UNIVERSITAT POLITÈCNICA
DE CATALUNYA
BARCELONATECH

Concepts, perspectives and implications of a hybrid system made of nucleic acids biopolymers and hydroxyapatite mineral

Pau Turon Dols

UNIVERSITAT POLITÈCNICA DE CATALUNYA
BARCELONATECH

PhD program in Polymers and Biopolymers

Concepts, perspectives and implications of a hybrid system made of nucleic acids biopolymers and hydroxyapatite mineral

Doctoral thesis by:
Pau Turon Dols

Thesis advisor:
Prof. Dr. Carlos Alemán

Chemical Engineering Department. Innovation in materials
Barcelona, September 2019

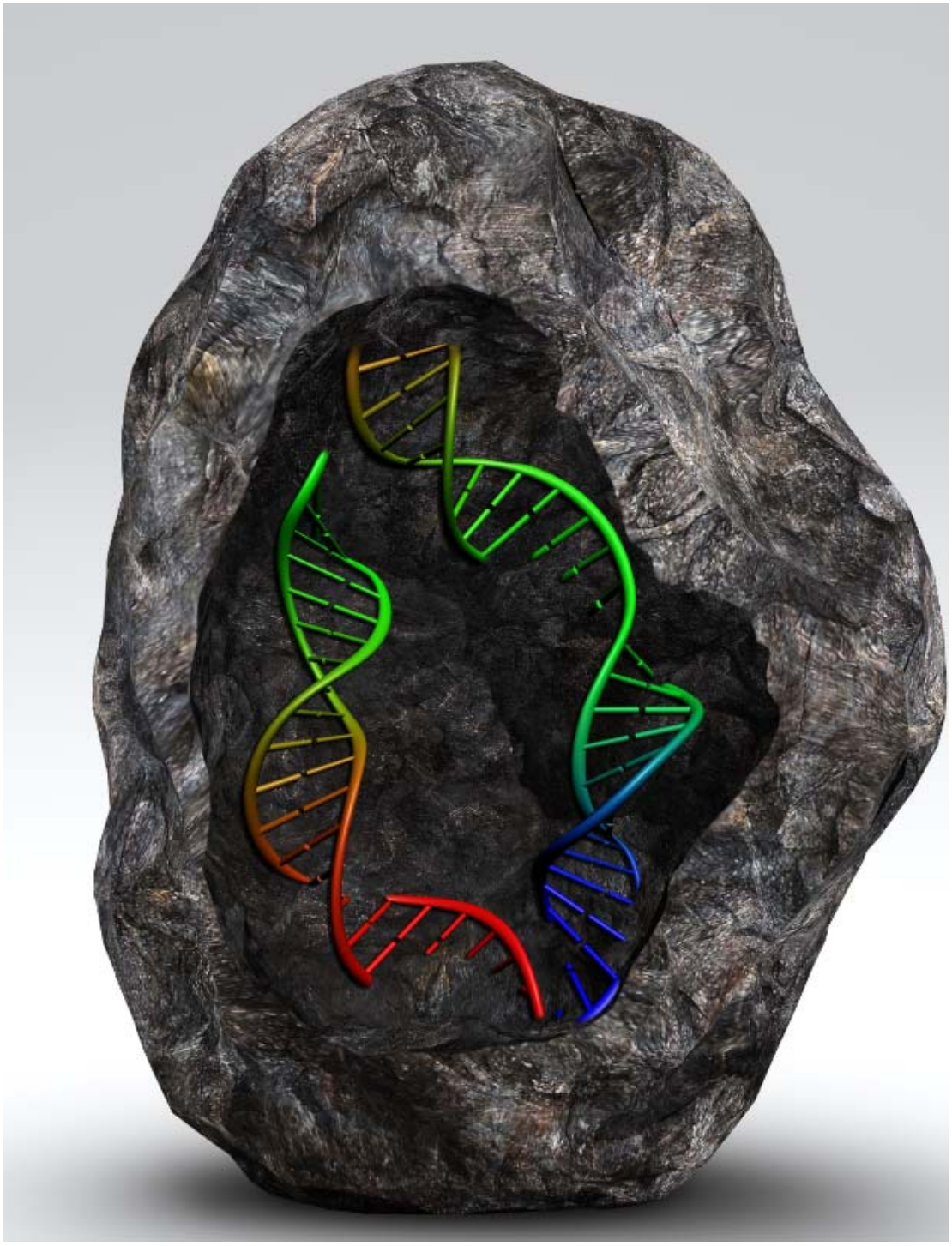

To my wife Elisabet and to my daughters Aina and Natàlia,

who always believed in my dream: "*El Projecte OLi*"

Foreword

Cancer research captured my interest since the first time I realized that a hydroxyolite, a hybrid system made of hydroxyapatite mineral and DNA, could be related to that disease. Every day, since I started the OLi Project, I remember my family and friends who I lost due to such disease (Txema A., M. M. Carmen S., Ángel C., Teresa F., Xavi G.). I made a commitment them to dedicate the rest of my life to making research about cancer and I will never give up. What I did not expect was that such research would end up in a thesis related to Chemistry, one of my long lasting dreams and life objectives. The thesis has been a long journey through the frontier of inorganic and organic worlds, working with non-viral vectors of transfection, synthesizing new catalysts for recycling CO_2, designing a prebiotic scenario and making hypotheses about how DNA survived in early Earth when undergoing events of mass extinction. After several years of work on the topic, I can confirm that no dream is achieved without a long term effort, and the least of the initial ideas consumes a huge amount of resources. However, long term objectives produce a long term satisfaction when accomplished. The main reward I aspire to is to enjoy the journey, sharing challenges with my travel companions, the ones who share the vision and continue walking towards the target despite the difficulties. Thanks for joining OLi Project.

Acknowledgements

I truly thank my Dissertation Advisor, Prof. Dr. Carlos Alemán, for being the one who believed that this thesis was possible. I owe him a myriad of hours discussing new concepts around OLi Project, analyzing amazing results and developing new hypotheses while struggling with daily business. I really appreciate his continued support to me and to the OLi Project.

I also take the opportunity to thank all Project team members and their institutions, Institut Recerca Germans Trias i Pujol (ICS), Institut Recerca Vall d'Hebron (ICS), Institut de Ciències Fotòniques (ICFO), Universitat Politècnica de Catalunya (UPC) and B. Braun Group, Aesculap division and CoE Closure Technologies in Rubí for supporting the Project.

I specially thank Dr. Joan Francesc Julián for his optimistic and passionate perspective of life, who decisively influenced the development of OLi Project and basic concepts of this thesis, and for leading an exceptional clinical team who I also thank for all their contributions, Dr. Jordi Navinés (since early days), Dr. Maite Fernández Figueres, Dr. Joan Ramon Grifols, Dr. Laia Roca, Dr. Ana Muñoz, Dr. Eva Castellà, Dr. Aurelio Ariza, Dr. Antonio Mariscal, Dr. Ignacio Blanco, Dr. Pedro Fernández, Dr. Maria Antònia Arbós, Dr. Maite Quiles, Dr. Francesc García Cuyàs, and Prof. Dr. Jaume Fernández-Llamazares.

I express my gratitude to Dr. Susana Santos, Dr. Silvia Carrasco, Dr. Johann Osmond, Dr. Soledad Royo, Dr. Lluis Torner for their support for the OLi project since the first day I shared it with ICFO. Thanks for introducing it to the ICFO's outstanding research groups, whose cooperation led by Prof. Dr. Romain Quidant and by Dr. Pablo Loza and their teams was really fruitful, Dr. Cuauhtemoc Araujo, Dr. Clara Vilches, Dr. Cesar Alonso, Dr. José García and particularly to Dr. Mónica Marro for finding hydroxyolites in breast cancer tissue and to Dr. Vanesa Sanz for identifying hydroxyolites in vitro cultured cells.

Moreover, I thank Mr. Rafael Moreno (Oficina Ponti) and Dr. Christoph Gerspacher (Ruff Wilhelm, Beier, Dauster & Partner), for their contribution to the development of the permanently polarized hydroxyapatite patent. I thank Dr. José Salas for his contribution to the design and performance of the reactor. I thank Mr. A. Lacasa and Mr. A. Rodríguez for designing the graphical abstract and some figures and Mr. P. Wakely for the English revision.

I acknowledge Prof. Dr. Jordi Puiggalí and his excellent team at UPC (Gustavo Chaves, Lluís Cardús, Dr. Maria Teresa Casas, Dr. Manolo Rivas and Dr. Luis Javier del Valle) for contributing to the experimental part of some papers related to this thesis and for achieving the synthesis of amino acids based on the polarized hydroxyapatite catalyst.

I credit Prof. Dr. Jordi Llorca for inoculating me with the scientific curiosity in the 1980s. I am glad that more than thirty years later we have found the way to cooperate in the OLi Project, thank you!.

I am grateful to Prof. Dr. Carlos Alemán's team, Dr. Guillem Revilla-López, Dr. Oscar Bertrán, Dr. Jordi Casanovas, Dr. Elaine Armelin and Mr. Jordi Sans (future PhD) for their several contributions in the simulation field and electric measurements and for making many of the project ideas feasible.

I am thankful to all DTS team in B. Braun for their unvaluable support, in particular to Dr. Luis Felipe del Castillo, Mr. Jordi Vadell, Ms. Cristina Manjón, Ms. Cristina Timoneda, Mr. Roberto Fernández, Ms. Margarita Nieto, Mr. Jaume Renau, Ms. Irene Prieto, Ms. Paula Abellán, Mr. Francisco Vargas and Dr. Christine Weis. Thanks again to Dr. Vanesa Sanz for joining B. Braun and contributing with her expertise in developing the catalysis process in our firm. Specifically, thanks to Ms. Anna M. Rodríguez-Rivero who is always ready to face a new professional challenge and decided to dedicate a significant part of her life to the OLi Project and focus her PhD on the implications of hydroxyolites in the clinical field.

Finally, to B. Braun Group (Rubí, Tuttlingen and Melsungen) for their financial and technical support to the Project. I thank Mr. Manuel Jiménez, Mr. Jesús Donado, Mr. Modesto Ibáñez, Mr. Antonio Jodar, Dr. Jens Von Lackum, Dr. Katrin Sternberg, Prof. Dr. Boris Hoffman, Mr. Tobias Köller, Dr. Hans-Peter Tümmler, Dr. Hans-Otto Maier, Dr. Meinrad Lugan, Dr. Joachim Shulz and Mr. Otto-Philipp Braun and his family for supporting the OLi Project in their firm.

Last but not least, thanks to my brothers, Samuel and Joan Marc, for their long lasting support and for contributing with new ideas to the project, and to my parents Joan and Margarida, for giving me the opportunity to be educated in Chemistry and contributing when I was a child to become who I am today. To the rest of the extended family, particularly to Alicia, Juan Sebastián, Ana, Carlos, Beatriz, Andrés, Débora, Ismael and Eunice, Joan Ramon, nephews and your respective families, particularly to my father and mother in law, Eunice and Sebastián, thank you all for unconditional support and for believing in me and the Project.

My last acknowledgement is for my little family. It is a privilege to have a family always supporting me in any project I face. There are no words to thank my wife Elisabet and my daughters, Aina and Natàlia, for being at my side all these years while developing the basics of OLi Project and this thesis. Aina, Natàlia, you have the strength to achieve whatever you want in your life, the intense and refreshing power of water, the power of wind to reach wherever you want, the power of fire to melt the most difficult challenges, the power of earth to remain solid in your values. This thesis is only an example that anything you wish needs effort and committing your life to it. Eli, my gratitude is infinite for being my partner all these years. Years ago, we shared this dream, without you it would never be possible, we have made it possible together. ... "There is no mountain too high, no river too wide, sing out this song and I'll be there by your side".

Rubí, August 25th 2019

Abstract

The origin of building blocks of life and how life thrived on Earth remains a topic of high interest for researchers of the Origin of Life. In this thesis, we deal with concepts, perspectives and implications of the system termed *hydroxyolite*, a combination of outstanding biopolymers (nucleic acids such as DNA and RNA) and an exceptional mineral (hydroxyapatite). First we study, based on Revilla et al. (2013) and Bertran et al. (2014), how hydroxyapatite forms crystals able to encapsulate DNA or RNA when nucleic acids are used as a nucleating template. Later, in Bertran et al., (2016), we reported the mechanism of how the encapsulated nucleic acid is released to the surroundings when environmental conditions change, for instance becoming more acidic. As a consequence, we postulated that DNA existing in cells can be encapsulated and protected by hydroxyapatite against environmental attacks (i.e. poisonous gases, gamma radiation or enzymatic degradation) until they change, making feasible the reintroduction of nucleic acids in the mainstream of life. We hypothesized about the implications of such a system in the early history of life when mass extinction events occurred on Earth (Turon et al., 2015). Moreover, we extended the *hydroxyolite* concept, borrowed from the materials chemistry, to other disciplines such as paleontology, biology, biotechnology and medicine by considering hydroxyolites as equivalents to non-viral vectors that can introduce and release DNA into a cell (transfection). Such nucleic acid triggers the expression of foreign proteins if released in the cytosol or might be recombined with cell genome when DNA is released in the target cell nucleus.

In the second part of the thesis, we studied the hydroxyolite system from a complementary perspective. We speculate about the consequences of being hydroxyapatite the first actor and not the nucleic acid. We propose that hydroxyapatite might act as an inorganic mold if considered as a catalytic substrate that facilitates the synthesis of simple organic molecules as the building blocks of life. Thus, we identified a prebiotic scenario, a volcanic eruption under lightning, where a phenomenon known as dirty storm usually occurs under certain conditions. Hydroxyapatite is known in nature to be part of igneous rocks and volcanic ash in small but significant concentrations. We replicated in the laboratory such extreme conditions by developing a thermally and electrically stimulated polarization. A process performed at 1000 ºC and under a difference of potential of 300 $kV \cdot m^{-1}$, to obtain permanently polarized hydroxyapatite (Turon et al., 2016; PCT/EP2017/069437) that turned out to be an enhanced

catalyst compared to hydroxyapatite able to fix nitrogen and carbon from a gas mixture of N_2, CO_2 and CH_4 (Rivas et al., 2018). The catalyst, under UV light, converts them into amino acids (Glycine and D/L-Alanine) and small organic molecules by means of a new inorganic photosynthetic process. In this work, we develop an integrative prebiotic model that describes how simple molecules might be synthesized from mildly reducing atmospheres by combining previous models such as volcanos as giant reactors, minerals as catalysts and photochemical reactions in the atmosphere under prebiotic sun light. All of them under the framework of a prebiotic inorganic photosynthesis, a process that might be considered the corner stone of the rise of the building blocks of life.

Resum

L'origen de les molècules que van donar lloc a la vida i com la vida va prosperar a la Terra segueix essent un tema del màxim interès pels investigadors de l'origen de la vida. En aquesta tesi, discutim conceptes, perspectives de futur i implicacions del sistema que hem anomenat *hidroxiolita (hydroxyolite)*, una combinació de biopolímers amb característiques molt especials (àcids nucleics com l'ADN i l'ARN) i un mineral excepcional (hidroxiapatita). En primer lloc, en els treballs Revilla et al., (2013) i Bertran et al., (2014) estudiem com els cristalls d'hidroxiapatita tenen la capacitat d'encapsular ADN o ARN quan l'àcid nucleic es comporta com agent nucleant. Tot seguit, reportem com l'àcid nucleic prèviament encapsulat pot ser alliberat si les condicions ambientals canvien, per exemple tornant-se lleugerament més àcides (Bertran et al., 2016). Com a conseqüència, postulem que l'ADN existent a les cèl·lules pot ser encapsulat per la hidroxiapatita protegint-lo contra atacs de l'entorn (per exemple, la influència de gasos tòxics, la radiació gamma o la degradació enzimàtica) fins que les condicions externes canvien i els àcids nucleics poder ser reintroduïts en el torrent principal de la vida. A continuació, discutim les implicacions d'aquest sistema híbrid a la història primitiva de la vida a la Terra, quan van ocórrer les grans catàstrofes que van donar lloc a extincions massives d'éssers vius (Turon et al., 2015). Tanmateix, estenem el concepte d'hidroxiolita, encunyat a la ciència de materials, a altres disciplines com la paleontologia, la biologia cel·lular, la biotecnologia i la medicina, considerant les hidroxiolites com a vectors no virals que poden introduir i alliberar ADN dins una cèl·lula (transfecció). Aquest àcid nucleic, si s'allibera en el citosol pot desencadenar l'expressió de proteïnes codificades en l'ADN introduït, o si s'allibera en el nucli podria recombinar-se amb el propi ADN de la cèl·lula diana de manera transitòria o permanent.

A la segona part de la tesi, estudiem el sistema hidroxiolita des d'una perspectiva complementària. Especulem sobre les conseqüències de ser la hidroxiapatita l'actor principal del sistema i no l'àcid nucleic. Proposem que la hidroxiapatita pot actuar com un motlle inorgànic si es comporta com a substrat catalític que facilita la síntesi de molècules orgàniques, com les molècules que van donar lloc a la vida. A partir d'aquest concepte hem identificat un escenari prebiòtic, una erupció volcànica acompanyada de descàrregues elèctriques, fenomen que succeeix amb certa freqüència en funció de les característiques de l'erupció. La

hidroxiapatita a la natura és coneguda per formar part de la composició de roques ígnies i de la cendra volcànica en petites però significatives quantitats. Al laboratori hem replicat aquestes condicions extremes i hem desenvolupat un procés de polarització mitjançant estimulació elèctrica i tèrmica, aplicant 1000 ºC i una diferència de potencial de 300 $kV \cdot m^{-1}$, que dóna com a resultat hidroxiapatita polaritzada permanentment (Turon et al, 2016; PCT/EP2017/069437) que converteix el mineral en un catalitzador extraordinari comparat amb la hidroxiapatita i que té la capacitat de fixar nitrogen i carboni a partir d'una mescla de gasos composada per N_2, CO_2 i CH_4 (Rivas et al., 2018) en presència d'aigua.

El catalitzador, sota il·luminació de llum UV facilita la conversió d'aquests gasos en aminoàcids (Glicina i D/L-Alanina) i en molècules orgàniques simples a través d'un procés fotosintètic inorgànic. En aquest treball, desenvolupem un model prebiòtic que descriu com molècules senzilles van poder ser sintetitzades a partir d'atmosferes suaument reductores combinant models prebiòtics previs (volcans que es comporten com grans reactors, reaccions fotoquímiques que succeeixen a l'atmosfera sota el sol prebiòtic i minerals que actuen com a catalitzadors) sota el marc de la fotosíntesi inorgànica prebiòtica, un procés que podria ser considerat la pedra angular de l'aparició de les molècules que van donar lloc a la vida.

Resumen

El origen de las moléculas que dieron lugar a la vida y como la vida prosperó en la Tierra sigue siendo un tema del máximo interés para los investigadores del Origen de la Vida. En esta tesis discutimos conceptos, perspectivas de futuro e implicaciones del sistema que hemos denominado *hidroxiolita* (*hydroxyolite*), una combinación de biopolímeros con características muy especiales (ácidos nucleicos tales como el ADN y el ARN) y un mineral excepcional (hidroxiapatita). En primer lugar, en nuestros trabajos Revilla et al. (2013) y Bertran et al. (2014) estudiamos como los cristales de hidroxiapatita tienen la capacidad de encapsular ADN o ARN cuando el ácido nucleico se comporta como un agente nucleante. A continuación, reportamos como el ácido nucleico previamente encapsulado puede ser liberado cuando las condiciones ambientales cambian, por ejemplo, cuando se vuelven ligeramente más ácidas (Bertran et al., 2016). A consecuencia, postulamos que el ADN existente en las células puede ser encapsulado por la hidroxiapatita protegiéndolo contra ataques del entorno (por ejemplo, la influencia de gases tóxicos, la radiación gamma o la degradación enzimática) hasta que cambian las condiciones externas y los ácidos nucleicos pueden ser reintroducidos de nuevo en el torrente principal de la vida. A continuación discutimos las implicaciones de este sistema híbrido en la historia primitiva de la vida en la Tierra, cuando ocurrieron las grandes catástrofes que dieron lugar a extinciones masivas de seres vivos (Turon et al., 2015). Asimismo, extendemos el concepto hidroxiolita, acuñado en la ciencia de materiales, a otras disciplinas como la paleontología, la biologia celular, la biotecnología y la medicina, considerando las hidroxiolitas como vectores no virales que pueden introducir y liberar ADN dentro de una célula (transfección). Este ácido nucleico, si es liberado en el citosol puede desencadenar la expresión de proteinas codificades en el ADN introducido, o si se libera en el núcleo podría recombinarse con el propio ADN de la célula diana de forma transitoria o permanente.

En la segunda parte de la tesis, estudiamos el sistema hidroxiolita desde una perspectiva complementaria. Especulamos sobre las consecuencias de ser la hidroxiolita el actor principal y no el ácido nucleico. Proponemos que la hidroxiolita puede actuar como un molde inorgánico si se comporta como un sustrato catalítico que facilita la síntesis de moléculas orgánicas, como las moléculas que dieron lugar a la vida. Hemos identificado un escenario

prebiótico basado en una erupción volcánica con descargas eléctricas, fenómeno que ocurre con cierta frecuencia en función de las características de la erupción. La hidroxiapatita es conocida en la naturaleza por formar parte de la composición de rocas ígneas y ceniza volcánica en bajas pero significativas concentraciones. Hemos replicado en el laboratorio estas condiciones extremas y hemos desarrollado un proceso de polarización mediante estimulación térmica y eléctrica, aplicando 1000 ºC y una diferencia de potencial de 300 $kV \cdot m^{-1}$, que da como resultado hidroxiapatita permanentemente polarizada (Turon et al, 2016; PCT/EP2017/069437). Este proceso convierte el mineral en un catalizador extraordinario comparado con la hidroxiapatita y tiene la capacidad de fijar nitrógeno y carbono a partir de una mezcla de gases compuesta por N_2, CO_2 y CH_4 (Rivas et al., 2018) en presencia de agua. El catalizador, bajo iluminación de luz UV, facilita la conversión de estos gases en aminoácidos (Glicina y D/L-Alanina) y en ácidos orgánicos simples a través de un proceso de fotosíntesis inorgánica. En este trabajo desarrollamos un modelo prebiótico que describe como moléculas sencillas pudieron ser sintetizadas a partir de atmósferas suavemente reductoras combinando modelos prebióticos ya existentes (volcanes que se comportan grandes reactores, reacciones fotoquímicas que ocurren en la atmosfera bajo el sol prebiótico y minerales que actuan como catalizadores) bajo el marco de una fotosíntesis prebiótica inorgánica, un proceso que podría ser considerado la piedra angular en la que se basó la aparición de las moléculas que dieron lugar a la vida.

Contents

Scientific Publications

The results of this thesis have been reported through the following publications:

1. Revilla-López, G., Casanovas J., Bertran O, **Turon P.***, Puiggalí J., Alemán C.,* Modeling biominerals formed by apatites and DNA, *Biointerphases* (**2013**), *8*, 10,1-15. DOI:10.1186/1559-4106-8-10, Marked as "Highly accessed"

2. Bertran, O., del Valle L.J., Revilla-López G., Chaves G., Cardús L., Casas M.T., Casanovas J., **Turon P***, Puiggalí J.*, Alemán C*., Mineralization of DNA into nanoparticles of hydroxyapatite, *Dalton Transactions* (**2014**), *43*, 317-327. DOI:10.1039/c3dt52112e.

3. Casanovas J., Revilla-López G., Bertrán O., del Valle L.J., **Turon P***, Puiggalí J., Alemán C*., Restricted puckering of mineralized RNA-like riboses, *Journal of Physical Chemistry B,* (**2014**), *118*, 19, 5075–5081. DOI:10.1021/jp501714q.

4. Bertran, O, Revilla-López, G., Casanovas, J., del Valle, L., **Turon, P***, Puiggalí, J*, Alemán, C*, Dissolving Hydroxyolite: A DNA Molecule into Its Hydroxyapatite Mold, *Chemistry-A European Journal* (**2016**), *22*, 6631–6636. DOI: 10.1002/chem.201600703.

5. **Turon P***, Puiggalí J., Bertrán O, Alemán C.*, Surviving Mass Extinctions through Biomineralized DNA, *Chemistry - A European Journal* (**2015**), *21*, 18892 – 18898. **Concept article.** DOI:10.1002/chem.201503030.

6. Rivas M., del Valle L.J., Armelin E., Bertran O, **Turon P.***, Puiggali J.*, Alemán C.*, Hydroxyapatite with Permanent Electrical Polarization: Preparation, Characterization and Response Against Inorganic Adsorbates, *ChemPhysChem* (**2018**), *19*, 1–11. DOI: 10.1002/cphc.201800196.

7. Rivas, M., L.J. del Valle, **Turon P***, Alemán C.*, Puiggalí J*, Sustainable synthesis of amino acids by catalytic fixation of molecular dinitrogen and carbon dioxide, *Green Chemistry* (**2018**), *20*, 685-693. DOI: 10.1039/c7gc02911j.

8. **Turon P.***, Alemán C.*, Inorganic Photosynthesis in Early Earth, an Integrative Prebiotic Model, (submitted).

Patents

The following patent has been generated as a result of the work performed in the thesis:

Turon, P., del Valle L.J., Puiggalí J., Alemán C., Permanently Polarized Hydroxyapatite, a process for its manufacture and uses thereof, PCT/EP2017/069437.

List of Figures

Chapter 1. Introduction to hydroxyolite system

Chapter 3. Nucleic acids in a hydroxyapatite crystal

Chapter 4. Surviving Mass Extinctions through Biomineralized DNA

List of Tables

Nomenclature

Abbreviation	Description
A	Adenine
AA	Amino acid
ACP	Amorphous calcium phosphate
Ala	Alanine
ALP	Alkaline phosphatase
Ann	Annex
ATMP	Aminotris(methylenephosphonic acid)
ATP	Adenosine triphosphate
C	Cytosine
CaP	Calcium phosphate
CDHAp	Calcium-deficient hydroxyapatite
CPP	Calcium pyrophosphate
CTAB	Cetyl Trimethyl Ammonium Bromide
DC	Direct current
DCPA	Dicalcium phosphate anhydrous
DCPD	Dicalcium phosphate dehydrate
DNA	Deoxyribonucleic acid
DNAse	Endonuclease that cleaves DNA
ds-DNA	Double stranded DNA
E. coli	*Escherichia coli*
EDTA	Ethylenediaminetetraacetic acid
ER	Endoplasmic reticulum
FAp	Flouroapatite
FTIR	Fourier-transform infrared spectroscopy
G	Guanine
Gly	Glycine
GTP	Guanosine triphosphate
HAp	Hydroxyapatite
HAp/ap	As prepared hydroxyapatite
HAp/s	Sintered hydroxyapatite
HAp/tsp	Polarized hydroxyapatite, thermally and electrically stimulated
HAp–DNA	Hydroxyolite containing DNA
HOLi	Hydroxyolite
HPLC	High-performance liquid chromatography
MCPA	Monocalcium phosphate anhydrous
MCPM	Monocalcium phosphate monohydrate
MD	Molecular Dynamics

Abbreviation	Description
MW	Microwave
NMR	Nuclear Magnetic Resonance
OAp	Oxyapatite
OCP	Octacalcium phosphate
P	Phosphorus
pH	Acidity or alkalinity of a solution on a logarithmic scale
p*Ksp*	Degree to which a compound dissociates in water on logarithmic scale
r	Radial distance
RMSD	Root-mean-square deviation
RNA	Ribonucleic acid
ROS	Reacting oxygen substances
ss-DNA	Single stranded DNA
T	Thymine
TCP	Tricalcium phosphate
TEM	Transmission Electron Microscopy
TSP	Thermally and electrically stimulated polarization process
TTCP	Tetracalcium phosphate
U	Uracil
UCA	Universal Common Ancestor
UK	United Kingdom
UV-vis	Ultraviolet visible radiation
ZC	Zirconyl chloride
γ	Gamma irradiation
λ	Wavelength

Chemical substance	**Description**
$(Ca,Mg)_3(PO_4)_2$	Whitlockite
$(NH_4)_2HPO_4$	Ammonium hydrogen phosphate
$(NH_4)H_2PO_4$	Ammonium dihydrogen phosphate
$^{\bullet}CH_3$	Methyl radical
Cl^-	Chloride ion
Ca^{2+}	Calcium ion
$CaCO_3$	Calcium carbonate
$CaHPO_4$	Calcium hydrogen phosphate
$CaHPO_4 \cdot 2H_2O$	Calcium hydrogen phosphate dihydrate
$Ca(H_2PO_4)_2$	Calcium dihydrogen phosphate
$Ca(H_2PO_4)_2 \cdot H_2O$	Calcium dihydrogen phosphate monohydrate
$Ca(NO_3)_2$	Calcium nitrate
$Ca_2P_2O_7$	Calcium pyrophosphate
$Ca_2P_2O_7 \cdot nH2O$	Calcium pyrophosphate hydrate
$Ca_3(PO_4)_2$	Tricalcium phosphate
$Ca_3(PO_4)_2 \cdot nH_2O$	Amorphous calcium phosphate
$Ca_4(PO_4)_2O$	Tetracalcium phosphate
$Ca_8 H_2(PO_4)_6 \cdot 5H_2O$	Octacalcium phosphate
$Ca_{10}(PO_4)_6(F)_2$	Fluorapatite
$Ca_{10}(PO_4)_6O$	Oxyapatite
$Ca_{10}(PO_4)_6(OH)_2$	Hydroxyapatite
$Ca_{10-x}(HPO_4)_x(PO_4)_{6-x}(OH)_{2-x}$ $(0 < x < 1)$	Calcium deficient hydroxyapatite
CaO	Calcium oxide
CH_2O	Formaldehyde
CH_4	Methane
CN^-	Cyanide ion
CO_2	Carbon dioxide
CO_3^{2-}	Carbonate ion
F^-	Fluoride ion
Fe^{2+}	Iron (II) ion
H_2O	Water
HPO_4^{2-}	Hydrogen phosphate ion
$H_2PO_4^-$	Dihydrogen phosphate ion
H_2S	Hydrogen sulphide
H_3O^+	Hydronium ion
HCl	Hydrogen chloride
HCN	Hydrogen cyanide

Chemical substance	**Description**
Mg^{2+}	Magnesium ion
N_2	Nitrogen gas
NaCl	Sodium chloride
NH_3	Ammonia
O_2^-	Superoxide ion
$^{\bullet}O_2^-$	Superoxide radical
OH^-	Hydroxyl ion
$^{\bullet}OH$	Hydroxyl radical
$P_2O_7^{4-}$	Pyrophosphate ion
$P_3O_{10}^{5-}$	Triphosphate ion
PO_4^{3-}	Phosphate ion
$ZrOCl_2$	Zirconyl chloride

Units	**Description**
bar	Bar
C	Coulomb
g	Gram
Gy	Gray
h	Hour
m	Meter
M	Mol
ºC	Celsius degree
ppm	Parts per million
s	Second
t	Ton
V	Volt
yr	Year
Å	Angstrom
Ω	Ohm

Chapter 1

Introduction to hydroxyolite hybrid system

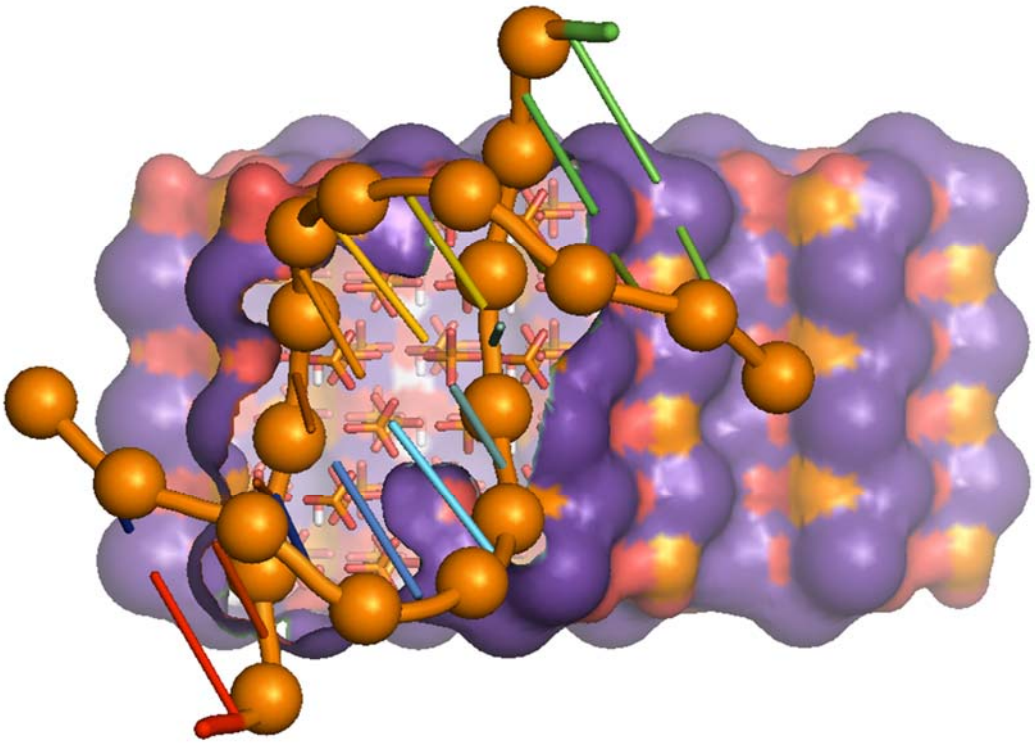

Chapter 1
Introduction to hydroxyolite hybrid system

1.1. Introduction

This thesis starts its course from a singular crossroad defined by one of the most interesting hybrid systems that binds organic and inorganic worlds together. Through this thesis we focus on the origin, theoretical implications and perspectives of a system built by the outmost biopolymer family related to life on Earth, the nucleic acids, and a highly polyvalent mineral, the most stable form of calcium phosphate, hydroxyapatite [$Ca_{10}(PO_4)_6(OH)_2$]. Such a hybrid system was termed by our group as *Hydroxyolite*,[1] a new brand name invented to define the adsorption and/or encapsulation of nucleic acids into hydroxyapatite, a name that recalls how ***hydroxy-****apati-****te*** is able to put the essence of life ("***-oli-***" meaning "Origin of Life") in a nutshell, making feasible the concept *hydroxy-oli-te*.

In this work, we use a multidisciplinary approach to study the hydroxyolite system, acknowledging its duality as a strategy to scrutinize the interaction between the organic biopolymers (i.e. deoxyribonucleic acid, henceforth DNA and ribonucleic acid, henceforth RNA) adsorbed or encapsulated by an exceptional inorganic mineral that is able to include in its lattice multiple ions without losing its structure, adsorb a long list of organic molecules on its surface and facilitate multiple heterogeneous catalytic processes.

We deal with the frontier of two well-defined areas of knowledge, inorganic and organic edges of Chemistry, merged together under the framework of materials chemistry to yield new concepts, models, hypotheses, materials and processes: i) a new catalyst that enables an inorganic photosynthetic process that converts gases into simple organic molecules; ii) a prebiotic model; iii) a hypothesis about how DNA survived mass extinctions events through the history of life on Earth protected by hydroxyapatite; and iv) we increase the knowledge and understanding of concepts such as nucleic acid mineralization and aim to extend such basics to other disciplines as Biotechnology (i.e. gene therapy, as hydroxyolite is known to be a non-viral vector of transfection) and Medicine (hydroxyapatite calcifications containing nucleic acids are recently described as appearing in breast cancer calcifications).

When performing the research, we analyzed from the perspective of each of the two components the interrelations between them. We discovered different viewpoints that made it possible to extract conclusions and then, create new concepts, hypothesis and models. For that reason, we have organized the thesis taking first the nucleic acid as a starting point, as a template of the hydroxyolite system (Chapters 3 and 4). Furthermore, in the second half of the thesis, we consider that hydroxyapatite is the substrate that triggers the system (Chapter 5).

1.2. Nucleic acids

We focus on a specific type of biopolymers, nucleic acids, being DNA and RNA two of the crucial molecules of living organisms. Nucleic acids are unique molecules that handle storage, transmission, processing, and regulation of genetic information and might act as catalysts and mechanochemical switches.[2] DNA and RNA differ in their building blocks. First, the sugar, as 2′-deoxyribose participates in DNA and 2′-ribose in RNA, and second, the nucleotides in DNA are built with four heterocyclic bases: adenine (A) and guanine (G) (purines) and cytosine (C) and thymine (T) (pyrimidines) but in RNA thymine is substituted by uracil (U), the other three are common in both biopolymers.[3]

The complete set of DNA of an organism, the genome, includes all genes (> 3 billion DNA base pairs in human cells) contained by each cell of the organism with nucleus. DNA encodes hereditary information that is transferred to the next generation, controlling how cells grow and replicate. The main characteristic of DNA is the entwining of two strands that are complementary in their nucleotide sequence, adenine pairs thymine and cytosine pairs guanine, to form a right-handed chiral double helix with a pitch of 3.4-3.6 nm, a diameter of 2 nm and usually packed around 50 nm length that can be extended to a linear length up to 10^8–10^9 nm.[4,5] DNA may adopt mainly two right-handed double-helical structures (i.e. A-DNA and B-DNA) but also a left-handed Z-DNA (Figure 1.1.) and other forms, such as triple and quadruple helices, junction (cruciform) structures and parallel helices,[6] but RNA, due to steric restrictions created by the 2'hydroxyl in ribose only adopts A-RNA.[7] Therefore, the functions of DNA can be explained by two features: a reservoir of information that encodes the sequences of proteins and RNA molecules (both specified in the base sequence) and a polymer allowing the replication, access and packaging of the previous information.

Through the process of gene transcription, DNA encodes RNA that eventually is translated to specify the proteins of a cell.[8]

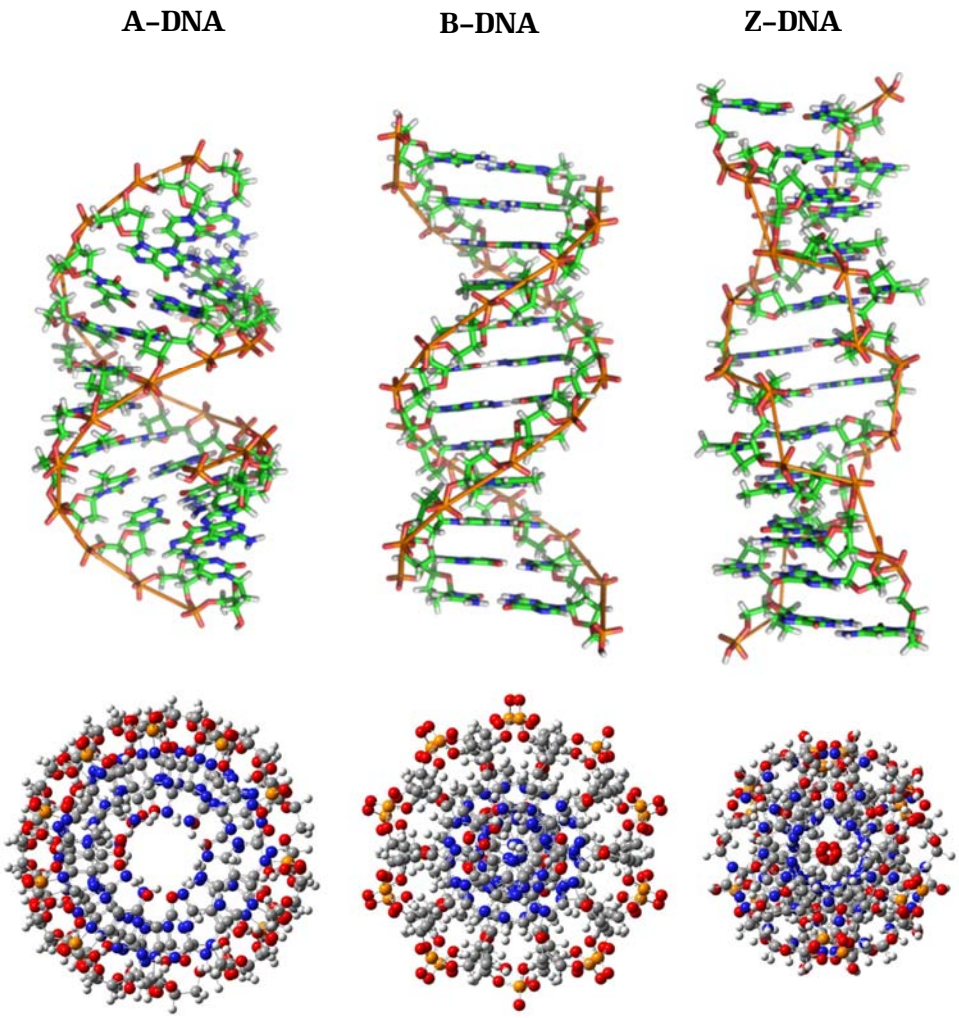

Figure 1.1. DNA in its A- B- and Z- form. Axial and equatorial views.

Despite their similarities, RNA is more labile than DNA. The RNA helix shows a pitch of 2.9 nm and a diameter of 2.6 nm, developing three-dimensional structures with an average size of 5 nm.[9] RNA easily folds in tertiary structures with capacity of recognition and retains some catalytic properties, not so different from those of proteins some of which make authors link them with the origin of life through a RNA world.[10] RNA is able to use energy from adenosine triphosphate (ATP) or guanosine triphosphate (GTP) in order to perform several

major tasks such as gene regulation, facilitating the protein synthesis and information processing.

The major stabilizing forces which contribute to the structural integrity of ds-DNA and ds-RNA are non-covalent interactions between their aromatic nucleobases.[11] Its C2-symmetrical structure with complementary hydrogen-bonded base pairs provides an effective means to store genetic information and transfer of the encoded messages.[12] The role of hydrogen bonds in stabilization of the helix and selective base-pair formation is still unclear despite the fact it has been generally accepted that the hydrogen bonds between the bases are critical to the stability of DNA. A Watson and Crick pair has two or three hydrogen bonds that contribute, depending on the molecular context, approximately with 0.5-1.8 $kcal \cdot mol^{-1}$ of stabilization per base pair of DNA. Such low values are increased in gas phase to 6 - 7 $kcal \cdot mol^{-1}$ where competition with water hydrogen bonds does not exist.[13,14]

The base stacking in explaining DNA function has received less attention than hydrogen bonds in the base pairs but, in B-DNA, neighboring pairs overlap one π system with the other (Figure 1.2.), making contact up to 115 $Å^2$. Thus, when forming a double helix from a random coil involves removing ~ 230 $Å^2$ of base π -surface area from the solvent per pair. The specific forces that contribute to stabilizing this stacking (i.e. electrostatic effects, induced dipole attractions and solvophobic effects) have been extensively studied, even though they are not completely understood despite the fact that significant advances and knowledge have been provided.[15-18]

Hydrogen bonds play an important role in specificity of biomolecular recognition. Energy studies forcing mismatches in the pairs A-T or C-G demonstrated that the energetic penalty is significant (i.e. T-C destabilizes within 3.2 - 5.8 $kcal \cdot mol^{-1}$ compared to the pair T-A. The effect of one hydrogen bond disrupted as occurs in T-C pair generates a destabilization that probably goes beyond the pair alone, distorting the polyphosphate backbone along the helix due to the different geometry that the pair should adopt due to the mismatch. Furthermore, the enzymatic replication of DNA is a critical process affected by hydrogen bonding and stacking stabilization. Such a process occurs with high efficiency and fidelity, quickly assembling within 20-1000 $nucleotides \cdot s^{-1}$, most of them without failures, the ratio of error being about one per 10^3 - 10^5 nucleotide insertions. Thus, both the stacking stabilization and hydrogen bonding stabilization are factors to be taken into consideration when discussing

the accuracy of the replication process, however such an effect was underestimated for years.[12]

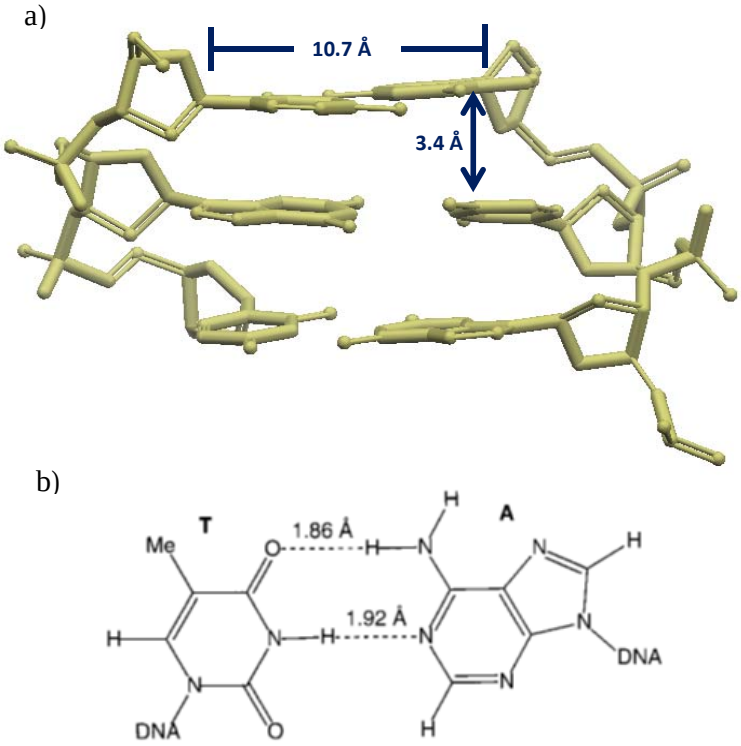

Figure 1.2. (a) Model of a three base-pair B-form DNA duplex with distances between strands and bases. (b) Watson and Crick A-T base pair. Adapted from ref. [12] with permission from John Wiley and Sons.

On the other hand, DNA may have the role of a scaffold for the structural support of multiprotein complexes in the cell. Despite DNA being rather rigid, proteins can use their binding energy to bend, wind or unwind it. Therefore, researchers develop strategies to use such structural properties to build artificial matrices for different uses in materials science and biomedical applications.[3,19]

Finally, it is worth mentioning that mammals' DNA contains two layers of information for generating the infrastructure required to shape an organism. The first layer is DNA itself, as we have been discussing in the previous paragraphs, the sequence of nucleotides. The second is more sophisticated and corresponds to the methylation of DNA. Such chemical modification along the DNA strand has been equated to a set of instructions about how to read the text already printed in the DNA sequence and how to control the transcription.

Therefore, DNA methylation is an epigenetic process. DNA is inherited from the parents, nevertheless a new methylation profile is established in each individual as the previous methylation pattern in the gametes is erased before implantation of the embryo.[20] After birth, programmed variation in genome methylation happens in response to environmental influences, recording such impacts in the genetic code that could significantly affect the individuals in their predisposition to some diseases (i.e. metabolic, autoimmune, and neurological). Additionally, DNA methylation can be advantageous as a diagnostic tool in order to detect cell death and allow the monitoring of some diseases by cell-free circulating-DNA blood test. Currently, this individualized methylation pattern is a hot topic in medicine as it can be correlated with ageing and cancer as well.[21]

1.3. Hydroxyapatite

Hydroxyapatite (HAp), $Ca_{10}(PO_4)_6(OH)_2$), is the most stable form of calcium phosphate. The name apatite was given by A. G. Werner in 1786 using the Greek word "απαταο" meaning "to deceive" or "to mislead" due to its unspecific aspect and similarities to other minerals.[22] Geological apatite, which is the most abundant phosphorus bearing mineral on Earth, can be found in igneous, sedimentary and metamorphic rocks and has various proportions of OH^-, F^-, and Cl^- forming the apatite group under the general formula of $Ca_5(PO_4)_3(F,OH,Cl)$. However, HAp is the one capturing the greatest interest and relevance in biological and materials sciences.[23] The mineral naturally formed in nature is usually known as hydroxylapatite instead of hydroxyapatite, its chemical name.

Calcium phosphate might adopt different phases that have in common the presence of calcium cations (Ca^{2+}) and anions containing phosphate as orthophosphate (PO_4^{3-}), metaphosphate (PO_3^-), or pyrophosphate ($P_2O_7^{4-}$) and their hydrogenated or hydroxylated forms. Furthermore, their crystal structure and properties are significantly different (i.e. space group, pK_{sp}, solubility, pH stability range and density as shown in Tables 1.1 and 1.2.).

In the following paragraphs we briefly highlight brushite, tricalcium phosphate, calcium phosphate amorphous and pyrophosphate among them as HAp will be discussed later. Brushite is the calcium phosphate compound easiest to be synthesized. It can be converted into monetite, its dehydrated form at pH < 6 or just heating brushite above 80 ºC; or into octacalcium phosphate at pH ≈ 6–7, or to HAp at pH above 7. Although brushite is biocompatible,[24] biodegradable, and osteoconductive, may form as an intermediary phase in

pathological calcifications occurring in slightly acidic media (for example, in dental calculi, urinary calculi, and urinary stones).[24] Brushite usually undergoes internal restructuration processes to yield HAp in biological environments.[25] β-Tricalcium phosphate has stoichiometric composition $Ca_3(PO_4)_2$ and can only be prepared by calcination (> 800 ºC) and not by precipitation. It transforms in α-tricalcium phosphate above 1125 ºC. Pure β-tricalcium phosphate never occurs in biological calcifications, only when containing magnesium (whitlockite; $(Ca,Mg)_3(PO_4)_2$) is found in dental, calculi urinary and salivary stones or some soft-tissue deposits. It is used as a bone cement or bone replacement in combination with HAp.[26]

Table 1.1. Main calcium phosphate phases, along with their chemical formulas, crystal systems, space group symmetries, solubility product values (pK_{sp}) and solubility at 25 ºC and pH 7.4. Adapted from ref. [22,27] with permission Royal Society of Chemistry and John Wiley and Sons.

Phase	Chemical formula	Space group	p*Ksp* *25ºC/37 ºC*	Solubility ($mg \cdot dm^{-3}$)
MCPA[a]	$Ca(H_2PO_4)_2$	Triclinic *P*1	1.14/n.d.	17 x 10^3
MCPM[a]	$Ca(H_2PO_4)_2 \cdot H_2O$	Triclinic *P*1	1.14/n.d.	18 x 10^3
DCPD[a]	$CaHPO_4 \cdot 2H_2O$	Monoclinic I_a	6.59/6.63	88
DCPA[a]	$CaHPO_4$	Triclinic *P*1	6.90/7.02	48
β-CPP[a]	$Ca_2P_2O_7$	Tetragonal $P4_1$	18.5/n.d.	7.6
ACP[a]	$Ca_3(PO_4)_2 \cdot nH_2O$	-	25/n.d.	0.8
α-TCP[a]	$Ca_3(PO_4)_2$	Monoclinic $P2_1/a$	25.5/25.5	2.5
β-TCP[a]	$Ca_3(PO_4)_2$	Rhombohedral *R3cH*	28.9/29.5	0.5
TTCP[a]	$Ca_4(PO_4)_2O$	Monoclinic $P2_1$	38-42/37-42	0.7
OAp[a]	$Ca_{10}(PO_4)_6O$	Hexagonal $P6_3/m$	69/n.d.	8.7
CDHAp[a]	$Ca_{10-x}(HPO_4)_x(PO_4)_{6-x}(OH)_{2-x}$ $(0 < x < 1)$	Hexagonal $P6_3/m$	≈85.1/85.1	9.4
OCP[a]	$Ca_8H_2(PO_4)_6 \cdot 5H_2O$	Triclinic *P*1	96,6/95.9	8.1
HAp[a]	$Ca_{10}(PO_4)_6(OH)_2$	Hexagonal $P6_3/m$	116.8/117.2	0.3
FAp[a]	$Ca_{10}(PO_4)_6(F)_2$	Hexagonal $P6_3/m$	120/n.d.	0.2

[a] MCPA = monocalcium phosphate anhydrous; MCPM = monocalcium phosphate monohydrate; DCPD = dicalcium phosphate dihydrate, a.k.a. brushite; DCPA = dicalcium phosphate anhydrous, a.k.a. monetite; CPP = calcium pyrophosphate; ACP = amorphous calcium phosphate (data pertain to the phase obtainable at pH 9–11); TCP = tricalcium phosphate; TTCP = tetracalcium phosphate; OAp = oxyapatite; CDHAp = calcium-deficient hydroxyapatite; OCP = octacalcium phosphate; HAp = hydroxyapatite; FAp fluoroapatite.

Amorphous calcium phosphate (ACP) is the first phase that precipitates from supersaturated solutions containing calcium cations and phosphate anions. Ca^{2+} and PO_4^{3-} and H_3O^+ ion concentrations in the mother liquor regulate the chemical composition of ACP. It is often found as a transient phase during the formation of calcium phosphates in aqueous systems. The compounds are amorphous, according to X-ray diffraction experiments but electron microscopy reveals spherical particles (20-200 nm). ACP calcifications containing

some ions such as Mg^{2+}, CO_3^{2-} and $P_2O_7^{4-}$ are also found in soft-tissue pathological calcifications (e.g. heart-valve calcifications of uremic patients). ACP might nucleate the crystallization of HAp. ACP is often used in calcium phosphate cements. ACP and cHAp interact with different phosphates and biophosphonates (BPs), which is a very relevant topic in the field of biomaterials for biomedical applications. Thus, polyphosphate, which is an orthophosphate polymer found in mammalian organisms, promotes mineralization and bone regeneration when adsorbed onto HAp by stabilizing basic cell growth and differentiation. On the other hand, the oxygen atom that links the phosphate groups of pyrophosphates is replaced by a carbon atom in BPs, which results in the inhibition of both hydrolytic and enzymatic degradations. The affinity of BPs towards HAp has been associated with the formation of strong interactions between the two species. Indeed, BPs are primary agents in the current pharmacological arsenal against different bone diseases (e. g. osteoporosis, Paget disease of bone and metastatic bone malignancies).[28-30]

Table 1.2. Selected calcium phosphate phases of interest for biomedical applications. Reproduced from ref [33] with permission from MDPI.

Ca/P Molar Ratio	Name	Formula	pH Stability Range	Density (g/cm^3)
0.5	MCPM (monobasic calcium phosphate monohydrate	$Ca(H_2PO_4)\cdot H_2O$	0.0-2.0	2.22
1.0	DCPA (dicalcium phosphate anhydrous, Monetite)	$CaHPO_4$	2.0-5.5 (> 80 ºC)	2.929
1.0	DCPD (dibasic calcium phosphate dehydrate, Brushite)	$CaHPO_4\cdot 2H_2O$	2.0-6.0	2.319
1.33	OCP (octacalcium phosphate)	$Ca_8H_2(PO_4)_6\cdot 5H_2O$	5.5-7.0	2.673
1.5	α-TCP (α-tricalcium phosphate)	$Ca_3(PO_4)_2$	Precipitated from aqueous solutoins only at T > 800 ºC	2.814[3]
1.5	β-TCP (β-tricalcium phosphate)	$Ca_3(PO_4)_2$	~ 5-12[1]	3.067[3]
1.2-2.2	ACP (amorphous calcium phosphate)	$Ca_3(PO_4)_2\cdot nH_2O$	6.5-9.5	-
1.50-1.67	CHDA (calcium deficient HAp)	$Ca_{10-x}(HPO_4)_x(PO_4)_{6-x}(OH)_{2-x}$ $(0 < x < 2)$[2]	9.5-12.0	-
1.67	HAp	$Ca_{10}(PO_4)_6(OH)_2$	Precipitated from aqueous solutoins only at T > 1300 ºC	3.155
2.0	TTCP (tetracalcium phosphate)	$Ca_4(PO_4)_2O$	-	3.056[3]

[1] Always metastable. The composition of the precipitate depends on the composition and pH of the electrolyte solution; [2] In the case x=1 (the boundary condition Ca/P = 1.5), the chemical formula looks as follows: $Ca_9(HPO_4)(PO_4)_5(OH)$, [3]These compounds cannot be precipitated from aqueous solutions.

Finally, pyrophosphate or diphosphate ($P_2O_7^{4-}$) is synthesized when monetite is heated above 300 ºC, however ammonium phosphate yields pyrophosphate at temperatures greater than 125 ºC.[31] Pyrophosphate ions inhibit HAp crystal formation being an important ion to regulate biomineralization. Calcium pyrophosphate hydrates (CPP, $Ca_2P_2O_7 \cdot nH_2O$) are involved in several forms of arthritis, including calcium pyrophosphate crystal deposition disease, also known as pseudogout.[32] Alkaline phosphatase (ALP), which is able to hydrolyze pyrophosphate ions, simultaneously causes a reduction of this ion's potent inhibiting effect on HAp formation and supersaturates the extra-cellular fluid with orthophosphates that consequently induce mineralization, regulating the bone re-mineralization.

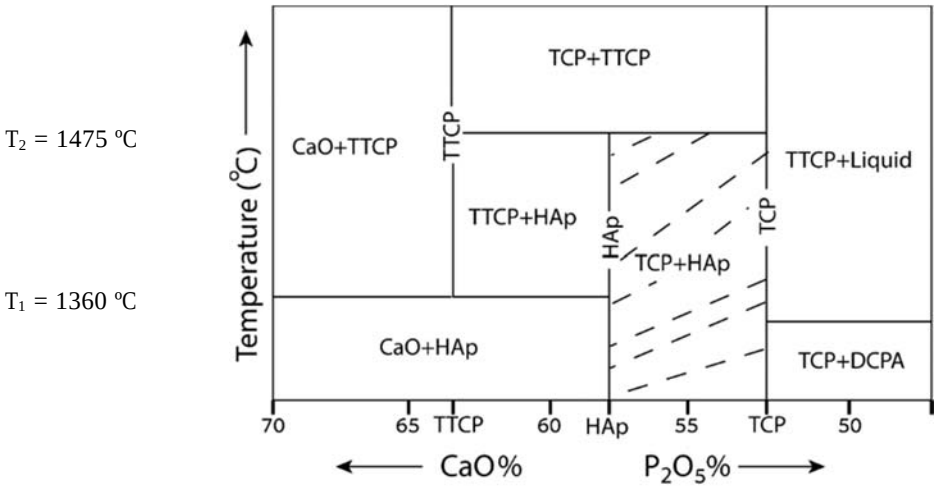

.

Figure 1.3. Equilibrium phase diagram of different calcium phosphates. The dashed region shows the phases of interest for biphasic calcium phosphate formation (TCP+HAp). In this figure, TTCP—tetracalcium phosphate, CaO—calcium oxide. Reproduced from ref [74] with permission from SAGE Publishing.

On the other hand, it is worth noting that temperature and pH are relevant parameters to obtain the desired calcium phosphate phase and to control its formation in different environments, while the transitions to be avoided or favored when synthesizing the chosen phase are multiple.

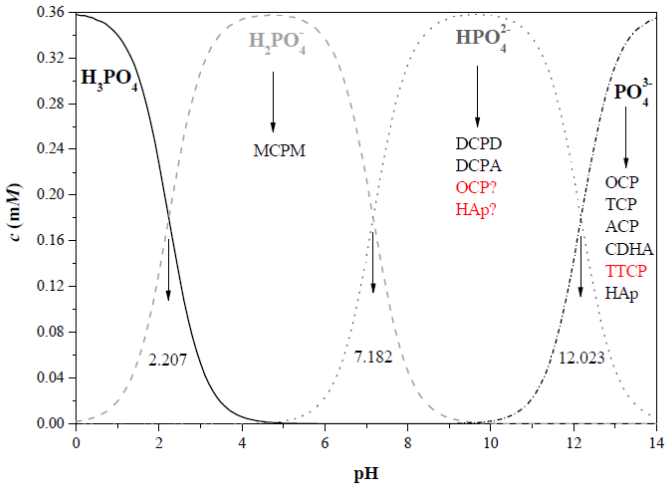

Figure 1.4. The distribution of phosphate species as a function of pH at 37 °C, 0.36 mM total analytical concentration of phosphate, free hydrogen concentration of 10^{-6} M. The values of the three dissociation constants are marked, along with the CaP phases that are likely to form from each species. As the pH increases, the Ca/P ratio in the solid phase increases, and the solubility of this phase decreases. Reproduced from ref [33] with permission from MDPI.

Considering the interest of HAp for heterogeneous catalysis, its synthesis has been under research in the last decades in order to obtain different structures, morphologies and textures. Production of HAp powders has been classified under four different methods:[34-37]

i) dry methods, based on homogeneous mixtures of the precursors, controlling precisely their composition and parameters,

ii) wet methods, extensively used as they are simple procedures comprising:

   a. double decomposition or coprecipitation (reacting source of PO_4^{3-} ligand with a source of Ca^{2+} with the assistance of additives (e.g., base or acid).

   b. emulsion, considered efficient, simple and suitable for producing a nano-structured HAp powder.

   c. hydrolysis (aqueous hydrolysis of CaP (i.e. OCP, DCPD, TCP) usually following dissolution and precipitation stages; sol-gel methods, from precursors in a solution, preferably organometallic.

   d. hydrothermal treatment, a reaction between the calcium and phosphate sources in water or solvents (solvothermal), in a confined environment with a higher temperature and pressure, inside an autoclave, a process that creates chemical bonds and forms nuclei that ensure a relatively stoichiometric and highly crystalline synthesis of HAp.

iii) microwave (MW)-assisted methods (intended to produce a higher yield of perfectly crystalline HAp powder homogeneous in terms of size, porosity and morphology) and ball-milling or ultrasound (used for its simplicity, reproducibility, and large-scale production of HAp) and

iv) miscellaneous methods (i.e. mimicking efficient biological systems or through pyrolysis).

HAp features have been compared by some authors with water due to its outstanding peculiarities as the role of water in the realm of liquids has been considered similar to the role of HAp is in the world of solids. Among its properties, its crystal lattice flexibility, the ability to conduct protons, improved osteoconductivity and a high bioactivity are particularly relevant. Furthermore, the structural hydroxyl ion channel in the direction of the *c*-axis is considered a specific feature of its crystal lattice that underlays its outstanding properties.

Stoichiometric pure HAp crystal is monoclinic and belongs to the space group $P2_1/b$, with 88 atoms per unit cell and its stoichiometry is $Ca_{20}(PO_4)_{12}(OH)_4$ and Ca/P = 1.67. However, the monoclinic form almost never occurs in such a form in nature, as the crystallization in hexagonal form is more feasible. Additionally at 207 ºC suffers a transition to hexagonal ($P6_3/m$). This is due to the fact that OH^- ion is not spherical, and the two mirror planes normal to the c-axis channel cannot be preserved. Conversely, the symmetry and the position of F^- is much better defined in the channel and, therefore, the fluoroapatite belongs to the hexagonal space group $P6_3/m$.

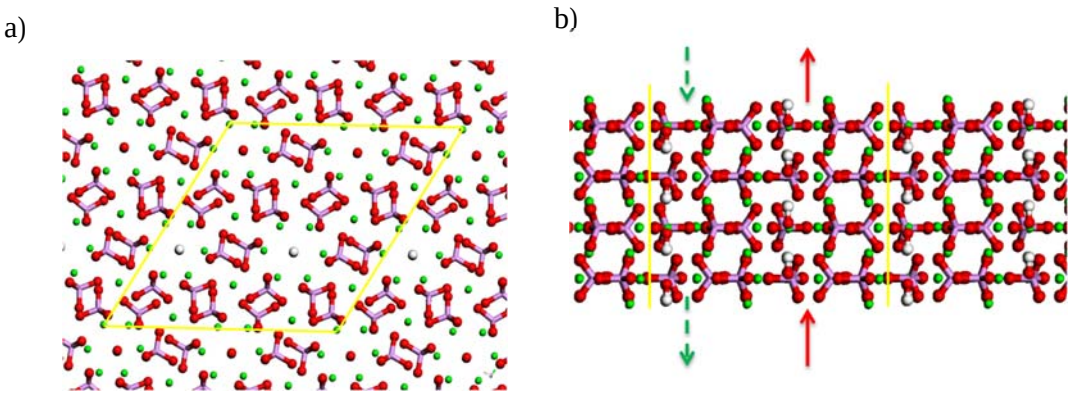

Figure 1.5. (a) Axial and longitudinal views of the HAp (0001). Yellow borders mark the 2x2 primitive surface cell reconstruction. (b) Green and red arrows mark the opposite direction of two consecutive OH columns. Ca^{2+} (green), Oxygen (red), Hydrogen (white), Phosphorus (in the center of violet bars).

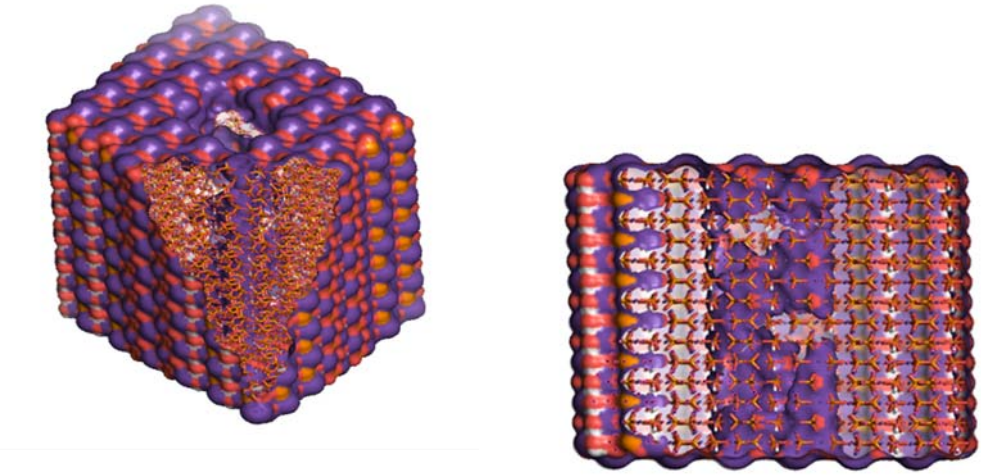

Figure 1.6. 3-D structure of hydroxyapatite lattice.

The theoretical lattice parameters are a = 9.418 Å and c = 6.884 Å for $P6_3/m$ (b = 2a, α = 120º for $P2_1/b$). However, depending on the synthesis and environmental factors, the lattice parameters can vary within the ranges of 9.41–9.44 Å and 6.84–6.94 Å, respectively, for the P63/m space group. The polymorphic transition from hexagonal to monoclinic is reversible at temperatures lower than 204 ºC. The number of atoms per cell in a $P6_3/m$ crystal is 44. It contains seven symmetrically independent atoms, two different calcium atoms: Ca_I forming single atomic columns parallel to the c axis and Ca_{II} surrounding the hexagonal channel of hydroxyl in groups of the three calcium atoms at different heights; one phosphor and three oxygen atoms forming PO_4^{3-} tetrahedral units (P, O_I, O_{II} and O_{III}); and the O(H) ions disordered along c about the mirror plane at z= ¼. The occupancy of the OH^- sites was 50%, as necessary in $P6_3/m$.

Regarding lattice flexibility it is worth noting that HAp can incorporate on half of the elements of the period table without losing its structure,[23] an important property that can influence the behavior of biomineralized DNA in HAp. As an example, when Mg^{2+} ions substitute up to 20% of Ca^{2+} ions some properties change significantly (e.g. the solubility is increased and the size of crystals is reduced). Interestingly, when ions with different charge are substituted, charge neutrality shall be maintained either by a second substitution with different charge or by creating vacancies, usually in the locations occupied by OH^-.

Substitutions may occur in several crystallographic sites and this feature is extremely useful in biological environments as toxic ions may be scavenged or they are just captured to maintain the homeostatic level in HAp forming bones or even to remove pollutants in toxic waters and environments. Those ions induce changes in the degree of crystallinity, solubility, thermal stability, morphology, and other surface and biological properties that are worth being studied in combination with nucleic acids.[22]

The surface of HAp is in constant evolution, particularly in biologic environments. The complexity of those processes makes it difficult to elucidate the mechanisms of transformation in calcium phosphates as the solution mediated dissolution/reprecipitation mechanism is the most supported. Moreover, the dynamics of the surface allow the system to be split as the surface properties are different from the inner part depending on slight differences in environmental parameters as low as a change of one pH unit from 6 to 7. Such an ability allows the possibility to obtain differences in reactivity in case HAp acts as a catalyst. The capacity of encapsulating and protecting molecules until the target is reached justifies the utilization of HAp as a drug delivery carrier. Thus, the slightly acidic pH inside some compartments of the cell would allow the dissolution of HAp capsules (pH 4.5-5.5). This feature might enable its use in gene delivery as HAp belongs to the group of non-viral transfection agents.

In terms of electrical properties, HAp exhibits piezoelectricity, ferroelectricity and pyroelectricity.[37] The first, related to the possibility of generating electrical charge at the surface when it is subjected to stress, is related to the polarization of OH^- groups trapped in the channel formed by the calcium atoms in Ca_{II} positions in the hexagonal form $P6_3/m$ but not in the monoclinic $P2_1/b$. HAp thin films exhibit the ferroelectric behavior with a remnant polarization being one-fourth of that exhibited by lead zirconate titanate films mostly due to OH^- in hydroxyl channel. Additionally, HAp pyroelectricity characterized by the pyroelectric coefficient pi = 12 $\mu C \cdot m^{-2} \cdot K^{-1}$ as HAp is able to generate electrical charge as a function of the rate of temperature change.[22]

The OH^- groups located in the characteristic column of HAp are located in the center of the overlapping triangles formed by the hexagonal Ca^{2+} ions, with an average distance of 2.5 Å between them. The calcium triangles of each layer are rotated by 60º with respect to the triangles below and above it, with both oxygen and hydrogen of the OH^- group lying on the c-axis in the higher, monoclinic symmetry, as they are all OH^- ordered in the same direction,

following a head-to-tail alignment. However, in $P6_3/m$ there is a 50 % likelihood for OH^- to point upwards or downwards. They are restricted to a channel resembling a line of interconnected ovoids, with the longest diameter, around 3 Å, in the basal plane and the shortest diameter in the plane of Ca_{II} triangles. The oxygen and hydrogen belonging to OH^- groups are disordered and such a situation is usually observed in hexagonal and defective HAp generated in biological environments. Piezoelectricity and the pyroelectricity effects exhibited by HAp are caused by the spontaneous polarization of the OH^- ions in the c-axis channel. Vacancies in the central channel allow room for mobility of OH^-, O_2^- and Ca^{2+} ions facilitating the restructure of the crystal or enhancing the catalytic properties of HAp. Such vacancies paired with vacancies in Ca^{2+} create a defective structure able to retain small molecules such as glycine.

The capacity of conducting H^+ is interesting as well due to its relationship with the catalytic properties of the mineral. The transmission of protons through the OH^- channel converts HAp into a good proton conductor useful for some industrial applications. The diffusion pathway is not linear but sinusoidal accompanied by the reorientation of OH^-. The diffusion of OH^- groups along the c-axis channel results in high ion mobility on the HAp surface and an intense local hydration expected to be responsible for the higher electrical conductivity exhibited by HAp. The mineral, using the same mechanism is able to transport O_2^- ions, particularly in B-type HAp where CO_3^{2-} substitute PO_4^{3-} groups causing an enlargement of the channel that facilitates the diffusion of ions through it. In terms of biomaterial for bone regeneration it is worth mentioning that thermally and electrically polarized HAp (semi-permanently polarized) stored charge density of 3.9 $\mu C \cdot cm^{-2}$, enhancing osteobonding and osteoconductivity when implanted in cortical bone of femoral diaphysis in white rabbits.[22]

1.3.1. Hydroxyapatite as a catalyst

HAp is a versatile and exceptional catalyst compared to other minerals.[38] Buvaneswari and Valsalan[39] reported that pure forms of HAp and fluorapatite show less activity compared to systems that were modified or enriched with certain metal ions. HAp brings several options related to the diversity of reaction sites, high surface of reaction and high adsorption capacity. Additionally, this mineral contributes with an unusual property of containing both basic and acid sites in a single crystal lattice. It is known that when HAp is highly crystalline

and ratio Ca/P = 1.5 it acts as an acid catalyst, when the ratio Ca/P is around 1.67 it acts as a basic catalyst. When 1.50 < Ca/P < 1.67 HAp catalyst behaves as both acid and basic.[40] HAp has already been used to catalyze in dehydration and dehydrogenation of alcohols,[41] in oxidation of alkanes, Friedel-Frakft alkylation,[42] aldol condensation reactions (reaction of an enolate ion enolate (alkaline media) or enol (acidic media) with a carbonic group to yield a β-hydroxyaldehid (aldol) or a β-hydroxyacetone), Diels-Alder (a reaction between a diene and a dienophile to build a substituted cyclohexene system), aerobic oxidation of alcohols (transforming ethanol in chemical substance of high added value and to decompose hydrogen peroxide among others). In pure form, HAp catalyzes the combustion of formahaldehide at room temperature.[43] The Knoevenagel's condensation (nucleophilic addition to a carbonic group, aldehyde or ketone of an activated carbon (acid) located between two acceptor groups of resonant electrons) can be easily performed without solvent at room temperature by using HAp.[44] It is worth noting that HAp has been used in combination with microwaves to catalyze Knoevenagel's condensation.[45]

The Green Chemistry approach is expected to develop sustainable heterogeneous catalysts by using highly functionalized metals based on the specific features of inorganic crystals as HAp, considered as nanostructured catalyst that allow the location of active metallic species (e.g. in the lattice, in the surface or between layers).[46] In high temperature conditions (> 350 ºC), HAp results in a high conversion yield from lactic acid to acrylic acid. The catalyst in such conditions is highly stable and it inactivation is not observed even after 300 hours of reaction. In such a reaction the dehydration ration is correlated with the deficiency in calcium and the increment in groups P-OH.[47]

The photocatalytic performance of HAp has attracted researchers as it makes the decomposition pharmaceutical pollutants, dyes and bacteria inactivation feasible. HAp composites, such as Ti-doped HAp are promising.[48] The origin of the photocatalytic activity of HAp has been attributed to effect of UV on the near-surface vacancies, presence of ·OH radical and the production of superoxide $O_2^{\bullet-}$ radical, and subsequent electron transfer to oxygen in the atmosphere.[49]

Recently, HAp has been described as the catalyst yielding ribose from formaldehyde and glycolaldehyde through a cross-aldol reaction and Lobry de Bruyn–van Ekenstein transformations. The continuous reaction needed one pot in hot water, without any fine pH control or any complicated condition control at each reaction step. The authors claimed that

ribose production by HAp may be a reason why a pentose backbone was incorporated into nucleic acids in the prebiotic world.[50]

1.4. Mineralization of nucleic acids

The research about how organic molecules become trapped in a mineral or how they template an inorganic matrix is of outmost interest, particularly to understand how mineralization processes work in biological environments and as a strategy to design new hybrid composites.

Literature mentions two types of mineralization related with biological processes: biomineralization and biocrystallization. Firstly, *biomineralization* is an important phenomenon in nature. Many researchers have focused on two subcategories of biomineralization: i) interfacial interactions organic-inorganic associated with biological mineralization, traditionally known as biomineralization; and ii) template-directed crystallization (i.e. organic molecules or structures that play a templating function, serve to fill space, direct the structure, and balance the charge of the resulting inorganic open-framework material).[51] Their objective, when studying natural mineralization phenomena (creation of shells, growth of teeth and bone) has been to apply biomimetic strategies in order to develop new materials (advanced composites and coatings) for several applications in different sectors (i.e. medical, chemical, optical, and electronic applications).[52] Biomineralization research, from a chemical perspective, can be divided into three different contributing areas: i) crystallographic characterization, composition elucidation, and biochemistry of the biological materials; ii) design of in vitro models, intended to test hypotheses referred to the role of biomacromolecules in controlling nucleation growth of crystals or the interactions between the organic matrix and the crystals; and recently iii) the development of new approaches to methods of synthesis, based on biological systems, with the objective of controlling crystal morphology, polymorphism, and material properties, resulting in new organic-inorganic hybrid composites (controlling complex patterns in inorganic structures will contribute developing new types of catalyst supports and membranes for the separation of large polymers, colloids and cells).[53] In the biomedical field, mimicking the biological mineralization is expected to result in implants with customized macroporosity, drug delivery systems and more efficient vectors for delivery of DNA in transfection procedures.[54,55]

Secondly, the concept of *biocrystallization* has been used by some authors to describe the process that some organisms use to encapsulate crucial biomolecules when they undergo external attacks.[56,57] It is well known that life is not compatible with the crystalline state. However, in some living systems such as bacteria, when exposed to severe environmental conditions, vital macromolecules are captured in intracellular crystalline assemblies that may give protection against the environmental event (i.e. *E. coli* has developed a defense strategy involving co-crystallization of its DNA with the stress-induced protein Dps). These intracellular hybrids are thermodynamically stable in a state that corresponds to free energy minima of the system. They are considered reminiscent of ordered states in the inanimate world such as crystals and liquid crystals, the last step to preserve high ordered molecules such as biopolymers.[58] The preservation of DNA, by eukaryotic cells under certain aggressive circumstances, has been part of the theoretical research performed in the thesis as we discuss in the results and discussion chapters.

Through evolution of life, some organisms have been capable of developing the ability to produce organic–inorganic hybrid materials templated by biomolecules (i.e. moluscus through calcium carbonate, diatoms and marine multicellular sponges via protein-based silica biomineralization). Nucleic acids, as templates for the synthesis of hybrid materials, have received considerable attention in recent years.[59] Such interest is grounded in several of DNA's main characteristics, chirality is one of them which is particularly relevant.[60] Chirality is a crucial feature that sustains life. It is present in a myriad of molecules and biopolymers (i.e. amino acids, sugars, (poly)peptides, and DNA or RNA) but also in macroscopic objects such as snails, helical trees and even hair vortices.[61,62] Chirality opens routes of molecular recognition and the use of selective mechanisms for natural self-assembly strategies that result in materials with hierarchical structures in the nano-, meso- and macroscale. Among chiral molecules, helical biopolymers such as nucleic acids, are of particular interest. Helical biomolecules present rod-like structures with a highly charged surface, a distinct uniform diameter, functionality, persistence length. Therefore, helical biomolecules undergo distinctive hierarchical self-assembly to form complexes with minerals (i.e. silica) making them important structural and signaling molecules in biological systems.[59] The use of chiral biomolecules to direct the "bottom-up" in vitro synthesis of inorganic silica materials is interesting for understanding the formation of complex architectures in living organisms, but also assists the applications of nanostructured materials.[59] For instance, rigid DNA rods, approx. 50 nm, in aqueous solution easily self-

assemble into multiple liquid-crystal phases. Conversely, when longer than 100 nm, they are flexible and can result in highly compact forms through cooperative conformational transitions. Therefore, DNA molecules can transcript into multiple molecule-length-dependent silica structures by using the combination of DNA self-assembly and silica biomineralization. Recently, Grass and co-workers (2015) showed that silica is a perfect environment to preserve nucleic acids for information storage and biomedical purposes.[63] Moreover, the long term preservation of DNA has been a matter of research for paleontologists looking for well preserved DNA of ancient species. It has been postulated that DNA in ancient fossil bones has the greatest chance of survival if encapsulated within bone apatite/collagen structures[64] and crystal aggregates.[65]

DNA has been used to template calcium carbonate. Calcium carbonates such as calcite, aragonite, vaterite and amorphous have industrial interest as pigments, brighteners and fillers and also biological (structural support and gravity sensors). The control of their crystal shape and texture is an important feature for such applications. Regarding nucleic acids interaction with calcium carbonate, Chen, Cai and Yu (2010) found that ss-DNA and linear structures show greater influence on the particle morphology than ds DNA, probably due to the fact that linear DNA is more easily adsorbed on $CaCO_3$, facilitating the interaction and because its rigidity decreases and flexibility increases.[66]

To finalize this section, we review CaP biomineralization focusing on some aspects that have been relevant in our work. CaP biomineralization has a prominent place over 60 different biological minerals since they play an important role as constituents of hard tissues in vertebrates. Reasonably high concentrations of Ca^{2+} and PO_4^{3-} (1 to 5 mM), but nontoxic, occur in all vertebrates, sometimes such a high concentration is allowed to be in solution by specific proteins (i.e. Fetuin-A) that keep nanosized HAp clusters in solution and inhibit their precipitation and posterior calcification. CaP, the major constituent of bone, teeth and tendons gives these organs stability, hardness, and function.[67] Biologically formed calcium phosphates are often nanocrystals, from tens to a few hundred nanometers, that are precipitated under mild conditions in contrast with calcium phosphates precipitated from aqueous solutions from supersaturated solutions. Calcium phosphates constitute a specific area of interest in nanotechnology, which may be applied in the repair of hard and soft skeletal tissues.[55,68]

Other interesting areas include the design and creation of cellular therapy carriers as non-viral vectors of transfection.[69] The process of nucleic acids going through the cytoplasmic membrane into the cells is termed transfection. In such a process, DNA is read out by the cell, and the machinery of the cell allows the biosynthesis of the encoded protein. As naked DNA (negatively charged) cannot cross the cell membrane due to its negative charge, a suitable carrier is required. The calcium phosphate family are known to be adequate vehicles to transport nucleic acids through that journey to the cytosol and cell nucleus where a recombination of DNA with the one originally belonging to the cell is feasible temporarily (transient) or permanently.[70] Almost 50 years after its discovery they are still under intense research, especially after transfection using viral vectors has shown some drawbacks.[71]

Coprecipitation of DNA with calcium phosphate which is based on HAp, is one of the most commonly used non-viral vectors since it was proposed in the early 1970s[72] Modification of the original process through the use of calcium phosphate nanoparticles has gained some attention because of their biocompatibility, their easy preparation, the capacity to be loaded with biomolecules and once inside the cell, their biodegradation/dissolution after cellular uptake in the lysosome.[73] However, their use has been limited through time due to the low efficiency of the process.[74] Interestingly, most of the authors consider DNA adsorbed in the surface of the HAp particles and they do not consider DNA as a template during the coprecipitation. A fact, that from the perspective of this thesis requires more research. In order to increase the efficiency of transfection some strategies were followed as to include Mg^{2+} in a initial stage of the coprecipitation in order to reduce the particle size.[69]

Additionally, DNA can be protected against intracellular attacks by DNAse if an additional shell of calcium phosphate layers is given to cover adsorbed DNA. This strategy leads to an increase in the transfection efficiency compared to single-shell calcium.[74]

In summary, the hybrid system we study in this thesis shows extraordinary features and potential applications in several fields that makes the research exciting. As the potential aspects to be analyzed are multiple, we are going to describe the objectives of this thesis and their justification in Chapter 2.

1.5. References

1. Turon P., Puiggalí J., Bertrán O., Alemán C., Surviving Mass Extinctions through Biomineralized DNA, *Chemistry - A European Journal* (**2015**), *21*, 18892 – 18898, DOI:10.1002/chem.201503030.

2. Lipfert J., Doniach S., Das R., Herschlag, D., Understanding Nucleic Acid–Ion Interactions, Annual Review of Biochemistry (**2014**), *83*, 813–841. DOI:10.1146/annurev-biochem-060409-092720.

3. Kumar A., Kumar V., Biotemplated Inorganic Nanostructures: Supramolecular Directed Nanosystems of Semiconductor(s)/Metal(s) Mediated by Nucleic Acids and Their Properties, *Chemical Reviews* (**2014**), *114*, 7044−7078. DOI: 10.1021/cr4007285.

4. Watson J.D., Crick F.H., Molecular structure of nucleic acids; a structure for deoxyribose nucleic acid, *Nature* (**1953**), *171*, 737–738. DOI: 10.1038/171737a0.

5. Seeman, N. C., DNA in a material world, *Nature* (**2003**), *421*, 6921, 427-431. DOI: 10.1038/nature01406.

6. Svozil D., Kalina J., Omelka M. Schneider B., DNA conformations and their sequence preferences, *Nucleic Acids Research* (**2008**), *36*, 11, 3690–3706. DOI:10.1093/nar/gkn260.

7. Dickerson R.E., Drew H.R., Conner B.N., Wing R.M., Fratini A.V., Kopka M.L., The anatomy of A-, B-, and Z-DNA. *Science* (**1982**), *216*, 475–485. DOI:10.1126/science.7071593.

8. Alberts B., DNA replication and recombination, *Nature* (**2003**), *421*, 431-435. DOI:10.1038/nature01407.

9. Jaeger L., Chworos A., The architectonics of programmable RNA and DNA nanostructures, *Current Opinion in Structural Biology* (**2006**), *16*, 531–543. DOI: 10.1016/j.sbi.2006.07.001.

10. Gilbert W., Origin of life; The RNA world, *Nature* (**1986**), *319*, 618. DOI:10.1038/319618a0.

11. Matray T.J., Kool E.T., Selective and Stable DNA Base Pairing without Hydrogen Bonds, *Journal of American Chemical Society* (**1998**), *120*, 6191-6192. DOI: 10.1021/ja9803310.

12. Kool E.T., Morales J.C., Guckian K.M., Mimicking the Structure and Function of DNA: Insights into DNA Stability and Replication, *Angewandte Chemie International Edition* (**2000**), *39*, 990-1009. DOI: 10.1002/(SICI)1521-3773(20000317)39:6<990::AID-ANIE990>3.0.CO;2-0.

13. Fersht A.R., The hydrogen bond in molecular recognition, *Trends in Biochemical Sciences* (**1987**), *2*, 301-304.
DOI:10.1016/0968-0004(87)90146-0.

14. Gould I.R., Kollman P.A., Theoretical Investigation of the Hydrogen Bond Strengths in Guanine-Cytosine and Adenine-Thymine Base Pairs, *Journal of American Chemical Society* (**1994**), *116*, 6, 2493-2499.
DOI:10.1021/ja00085a033.

15. Friedman, R.A., Honig B., A Free Energy Analysis of Nucleic Acid Base Stacking in Aqueous Solution, *Biophysical Journal* (**1995**), *69*, 1528-1535.
DOI: 10.1016/S0006-3495(95)80023-8.

16. Šponer J.,, Jurečka P., Marchan I., Luque F.J., Orozco M., Hobza P., Nature of base stacking: reference quantum ‐ chemical stacking energies in ten unique B ‐ DNA base ‐ pair steps, *Chemistry–A European Journal* (**2006**), *12*, 10, 2854-2865.
DOI: 10.1002/chem.200501239.

17. Alhambra C., Luque F.J., Gago F., Orozco M., Ab initio study of stacking interactions in A-and B-DNA, *The Journal of Physical Chemistry B* (**1997**), *101*, 19, 3846-3853.
DOI:10.1021/jp962626a.

18. Rueda M., Luque F.J., Lopez J.M., Orozco M., Amino−imino tautomerism in derivatives of cytosine: effect on hydrogen-bonding and stacking properties, The Journal of Physical Chemistry A, (**2001**), *105*, 26, 6575-6580.
DOI: 10.1021/jp010838o.

19. Jones M.R., Seeman N.C. Mirkin C.A., Programmable materials and the nature of the DNA bond, *Science* (**2015**), *347*, 6224, 1260901-1-11.
DOI: 10.1126/science.1260901.

20. Smith ZD, Chan MM, Humm KC, Karnik R., Mekhoubad S., Regev A., Eggan K., Meissner A., DNA methylation dynamics of the human preimplantation embryo, *Nature* (**2014**), *511*: 611–615.
DOI:10.1038/nature13581.

21. Dor Y., Cedar H., Principles of DNA methylation and their implications for biology and medicine, *Lancet* (**2018**), *392*: 777–786.
DOI: 10.1016/S0140-6736(18)31268-6.

22. Uskoković V., The role of hydroxyl channel in defining selected physicochemical peculiarities exhibited by hydroxyapatite, *RSC Advances* (**2015**), *5*, 36614-36633.
DOI: 10.1039/c4ra17180b.

23. Wopenka B., Pasteris J.D., A mineralogical perspective on the apatite in bone, *Materials Science and Engineering C* (**2005**), *25*, 131–143.
DOI:10.1016/j.msec.2005.01.008.

24. Dorozhkin, S.V., Calcium orthophosphates in nature, biology and medicine. *Materials* (**2009**), *2*, 399–498.
DOI:10.3390/ma2020399.

25. Constantz B.R., Barr B.M., Ison I.C., Fulmer M.T., Baker J., McKinney L., Goodman S.B., Gunasekaren S., Delaney D.C., Ross J., Poser R.D., Histological, chemical, and crystallographic analysis of four calcium phosphate cements in different rabbit osseous sites. *Journal Biomedical Material Research* (**1998**), *43*, 451e61.
DOI:10.1002/(SICI)1097-4636(199824)43:4<451::AID-JBM13>3.0.CO;2-Q.

26. Wang J., Chen W., Li Y., Fan S., Weng J., Zhang X., Biological evaluation of biphasic calcium phosphate ceramic vertebral laminae, *Biomaterials* (**1998**), *19*, 1387-1392.
DOI:10.1016/S0142-9612(98)00014-3.

27. Dorozhkin, S.V., Epple, M. Biological and medical significance of calcium phosphates, *Angewandte Chemie International Edition* (**2002**), *41*, 3130–3146.
DOI: 10.1002/1521-3773(20020902)41:17<3130::AID-ANIE3130>3.0.CO;2-1.

28. Rivas M., del Valle L.J., Armelin E., Bertran O, Turon P., Puiggali J., Alemán C., Hydroxyapatite with Permanent Electrical Polarization: Preparation, Characterization and Response Against Inorganic Adsorbates, *ChemPhysChem* (**2018**), *19*, 1–11.
DOI: 10.1002/cphc.201800196.

29. Verron E., Gauthier O., Janvier P., Pilet P., Lesoeur J., Bujoli B., Guicheux J., Bouler J.M., In vivo bone augmentation in an osteoporotic environment using bisphosphonate-loaded calcium deficient apatite, *Biomaterials* (**2010**), *31*, 7776-7784.
DOI:10.1016/j.biomaterials.2010.06.047.

30. Schnitzler V., Fayon F., Despas C., Khairoun I., Mellier C., Rouillon T., Massiot D., Walcarius A., Janvier P., Gauthier O., Montavon G., Bouler J.M., Bujoli B., Investigation of alendronate-doped apatitic cements as a potential technology for the prevention of osteoporotic hip fractures: critical influence of the drug introduction mode on the in vitro cement properties, *Acta Biomaterialia* (**2011**), *7*, 2, 759-70.
DOI: 10.1016/j.actbio.2010.09.017.

31. Schwartz A.W., Phosphorus in prebiotic chemistry, *Philosophical Transactions of the Royal Society B: Biological Sciences* (**2006**) *361*, 1743–1749.
DOI:10.1098/rstb.2006.1901.

32. Gras P., Rey C., Marsan O., Sarda S., Combes C., Synthesis and Characterisation of Hydrated Calcium Pyrophosphate Phases of Biological Interest, *European Journal of. Inorganic Chemistry* (**2013**), *34*, 5886–5895.
DOI:10.1002/ejic.201300955.

33. Eliaz N., Metoki N., Calcium Phosphate Bioceramics: A Review of Their History, Structure, Properties, Coating Technologies and Biomedical Applications, *Materials* (**2017**), *10*, 334, 1-104.
DOI:10.3390/ma10040334.

34. Fihri A., Len C., Varma R.S., Solhy A., Hydroxyapatite: A review of syntheses, structure and applications in heterogeneous catalysis, *Coordination Chemistry Reviews* (**2017**), *347*, 48-76.
DOI:10.1016/j.ccr.2017.06.009.

35. Kim H-W., Koh Y-H., Li L-H., Lee S., Kim H-E., Hydroxyapatite coating on titanium substrate with titania buffer lay er processed by sol-gel method, *Biomaterials* (**2004**), *25*, 2533-2538.
DOI:10.1016/j.biomaterials.2003.09.041.

36. Yamasaki N., Kai T., Nishioka M., Yanagisawa K., Ioku K., Porous hydroxyapatite ceramics prepared by hydrothermal hotpressing. *Journal of Materials Science* (**1990**), *9*, 1150-1151.
DOI:10.1007/BF00721872.

37. Hu S., Ji F., Marinescu C., Cimpoesu F., Qi Y., Tao Y., Stroppa A., Ren W., Ferroelectric polarization of hydroxyapatite from density functional theory, *RSC Advances* (**2017**), *7*, 21375–21379.
DOI: 0.1039/C7RA01900A.

38. Rodrigues E. G., Keller T.C., Mitchell S., Pérez-Ramírez J., Hydroxyapatite, an exceptional catalyst for the gas-phase deoxygenation of bio-oil by aldol condensation, *Green Chemistry* (**2014**), *16*, 4870-4874.
DOI: 10.1039/C4GC01432D.

39. Buvaneswari G., Valsalan K., Single step conversion of β-TCP to Na-modified hydroxyapatite and its application in green chemical synthesis of α, β-unsaturated compounds, *Materials Letters* (**2014**), *134*, 252–255.
DOI:10.1016/j.matlet.2014.07.098.

40. Stošić D., Bennici S., Sirotin S., Calais C., Couturier J-L., Dubois J-L., Travert A., Auroux A., Glycerol dehydration over calcium phosphate catalysts: Effect of acidic–basic features on catalytic performance, *Applied Catalysis A: General* (**2012**), *447– 448*, 124– 134.
DOI:10.1016/j.apcata.2012.09.029.

41. Tsuchida T., Kuboa J., Yoshioka T., Sakuma T., Takeguchi T., Ueda W., Reaction of ethanol over hydroxyapatite affected by Ca/P ratio of catalyst, *Journal of Catalysis*, (**2008**), *259*, 183–189.
DOI:10.1016/j.jcat.2008.08.005.

42. Sebti S., Tahir R., Nazih R., Boulaajaj S., Comparison of different Lewis acid supported on hydroxyapatite as new catalysts of Friedel–Crafts alkylation, *Applied Catalysis A: General* (**2001**), *218*, 25–30.
DOI:10.1016/S0926-860X(01)00599-3.

43. Xu J., White T., Li P, He C., Han Y., Hydroxyapatite foam as a catalyst for formaldehyde combustion at room temperature, *Journal of American Chemical Society* (**2010**), *132*, 13172–13173.
DOI:10.1021/ja1058923.

44. Sebti S., Tahir R., Nazih R., Saber A., Boulaajaj S., Hydroxyapatite as a new solid support for the Knoevenagel reaction in heterogeneous media without solvent, *Applied Catalysis A: General* (**2002**), *228*, 155–159.
DOI:10.1016/S0926-860X(01)00961-9.

45. Mallouk S., Bougrin K., Laghzizil A., Benhida R., Microwave-Assisted and Efficient Solvent-free Knoevenagel Condensation. A Sustainable Protocol Using Porous Calcium Hydroxyapatite as Catalyst, *Molecules* (**2010**), *15*, 813–823.
DOI:10.3390/moleculeγ5020813.

46. Kaneda K., Mizugaki T., Development of concerto metal catalysts using apatite compounds for green organic syntheses, *Energy & Environmental Science* (**2009**), *2*, 655–673.
DOI:10.1039/B901997A.

47. Ghantani V., Lomate S.T., Dongare M.K, Umbarkar S.B., Catalytic dehydration of lactic acid to acrylic acid using calcium hydroxyapatite catalysts, *Green Chemistry* (**2013**), *15*, 1211–1217.
DOI:10.1039/C3GC40144H.

48. Nishikawa H., Kato S., Ando T., Rapid and complete oxidation of acetaldehyde on TiO_2 photocatalytic filter supported by photo-induced activated hydroxyapatite, *Journal of Molecular Catalysis A: Chemical* (**2005**), *236*, 1-2, 145–148.
DOI:10.1016/j.molcata.2005.04.013.

49. Avakyan, L.A., Paramonova E.V., Coutinho J., Öberg S., Bystrov V.S., L.A. Bugaev, Optoelectronics and defect levels in hydroxyapatite by first-principles, *Journal of Applied Physics* (**2018**), *148*, 154706, 1–14.
DOI:10.1063/1.5025329.

50. Usamia K., Okamoto A., Hydroxyapatite: catalyst for a one-pot pentose formation, *Organic & Biomolecular Chemistry* (**2017**), *15*, 8888–8893.
DOI:10.1039/C7OB02051A.

51. Ozin G.A., Morphogenesis of Biomineral and Morphosynthesis of Biomimetic Forms, Accounts Chemical Research (**1997**), *30*, 17-27.
DOI:10.1021/ar960021r.

52. Zhang L.J., Liu H.G., Feng X.S., Zhang R.J., Zhang L., Mu Y.D., Hao J.C., Qian D.J., Lou Y.F., Mineralization mechanism of calcium phosphates under three kinds of Langmuir monolayers, *Langmuir* (**2004**), *20*, 6, 2243-2249.
DOI:10.1021/la035381j.

53. Estroff L.A., Introduction: Biomineralization, *Chemical Reviews* (**2008**), *108*, 11, 4329-4331.
DOI: 10.1021/cr8004789.

54. Mann S., The chemistry of form, *Angewandte Chemie International Edition* (**2000**), *39*, 3392–3406.
DOI:10.1002/1521-3773(20001002)39:19<3392::AID-ANIE3392>3.0.CO;2-M.

55. Engel E., Michiardi A., Navarro M., Lacroix D., Planell J.A., Nanotechnology in regenerative medicine: the materials side, *Trends in biotechnology* (**2008**), *26*, 1, 39-47.
DOI:10.1016/j.tibtech.2007.10.005.

56. Wolf S.G., Frenkiel-Krispin D., Arad T., Finkel S.E., Kolter R., Minsky A., DNA protection by stressinduced biocrystallization, *Nature* (**1999**), *400*, 83–85.
DOI:10.1038/21918.

57. Krupyanskii Y.F., Loiko N.G., Sinitsyn D.O., Tereshkina K.B., Tereshkin E.V., Frolov I.A., Chulichkov A.L., Bokareva D.A., Mysyakina I.S., Nikolaev Y.A., El'-Registan G.I., Popov V.O., Sokolova O.S., Shaitan K.V., Popov A.N., Biocrystallization in Bacterial and Fungal Cells and Spores, *Crystallography Reports* (**2018**), *63*, 4, 594–599.
DOI: 10.1134/S1063774518040144.

58. Kachroo A.H., Order in stress — Lessons from the inanimate world, *Journal of Biosciences* (**2004**), *29*, 4, 369–372.
DOI:10.1007/BF02712104.

59. Liu B., Cao Y., Huang Z., Duan Y., Che S., Silica biomineralization via the self-assembly of helical biomolecules, *Advanced Materials* (**2015**), *27*, 479–497.
DOI: 10.1002/adma.201401485.

60. Vybornyi M., Vyborna Y., Häner R., Silica Mineralization of DNA-Inspired 1D and 2D Supramolecular Polymers, *ChemistryOpen* (**2017**), *6*, 4, 488-491.
DOI:10.1002/open.201700080.

61. Qiu H., Che S., Chiral mesoporous silica: Chiral construction and imprinting via cooperative self-assembly of amphiphiles and silica precursors, *Chemical Society Reviews* (**2011**), *40*, 1259-1268.
DOI: 10.1039/c0cs00002g.

62. Wang Y., Xu J., Wang Y., Chen H., Emerging chirality in nanoscience, *Chemical Society Reviews* (**2013**), *42*, 2930-2962.
DOI: 10.1039/C2CS35332F.

63. Grass R.N., Heckel R., Puddu M., Paunescu D., Stark W.J., Robust chemical preservation of digital information on DNA in silica with error ‐ correcting codes, Angewandte Chemie International Edition (**2015**), *54*, 2552–2555.
DOI:10.1002/anie.201411378.

64. Campos P.F., Craig O.E., Turner-Walker G., Peacock E., Willerslev E., Gilbert M.T.P, DNA in ancient bone – Where is it located and how should we extract it?, Annals of Anatomy (**2012**), *194*, 7-16.
DOI: 10.1016/j.aanat.2011.07.003.

65. Salamon M., Tuross N., Arensburg B., Weiner S., Relatively well preserved DNA is present in the crystal aggregates of fossil bones, *Proceedings of National Academy of Sciences* (**2005**), *102*, 13783-13788.
DOI:10.1073/pnas.0503718102.

66. Cheng B., Cai W., Yu J., DNA-Mediated Morphosynthesis of Calcium Carbonate Particles*, Journal of Colloid and Interface Science* (**2010**), *352*, 43−49.
DOI:10.1016/j.jcis.2010.08.050.

67. Caiab Y., Tang T., Calcium phosphate nanoparticles in biomineralization and biomaterials, *Journal of Materials Chemistry* (**2008**), *18*, 3775–3787.
DOI:10.1039/B805407J.

68. Xu H.H.K., Weir M.D., Burguera E.F., Fraser A.M., Injectable and macroporous calcium phosphate cement scaffold, *Biomaterials* (**2006**), *27*, 4279-4287.
DOI:10.1016/j.biomaterials.2006.03.001.

69. Chowdhury E.H., Kunou M., Nagaoka M., Kundu A.K., Hoshiba T., Akaike T., High efficiency gene delivery for expression in mammalian cells by nanoprecipitates of Ca–Mg phosphate, *Gene* (**2004**), *341*, 77-82.
DOI:10.1016/j.gene.2004.07.015.

70. Epple M., Ganesan K., Heumann R., Klesing J., Kovtun A., Neumann S., Sokolova V., Application of calcium phosphate nanoparticles in biomedicine, *Journal of Materials Chemistry* (**2010**), *20*, 18–23.
DOI:10.1039/B910885H.

71. Crystal R.G., Transfer of Genes to Humans: Early Lessons and Obstacles to Success, *Science* (**1995**), *270*, 404-410.
DOI:10.1126/science.270.5235.404.

72. Graham F.L., van der Eb A.J., Transformation of rat cells by DNA of human adenovirus 5, *Virology* (**1973**), *52*, 456– 467.
DOI:10.1016/0042-6822(73)90163-3.

73. Chernousova S., Epple M., Live-cell imaging to compare the transfection and gene silencing efficiency of calcium phosphate nanoparticles and a liposomal transfection agent, *Gene Therapy* (**2017**) *24*, 282–289.
DOI: 10.1038/gt.2017.13.

74. Sokolova V.V., Radtke I., Heumann R., M. Epple, Effective transfection of cells with multi-shell calcium phosphate-DNA nanoparticles, *Biomaterials* (**2006**), *27*, 3147-3153.
DOI: 10.1016/j.biomaterials.2005.12.030.

75. Manjubala, I.; Sastry, T.P.; Suresh Kumar, R.V., Bone in-growth induced by biphasic calcium phosphate ceramic in femoral defect of dogs., *Journal Biomaterials Application*, (**2005**), *19*, 341–360.
DOI:10.1177.0885328205048633.

Chapter 2

Objectives

Chapter 2
Objectives

2.1 Introduction

This thesis is intended to develop a new conceptual framework around an idea that was envisioned to become a new line of research. We acknowledge that the main concept has several ramifications, and some of them in different disciplines that we cannot totally include in this work. However, we expect to outline the basic theoretical background that will identify the Gordian nodes of the whole picture, expecting that a full set of details about the nodes and their connections will be developed elsewhere in separate works. The conceptual framework we are going to expose in the following chapters is the result of several contributions from researchers belonging to different fields, who we thank, and with whom the author has discussed the idea in order to establish the overall consistency of the concepts across the fields.

The thesis is planned to be more conceptual than rather focused on empirical work. Nevertheless, we investigated experimentally some of the concepts and hypothesis we develop here. This is the reason why the objectives of the thesis are structured around the concepts, hypothesis and models and the complete empirical work is separated in the corresponding annexes. Due to the interdisciplinary scope of the research, several scientists from different fields, who we thank, contributed to the empirical research where they are experts. Thus, through the thesis, we introduce and discuss the most relevant results in the corresponding sections, using them as pillars to build the theoretical framework.

We have followed a general strategy through the thesis. First, we have compiled the current state of the art. Second, when possible, we have used a theoretical-experimental synergistic approach, in order to first simulate the system in silico by means of molecular mechanics or quantum mechanics, and later confirm empirically the behavior of the hydroxyolite system using classical wet chemistry. Third, we extracted the main features of the hydroxyolite system from previous simulations and experiments in order to create models or confirm hypothesis intended to be applicable to different fields of Chemistry (i.e. material chemistry, catalysis or prebiotic research), extending the concept when possible to

other life sciences using as a common denominator the relevant characteristics of the hybrid system made of nucleic acids and HAp.

The objectives have been structured as follows. First, we define a general objective that we split into four sub-objectives, each of them interlinked with the main concept of a hybrid system made of nucleic acids and HAp. Each of them is intended to develop a specific topic according to the perspective from which we approached the hybrid system:

a) Nucleic acids as a template of a HAp crystal, a biocompatible carrier of genetic information that can be delivered after re-dissolution.
b) HAp as a protective shield of nucleic acids, and
c) HAp as a catalyst (after a polarization process).

We detail such sub-objectives and their justification in the next section.

2.2. Main Objective

DNA/HAp biominerals formed by the combination of DNA with a HAp matrix can be viewed from two different perspectives. The first refers to the fact that DNA in combination with HAp nanoparticles is able to transfect (transport + infect) living cells (e.g. liver cells, fibroblasts, osteoblasts and tumor cells).[1-5] It has been proposed the interaction between the two entities of the biomineral occurs because of the affinity between the calcium of HAp and the phosphate backbone of DNA.[6-9] It should be noted that this proposal makes the nucleotide sequence of DNA unimportant, whereas its length takes on major importance. A second perspective is the one reported by Kostetsky,[10] who observed that the period of translation along the c-axis of the HAp lattice, 3.4 Å, is relatively similar to the period of the DNA double helix. This feature combined with the fact that HAp is able to catalyze the abiogenic synthesis of: D-ribose from ammonia, methane and water; nucleotides from nucleosides condensing agents and ammonium oxalate;[11] and polynucleotides with a 3',5'-phosphodiether bond under conditions similar to those of primaveral Earth, led Kostetsky to propose a model for the synthesis of DNA through the interaction of its different elements with the lattice of HAp mineral. According to this model, the DNA double helix might be embedded into the crystalline network of HAp forming a biomineral similar to that obtained by encapsulating therapeutic DNA into HAp nanoparticles. Considering the relevance of both perspectives we realized the need to establish a solid theoretical framework and a robust

empirical background that could make such a hybrid system more understandable in order to foresee its implications in life sciences. For that reason, we define the main objective as:

Main objective "*To determine the theoretical implications of the hydroxyolite system, made by a combination of nucleic acids and the mineral HAp, in terms of its origin, role and consequences related to its formation under certain specific circumstances, particularly during the history of life on Earth"*.

2.3. Sub-objectives

2.3.1. Sub-objective 1

We consider that the nucleic acid is the one which triggers the generation of the hydroxyolite system. Interactions between HAp and DNA are believed to play an important role in different fields, including the biomedical one.[12,13] For example, recent spectroscopic studies reported a contribution of vibrational modes of DNA, phospholipids and proteins in HAp breast cancer microcalcifications formed in the organism.[12] Additionally, HAp nanoparticles have been described as non-viral inorganic gene carriers.[13-16] DNA-HAp complexes were found to be able to cross cell membranes, integrating DNA into the cell genome. Brundin et al.[17] showed a specific binding affinity of HAp for DNA. The direct encounter between DNA and HAp in biological systems suggests that investigation of the interaction between these two materials and particularly, of the formation of biominerals through the nucleation of HAp at a DNA template would be very useful for the development of novel strategies for gene therapy. Amazingly, the number of studies devoted to examining the interaction between HAp and DNA is still very scarce. In an early study, Jordan et al.[18] reported on DNA-calcium phosphate co-precipitation for transfection purposes, even though such co-precipitation was described only in a narrow range of physical-chemical conditions. More recently, Okazaki et al.[19] investigated the effect of DNA on the crystal growth of HAp by synthesizing the mineral in the presence of the biomolecule. However, those authors reported that DNA inhibits the HAp crystal growth, indicating that DNA molecules are not in the HAp structure but adsorbed at the surface.

On the basis of these observations, as stated in the first objective, we investigate the feasibility of DNA encapsulation into HAp nanoparticles, with DNA as the template of such

a crystal, using a rational design approach that combines theoretical and experimental methodologies. Atomistic molecular dynamics simulations of B-DNA immersed in an inorganic solution show the rapid formation of calcium phosphate clusters at the biomolecule template. Thus, we define the sub-objective 1 as:

Sub-objective 1. "*We aim to demonstrate that nucleic acids play the role of a nucleating agent in an aqueous solution that contains calcium and phosphate ions and a crystal (hydroxyolite) that encapsulates both DNA or RNA is formed spontaneously because it is thermodynamically favored"*.

2.3.2. Sub-objective 2

Demineralization of double-stranded DNA (ds-DNA) in HAp is at the forefront of the emerging clinical and medical applications (gene therapy) because of its importance in the development of controlled vehicles for gene delivery to replace damaged DNA. In addition, clinical observations have shown that bone HAp dissolution in acid environments is directly related with the pathophysiology of cancer-associated bone pain and osteoporosis, even though their mechanisms remain poorly understood.[20,21] Bioactive particles made of HAp-DNA exhibit good cell absorption, significant transfection efficiency, and high biocompatibility. They are obtained by covering genetic material with HAp.[22-24] Dissolution of such particles is worthy of study because it is directly related to the transfection efficiency and, additionally, it can be connected with other biological processes because HAp-DNA particles might release protected information encoded in DNA under certain conditions.[25] The molecular mechanism that drives the particle dissolution and DNA demineralization remains widely unknown and controversial.[26-28] We use a four-step approach based on atomistic molecular dynamics simulations to clarify the dissolution mechanism of HAp-DNA particles in acid environments, mimicking the physiological pH variations of the intracellular fluid encountered inside the cell cytosol and nucleus. Thus, we define sub-objective 2 as:

Sub-objective 2. "*We aim to demonstrate that a hydroxyolite crystal, carrier of genetic information, dissolves when the environmental conditions change, particularly when it becomes more acidic, releasing the entrapped nucleic acid into the surrounding media"*.

2.3.3. Sub-objective 3

Third, we deliberate about the implications of HAp shielding the biopolymer from external assaults. We postulate that hydroxyolite is a hybrid system where HAp acts as an inorganic shell that protects nucleic acids from environmental attacks. The importance of calcification processes, such as fossilization, for the understanding of the development of life on Earth is well documented.[29-31] Biomineralization of DNA was studied at atomic level[32-35] revealing that DNA acts as a template for HAp crystallization, as we demonstrate in the first set of sub-objectives. As a consequence, HAp adsorbs or encapsulates DNA and might protect the biomolecule from external attacks.[36] We note that we focus on the scenario related to periods of mass extinction, one of the most aggressive events that life has faced. We consider it is worth reviewing them within the third sub-objective from the perspective of DNA–HAp interactions and the synergistic effect against aggressive environmental conditions. This is the aim of this objective, to determine the physical, chemical, and biological implications of the mineralization of DNA for the persistence of life after aggressive events. Thus, the sub-objective has been defined 3 as:

Sub-objective 3. "*To develop a conceptual model about the implications of DNA being protected by HAp when facing environmental attacks and its consequences for other disciplines such as paleontology (i.e. in mass extinction events on early Earth), biology, biotechnology and medicine"*.

2.3.3. Sub-objective 4

We consider HAp as a catalytic substrate where simple organic molecules, particularly the ones related to the building blocks of life, could be synthesized. Starting from that premise we analyze the specific catalytic features of HAp. An important difference between ACP and synthetic HAp is the alignment of the OH^- ions along the c-axis in the latter. The crystal structure of stoichiometric HAp, which contains no OH^- defects, is monoclinic at room temperature. However, the monoclinic HAp changes to hexagonal phase at about 207 ºC, which means a change from an ordered to a disordered distribution of OH^- ions along the c-axis. The hexagonal phase becomes the most stable form of HAp in the pH range of 4–12 because of the disorder caused by the presence of vacancies and presence of O_2^- ions in the columns of OH^- groups. Although the properties of HAp were altered by thermally induced

changes in the positions of OH^- ions, the observed effects were not stable at room temperature (i. e. the OH^- reorientation has a short relaxation time).

In the last decades, Yamashita and co-workers[37-41] caused polarization effects in HAp samples by applying a constant DC electric field of 1.0–10.0 kV/cm at elevated temperature (300 – 850 ºC) to samples previously sintered at 1250 ºC for 2 h. Results indicated that the polarization effects were consequence of the electrical dipoles associated with the formation of defects inside crystal grains and of the space charge polarization originated in the grain boundaries. The slow relaxation of such dipoles suggested that polarization was only partially maintained (semi-permanently), even though this effect was not quantified. In addition, the above mentioned thermally stimulated polarization process (TSP) was found to affect some surface properties as for example the wettability and adhesion of osteoblastic cells, which were higher onto semi-permanently polarized samples than onto non-polarized ones.[42,43]

In this thesis, we develop an alternative TSP strategy, based on the conditions reported to be found in a volcano eruption and its plume (~1000 ºC and 3 $kV \cdot cm^{-1}$). Such TSP treatment resulted in an electrophotocatalyst where the electrical properties of polarized HAp become permanent. For that reason it is currently on its way to patenting (PCT/EP2017/069437 in Annex VII).[44] More specifically, the new catalyst allows the fixing of nitrogen from N_2 and carbon from CO_2 and CH_4 to obtain both glycine and Alanine (D/L racemic mixture), the two simplest amino acids, using mild reaction conditions. Results reflect the significant impact of the alternative conditions used for the TSP treatment on the adsorption of several organic molecules in its surface that can be tailored by controlling the conditions used for HAp treatment, suggesting new applications for permanently polarized HAp.

As a result, we revisit HAp as a mineral which might catalyze the synthesis of simple organic molecules after polarization and consequently might build hybrid systems composed of the polarized catalytic substrate and the recently synthesized molecules adsorbed in its surface. All in all, taking into consideration all our previous empirical findings, we aim to develop a prebiotic model where HAp plays the role of a catalytic substrate where simple organic molecules, such as the building blocks of life, can be generated and assembled to develop biopolymers such as nucleic acids. Then, we define sub-objective 4 as:

Sub-objective 4. "*To develop a prebiotic model that considers HAp as a catalyst that might facilitate the rise of the building blocks of life that are assembled to synthesize biopolymers in its surface"*.

All sub-objectives are somehow interlinked and through their development we cannot avoid referring from one to the other in order to build the whole picture of the conceptual framework we are going to describe in the next chapters.

2.4. References

1. Liu Y., Wang T., He F., Liu Q., Zhang D., Ziang S., Su S., Zhang J., An efficient calcium phosphate nanoparticle-based nonviral vector for gene delivery, *International Journal of Nanomedicine* (**2011**), *6*, 721–727.
DOI:10.2147/IJN.S17096.

2. Olton D., Li J., Wilson M.E., Rogers T., Close J., Huang L., Kumta P.N., Sfeir C., Nanostructured calcium phosphates (NanoCaPs) for non-viral gene delivery: Influence of the synthesis parameters on transfection efficiency, *Biomaterials* (**2007**), *28*, 1267–1279.
DOI:10.1016/j.biomaterials.2006.10.026.

3. Sokolova V.V., Radtke I., Heumann R., Epple M., Effective transfection of cells with multi-shell calcium phosphate-DNA nanoparticles, *Biomaterials* (**2006**), *27*, 3147–3153.
DOI: 10.1016/j.biomaterials.2005.12.030.

4. Cao X., Deng W., Wei Y., Su W., Yang Y., Wei Y., Yu J., Xu X., Encapsulation of plasmid DNA in calcium phosphate nanoparticles: stem cell uptake and gene transfer efficiency. *International Journal of Nanomedicine* (**2011**), *6*, 3335–3349.
DOI:10.2147/IJN.S27370.

5. Liu T., Tang A., Zhang G., Chen Y., Zhang J., Peng S., Cai Z., Calcium phosphate nanoparticles as a novel nonviral vector for efficient transfection of DNA in cancer gene therapy, *Cancer Biotherapy and Radiopharmaceuticals* (**2005**), *20*,141–149.
DOI:10.1089/cbr.2005.20.141.

6. Maitra A., Calcium phosphate nanoparticles: second-generation nonviral vectors in gene therapy. *Expert Review of Molecular Diagnostics* (**2005**), *5*, 893–905.
DOI:10.1586/14737159.5.6.893.

7. Jordan M., Schallhorn A., Wurm F.M., Transfecting mammalian cells: optimization of critical parameters affecting calcium-phosphate precipitate formation, *Nucleic Acids Research*, (**1996**), *24*, 596–601.
DOI:10.1093/nar/24.4.596.

8. Jordan M., Wurm F., Transfection of adherent and suspended cells by calcium phosphate. *Methods* (**2004**), *33*, 136–143.
DOI: 10.1016/j.ymeth.2003.11.011.

9. Sokolova V., Kovtun A., Prymak O., Meyer-Zaika W., Kubareva E.A., Romanova E.A., Oretskaya T.S., Heumann R., Epple M., Functionalisation of calcium phosphate nanoparticles by oligonucleotides and their application for gene silencing. *Journal of Materials Chemistry* (**2007**), *17,* 721–727.
DOI: 10.1039/B612699E.

10. Kostetsky E.Y., The possibility of the formation of protocells and their structural components on the basis of the apatite matrix and cocrystallizing minerals, *Journal of Biological Physics* (**2005**), *31*, 607–638.
DOI:10.1007/s10867-005-2383-x.

11. Schwartz A.W., Prebiotic phosphorylation-nucleotide synthesis with apatite. *Biochimica et Biophysica Acta - Nucleic Acids and Protein Synthesis* (**1972**), *281*, 477–480.
DOI:10.1016/0005-2787(72)90147-5.

12. Baker R., Rogers K.D., Shepherd N., Stone N., New relationships between breast microcalcifications and cancer, *British Journal of Cancer* (**2010**), *103*, 1034–1039.
DOI:10.1038/sj.bjc.6605873.

13. Zhu S.H., Huang B.Y., Zhou K.Z., Huang S.P., Liu F., Li Y.M., Xue Z.G..Long Z.G., Hydroxyapatite Nanoparticles as a Novel Gene Carrier, *Journal of Nanoparticle Research* (**2004**), *6*, 307–311.
DOI:10.1023/B:NANO.0000034721.06473.23.

14 Kozlova D., Chernousova S., Knuschke T., Buer J., Westendorf A.M., Epple M., Cell targeting by antibody-functionalized calcium phosphate nanoparticles, *Journal of Materials Chemistry* (**2012**), *22*, 396–404.
DOI: 10.1039/C1JM14683A.

15. Bisht S., Bhakta G., Mitra S., Maitra A., pDNA loaded calcium phosphate nanoparticles: highly efficient non-viral vector for gene delivery, *International Journal of Pharmaceutics* (**2005**), *288*, 157–168.
DOI:10.1016/j.ijpharm.2004.07.035.

16. Olton D., Li J., Wilson M.E., Rogers T., Close J., Huang L., Kumta P.N., Sfeir C., Nanostructured calcium phosphates (NanoCaPs) for non-viral gene delivery: influence of the synthesis parameters on transfection efficiency, *Biomaterials* (**2007**), *28*, 1267–1279.
DOI:10.1016/j.biomaterials.2006.10.026.

17. Brundin M., Figdor D., Sundqvist G., Sjögren U., DNA binding to hydroxyapatite: a potential mechanism for preservation of microbial DNA, *Journal of Endodontics* (**2013**), *39*, 211–216.
DOI:10.1016/j.joen.2012.09.013.

18. Jordan M., Schallhorn A., Wurm F.M., Transfecting mammalian cells: optimization of critical parameters affecting calcium-phosphate precipitate formation, *Nucleic Acids Research* (**1996**), *24*, 596–601.
DOI:10.1093/nar/24.4.596.

19. Okazaki M., Yoshida Y., Yamaguchi S., Kaneno M., Elliot J.C., Affinity binding phenomena of DNA onto apatite crystals, *Biomaterials* (**2001**), *22*, 2459–2464.
DOI:10.1016/S0142-9612(00)00433-6.

20. Yoneda T., Hata K., Nakanishi M., Nagae M., Nagayama T., Wakabayashi H., Nishisho T., Sakurai T., Hiraga T., Involvement of acidic microenvironment in the pathophysiology of cancer-associated bone pain, *Bone* (**2011**), *48*, 100 –105. DOI:10.1016/j.bone.2010.07.009.

21. Rachner T.D., Khosla S., Hofbauer L.D., Osteoporosis: now and the future, *Lancet* (**2011**), *377*, 1276 –1287. DOI:10.1016/S0140-6736(10)62349-5.

22. Shen H., Tan J., Saltzman W.M., Surface-mediated gene transfer from nanocomposites of controlled texture, *Nature Materials* (**2004**), *3*, 569 –574. DOI:10.1038/nmat1179.

23. Sun B., Yi M., Yacoob C.C., Nguyen H.T., Shen H., Effect of surface chemistry on gene transfer efficiency mediated by surface-induced DNA-doped nanocomposites, *Acta Biomaterialia* (**2012**), *8*, 1109–1116. DOI:10.1016/j.actbio.2011.12.005.

24. Sun B., Tran K.K., Shen H., Enabling customization of non-viral gene delivery systems for individual cell types by surface-induced mineralization, *Biomaterials* (**2009**), *30*, 6386 –6393. DOI:10.1016/j.biomaterials.2009.08.006.

25. Turon P., Puiggalí J., Bertran O., Alemán C., Surviving Mass Extinction through biomineralized DNA, *Chemistry – A European Journal* (**2015**), *21*, 18892 –18898. DOI:10.1002/chem.201503030.

26. Wang L., Nancollas G.H., Calcium orthophosphates: crystallization and dissolution, *Chemical Reviews* (**2008**), *108*, 4628 –4669. DOI:10.1021/cr0782574.

27. Dorozhkin S.V., Dissolution mechanism of calcium apatites in acids: A review of literature, *World Journal of Methodology* (**2012**), *2*, 1–17. DOI:10.5662/wjm.v2.i1.1.

28. Tang R.K., Orme C.A., Nancollas G.H., A new understanding of demineralization: The dynamics of brushite dissolution, *Journal of Physical Chemistry B* (**2003**), *107*, 10653– 10657. DOI:10.1021/jp0346312.

29. Donoghue P.C.J., Benton M.J., Rocks and clocks: calibrating the Tree of Life using fossils and molecules, *Trends in Ecolology and Evolution* (**2007**), *22*, 424 –431. DOI:10.1016/j.tree.2007.05.005.

30. Knoll A.H., Biomineralization and evolutionary history, Reviews in Mineralogy and Geochemistry (**2003**), *54*, 329 –356. DOI:10.2113/0540329.

31. Porter S.M., Seawater chemistry and early carbonate biomineralization, *Science* (**2007**), *316*, 1302 –1304.
DOI:10.1126/science.1137284.

32. Revilla-López G., Casanovas J., Bertran O., Turon P., Puiggalí J., Alemán C., Modeling biominerals formed by apatites and DNA, *Biointerphases* (**2013**), *8*, 10.
DOI:10.1186/1559-4106-8-10.

33. Takeshita T., Matsuura Y., Arakawa S., Okamoto M., Biomineralization of hydroxyapatite on DNA molecules in SBF: morphological features and computer simulation, *Langmuir* (**2013**), *29*, 11975 – 11981.
DOI:10.1021/la402589j.

34. Vasconcellos K.B., McHugh S.M., Dapsis K.J., Petty A.R., Gerdon A.E., Biomimetic nanoparticles with polynucleotide and PEG mixed-monolayers enhance calcium phosphate mineralization, *Journal of Nanoparticle. Research* (**2013**), *15*, 1942.
DOI:10.1007/s11051-013-1942-5.

35. Bertran O., del Valle L.J., Revilla-López G., Chaves G., Cardús L., Casas M.T., Casanovas J., Turon P., Puiggalí J., Alemán C., Mineralization of DNA into nanoparticles of hydroxyapatite, *Dalton Transactions* (**2014**), *43*, 317 –327.
DOI: 10.1039/C3DT52112E.

36. del Valle L.J., Bertran O., Chaves G., Revilla-López G., Rivas M., Casas M.T., Casanovas J., Turon P., Puiggalí J., Alemán C., DNA adsorbed on hydroxyapatite surfaces, *Journal of Material Chemistry B* (**2014**), *2*, 6953 –6966.
DOI:10.1039/C4TB01184H.

37. Ueshima M., Nakamura S., Ohgaki M., Yamashita K., Electrovectorial effect of polarized hydroxyapatite on quasi-epitaxial growth at nano-interfaces, *Solid State Ionics* (**2002**), *151*, 29–34.
DOI:10.1016/S0167-2738(02)00600-8.

38. Ueshima M., Nakamura S., Yamashita K., Huge, millicoulomb charge storage in ceramic hydroxyapatite by bimodal electric polarization, *Advanced Materials* (**2002**), *14*, 591–595.
DOI:10.1002/1521-4095(20020418)14:8<591::AID-ADMA591>3.0.CO;2-7.

39. Nakamura, M., Sekijima Y., Nakamura S., Kobayashi T., Niwa K., Yamashita K., Role of blood coagulation components as intermediators of high osteoconductivity of electrically polarized hydroxyapatite, *Journal Biomedical Materials Research* (**2006**), *79A*, 627– 634.
DOI:10.1002/jbm.a.30827.

40. Horiuchi N., Nakamura M., Nagai A., Katayama K., Yamashita K., Proton conduction related electrical dipole and space charge polarization in hydroxyapatite, *Journal of Applied Physics* (**2012**), *112*, 074901.
DOI:10.1063/1.4754298.

41. Horiuchi N., Nakaguki S., Wada N., Nakamura M., Nagai A., Katayama K., Yamashita K., Polarization-induced surface charges in hydroxyapatite ceramics, *Journal of Applied Physics* (**2014**), *116*, 014902.
DOI:10.1063/1.4886235.

42. Nakamura M., Hori N., Namba S., Toyama T., Nishimiya N., Yamashita K., Wettability and surface free energy of polarised ceramic biomaterials, *Biomedical Materials* (**2015**), *10*, 011001.
DOI:10.1088/1748-6041/10/1/011001.

43 Nakamura M., Nagai A., Hentunen T., Salonen J., Sekilima Y., Okura T., Hashimoto K., Toda Y., Monma H., Yamashita K., Surface Electric Fields Increase Osteoblast Adhesion through Improved Wettability on Hydroxyapatite Electret, *ACS Applied Materials and Interfaces* (**2009**), *1*, 2181–2189.
DOI:10.1021/am900341v.

44. Rivas M., del Valle L.J., Turon P., Alemán C., Puiggalí J., Sustainable synthesis of amino acids by catalytic fixation of molecular dinitrogen and carbon dioxide, *Green Chemistry* (**2018**), *20*, 685–693.
DOI:10.1039/C7GC02911J.

Chapter 3

Nucleic acids in a hydroxyapatite crystal

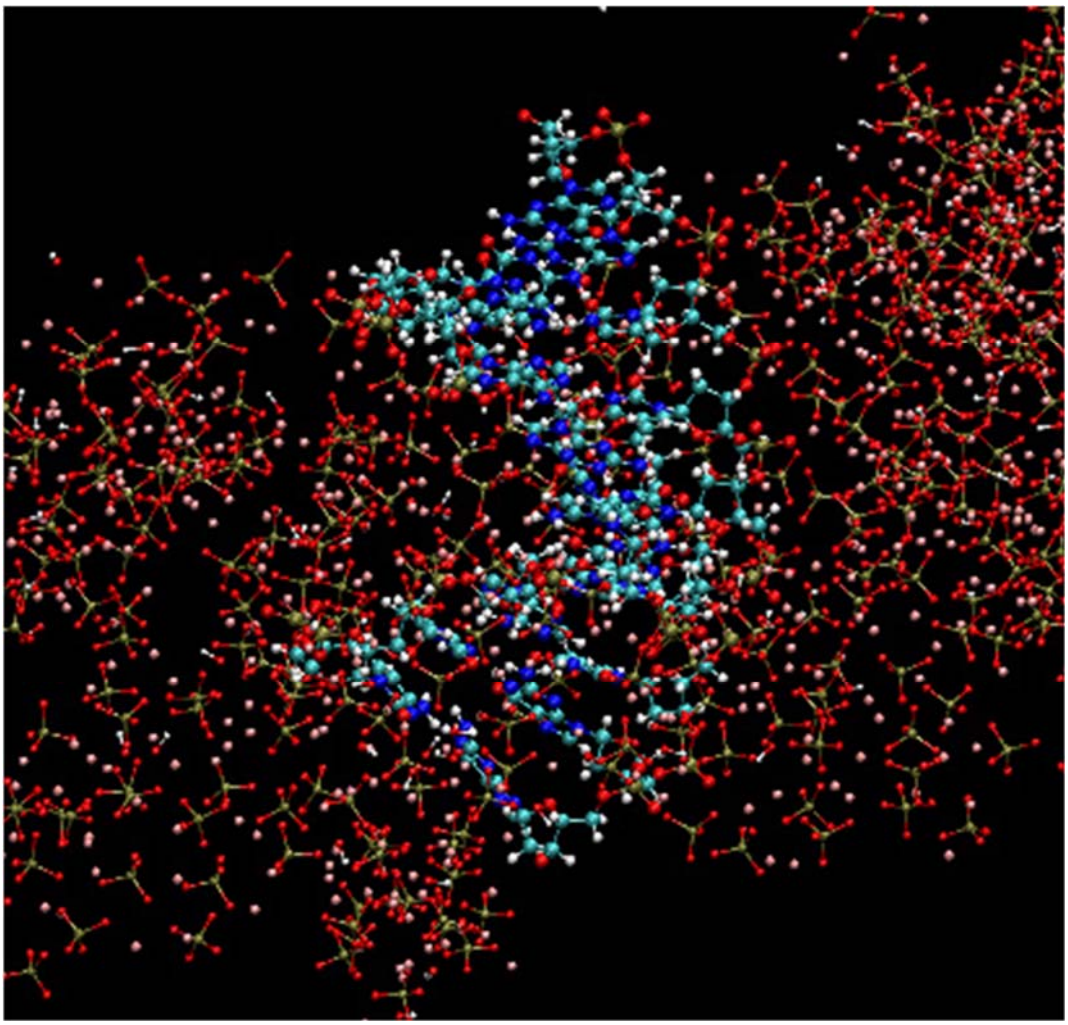

Chapter 3

Nucleic acids in a hydroxyapatite crystal

3.1. Introduction

Okazaki et al.[1] (2001) indicated that DNA inhibits the crystal growth of HAp, which makes the formation of biominerals through the encapsulation of the biomolecule difficult. In a more recent study, parallel to our own research, Gerdon and co-workers (2012)[2] demonstrated empirically the ability of DNA to template the mineralization of calcium phosphate. These authors developed a quartz crystal microbalance sensor for the quantification of HAp formation and the assessment of DNA as a template molecule. The results, which were also supported by optical density and dynamic light scattering measures, FTIR spectroscopy and scanning electron microscopy, suggested that DNA sequesters calcium and phosphate ions, thereby supersaturating the microenvironment and acting as a scaffold on which mineral forms.[2] Moreover, small differences in DNA length, hybridization, and secondary structure were found to provoke differences in affinity for HAp and appear to influence mineralization. However, the molecular mechanism that enable nucleic acids to template of a HAp crystal was not described.

In the first part of the chapter, according to sub-objective 1, we dive into such research, seeking the basic concepts that justify that a hydroxyolite system can be generated in nature under certain circumstances. Furthermore, we assess if DNA or RNA acting as a template would make it feasible to encapsulate themselves in HAp, minimizing the total energy of the system.

In the second part of the chapter, according to sub-objective 2, we discuss the mechanism that drives the dissolution of such hybrid particles when they are endocyted and released in the cytosol or the cell nucleus, which is usually slightly acidic. Despite the clinical importance of the dissolving mechanism of HAp for some diseases as vascular calcifications, osteoporosis or bone cancer, the underlying mechanism that controls its dissolution in acidic environments remains unclear. However, deep knowledge about such a process is highly desirable in order to provide better understanding of different pathologies and of the HAp as a vehicle for gene delivery to replace damaged DNA. The mechanism of dissolution in acidic conditions of HAp nanoparticles encapsulating ds-DNA has been

investigated at the atomistic level using computer simulations. For this purpose, four consecutive (multi-step) molecular dynamics simulations, involving different temperatures and proton transfer processes, have been carried out.

3.2. Purpose

In this chapter we focus on the two sub-objectives defined in Chapter 1 as sub-objective 1 and sub-objective 2. We recall them in this section to put into context the concepts we are going to outline in the following sections in order to demonstrate each one. We note that we have extracted the main findings to support the achievement of the objectives from the full research documents enclosed in Annex I, II, III and IV that were published in international scientific peer-reviewed journals.

Sub-objective 1. "*We aim to demonstrate that nucleic acids play the role of a nucleating agent in an aqueous solution that contains calcium and phosphate ions and a crystal (hydroxyolite) that encapsulates both DNA or RNA is formed spontaneously because it is thermodynamically favored"*.

Sub-objective 2. "*We aim to demonstrate that a hydroxyolite crystal, carrier of genetic information, dissolves when the environmental conditions change, particularly when they becomes more acidic, releasing the entrapped nucleic acid into the surrounding media"*.

The chapter is organized as follows. Section 3.3. summarizes the main results in terms of DNA as a template of a HAp crystal (Section 3.3.1.) and the dissolution mechanism of a hydroxyolite (Section 3.3.2.). Firstly, we introduce the concept of a shared crystallization plane by HAp and nucleic acids (Section 3.3.1.1.). Secondly, we confirm the role of DNA as a template in an aqueous solution containing Ca^{2+} and PO_4^{3-} ions (Section 3.3.1.2.). Thirdly, we confirm the synthesis in vitro of hydroxyolites using DNA as a template (Section 3.3.1.3). Finally, the mechanism of hydroxyolite dissolution is unveiled (Section 3.3.2.1). Discussion of all results is integrated with the exposition of the results. The chapter ends with conclusions (Section 3.4).

3.3. Results and discussion

3.3.1. DNA as a template of a hydroxyapatite crystal

3.3.1.1 The common shared crystallization plane

First, a Molecular Dynamics (MD) study of the nucleation and crystal growth of HAp at the ds-DNA, which was arranged in a B double helix (B-DNA), was performed, as described in detail in Annex I. Detailed atomistic information was extracted from models describing the initial stages of nucleation and cluster formation of calcium phosphate at a B-DNA molecule.

It is worth noting an important result which appeared after a detailed comparison of B-DNA and HAp structures that allowed us to identify two planes, the first defined by four phosphate groups of HAp and the second by two pairs of phosphates belonging to the polyphosphate backbone of ds-DNA. The phosphate groups are located at similar distances in the two planes, making the match between them feasible and facilitating the initial nucleating site of the crystallization process (Figure 3.1.). Specifically, for HAp such a plane is defined by u = 6.87 Å (i.e. the crystallographic parameter (c) and v = 11.66 Å, with an angle $\gamma = 120^{O}$; while some minor variability is observed for B-DNA depending on the sequence, however we tested different models for DNA and RNA and we extracted similar conclusions, the sequence is not significantly influencing the identified plane. Thus, the average values of the rectangle sides in B-DNA are u' = 6.72 Å and v' = 13.75 Å, the largest variability being shown by changes in the angle, considering values ranging from 108º to 141º.

A HAp model was generated starting from the phosphate groups located at the crystallization plane, using the plane identified as a nucleating site in the 5'-CGCGAATTCGCG-3', a representative DNA sequence, and allowing the crystal to grow. Accordingly, the four phosphate groups of the plane identified in B-DNA, as displayed in Figure 3.1a, were embedded into the HAp crystal. The growing process of the crystal is schematized in Figure 3.2a for HAp, whilst Figure 3.2b displays the resulting structure viewed from a frontal perspective of the B-DNA in the mineral. Thus, we corroborated that the geometric positions of the phosphate groups of ds B-DNA are suitable to grow a HAp crystal. This result allowed us to conclude, from a geometric point of view, that such biomolecules have the suitable nucleating sites to act as a nucleating agent of the mineral.

However, an energy analysis was also required to provide a complete assessment of this behavior of B-DNA as a mineral nucleator.

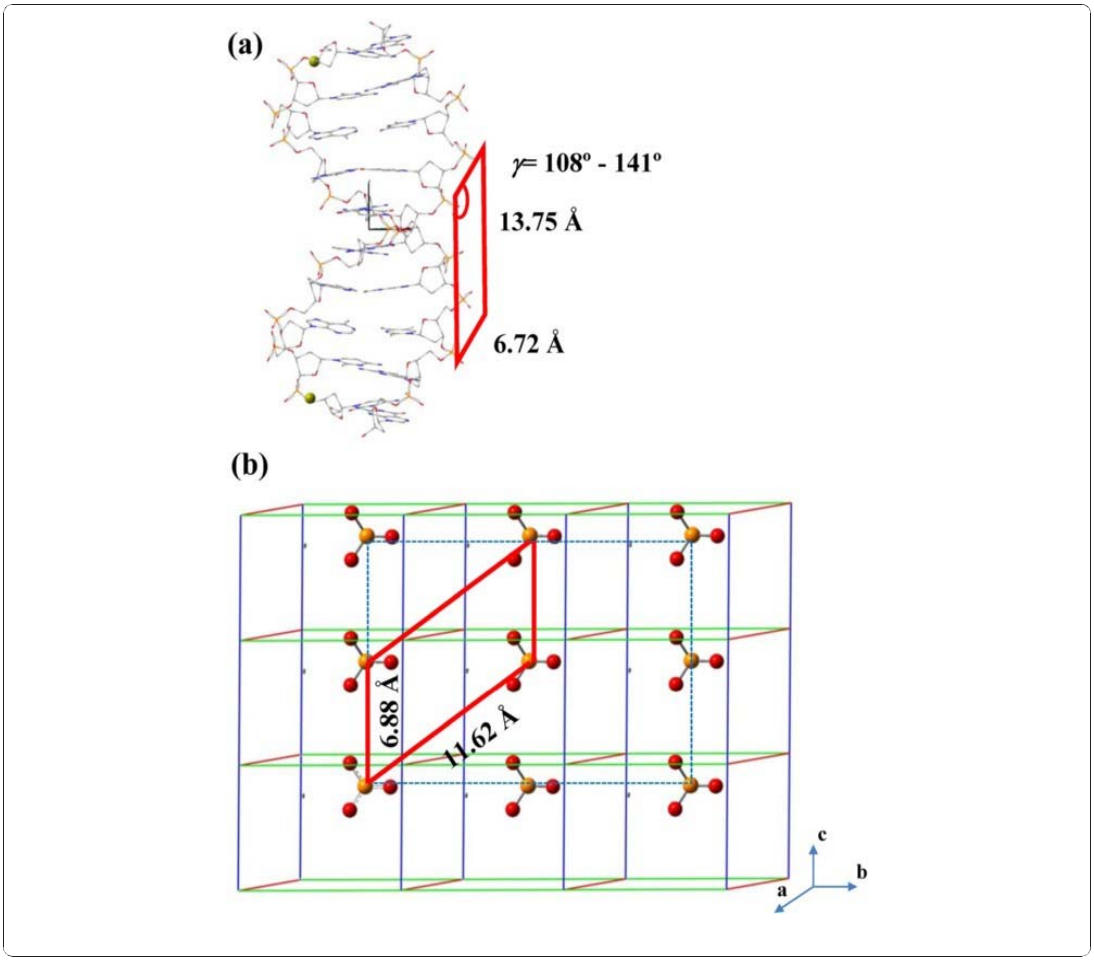

Figure 3.1. Isomorphic planes identified in (a) the double helix of B-DNA and (b) HAp. Reproduced with permission AIP Publishing ref [8].

The variation of the total energy, which is clearly dominated by the electrostatic contribution of the mineral as the size of the crystal grows (i.e. increasing thickness) is summarized in Annex I, Figure I.7. (henceforth Figure Ann.I.7.). The size or thickness of the crystal is represented by a cutoff distance defined with respect to the center of masses of the phosphate groups belonging to the planes used to nucleate the crystals. The energy profiles obtained for B-DNA/HAp and HAp, which are practically identical, clearly reflect the lack of influence of the double helix DNA on the energy of the system from the first steps of mineralization (i.e. mineral thickness < 10 Å).

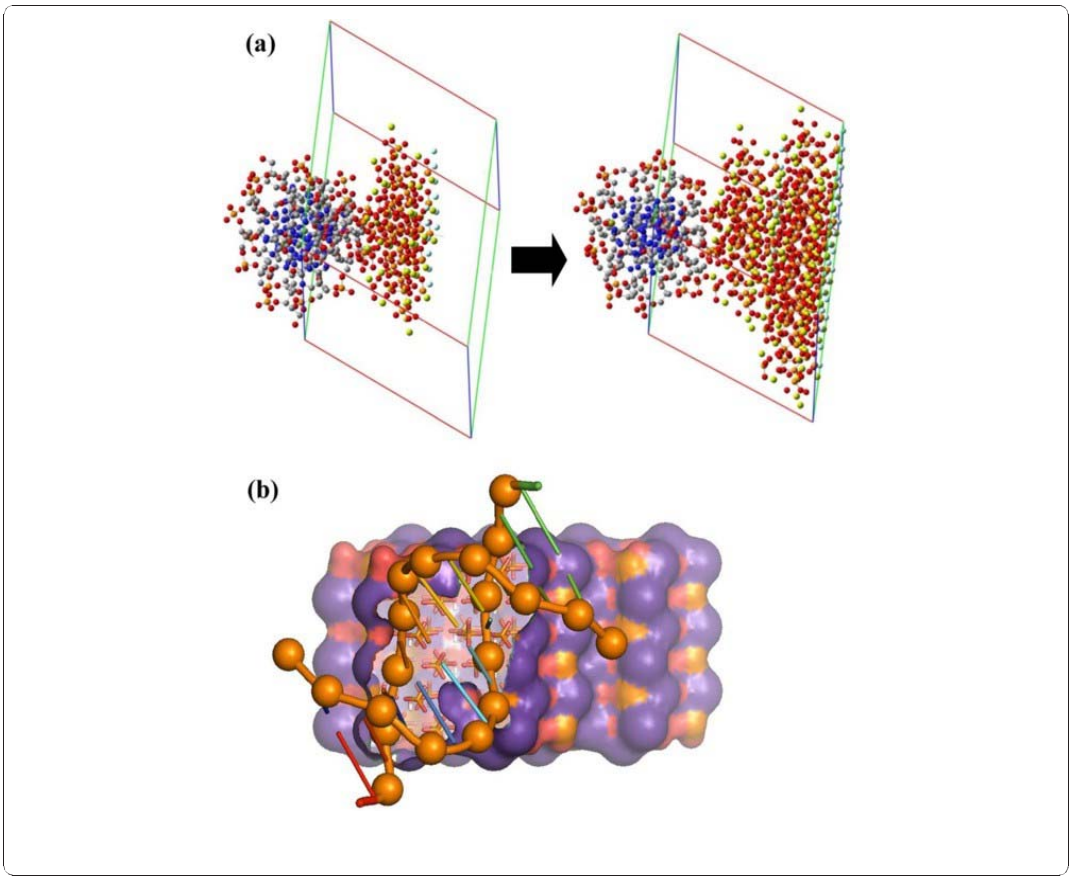

Figure 3.2. (a) Growing process of HAp using the double helix of B-DNA as a nucleating agent and (b) Biomineral obtained by such a growing mechanism where DNA strands are highlighted in brown balls. Reproduced with permission AIP Publishing ref [8].

Moreover, we compared the pattern of B-DNA embedded in HAp with a different apatite, fluoroapatite (FAp), noting that despite the fact that patterns are quite similar there is an energetic mismatch in the pair B-DNA/FAp and FAp (Figure Ann.I.7b), which suggests a stronger distortion of the ds DNA in FAp compared to HAp.

3.3.1.2. DNA as a template in an aqueous solution containing Ca^{2+} and PO_4^{3-} ions

In this section, we introduce the effect of an aqueous solution containing Ca^{2+} and PO_4^{3-} on the capacity of B-DNA to template the mineral.

Atomistic molecular dynamics simulations of B-DNA immersed in the above mentioned solution showed the rapid formation of calcium phosphate clusters at the biopolymer

template. The temporal evolution of those clusters suggests the growing of HAp crystal around the DNA matrix. Although 50 ns trajectories only represent the initial stages of nucleation of HAp around the DNA template, the analyses support the view that the biomolecules promote but do not inhibit the mineral growth (more details in Annex II).

The systems with presence and absence of B-DNA were simulated for 50 and 25 ns, respectively, to gain insights not only of the clustering process but also of the mineral (or crystal) nucleation process. Figures 3.3. and 3.4. show the distribution of Ca^{2+}, PO_4^{3-} and OH^- ions at selected snapshots extracted from the simulations in the presence and absence of B-DNA, respectively. As can be seen, the DNA favors the formation of embryonic clusters surrounding the double helix from the first stages of the MD simulation (i.e. after 1 ns). These initial clusters mainly involve Ca^{2+} and PO_4^{3-} ions, the incorporation of OH^- anions being apparently very scarce at such an early part of the trajectory. Snapshots recorded after 25 and 50 ns of simulation show not only the incorporation of OH^- anions, but also a change in the distribution of the Ca^{2+} and PO_4^{3-} clustering. This feature suggests that B-DNA may act as a stable nucleating template for the formation of HAp. More specifically, the DNA double helix may behave as a nucleating motif that initially helps to nucleate amorphous-like calcium phosphate clusters, which subsequently tend to re-organize for transformation into HAp.

The templating role of the biomolecule in the nucleation of HAp is clearly demonstrated when the distribution of inorganic ions is examined for the trajectory without B-DNA. Figure 3.4. shows extensive inorganic clusters after 1 ns, which is consistent with the formation of multiple nucleation centers for amorphous phosphate precipitation. This observation is consistent with nucleation from a supersaturated solution. In subsequent stages of the trajectory, these clusters grow similarly and ions tend to re-organize, suggesting that the system evolves towards poly-organized HAp. This multi-nucleation behavior is fully consistent with previous studies devoted to investigating HAp crystal growth[3] and differs from that displayed in Figure 3.3. which shows the preferential nucleation around the DNA template. The radial distribution functions of P···P pairs, $g_{P-P}(r)$, were calculated for the crystal structure of natural HAp,[4] the backbone of the DNA double helix and the PO_4^{3-} anions in the inorganic solution with and without DNA. As displayed in Figure 3.5., the $g_{P-P}(r)$ for the B-DNA shows a broad and high peak centered at 6.45 Å, which is consistent with

the dynamics and structural regularity of the biomolecule. This peak contains the two peaks found for the HAp crystal at r = 6.2 and 6.6 Å.

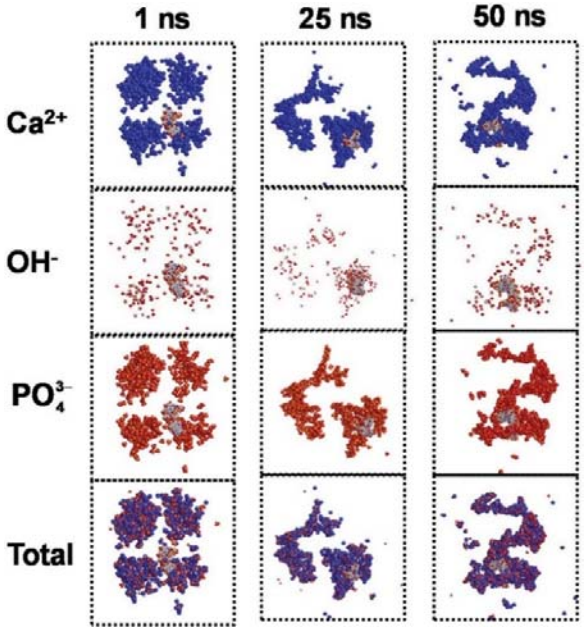

Figure 3.3. Distribution of Ca^{2+}, PO_4^{3-} and OH^- ions around DNA double helix at selected snapshots of the MD trajectory. The distributions of ions are displayed separately and all together. Solvent molecules have been omitted for clarity. Reproduced from ref. [13] with permission from The Royal Society of Chemistry.

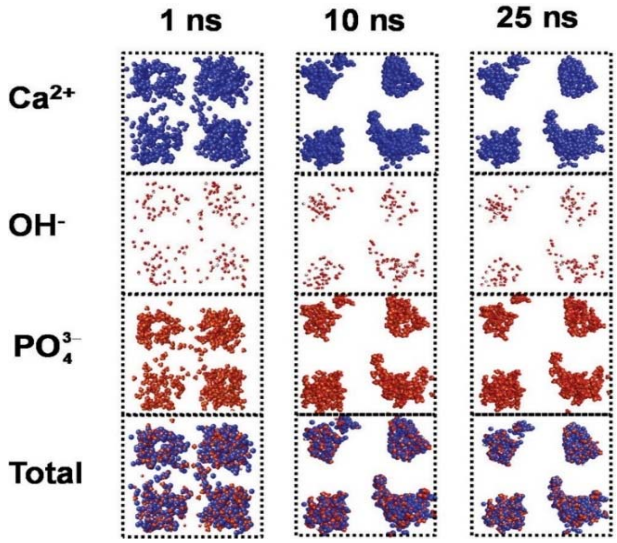

Figure 3.4. Distribution of Ca^{2+}, PO_4^{3-} and OH^- ions at selected snapshots of the MD trajectory in the absence of DNA. The distributions of ions are displayed separately and all together. Solvent molecules have been omitted for clarity. Reproduced from ref. [13] with permission from The Royal Society of Chemistry.

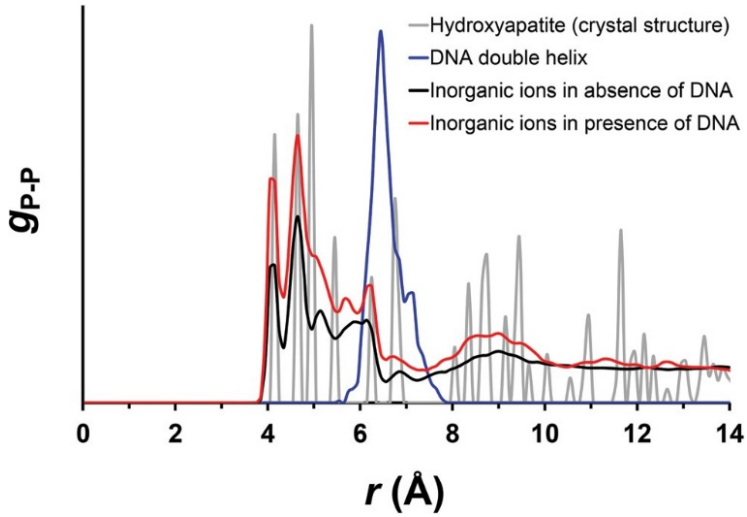

Figure 3.5. Radial distribution functions of P···P atom pairs for: the crystal structure of natural HAp (grey line); the DNA double helix (blue line); the PO_4^{3-} anions in the solution without DNA (black line); and the PO_4^{3-} anions in the solution with DNA (red line). The profiles for DNA and PO_4 anions were calculated using MD simulations performed in this work while the profile for natural HAp was obtained using the crystallographic coordinates reported in ref. [4] Reproduced from ref. [13] with permission from The Royal Society of Chemistry.

However, as expected, none of the four characteristic peaks of HAp at $r \leq 5.4$ Å appears in the profile obtained for the biopolymer. This is overcome in the $g_{P-P}(r)$ calculated for the PO_4^{3-} containing solutions. Thus, all the peaks found at $r < 6.7$ Å for the HAp crystal are identified in the profile derived for the inorganic solution with B-DNA.

Furthermore, the six peaks found for the HAp crystal in the 8–10 Å interval fit within a broad peak that contains multiple shoulders. This is consistent with an ordered enlargement of the clusters. Although quantitative comparison of the two profiles still reveals some discrepancies (i.e. in the $g_{P-P}(r)$ derived from MD the peak at $r = 4.9$ Å is a shoulder, the peak at $r = 5.4$ Å is shifted by ~0.2 Å, and the intensity of the peak at $r = 6.7$ Å is low after 50 ns trajectory), the qualitative concordance clearly indicates that B-DNA favors the mineral formation or even crystallization of HAp around it.

The agreement between the profiles derived from the HAp crystal structure and the snapshots recorded from the MD trajectory in the absence of DNA is also very remarkable (Figure Ann.II.4.), even though the definition of the peaks in the latter is not very high. This should be attributed not only to the length of the trajectory (i.e. 25 ns only) but also to the

organization mechanism discussed above, which is based on the simultaneous formation and growing of multiple clusters (nucleation centers).

The radial distribution functions of Ca···Ca and Ca···P pairs ($g_{Ca–Ca}(r)$ and $g_{Ca–P}(r)$, respectively) obtained for the crystal structure of natural HAp and the simulated systems, corroborate the role of DNA as a template. Thus, the similitude of the profiles derived from the trajectories in the presence and absence of DNA as well as the rapid definition of such profiles (i.e. the profile remain practically invariant after 10 ns) indicate that DNA does not inhibit the nucleation of HAp around it, as recently suggested.[1] Indeed, the correspondence between the peaks derived from simulations and the peaks calculated using the crystallographic coordinates of HAp confirms that, after a few ns, the inorganic clusters tend to organize into pseudo-ordered structures.

Figure 3.6a depicts a representative calcium phosphate cluster obtained at the first stages of the simulation (<1 ns) without B-DNA. The formation of such simple clusters seems to be a requisite for the growth of HAp from inorganic solutions. Figure 3.6b and 3.6c show clusters involving Ca^{2+}, PO_4^{3-} and OH^- ions from simulations without and with DNA, respectively, which suggest the nucleation of HAp.

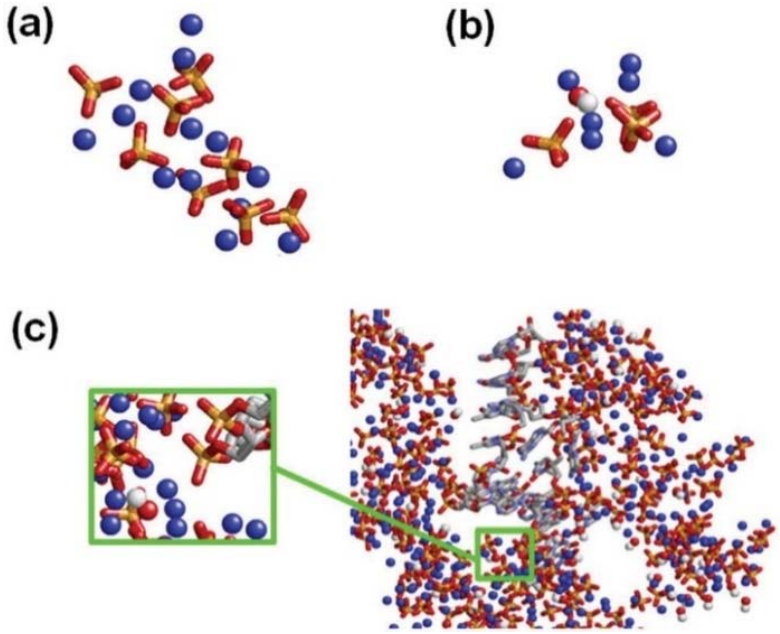

Figure 3.6. (a). Representative calcium phosphate cluster obtained at the first stages of the simulation without DNA. Representative clusters including OH^- ions extracted from the simulation (b) without and (c) with DNA. Reproduced from ref. [13] with permission from The Royal Society of Chemistry.

3.3.1.3. Synthesis of hydroxyolites in vitro

In this section, experimental studies for the biomineralization of DNA into HAp have been conducted by mixing aqueous solutions containing Ca^{2+}, PO_4^{3-} and OH^- ions with DNA. Corroboration of the formation of hydroxyolites and characterization of the biomineral were carried out after the removal of superficially adsorbed DNA by enzymatic digestion.

Figure 3.7. shows the morphologies of HAp samples prepared using $Ca(NO_3)_2$, $(NH_4)_2HPO_4$ and fish sperm DNA in aqueous solution and under two well differentiated conditions based on previously established methodologies.[5-7] In order to obtain nanocapsules the solutions containing Ca^{2+} and PO_4^{3-} ions were quickly mixed at high pH, which favored rounded morphologies. Aggregation was avoided by adding a surfactant (CTAB), highly diluted solutions being used. DNA molecules should form micelles in solution that adsorbed Ca^{2+} ions on their surface by electrostatic interaction.[7] After the addition of the solution containing PO_4^{3-}, the reaction took place forming HAp around the initial DNA micelles.

Figure 3.7a clearly shows the presence of hollow nanospheres with a diameter close to 20 nm, which may contain the DNA molecules inside. In contrast, solid nanospheres of similar size (inset of Figure 3.7a) were obtained when DNA was not added to any of the initial inorganic solutions. A high concentration of DNA was employed for the preparation of nanocrystals and, consequently, it was added to the PO_4^{3-} solution instead of the Ca^{2+} one in order to avoid the formation of complexes that could limit solubility. The crystal anisotropy and, specifically, a preferred growth along the crystallographic c axis were favoured by decreasing the pH to 10.31. The phosphate solution was slowly added over the Ca^{2+} solution to avoid a rapid precipitation, allowing the development of well formed crystals from a primary nucleus. Figure 3.7b shows the crystalline aggregates that were attained under these selected conditions. Aggregates had a length close to 2 μm and a variable width that was found to depend on the number of constitutive nanorods, each with a width close to 20 nm.

UV-vis spectra, which are displayed in Figure 3.8., clearly demonstrate the presence of DNA molecules in both nanocapsules and nanorod preparations since a characteristic absorption peak at 260 nm was detected in both cases.

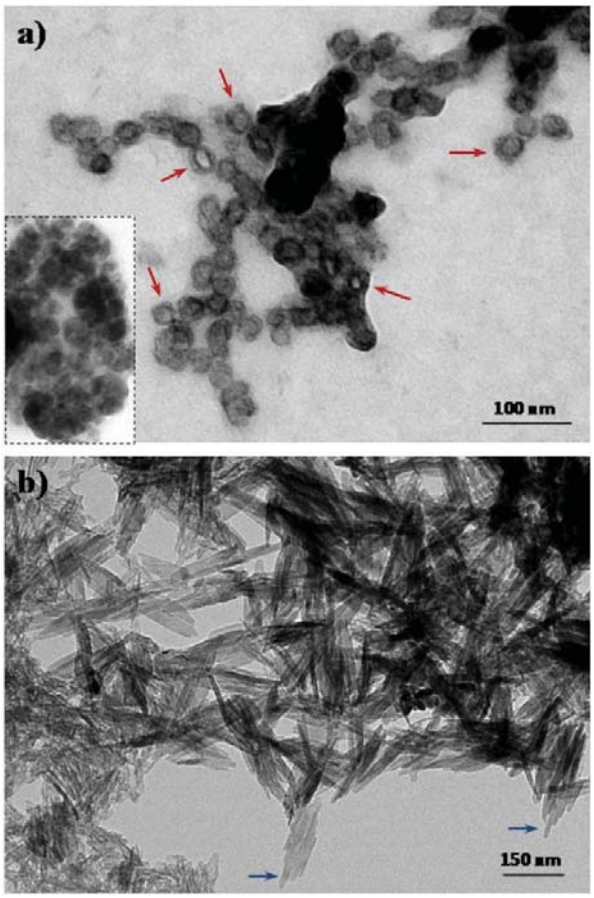

Figure 3.7. TEM micrographs showing HAp-DNA nanocapsules (a) and nanocrystals (b). Red arrows point out capsules with a clearly distinctive contrast that suggest the incorporation of DNA in their inner part. For comparison purposes the inset shows nanocapsules prepared under the same experimental conditions but in absence of fish sperm DNA. Blue arrows emphasize the nanorods that constitute the crystal aggregates. Reproduced from ref. [13] with permission from The Royal Society of Chemistry.

This absorbance increases after dissolution of the sample with the acid medium, as expected for DNA molecules encapsulated inside the HAp nanoparticles. It should be emphasized that such an increment is very remarkable in the nanorod preparation, corroborating the shielding effect hypothesis discussed above. Figure 3.8. also shows the spectra of digested samples. As expected, the absorbance at 260 nm decreases considerably after enzymatic treatment, reaching a value practically zero for the nanorod sample. However, the significant absorbance detected after dissolution of the sample in acid medium unambiguously demonstrates the incorporation of DNA inside nanoparticles.

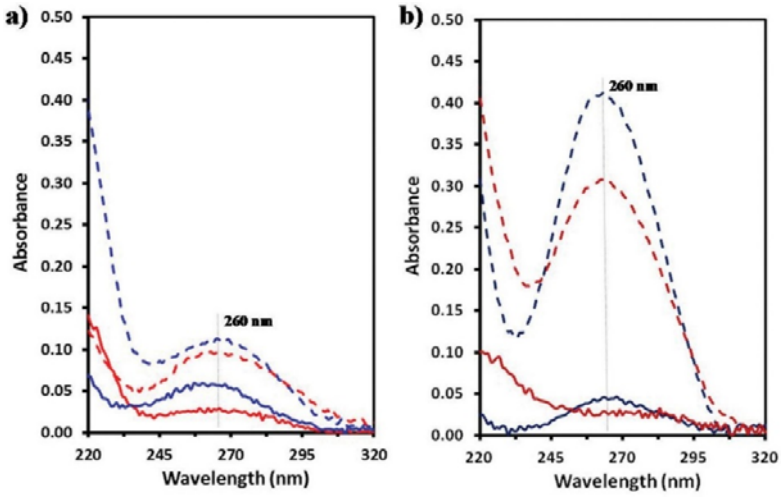

Figure 3.8. UV-vis absorption spectra of the aqueous solution/dispersion of HAp-DNA nanocapsules (a) and nanocrystals (b) (with blue traces). Spectra from samples digested with deoxyribonuclease to eliminate adsorbed DNA are indicated with red traces, whereas those corresponding to samples dissolved with the acid medium are indicated with dashed traces. Reproduced from ref. [13] with permission from The Royal Society of Chemistry.

The quantification of DNA in nanoparticles was performed for the nanorod preparation due to a greater amount of sample being available. For this purpose, the absorbance measurement (A260) was multiplied by the well-known conversion factor of 50 $\mu g \cdot mL^{-1}$ (for double-strand DNA) to obtain the total amount of DNA. Results indicate that approximately 11 µg and 33 µg of DNA are adsorbed on the surface or encapsulated inside the 1 mg of HAp nanorods, respectively. Accordingly, an encapsulating efficiency close to 25% is derived, considering that the DNA/HAp ratio from synthesis was 127 $\mu g \cdot mg^{-1}$.

Similar conclusions are derived from the electrophoretic pattern of HAp/DNA nanorods Figure 3.9.. Both the DNA superficially adsorbed and that incorporated inside the particles give rise to the high intense spot observed on lane 4. This corresponds to the particles digested with EDTA, which is capable of chelating calcium ions. The intensity of the latter spot is clearly higher than that observed for the spot of lane 3, which refers to the initially loaded particles (i.e. it is basically attributed to both DNA adsorbed on the surface and DNA internally loaded but able to migrate).

.

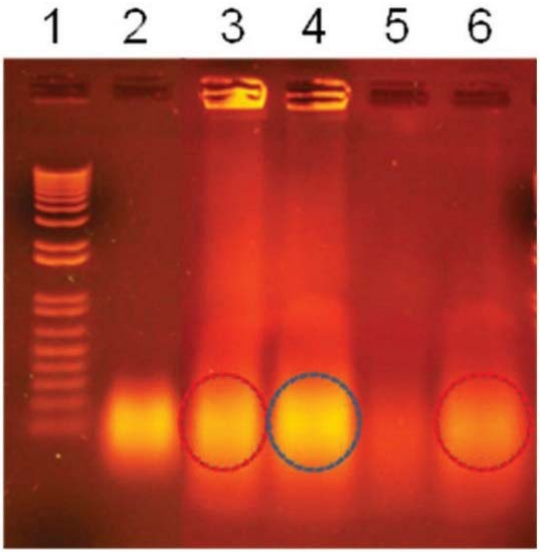

Figure 3.9. Electrophoretic pattern of HAp-DNA nanocrystals. Lane 1: molecular weight marker. Lane 2: Fish sperm DNA. Lane 3: HAp-DNA nanocrystals. Lane 4: HAp-DNA nanocrystals dissolved with EDTA. Lane 5: HAp-DNA nanocrystals digested with deoxyribonuclease. Lane 6: HAp-DNA nanocrystals digested with deoxyribonuclease and then dissolved with EDTA. Note that the intensity of the DNA signal in lane 4 (blue circle) is similar to the addition of the intensity of DNA signals in lanes 3 and 6 (red circles). Reproduced from ref. [13] with permission from The Royal Society of Chemistry.

The fluorescence observed in the wells of lanes 3 and 4, and even the continuous smear, reflect the restricted mobility of DNA in the gel, which is caused by a progressive release from the bigger particles. Lanes 5 and 6 correspond to particles in which the adsorbed DNA was previously digested with deoxyribonuclease to eliminate this superficial DNA. A high intense spot is observed after dissolution with EDTA (lane 6) while a low signal is detected before dissolution (lane 5), as expected for encapsulated DNA. Finally, Figure 3.9. points out that the intensity of the DNA spot of lane 4 results from the addition of the signals of DNA adsorbed in the surface (lane 3) and DNA incorporated inside the particle (lane 6).

3.3.2. Dissolution of a hydroxyolite crystal

A HAp nanoparticle of composition similar to that found in previous experimental studies[8] was constructed using Ca^{2+}, Mg^{2+} , OH^{-} , PO_4^{3-}, and CO_3^{2-} ions (Figure 3.10.). For this purpose, we used one of the small aggregates obtained in a previous work[8] as a starting

point, which was spontaneously formed in neutral water from a bulk solution of the same ions (details in Annex IV). The resulting mineral mold, which contained 656 Ca^{2+}, 42 Mg^{2+}, 112 OH^{-}, 412 PO_4^{3-}, and 14 CO_3^{2-} ions, was surrounded by 50,552 water molecules, 1,000 H_3O^{+}, and 1,000 Cl^{-}. The total number of explicit atoms, including ds-DNA, was 160,328.

Two independent molecular models were constructed using this strategy because the study was performed using two sets of independent MD simulations. Although results discussed in this work correspond to one of such sets only, similar observations were obtained from the second set, giving consistency to their interpretation and discussion.

The dissolution of the hydroxyolite was followed through changes in the Ca^{2+} distribution using two parameters: 1) the partial radial distribution function of Ca^{2+} ·Ca^{2+} pairs, g_{CaCa}, which is not expected to detect the first stages of the dissolution process; and 2) a ρ(L)–L profile, where ρ(L) = 656/M(L), 656 is the total number of Ca^{2+} ions in the model, L is the edge of the identical cubes in which the simulation box was divided, and M(L) is the number of cubes of edge L containing at least one Ca^{2+}. Accordingly, ρ(L) defines the average number of Ca^{2+} per occupied cube of edge L, the shape of the ρ(L)–L profile being very sensitive to the migration of ions from the initial nanoparticle to the bulk solution. The distribution of the Ca^{2+} in equilibrated hydroxyolite is described in Figure 3.11..

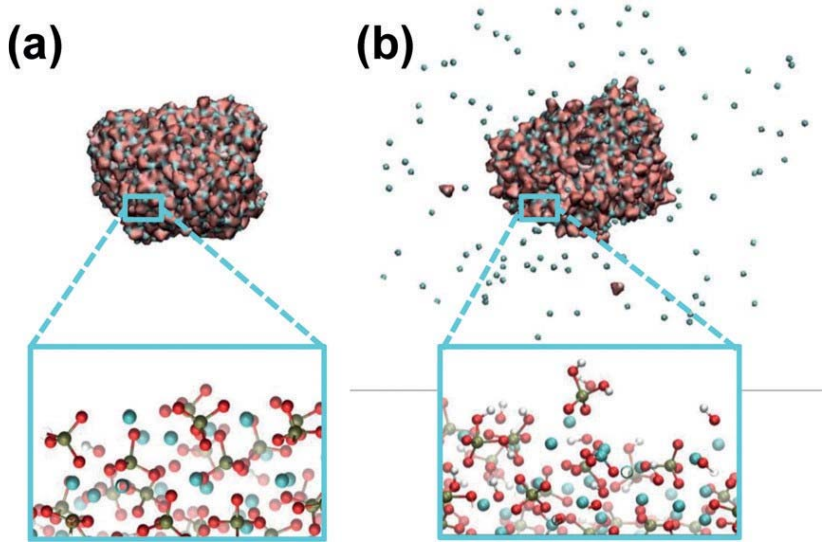

Figure 3.10. Hydroxyolite nanoparticle: (a) after equilibration; and (b) after multi-step MD simulation (last snapshot). The distribution of the ions at the surface is illustrated in the magnifications. Brown, red, light grey, and blue balls represent P, O, H, and Ca, respectively. Reproduced from ref. [14] with permission from John Wiley and Sons.

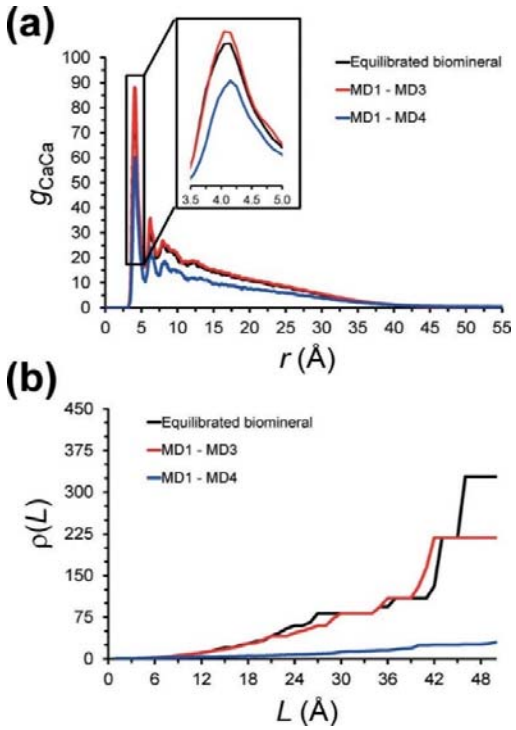

Figure 3.11. a) Radial distribution functions of $Ca^{2+}\cdots Ca^{2+}$ pairs and b) ρ(L)–L curves calculated for hydroxyolite after equilibration, three consecutive runs at temperatures increasing from 298 to 350 K (MD1–MD3), and the latter trajectories plus a run of 1.75 ms at 350 K with proton transfer (MD1–MD4). The inset in (a) evidences the migration of the Ca^{2+} from the hydroxyolite surface to the solution during MD4. Reproduced from ref. [14] with permission from John Wiley and Sons.

The equilibrated hydroxyolite was the starting point of the first MD run (MD1), which corresponded to 300 ns of NPT MD at 298 K and 1 bar pressure. After this, both the g_{CaCa} and ρ(L)–L profiles remained practically unchanged, evidencing that the dissolution process had not start yet. Then, the temperature was slowly increased to 320 K, a production run of 200 ns being subsequently conducted (MD2). The g_{CaCa} profile calculated for the last snapshot was again identical to that of the equilibrated hydroxyolite, whereas the ρ(L)–L profile exhibited some differences. However, a careful analysis of the results showed that such variations were not due to the migration of ions but to a change in the volume of the biomineral. Similar features were obtained when the temperature was slowly increased from 320 to 350 K and a production run of 20 ns (MD3) was conducted (Figure 3.11.). Accordingly, the nanoparticle underwent small rearrangements produced by a thermal expansion, which resulted in a variation in the corresponding ρ(L)–L curve. More

specifically, the volume of the nanoparticle increased from 86,368 $Å^3$ at 298 K to 88,436 $Å^3$ (2.4 %) and 88,509 $Å^3$ (2.5 %) at 320 and 350 K, respectively.

The solubility of HAp in acid environments is known to increase with temperature.[1] However, simulations indicate that the description of the interactions at the nanoparticle/bulk interface is not enough to promote the hydroxyolite dissolution, independently of the temperature. The influence of the acidic conditions was introduced in the mechanism by considering reactions (1) [Eq. (1)] and (2) [Eq. (2)] in the next MD step:

$$PO_4^{3-} + H_3O^+ \rightarrow HPO_4^{2-} + H_2O \qquad (1)$$

$$HPO_4^{2-} + H_3O^+ \rightarrow H_2PO_4^- + H_2O \qquad (2)$$

Changes in the g_{CaCa} and ρ(L)–L profiles after 0.75 ms demonstrated that the nanoparticle was dissolving (i.e. 25 Ca^{2+} migrated from the hydroxyolite surface to the solution). This dissolution process continued for the next 1 ms (Figure 3.11.). At the end of MD4, the intensity of the sharp peak at ≈ 4.1 Å in the g_{CaCa} profile decreased significantly (28 %) with respect to the equilibrated mineral, which was consistent with the drastic reduction of ρ(L) at relatively small L values. The number of Ca^{2+} that migrated from the nanoparticle to the solution accounted for 144 (i.e., 22 %) after 1.75 ms (Figure 3.10.). In addition, the proton transfer mechanism facilitated the dissolution of 7 Mg^{2+} (17 %), 4 OH^- (4 %), 63 PO_4^{3-} (16 %), 2 HPO_4^{2-}, and 1 CO_3^{2-} (7 %). This demineralization is dominated by the detachment of Ca^{2+} from the hydroxyolite nanoparticle (i.e., decalcification), the participation of Mg^{2+} ions in such process being very small at this stage.

Multi-step simulations suggested a decalcification for hydroxyolite dissolution, triggered by proton transfer and acid–base-based reactivity of the phosphate species. These results are in complete agreement with experimental observations on the dissolution of HAp with different acids.[9,10] On the other hand, results reflect a polynuclear detachment of Ca^{2+} (Figure 3.12.). Although some authors suggested that this mechanism is more probable for HAp dissolution in mild acid environments (pH within 5.0–7.2 and Ca/P molar ratios of 1.0–2.0),[11] other authors reported a mononuclear mechanism driven by the formation and growth of pits.[12]

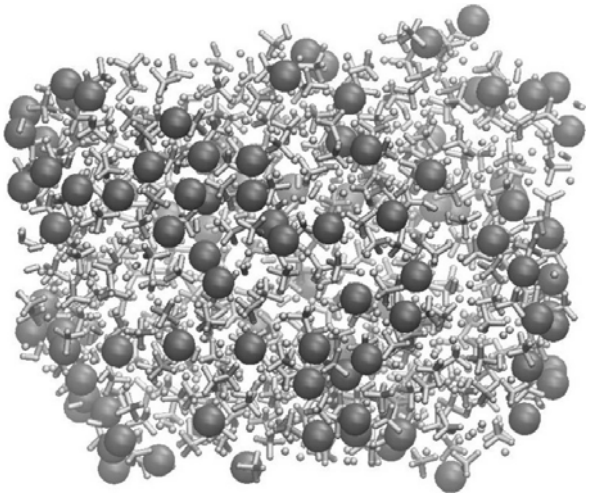

Figure 3.12. Dissolution of the hydroxyolite particle following a polynuclear mechanism. The initial nanoparticle (i.e., starting point for MD1) is displayed. All atoms are depicted with small light grey balls with the exception of Ca^{2+} detached from the surface along MD4 (i.e., the simulation considering proton transfer), which are represented by large dark grey balls. As it can be seen, Ca^{2+} ions detach from multiple centers widely distributed through the surface in the initial configuration. Accordingly, the decalcification process follows a poly-nuclear mechanism rather than a mononuclear one (i.e., detachment of Ca^{2+} ions from a few close centers). Reproduced from ref. [14] with permission from John Wiley and Sons.

Results obtained in this work provide direct evidence that Ca^{2+} is detached from multiple centers widely distributed on the surface. In addition, results show that Ca^{2+} mobility increases following the transformation of phosphates into $H_2PO_4^-$, thus reflecting changes in the coordination caused by the steric and electrostatic components. The latter promotes dissolution of the biomineral.

The structural stability of the ds-DNA can be assessed in Figure 3.13., which displays the temporal evolution of the root-mean-square deviation (RMSD) with respect to the ideal B-DNA double helix. The RMSD was calculated by considering all atoms different from hydrogen. The ds-DNA remains mostly unaltered through the whole range of examined temperatures. The average RMSD values calculated for MD1 (298 K), MD2 (320 K), and MD3 (350 K) are 0.42 ± 0.06, 1.02 ± 0.03, and 1.51 ± 0.01 Å, respectively. The RMSD increases slowly along MD4 as a consequence of the penetration of the protons. In spite of this, the average RMSD for the last 500 ns of MD4 (2.03 ± 0.04 Å) is still very low. This

stability has been attributed to the reduction of the electrostatic strain at the biomolecule associated to the hydrogenated phosphates at the internal regions.

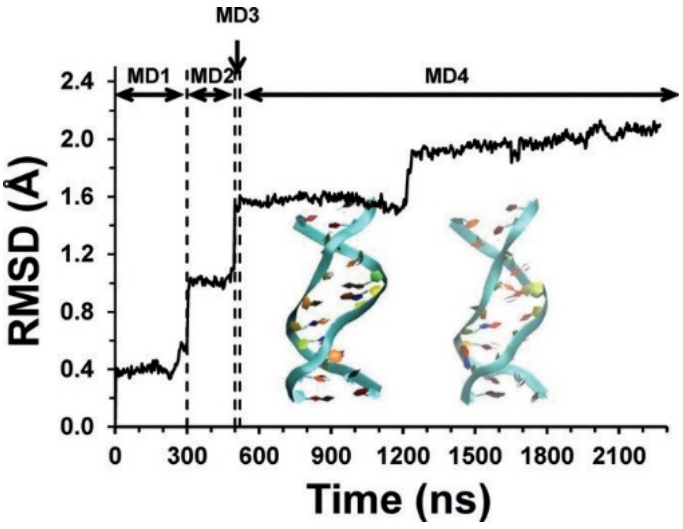

Figure 3.13. Evolution of the RMSD along the multi-step MD for the ds-DNA relative to the canonical B-DNA. The double helix is represented by using a ribbon model for the equilibrated system (starting point of MD1) and for the last snapshot of MD4. Reproduced from ref. [14] with permission from John Wiley and Sons.

3.4. Conclusions

The mechanism proposed for the growth of apatite crystals using the double helix of B-DNA as nucleating agent represents an alternative to classical encapsulation processes (i.e. loading of biomolecules at the nanopores and/or on the surface). Thus, the controlled formation of biominerals (i.e. porous nanoparticles of mineral growing from biomolecules) combined with conventional encapsulation approaches may be used to design therapies with higher efficacy and durability. MD simulations have been used to investigate the initial stages of nucleation and cluster formation of calcium phosphate at a B-DNA double helix in aqueous solution. At room temperature, calcium ions interact with DNA phosphates to form ion complexes, but attracted by electrostatic forces, they coordinate to PO_4^{3-} and other calcium ions starting the formation of clusters.

The overall observation of the results reported in this chapter indicates that the DNA double helix promotes the nucleation of HAp, acting as a template. The embryonic calcium phosphate clusters formed at the first stages of the simulation grow and transform into

complex clusters, in which Ca^{2+}, PO_4^{3-} and OH^- ions occupy positions that resemble those of crystalline HAp. This re-organization, which is largely influenced by the incorporation of OH^- into the clusters, supports the benefit of the interaction between the DNA and the inorganic ions for the formation of HAp. Experimental studies demonstrated the biomineralization of DNA into HAp obtained by mixing aqueous solution containing Ca^{2+}, PO_4^{3-} and OH^- ions with DNA. The existence of encapsulated DNA inside of the HAp crystal was confirmed after removal of superficially adsorbed DNA by enzymatic digestion and further redissolution of the mineral that led to the release of the entrapped DNA.

Concerning the dissolution mechanism, atomic-level studies shed light on the acidic dissolution of HAp and hydroxyolites. Those processes happen following a decalcification mechanism where calcium ions detachment is triggered by the initial hydration of phosphates and it is enhanced by their further hydrogenation resulting from hydronium reactivity. The decalcification occurs through a polynuclear process: the escape of the calcium ions occurs through multiple independent centers widely distributed on the surface. Thus, the detachment of the calcium ions is caused by the important electrostatic alterations induced by the HPO_4^{2-} and $H_2PO_4^-$ species rather than by the detachment of neighboring calcium ions. This result has enormous implications for the development of therapies in which fixation of Ca^{2+} is crucial, as for example those related with the fight against osteoporosis. Also, results prove that HAp acts as a shield for ds-DNA biopolymer, protecting their functionality from temperature-stressing conditions and chemicals. Accordingly, the mechanism unveiled in the chapter contribute to the understanding about how hydroxyolite particles are able to deliver nucleic acids in the cytosol or in the cell nucleus to carry out the transfection processes.

The approach discussed in this chapter, using DNA as a nucleator of the non-viral vectors of transfection, represents an alternative to conventional gene therapy strategies, in which plasmids are transported at the surface of the mineral and, therefore, are exposed to undergoing the attack of enzymes. With the strategy discussed here, DNA remains protected against external degradation until the hydroxyolite crosses the cell membrane and starts the dissolution process. From that moment, the dissolution profile would be dependent on the surrounding pH and calcium concentration. Lysosomes, acidic vacuoles that contain hydrolytic enzymes able to degrade most biomolecules will start degrading the hydroxyolites after endocytosis. The result of such a degradation process will be the release of DNA or

RNA inside the cell, meaning that foreign genetic information may interact with the cellular ribosomes in order to synthesize the proteins encoded in its sequence (in case the release happens in the cytosol) or be recombined with the own genome of the cell if the release happens inside the cell nucleus, completing the transfection process. Such processes are highly interesting from the perspective of some diseases and we have contributed through this chapter to increasing the knowledge about such a process mediated by hydroxyolites.

3.5. References

1. Okazaki M., Yoshida Y., Yamaguchi S., Kaneno M., Elliot J.C., Affinity binding phenomena of DNA onto apatite crystals, *Biomaterials* (**2001**), *22*, 2459–2464. DOI:10.1016/S0142-9612(00)00433-6.

2. Ngourn S.C., Butts H.A., Petty A.R., Anderson J.E., Gerdon A.E., Quartz crystal microbalance analysis of DNA-templated calcium phosphate mineralization. *Langmuir* (**2012**), *28*, 12151–12158. DOI: 10.1021/la300949y.

3. Harding, J.H., Duffy D.F., Sushko M.L., Rodger P.M., Quigley D., Elliot J.A., Computational techniques at the organic−inorganic interface in biomineralization, *Chemical Reviews* (**2008**), *108*, 4823–4854. DOI: 10.1021/cr078278y.

4. Hiughes J.M., Cameron M., Corwley K.D. Structural variations in natural F, OH, and Cl apatites. *American Mineralogist* (**1989**) *74*, 870–876. DOI: Not assigned.

5. Zhang Y., Lu J., A simple method to tailor spherical nanocrystal hydroxyapatite at low temperature, *Journal of Nanoparticle Research* (**2007**), *9*, 589–594. DOI: 10.1007/s11051-006-9177-3.

6. Wang P., Li C., Gong H., Jiang X., Wang H., Li K., Effects of synthesis conditions on the morphology of hydroxyapatite nanoparticles produced by wet chemical process, *Powder Technology* (**2010**), *203*, 315–321. DOI: 10.1016/j.powtec.2010.05.023.

7. Qi C., Zhu Y-J., Lu B-Q., Zhao X-Y., Zhao J., Chen F., Hydroxyapatite nanosheet-assembled porous hollow microspheres: DNA-templated hydrothermal synthesis, drug delivery and protein adsorption, *Journal of Materials Chemistry* (**2012**), *22*, 22642–22650. DOI: 10.1039/C2JM35280J.

8. Revilla-López G., Casanovas J., Bertran O., Turon P., Puiggalí J., Alemán C., Modeling biominerals formed by apatites and DNA, *Biointerphases* (**2013**), *8*, 10. DOI:10.1186/1559-4106-8-10.

9. Dorozhkin S.V., Dissolution mechanism of calcium apatites in acids: A review of literature, *World Journal of Methodology* (**2012**), *2*, 1–17. DOI:10.5662/wjm.v2.i1.1.

10. Yoshioka M., Yoshida Y., Inoue S., Lambrechts P., Vanherle G., Nomura Y., Okazaki M., Shintani H., Van Meerbeek B., Adhesion/decalcification mechanisms of acid interactions with human hard tissues, *Journal of Biomedical Materials Research* (**2002**), *59*, 56–62. DOI: 10.1002/jbm.1216.

11. Christoffersen M.R., Dohrup J., Christoffersen J., Kinetics of growth and dissolution of calcium hydroxyapatite in suspensions with variable calcium to phosphate ratio, *Journal of Crystal Growth* (**1998**), *186*, 283–290.
DOI:10.1016/S0022-0248(97)00473-9.

12. Tang R.K., Orme C.A., Nancollas G.H., A new understanding of demineralization: The dynamics of brushite dissolution, *Journal of Physical Chemistry B* (**2003**), *107*, 10653– 10657.
DOI:10.1021/jp0346312.

13. Bertran, O., del Valle L.J., Revilla-López G., Chaves G., Cardús L., Casas M.T., Casanovas J., **Turon P***, Puiggalí J.*, Alemán C*., Mineralization of DNA into nanoparticles of hydroxyapatite, *Dalton Transactions* (**2014**), *43*, 317-327.
DOI:10.1039/c3dt52112e.

14. Bertran, O, Revilla-López, G., Casanovas, J., del Valle, L., **Turon, P***, Puiggalí, J*, Alemán, C*, Dissolving Hydroxyolite: A DNA Molecule into Its Hydroxyapatite Mold, *Chemistry-A European Journal* (**2016**), *22*, 6631–6636.
DOI: 10.1002/chem.201600703.

Chapter 4

Surviving Mass Extinctions through Biomineralized DNA

Chapter 4

Surviving mass extinctions through biomineralized DNA[1]

4.1. Preamble

As a consequence of the research that withstands the previous chapter, we validated that HAp protects ds-DNA against both temperature and chemicals effects, being noteworthy that despite its fragility the double helix is preserved through the encapsulation process keeping it functional. Furthermore, during its dissolution, HAp totally or partially protects DNA from physical and biochemical stressing factors, like enzymatic degradation until DNA is completely released (i.e. by regulating the pH in the cytosol or cell nucleus due to the release of HPO_4^{2-} and $H_2PO_4^-$ ions from protonated HAp surface). Thus, we concluded that both biomineralization process based on DNA encapsulation by the surrounding ions, as calcium and phosphate usually ubiquitous in cells and extracellular matrix, and dissolution process should protect the genetic information contained in the hydroxyolite capsule. However, when DNA is only adsorbed at the surface of the mineral, it should be easily attacked by endonucleases triggering its degradation and disappearance of genetic information, that from a certain perspective is a waste that nature only would allow if a higher benefit would be achieved (i.e. to degrade some mutations that should not be preserved).[1]

The hydroxyolite, which has to be understood as a DNA molecule in its HAp mold, might have important implications in several fields (i.e. for the development of novel strategies for gene therapy or for its potential relation with some diseases). Moreover, we postulate that the HAp microcalcifications in certain diseases such as breast cancer might be related to the formation of hydroxyolites and we are convinced that such investigation merits specific attention. As we are performing such research in a clinical context, we decided not to include that part in this thesis and will be disclosed elsewhere. However, we decided to extend the hydroxyolite concept to other disciplines as paleontology, looking for some clues that could explain why after mass extinctions events life was reborn with even more diversity and

---

[1] Concepts article. Turon P*, Puiggalí J., Bertrán O, Alemán C.*, Surviving Mass Extinctions through Biomineralized DNA, *Chemistry - A European Journal* (**2015**), *21*, 18892 – 18898.
DOI:10.1002/chem.201503030. Reproduced with permision from John Wiley and Sons.

strength. In this chapter, we do not pretend to close the full gap about how life survived through mass extinction events but we intend to give a new insight on that debate using as a basic premise of our hypothesis that DNA templates HAp capsules and can be release again to the life mainstream when environmental conditions become more favorable.

From the mass extinction events perspective, we discuss the formation and resilience of hydroxyolite particles that may have made the difference for the survival of life in early Earth.[2] Results from this work suggests that once formed, hydroxyolite particles can be viewed as nanocontainers that store and preserve DNA or RNA from changing environmental conditions.

4.2. Purpose

In this chapter we focus on the third sub-objective defined in Chapter 1. We revisit it in this section to be used as an initiator of the hypothesis we are going to developed that is fully based on our research detailed in Annex I, II, III and IV, and summarized in Chapter 3.

We note that we focus in the scenario related to periods of mass extinction, one of the most aggressive events that life has faced. This is the aim of this objective is to determine the physical, chemical, and biological implications of the mineralization of DNA for the persistence of life after aggressive events. Thus, we define the sub-objective 3 as:

Sub-objective 3. "*To develop a conceptual model about the implications of DNA being protected by hydroxyapatite facing environmental attacks and its consequences for other disciplines as paleontology (i.e. in mass extinction events on early Earth), biology, biotechnology and medicine"*

Then, through the chapter we discuss the potential implications of encapsulating a nucleic acid inside a HAp shield, a mineral that wraps DNA and RNA as a mold.

4.3. Introduction

Even in the worst of conditions, such as those which occurred during mass extinction events, life on Earth never totally stopped. Aggressive chemical and physical attacks able to sterilize or poison living organisms occurred repeatedly. Surprisingly, DNA was not degraded, denatured or modified to the point of losing the capability of transferring the genetic information to the next generations. After the events of mass extinction life was able to survive and thrive. DNA was passed on despite being an extremely fragile biomolecule. The potential implications of HAp protection of DNA are discussed in the following sections including how DNA acts as a template for HAp formation, how cell death can trigger biomineralization, and how DNA can be successfully released from HAp when the conditions are favorable for life.

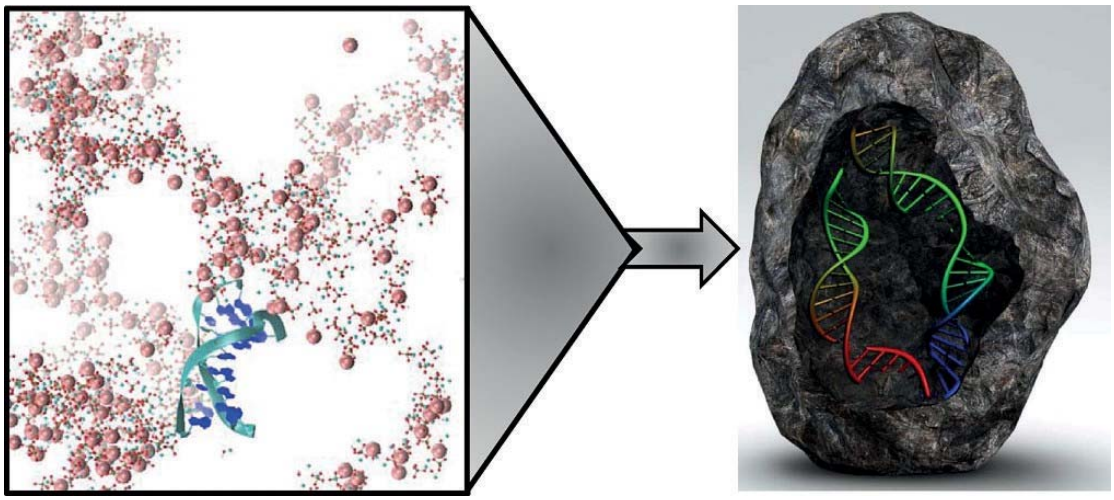

Figure 4.1. Schematic description of the hydroxyapatite encapsulation of DNA (hydroxyolite). The biomineralization process of DNA has not only been observed experimentally, but has also been described at the molecular level using atomistic computer simulations.[3,4] Reproduced from ref. [80] with permission from John Wiley and Sons.

From a simplified perspective a cell might be considered to be a soft organic DNA-protective capsule with all the functions for sustaining active life. In other words, it is a perfect mechanism for replicating and transmitting the genetic code to the next generation. The proposed existence of the universal common ancestry[5] (UCA), the grandfather of all living organisms, reinforces the robustness of DNA as a successful biochemical

infrastructure that has supported life through time. Since the time of UCA, and probably even earlier, the requirement of collecting, keeping, and transmitting information essential for life has been fulfilled using an extremely simple system based on a double pair of nitrogen bases bonded to a sugar phosphate backbone. The main hurdle for this finely tuned and fragile system is that it can easily be stopped by mild physical or chemical aggressions.

Conversely, an inactive inorganic long-lasting shield of calcium phosphate seems to be the opposite alternative to protect DNA. Are both approaches linked? From our point of view, the biomineralization process connects both, making them complementary, thus explaining the resilience of the DNA life based system.

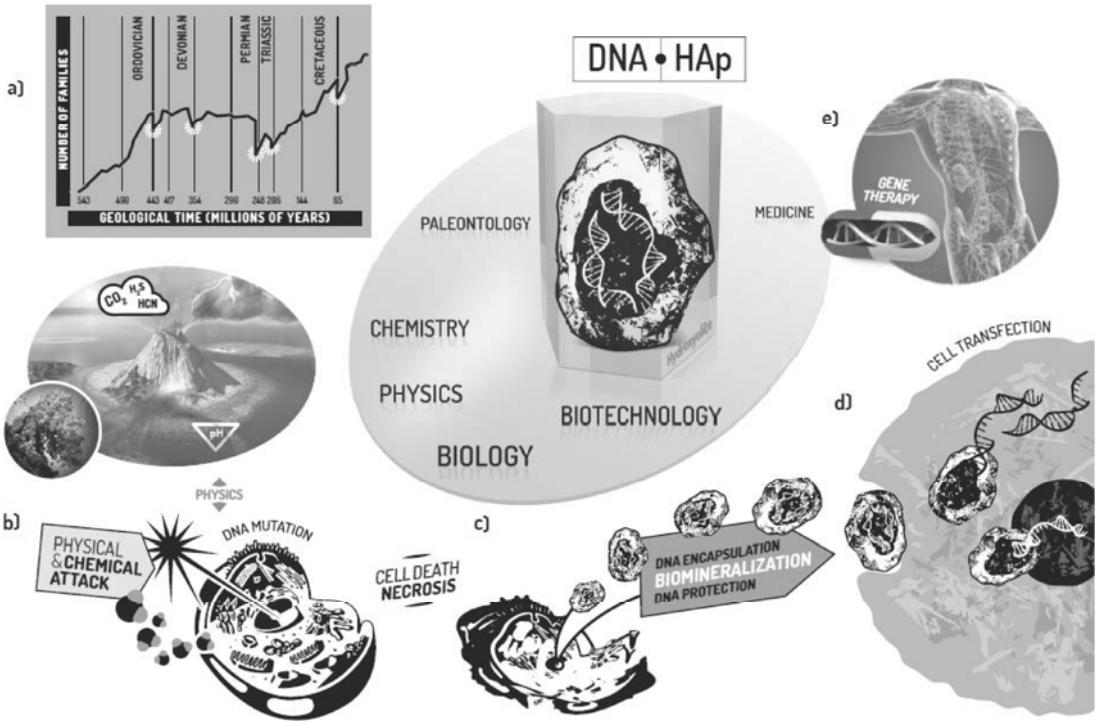

Figure 4.2. Proposed HAp–DNA (hydroxyolite) connections to multiple scientific disciplines. (a) Paleontology: number of families decrease during the Big Five mass extinction events when hydroxyolites are expected to be spontaneously formed. Graphic adapted with permission from reference.[6] Copyright 1987, Wiley. (b) Chemistry and physics: gases expulsed by volcanoes caused cell death acting as toxins or causing death by hypoxia. Radiation or temperature variations also caused cell death. (c) Biology: cells damaged or killed undergo cell death processes, like necrosis. The subsequent DNA encapsulation depends on the availability of Ca^{2+} and PO_4^{3-}. Encapsulated DNA remains functional for a long time. (d) Biotechnology: cell transfection by encapsulated DNA in HAp is likely to reintroduce DNA in the life cycle of a cell. (e) Medicine: gene therapy is based on the introduction of a gene into the cell with the objective of healing it. The use of HAp for encapsulating DNA is possible, but the rate of success is low and the process is not efficient. Reproduced from ref. [80] with permission from John Wiley and Sons.

Here we explore the synergies for life development based on bioinorganic interactions between DNA and HAp and the role of HAp in biochemical reactions. We consider cell death as a trigger of the biomineralization process and the processes of reintroduction of the biomineralized DNA in the life cycle, drawing conclusions on how DNA could survive through mass extinction events.

4.4. DNA–HAp interactions

Extinction events have occurred several times since life began. They had catastrophic consequences for living organisms, significantly reducing the number of living species (Figure 4.2.). The "Big Five", Ordovician (ca. 443 Myr), Devonian (ca. 359 Myr), Permian (ca. 251 Myr), Triassic (ca. 200 Myr) and Cretaceous (ca. 65 Myr), were remarkably intense (> 75 % reduction of species).[7] Surprisingly, DNA (the only mechanism for transferring the genetic code to next generations) was able to be passed on without being deactivated.

Current theories on the origins of life propose an initial RNA world[8] and posterior development of DNA, suggesting that both RNA and DNA biopolymers were likely to be synthesized through heterogeneous catalysis on mineral surfaces such as montmorillonite.[9-11] The DNA capacity of interaction with several inorganic substrates (not only silicates) is remarkable.[12,13] We highlight HAp for its strong capacity of interaction with biomolecules. DNA acts as a template of HAp in physiological conditions. Additionally, we note that the nature of DNA–HAp interaction on the crystal surface depends on the exposed face of the crystal (Figure 4.3.).[14] The binding on the (001) face, the most favorable, maintains the B-DNA double helix conformation. Conversely, the interaction on the (010) face terminated with Ca^{2+} , OH^- , and PO_4^{3-}—denoted (010; $Ca^{2+}OH^-$)— provokes DNA structural deformations and rejection. Finally, the binding on the side of the (010) face terminated with Ca^{2+} and PO_4^{3-} ions (010; Ca^{2+}) shows very strong attractive interactions, which are intense enough to distort the double helix structure and push the molecule towards the surface. Additionally, considering the morphological aspects of HAp, we observed that amorphous nanospheres and fusiform rods, synthesized under controlled reaction conditions, showed enhanced protection against the aggression of external factors like enzymatic degradation by DNAse compared to sheet crystals.[14]

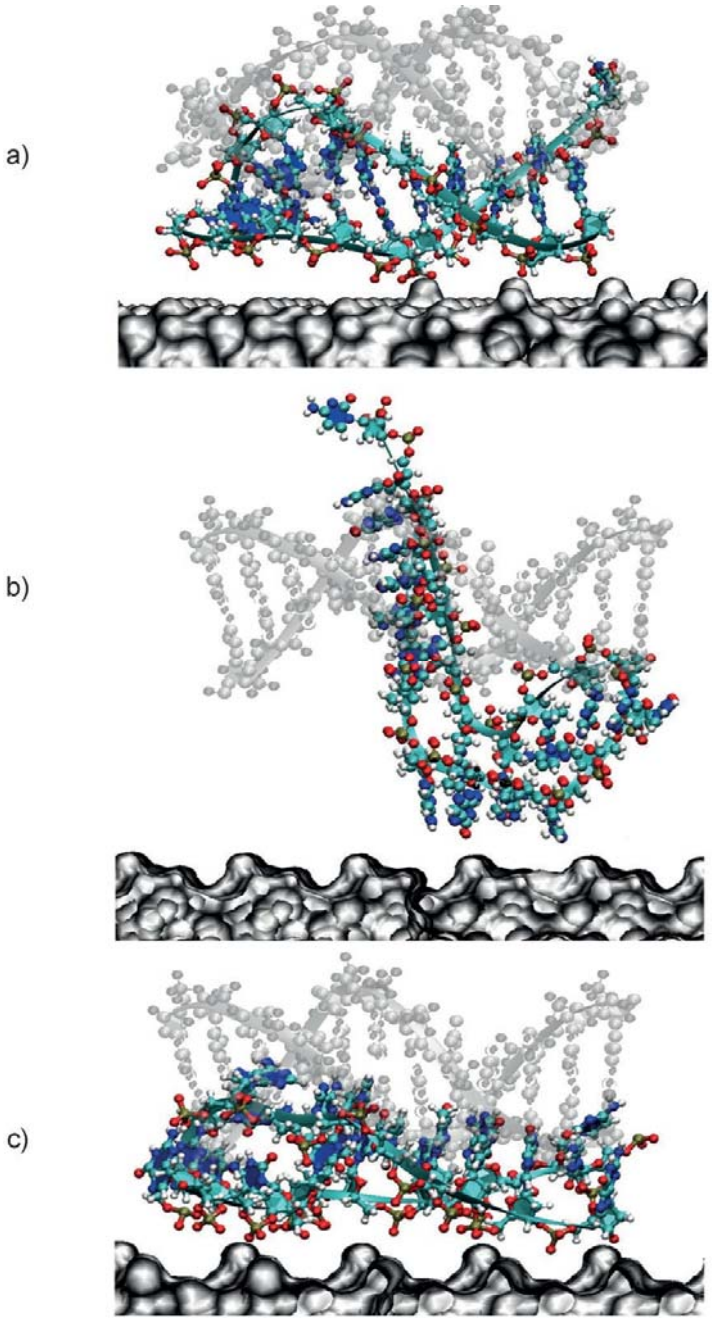

Figure 4.3. Interaction of DNA with three different HAp surfaces (in grey the initial state, in colour the final state): (a) DNA is attracted to the surface of face (001) and DNA double helix is not distorted, (b) DNA is distorted and repelled when it interacts with the face (010 ; Ca^{2+} -OH^{-}) terminated with Ca^{2+} , OH^{-} , and PO_4^{3-} , (c) DNA is strongly attracted to the side (010 ; Ca^{2+}) causing double helix distortion and pushing the molecule towards the surface. Reproduced from ref. [80] with permission from John Wiley and Sons.

Travelling back to the very origin of life it is worth noting that the finding of the first abiotic carbon was reported in 1996 by Mojzsis and co-workers[15] when they identified a ^{13}C depleted microscopic graphite inclusion inside apatite dated 3,830 million years old in Akilia (Greenland). It was interpreted as a possible biomarker indicating the early connection between apatites and life. Recently, well preserved soft tissue in fragments of demineralized cortical and/or medullary bone from the Cretaceous to the present day have been reported, and proteins have been detected in dinosaur bone microstructures.[16] The strong relationship between calcified structures and biopolymers can still be found in current organisms. The role of HAp as a catalyst of many organic basic reactions is not a minor one,[17-19] and of special interest are reactions in which the chemistry of surfaces is involved.[20] As an example, essential biochemical reactions take place around mineralized calcium phosphate scaffolds, such as bones (i.e. production of mesenchymal stem cells and platelets inside bone marrow).[21] Enhancing its role for homeostasis HAp incorporates fixed quantities of Mg^{2+} in its lattice;[22] this allows for the regulation of available Mg^{2+} that remains free to react in basic metabolic reactions as cell respiratory systems. Additionally, Mg^{2+} is able to stabilize DNA modulating its structure and dynamics.[25] Misbalances of Mg^{2+} are related to several diseases.

4.5. Triggers for DNA biomineralization

DNA is a biopolymer that is easily affected and degraded by chemicals[23] or physical treatment (radiation),[24] becoming mutated or denatured. The fragility of DNA-supported life systems becomes evident when unprotected cells are exposed to an excess of solar ultraviolet radiation: they become damaged, mutated, or carcinogenic.[25]

The question of how DNA was able to overcome the aggressive conditions of mass extinction events remains open.[5] Reviewing the hypotheses of how mass extinction events took place, we observe that during the Ordovician period repeated glacial episodes occurred. The uplift and weathering of the Appalachians affected the atmospheric and ocean chemistry, including the sequestration of CO_2. Additionally, at the end of the period, a gamma ray burst caused a severe depletion of the ozone layer and the Earth received intense solar ultraviolet radiation[26] that sterilized the earth's crust. The Devonian period was affected by a global cooling, weathering, and drawdown of global CO_2 with periods of anoxia. The Permian extinction event was determined by Siberian volcanic activity that led to elevated H_2S and CO_2 concentrations, which poisoned both marine and terrestrial ecosystems in conjunction

with a global temperature increase. As a consequence the oceans became more acidic and marine waters anoxic. The Triassic registered magmatic activity and elevated atmospheric CO_2 levels with an increase in global temperatures, which resulted in a calcification crisis in the world's oceans.[27] Finally, the Cretaceous period was characterized by a rapid cooling due to a bolide impact that provoked a global cataclysm. How could DNA survive as a coherent molecule keeping the ability of transmitting life despite these repeated aggressions? A plausible answer is that DNA was encapsulated or protected by HAp.

4.6. Cell death

When cells are affected by external aggressions they might undergo cell death, most likely through necrosis[28-30] but other mechanisms, such as apoptosis, necroptosis, or pyroptosis cannot be discounted.[31] Here, we use the explanation of necrosis as representative and the most likely process under these conditions. The necrotic status causes the cell membrane to collapse and release the cell content into the surrounding environment (usually the extracellular matrix). Several chemical mechanisms can trigger necrosis, such as calcium misbalance, hypoxia, ATP depletion, and excess of reacting oxygen substances (ROS). Necrosis can happen when cells suffer freezing and defreezing cycles or DNA is damaged by ultraviolet or gamma radiation. All of them can cause the uncontrolled release of DNA from the nucleus. When DNA is released in combination with calcium (Ca^{2+}) and phosphate (PO_4^{3-}) available in the cell, it can act as a calcifying template[4] and the biomineralization process will end up in a necrotic calcification.[32] Usually a calcium homeostasis system prevents this from happening. Calcium homeostatic systems appeared very early in the history of life as a survival mechanism preventing Ca^{2+} mediated cell damage. An excess of cytosolic calcium is incompatible with life, because it initiates the precipitation of phosphates, starts the aggregation of proteins and nucleic acids, and finally affects the integrity of lipid membranes.[33] Calcium, an extremely versatile ion, participates in several relevant cell processes like fertilization, embryonic pattern formation, cell differentiation, and cell death. The concentration of calcium is usually around 100 nm when the cell is at rest, but increases to 1000 nm when activated. Higher concentrations are cytotoxic. The availability of calcium in a cell is well regulated and depends on several interconnected factors.[34,35] Among them, we highlight both the role of the endoplasmic reticulum (ER), as the main store of calcium (total Ca^{2+} in ER is about 2 $mmol \cdot L^{-1}$, but free Ca^{2+} in ER is about

50–500 mmol·L^{-1}),[36] and the role of mitochondria due to their ability to rebalance the calcium concentration in the cytosol. The membrane systems of the endoplasmic reticulum (ER) hold the stores of calcium. The release is controlled by various channels (i.e. the inositol-1,4,5-trisphosphate receptor and the ryanodine receptor are the most studied), but it is interesting to note that the principal activator of these channels is Ca^{2+} itself and this autocatalytic process is central to the mechanism of Ca^{2+} signaling.[34] On the other hand, mitochondria are able to capture high concentrations of calcium ions from cytosol by allowing the precipitation of HAp inside of them.[37,38] Such reservoirs of calcium and phosphate are mobilized when mitochondria are damaged or cells are necrosed.[39] Additionally, mitochondria are able to release polyphosphates,[40,41] archaic polymers present in all living species from archae to eukaryotes, to the cytosol, in which they are then converted by hydrolysis to additional phosphates.[42] Polyphosphates might also be attracted to the HAp surface,[43] to specific sites recently defined at the atomic level, creating a polymeric outer layer on the HAp (Figure 4.4.).

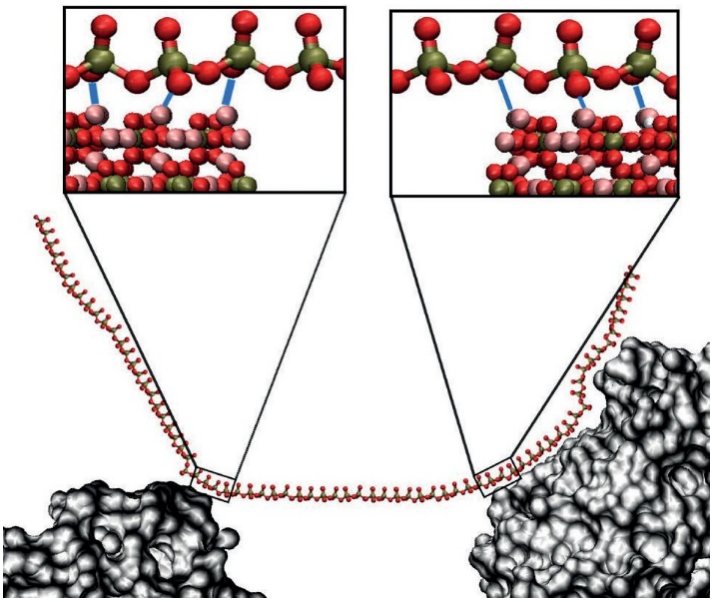

Figure 4.4. Polyphosphate binding to HAp surface. Reproduced from ref. [80] with permission from John Wiley and Sons.

The combination of both endoplasmic reticulum and mitochondria malfunctions due to external aggressions, might provide the source of both calcium and phosphate for HAp–DNA particle formation, particularly taking into consideration that mitochondria have their

own mtDNA that usually become mutated when cells are getting older.[44] Dead cells will not be viable, but DNA remains totally or partially protected from the environmental aggression when adsorbed or encapsulated. Transferring this fact to the mass extinction perspective we can expect that when cells were stressed by the aggressive environmental conditions, a significant part of them were damaged or killed. Thus a large quantity of HAp–DNA nanoparticles were likely to be formed preserving DNA from further attacks. In parallel, we recognize that other mechanisms of adaptation to environmental stressful conditions were developed during the recovery after each mass extinction event.[45]

4.7. Resilience of hydroxyapatite

The resilience of the hydroxyolite particles is also due to several additional intrinsic features of HAp that reinforce the probability of surviving the environmental attack unaltered, or with minor secondary effects. HAp is able to adsorb contaminants, like formaldehyde,[46] and can enhance their further catalytic oxidation[18] at room temperature. A high adsorption of cyanide ions by HAp is reported to be a promising air purification system.[47] Formaldehyde and cyanide are interesting because they are considered to be substances released by volcanic eruptions into the atmosphere, and they are molecules that are necessary for starting life reactions. HAp can be activated by strong chemical conditions that modify its surface texture giving high-performance properties.[48] Furthermore, HAp performs well under high radiation doses (< 30 kGy), similar to what is commonly used to sterilize medical devices, as HAp is able to protect organic polymers, like collagen, without losing their biocompatibility properties.[49] Interestingly, the radiation might generate active oxygen radicals on the HAp surface, such as $^{\cdot}OH$, $^{\cdot}O_2^-$ (UV) or $^{\cdot}CO_2^-$ (γ), which could lead to the enhancement of chemical reactions, including DNA mutations.[50,51] Ionized electrons by radiation remain trapped in the HAp crystalline structure, which is a useful feature as a bone dosimeter for recording the radiation history of skeleton or fossil dating. [52] Finally, HAp is able to retain a wide variety of heavy metal ions in its structure that could damage DNA, such as lead, copper, tin, uranium, aluminum, and nickel.[53,54]

HAp is not the only candidate for DNA protection: for example, silicates share some structural characteristics with apatite which would be compatible with DNA interactions.[55,56] Montmorillonite, illite, and kaolinite represent clay minerals that are able to protect DNA from nucleases during natural bacterial genetic transformation[57,58] and they are also useful

for gene delivery as silica nanoparticles, but their slow degradation rate decreases efficiency[59,60] compared to HAp.

4.8. Reintroducing DNA into the life cycle

The potential impact of a hydroxyolite, a nanometric particle, for life continuation is not negligible (Figure 4.2.). Since the 1970s calcium phosphate has been well known as a non-viral carrier used for gene therapy. Particles with transfection capability are in the range of 20–200 nm.[42] Hydroxyolites are capable of introducing plasmids into the nucleus,[61,62] where the plasmid recombines with cell DNA. For some decades HAp transfection was almost abandoned due to its low transfection efficiency, but recently it has become more attractive, as HAp is highly biocompatible and has less side effects compared to other transfecting agents, like viral vectors.[63,64]

The hydroxyolite capsules, once formed, can stay "on hold" and remain passive for years until the aggressive environment relaxes or totally disappears. After clearance, the encapsulated DNA could have the option of being reintroduced again into the life cycle by two main mechanisms: 1) redissolution of the particle or 2) uptake by a living cell. Looking at the first mechanism, several solubility factors affect HAp:[65] method of preparation, crystallinity, density and extent of ionic substitutions into the apatite lattice. Particularly interesting is the carbonate substitution extensively observed in living organisms, as it increases the solubility. Fluoride substitution observed in enamel decreases solubility. Finally, highly crystalline particles usually result in very insoluble structures, whilst particles that are less crystalline have higher relative solubilities.[66,67] The redissolution process by pure acid attack (HCl) is 10-fold easier when sodium (Na^+) and chloride (Cl^-) are present in the aqueous solution at low concentrations (in the millimolar range).[68] The molecular mechanism that drives solubility remains unclear despite the efforts for clarifying it and several models proposed in the literature.[69,70]

When considering the second mechanism, eukaryotic cells can internalize particles bigger than 10 nm through the endocytic pathways including phagocytosis, macropinocytosis, clathrin mediated endocytosis, and non-clathrin mediated endocytosis, such as internalization by caveolae.[71] As representative mechanisms for HAp internalization we mention endocytosis and macropinocytosis. In the first, the cell membrane invaginates before taking up the nanoparticle. In the second, macropinocytosis, the particle first goes to

the endosomes and then to the lysosomes, dissolving under the acidic conditions.[72] The combination of cell uptake and redissolution is especially relevant during the event of transfection when the particle releases DNA to the nucleus or cytosol. The buffering properties of HAp are important for protecting DNA against DNAse degradation during this process.[73] Additionally, it is worth mentioning that it is not difficult to release DNA from HAp. Only a slight increase in temperature or a decrease in pH is necessary to discharge DNA from HAp.[74] An increase in ionic strength, phosphate gradients, or other solvents mimicking the chromatographic conditions used for DNA separation in HAp columns also result in DNA release from HAp.[75,76]

Summarizing, DNA is protected from the environment after cell death, but is not isolated forever. When favorable life conditions reappear, hydroxyolite particles have the ability of delivering DNA to a new cell, promoting a recombination of genetic code and potentially starting diversification, as usually observed after the event of mass extinction (Figure 4.2.).[77] Single- or double-stranded RNA have the same potential of templating HAp and becoming encapsulated or adsorbed as an hydroxyolite[78] without losing functionality that will be essential for restarting life.

4.9. Conclusion

This work provides an example of how chemical concepts extracted from both laboratory and computer simulation experiments can be extended to very diverse and relatively far fields of science, such as evolution, to correlate and explain important observations about life itself.

It is highly likely that life has evolved up to now using several mechanisms to protect the information encoded in DNA. HAp is currently intensively interlinked with biochemical processes. All of these processes run at physiological conditions of temperature and pH. Its unique properties of accepting different ions on its flexible lattice, gases on its surfaces, and biomolecules on its interior makes it likely that HAp played an outstanding role during the relevant life events on earth.

Environmental stressing conditions are expected to damage DNA. At first glance, looking at its lability, fragility, and instability, DNA is not expected to survive unscathed after being exposed to damaging conditions with unfavorable circumstances. However, the evidence of life today confirms that even the most aggressive events that occurred in the past could not

stop life thriving; therefore, despite the fact that DNA was probably modified or mutated during the events of mass extinction, it was not denatured or destroyed. Its resilience is remarkable, thus the hypothesis of a combination of DNA with an inorganic shell of HAp gains credibility. Hydroxyolites (DNA–HAp nanoparticles) are thermodynamically favored. HAp is easily redissolved and able to carry the encoded information without modifying it. The power of these particles for transmitting information to living cells has led to the fact that HAp has been used as a gene therapy vector. Only its low efficiency prevents it from being the most used mechanism for transfecting cells. Thus, its ability to protect and transmit DNA probably made the difference throughout the mass extinction events for the survival of life. This hypothesis is reinforced by the biomineralization process observed when a cell dies under certain stressing conditions. After a while, a necrotic calcification appears that frequently is no more than a particle containing DNA (on its surface or in its interior) trying to protect the invaluable information for life. It can be considered to be the first survival mechanism of the cell.

Considering all the reviewed arguments, the potential of hydroxyolites to help us understand the evolution of life remains an interesting field to be explored in depth. Further research is necessary to confirm the process of DNA encapsulation after cell death, how and where DNA remains preserved and how the reintroduction of DNA into the life cycle really works.

Watson and Crick[79] realized the importance of the double helix for life, thus changing the understanding of medicine, diseases, genetics, and the origin of life. From our perspective, the DNA–HAp particle has to be understood as a molecule in its mold. HAp has the potential to be the Trojan horse that protected and hid DNA through mass extinction events and this throughout the whole history of life on Earth.

4.10. References

1. Donoghue P.C.J., Benton M.J., Rocks and clocks: calibrating the Tree of Life using fossils and molecules, *Trends in Ecology and Evolution* (**2007**), *22*, 424 –431. DOI: 10.1016/j.tree.2007.05.005.

2. Porter S.M., Seawater chemistry and early carbonate biomineralization, *Science* (**2007**), *316*, 1302 –1304. DOI: 10.1126/science.1137284.

3. Revilla-López G., Casanovas J., Bertran O., Turon P., Puiggalí J., Alemán C., Modeling biominerals formed by apatites and DNA, *Biointerphases* (**2013***), 8*, 10. DOI:10.1186/1559-4106-8-10.

4. Bertran O., del Valle L.J., Revilla-López G., Chaves G., Cardus L., Casas M.T., Casanovas J., Turon P., Puiggalí J., Alemán C., Mineralization of DNA into nanoparticles of hydroxyapatite, *Dalton Transactions* (**2014**), *43*, 317 –327. DOI: 10.1039/C3DT52112E.

5. Theobald D.L., A formal test of the theory of universal common ancestry, *Nature* (**2010**), *465*, 219 –222. DOI:10.1038/nature09014.

6. Erwin D.H., Valentine J.W, Sepkoski Jr J.J., A comparative study of diversification events: the early Paleozoic versus the Mesozoic, *Evolution* (**1987**), *41*, 1177 – 1186. DOI:10.1111/j.1558-5646.1987.tb02459.x.

7. Barnosky D.A., Matzke N., Tomiya S., Wogan G.O.U., Swartz B., Quental T.B., Marshall C., McGuire J.L., Lindsey E.L., Maguire K.C., Mersey B., Ferrer E.A., Has the Earth's sixth mass extinction already arrived?, *Nature* (**2011**), *471*, 51– 57. DOI:10.1038/nature09678.

8. Gilbert W., Origin of life; The RNA world, *Nature* (**1986**), *319*, 618. DOI:10.1038/319618a0.

9. Joshi P.C., Aldersley M.F., Ferris J.P., Progress in demonstrating total homochiral selection in montmorillonite-catalyzed RNA synthesis, *Biochemical and Biophysical Research Communications* (**2011**), *413*, 594 –598. DOI: 10.1016/j.bbrc.2011.09.008.

10. Ertem G., Ferris J.P., Synthesis of RNA oligomers on heterogeneous templates, *Nature* (**1996**), *379*, 238 –240. DOI: 10.1038/379238a0.

11. Rimola A., Ugliengo P., Sodupe M., A Adsorción y polimerización de aminoácidos en superficies de minerales. Simulaciones computacionales de procesos prebióticos. *Anales de Química* (**2011**), *107*, 2, 137–143.

12. Cleaves II H.J., Crapster-Pregont E., Jonsson C.M., Jonsson C.L., Sverjensky D.A., Hazen R.A., The adsorption of short single-stranded DNA oligomers to mineral surfaces, *Chemosphere* (**2011**), *83*, 1560 –1567.
DOI: 10.1016/j.chemosphere.2011.01.023.

13 Mignon, P., Sodupe M., Theoretical study of the adsorption of DNA bases on the acidic external surface of montmorillonite, *Physical Chemistry Chemical Physics*, (**2012**), *14*, 945-954.
DOI:10.1039/c1cp22454a.

14. del Valle L.J., Bertran O., Chaves G., Revilla-López G., Rivas M., Casas M.T., Casanovas J., Turon P., Puiggalí J., Alemán C., DNA adsorbed on hydroxyapatite surfaces, *Journal of Material Chemistry B* (**2014**), *2*, 6953 –6966.
DOI:10.1039/C4TB01184H.

15. Mojzsis, G. Arrhenius, K. D. McKeegan, K. D. Harrison, T. M. A. P. Nutman, C. R. L. Friend, Evidence for life on Earth before 3,800 million years ago, *Nature* (**1996**), *384*, 55– 59.
DOI: 10.1038/384055a0.

16. Schweitzer M.H., Wittmeyer J.L., Horner J.R., Molecular analyses of dinosaur osteocytes support the presence of endogenous molecules, *Bone* (**2013**), *52*, 414 –423.
DOI: 10.1016/j.bone.2012.10.010.

17. Orgel L.E., Prebiotic chemistry and the origin of the RNA world, *Critical Reviews in Biochemistry and Molecular Biology* (**2004**), *39*, 99 –123.
DOI: 10.1080/10409230490460765.

18. Xu J., White T., Li P., He C., Han Y., Hydroxyapatite foam as a catalyst for formaldehyde combustion at room temperature, *Journal of American Chemical Society* (**2010**), *132*, 13172 – 13173.
DOI: 10.1021/ja1058923.

19. Benner S.A., Kim H-J., Carrigan M.A., Asphalt, water, and the prebiotic synthesis of ribose, ribonucleosides, and RNA, *Accounts of Chemical Research* (**2012**), *45*, 2025 – 2034.
DOI: 10.1021/ar200332w.

20. Ducheyne P., Qiu Q., Bioactive ceramics: the effect of surface reactivity on bone formation and bone cell function, *Biomaterials* (**1999**), *20*, 2287 –2303.
DOI: 10.1016/S0142-9612(99)00181-7.

21. Bianco P., Riminucci M., Gronthos S., Gehron P., Bone marrow stromal stem cells: nature, biology, and potential applications, *Stem Cells* (**2001**), *19*, 180 –192.
DOI: 10.1634/stemcells.19-3-180|.

22. Bertran O., del Valle L.J., Revilla-López G., Rivas M., Chaves G., Casas M.T., Casanovas J., Turon P., Puiggalí J., Alemán C., Synergistic approach to elucidate the incorporation of magnesium ions into hydroxyapatite, *Chemistry- A European Journal* (**2015**), *21*, 2537 –2546.
DOI: 10.1002/chem.201405428.

23. Cheung-Ong K., Giaever G., Nislow C., DNA-damaging agents in cancer chemotherapy: serendipity and chemical biology, Chemistry and Biolology (**2013**), *20*, 648 –659.
DOI:10.1016/j.chembiol.2013.04.007.

24. Suzuki K., Ojima M., Kodama S., Watanabe M., Radiation-induced DNA damage and delayed induced genomic instability, *Oncogene* (**2003**), *22*, 6988 –6993.
DOI:10.1038/sj.onc.1206881.

25. Cadeta J., Sageb E., Doukia T., Ultraviolet radiation-mediated damage to cellular DNA, *Mutation Research/Fundamental and Molecular Mechanisms of Mutagenesis* (**2005**), *571*, 3 –17.
DOI:10.1016/j.mrfmmm.2004.09.012.

26. Melott A.L., Lieberman B.S., Laird C.M., Martin L.D., Medvedev M.V., Thomas B.C., Cannizzo J.C., Gehrels N., Jackman D.H., Did a gamma-ray burst initiate the late Ordovician mass extinction? *International Journal of Astrobiology* (**2004**), *3*, 55– 61.
DOI:10.1017/S1473550404001910.

27. Hinojosa J.L., Brown S.T., Chen J., DePaolo J.D., Paytan A., Shen S-z., Payne J.L., Evidence for end-Permian ocean acidification from calcium isotopes in biogenic apatite, *Geology* (**2012**), *40*, 743–746.
DOI:10.1130/G33048.1.

28. Proskuryakov S.Y., Gabai V.L., Mechanisms of tumor cell necrosis, *Current Pharmaceutical Design* (**2010**), *16*, 56– 68.
DOI:10.2174/138161210789941793.

29. Proskuryakov S.Y., Konoplyannikov A.G. Gabai V.L., Necrosis: a specific form of programmed cell death?, *Experimental Cell Research* (**2003**), *283*, 1 –16.
DOI:10.1016/S0014-4827(02)00027-7.

30. Hotchkiss R.S., Strasser A., McDunn J.E., Swanson P.E., Cell death, *New England Journal of Medicine* (**2009**), *361*, 1570 –1583.
DOI: 10.1056/NEJMra0901217.

31. Tait S.W.G., Ichim G., Green D.R., Die another way–non-apoptotic mechanisms of cell death, *Journal of Cell Science* (**2014**), *127*, 2135 –2144.
DOI: 10.1242/jcs.093575.

32. Kalantari F., Miao D., Emadali A., Tzimas N.G., Goltzman D., Vali H., Chevet E., Auguste P., Cellular and molecular mechanisms of abnormal calcification following ischemia–reperfusion injury in human liver transplantation, *Modern Pathology* (**2007**), *20*, 357 –366.
DOI: 10.1038/modpathol.3800747.

33. Case R.M., Eisner D., Gurney A., Jones O., Muallemd S., Verkhratsky A., Evolution of calcium homeostasis: from birth of the first cell to an omnipresent signalling system, *Cell Calcium* (**2007**), *42*, 345 –350.
DOI:10.1016/j.ceca.2007.05.001.

34. Berridge M.J., Lipp, P., Bootman M.D., The versatility and universality of calcium signaling, *Nature Reviews. Molecular Cell Biology* (**2000**), *1*, 11 –21.
DOI: 10.1038/35036035.
35. Clapham D.E., Calcium signaling, *Cell* (**2007**), *131*, 1047 –1058.
DOI: 10.1016/j.cell.2007.11.028.

36. Coe H., Michalak M., Calcium binding chaperones of the endoplasmic reticulum, *General Physiology and Biophysics* (**2009**), *28*, 96– 103.
DOI: No assigned.

37. Contreras L., Drago I., Zampese E., Pozzan T., Mitochondria: the calcium connection, *Biochimica et Biophysica Acta (BBA) - Bioenergetics* (**2010**), *1797*, 607 –618.
DOI: 10.1016/j.bbabio.2010.05.005.

38. Greenawalt J.W., Rossi C.S., Lehninger A.L., Effect of active accumulation of calcium and phosphate ions on the structure of rat liver mitochondria, *Journal of Cell Biology* (**1964**), *23*, 21– 38.
DOI:10.1083/jcb.23.1.21.

39. Rizzuto R., De Stefani D., Raffaello A., Mammucari C., Mitochondria as sensors and regulators of calcium signaling, *Nature Reviews. Molecular Cell Biolology* (**2012**), *13*, 566 –578.
DOI: 10.1038/nrm3412.

40. Omelon S., Georgiou J., Henneman Z.J., Wise L.M., Sukhu B., Hunt T, Wynnyckyj, C., Holmyard D., Bielecki R., Grynpas R.D., Control of vertebrate skeletal mineralization by polyphosphates, *PLoS ONE* (**2009**), *4*, e5634.
DOI: 10.1371/journal.pone.0005634.

41. Seidlmayer K., Gomez-Garcia M.R., Blatter L.A., Pavlov E., Dedkova E.N., Inorganic polyphosphate is a potent activator of the mitochondrial permeability transition pore in cardiac myocytes, *Journal of General Physiology* (**2012**), *139*, 321 –331.
DOI: 10.1085/jgp.201210788.

42. Cao X., Deng W., Wei Y., Su W., Yang Y., Wei Y., Yu J., Xu X., Encapsulation of plasmid DNA in calcium phosphate nanoparticles: stem cell uptake and gene transfer efficiency, *International Journal of Nanomedicine* (**2011**), *6*, 3335 –3349.
DOI: 10.2147/IJN.S27370.

43. Rivas M., Casanovas J., del Valle L.J., Bertran O., Revilla-López G., Turon P., Puiggalí J., Alemán C., An experimental-computer modeling study of inorganic phosphates surface adsorption on hydroxyapatite particles, *Dalton Transactions* (**2015**), *44*, 9980–9981.
DOI: 10.1039/C5DT00209E.

44. Kim H-R., Won S.J., Fabian C., Kang M., Szardenings M., Shin M-G., Mitochondrial DNA aberrations and pathophysiological implications in hematopoietic diseases, chronic inflammatory diseases, and cancers, *Annals of Laboratory Medicine* (**2015**), *35*, 1–14.
DOI: 10.3343/alm.2015.35.1.1.

45. Erwin D.H., The end and the beginning: recoveries from mass extinctions, *Trends in Ecology and Evolution* (**1998**), *13*, 344 –349.
DOI: 10.1016/S0169-5347(98)01436-0.

46. Kawai T., Ohtsuki C., Kamitakahara M., Tanihara M., Miyazaki T., Sakaguchi Y., Konagaya S., Removal of formaldehyde by hydroxyapatite layer biomimetically deposited on polyamide film, *Environmental Science & Technology* (**2006**), *40*, 4281 – 4285.
DOI: 10.1021/es050098n.

47. Parga J.R., Valenzuela J.L., Vázquez V., Rodríguez M., Moreno H., Removal of aqueous lead and copper ions by using natural hydroxyapatite powder and sulphide precipitation in cyanidation process, Materials Sciences and Applications (**2013**), *4*, 231–237.
DOI:10.4236/msa.2013.44028.

48. Iriarte-Velasco U., Ayastuy J.L., Zudaire L.,Sierra I., An insight into the reactions occurring during the chemical activation of bone char*, Chemical Engineering Journal.* (**2014**), *251*, 217 –227.
DOI: 10.1016/j.cej.2014.04.048.

49. Kawasaki Y., Sotome S., Yoshii T., Torigoe I., Maehara H., Sugata Y., Hirano M., Mochizuki N., Shinomiya K., Okawa A., Effects of gamma ‐ ray irradiation on mechanical properties, osteoconductivity, and absorption of porous hydroxyapatite/collagen, *Journal of Biomedical Materials Research. Part B* (**2009**), *92*, 161 –167.
DOI: 10.1002/jbm.b.31502.

50. Ishchenko S.S., Vorona I.P., Okulov S.M., Baran N.P., Rudko V.V., ENDOR study of CO_2^- radicals in hydroxyapatite of γ-irradiated bone, *Radiation Measurements* (**2011**), *46*, 37–39.
DOI: 10.1016/j.radmeas.2010.07.025.

51. Nishikawa H., Radical generation on hydroxyapatite by UV irradiation, *Materials Letters* (**2004**), *58*, 14–16.
DOI: 10.1016/S0167-577X(03)00396-3.

52. Breen S.L., Battista J.J., Radiation dosimetry in human bone using electron paramagnetic resonance, *Physics in Medicine and Biolology* (**1995**), *40*, 2065–2077. DOI: 10.1088/0031-9155/40/12/005.

53. Aklil, A., Mouflihb M., Sebti S., Removal of heavy metal ions from water by using calcined phosphate as a new adsorbent, *Journal of Hazardous Materials* (**2004**), *112*, 183–190. DOI: 10.1016/j.jhazmat.2004.05.018.

54. Seaman, J., Arey J.C., Bertsch P.M., Immobilization of nickel and other metals in contaminated sediments by hydroxyapatite addition*, Journal of Environmental Quality*. (**2001**), *30*, 460–469. DOI: 10.2134/jeq2001.302460x.

55. Porter A.E., Botelho C.M., Lopes M.A., Santos J.D., Best S.M., Bonfield W., Ultrastructural comparison of dissolution and apatite precipitation on hydroxyapatite and silicon‐substituted hydroxyapatite in vitro and in vivo, *Journal of Biomedical Materials Research* (**2004**), *69*, 670 –679. DOI:10.1002/jbm.a.30035.

56. Porter A.E., Patel N., Skepper J.N., Best S.M., Bonfield W, Comparison of in vivo dissolution processes in hydroxyapatite and silicon-substituted hydroxyapatite bioceramics, *Biomaterials* (**2003**), *24*, 4609 –4620. DOI:10.1016/S0142-9612(03)00355-7.

57. Kawase M., Hayashi Y., Kinoshita F., Yamato E., Miyazaki J-i., Yamakawa J., Ishida T., Tamura M., Yagi K., Protective effect of montmorillonite on plasmid DNA in oral gene delivery into small intestine, *Biological and Pharmaceutical Bulletin* (**2004**), *27*, 2049 –2051. DOI: 10.1248/bpb.27.2049.

58. Blum S.A.E., Lorentz M.G., Wackernagel W., Mechanism of retarded DNA degradation and prokaryotic origin of DNases in nonsterile soils, *Systematic and Applied Microbiology* (**1997**), *20*, 513–521. DOI: 10.1016/S0723-2020(97)80021-5.

59. Tang L., Cheng J., Nonporous silica nanoparticles for nanomedicine application, *Nano Today* (**2013**), *8*, 290 –312. DOI:10.1016/j.nantod.2013.04.007.

60. Wu S-H., Hung Y., Mou C-Y-, Mesoporous silica nanoparticles as nanocarriers, Chemical Communications (**2011**), *47*, 9972 –9985. DOI: 10.1039/C1CC11760B.

61. Sokolova V.V., Radtke I., Heumann R., Epple M., Effective transfection of cells with multi-shell calcium phosphate-DNA nanoparticles, *Biomaterials* (**2006**), *27*, 3147 – 3153. DOI:10.1016/j.biomaterials.2005.12.030.

62. Motskin M., Wright D.M., Muller K., Kyle N., Gard T.G., Porter A.E., Skepper J.N., Hydroxyapatite nano and microparticles: correlation of particle properties with cytotoxicity and biostability, *Biomaterials* (**2009**), *30*, 3307 –3317. DOI:10.1016/j.biomaterials.2009.02.044.

63. Chowdhury E.H., Akaike T., High performance DNA nano-carriers of carbonate apatite: Multiple factors in regulation of particle synthesis and transfection efficiency, *International Journal of Nanomedicine* (**2007**), *2*, 101 –106. PMCID: PMC2673822.

64. Crystal R.G., Transfer of genes to humans: early lessons and obstacles to success, *Science* (**1995**), *270*, 404–410. DOI:10.1126/science.270.5235.404.

65. Fulmer M.T., Ison I.C., Hankermayer C.R., Constantz B.R., Ross J., Measurements of the solubilities and dissolution rates of several hydroxyapatites, *Biomaterials* (**2002**), *23*, 751–755. DOI: 10.1016/S0142-9612(01)00180-6.

66. Liu Q., Chen Z., Pan H., Darvell B.W., The effect of excess phosphate on the solubility of hydroxyapatite, *Ceramics International* (**2014**), *40*, 2751 –2761. DOI: 10.1016/j.ceramint.2013.10.044.

67. Pan H., Darvell B.W, Effect of carbonate on hydroxyapatite solubility, *Crystal Growth & Design* (**2010**), *10*, 845–850. DOI: 10.1021/cg901199h.

68. Hankermeyer C.R., Ohashi K.L., Delaney D.C., Ross J., Constantz B.R., Dissolution rates of carbonated hydroxyapatite in hydrochloric acid, *Biomaterials* (**2002**), *23*, 743–750. DOI:10.1016/S0142-9612(01)00179-X.

69. Dorozhkin S.V., Dissolution mechanism of calcium apatites in acids: A review of literature, *World Journal of Methodology* (**2012**), *2*, 1–17. DOI:10.5662/wjm.v2.i1.1.

70. Wang L., Nancollas G.H., Calcium orthophosphates: crystallization and dissolution, *Chemical Reviews* (**2008**), *108*, 4628 –4669. DOI:10.1021/cr0782574.

71. Bauer I.W., Li S-P., Han Y-C, Yuan L., Yin M-Z, Internalization of hydroxyapatite nanoparticles in liver cancer cells, *Journal of Materials Science: Materials in Medicine* (**2008**), *19*, 1091 –1095. DOI: 10.1007/s10856-007-3124-4

72. Sokolova V., Kozlova D., Knuschke T., Buer J., Westendorf A.M., Epple M., Mechanism of the uptake of cationic and anionic calcium phosphate nanoparticles by cells, *Acta Biomaterialia* (**2013**), *9*, 7527 –7535. DOI: 10.1016/j.actbio.2013.02.034.

73. Chowdhury E.H., Maruyama A., Kano A., Nagaoka M., Kotaka M., Hirose S., Kunou M., Akaike T., pH-sensing nano-crystals of carbonate apatite: effects on intracellular delivery and release of DNA for efficient expression into mammalian cells, *Gene* (**2006**), *376*, 87– 94.
DOI:10.1016/j.gene.2006.02.028.

74. Martinson H.G., Nucleic acid-hydroxylapatite interaction. II. Phase transitions in the deoxyribonucleic acid-hydroxylapatite system, *Biochemistry* (**1973**), *12*, 145–150.
DOI: 10.1021/bi00725a024.

75. Bernardi G., Chromatography of nucleic acids on hydroxyapatite, *Nature* (**1965**), *206*, 770 –779.

76. Watanabea T., Makitsurua K., Nakazawa H., Hara S., Suehiro T., Yamamoto A., Hiraide T., Ogawa T., Separation of double-strand DNA fragments by high-performance liquid chromatography using a ceramic hydroxyapatite column, *Analytica Chimica Acta* (**1999**), *386*, 69– 75.
DOI: 10.1016/S0003-2670(99)00024-0

77. Benton M.J., Diversification and extinction in the history of life, *Science* (**1995**), *268*, 52–58.
DOI: 10.1126/science.7701342.

78. Donoghue P.C.J., Benton M.J., Rocks and clocks: calibrating the Tree of Life using fossils and molecules, *Trends in Ecology and Evolution* (**2007**), *22*, 424 –431.
DOI: 10.1016/j.tree.2007.05.005.

79. Watson J.D., Crick F.H., Molecular structure of nucleic acids; a structure for deoxyribose nucleic acid, *Nature* (**1953**), *171*, 737–738.
DOI: 10.1038/171737a0.

80. Turon P*, Puiggalí J., Bertrán O, Alemán C.*, Surviving Mass Extinctions through Biomineralized DNA, *Chemistry - A European Journal* (**2015**), *21*, 18892 – 18898.
DOI:10.1002/chem.201503030.

Chapter 5

Inorganic photosynthesis on polarized hydroxyapatite, an integrative prebiotic model

Chapter 5

Inorganic photosynthesis on polarized hydroxyapatite, an integrative prebiotic model

5.1. Preamble

5.1.1. Challenges in prebiotic research

How life was initiated and thrived on Earth is still one of the most challenging topics in prebiotic and early life research. Many researchers have contributed to the debate from different perspectives, however, key topics are still partially understood or unsolved, and this fact makes the research in that field extremely exciting. In this preamble we highlight four challenges that give framework to our research. They put in perspective the prebiotic model we introduce in this chapter about the role calcium phosphate might have played, in the form of HAp, more than 3.6 billion years ago, before any form of life reigned on Earth.

As a first challenge, we mention the rise of the building blocks of life. Some theories and models have been developed in order to explain how the first organic molecules were synthesized. They range from atmospheric photochemistry, mineral surfaces, sea vents, volcanos, comets and meteorites. None of them totally explain how the building blocks of life appeared, all of them showing some important drawbacks that keep the debate open. In this chapter we aim to contribute to the prebiotic research with an integrative prebiotic model based on our recent findings in inorganic photosynthesis that we are going to review in section 5.3.

A second challenge, that we are not addressing in the thesis, but which has always captured our attention, is the enigma behind chirality. Up to now, remains unveiled why only enantiomeric molecules are used to build the molecular infrastructure of life (i.e. D-sugars, L-amino acids and D-nucleic acids and not L-sugars, D-amino acids and L-nucleic acids). How they ended up in a totally unbalanced ratio in cell mechanics, knowing that a regular synthetic reaction in the laboratory usually yields a 50:50 racemic mixture of such enantiomeric pairs, remains a paradox. From our perspective, it can only be conjectured that nature tends to use minimal energy pathways to build complex systems. However, they are

not yet known and chirality remains as a major challenge for prebiotic chemistry researchers, despite the fact that some authors claim there is a selective recrystallization that favors one of the enantiomers over the other, that still seems to be too simplistic explanation for such an intricate system.

Assuming that biopolymers such as proteins and nucleic acids should be synthesized before life started, a third challenge should be to determine how monomers of such biopolymers were concentrated enough and assembled together. Some authors theoretically and empirically proved that mineral surfaces, such as silicates and calcium phosphates (i.e. montmorillonite, feldspar and HAp) may act as catalysts that enabled such polymerization.

Last but not least, we reach the fourth challenge, to determine whether the first living system, a protocell, used a coupled system made by proteins and nucleic acids becoming integrated and fully functional with replicative capacity to transmit their own genetic information to the next generation. The hypothesis of RNA world is currently the most accepted, as this biopolymer is considered one of the corner stones of life due to its capacity to transmit information and catalyze some metabolic pathways. Therefore, we note that for replicative purposes, a template or a mold is usually necessary, two concepts we deal with extensively in this thesis. This is the reason why we support the idea that that HAp might be involved in the first replicative processes, probably in the format of an early made hydroxyolite, a concept beyond the scope of this thesis but in our radar.

In summary, what the origin of RNA or DNA was, how the polyphosphate backbone, sugars (D-ribose or D-deoxyribose) and nitrogen bases were synthesized and assembled is still under research. To our knowledge, the full chain of events has not been achieved without human intervention. Hence, the complete challenge starts from a mixture of simple molecules (i.e. a mildly reducing gas mixture composed of nitrogen (N_2), carbon dioxide (CO_2) and less than 100 ppm of CH_4, (ratio CH_4/CO_2=0,1) to be populating the early Earth's atmosphere and considering the existence of liquid water) and it ends with a functional replicating unit able to transmit their own features to the next generation, including the option to mutate and evolve into different species.

At this point, we return to the central concept of this thesis. As we mention in Chapter 3, a hydroxyolite can be understood as a nucleic acid in its mold. For that reason, in this chapter we change the perspective from the DNA as a template to the HAp as a prebiotic mold. In the next sections, we are going to put the focus on the mold and its consequences. As a

premise, we hypothesize that HAp, that is able to encapsulate nucleic acids, might be the catalytic substrate that originated the building blocks of life.

J. D. Bernal (1949)[1] and V. Goldschmidt (1952)[2] speculated independently on the mineral's role in the origins of life. After them, a long list of authors have contributed with detailed scenarios for mineral-mediated biogenesis. However, the list of ones focusing on HAp is short, and they basically mentioned their properties as a good adsorbent substrate or as a phosphorylation agent.[3,4] As we mentioned in the introductory chapter, HAp is a good catalyst by itself, many reactions are known where HAp is involved, some of them being interesting from the origin of life perspective. However, few authors centered their attention in the potential of HAp as a catalyst related to the building blocks of life, some of them are Reid and Orgel (1967),[5,] Weber (1982),[6] Acevedo and Orgel (1986).[7] Schwartz and De Graaf (1993),[8] Kostetsky (2005) and more recently Usami and Ukamoto (2017)[9] but, surprisingly, relevant contributions to minerals as a prebiotic catalytic substrate do not put the focus on HAp in their work (i.e. Cairns-Smith,[10] and Cleaves et al.,).[11]

To develop our prebiotic model, we were inspired by the Miller and Urey experiment (1953), who synthesized amino acids from a reducing gas mixture containing CH_4, NH_3, H_2O and H_2 under sparks for a week. Such an impressive result gave a boost to almost 70 years of origin of life research that is still on going and it is reviewed elsewhere.[12-14] We introduced some major modifications to Urey experiment: i) lightning over the gas mixture was removed and, the source of energy was UV light irradiation and temperature, ii) H_2 was removed as a reducing gas, iii) NH_3 was replaced by N_2 as a source of nitrogen, iv) the reaction temperature was defined at around 95 ºC (< 100 ºC). The idea of simulating the effect of a volcano lightning storm on HAp was attractive because volcanic ash is known to contain a certain amount of apatitic minerals, including HAp, and we were particularly interested in the effect of a high difference of potential on HAp at high temperature. Therefore, we defined a laboratory process that simulates the extreme conditions of a volcano plume during a volcano lightning storm (known by volcanologists as a *dirty storm*). A polarization process at 1,000 ºC and 500 V (3 $kV \cdot cm^{-1}$) was applied to HAp resulting in an improved catalyst (see Annex V). The process caused a permanent polarization of HAp, up to now a mineral known to become polarized under the effect of an electric field but only for a short period of time, a phenomenon known as quasi-permanent polarization.[15,16] However, the process we applied transformed the transient electrical properties into

permanent, a decisive feature to significantly enhance the catalytic performance. Since then, we have tested its catalytic properties in different conditions obtaining newsworthy results.

In this chapter we retrieve one of the reactions we reported using HAp/tsp as a catalyst, which is the synthesis of the two simplest amino acids starting from an extremely simple gas mixture composed of N_2, CO_2, CH_4 and H_2O, the same components of the current accepted prebiotic atmosphere model, a mildly reducing atmosphere (we note that the nitrogen source was N_2 instead of NH_3 the reaction thus becoming more challenging). To complete the prebiotic model, we irradiated the reactor vessel containing the catalyst and the gas mixture with UV light (λ=254 nm), simulating UV irradiation coming from the prebiotic sun and UV radiation emitted by lightning. In short, we developed a photosynthetic process catalyzed by HAp/tsp.

The major implications of this new synthetic process is that we developed an inorganic photosynthesis that has the potential to fix molecular nitrogen to obtain amines and also carbon, from carbon dioxide and methane, to obtain a carboxylic group attached to the carbon backbone of the amino acid. We will discuss some more aspects of such a finding in the next sections.

Finally, using the inorganic photosynthesis as a central pillar, we were able to integrate some prebiotic models (photochemistry of atmospheres, volcanos, minerals as catalytic substrates) in a unique prebiotic model. We include such a model in the last section of the chapter to close this thesis about the hydroxyolite system.

5.2. Purpose

In this chapter we concentrate on the fourth sub-objective defined in Chapter 1. We examine the basics of HAp as a catalyst that we use as a framework for exposing some perspectives on prebiotic concepts based on our research detailed in Annexes V, VI and VII.

Starting from the hydroxyolite concept, we hypothesized that HAp, being a good catalyst by itself should become a better one under extreme conditions usually observed in volcano plume. Such a premise ended up in the development of a new catalyst that we named permanently polarized hydroxyapatite (HAp/tsp), the result of a thermal and electrical stimulation process of polarization. Such a catalyst presents extraordinary features as an inorganic photosynthesis facilitator. We are going to summarize the main features of the

catalyst in the results section. Again, all the experimental research collected in Annex V, VI and VII is used as a pillar to develop a model, in this case, a prebiotic model that we defined as the main objective of this chapter. Consequently, we recall sub-objective 4:

Sub-objective 4. "*To develop a prebiotic model that considers hydroxyapatite as a catalyst that might facilitate the rise of the building blocks of life that are assembled to synthesize biopolymers in its surface".*

The rest of this chapter is organized as follows: We summarize the synthesis of polarized hydroxyapatite catalyst in section 5.3.1. and the basics of the inorganic photosynthesis in section 5.3.2. Furthermore, we introduce the integrative prebiotic model based on inorganic photosynthesis in section 5.4. We end up with conclusions in section 5.5.

5.3. Results and discussion

5.3.1. Permanently polarized HAp

HAp/tsp was obtained after applying a thermally (1000 ºC) and electrically (DC voltage of 500 V; DC field of 300 $kV \cdot m^{-1}$) stimulated polarization process (henceforth TSP) for 1 h. to sintered HAp (HAp/s). HAp/s was achieved by heating HAp as prepared (HAp/ap) at 1,000 °C for 2 h in air. Previously, HAp/ap was obtained by adding $(NH_4)_2HPO_4$ in de-ionized water to $Ca(NO_3)_2$ in ethanol, and applying hydrothermal conditions to the resulting suspension for 24 h.

Analyses of the chemical and structural properties of the resulting cHAp/tsp show: i) the disappearance of HPO_4^{2-} ions from the surface layer, which are typically identified in HAp/ap and, specially, HAp/s, ii) the appearance of OH^- vacancies and, iii) the enhancement of the crystallinity. Figure 5.1. compares the solid state ^{31}P NMR spectra of HAp/ap, HAp/s and HAp/tsp.

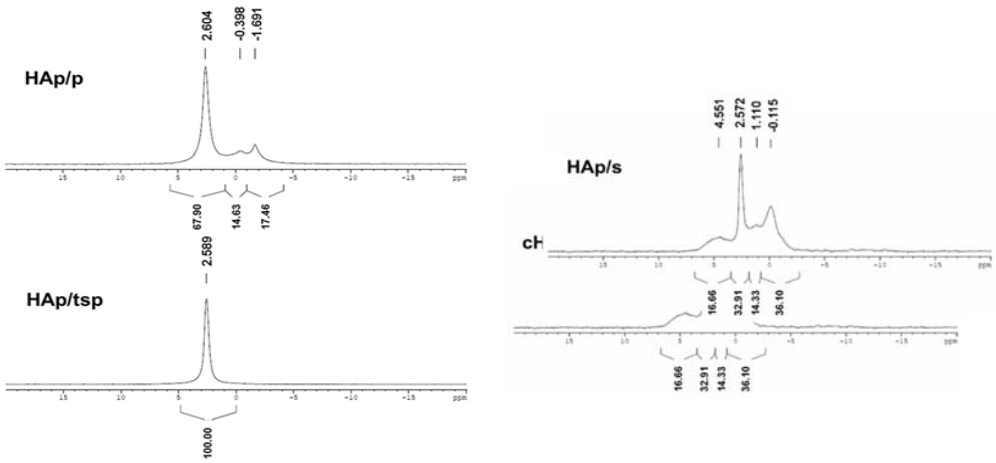

Figure 5.1. Solid-state ^{31}P NMR spectra of HAp/ap, HAp/s and HAp/tsp. Reproduced from ref. [66] with permission from John Wiley and Sons.

The main resonance peak in all samples (~2.59 ppm) corresponds to bulk phosphate groups of HAp.[17] This peak is narrower for HAp/s and HAp/tsp than for HAp/ap, which is consistent with the increment of crystallinity mentioned above. The broad signals at approximately [-1,0] ppm and the shoulder at [0,1] ppm in both HAp/ap and HAp/s are usually assigned to the lone protonated surfaces of phosphate groups arising from the disordered near surface layer.[18] Indeed, HAp particles are frequently described as an ordered crystalline core surrounded by a disordered non-apatitic surface layer.[19] The shoulder at 4–6 ppm in HAp/s has been attributed to the increment of HPO_4^{2-} ions at the disordered surface layer.[20,21] However, the most amazing result is the single peak observed in HAp/tsp, which corresponds to phosphate groups. This shows that the TSP exerts an important effect on the surface layer. Thus, the fingerprints of the surface OH^- ions leaving from the columns due to the TSP process are the disappearance of the surface HPO_4^{2-} ions and the formation of holes in the valence band to achieve the corresponding charge neutralization. The most distinctive characteristics of HAp/tsp are the electrochemical properties: i) electrochemical activity, HAp/tsp is ~150% higher than that of HAp/ap, which proves that the polarization treatment facilitates the diffusion of ions through the mineral matrix; ii) stability, the bulk resistance increases by only 4% after 3 months; and iii) the electrical conductivity, the bulk resistance of HAp/tsp (~0,67 M $\Omega \cdot cm^2$) is significantly lower than that of the HAp/ap (~134.6 M $\Omega \cdot cm^2$), indicating that the ionic conductivity increases by three orders of magnitude, which represents a significant improvement with respect to those achieved by other authors[15,16,22-24] applying lower polarization temperatures to samples sintered in a

saturated water vapor atmosphere. Re-evaluation of samples that were polarized three months before has shown that both the electrochemical and electrical properties of the HAp/tsp remain practically unaltered, proving that the acquired polarization effects are permanent. This represents a very important advantage with respect to previously reported strategies since the properties of samples polarized at lower temperatures (≤ 800 ºC) are very similar to those of HAp/s after three months.

Thus, the requirements of the catalyst were, on one hand, a material able to transform an energy source, as for example UV radiation, into electron/hole pairs and, on the other hand, materials to bring the gases used as reactants into contact with the catalyst (i.e. adsorb the gases), which was essential to conduct the reactions. Obviously, the success of the catalyst was also based on the fact that it could avoid unfavorable synergies among the materials when they were combined. After evaluating different options, two materials, which correspond to those presented in this work, were selected to be part of the coating: zirconia (through its precursor zirconyl chloride) and a phosphonic acid with chelating properties (ATMP). The details about the roles played by each component of the catalytic system are given throughout the whole Annex VI.

The ability to adsorb $P_3O_{10}^{5-}$, $P_2O_7^{4-}$ and ATMP is a remarkable characteristic of HAp/tsp. XPS and FTIR results indicated that the adsorption of inorganic phosphates and phosphonates onto HAp/tsp is around 1.5–2 times higher than onto HAp/s, which in turn is about twice that of HAp/ap. A feature that we use to prepare the coating of the catalyst by placing two layers of ATMP and one of $ZrOCl_2$ (ZC) in the middle of them. The adsorption capacity of phosphonates ensures an efficient contact between the HAp/tsp and the ATMP-ZC-ATMP three-layer coating of the HAp/tsp catalyst (Figure 5.2a). Besides, ZC and ATMP layers have been used to adsorb the gaseous reactants, essentially N_2 and CO_2, facilitating their reactivity (coating preparation details in Annex VI).

Additionally, these results are very important for biomedical applications, as for example the fabrication of HAp scaffolds with improved phosphate and phosphonate adsorption capacity for bone regeneration. In addition, the adsorption of inorganic phosphates and phosphonates imparts electrochemical stability and reduces the electrical resistance, opening new possibilities to the electro-stimulation.

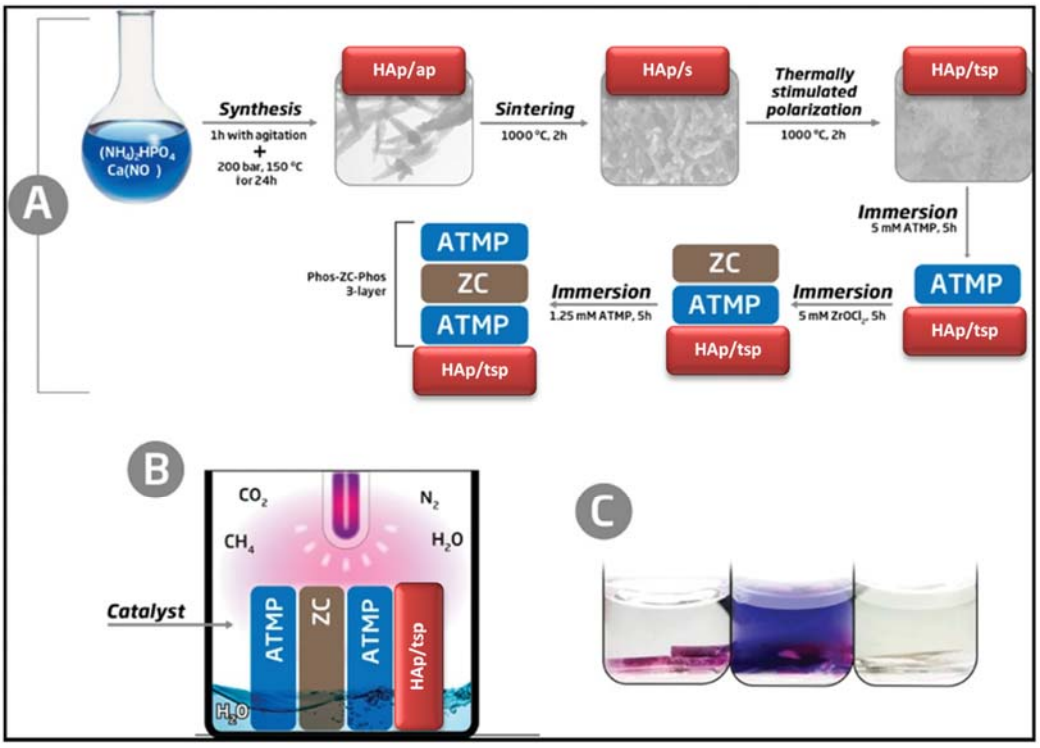

Figure 5.2. Schemes describing (a) the preparation of the HAp/tsp + ATMP-ZC-ATMP catalytic system and (b) the reaction medium used to produce AAs. (c) Representative results of the ninhydrin test for a positive reaction before stirring (left) and after stirring (middle) and a negative reaction (right). Reproduced from ref. [67] with permission from Royal Society of Chemistry.

5.3.2. Inorganic photosynthesis mediated by HAp/tsp

The synthesis of AAs was carried out in an inert reaction chamber under a weakly reducing atmosphere constituted of N_2 (0.33 bar), CO_2 (0.33 bar), CH_4 (0.33 bar) and liquid H_2O, using a UV lamp directly irradiating the catalyst and gas mixture (Figure 5.2b). The formation of primary amines adsorbed onto the solid substrate was shown by positive ninhydrin tests through the development of purple spots inside the catalyst recovered after the reaction (Figure 5.2c, left). Amine compounds were well dissolved in an acetone solution after vigorous stirring (Figure 5.2c, middle), contrasting with the uncolored solid and solution (Figure 5.2c, right) observed under many other assayed reaction conditions and catalytic systems (see below).

After 72 h at 95 °C, the synthesis of both Gly and Ala is demonstrated by the NMR spectra displayed in Figure 5.3. The ^{1}H NMR spectrum of the samples obtained by dissolving the catalyst and products of the reaction (Figure 5.3a) shows the presence of the catalyst signal corresponding to the ATMP methylene group (doublet at 3.79–3.76 ppm) and the signals corresponding to the newly produced AAs such as methylene protons (singlet at 3.65 ppm) of Gly and both methine (quadruplet at 3.91–3.85 ppm) and methyl (doublet at 1.54–1.52 ppm) groups of Ala. The same compounds are also observed in the solid-state ^{13}C NMR spectrum (Figure 5.3b), where only peaks assigned to the ATMP (54.34 and 53.00 ppm), Gly (171.95 and 41.26 ppm) and Ala (175.25, 50.25 and 16.01 ppm) units are detected. The ^{31}P NMR spectrum of the catalyst in dissolution (Figure 5.3c) shows the presence of the HAp/tsp (7.21 ppm) and ATMP (−0.03 ppm) peaks, but additional signals related to the products coming from the decomposition of the catalyst were not detected. With respect to CH_4 or CO_2, the Gly and Ala molar yields at 95 °C after 72 h are 1.9% and 1.6%. Instead, after 24 h at 95 °C no trace of Gly and Ala is detected by NMR. Furthermore, the formation of AAs is unsuccessful without sustained exposure to the UV radiation, which appears to be a fundamental issue to generate radicals (e.g. $^{\bullet}CH_3$ and $^{\bullet}OH$) needed for further reaction intermediates towards the final yielding of Ala and Gly.

On the other hand, the formation of AAs on the surface of the catalyst has also been proven by FTIR and Raman spectroscopy, which shows intense absorption bands in the amine region of the corresponding spectra. Finally, chiral high-performance liquid chromatography (HPLC) analyses were carried out to quantify the ratio of D- and L-Ala adsorbed into the catalysts. As was expected, after dissolution of the catalysts after the reaction in a 0.1 M HCl solution with 50 mM NaCl, a racemic D-Ala: L-Ala mixture was determined.

In this section, we have introduced a new catalyst based on permanently polarized HAp (HAp/tsp-[ATMP/ZC/ATMP]) with enhanced electrical and photochemical properties that allows the coupling of nitrogen and carbon fixation processes. Such a catalyst family opens an interesting field of research where simple gas mixtures that usually do not react among themselves are combined to yield basic organic molecules, such as amino acids, one of the main building blocks of life. More specifically, in this work we proved that Gly and Ala are produced at atmospheric pressure through an artificial photosynthetic nitrogen and carbon fixation reaction, starting from a weakly reducing atmosphere (N_2, H_2O, CO_2 and CH_4) and

using UV radiation as a source of energy. This reaction represents a very simple alternative to the costly chemical and enzymatic processes used to produce commercially Gly and Ala.

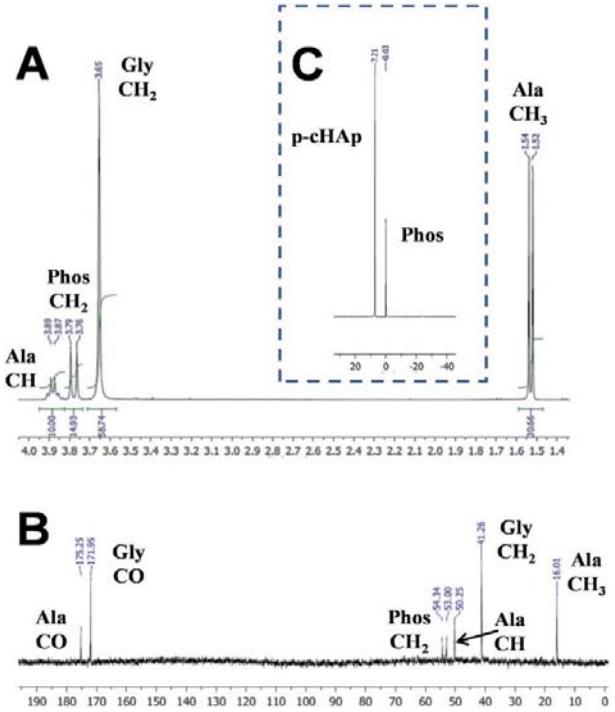

Figure 5.3. For samples obtained after the reaction (95 °C and 24 h) using a chamber pressure of 1 bar (i.e. 0.33 bar of each feeding reaction gas): (a) ^{1}H NMR spectrum of the solution obtained after the extraction of the AAs from the catalyst by dissolving the sample in deuterated water containing 100 mM of HCl and 50 mM of NaCl; and the solid state (b) ^{13}C - and (c) ^{31}P NMR spectra of the catalyst with the synthesized AAs. Reproduced from ref. [67] with permission from Royal Society of Chemistry.

It is worth noting that nitrogen fixation is an extremely relevant process from an industrial perspective.[25] It is difficult to overestimate the impact of the Haber–Bosch process that from N_2 and H_2 yields ammonia and furthermore results in more than 450 million tons of fertilizers per year, using more than 1% of the global energy supply.[26] Moreover, the synthesis of ammonia from nitrogen is constantly under research and only in the last decade have new catalysts based on ruthenium and zirconium been developed.[27] However, the environmental impact of the Haber–Bosch process is not negligible as natural gas or coal is used as an energy source (i.e. 1.87 tons of CO_2 are released per ton of ammonia produced and globally 245 million tons of CO_2 were released by the ammonia industry in 2010, equivalent to about 50% of the UK CO_2 emissions).[28] Thus, the outstanding benefits of nitrogen fixation are shadowed by their impact on environmental contamination.

Furthermore, the catalytic reduction of dinitrogen under mild conditions has been achieved by using molybdenum catalysts. Shilov, in the 1980s, obtained a mixture of hydrazine and ammonia[29] and Schrock and co-workers[30,31] converted dinitrogen into ammonia with excellent yield using protons and electrons. Very recently, Kuriyama et al.[32] reported the catalytic reduction of molecular dinitrogen into ammonia and hydrazine by using iron complexes bearing an anionic ligand as catalysts under mild reaction conditions. However, to our knowledge, the nitrogen fixation into amino acids using HAp/tsp was not reported until we published our findings (Annex VI).

On the other hand, CO_2 recycling is an absolute necessity for our society knowing that its accumulation in the atmosphere is now approaching 1 Tera ton.[33] Significant steps have been taken towards the utilization of CO_2 in order to convert it into valuable chemicals (150 Mt urea, 100 Mt methanol, 70 Mt salicylic acid, 9.7 Mt formaldehyde and 0.7 Mt formic acid are the most produced).[34-36] In the last few years, catalytic reactions via carbon dioxide fixation have gained a prominent role as representative green processes with enhanced sustainability.[37-40] However, by learning from nature, photosynthesis as performed by living organisms is the carbon fixation process par excellence. Efforts to mimic it synthetically have been elusive through time. The development of photosynthetic processes requires significant advances in new materials for light harvesting and the development of fast, stable, and efficient electrocatalysts.[41,42] Our contribution in this section has been in that direction. Nevertheless, we use this finding as a starting point to our next section where we deal with the implications of such inorganic photosynthesis in regard to prebiotic chemistry.

5.4. Perspectives. Integrative Prebiotic Model: Inorganic photosynthesis

5.4.1. Introduction

Synthesizing precursors of complex biomolecules, such as proteins and nucleic acids without human intervention under prebiotic conditions has attracted the interest of origin of life researchers. Until now, how and where such molecules appeared and sufficiently concentrated to develop life still remains under debate.[43,44] Several theories have been considered in the last decades as originators of such molecules:[13,45] extraterrestrial meteorites,[46] volcanoes as giant reactors,[47-49] atmospheric gases under lightning and UV irradiation,[50-52] catalytic surfaces of minerals[10,11,53-55] and hydrothermal vents.[55,57] In order

to give a new insight based on our findings in an inorganic photosynthesis, we propose a prebiotic inorganic photosynthetic model where a gas mixture containing N_2, CO_2, CH_4 and H_2O in the presence of a polarized HAp catalyst results in simple organic molecules (i.e. amino acids and organic acids). Such a model combines several of the most relevant features of the previous ones that are complemented with the enhanced catalytic properties of HAp/tsp.[58,59]

Currently, the most accepted composition of early Earth atmosphere indicates that it was weakly reducing (i.e.N_2, CO_2 and CH_4 in much lower quantities and H_2O in equilibrium with liquid water; CH_4 less than 100 ppm and CH_4/CO_2 ~ 0,1).[60-63] Since 1950s, many experiments have been performed, most of them with ammonia (NH_3) as a source of nitrogen. However, starting gas mixtures using N_2 instead of NH_3 signified a bigger challenge because usually low yields of amino acids were observed as activating the triple bond of N_2 is much more difficult. To synthesize simple organic molecules using neutral atmospheres containing mixtures of N_2, CO_2, (CO) and H_2O required high energy sources (i.e. electrical discharges, laser pulses, protons or soft X-ray) to obtain glycine and α-alanine in relatively high concentrations while other amino acids were obtained in lower concentrations.[44] However, Cleaves et al. (2008) improved the amino acid yield up to 2.5% of the initial nitrogen using a N_2/CO_2 gas mixture under sparks, by including $CaCO_3$, buffering the collecting solution to maintain a pH value close to 7, and using oxidation inhibitors such as Fe^{2+}. Furthermore, following a lower energy route, some authors tried to obtain amino acids by irradiating the initial gases with UV light (i.e. Sagan and Khare (1971); Becker et al. (1974); Muñoz Caro et al. (2002)), however, none of them used N_2 in the starting mixture due to the difficulty of activating the dinitrogen triple bond.[64-66]

Recently, the synthesis of HAp/tsp was reported.[67] The HAp/tsp was obtained by exposing HAp to a high temperature and difference of potential (1000 ºC, 300 $kV \cdot m^{-1}$) simultaneously. HAp, after polarization, shows two outstanding features: i) enhanced catalytic performance and ii) higher adsorption capacity of organic molecules.[68,69] Such catalyst, irradiated by UV light (λ=254 nm), was able to fix carbon and nitrogen through an inorganic photosynthesis as described in the previous section. The inorganic photosynthesis reaction yielded glycine and a racemic mixture of α-alanine at mild temperature (< 100 ºC) using a gas mixture of N_2, CO_2 and CH_4 at 1 bar, including liquid water in the reaction mixture.

Environmental conditions in nature that might make feasible to obtain HAp/tsp are likely to occur in a volcanic eruption, specifically inside of a lightning volcano plume, a phenomenon known by volcanologists as dirty storms. Furthermore, apatitic material, such as HAp, is found in igneous material and volcanic ash in low but significant quantities (i.e. < 0.1%).[70-74] Lightning in dirty storms is an indicator that volcanic ash is exposed to large differences in potential and strong electric fields because high differences of potential, similar to those needed to polarize HAp, usually end up generating an electric discharge.[75-77] Lightning in volcanos is related to the intensity of the eruption, ash plume height and the high water content of magma. Consequently, we consider that HAp polarization should be possible in a lightning volcano where temperatures are above 800 ºC, similar to the ones needed in the HAp polarization process to obtain HAp/tps. We take into consideration that in the prebiotic era volcanic activity was much more intense than in present days and magma might even have been at higher temperatures than today, facts that might facilitate the polarization of HAp.

5.4.2. The integrative prebiotic model

Volcanism was much more intense in the Archean period than today. The prebiotic model we propose implies that volcanic ash clouds, containing prebiotic atmospheric gases, gases coming from the eruption and minerals such as metal oxides and HAp, were simultaneously exposed to high temperature and strong electric fields that resulted in HAp polarization. Additionally, intense UV radiation (i.e. coming from lightning and the prebiotic sun) generated radicals on the surface of HAp (i.e. hydroxyl radical $^{\cdot}OH$ and/or superoxide $^{\cdot}O_2^-$) as demonstrated in laboratory conditions. Such radicals are important intermediates of the inorganic photosynthesis we reported and, interestingly, they are known to remain captured in the HAp lattice[78-80] for long periods (up to a year), much longer than their expected shelf life in aqueous environments where their reactivity is extremely high.

The proposed prebiotic model of an inorganic photosynthesis is expected to explain the synthesis of molecules such as amino acids, formaldehyde (CH_2O),[81] precursors of sugars and simple organic acids, among others. Among other important molecules hydrogen cyanide (HCN) is expected to be outgassed from volcanos or synthesized by direct atmospheric photochemistry. Therefore, HCN is known to be adsorbed on HAp in large quantities in the form of cyanide (CN^-),[82,83] and such adsorption on the HAp/tsp catalyst

might facilitate the synthesis of nitrogen containing compounds as nucleobases and nucleotides,[84] necessary blocks to produce RNA and DNA.[85] Moreover, the high temperature inside the volcano plume favors condensation and polymerization reactions where the removal of water molecules is necessary for the synthesis of biopolymers as proteins.[86,87] On the other hand, HCN, by exposure to ·OH radicals contained in HAp, decompose to CN + H under UV in order to generate HCNOH substances.[88] HCN is known to hydrolyze to formamide, a major precursor of nucleic acids that is strongly adsorbed on HAp surface as well.[89] The capacity of polarized HAp to adsorb several key prebiotic molecules is outstanding. It is worth noting that HAp/tsp, when catalyzing the inorganic photosynthesis in the lab was able to adsorb amino acids, large quantities of CH_2O and other organic molecules.[90] The adsorption of polyphosphates, as we reported in previous works, should facilitate the phosphorylation processes,[68] particularly by pyrophosphate, as is known to be formed in the volcano scenario and some authors mention it as one credible candidate to be a prebiotic phosphorylating agent. In summary, the simultaneous ability of HAp to be a catalyst and an adsorptive substrate facilitates both the synthesis and concentration of monomers involved in more complex reactions.

The proposed inorganic photosynthesis model implies that HAp expulsed by a volcano was polarized and catalyzed the fixation of nitrogen and carbon containing molecules, adsorbing them in its surface. During the ash cloud flight, the particles underwent a decreasing temperature gradient in contact with the upper layers of the atmosphere, cooling down until they landed on the ground, making feasible the seeding of the earth's crust and sea waters with freshly synthesized building blocks of life. Such a model might give a plausible explanation to the early findings of Markhinin and Podkletnov (1977) that found evidence of organic matter in volcanic ash (i.e. free and combined amino acids, amino sugars and other hetero-atomic compounds, containing also sulphur, chlorine, oxygen and nitrogen).[46] Following that argument, HAp/tsp might play a role of a catalytic substrate that made feasible the synthesis of molecules and facilitated the assembly of monomers to form biopolymers as well. Furthermore, we note that those molecules remaining adsorbed in such a catalytic substrate would be ready to participate in subsequent reactions driven by, for instance, the weathering effect. Thus, they could be selectively eluted from HAp/tsp by aqueous solutions containing different concentrations of salts, mimicking a chromatographic process that retains different molecules depending on their polarity and their interaction with

the chromatographic column substrate, as happens with the known HAp substrate to separate nucleic acids.[91]

Summarizing, we propose an inorganic photosynthetic model that integrates concepts from models based on lightning atmospheres, volcanos as giant reactors, and mineral surfaces as catalysts in one single picture. Therefore, we postulate that the polarized HAp catalyst is an outstanding candidate to become a key player in prebiotic chemistry that facilitated the raising of the building blocks of life and their posterior assembly, forming more complex biomolecules on a common catalytic substrate.

5.5. Conclusions

In this chapter, we have theorized about the role of HAp/tsp, an outstanding catalyst obtained by means of a thermally and electrically stimulated polarization process. The new catalyst is able to catalyze an inorganic photosynthesis, a highly desired process due to its ability to fix nitrogen and carbon to generate organic molecules. From simple gases as dinitrogen (79 % free of charge in atmosphere), carbon dioxide (a greenhouse gas that society is struggling to control its increment in the atmosphere), methane (greenhouse gas currently being burnt because it is produced in excess by the petrochemical industry) and water we made it feasible to obtain organic matter useful for feeding. Despite the potential impact of such a discovery, still under research to convert it into an industrial process, in this chapter we aim to focus on the role of HAp as a potential catalytic mold of biopolymers such as nucleic acids and their monomers that would fit in our central topic of the thesis, the hydroxyolite concept. Consequently, we develop a scenario that integrates concepts and perspectives around HAp as a key catalyst that allows us to contribute to prebiotic chemistry with a model based on an inorganic photosynthesis enabled by polarized HAp.

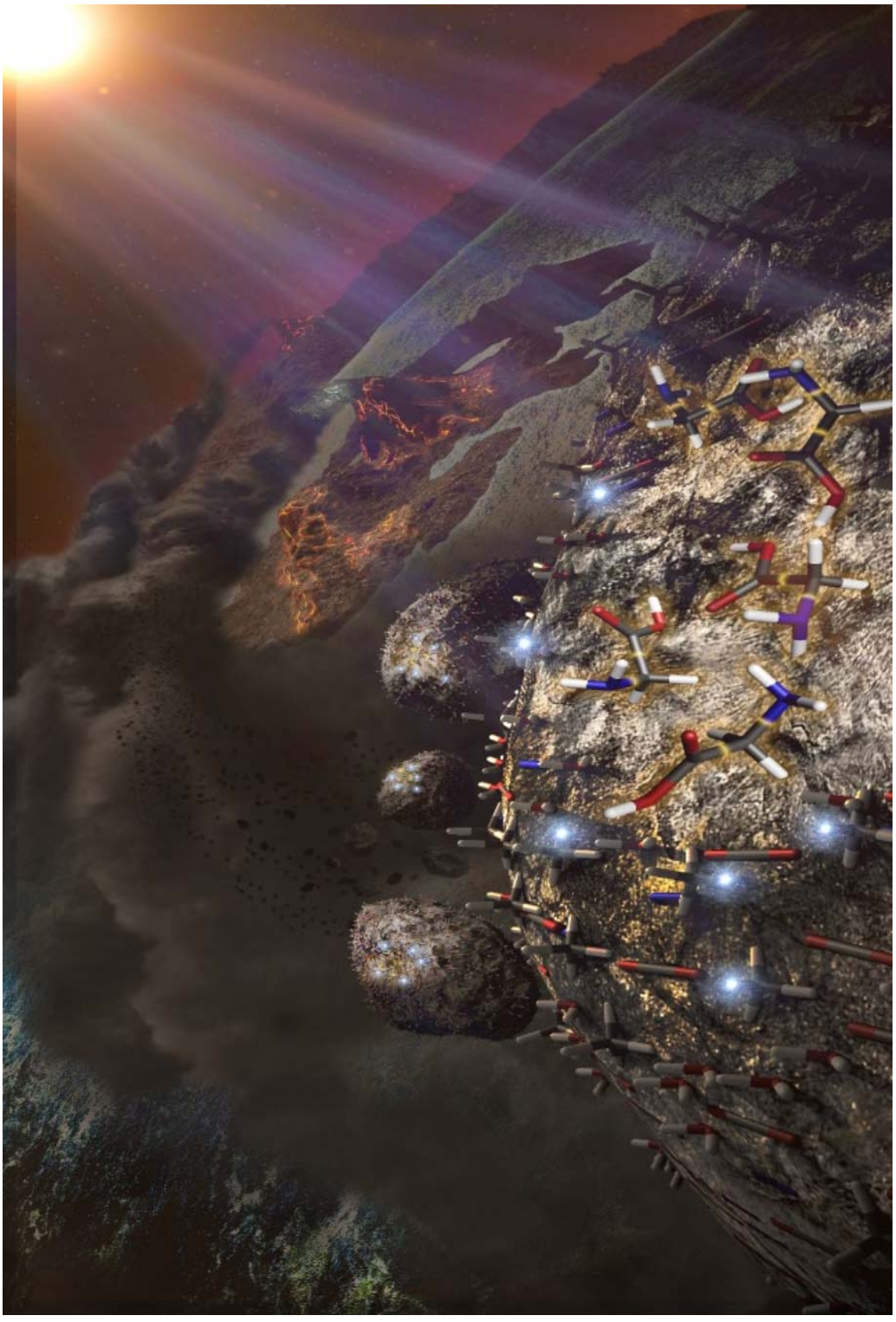

Figure 5.4. Figurative representation of the inorganic photosynthetic model. Volcano ash under lightning storms polarizes HAp, a mineral catalyst able to synthesize organic molecules from mildly reducing gas mixtures made of N_2, CO_2, CH_4 and H_2O.

5.7. References

1. Bernal J.D., The Physical Basis of Life, *Proceedings Physical Society A* (**1949**), *62***,** 537-558.

2. Goldschmidt V.M., Geochemical aspects of the origin of complex organic molecules on the Earth, as precursors to organic life. *New Biology* (1952), *12*, 97–105 cited in Hazen R.M., Chance, necessity and the origins of life: a physical sciences perspective. Philosophical Transactions Royal Society A (**2017**), *375*: 20160353, 1-12. DOI: 10.1098/rsta.2016.0353.

3. Orgel, L.E., Polymerization on the Rocks: Theoretical Introduction, *Origins of Life and Evolution of Biospheres* (**1998**), *28*,3, 227-234. DOI:10.1023/A:1006595411403.

4. Karki M., Gibard C., Bhowmik S., Krishnamurthy R., Nitrogenous Derivatives of Phosphorus and the Origins of Life: Plausible Prebiotic Phosphorylating Agents in Water, *Life* (**2017**), *7*, 32. DOI:10.3390/life7030032.

5. Reid C., Orgel L.E. , Model for Origin of Monosaccharides: Synthesis of Sugars in Potentially Prebiotic Conditions, *Nature* (**1967**), *216*, 455. DOI: 10.1038/216455a0.

6. Weber, A, Formation of pyrophosphate on hydroxyapatite with thioesters as condensing agents, *BioSystems*, (**1982**), *15*, 3, 1872-8324. DOI: 10.1016/0303-2647(82)90002-8.

7. Acevedo O.L., Orgel L.E., Template-directed oligonucleotide ligation on hydroxylapatite. Nature (**1986**), *321*, 790–792. DOI:10.1038/321790a0.

8 Schwartz A.W., de Graaf R.M., The prebiotic synthesis of carbohydrates: a reassessment, *Journal of Molecular Evolution* (**1993**), *36*, 101–106. DOI: 10.1007/BF00166245.

9. Usami K., Okamoto A., Hydroxyapatite: catalyst for a one-pot pentose formation, *Organic and Biomolecular Chemistry* (**2017**), *15*, 8888-8893. DOI: 10.1039/C7OB02051A.

10. Cairns-Smith A.G., Ingram P., Walker G.L., Formose Production by Minerals: Possible Relevance to the Origin of Life It, *Journal of Theoretical Biology* (**1972**), *35*, 3,601-604. DOI: 10.1016/0022-5193(72)90153-1.

11. Cleaves H.J., Scott A.M., Hill F.C., Leszczynski J., Sahaide N., Hazen R., Mineral–organic interfacial processes: potential roles in the origins of life, *Chemical Society Reviews* (**2012**), *41*, 5502–5525. DOI: 10.1039/C2CS35112A.

12. Kitadai N., Maruyama S., Origins of building blocks of life: A review, *Geoscience Frontiers* (**2018**), *9*, 1117-1153.
DOI: 10.1016/j.gsf.2017.07.007.

13. Ruiz-Mirazo K., Briones C., de la Escosura A., Prebiotic Systems Chemistry: New Perspectives for the Origins of Life, *Chemical Reviews* (**2014**), *114*, 285−366.
DOI: 10.1021/cr2004844.

14. Hazen R.M., Chance, necessity and the origins of life: a physical sciences perspective. *Philosophical Transactions. Royal Society A* (**2017**), *375*: 20160353. 1-12.
DOI: 10.1098/rsta.2016.0353.

15. Horiuchi N., Nakamura M., Nagai A., Katayama K., Yamashita K., Proton conduction related electrical dipole and space charge polarization in hydroxyapatite, *Journal of Applied Physics* (**2012**), *112*, 074901.
DOI: 10.1063/1.4754298.

16. Horiuchi N., Nakaguki S., Wada N., Nakamura M., Nagai A., Katayama K., Yamashita K., Polarization-induced surface charges in hydroxyapatite ceramics, *Journal of Applied Physics* (**2014**), *116*, 014902, 1-8.
DOI: 10.1063/1.4886235.

17. Jarlbring M., Sandström D.E., Antzutkin O.N., Forsling W., Characterization of Active Phosphorus Surface Sites at Synthetic Carbonate-Free Fluorapatite Using Single-Pulse ^{1}H, ^{31}P, and ^{31}P CP MAS NMR, *Langmuir* (**2006**), *22*, 4787–4792.
DOI: 10.1021/la052837j.

18. Wang Y., Von Euw S., Fernandes F.M., Cassaignon S., Selmane M., Laurent G., Pehau-Arnaudet G., Coelho C., Bonhomme-Coury L., Giraud-Guillaume M-M., Babinneau F., Azars T., Nassif N., Water-mediated structuring of bone apatite, *Nature Material*s (**2013**), *12*, 1144–1153.
DOI: 10.1038/nmat3787.

19. Jager C., Welzel T., Meyer-Zaika W., Epple M.A., A solid‐state NMR investigation of the structure of nanocrystalline hydroxyapatite, *Magnetic Resonance in Chemistry* (**2006**), *44*, 573–580..
DOI: 10.1002/mrc.1774.

20. Osman M.B., Diallo-Garcia S., Herledan V., Brouri D., Toshioka T., Kubo J., Millot Y., Costentin G., Discrimination of surface and bulk structure of crystalline hydroxyapatite nanoparticles by NMR, *Journal of Physical Chemistry C* (**2015**), *119*, 23008–23020.
DOI:10.1021/acs.jpcc.5b08732.

21. Bertran O., Revilla-López G., Casanovas J., del Valle L.J., Turon P., Puiggalí J., Alemán C., Dissolving hydroxyolite: A DNA molecule into its hydroxyapatite mold, *Chemistry - A European Journal* (**2016**), *22*, 6631–6636.
DOI:10.1002/chem.201600703.

22. Ueshima M., Nakamura S., Ohgaki M., Yamashita K., Electrovectorial effect of polarized hydroxyapatite on quasi-epitaxial growth at nano-interfaces, *Solid State Ionics* (**2002**), *151*, 29–34.
DOI:10.1016/S0167-2738(02)00600-8.

23. Ueshima M., Nakamura S., Yamashita K., Huge, millicoulomb charge storage in ceramic hydroxyapatite by bimodal electric polarization, *Advanced Materials* (**2002**), *14*, 591–595.
DOI:10.1002/1521-4095(20020418)14:8<591::AID-ADMA591>3.0.CO;2-7

24. Nakamura, M., Sekijima Y., Nakamura S., Kobayashi T., Niwa K., Yamashita K., Role of blood coagulation components as intermediators of high osteoconductivity of electrically polarized hydroxyapatite, *Journal Biomedical Materials Research* (**2006**), *79A*, 627– 634.
DOI:10.1002/jbm.a.30827.

25. Editorial comment, The Nitrogen Fix, *Nature* (**2013**), *501*, 6–6.
DOI:10.1038/501006a.

26. Smith B.E., Nitrogenase reveals its inner secrets, *Science* (**2002**), **2*9*7**, 1654–1655.
DOI:10.1126/science.1076659.

27. Macleod K.C., Holland P.L., Recent developments in the homogeneous reduction of dinitrogen by molybdenum and iron, *Nature Chemistry* (**2013**), *5*, 559–565.
DOI:10.1038/nchem.1620.

28. Lan R., Irvine J.T.S., Tao S., Synthesis of ammonia directly from air and water at ambient temperature and pressure, *Scientific Reports* (**2013**), *3*, 1145.
DOI:10.1038/srep01145.

29. Shilov A.E., Catalytic reduction of molecular nitrogen in solutions, *Russian Chemical Bulletin International Edition* (**2003**), *52*, 2555–2562.
DOI: 10.1023/B:RUCB.0000019873.81002.60.

30. Yandulov D.V., Schrock R.R., Catalytic reduction of dinitrogen to ammonia at a single molybdenum center, *Science* (**2003**), *301*, 76–78.
DOI:10.1126/science.1085326.

31. Schrock R.R., Reduction of dinitrogen, *Proceedings of National Academy of Sciencies. U. S. A.* (**2006**), *103*, 17087–17087.
DOI:10.1073/pnas.0603633103.

32. Kuriyama S., Arashiba K., Nakajima K., Matsuo Y., Tanaka H., Ishii K.,Yoshizawa K., Catalytic transformation of dinitrogen into ammonia and hydrazine by iron-dinitrogen complexes bearing pincer ligand, *Nature Communications* (**2016**), *7*, 12181.
DOI: 10.1038/ncomms12181.

33. Mikkelsen M., Jorgensen M., Krebs F.C., Synthesis and characterization of zwitterionic carbon dioxide fixing reagents, *International Journal of Greenhouse Gas Control* (**2010**), *4*, 452–458.
DOI:10.1016/j.ijggc.2009.11.008.

34. Alper E., Orhan O.Y., CO_2 utilization: Developments in conversion processes, *Petroleum* (**2017**), *3*, 109–126.
DOI:10.1016/j.petlm.2016.11.003.

35. Ola O., Maroto-Valer M.M., Mackintosh S., Turning CO_2 into valuable chemicals, *Energy Procedia* (**2013**), *37*, 6704–6709.
DOI:10.1016/j.egypro.2013.06.603.

36. Aresta M., Dibenedetto A., Utilisation of CO_2 as a chemical feedstock opportunities and challenges, *Dalton Transactions* (**2007**), *28*, 2975–2992.
DOI:10.1039/B700658F.

37. Song Q-W., Zhou Z-H., He L-N., Efficient, selective and sustainable catalysis of carbon dioxide, *Green Chemistry* (**2017**), *19*, 3707–3728.
DOI:10.1039/C7GC00199A.

38. Zhao B., Su Y., Process effect of microalgal-carbon dioxide fixation and biomass production: A review, *Renewable Sustainable Energy Reviews* (**2014**), *31*, 121–132.
DOI:10.1016/j.rser.2013.11.054.

39. Fleischer M., Blattmann H., Mülhaupt R., Glycerol-, pentaerythritol- and trimetylolpropane based polyurethanes and their cellulose carbonate composites prepared via the non-isocyanate route with catalytic carbon dioxide fixation, *Green Chemistry* (**2013**), *15*, 934–942.
DOI:10.1039/C3GC00078H.

40. Molla R.A., Iqubal Md. A., Ghosh K., Islam S.M., A route for direct transformation of aryl halides to benzyl alcohols via carbon dioxide fixation reaction catalyzed by a (Pd@N-GMC) palladium nanoparticle encapsulated nitrogen doped mesoporous carbon material, *Green Chemistry* (**2016**), *18*, 4649–4656.
DOI:10.1039/C6GC01038E.

41. Bar-Even A,, Noor E., Lewis N.E., Milo R., Design and analysis of synthetic carbon fixation pathways, *Proceedings of National Academy of Sciences. U. S. A*. (**2010**), *107*, 8889–8894.
DOI:10.1073/pnas.0907176107.

42. Dubois M.R., Dubois D.L., Development of molecular electrocatalysts for CO_2 reduction and H_2 production/oxidation, *Accounts of Chemical Research* (**2009**), *42*, 1974–1982.
DOI: 10.1021/ar900110c.

43. Miller S.L., A production of amino acids under possible primitive earth conditions. *Science* (**1953**) *117*, 528-529.
DOI: 10.1126/science.117.3046.528.

44. Miller S.L., Urey H.C., Organic compound synthesis on the primitive Earth. *Science* (**1959**), *130*, 246-251.
DOI: 10.1126/science.130.3370.245.

45. Zaia D.A.M., Thaïs C., Zaia B.V., De Santana H., Which Amino Acids Should Be Used in Prebiotic Chemistry Studies?. *Origins of Life and Evolution of Biospheres* (**2008**), *38*, 469–488.
DOI: 10.1007/s11084-008-9150-5.

46. Burton A.S., Stern J.C., Elsila J.E., Glavin D.P., Dworkin J.P., Understanding prebiotic chemistry through the analysis of extraterrestrial amino acids and nucleobases in meteorites. *Chemical Society Reviews* (**2012**), *41*, 5459-5472.
DOI: 10.1039/c2cs35109a.

47. Markhinin E.K., Podkletnov N.E., The phenomenon of formation of prebiological compounds in volcanic processes. *Origins of Life* (**1977**), *8,* 225-235.
DOI:10.1007/BF00930684.

48. Podkletnov N. E., Markhinin E.K., New data on abiogenic synthesis of prebiological compounds in volcanic processes. *Origins of Life* (**1981**), *11*, 303-315.
DOI:10.1007/BF00931484.

49. Lavrentiev G.A., Strigunkova T.F., Egorov I.A., A biological synthesis of aminoacids, pyrines and pyrimidines under conditions simulating the volcanic ash-cloud. *Origins of Life,* (**1984**), *14*, 205-212.
DOI:10.1007/BF00933659.

50. Bada J.L., New insights into prebiotic chemistry from Stanley Miller's spark discharge experiments. *Chemical Society Reviews* (**2013**), *42*, 2186-2196.
DOI: 10.1039/C3CS35433D.

51. Chittenden G.J.F., Schwartz A.W., Prebiotic photosynthetic reactions. *Biosystems* (**1981**), *14*, 15-32.
DOI:10.1016/0303-2647(81)90018-6.

52. Trainer M.G., Atmospheric Prebiotic Chemistry and Organic Hazes, *Current Organic Chemistry* (**2013**), *17*, 1710-1723.
DOI: 10.2174/13852728113179990078.

53. Erastova V., Degiacomi M.T., Fraser D.G., Greenwell, H.C., Mineral surface chemistry control for origin of prebiotic peptides. Nature Communications (**2017**), *8*: 2033, 1-9.
DOI: 10.1038/s41467-017-02248-y.

54. Rimola A., Ugliengo P., Sodupe M., Formation versus Hydrolysis of the Peptide Bond from a Quantum-mechanical Viewpoint: The Role of Mineral Surfaces and Implications for the Origin of Life, *International Journal of Molecular Sciences*, (**2009**), *10*, 746-760.
DOI:10.3390/ijms10030746.

55. Rimola A., Tosoni S., Sodupe M., Ugliengo P., Does silica surface catalyse peptide bond formation? New insights from first-principles calculations, *ChemPhysChem* (**2006**), *7*, 157-163.
DOI: 10.1002/cphc.200500401.

56. Martin W., Baross J., Kelley D., Russell M.J., Hydrothermal vents and the origin of life. *Nature Reviews Microbiology* (**2008***), 6*, 805-814.
DOI: 10.1038/nrmicro1991.

57. Stüeken E.E., Anderson R.E., Bowman J.W., Brazelton W.J., Colangelo-Lilis J., Goldman A.D., Som S.M., Baross J.A., Did life originate from a global chemical reactor?. *Geobiology* (**2013**), *11*, 101-126.
DOI: 10.1111/gbi.12025.

58. Hartman H., Photosynthesis and the origin of life. *Origins of Life and Evolution of Biospheres* (**1998**), *28*, 515-521.
DOI:10.1023/A:1006548904157.

59. Kasting J.F., Siefert J.L., Life and the evolution of Earth's atmosphere. *Science* (**2002**), *296*, 1066-1068.
DOI: 10.1126/science.1071184.

60. Kasting J.F., Earth's early atmosphere. *Science* (**1993**), *259*, 920-926.
DOI: 10.1126/science.11536547.

61. Cleaves H.J., Chalmers J.H., Lazcano A., Miller S.L., Bada J.L., A reassessment of prebiotic organic synthesis in neutral planetary atmospheres. *Origins of Life and Evolution of Biospheres* (**2008**), *38*, 105-115.
DOI: 10.1007/s11084-007-9120-3

62. Kasting J.F., Catling D., Evolution of a habitable planet. Annual Review of Astronomy and Astrophysics (**2003**), *41*, 429-463.
DOI: 10.1146/annurev.astro.41.071601.170049.

63. Tian F., Toon O.B., Pavlov A.A., De Sterck H., A hydrogen-rich Earth atmosphere. *Science* (**2005**), *308*, 1014-1017.
DOI: 10.1126/science.1106983.

64. Sagan C., Khare B.N., Long-wavelength ultraviolet photoproduction of amino acids on the primitive Earth. *Science* (**1971**), *173*, 417-420.
DOI: 10.1126/science.173.3995.417.

65. Becker R.S., Hong K., Hong J.H., Hot hydrogen atoms reactions of interest in molecular evolution and interstellar chemistry, *Journal of Molecular Evolution* (**1974**), *4*, 157–172.
DOI:10.1007/BF01732020.

66. Muñoz Caro G.M., Meierhenrich U.J., Schutte W.A., Barbier B., Arcones Segovia A., Rosenbauer H., Thiemann W. H-P., Brack A., Greenberg J.M., Amino acids from ultraviolet irradiation of interstellar ice analogues, *Nature* (**2002**), *416*, 403-406.
DOI: 10.1038/416403a.

67. Rivas M., del Valle L.J., Armelin E., Bertran O., Turon P., Puiggalí J., Alemán C., Hydroxyapatite with Permanent Electrical Polarization: Preparation, Characterization and Response Against Inorganic Adsorbates, *ChemPhysChem* (**2018**), *19*, 14, 1746-1755.
DOI:10.1002/cphc.201800196.

68. Rivas M., del Valle L.J., Turon P., Alemán C., Puiggalí J., Sustainable synthesis of amino acids by catalytic fixation of molecular dinitrogen and carbon dioxide. *Green Chemistry* (**2018**), *20*, 685–693.
DOI: 10.1039/C7GC02911J.

69. Rodrigues E.G., Keller T.C., Mitchell S., Pérez-Ramírez J., Hydroxyapatite, an exceptional catalyst for the gas-phase deoxygenation of bio-oil by aldol condensation. *Green Chemistry* (**2014**), *16***,** 4870-4870.
DOI: 10.1039/C4GC01432D.

70. Kim H-J., Ricardo A., Illangkoon H.I., Kim M.J., Carrigan M.A., Frye F., Benner S.A., Synthesis of carbohydrates in mineral-guided prebiotic cycles. *Journal of American Chemical Society* (**2011**), *133*, 9457-9468.
DOI: 10.1021/ja201769f.

71. Piccoli P.M., Candela P.A., Apatite in igneous systems, *Reviews in Mineralogy and Geochemistry* (**2002**), *48*, 255-292.
DOI: 10.2138/rmg.2002.48.6.

72. de Graaf R.M., Schwartz A.W., Reduction and activation of phosphate on the primitive Earth. *Origins of Life and Evolution of Biospheres* (**2000**), *30*, 405-410.
DOI:10.1023/A:1006700512902.

73. Holm N.G., Glasses as sources of condensed phosphates on the early earth. *Geochemistry* (**2014**), *T 15*, 1-4.
DOI:10.1186/1467-4866-15-8.

74. Schwartz A.W., Phosphorus in prebiotic chemistry. *Philosophic Transactions Royal Society B* (2006), *361*, 1743-1749 (**2006**).
DOI:10.1098/rstb.2006.1901.

75. Liao C-J., Lin F-H., Chen K-S., Sun J-S., Thermal decomposition and reconstitution of hydroxyapatite in air atmosphere. *Biomaterials* (**1999**), *20*, 1807-1813. DOI:10.1016/S0142-9612(99)00076-9.

76. McNutt S.R., Williams E.R., Volcanic lightning: global observations and constraints on source mechanisms. *Bulletin of Volcanology* (**2010**), *72*, 1153-1167. DOI:10.1007/s00445-010-0393-4.

77. Basiuk V.A., Navarro-González R., Possible role of volcanic ash-gas clouds in the Earth's prebiotic chemistry, *Origins of Life and Evolution of Biospheres* (**1996**), *26*, 173-194. DOI:10.1007/BF01809854.

78. Matsumura Y., Kanai H., Moffat J.B., Formation of oxygen radicals by coordinatively unsaturated oxygen anions on hydroxyapatite. *Journal of Molecular Catalysis A: Chemical*, (**1998**), *135*, 317-320. DOI:10.1016/S1381-1169(98)00003-X.

79. Nishikawa H., Radical generation on hydroxyapatite by UV irradiation. Materials Letters (**2004**), *58*, 14-16. DOI:10.1016/S0167-577X(03)00396-3.

80. Langmann B., Volcanic Ash versus Mineral Dust: Atmospheric Processing and Environmental and Climate Impacts. *ISRN Atmospheric Sciences* (**2013**), Article ID 245076, 1-17. DOI:10.1155/2013/245076.

81. Pinto J.P., Gladstone G.R., Yung Y.L., Photochemical production of formaldehyde in Earth's primitive atmosphere. *Science* (**1980**), *210*, 183-185. DOI: 10.1126/science.210.4466.183.

82. Casanovas J., Revilla-López G., Bertrán O., del Valle L.J., Turon P., Puiggalí J., Alemán C.. Restricted puckering of mineralized RNA-like riboses, *Journal of Physical Chemistry B*, (**2014**), *118*, 5075-5081. DOI:10.1021/jp501714q.

83. Zahnle K.J., Photochemistry of methane and the formation of hydrocyanic acid (HCN) in the Earth's early atmosphere. Journal of Geophysical Research (**1986**). *91*, 2819-2834. DOI:10.1029/JD091iD02p02819|.

84. Oro J., Mechanism of synthesis of adenine from hydrogen cyanide under possible primitive Earth conditions, *Nature* (**1961**), *191*, 1193-1194. DOI:10.1038/1911193a0.

85. Schrader M.E., The RNA world: conditions for prebiotic synthesis. *Journal of Geophysical Research* (**2009**), *114*, D15305. DOI:10.1029/2008JD010810.

86. Deamer D., Weber A.L., Bioenergetics and life's origins, *Cold Spring Harbor Perspectives in Biology* (**2010**), *2*, a004929.
DOI:10.1101/cshperspect.a004929.

87. Rimola A., Sodupe M., Ugliengo P., Aluminosilicate Surfaces as Promoters for Peptide Bond Formation: An Assessment of Bernal's Hypothesis by ab Initio Methods, *Journal of American Chemical Society*, (**2007**), *129*, 8333-8344.
DOI: 10.1021/ja070451k.

88. Tian F., Kasting J.F., Zahnle K., Revisiting HCN formation in Earth's early atmosphere. *Science Letters* (**2011**), *308*, 417-423.
DOI: 10.1016/j.epsl.2011.06.011.

89. Saladino R., Neri V., Crestini C., Costanzo G., Graciotti M., Di Mauro E., The role of the formamide/zirconia system in the synthesis of nucleobases and biogenic carboxylic acid derivatives. *Journal of Molecular Evolution* (**2010**), *71*, 100-110.
DOI:10.1007/s00239-010-9366-7.

90. Kawai T., Ohtsuki C., Kamitakahara M., Tanihara M., Miyazaki T., Sakaguchi Y., Konagaya S., Removal of formaldehyde by hydroxyapatite layer biomimetically deposited on polyamide film. *Environmental Science and Technology* (**2006**), *40*, 4281-4285.
DOI:10.1021/es050098n.

91. Valle L.J., Bertrán O., Chaves G, Revilla-López G., Rivas M., Teresa Casas M., Casanovas J., Turon P., Puiggalí J., Alemán C., DNA adsorbed on hydroxyapatite surfaces *Journal of Materials Chemistry B* (**2014**), *2*, 6953-6966.
DOI:10.1039/C4TB01184H.

Chapter 6.
General Conclusions

The main conclusions of this thesis are summarized in this last Chapter. As we stated in Chapter 2, the main objective is to define a theoretical framework around the hydroxyolite concept that we split into four sub-objectives that deal with its origin, role and consequences.

6.1. Main conclusion

We conclude that hydroxyolite, a hybrid system made by the combination of a nucleic acid biopolymer and a HAp mineral, is an extremely fruitful concept that can be studied and interpreted from several angles. Each of them leads to specific conclusions that can be applied to different fields of knowledge. For that reason, we developed through the thesis a deep knowledge about the basic concepts that make it possible to understand the principles that regulate its formation in vitro and in natural environments. Such basic knowledge allowed us to speculate and develop concepts and perspectives about its role through the history of life, from the abiotic synthesis of simple molecules, through the mass extinction events and its relation with some diseases. In parallel, we have been able to prove that an inorganic photosynthetic process facilitated by HAp/tsp is feasible, opening a door to a low energy process to fixate nitrogen that allows a simultaneous recycling of carbon dioxide and methane, the main promoters of the greenhouse effect.

Accordingly, the following sections detail the conclusion we obtained around the hydroxyolite concept.

6.2. Crystallization plane

We proved that four phosphate groups belonging to the polyphosphate backbone of nucleic acid double helix form a plane that matches with a four phosphate group plane. Such a common shared plane, that repeats through the double helix, is the site where an HAp crystal initiates. Therefore nucleic acids act as a template for the nucleation of HAp clusters that permits their encapsulation and adsorption on the HAp surface. The calcium phosphate clusters formed in the first stages of the nucleation transform into complex clusters, in which Ca^{2+}, PO_4^{3-} and OH^- ions occupy positions according to crystalline HAp.

6.3. Encapsulation of DNA in aqueous solutions containing Ca^{2+} and PO_4^{3-}

The biomineralization of DNA into HAp is confirmed experimentally by mixing aqueous solution containing Ca^{2+}, PO_4^{3-} and OH^- ions with DNA. The existence of encapsulated DNA inside of the HAp crystal was confirmed after the removal of superficially adsorbed DNA by enzymatic digestion and further redissolution of the mineral that led to the release of the entrapped DNA.

6.4. Elucidation of the dissolving mechanism of a hydroxyolite

The dissolution mechanism on the acidic dissolution of HAp and hydroxyolites was revealed at atomic-level. An initial hydration of phosphate, enhanced by the reactivity of hydronium ion, that further hydrogenates the phosphate ion, triggers calcium ions detachment. The release of calcium ions occurs through a polynuclear process and involves multiple independent centers widely distributed on the surface. The detachment of the calcium ions is caused by electrostatic alterations induced by the HPO_4^{2-} and $H_2PO_4^{3-}$ species and not by the detachment of neighboring calcium ions. Mg^{2+} ions included in the hydroxyolite system are not playing a relevant role in the dissolution process. We highlight two main consequences of unveiling such a mechanism:

a) New strategies for Ca^{2+} fixation to fight against osteoporosis
b) Deep understanding about how hydroxyolite particles deliver nucleic acids in the cytosol or in the cell nucleus to carry out the transfection processes. HAp is easily redissolved in slightly acidic media and are able to carry and deliver the encoded information without modifying it, whilst keeping it functional.

6.5. Nucleic acid protection by HAp shell

We concluded through a synergistic theoretical-empirical approach that HAp acts as a shield for nucleic acids biopolymer, protecting their functionality from temperature-stressing conditions and chemicals such as enzymatic degradation. Additionally, the dissolution process releases buffering species (i.e. HPO_4^{2-} and $H_2PO_4^-$) that stabilizes the pH around the nucleic acid contributing with additional protection against enzymatic degradation while the hydroxyolite is dissolved.

6.6. Surviving mass extinction events through biomineralized DNA

A hydroxyolite can be understood as an antagonist of a cell in the sense that a cell is a finely tuned living system specialized in transmitting genetic information to the next generation, while a hydroxyolite is a passive seed made of genetic information and a mineral but has the potential to deliver such genetic information in a new cell. Using such a concept we concluded HAp might protect DNA through mass extinction events, where environmental conditions were expected to damage the delicate molecule of DNA. We use the concept of a hydroxyolite to hypothesize how life was able to thrive on Earth through biomineralized DNA. In such a discussion, we extend the hydroxyolite concept based on materials chemistry to several disciplines such as chemistry, biology, biotechnology and medicine. From our perspective, the DNA–HAp particle has to be understood as a molecule in its mould. HAp has the potential to be the Trojan horse that protected and helped DNA to survive through mass extinction events. Its ability to be reused when environmental conditions become more friendly facilitates the transfection of other cells to reintroduce such DNA in the mainstream of life.

6.7 Prebiotic model based on inorganic photosynthesis

Based on the hydroxyolite concept where DNA is encapsulated in a HAp mold, we focused on the HAp substrate as a catalyst that might be the facilitator of the prebiotic synthesis of the building blocks of life. Consequently, we developed a prebiotic scenario where HAp, known as a component of igneous rocks, was expulsed in volcanic eruptions suffering the effects of high temperature (within 800 and 1,000 ºC) and elevated differences of potential (i.e. 500 V) under the UV light of sun and lightning in the volcano plume. Such treatment converts HAp in an enhanced catalyst able to deliver simple molecules as building blocks of life. The high adsorption ability of HAp allows the retention of such molecules facilitating coupled reactions of polymerization to obtain biopolymers such as proteins and nucleic acids. Such a model incorporates concepts from atmospheric photochemistry, volcanos as giant reactions, minerals as catalytic surfaces that we integrate altogether in a model based on inorganic photosynthesis.

6.7. Permanently polarized HAp

Based on the theoretical concept that HAp might be the mold where basic molecules for life were synthesized, we concluded that HAp should be treated with a high temperature and high differences of potential, as happens in a volcanic storm, to simulate prebiotic conditions. As a result, we have obtained HAp/tsp, an outstanding catalyst developed by means of a thermally and electrically stimulated polarization process. The new catalyst is able to catalyze important reactions but we focus in this thesis on an inorganic photosynthesis, a highly desired process due to its ability to fix nitrogen and carbon to generate organic molecules. Starting from simple gases as dinitrogen, carbon dioxide, methane and liquid water, organic matter and amino acids were obtained under UV light and using mild reaction conditions in regards of temperature (< 100 ºC) and pressure (gas mixture within 1-6 bar).

6.8 Final word

All in all, we established a conceptual framework that extends its impact to Chemistry through catalysis and a prebiotic model as well as Biology and Biotechnology as it deals with a non-viral vector of transfection that can transport and release DNA to a new cell. It also impacts Medicine, for its potential consequences in calcifying diseases (i.e. breast cancer) where tumoral DNA might be encapsulated and protected by HAp, ready to migrate and transfect distant cells.

Annex I

Modeling biominerals formed by apatites and DNA[2]

Abstract

Different aspects of biominerals formed by apatite and DNA have been investigated using computer modeling tools. Firstly, the structure and stability of biominerals in which DNA molecules are embedded into hydroxyapatite and fluoroapatite nanopores have been examined by combining different molecular mechanics methods. After this, the early processes in the nucleation of hydroxyapatite at a DNA template have been investigated using molecular dynamics simulations. Results indicate that duplexes of DNA adopting a B double helix can be encapsulated inside nanopores of hydroxyapatite without undergoing significant distortions in the inter-strand hydrogen bonds and the intra-strand stacking. This ability of hydroxyapatite is practically independent of the DNA sequence, which has been attributed to the stabilizing role of the interactions between the calcium atoms of the mineral and the phosphate groups of the biomolecule. In contrast, the fluorine atoms of fluoroapatite induce pronounced structural distortions in the double helix when embedded in a pore of the same dimensions, resulting in the loss of its most relevant characteristics. On the other hand, molecular dynamics simulations have allowed us to observe the formation of calcium phosphate clusters at the surface of the B-DNA template. Electrostatic interactions between the phosphate groups of DNA and Ca^{2+} have been found to essential for the formation of stable ion complexes, which were the starting point of calcium phosphate clusters by incorporating PO_4^{3-} from the solution.

---

[2] Published in Revilla-López G., Casanovas J., Bertran O., Turon P., Puiggalí J., Alemán C., Modeling biominerals formed by apatites and DNA, *Biointerphases* (**2013**), *8*, 10. Reproduced with permission of AIP Publishing.

Annex I

Modeling biominerals formed by apatites and DNA

I.1. Background

Hydroxyapatite (HAp), a mineral with formula $Ca_{10}(PO_4)_6(OH)_2$ and hexagonal symmetry, is the most stable form of calcium phosphate at room temperature and in the pH range of 4–12.[1] This mineral, which is the main component of bones and teeth, is considered as an important biomaterial since several decades ago.[2] Thus, due to both its outstanding biological responses to the physiological environment and its very close similarity to natural bone structure, HAp is currently applied in biomedicine. For example, it is used as a bioactive and osteoconductive bone substitute material in clinical surgery,[3,4] and as a system for the delivery of antitumor agents and antibodies in the treatment of cancer.[5-7] Furthermore, as HAp also has the advantage of absorbability and high binding affinity with a variety of molecules, it has been also used as a purification platform. For example, HAp is applied for the removal of heavy atoms from waste water,[8] and for the separation, extraction and purification of proteins[9] and DNA.[10]

DNA/HAp biominerals formed by the combination of DNA with a HAp matrix can be viewed from different perspectives. The first refers to the fact that therapeutic DNA is encapsulated in HAp nanoparticles for its subsequent transfection into living cells (e.g. liver cells, fibroblasts, osteoblasts and tumor cells).[5-7,11,12] Specifically, HAp nanoparticles with embedded DNA chains can be obtained using different approaches, even though the more popular are those based on the in situ precipitation of the inorganic salt in presence of DNA[13,14] and on the use of a HAp core that is coated using colloidal solutions to give a multishell particle.[7] Nanostructured HAp has been shown to be superior for the transfection to other gene delivery methods in terms of immunogenicity and toxicity (i.e. safety).[15] Moreover, the transfection efficiency can be stabilized and enhanced by modulating properties such as extent of DNA binding and encapsulation, particle size, and dissolution behavior of the HAp phases.[15,16] The interaction between the two entities of the biomineral has been proposed to occur because of the affinity between the calcium of HAp and the phosphate backbone of DNA.[17-20] It should be noted that this proposal makes the nucleotide sequence of DNA unimportant, whereas its length takes major importance. Another

perspective is the one reported by Kostetsky,[21] who observed that the period of translation along the c-axis of the HAp lattice, 3.4 Å, is relatively similar to the period of the DNA double helix. This feature combined with the fact that the phosphate groups of HAp are able to catalyze the abiogenic synthesis of: D-ribose from ammonia, methane and water;[22,23] nucleotides from nucleosides condensing agents and ammonium oxalate;[24] and polynucleotides with a 3',5'-phosphodiether bond[24] under conditions similar to those of primaveral Earth, led Kostetsky to propose a model for the synthesis of DNA through the interaction of its different elements with the lattice of HAp mineral.[25] According to this model, the DNA double helix is embedded into the crystalline network of HAp forming a biomineral similar to that obtained by encapsulating therapeutic DNA into HAp nanoparticles.

On the other hand, in a very recent study Gerdon and co-workers[26] demonstrated the ability of DNA to template the mineralization of calcium phosphate. These authors developed a quartz crystal microbalance sensor for the quantification of HAp formation and the assessment of DNA as a template molecule. The results, which were also supported by optical density and dynamic light scattering measures, FTIR spectroscopy and scanning electron microscopy, suggested that DNA sequesters calcium and phosphate ions, thereby supersaturating the microenvironment and acting as a scaffold on which mineral forms.[26] Moreover, small differences in DNA length, hybridization, and secondary structure were found to provoke differences in affinity for HAp and appear to influence mineralization.

In this work we have used molecular modeling tools to investigate the structure of DNA/HAp biominerals, in which single stranded (ss) and double stranded (ds) DNA are embedded into HAp nanopores. We have focused our analyses on the following aspects: (i) the smallest nanopore size required for the accommodation of ds DNA arranged in the typical B structure[27] (ds B-DNA) during the encapsulation process; (ii) the strain induced by the HAp crystalline field into the B-DNA structure; (iii) the importance of the chemical nature of the inorganic part of the biomineral in the DNA, which has been investigated by comparing DNA/HAp with the biomineral constructed by combining DNA with fluoroapatite [$Ca_{10}(PO_4)_6F_2$, abbreviated FAp], hereafter denoted DNA/FAp; (iv) the encapsulation of ssDNA in terms of molecular strain and relative stability with respect to ds DNA; and (v) the stability of HAp crystals formed around the ds B-DNA core. Furthermore, in order to contribute to a better understanding of the interaction of B-DNA with HAp at the

atomic level, we have performed a simulation study of the nucleation and crystal growth of HAp at the ds B-DNA matrix. More specifically, we have used Molecular Dynamic (MD) simulations to provide detailed atomistic models for the initial stages of nucleation and cluster formation of calcium phosphate at a B-DNA molecule. The rest of the paper has been organized as follows. In the next section, we briefly summarize the main characteristics of the crystal structures of natural HAp and FAp, and the chemical structures of the three B-DNA duplexes studied in this work. After this, the strategy and computational details used for both the encapsulation of DNA in apatites and the early processes in the nucleation of HAp at a BDNA template are described. The results have been organized in several sub-sections, which are devoted to the encapsulation of ds and ss DNA in both HAp and FAp, the validation of the force-field to reproduce organic···inorganic interactions in biominerals, and both the modeling and dynamics of HAp crystals growth around the ds B-DNA template. Finally, conclusions are summarized in the last section of Annex I.

I.2. Structures of apatites and DNA

Natural HAp has a hexagonal crystal structure with space group $P6_3/m$ and periods a=b= 9.42 Å, and c= 6.87 Å. The total number of atoms in the unit cell is 44, even though it only contains seven symmetrically independent atoms: two calcium ions, one forming single atomic columns parallel to the c axis (Ca_I) and the other surrounding the hexagonal channel of hydroxyl in groups of the three calcium atoms at different heights (Ca_{II}); one phosphor and three oxygen atoms (P, O_I, O_{II} and O_{III}) forming PO_4 tetrahedral units; and the O(H) ions disordered along c about the mirror plane at z= ¼. The occupancy of the OH^- sites was 50%, as necessary in a $P6_3/m$. FAp shows a very similar crystal structure with 42 atoms in the $P6_3/m$ hexagonal cell (a= b= 9.40 Å, c = 6.88 Å).[28] In this case, the OH^- ions of HAp are replaced by F^-, which are located on the c-axis.

Three different ds dodecamers, which adopt a B-DNA double helix, have been examined. The chemical structures of the three duplexes, hereafter denoted **I**, **II** and **III**, are 5'-CGCGAATTCGCG-3', 5'-GCGAGATCTGCG-3' and 5'-CGCGAATTC*GCG-3', respectively. Sequence **I** is known as the Dickerson's dodecamer[29] and consists in a well-known sequence with three primary characteristic tracts: CG, AA and TT. Sequence **II** is a conventional sequence that becomes involved in different cellular processes, including carcinogenic ones.[30] Finally, **III** involves methylation of the C5 position of cytidine base,

identified as C*.[31] This methylation is known to suppress hydrolysis by *Eco*RI restriction enzyme. The 3D structure of the three dodecamers was studied in solution and/or solid state,[29-32] a B-DNA arrangement being observed in all cases. On the other hand, ssDNAs were constructed by removing one of the strands from the three selected duplexes.

I.3. Encapsulation of DNA in apatites and nucleation of HAp

Giving the hexagonal symmetry of the two investigated apatites and the molecular dimensions of the B-DNA dodecamers, HAp and FAp models (super-cells) were constructed considering 6×6×7 unit cells. After this, a hole was generated in the center of each super-cell, the dimensions of such hole being defined by the ds B-DNA (i.e. steric conflicts between the apatite atoms and the BDNA were not allowed). After several trials, we found that a hole of 2×2×7 units cells (Figure Ann.I.1a) was the minimum required to accommodate the double helix without severe steric contacts. In order to completely avoid unfavorable steric interactions between the apatite and the biomolecule, some additional atoms and groups of atoms were translated at their border regions (Figure Ann.I.1b) allowing us to maintain the electroneutrality of the super-cells. The side length of this hole is 19 Å and its angle γ is 120. The resulting models (i.e. super-cells with a hole of appropriated dimensions at the center) consist of 9,856 and 9,408 atoms for HAp and FAp, respectively. The atomic coordinates for the ds DNAs were generated using the NAB (Nucleic Acid Builder) program of the AMBER software,[33] which constructed the double helix in the canonical B form. In order to maintain the electrical neutrality of the system, Ca^{2+} ions were put at the minor groove of the double helix, as is frequently observed by X-ray diffraction.[34-36] The positions of these ions were optimized by energy minimization while the coordinates of the rest of the atoms of the system were kept fixed. Models for encapsulated ssDNAs were constructed by removing one of the two strands from the ds B-DNAs embedded in HAp or FAp. In these cases, Ca^{2+} ions were put at random positions around the backbone phosphate groups and subsequently optimized by energy minimization.

The simulation system used to investigate the initial stages of nucleation and cluster formation of calcium phosphate at a B-DNA double helix consisted of the Dickerson's dodecamer duplex (**I**), which was located at the center of the simulation box, 945 Ca^{2+} ions, 567 PO_4^{3-} ions, 189 OH^- ions, and 29,560 water molecules (Figure Ann.I.1c). In order to provide a comprehensive view of the templating role of the double helix, additional simulations of the same system but without B-DNA were carried out. Several factors are expected to affect the nucleation and growth of the HAp at the B-DNA, ionic concentration being among them. We are aware that the concentration of ions in the simulation systems is higher than in biological conditions. However, modeling much lower concentrations would require computationally prohibitively large simulation boxes. Furthermore, increasing the ion concentration is a practical way to accelerate the simulation of HAp nucleation and growth.[37,38]

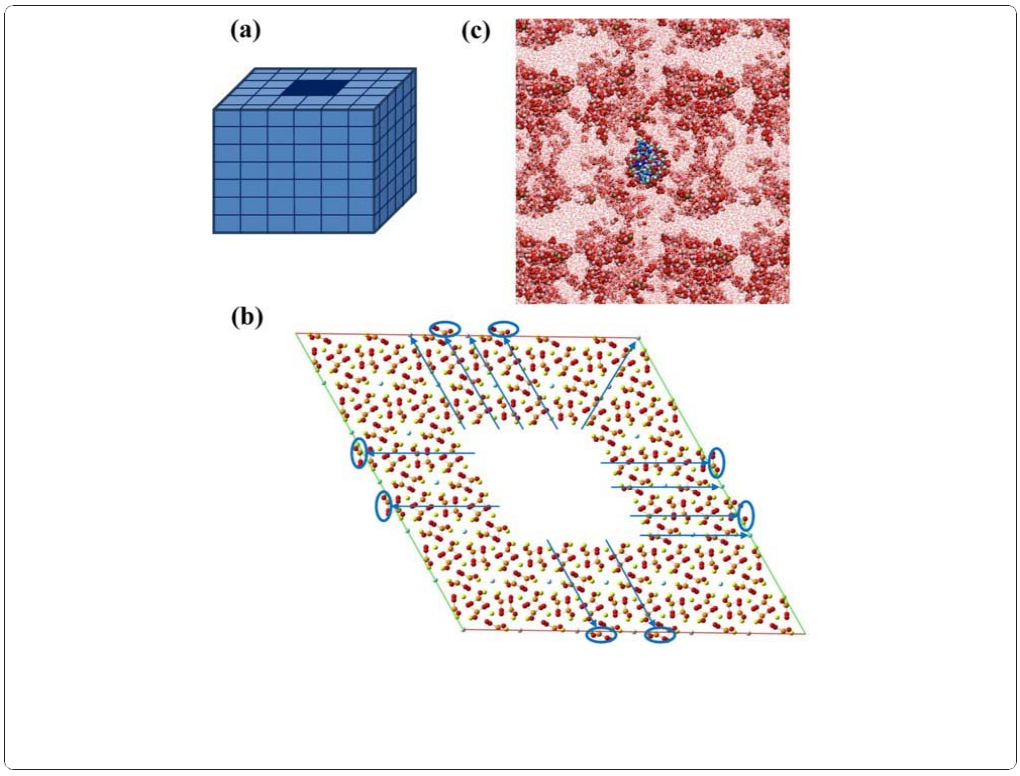

Figure Ann.I.1. (a) Simplified scheme of the HAp and FAp super-cells and the hole used to encapsulate ds B-DNA. (b) Atomistic depiction of the FAp super-cell projected onto the (001) plane showing the atoms (blue arrows) and groups of atoms (blue arrows and circles) translated to the border regions of the super-cell. (c) Graphical representation of the system used to investigate the initial stages HAp nucleation and growth at a B-DNA in aqueous solution: Dickerson's dodecamer double helix in the center of the simulation box, which also contains water solvent molecules and Ca^{2+}, PO_4^{3-} and OH^- ions.

I.4. Methods

I.4.1. Encapsulation of DNA

In order to relax and investigate the stability of the models constructed in the previous section, molecular mechanics calculations based on both energy minimization and MD simulations were applied using the NAMD 2.6 program.[39] Initially, all the models were minimized by applying 5×10^3 steps of steepest descent to relax the more important conformational and structural tensions. Then, a MD run of 3.0 ns in the NVT ensemble (constant number of particles, volume and temperature) at 298 K was carried out to equilibrate the systems and eliminate small structural tensions.

After such thermal relaxation, the saved coordinates were submitted to a new energy minimization by applying 5×10^3 steps of steepest descent. In both energy minimizations and MD simulation, atoms contained in ds and ss DNAs were the only ones allowed to move from their positions, the coordinates of the mineral being kept fixed at their crystallographic positions in all cases. It should be emphasized that all the systems were calculated in triplicate considering starting points that differ in the orientation of the DNA with respect to the apatite.

The potential energy was computed using the Amber force-field.[40,41] All force-field parameters for DNA as well as the phosphate and hydroxyl groups of apatites were extracted from Amber ff03.[42] This is a variant of Amber ff99[43] in which charges and main chain torsion potentials have been re-derived from quantum mechanical calculations in solution. It should be noted that the ff03 parameters are identical to the ff99-SB[44] ones for nucleic acids, phosphate and hydroxyl groups. Force-field parameters of Ca^{2+} and F^- were extracted from the works reported by Bradbrook et al.[45] and Dang,[46]. The geometric distortion induced by the apatite in the secondary structure of DNA ($\Delta\tau$) has been measured as an energy penalty in the bonding contributions using Eqn 1:

$$\Delta\tau = \Delta E_{str} + \Delta E_{bnd} + \Delta E_{tor} \qquad (1)$$

where ΔE_{str}, ΔE_{bnd} and ΔE_{tor} refer to the differences in the stretching, bending and torsional energies, respectively. It should be remarked that $\Delta\tau$ exclusively refers to the geometric stress of the double helix, the omission of non-bonding contributions in Eqn 1 allowing us to avoid masking effects associated with strong electrostatic interactions. These

differences were calculated by subtracting the energy values associated with the relaxed structure (i.e. the structure obtained for the DNA embedded in apatite after relaxation by energy minimization and MD simulations) and canonical Bform of DNA (i.e. the structure directly provided by the NAB module). It should be noted that $\Delta\tau$ accounts for the structural stress induced by the apatite atoms in DNA.

I.4.2. Validation of the force-field

The reliability of the force-field parameters used in this work to reproduce apatite···DNA interactions in biominerals has been evaluated by comparing the interaction energies derived from molecular mechanics and quantum mechanics calculations. A total of 22 small model complexes containing a fragment of DNA and a fragment of apatite were taken from the modeled biominerals. These complexes, which involved a number of atoms ranging from 53 to 98, were selected to cover the modeling of both attractive and repulsive interactions. The interaction energies, which were estimated as the difference between the total energy of the complex and the energies of the isolated fragments, were calculated using both the AMBER forcefield and the B3LYP/6-31G(d)[46-48] quantum mechanical method. The basis set superposition error (BSSE) of the interaction energies calculated at the B3LYP/6-31G(d) level was corrected using the counterpoise (CP) method.[49] All quantum mechanical calculations were performed using the Gaussian 09 computer program.[50]

I.4.3. Nucleation of HAp

MD simulations in NPT conditions (constant number of particles, temperature of 298 K and pressure of 1 atm) were performed using the NAMD 2.6[39] code to investigate the process of formation and growth of HAp round ds B-DNA molecule in a bath of water molecules. Before the incorporation of DNA, the density of the water in the simulation box was 1.00 g/cm^3 at a temperature of 298 K. The force-field parameters for DNA, phosphate and hydroxyl groups, and Ca^{2+} were identical to those for the encapsulation study. The water molecules were represented using the TIP3P model.[51] The initial simulation box (92.0×91.5×108.0 Å^3) was equilibrated using the following strategy. Before any MD trajectory was run, 5×10^3 steps of energy minimization were performed in order to relax conformational and structural tensions. Next, different consecutive rounds of short MD runs were performed in order to equilibrate the density, temperature, and pressure. First, solvent

and ions were thermally relaxed by three consecutives runs, while the B-DNA was kept frozen: 0.5 ns of NVT-MD at 500 K were used to homogeneously distribute the solvent and ions in the box. After this, 0.5 ns of isothermal (298 K) and 0.5 ns isobaric (1 atm and 298 K) relaxation were run. Finally, all the atoms of the system were submitted to 0.15 ns of steady heating until the target temperature was reached (298 K), 0.25 ns of NVT-MD at 298 K (thermal equilibration) followed by 0.5 ns of density relaxation (NPT-MD).

Atom pair distance cut-offs were applied at 16.0 Å to compute the van der Waals interactions. In order to avoid discontinuities in the Lennard-Jones potential, a switch function was applied to allow a continuous decay of the energy when the atom pair distances are larger than 14.0 Å. For electrostatic interactions, we computed the nontruncated electrostatic potential throughout Ewald Summations.[52] The real space term was determined by the van der Waals cut-off (16 Å), while the reciprocal term was estimated by interpolation of the effective charge into a charge mesh with a grid thickness of 5 points per volume unit, i.e. Particle-Mesh Ewald (PME) method.[52] Both temperature and pressure were controlled by the weak coupling method, the Berendsen thermobarostat.[53] The relaxation times used for the coupling were 1 and 10 ps for temperature and pressure, respectively. Bond lengths were constrained using the SHAKE algorithm[54] with a numerical integration step of 1 fs. Periodic boundary conditions were applied using the nearest image convention, and the nonbonded pair list was updated every 1,000 steps (1 ps). The end of the density relaxation simulation was the starting point of the 10 ns production simulations presented in this work. The coordinates of all the production runs were saved every 500 steps (1 ps intervals).

I.5. Results and discussion

I.5.1. Embedding double stranded B-DNA in hydroxyapatite

Figure Ann.I.2a represents the structure of Dickerson's dodecamer (sequence **I**) embedded in HAp before relaxation. As it can be seen, the B-DNA occupies practically the whole pore, indicating that its dimensions are appropriated to accommodate the double helix. Figure Ann.I.2b depicts the double helix after complete relaxation through energy minimizations and MD. Although interactions with HAp atoms induce some distortions in the backbone of B-DNA, both the intra-strand stacking and the inter-strand hydrogen bonds are clearly preserved. The influence of the sequence on the B-DNA distortion induced by the mineral was examined by considering the double helices of **II** and **III** embedded in the same pore of

HAp. Inspection of the relaxed structures, which are also included in Figure I.2b, indicates that, as observed for **I**, apparently the initial double helices do not undergo significant distortions. This result is fully consistent with previous suggestions, which attributed the binding between HAp and ds DNA to the attractive interaction between the Ca^{2+} ions of the former and the PO_4^{3-} groups of the latter.[17-20] According to this feature, the role of the nucleotide sequence is relatively unimportant and the stability of the B-DNA inside the pore is essentially due to the dimensions of the latter.

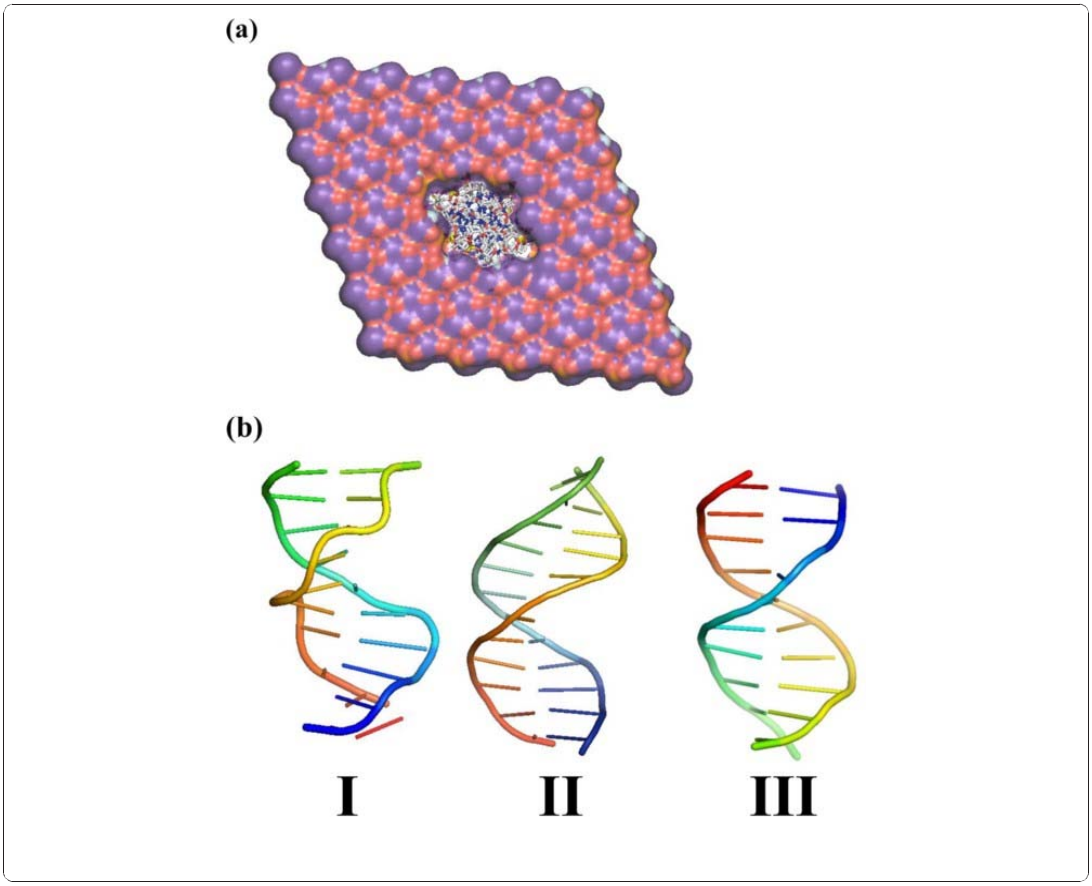

Figure Ann.I.2. (a) Equatorial perspective of the B-DNA double helix (I) embedded in HAp before relaxation. (b) Axial perspective of the double helix of I, II and III after relaxation.

The distortion induced by the mineral in the double helix of each of the three investigated sequences was quantified using the parameters displayed in Table Ann.I.1, which correspond to: (i) $\Delta\tau$, which measures energy differences of the bonding contributions (Eqn 1); (ii) the root mean square deviation (RMSD) between the canonical double helix (i.e. the starting structure) and the relaxed double helix; and (iii) the inter-chain distance (IC) measured with

respect to the centers of mass of each strand. Interestingly, the $\Delta\tau$ obtained for **I** was one order of magnitude higher than for **II** and **III**, even though the difference between the bonding contributions was attractive in all cases. Thus, distortion of the backbone produces an energy penalty in the torsional energy but favorable stretching and, especially, bending contributions, resulting in an attractive $\Delta\tau$ value. However, the unfavorable torsional energy contributions, which reflect the conformational distortions induced by the mineral in the canonical B-DNA, are relatively small. The RMSDs ranged from 1.7 to 4.2 Å, which are relatively low considering that they were derived using all the atoms of ds DNA. Finally, the IC showed very small distortions (i.e. ranging from −0.5 to +2.8 Å) since the IC of the starting structures varied from 19.0 to 20.3 Å, depending on the sequence.

Table Ann.I.1. Stress induced by the minerals in the DNA molecules ($\Delta\tau$; in kcal/mol)

Stretching, bending and torsional contributions to the stress (ΔE_{str}, ΔE_{bnd} and ΔE_{tor}, respectively), inter-chain distance (IC; in Å) and root mean square deviations (RMSD; in Å) between the initial and the relaxed conformations of the biomolecule for different systems encapsulated in HAp and FAp

	$\Delta\tau$[a]	ΔE_{str}[b]	ΔE_{bnd}[c]	ΔE_{tor}[d]	IC [e]	RMSD [f]
			HAp···ds B-DNA			
I	-277	-32	-291	+46	22.8	3.5
II	-2460	-311	-2160	+11	19.8	1.7
III	-1975	-228	-1903	+156	18.7	4.2
			FAp···ds B-DNA			
I	+698	+961	-385	+122	17.6	9.7
			HAp···ss DNA			
I	-239	-22	-236	+19.2	-	10.3
			FAp···ss DNA			
I	-204	-18	-234	+48	-	11.1

[a] Eqn (2). [b] Eqn (3). [c] Eqn (4). [d] Eqn (5). [e] Calculated with respect to the center of masses of each strand. [f] The RMSD was calculated considering all the atoms of the duplexes.

The overall of these results indicates that the cavity displayed in Figure Ann.I.1b allows encapsulate B-DNA double helices without produce mineral-induced stress. Moreover, the dimensions of the pore combined with the crucial role played by the Ca^{2+} are appropriated to avoid any dependence on the nucleotide sequence. Accurate definition of the cavity is provided by the maximum distances between pairs of atoms of the mineral at the internal diagonals of the pore, which are 30.5 and 21.1 Å.

I.5.2. Embedding double stranded B-DNA in fluoroapatite

Relaxation of ds Dickerson's dodecamer embedded in FAp led to the structure displayed in Figure Ann.I.3a.

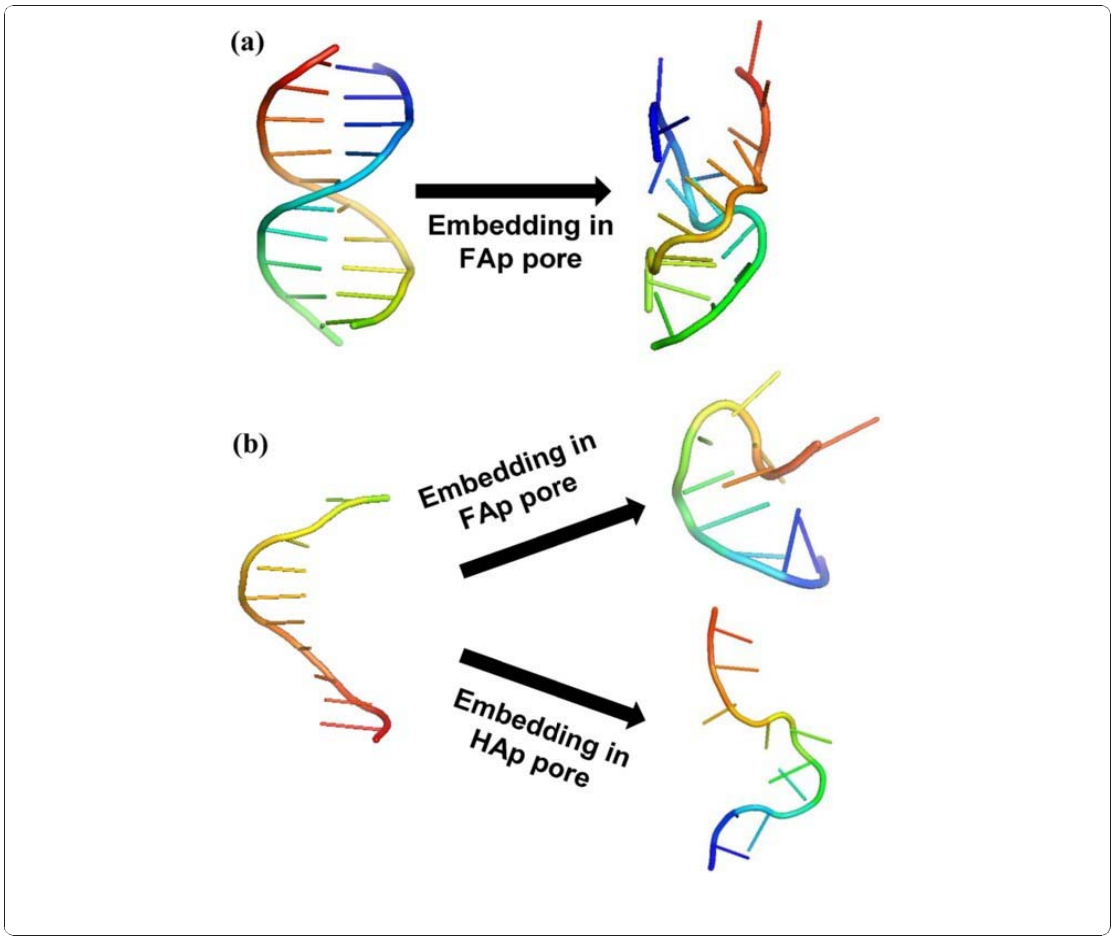

Figure Ann.I.3. Axial perspectives of (a) the double helix of I before and after relaxation in FAp and of (b) a single strand of I before and after relaxation in FAp (top) and HAp (down).

Although the general shape of the double helix is retained after energy minimizations and MD, it underwent geometric distortions that affected significantly both the inter-strand hydrogen bonds and the intra-strand π-stacking. Thus, the RMSD calculated with respect to the canonical B-DNA used as starting point was 9.7 Å (Table Ann.I.1), this value being significantly higher than those obtained for complexes with HAp. Moreover, the energy penalty is repulsive, $\Delta\tau$ = 698 kcal/mol, evidencing the significant geometric stress induced by FAp in the double helix. This stress is essentially concentrated in the bond lengths, the ΔE_{str} being not only repulsive but also significantly higher than the ΔE_{bnd} and ΔE_{tor} contributions. Finally, it should be noted that the repulsive interactions between the FAp and the double helix produces a significant reduction in the IC with respect to the initial value. Thus, the distance between the centers of masses of the two strands in the canonical B-DNA form of I was 20.0 Å, decreasing to 17.6 Å after relaxation inside of the FAp pore. This contraction is in opposition with the expansion of 2.8 Å observed when I was embedded in HAp, reflecting the repulsive force exerted by fluorine atoms of FAp in the double helix.

I.5.3. Embedding single stranded DNA in apatites

As expected, ssDNA molecules encapsulated in HAp and FAp underwent drastic conformational changes upon relaxation. Obviously, this should be attributed to the lack of inter-strand hydrogen bonding, which facilitates the distortions induced by the interactions with the mineral. Figure Ann.I.3b reflects such important variations for ss-**I**. The RMSD obtained for the strand encapsulated in HAp and FAp after relaxation is 10.3 and 11.1 Å, respectively,

suggesting that distortions are similar in both cases. The latter is corroborated by $\Delta\tau$ values (Table Ann.I.1). Thus, the pore is large enough to minimize repulsive interactions, independently of the composition of the mineral, through the complete conformational reorganization of the biomolecule. The relaxed conformation displayed in Figure Ann.I.3b should be simply considered as one of the many possible disordered conformational states of the ss DNA molecules (i.e. the pore allows multiple disordered conformational states for the DNA strand, as was observed during the MD simulation). Similar results were obtained for ss-**II** and ss-**III** (not shown).

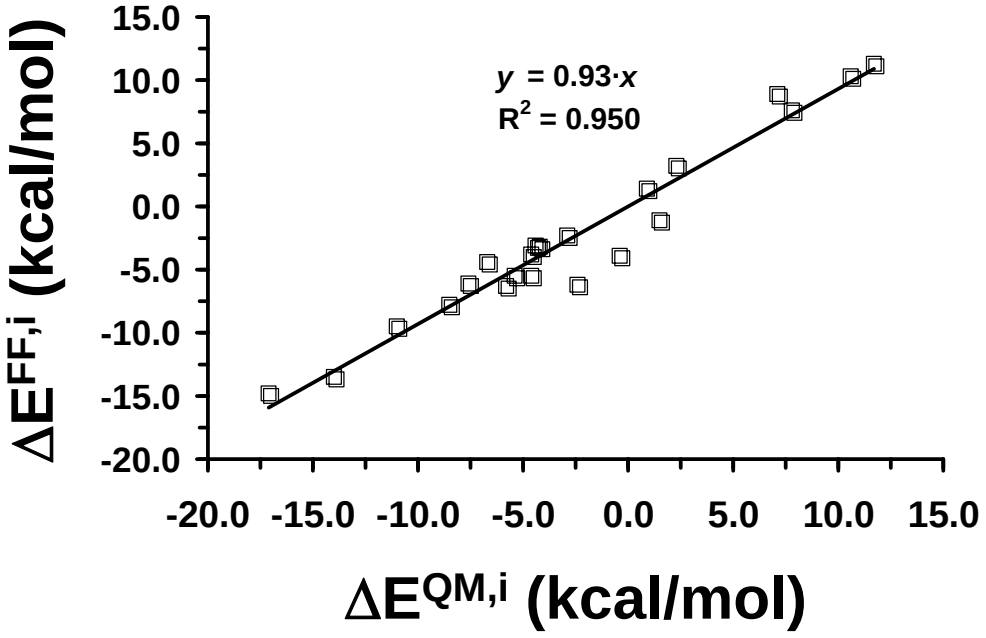

Figure Ann.I.4. Representation of the interaction energies calculated for inorganic···organic model complexes using quantum mechanical calculations at the B3LYP/6-31G(d) level ($\Delta E^{QM,i}$) and the AMBER force-field ($\Delta E^{FF,i}$).

I.5.4. Validation of the force-field

We are aware that the molecular mechanics calculations presented in the above sub-sections were carried out using force-field parameters that were not explicitly designed to investigate the inorganic···organic interactions found in biominerals. Specifically, the parameters used to simulate the phosphate and hydroxyl groups of apatites were extracted from Amber ff03,[41] which was explicitly developed to study the dynamics of proteins and nucleic acid in condensed phases, while those used for Ca^{2+} and F^- were set to study the crystallographic structure of monosaccharides[44] and the solvation of LiF in polarizable water,[45] respectively. Before to investigate the nucleation of HAp at a B-DNA double helix, we performed quantum mechanical calculations on model systems to demonstrate that such force-field parameters satisfactorily reproduce inorganic···organic interactions. A total of 22 model complexes, each containing a fragment of HAp and a fragment of B-DNA, were taken from the model obtained for **I** embedded in the mineral.

These model complexes were selected to cover a wide range of interactions, both attractive and repulsive. The interaction between the HAp and B-DNA fragments was calculated for all the complexes using both the force-field potential ($\Delta E^{FF,i}$) and the

B3LYP/6-31G(d) quantum mechanical method ($\Delta E^{QM,i}$), the CP procedure being applied in the latter to correct the BSSE. The $\Delta E^{QM,i}$ against $\Delta E^{FF,i}$ values range from 11.7 to −17.1 kcal/mol and from 11.3 to −14.8 kcal/mol, respectively. Figure Ann.I.4., which represents $\Delta E^{QM,i}$ against $\Delta E^{FF,i}$, evidences a close agreement between the forcefield and quantum mechanical estimates. Thus, the root mean square deviation between the interaction energies provided by the two methodologies only amounts 1.6 kcal/mol, while the ratio $\Delta E^{FF,i}/\Delta E^{QM,i}$ and the regression coefficient R^2 are 0.93 and 0.950, respectively. These results demonstrate the ability of the force-field parameters used in this work to reproduce inorganic···organic interactions in biominerals with an accuracy better than expected.

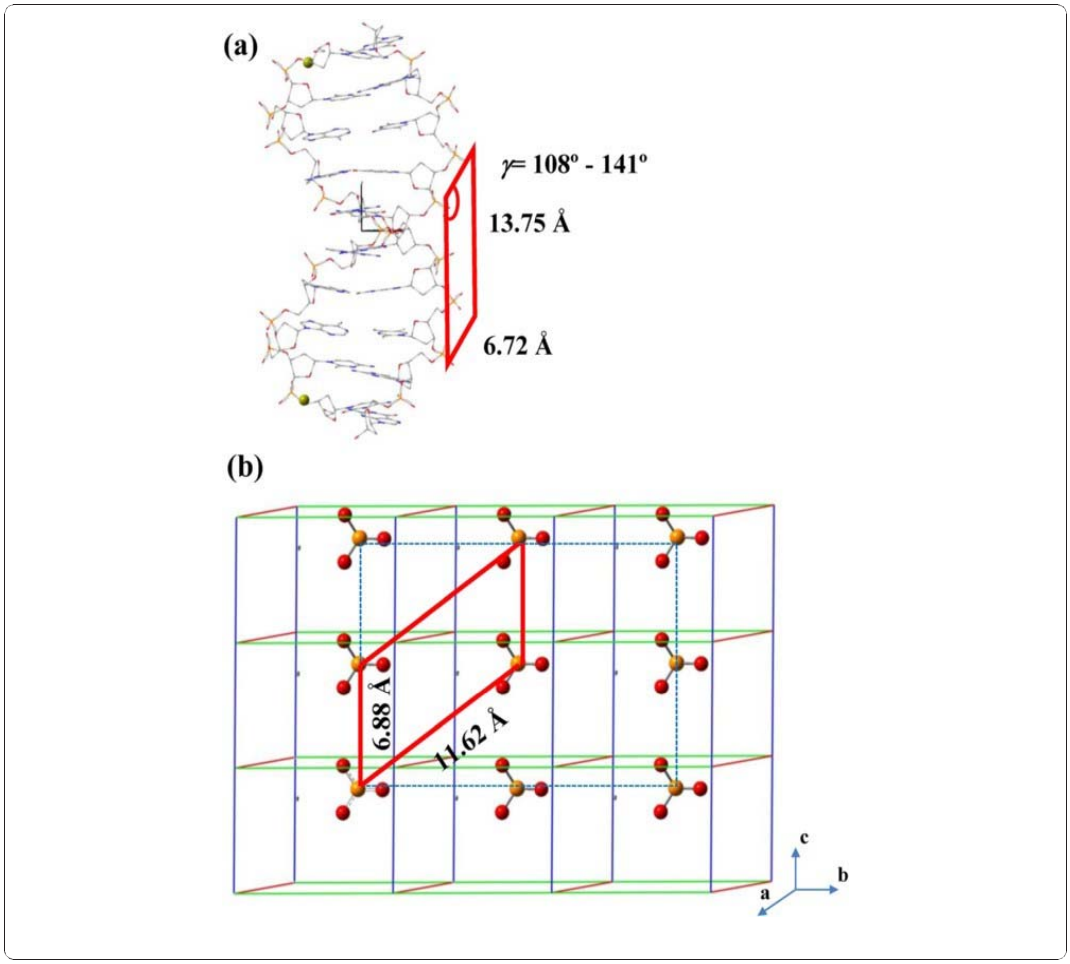

Figure Ann.I.5. Isomorphic planes identified in (a) the double helix of B-DNA and (b) HAp.

I.5.5. Nucleation of apatites using B-DNA

Detailed comparison of B-DNA and apatites structures allowed us to identify a plane defined by four phosphate groups that are located at similar distances in the two systems (Figure Ann.I.5.). Specifically, for HAp / FAp such plane is defined by u = 6.87/6.88 Å (i.e. the crystallographic parameter (c) and v= 11.66/11.62 Å, with an angle γ of 120^{o}; while some variability is observed for B-DNA depending on the sequence. Thus, the average values of the sides are u= 6.72 Å and v= 13.75 Å, the largest variability being shown by the angle with values ranging from 108° to 141°.

Starting from the plane identified in sequence **I**, HAp and FAp models were generated from the phosphate groups located at such plane and growing the crystal through the positional parameters displayed in Table Ann.I.2. Accordingly, the four phosphate of the plane identified in B-DNA, as displayed in Figure Ann.I.5a, were embedded into the apatite crystal. The latter growing process is schematized in Figure Ann.I.6a for HAp,

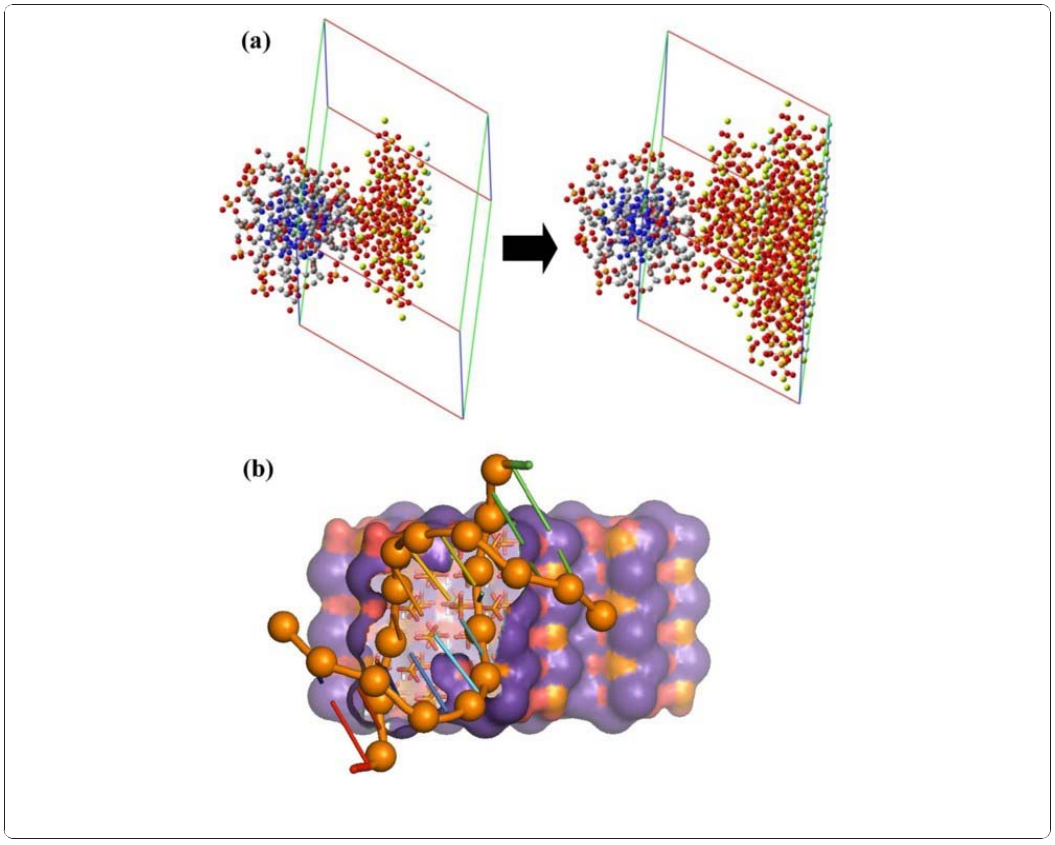

Figure Ann.I.6.(a) Growing process of HAp using the double helix of B-DNA as a nucleating agent. (b) biomineral obtained such growing mechanism.

Table Ann.I.2. Positional parameters used to construct the crystal structures of natural HAp and FAp.

Atom	*x*	*y*	**z**
Ca_I			
HAp	2/3	1/3	0.0010
FAp	2/3	1/3	0.00144
Ca_{II}			
HAp	-0.00657	0.24706	1/4
FAp	-0.00712	0.24227	1/4
P			
HAp	0.36860	0.39866	1/4
FAp	0.36895	0.39850	1/4
O_I			
HAp	0.4850	0.3289	1/4
FAp	0.4849	0.3273	1/4
O_{II}			
HAp	0.4649	0.5871	1/4
FAp	0.4667	0.5875	1/4
O_{III}			
HAp	0.2580	0.3435	0.0703
FAp	0.2575	0.3421	0.0705
O(H) / F			
HAp	0	0	0.1979
FAp	0	0	1/4

while Figure Ann.I.6b displays the resulting structure viewed from a perspective in front of the B-DNA. In order to make understandable the procedure used to build the models, Figure Ann.I.6. illustrates the procedure considering a single plane of phosphates. The same procedure was applied to build the crystal FAp model (not shown). As suggested from the comparison displayed in Figure Ann.I.5., we corroborated that the geometric position of the phosphate groups of ds B-DNA is suitable to grow both HAp and FAp crystals. This feature allowed us to conclude that, from a geometric point of view, such biomolecule may act as nucleating agent of the mineral. However, an energy analysis is also required to provide a complete evaluation of this nucleation in the biomineral.

Figure Ann.I.7. compares the variation of the total energy, which is clearly dominated by the electrostatic contribution, of the two biominerals with those of the two minerals as the size of the crystal grows (i.e. increasing thickness).

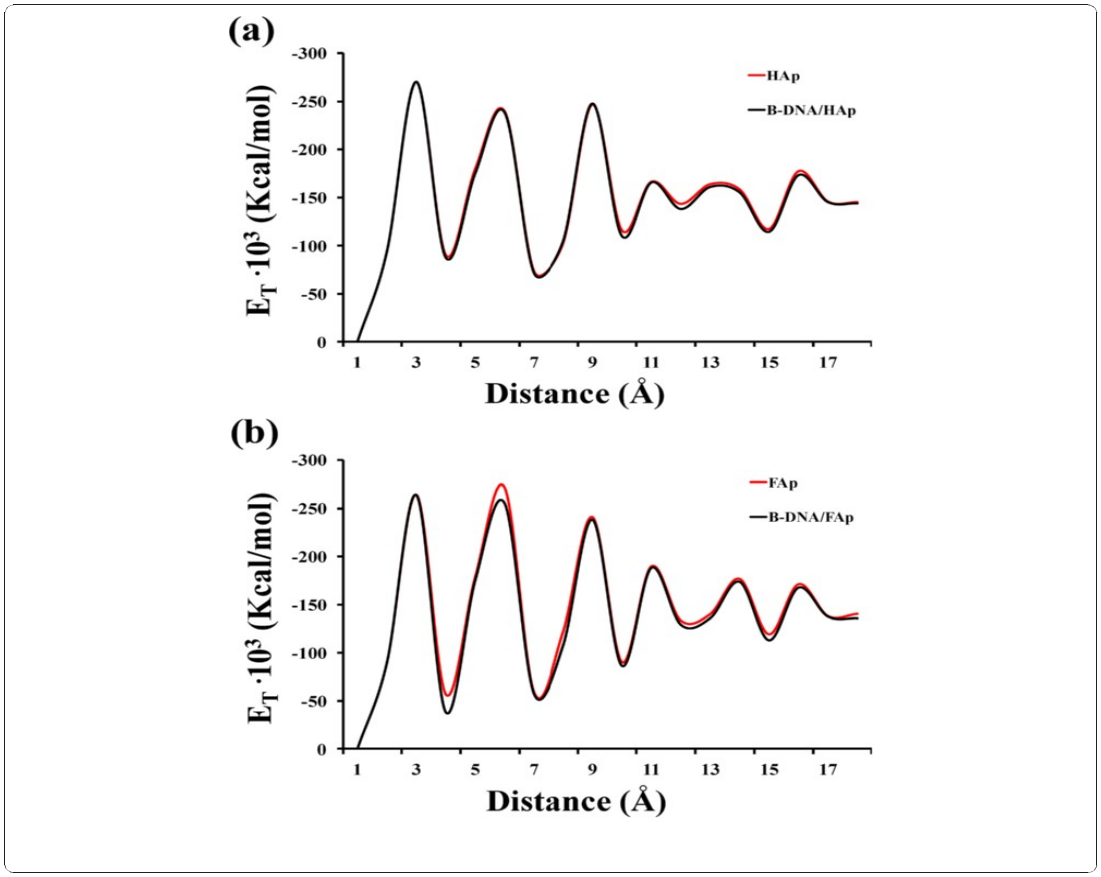

Figure Ann.I.7. Variation of the total energy (ET) against the distance from the center of masses of B-DNA for the biomineral and mineral of (a) HAp and (b) FAp.

It should be noted that biominerals refer to the apatite crystals grown around a B-DNA molecule, which is used as a template (i.e. B-DNA/HAp and B-DNA/FAp) while minerals correspond to pure apatite crystals (i.e. HAp and FAp without B-DNA). Also, the size or thickness of the crystal is represented by a cutoff distance defined with respect to the center of masses of the phosphate groups belonging to the planes used to nucleate the crystals. The energy profiles obtained for B-DNA/HAp and HAp, which are practically identical (Figure Ann.I.7a), clearly reflect the lack of influence of the double helix DNA on the energy of the system from the first steps of mineralization (i.e. mineral thickness < 10 Å). The pattern for B-DNA/FAp and FAp is fairly similar but there is an energetic mismatch between the

biomineral and the mineral (Figure Ann.I.7b), which suggests a stronger distortion of the ds DNA. These results are in agreement with those provided above, which evidenced that FAp distorts more severely the double helix of B-DNA than HAp. Dynamics of the initial stages of nucleation of apatites at B-DNA.

In order to simulate the early formation and growing of calcium phosphate clusters in the nucleation of HAp at B-DNA double helix template, MD simulations of two systems based on stoichiometric aqueous solutions of Ca^{2+}, PO_4^{3-} and OH^- ions were carried out. In the first system, hereafter denoted HAp/DNA, a double helix B-DNA molecule was immersed in the stoichiometric solution described in the Methods section. The second system, hereafter denoted HAp, no DNA was incorporated to the water box thus remaining the Ca^{2+}, PO_4^{3-} and OH^- ions. The analysis of the results was performed on the bases of a 10 ns production run (i.e. the trajectory after equilibration of the density, temperature, and pressure; see Methods section) in the NPT ensemble. It is worth noting that these simulations are two times larger than those used to examine the early stages of nucleation of HAp at a collagen template[39] and, therefore, the clustering process is expected to occur within such time scale. Figure Ann.I.8. compares the radial distribution functions (RDF) of $Ca^{2+}\cdots OH^-$ and $Ca^{2+}\cdots PO_4^{3-}$ pairs obtained from HAp and HAp/DNA simulations. As it can be seen, the B-DNA template does not have any significant effect in the RDF of the $Ca^{2+}\cdots OH^-$ pair at distances smaller than 4.5 Å, even though the peaks centered at 5.45 and 6.18 Å are more pronounced in the HAp/DNA system than in the HAp ones. The latter feature indicates that the clustering is higher in the former than in the latter. Differences are more pronounced, especially at short distances, in the RDFs calculated for the $Ca^{2+}\cdots PO_4^{3-}$ pair in HAp and HAp/DNA. Thus, for the HAp system the first peak appears at 4.22 Å, whereas two well-defined sharp peaks centered at 3.14 and 3.82 Å are clearly identified for the HAp/DNA one. This is consistent with the growing of embryonic clusters in the latter system. Inspection of atomistic configurations extracted from the dynamics indicates that peaks identified for the $Ca^{2+}\cdots PO_4^{3-}$ pair at distances lower than 4 Å correspond to PO3 4 groups surrounded by several (frequently 3) Ca^{2+} atoms.

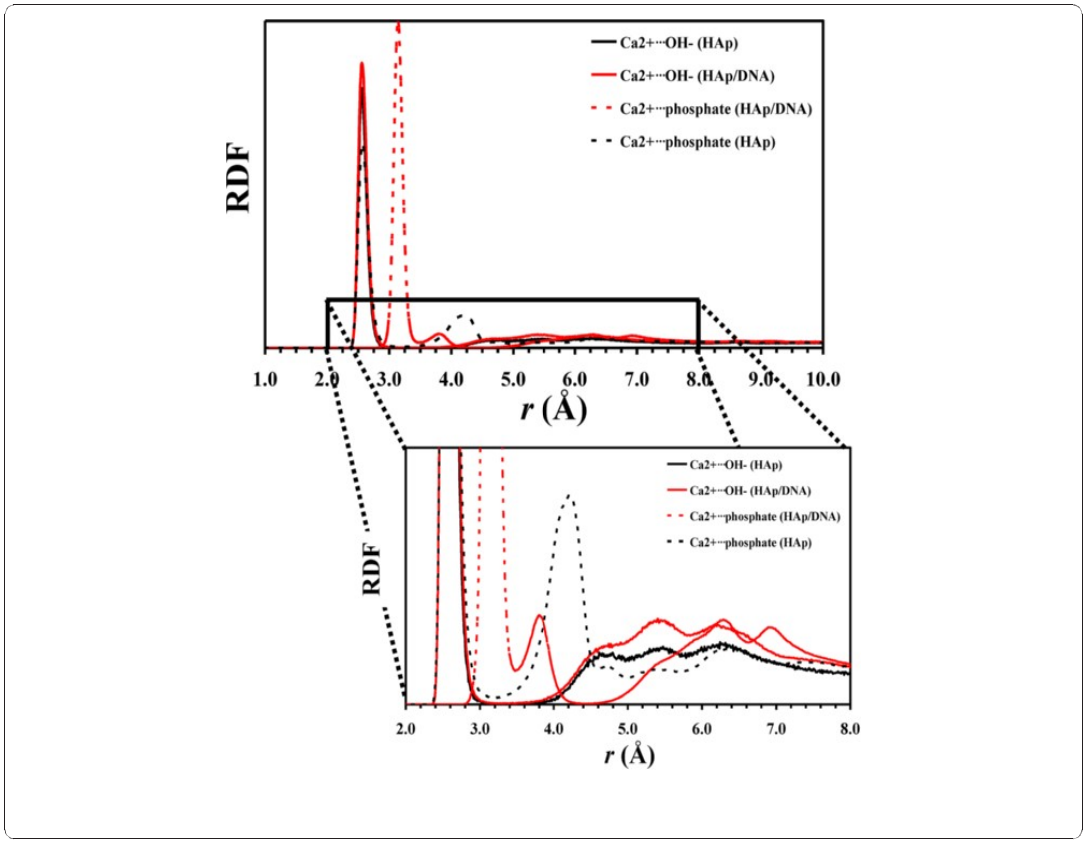

Figure Ann.I. 8. Radial distribution functions of $Ca^{2+}\cdots OH^{-}$ and $Ca^{2+}\cdots PO_4^{3-}$ pairs calculated for HAp and HAp/DNA systems. Both general and detailed views are displayed.

The nucleation of HAp at the DNA molecule is clearly corroborated in Figure Ann.I.9., which represents the RDF of $Ca^{2+}\cdots PO_4^{2-}$, $OH-\cdots PO_4^{2-}$ and PO_4^{3-} . . . PO_4^{2-} pairs (where PO_4^{2-} corresponds to the phosphate group of DNA). As it can be seen, the $Ca^{2+}\cdots PO_4^{2-}$ profile shows a peak at 2.58 Å, indicating that the PO_4^{2-}groups of B-DNA are coordinated with Ca^{2+} forming stable ion complexes. Although the role of Ca^{2+} in this complexes may be initially reduced to that of a simple counterion, the peaks observed at 3.14 and 3.84 Å in the $PO_4^{3-}\cdots PO_4^{2-}$ RDF can be only attributed to the nucleation of inorganic crystals at the biomolecule template. Thus, MD simulations reflect that the phosphate groups of DNA interact with Ca^{2+} to form ion complexes, which subsequently coordinate with PO_4^{3-} groups of the solution giving place to the stabilization of calcium phosphate clusters at the template. Electrostatic attractions between Ca^{2+} and the phosphate groups of both the DNA and the solution were crucial for the nucleation of the crystals at the template surface. On the other hand, the $OH^{-}\cdots PO_4^{2-}$ RDF suggests that the role of the OH^{-} is much less decisive in the

formation of clusters at the B-DNA surface. Thus, although the profile shows a very broad peak centered at 3.28 Å, it is very poorly defined indicating that the OH^- anions are incorporated only occasionally to the calcium phosphate clusters formed at the surface of the B-DNA. Accordingly, the combination of the $OH^{-}\cdots$ PO_4^{2-} and $Ca^{2+}\cdots OH^-$ RDFs (Figures Ann.I.8. and Ann.I.9., respectively) evidences that the OH^- remain essentially at the bulk forming complexes and clusters with Ca^{2+}. It should be remarked that the low relevance of the OH^- anions in the formation of clusters to nucleate HAp crystal at the B-DNA surface is fully consistent with experimental observations. Thus, Tarasevich et al.[55] reported that the calcium phosphate clusters act as precursors of HAp (i.e. typically octacalcium phosphate) do not incorporate OH^- groups.

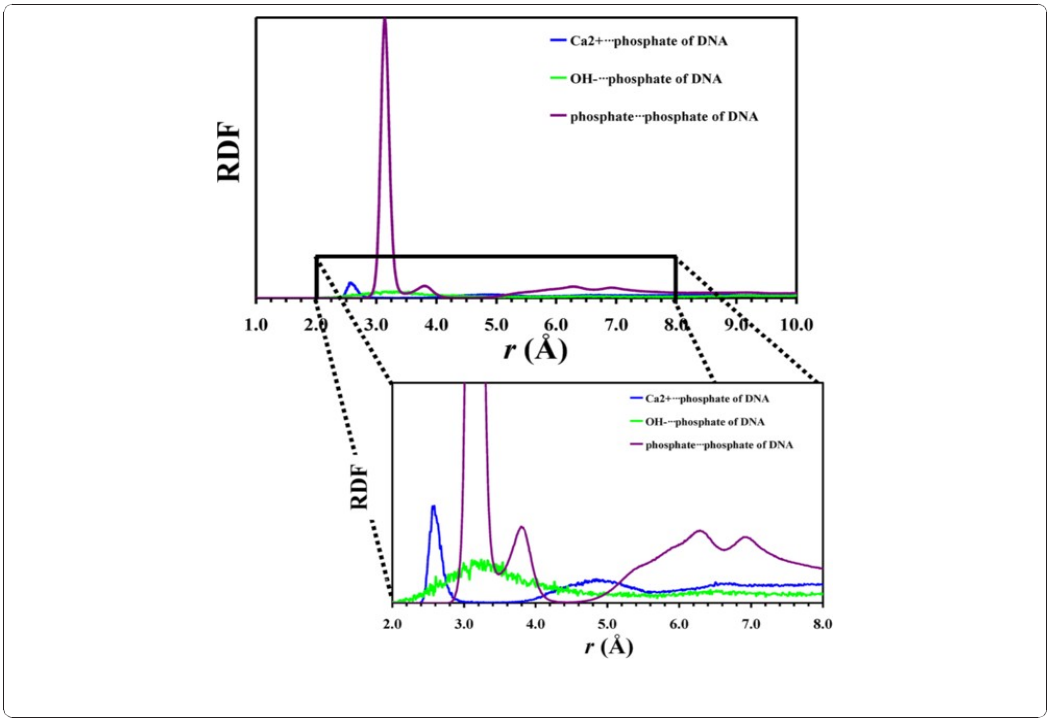

Figure Ann.I.9. Radial distribution functions of $Ca^{2+}\cdots PO_4^{2-}$; $OH^-\cdots PO_4^{2-}$ and $PO_4^{3-}\cdots PO_4^{2-}$ pairs calculated for HAp/DNA. Both general and detailed views are displayed.

I.6. Conclusions

In this study, biominerals made of apatite and DNA have been modeled at the atomistic level. The aims of the work were to provide understanding of the influence of the mineral on the conformation of the biomolecule and to determine the possible role of the latter as nucleating agent of the mineral. Encapsulation of the B-DNA double helix in rhombohedric pores ($\gamma = 120^{O}$) of HAp does not induce significant structural distortions in the biomolecule. This observation has been found to be independent of the DNA sequence, which has been attributed to the strong stabilizing interactions between the Ca^{2+} atoms of HAp and the phosphate groups of DNA. The minimum dimensions of the pore needed to encapsulate B-DNA are defined by the maximum distances between atoms of the mineral at the internal diagonals, which are 30.5 and 21.1 Å. This result is fully consistent with experimental investigations devoted to encapsulate DNA into HAp nanoparticles, which show a relatively high loading capacity through their pores. The structural stability of the encapsulated double helix is an important finding that offers new possibilities for the design of efficient therapeutic biomedical applications. These results are particularly relevant considering recent findings like the mechanism used by carcinogenic cells to capture HAp nanoparticles.[56]

On the other hand, the mechanism proposed for the growing of apatite crystals using the double helix of B-DNA as nucleating agent represents an alternative to classical encapsulation processes (i.e. loading of biomolecules at the nanopores and/or the surface). Thus, the controlled formation of biominerals (i.e. porous nanoparticles of mineral growing from biomolecules) combined with conventional encapsulation approaches may be used to design therapies with higher efficacy and durability. MD simulations have been used to investigate the initial stages of nucleation and cluster formation of calcium phosphate at a B-DNA double helix in aqueous solution. At room temperature, calcium ions interact with DNA phosphates to form ion complexes, but attracted by electrostatic forces, they coordinate to PO_4^{3-} and other calcium ions starting the formation of clusters. Finally, it should be mentioned that this growing mechanism of the biomineral is compatible with the theory and models proposed by Kostetsky[21] to explain the origin of organic matter and life on the Earth.

I.7. References

1. Koutsopoulos S., Synthesis and characterization of hydroxyapatite crystals: A review study on the analytical methods. *Journal of Biomedical Materials Research* (**2002**), *62*, 600–612.
DOI: 10.1002/jbm.10280.

2. LeGeros R.Z., *Hydroxyapatite and related materials*. CRC Press, Boca Raton, (**1979**).

3. Noro T., Itoh K., Biomechanical behaviour of hydroxyapatite as bone substitute material in a loaded implant model. On the surface strain measurement and the maximum compression strength determination of material crash. *Biomedical Materials Engineering* (**1999**), *9*, 319–324.
PMID: 10822487

4. Ebaretonbofa E., Evans J.R.G. Porosity hydroxyapatite foam scaffolds for bone substitute. *Journal of Porous Mat*erials (**2002**), *9*, 257–263.
DOI: 10.1023/A:1021696711468

5. Liu Y., Wang T., He F., Liu Q., Zhang D., Ziang S., Su S., Zhang J., An efficient calcium phosphate nanoparticle-based nonviral vector for gene delivery. *International Journal of Nanomedicine* (**2011**), *6*, 721–727.
DOI: 10.2147/IJN.S17096.

6. Olton D., Li J., Wilson M.E., Rogers T., Close J., Huang L., Kumta P.N., Sfeir C., Nanostructured calcium phosphates (NanoCaPs) for non-viral gene delivery: Influence of the synthesis parameters on transfection efficiency. *Biomaterials* (**2007**), *28*, 1267–1279.
DOI: 10.1016/j.biomaterials.2006.10.026.

7. Sokolova V.V., Radtke I., Heumann R., Epple M., Effective transfection of cells with multi-shell calcium phosphate-DNA nanoparticles. *Biomaterials* (**2006**) *27*, 147–3153.
DOI:10.1016/j.biomaterials.2005.12.030.

8. Van Der Houwen J.A.M., Valsami-Jones E., The application of calcium phosphate precipitation chemistry to phosphorus recovery: The influence of organic gigands. *Environmental Technology* (**2001**), *22*,1325–1335.
DOI: 10.1080/09593332108618187.

9. Cummings L.J., Snyder M.A., Brisack K. Protein chromatography on hydroxyapatite columns. *Methods in Enzymology* (**2009**), *463*,387–404.
DOI: 10.1016/S0076-6879(09)63024-X.

10. Andrews-Pfannkoch C., Fadrosh D.W., Thorpe J., Williamson S.J., Hydroxyapatite-mediated separation of double-stranded DNA, singlestranded DNA, and RNA genomes from natural viral assemblages. *Applied and Environmental Microbiology* (**2010**), *76*, 5039–5045.
DOI:10.1128/AEM.00204-10.

11. Cao X., Deng W., Wei Y., Su W., Yang Y., Wei Y., Yu J., Xu X., Encapsulation of plasmid DNA in calcium phosphate nanoparticles: stem cell uptake and gene transfer efficiency. *International Journal of Nanomedicine* (**2011**), *6*, 3335–3349. DOI: 10.2147/IJN.S27370.

12. Liu T., Tang A., Zhang G., Chen Y., Zhang J., Peng S., Cai Z, Calcium phosphate nanoparticles as a novel nonviral vector for efficient transfection of DNA in cancer gene therapy. *Cancer Biotherapy and Radiopharmaceuticals* (**2005**), *20*,141–149. DOI: 10.1089/cbr.2005.20.141.

13. Kakizawa Y., Miyata K., Furukawa S., Kataoka K., Size-controlled formation of a calcium phosphate-based organic–inorganic hybrid vector for gene delivery using poly(ethylene glycol)-block-poly(aspartic acid). *Advanced Materials* (**2004**), *16*, 699–702. DOI: 10.1002/adma.200305782|.

14. Urabe M,. Kume A., Tobita K., Ozawa K. DNA/Calcium phosphate precipitates mixed with medium are stable and maintain high transfection efficiency. *Analytical Biochemistry* (**2000)**, *278*, 91–92. DOI:10.1006/abio.1999.4429.

15. Sokolova V., Radtke I., Heumann R., Eppel M., Nano-sized calcium phosphate (CaP) carriers for non-viral gene deilvery. *Materials Science and Engineering B* (**2012**), *177*, 289–302. DOI: 10.1016/j.mseb.2011.11.001

16. Wu G-J., Zhou L-Z., Wang K-W., Cheng F., Sun Y., Duan Y-R., Zhu Y-J., Gu H-C. Hydroxylapatite nanorods: An efficient and promising carrier for gene transfection. *Journal of Colloid and Interface Science* (**2010**), *345*, 427–432. DOI:10.1016/j.jcis.2010.01.048.

17. Maitra A., Calcium phosphate nanoparticles: second-generation nonviral vectors in gene therapy. *Expert Review of Molecular Diagnostics* (**2005**) *5*, 893–905. DOI:10.1586/14737159.5.6.893.

18. Jordan M., Schallhorn A., Wurm F.M., Transfecting mammalian cells: optimization of critical parameters affecting calcium-phosphate precipitate formation, *Nucleic Acids Research*, (**1996**), *24*, 596–601. DOI: 10.1093/nar/24.4.596.

19. Jordan M., Wurm F., Transfection of adherent and suspended cells by calcium phosphate. *Methods* (**2004**) *33*,136–143. DOI:10.1016/j.ymeth.2003.11.011.

20. Sokolova V., Kovtun A., Prymak O., Meyer-Zaika W., Kubareva E.A., Romanova E.A., Oretskaya T.S., Heumann R., Epple M., Functionalisation of calcium phosphate nanoparticles by oligonucleotides and their application for gene silencing, *Journal of Materials Chemtry* (**2007**), *17*, 721–727. DOI: 10.1039/B612699E.

21. Kostetsky E.Y., The possibility of the formation of protocells and their structural components on the basis of the apatite matrix and cocrystallizing minerals. *Journal of Biological Physics* (**2005**), *31*, 607–638.
DOI:10.1007/s10867-005-2383-x.

22. Simionescu C.I., Dumitriu S., Bulacovski V., Popa V.I., Synthesis of saccharides by cold plasma decomposition in methane-water-apatite system. *Cellulose Chemistry and Technology* (**1978**), *12*, 143–152.

23. Simionesku C.I., Denes F. *Origin of life. The chemical theories*, Mir, Moskow (**1986**).

24. Schwartz A.W. Prebiotic phosphorylation-nucleotide synthesis with apatite. *Biochimica et Biophysica Acta (BBA) - Nucleic Acids and Protein Synthesis* (**1972**) *281*:477–480.
DOI: 10.1016/0005-2787(72)90147-5.

25. Kostetsky E.Y. On the origin of life and the possibility of the development of protocells and their structural elements in apatite crystals. *Journal of Evolutionary Biochemistry and Physiology* (**1999**) *35*, 249–256.

26. Ngourn S.C., Butts H.A., Petty A.R., Anderson J.E., Gerdon A.E., Quartz crystal microbalance analysis of DNA-templated calcium phosphate mineralization. *Langmuir* (**2012**), *28*, 12151–12158.
DOI: 10.1021/la300949y.

27. Wang J.C., Helical repeat of DNA in solution. *Proceedings of National Academy of Sciencies* (**1979**), *76*, 200–203.
DOI: 10.1073/pnas.76.1.200.

28. Hiughes J.M., Cameron M., Corwley K.D. Structural variations in natural F, OH, and Cl apatites. *American Mineralogist* (**1989**) *74*, 870–876.
DOI: Not assigned.

29. Grzeskowiak K., Goodsell D.S., Kaczor-Grzeskowiak M., Cascio D., Dickerson R.E., Crystallographic analysis of C-C-A-A-G-C-T-T-G-G and its implications for bending in B-DNA. *Biochemistry* (**1993**) *32*, 8923–8931.
DOI:10.1021/bi00085a025.

30. Bang J., Bae S-H., Park C-J., Lee J-H., Choi B-S., Structural and dynamics study of DNA dodecamer duplexes that contain un-, hemi-, or fully methylated GATC sites. *Journal of American Chemical Society* (**2008**), *130*, 17688–17696.
DOI:10.1021/ja8038272.

31. Geahigan K.B., Meints G.A., Hatcher M.E., Orban J., Drobny G.P., The dynamic impact of CpG methylation in DNA. *Biochemistry* (**2000**), *39*, 4939–4946.
DOI: 10.1021/bi9917636.

32. Bae S.H., Cheong H.K., Cheong C., Kang S., Hwang D.S., Choi B.S., Structure and dynamics of hemimethylated GATC sites: implications for DNA-SeqA recognition. *Journal of Biological Chemistry* (**2003**), *278*, 45987–45993
DOI: 10.1074/jbc.M306038200.

33. Case D.A., Darden T.A., Cheatham T.E., III, Simmerling C.L., Wang J., Duke R.E., Luo R., Walker R.C., Zhang W., Merz K.M., Roberts B., Hayik S., Roitberg A., Seabra G., Swails J., Götz A.W., Kolossváry I., Wong K.F., Paesani F., Vanicek J., Wolf R.M., Liu J., Wu X., Brozell S.R., Steinbrecher T., Gohlke H., Cai Q., Ye X., Wang J., Hsieh M-J., Cui G., Roe D.R., Mathews D.H., Seetin M.G., Salomon-Ferrer R., Sagui C., Babin V., Luchko T., Gusarov S., Kovalenko A., Kollman P.A., AMBER 12. University of California, San Francisco, (**2012**).

34. Hud N.V., Polak M., DNA-cation interactions: The major and minor grooves are flexible ionophores. *Current Opinion in Structural Biology* (**2001**) *11*, 293–301.
DOI:10.1016/S0959-440X(00)00205-0.

35. Sines C.C., McFail-Isom L., Howerton S.B., Van Derveer D., Williams L.D., Cations mediate B-DNA conformational heterogeneity. *Journal of American Chemical Society* (**2000**), *122*, 11048–11056.
DOI:10.1021/ja002244p.

36. Chiu T.K., Dickerson R.E., A crystal structures of B-DNA reveal sequence specific binding and groove-specific bending of DNA by magnesium and calcium. *Journal of Molecular Biology* (**2000**), *301*, 915–945.
DOI: 10.1006/jmbi.2000.4012.

37. Zhang R.Y., Ma P.X. Biomimetic polymer/apatite composite scaffolds for mineralized tissue engineering. *Macromolecular Bioscience* (**2004**), *4*, 100–111.
DOI: 10.1002/mabi.200300017.

38. Almora-Barrios N., De Leeuw N.H., Molecular dynamics simulation of the early stages of nucleation of hydroxyapatite at a collagen template. *Crystal Growth & Design* (**2012**) *12*, 756–763.
DOI: 10.1021/cg201092s.

39. Phillips J.C., Braun R., Wang W., Gumbart J., Tajkhorshid E., Villa E., Chipot C., Skeel R.D., Kale L., Schulten K., Scalable molecular dynamics with NAMD. *Journal of Computational Chemistry* (**2005**), *26*, 1781–1802.
DOI: 10.1002/jcc.20289|

40. Cornell W.D,. Cieplak P., Bayly C.I., Gould I.R., Merz K.M., Ferguson D.M., Spellmeyer D.C., Fox T., Caldwell J.W., Kollman P.A., A second generation force field for the simulation of proteins, nucleic acids, and organic molecules. *Journal of American Chemical Society* (**1995**), *117*, 5179–5197.
DOI:10.1021/ja00124a002.

41. Duan Y., Chowdhury S., Lee M.C., Xiong G., Zhang W., Yang R., Cieplak P., Luo R., Lee T., Caldwell J., Wang J., Kollman P.A., A point-charge force field for molecular mechanics simulations of proteins based on condensed-phase quantum mechanical calculations. *Journal of Computational Chemistry* (**2003**), *24*, 1999–2012. DOI:10.1002/jcc.10349.

42. Wang J., Cieplak P., Kollman P.A., How well does a restrained electrostatic potential (RESP) model perform in calculating conformational energies of organic and biological molecules? *Journal of Computational Chemistry* (**2000**), *21*, 1049–1074. DOI:10.1002/1096-987X(200009)21:12<1049::AID-JCC3>3.0.CO;2-F.

43. Hornak V., Abel R., Okur A., Strockbine B., Roitberg A., Simmerling C., Comparison of multiple Amber force fields and development of improved protein backbone parameters. *Proteins* (**2006**), *65*, 712–725. DOI:10.1002/prot.21123.

44. Bradbrook G.M., Gleichmann T., Harrop S.J., Habash J., Raftery J., Kalb J., Yariv J., Hillier I.H., Helliwell J.R., X-Ray and molecular dynamics studies of concanavalin-A glucoside and mannoside complexes Relating structure to thermodynamics of binding. *Journal of Chemical Society, Faraday Transactions* (**1998**), *94*, 1603–1611. DOI:10.1039/A800429C.

45. Dang L.X., Development of nonadditive intermolecular potentials using molecular dynamics: solvation of Li^+ and F^- ions in polarizable water. *Journal of Chemical Physics* (**1992**), *96*, 6970–6977. DOI: 10.1063/1.462555.

46. Becke A.D., A new mixing of Hartree–Fock and local density-functional theories. *Journal of Chemical Physics* (**1993**), *98*, 1372–1377. DOI:10.1063/1.464304.

47. Lee C., Yang W., Parr R.G., Development of the Colle-Salvetti correlation-energy formula into a functional of the density. *Physical Reviews B* (**1988**), *37*, 785–789. DOI:10.1103/PhysRevB.37.785

48. Hariharan P.C., Pople J.A., The effect of d-functions on molecular orbital energies for hydrocarbons. *Chemical Physics Letters* (**1972**), *16*, 217–219. DOI:10.1016/0009-2614(72)80259-8.

49. Boys S.F., Bernardi F., The calculation of small molecular interactions by the differences of separate total energies. Some procedures with reduced errors. *Moleular Physics* (**1970**), *19*, 553–566. DOI:10.1080/00268977000101561.

50. Frisch M.J., Trucks G.W., Schlegel H.B., Scuseria G.E., Robb M.A., Cheeseman J.R., Scalmani G., Barone V., Mennucci B., Petersson G.A., Nakatsuji H., Caricato M., Li X., Hratchian H.P., Izmaylov A.F., Bloino J., Zheng G., Sonnenberg J.L., Hada M., Ehara M., Toyota K., Fukuda R., Hasegawa J., Ishida M., Nakajima T., Honda Y., Kitao O., Nakai H., Vreven T., Montgomery J.A., Jr, et al. (**2009**) Gaussian 09, revision A.01. Gaussian, Inc, Wallingford, CT.

51. Jorgensen W.L., Chandrasekhar J., Madura J.D., Impey R.W., Klein M.L. Comparison of simple potential functions for simulating liquid water. *Journal of Chemical Phy*sics (**1983**), *79*, 926–935.
DOI:10.1063/1.445869.

52. Darden T., York D., Pedersen L., Particle Mesh Ewald-an N.Log(N) method for Ewald sums in large systems. *Journal of Chemical Physics* (**1993**), *98*, 10089–10092.
DOI:10.1063/1.464397.

53. Berendsen H.J.C., Postma J.P.M., van Gunsteren W.F., DiNola A., Haak J.R., Molecular dynamics with coupling to an external bath. *Journal of Chemical Physics* (**1984**), *81*, 3684–3690.
DOI:10.1063/1.448118.

54. Ryckaert J.P., Ciccotti G., Berendsen H.J.C., Numerical integration of the Cartesian Equations of Motion of a System with Constraints: Molecular Dynamics of n-Alkanes. *Journal of Computational Physics* (**1977**), *23*, 327–341.
DOI:10.1016/0021-9991(77)90098-5.

55. Tarasevich B.J., Howard C.J., Larson J.L., Snead M.L., Simmer J.P., Paine M., Shaw W.J., The nucleation and growth of calcium phosphate by amelogenin. *Journal of Crystal Growth* (**2007**), *304*, 407–415
DOI: 10.1016/j.jcrysgro.2007.02.035.

56. Motskin M., Müller K.H., Genoud C., Monteith A.G., Skepper J.N., The sequestration of hydroxyapatite nanoparticles by human monocytemacrophages in a compartment that allows free diffusion with the extracellular environment. *Biomaterials* (**2011**), *32*, 9470–9482.
DOI:10.1016/j.biomaterials.2011.08.060.

Annex II

Mineralization of DNA into nanoparticles of hydroxyapatite[3]

Abstract

Encapsulation of DNA into hydroxyapatite (HAp) has been investigated using a rational approach that involves computer simulation and experimental techniques. The temporal evolution of the radial distribution functions derived from atomistic molecular dynamics simulations of Ca^{2+}, PO_4^{3-} and OH^- containing aqueous solutions in the presence and absence of B-DNA has been used to conclude that the backbone of the double helix acts as a template for HAp growth. More specifically, results reveal the formation of calcium phosphate clusters at the first stages of the simulations, which subsequently reorganize to nucleate HAp. This effect is produced in the absence and, especially, presence, of DNA indicating that the biomolecules do not inhibit but even promote mineral growth. Furthermore, computer simulations suggest that the diffusion of the OH^- anions through the inorganic solution is the limiting step for the nucleation of the biomineral. Nanocapsules and crystalline nanorods of HAp containing DNA molecules inside have been prepared by mixing solutions containing Ca^{2+} and PO_4^{3-} ions with fish sperm DNA at high pH. The dimensions and morphology of such nanostructures have been examined by transmission electron microscopy, while the characterization of the biomineral has been focused on the identification of DNA inside HAp using infrared, X-ray photoelectron and UV-vis spectroscopies, as well as gel electrophoresis. The biominerals reported in this work are important for biomedical applications requiring the protection of DNA from aggressive environmental conditions.

---

[3] Published in Bertran O., del Valle L.J., Revilla-López G., Chaves G., Cardus L., Casas M.T., Casanovas J., Turon P., Puiggalí J., Alemán C., Mineralization of DNA into nanoparticles of hydroxyapatite, *Dalton Transactions* (**2014**), *43*, 317 –327. Reproduced with permission of Royal Society of Chemistry.

Annex II

Mineralization of DNA into nanoparticles of hydroxyapatite

II.1. Introduction

Hydroxyapatite (HAp), $Ca_{10}(PO_4)_6(OH)_2$, is a complex mineral which is becoming increasingly important as a candidate for use as a biomaterial. HAp is the main mineral phase of mammalian tooth enamel and bone,[1] where it grows as nano-sized mineral platelets at nucleating sites on a protein template.[2,3] More specifically, very thin HAp platelets adopt an ordered arrangement within and around collagen fibrils, the mineral being aligned with its c-axis along the fibril.[2] HAp-collagen composites are biodegradable and good matrices for bone cell attachment and proliferation, as well as new bone formation.[4] Several non-collagenous proteins have been also associated with HAp. Specifically, the growth of the bone is controlled by naturally evolved proteins,[5–7] and malfunction of these proteins may lead to severe skeletal diseases.[8]

In the last few years interactions between HAp and DNA are believed to play an important role in different fields, including the biomedical one.[9,10] For example, recent spectroscopic studies showed the contribution of vibrational modes of DNA, phospholipids and protein appears in HAp microcalcifications formed in the organism.[9] More recently, HAp nanoparticles (NPs) have been used as non-viral gene carriers.[10–13] Thus, DNA-HAp NPs complexes were found to cross cell membranes, integrating into the cell genome. In a very recent study, Brundin et al.[14] showed a specific binding affinity of HAp for DNA. These same authors found that HAp-bound DNA is more resistant to decay and less susceptible to degradation by serum and nucleases, which may account for the long-term persistence of DNA in bone and tooth.[14]

The direct encounter between DNA and HAp in biological systems suggests that investigation of the interaction between these two materials and particularly, of the formation of biominerals through the nucleation of HAp at a DNA template would be very useful for the development of novel strategies for gene therapy. Thus, biomineralization would facilitate DNA protection by the surrounding inorganic material. Amazingly, the number of studies devoted to examining the interaction between HAp and DNA is still very scarce. In an early study, Jordan et al.[15] reported on DNA-calcium phosphate co-precipitation for

transfection purposes, even though such co-precipitation was described only in a narrow range of physico-chemical conditions. More recently, Okazaki et al.[16] investigated the effect of DNA on the crystal growth of HAp by synthesizing the mineral in the presence of the biomolecule. Those authors reported that DNA inhibits the HAp crystal growth, indicating that DNA molecules are not in the HAp structure but adsorbed at the surface. Finally, in a very recent study we used molecular modeling tools to examine the structure and stability of biominerals in which DNA molecules are embedded into HAp nanopores.[17] Results indicated that duplexes of DNA adopting a B double helix can be encapsulated inside nanopores of HAp without undergoing significant conformational distortions.

On the basis of these observations, in this work we investigate the encapsulation of DNA into HAp nanoparticles using a rational design approach that combines theoretical and experimental methodologies. Atomistic molecular dynamics (MD) simulations of B-DNA immersed in an inorganic solution show the rapid formation of calcium phosphate clusters at the biomolecule template. The temporal evolution of these clusters suggests the growing of HAp around the DNA matrix. Although 50 ns trajectories only represent the initial stages of nucleation of HAp around the DNA template, analyses support the view that the biomolecules promote, or at least does not inhibit, mineral growth. The inorganic solutions used for the simulations have been experimentally applied to fabricate nanocapsules and crystalline nanorods with DNA inside. Corroboration of this experimental achievement and characterization of the biomineral after the removal of superficially adsorbed DNA by enzymatic digestion were carried out through transmission electron microscopy (TEM), infrared spectroscopy (FTIR), X-ray photoelectron spectroscopy (XPS), UV-vis spectroscopy and gel electrophoresis.

II.2. Methods

II.2.1. Computational methods

The simulation system consisted of the Dickerson's dodecamer (5′-CGCGAATTCGCG-3′), which is a well-known sequence that adopts a B-DNA double helix,[18] 955 Ca^{2+} ions, 567 PO_4^{3-} ions, 189 OH^- ions, and 29,523 water molecules. In addition, simulations of a system made of 945 Ca^{2+} ions, 567 PO_4^{3-} ions, 189 OH^- ions and 29,554 water molecules were carried out to get more insights on the role of the B-DNA template in mineral growth. MD simulations in NPT conditions (constant number of particles, temperature of 298 K and

pressure of 1 atm) were performed using the NAMD 2.6[19] code. The potential energy was computed using the Amber force-field.[20] All force-field parameters for DNA as well as the phosphate and hydroxyl groups were extracted from Amber ff03.[21] It should be noted that the ff03 parameters are identical to the ff99-SB[22] ones for nucleic acids, phosphate and hydroxyl groups. Force-field parameters of Ca^{2+} were extracted from the work reported by Bradbrook et al.[23] The ability of this set of force-field parameters to reproduce the inorganic–organic interactions found in biominerals was recently proved.[17] The density of water in the simulation box was 1.00 $g \cdot cm^{-3}$ at a temperature of 298 K. The water molecules were represented using the TIP3P model.[24] The initial simulation box (92.0 × 91.5 × 108.0 $Å^3$) was equilibrated using the following strategy. Before any MD trajectory, 5000 steps of energy minimization were performed to relax conformational and structural tensions. Next, different consecutive rounds of short MD runs were performed to equilibrate the density, temperature, and pressure. First, solvent and ions were thermally relaxed by three consecutive runs, while the B-DNA was kept frozen: 0.5 ns of NVT-MD (volume conserved) at 500 K were used to homogeneously distribute the solvent and ions in the box. After this, 0.5 ns of isothermal (298 K) and 0.5 ns of isobaric (1 atm and 298 K) relaxation were run. Finally, all the atoms of the system were submitted to 0.15 ns of steady heating until the target temperature was reached (298 K), 0.25 ns of NVT-MD at 298 K (thermal equilibration), followed by 0.5 ns of density relaxation (NPT-MD).

Atom pair distance cut-offs were applied at 16.0 Å to compute the van der Waals interactions. In order to avoid discontinuities in the Lennard-Jones potential, a switch function was applied to allow a continuous decay of energy when the atom pair distances are larger than 14.0 Å. For electrostatic interactions, we computed the non-truncated electrostatic potential throughout Ewald Summations.[25] The real space term was determined by the van der Waals cut-off (16 Å), while the reciprocal term was estimated by interpolation of the effective charge into a charge mesh with a grid thickness of 5 points per volume unit, i.e. Particle-Mesh Ewald (PME) method.[25] Both temperature and pressure were controlled by the weak coupling method, the Berendsen thermobarostat.[26] The relaxation times used for the coupling were 1 and 10 ps for temperature and pressure, respectively. Bond lengths were constrained using the SHAKE algorithm[27] with a numerical integration step of 1 fs. Periodic boundary conditions were applied using the nearest image convention, and the nonbonded pair list was updated every 1,000 steps (1 ps). The end of the density relaxation simulation was the starting point of the production simulations presented in this work, which

were 50 and 25 ns long for the system with and without the DNA template, respectively. The coordinates of all the production runs were saved every 1,000 steps (1 ps interval).

II.2.2. Experimental methods

II.2.2.1. Materials

The materials used in the present work included fish sperm DNA, DNase I (bovine pancreas, > 400 Kunitz units per mg), hexadecyltrimethylammonium bromide (CTBA), calcium nitrate [$Ca(NO_3)_2 \cdot 4H_2O$], diammonium hydrogen phosphate [$(NH4)_2HPO_4$], ethylenediaminetetraacetic acid (EDTA), NH_4OH, HCl, NaCl, ethanol and deionized water. Fish sperm DNA, DNase I and CTBA were purchased from Sigma-Aldrich. Other reagents were provided by Panreac. All chemicals were of analytical grade and were used without further modification and purification.

II.2.2.2. Synthesis of HAp-DNA nanocrystals

0.1 g of fish sperm DNA were added to 15 mL of a 0.3 M $(NH_4)_2HPO_4$ solution in de-ionized water. The pH of such solution was previously adjusted to 10 with aqueous ammonia. The mixture was added drop-wise (rate of 2 $mL \cdot min^{-1}$) and under agitation (400 rpm) to 25 mL of 0.3 M $Ca(NO_3)_2$ solution in de-ionized water and the appropriate amount of aqueous ammonia to adjust pH to 10. Temperature was maintained at 40 °C during the addition process. After that, the reaction mixture was stirred at 80 °C for 1.5 h and then naturally cooled to room temperature. The resultant suspension was aged for 24 h at room temperature. Then, the precipitate was separated by centrifugation and washed sequentially with de-ionized water and a 60/40 v/v mixture of ethanol–water (twice). A white powder was obtained after freeze-drying. The same protocol without the addition of fish sperm DNA was followed to get HAp nanocrystals, which were used as a control.

II.2.2.3. Synthesis of HAp-DNA nanocapsules

0.382 g of fish sperm DNA were added to 5 mL of a 0.5 mM $Ca(NO_3)_2$ solution in ethanol containing ammonia to adjust the pH to 11. Specifically, the DNA/Ca^{2+} ratio was 0.15 $g \cdot mmol^{-1}$. The mixture was quickly added under agitation (400 rpm) to 3 mL of 0.5 mM $(NH_4)_2HPO_4$ solution in de-ionized water and 0.5 mg of CTAB surfactant (calculated to be half the value of the critical micellar concentration, CMC). The mixture was maintained under agitation at room temperature for 1 h and subsequently allowed to stand overnight at 37 °C. The precipitate was separated by centrifugation and washed sequentially with de-

ionized water and a 60/40 v/v mixture of ethanol–water (twice). A white powder was obtained after freeze-drying. The same protocol without the addition of fish sperm was followed to get HAp nanocapsules, which were used as a control.

II.2.2.3. Transmission electron microscopy (TEM)

A Philips TECNAI 10 electron microscope was used and operated at 80 kV for a bright field mode. Micrographs were taken with an SIS MegaView II digital camera. Nanocrystals were recovered from the mother liquor by centrifugation, repeatedly washed with water and ethanol and deposited on carbon- coated grids. Nanocapsules were directly recovered from the highly diluted synthesis medium.

II.2.2.4. FTIR spectroscopy

Infrared absorption spectra were recorded from powder samples with a Fourier Transform FTIR 4100 Jasco spectrometer in the 1800–800 cm^{-1} range. A Specac model MKII Golden Gate attenuated total reflection (ATR) equipment with a heated Diamond ATR Top-Plate was used.

II.2.3.5. X-ray photoelectron microscopy (XPS)

XPS analyses were performed in a SPECS system equipped with a high-intensity twin-anode X-ray source XR50 of Mg/Al (1253 eV/1487 eV) operating at 150 W, placed perpendicular to the analyzer axis, and using a Phoibos 150 MCD-9 XP detector. The X-ray spot size was 650 μm. The pass energy was set to 25 and 0.1 eV for the survey and the narrow scans, respectively. Charge compensation was achieved with a combination of electron and argon ion flood guns. The energy and emission current of the electrons were 4 eV and 0.35 mA, respectively. For the argon gun, the energy and the emission current were 0 eV and 0.1 mA, respectively. The spectra were recorded with a pass energy of 25 eV in 0.1 eV steps at a pressure below 6×10^{-9} mbar. These standard conditions of charge compensation resulted in a negative but perfectly uniform static charge. The C1s peak was used as an internal reference with a binding energy of 284.8 eV. High-resolution XPS spectra were acquired by Gaussian–Lorentzian curve fitting after s-shape background subtraction. The surface composition was deter- mined using the manufacturer's sensitivity factors.

II.2.3.6. UV-Vis spectroscopy

A UV-3600 (Shimadzu) UV-Vis-NIR spectrophotometer controlled by the UVProbe 2.31 software was used to record the UV-Vis spectra of HAp-DNA nanoparticles at room temperature, in the 200–400 nm range, with a bandwidth of 0.2 nm and a scan speed of 600 $nm \cdot min^{-1}$. Spectra were recorded from aqueous suspensions of 0.5 mg of HAp-DNA nanoparticles in 1 mL of sterile milliQ water. Spectra were also acquired after dissolution of HAp-DNA nanoparticles by the addition of 100 µL of an acid medium (100 mM HCl and 50 mM NaCl) in the cuvette. Samples were homogenized by pipetting and maintained at room temperature for 5–10 min before recording the spectra. The same procedure was followed to analyze HAp-DNA nanoparticles previously digested overnight with deoxyribonuclease which was used to eliminate the adsorbed DNA on the nanoparticle surface. Samples were recovered after digestion by centrifugation, washed twice with deionized water and re-suspended in 1 mL of deionized water. Spectra were recorded from this aqueous suspension and from the dissolution attained after the addition of 100 µL of the acid medium.

II.2.3.7 Gel electrophoresis

Five samples were prepared for analysis by agarose gel electrophoresis: HAp nanoparticles, HAp-DNA nanoparticles before and after dissolution with EDTA and deoxyribonuclease digested HAp-DNA nanoparticles before and after dissolution with EDTA. This was performed by adding 5 µL of a 250 mM solution of EDTA. In each case, 25 µL of an aqueous dispersion of the selected HAp-DNA nanoparticles (10 $\mu g \cdot \mu L^{-1}$) were mixed with an aliquot (5 µL) of 6×gel loading buffer. Subsequently, an aliquot of 15 µL was introduced in the well of a 1% agarose gel containing ethidium bromide (0.5 $\mu g \cdot mL^{-1}$ of gel) in 1× tris-borate-EDTA buffer (TBE).

II.3. Results and discussion

II.3.1. Computational design

In an early study Okazaki et al.[16] indicated that DNA inhibits the crystal growth of HAp, which makes the formation of biominerals through the encapsulation of the biomolecule difficult. In order to investigate this feature, the temporal evolution of stoichiometric inorganic solutions of Ca^{2+}, PO_4^{3-} and OH^- ions in the presence and absence of B-DNA has been investigated using MD simulations. The former and latter systems were simulated for 50 and 25 ns, respectively, to gain insights not only from the clustering process but also from the mineral (or crystal) nucleation process, if it exists. Figure Ann.II.1. and Ann.II.2. show the distribution of Ca^{2+}, PO_4^{3-} and OH^- ions at selected snapshots extracted from the simulations in the presence and absence of B-DNA, respectively.

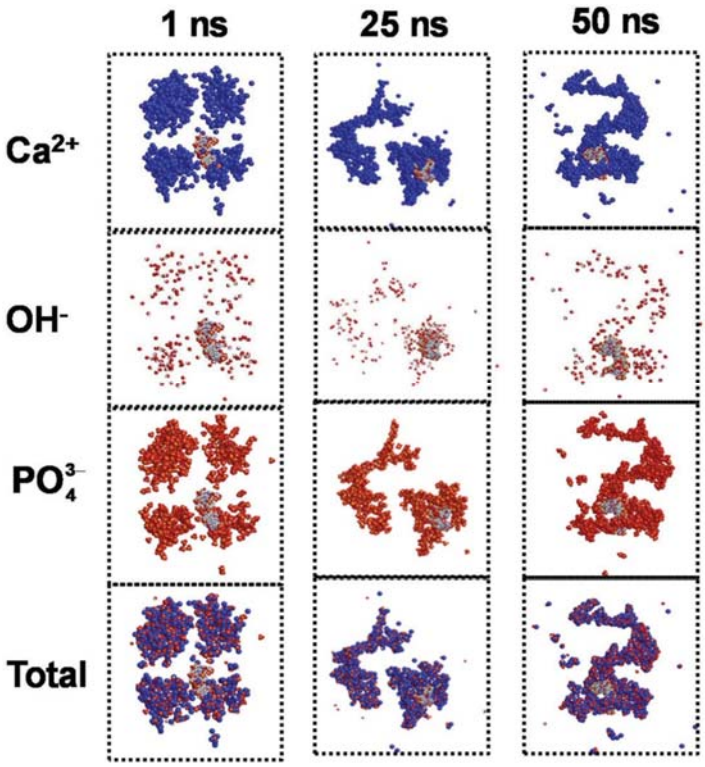

Figure Ann.II.1. Distribution of Ca^{2+}, PO_4^{3-} and OH^- ions around DNA double helix at selected snapshots of the MD trajectory. The distributions of ions are displayed separately and all together. Solvent molecules have been omitted for clarity.

As can be seen, the DNA favors the formation of embryonic clusters surrounding the double helix from the first stages of the MD simulation (i.e. after 1 ns). These initial clusters mainly involve Ca^{2+} and PO_4^{3-} ions, the incorporation of OH^- anions being apparently very scarce at such an earlier part of the trajectory. Snapshots recorded after 25 and 50 ns of simulation show not only the incorporation of OH^- anions, but also a change in the distribution of the Ca^{2+} and PO_4^{3-} clustering. This feature suggests that DNA may act as a stable nucleating template for the formation of HAp. More specifically, the DNA double helix may behave as a nucleating motif that initially helps to nucleate amorphous-like calcium phosphate clusters, which subsequently tend to re-organize for transformation into HAp.

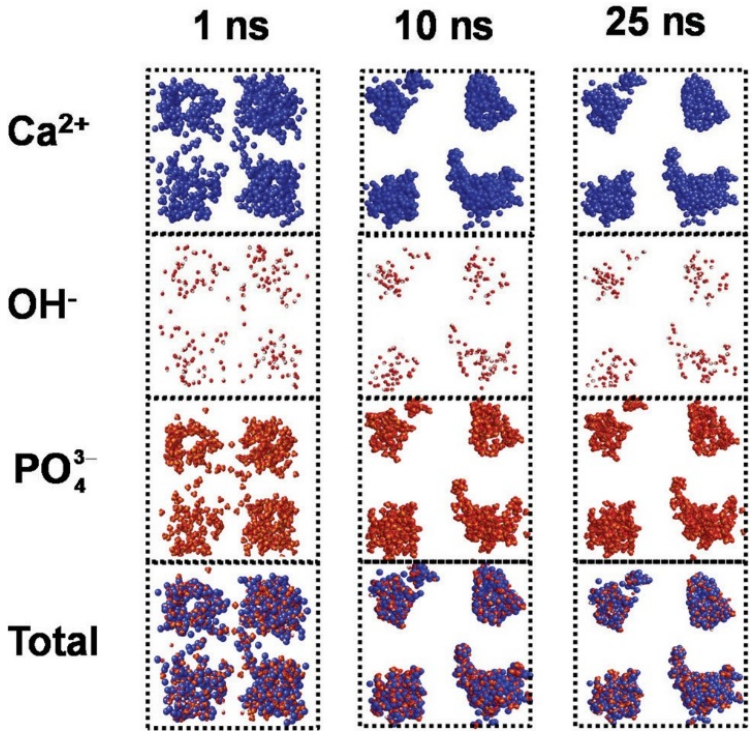

Figure Ann.II.2. Distribution of Ca^{2+}, PO_4^{3-} and OH^- ions at selected snapshots of the MD trajectory in the absence of DNA. The distributions of ions are displayed separately and all together. Solvent molecules have been omitted for clarity.

The templating role of the biomolecule in the nucleation of HAp is clearly evidenced when the distribution of inorganic ions is examined for the trajectory without DNA. Figure Ann.II.2. shows extensive inorganic clusters after 1 ns, which is consistent with the formation of multiple nucleation centers for amorphous phosphate precipitation. This observation is consistent with nucleation from a supersaturated solution. In subsequent stages of the trajectory, these clusters grow similarly and ions tend to re-organize, suggesting

that the system evolves towards poly-organized HAp. This multi-nucleation behavior is fully consistent with previous studies devoted to investigating HAp crystal growth[28] and differs from that displayed in Figure Ann.II.1., which shows the preferential nucleation around the DNA template. Figure Ann.II.3. compares the radial distribution functions of P···P pairs, $g_{P-P}(r)$, calculated for the crystal structure of natural HAp,[29] the backbone of the DNA double helix and the PO_4^{3-} anions in the inorganic solution with and without DNA.

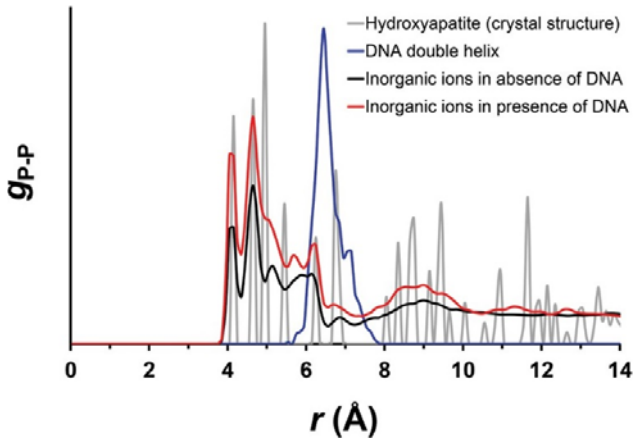

Figure Ann.II.3. Radial distribution functions of P···P atom pairs for: the crystal structure of natural HAp (grey line); the DNA double helix (blue line); the PO_4^{3-} anions in the solution without DNA (black line); and the PO_4^{3-} anions in the solution with DNA (red line). The profiles for DNA and PO_4 anions were calculated using MD simulations performed in this work while the profile for natural HAp was obtained using the crystallographic coordinates reported in ref. [29].

Thus, the trajectory of the inorganic solution with DNA was used to calculate the $g_{P-P}(r)$ of the DNA backbone (i.e. the double helix was preserved during the whole trajectory) and the PO_4^{3-} anions. The $g_{P-P}(r)$ for the DNA shows a broad and high peak centered at 6.45 Å, which is consistent with the dynamics and structural regularity of the biomolecule. This peak contains the two peaks found for the HAp crystal at r = 6.2 and 6.6 Å. However, as expected, none of the four characteristic peaks of HAp at $r \leq 5.4$ Å appears in the profile obtained for the biomolecule. This limitation is overcome in the $g_{P-P}(r)$ calculated for the PO_4^{3-} containing solutions. Thus, all the peaks found at $r < 6.7$ Å for the HAp crystal are identified in the profile derived for the inorganic solution with DNA. Further- more, the six peaks found for the HAp crystal in the 8–10 Å interval fit within a broad peak that contains multiple shoulders. This is consistent with an ordered enlargement of the clusters. Although

quantitative comparison of the two profiles still reveals some discrepancies (i.e. in the $g_{P–P}(r)$ derived from MD the peak at r = 4.9 Å is a shoulder, the peak at r = 5.4 Å is shifted by ~0.2 Å, and the intensity of the peak at r = 6.7 Å is low after 50 ns trajectory), the qualitative concordance clearly indicates that DNA favors the mineral formation or even crystallization of HAp around it.

The agreement between the profiles derived from the HAp crystal structure and the snapshots recorded from the MD trajectory in the absence of DNA is also very remarkable, even though the definition of the peaks in the latter is not very high. This should be attributed not only to the length of the trajectory (i.e. 25 ns only) but also to the organization mechanism discussed above, which is based on the simultaneous formation and growing of multiple clusters (nucleation centers).

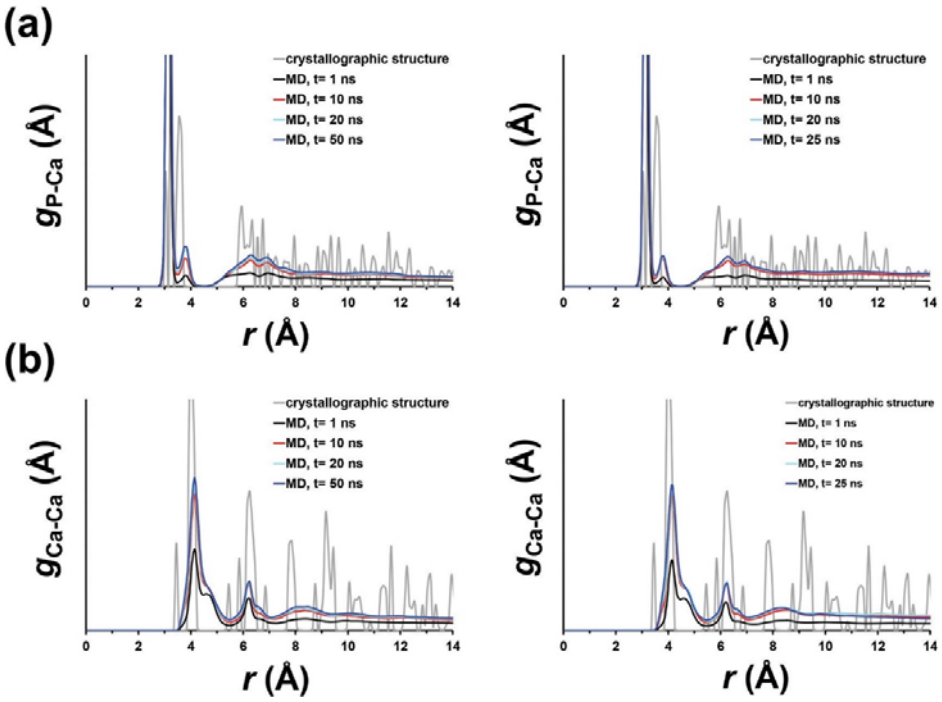

Figure Ann.II.4. Radial distribution functions of (a) P···Ca and (b) Ca···Ca atom pairs calculated at different time intervals for the simulated inorganic solutions with and without DNA (left and right, respectively). The profile obtained using the crystallographic coordinates of natural HAp (grey line) has been included in all cases for comparison.

Inspection of Figure Ann.II.4., which displays the radial distribution functions of Ca···Ca and Ca···P pairs ($g_{Ca–Ca}(r)$ and $g_{Ca–P}(r)$, respectively) obtained for the crystal structure of natural HAp and the simulated systems, corroborates the role of DNA as a template. Thus, the similitude of the profiles derived from the trajectories in the presence and absence of

DNA as well as the rapid definition of such profiles (i.e. the profile remain practically invariant after 10 ns) indicate that DNA does not inhibit the nucleation of HAp around it, as recently suggested.[16] Indeed, the correspondence between the peaks derived from simulations and the peaks calculated using the crystallographic coordinates of HAp confirms that, after a few ns, the inorganic clusters tend to organize into pseudo-ordered structures.

As mentioned above, Figure Ann.II.1. and Ann.II.2. suggest that the diffusion of OH^- anions through the inorganic solution and their incorporation into the calcium phosphate clusters is the limiting step for the formation of HAp. To clarify this feature, the radial distribution functions of $Ca\cdots OH^-$ and $OH^-\cdots OH^-$ pairs ($g_{Ca–OH}(r)$ and $g_{OH–OH}(r)$, respectively) for the simulated systems have been calculated (Figure Ann.II.5.). Interestingly, comparison of the $g_{Ca–OH}(r)$ profiles derived from the simulations in the absence and presence of DNA indicates that, apparently, the diffusion of OH^- is slower in the former than the in the latter. Thus, the height of the peaks found at r values ranging from 4 to 7 Å changes progressively during the simulation of the inorganic solution without DNA. In contrast, the peaks at such regions remain practically unchanged after 10 ns of MD when the bio-molecule has been included in the simulation. The role of DNA as template is also reflected by the peak appearing in the $g_{Ca–OH}(r)$ profile after 40 ns at 3.1 Å (Figure Ann.II.5.).

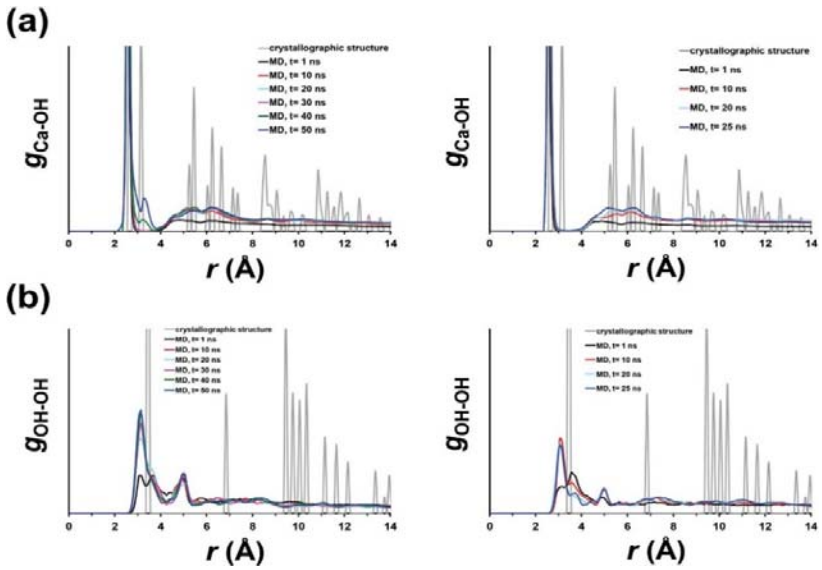

Figure Ann.II.5. Radial distribution functions of (a) $Ca\cdots OH^-$ and (b) $OH–\cdots OH^-$ atom pairs calculated at different time intervals for the simulated inorganic solutions with and without DNA (left and right, respectively). The profile obtained using the crystallographic coordinates of natural HAp (grey line) has been included in all cases for comparison.

This peak gives evidence that OH^- anions slowly diffuse towards the positions typically occupied at Hap, indicating that the biomolecule promotes, or at least does not inhibit, mineral growth. Similar features are concluded from the $g_{OH–OH}(r)$ profiles.

The diffusion of OH− during the MD simulation in the presence of DNA is clearly shown in Figure Ann.II.6., which represents the temporal evolution of the radial distribution function for $OH^-\cdots P(DNA)$ pairs, $g_{OH–DNA}(r)$. The profiles calculated at different time intervals provide information about the temporal evolution of the number and relative position of OH^- anions located at a distance smaller than 21 Å from a phosphate group belonging to DNA. As can be seen, OH^- anions progressively incorporate to different clusters during the whole simulation, reinforcing the hypothesis that their diffusion through the inorganic solution is the limiting step for the growth of the mineral structure.

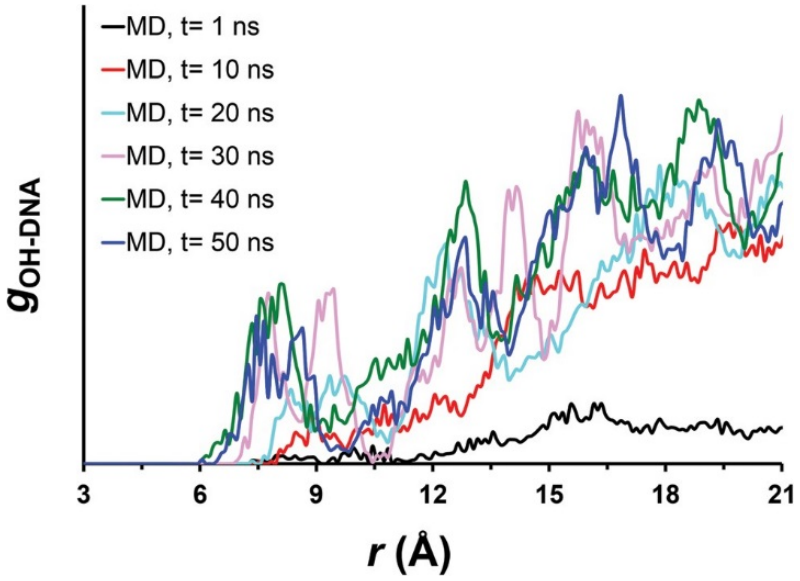

Figure Ann.II.6. Radial distribution functions of $OH^-\cdots P$ pair, where P represents the phosphorous atom of DNA backbone, calculated at different time intervals for the simulated inorganic solution with DNA.

Figure Ann.II.7a depicts a representative calcium phosphate cluster obtained at the first stages of the simulation (<1 ns) without DNA. This formation of such simple clusters seems to be a requisite for the growth of HAp from inorganic solutions. Figure Ann.II.7b and II.7c show clusters involving Ca^{2+}, PO_4^{3-} and OH^- ions from simulations without and with DNA, respectively, which suggest the nucleation of HAp.

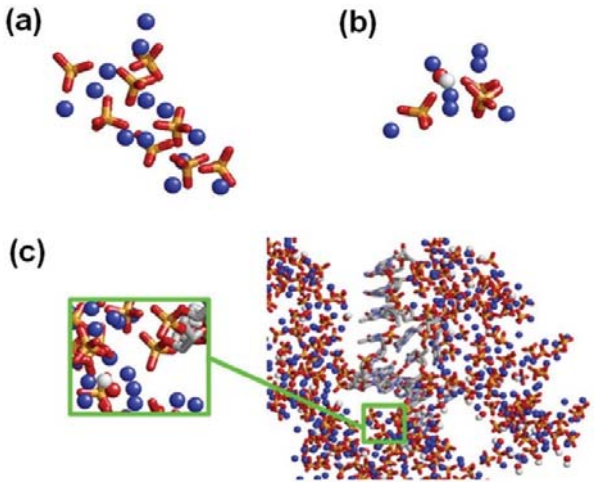

Figure Ann.II.7. (a). Representative calcium phosphate cluster obtained at the first stages of the simulation without DNA. Representative clusters including OH^- ions extracted from the simulation (b) without and (c) with DNA.

The overall observation of the results reported in this section indicates that the DNA promotes the role of the double helix backbone as a template for the nucleation of HAp. The embryonic calcium phosphate clusters formed at the first stages of the simulation grow and transform into complex clusters, in which Ca^{2+}, PO_4^{3-} and OH^- ions occupy positions that resemble those of crystalline HAp. This re-organization, which is largely influenced by the incorporation of OH^- into the clusters, supports the benefit of the interaction between the DNA and the inorganic ions for the formation of HAp. Accordingly, experimental studies for the biomineralization of DNA into HAp have been conducted in the next section by mixing aqueous containing Ca^{2+}, PO_4^{3-} and OH^- ions with DNA. Incorporation of DNA in HAp nanocapsules and nanocrystals.

Figure Ann.II.8. shows the morphologies of HAp samples prepared using $Ca(NO_3)_2$, $(NH_4)_2HPO_4$ and fish sperm DNA in aqueous solution and under two well differentiated conditions based on previously established methodologies.[30–32] In order to get nanocapsules the solutions containing Ca^{2+} and PO_4^{3-} ions were quickly mixed at high pH, which favored rounded morphologies. Aggregation was avoided by adding a surfactant (CTAB), highly diluted solutions being used. DNA molecules should form micelles in solution that adsorbed

Ca^{2+} ions on their surface by electrostatic interaction.[32] After the addition of the PO_4^{3-} containing solution, the reaction took place forming HAp around the initial DNA micelles.

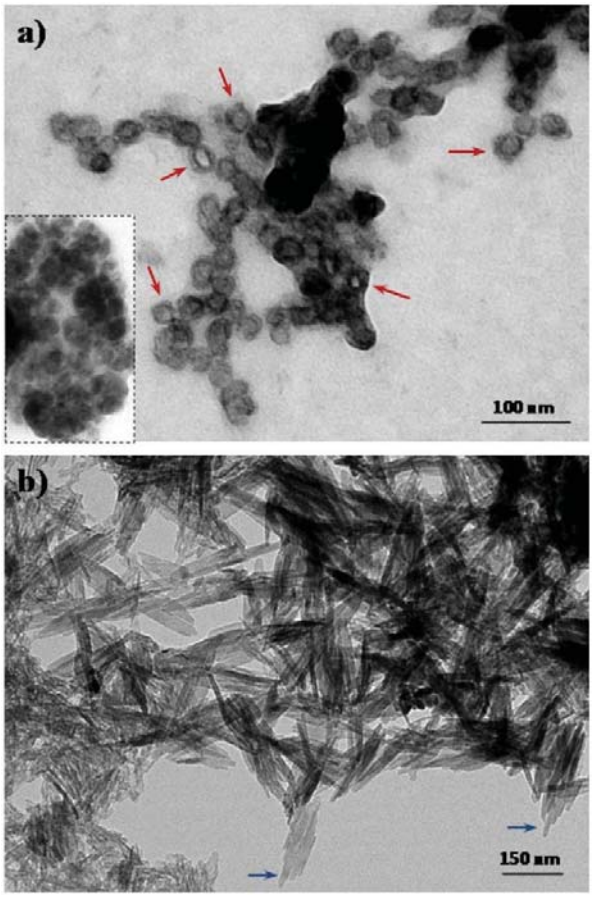

Figure Ann.II.8. TEM micrographs showing HAp-DNA nanocapsules (a) and nanocrystals (b). Red arrows point out capsules with a clearly distinctive contrast that suggest the incorporation of DNA in their inner part. For comparison purposes the inset shows nanocapsules prepared under the same experimental conditions but in absence of fish sperm DNA. Blue arrows emphasize the nanorods that constitute the crystal aggregates.

Figure Ann.II.8a clearly shows the presence of hollow nanospheres with a diameter close to 20 nm, which may contain the DNA molecules inside. In contrast, solid nanospheres of similar size (inset of Fig. Ann.II.8a) were obtained when DNA was not added to any of the initial inorganic solutions. A high concentration of DNA was employed for the preparation of nanocrystals and, consequently, it was added to the PO_4^{3-} solution instead of the Ca^{2+} one in order to avoid the formation of complexes that could limit solubility. The crystal anisotropy and, specifically, a preferred growth along the crystallographic c axis were favored by decreasing the pH to 10.31. The phosphate solution was slowly added over the

Ca^{2+} solution to avoid a rapid precipitation, allowing the development of well formed crystals from a primary nucleus. Figure Ann.II.8b shows the crystalline aggregates that were attained under these selected conditions. Aggregates had a length close to 2 μm and a variable wideness that was found to depend on the number of constitutive nanorods, each with a width close to 20 nm.

Different techniques (FTIR, XPS UV-vis and electrophoresis) have been applied to demonstrate the incorporation of DNA inside the nanocapsules/nanorods. Figure Ann.II.9. shows the FTIR spectra of synthesized HAp with typical PO_4^{3-} bands at 1093, 1033 and 962 cm^{-1} and any significant signal in the 1800–800 cm^{-1} region. The spectra of HAp nanocapsules prepared in the presence of DNA is significantly more complex, and multiple bands associated with the biomolecule can be distinguished with relatively high intensity. It should be remarked that the spectrum was recorded after removal of all superficially adsorbed DNA by digestion with deoxyribonuclease, signals of the included DNA being clearly detected because of the small thickness of the HAp wall. In particular, amide bands at 1653 and 1558 cm^{-1}, phosphate bands at 1050 cm^{-1} and NH and methylene bands at 1480–1300, 1220–1210 and 890–840 cm^{-1}.

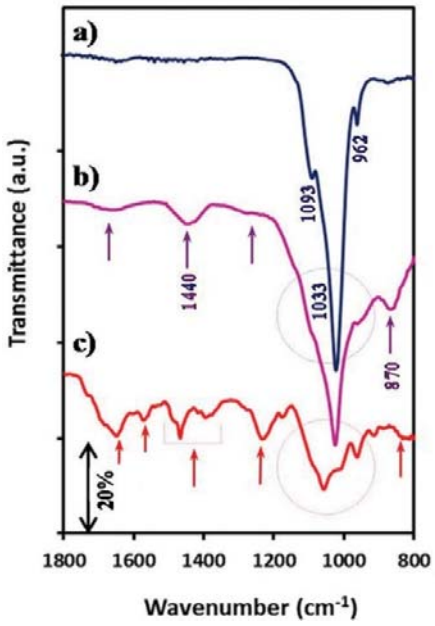

Figure Ann.II.9. FTIR spectra of HAp nanocapsules (a), HAp-DNA nanocrystals (b) and HAp-DNA nanocapsules (c). Nanocapsules prepared in presence of fish sperm DNA were previously digested with deoxyribonuclease to eliminate adsorbed DNA. Arrows and circles point out DNA distinctive signals and the complex phosphate region, respectively.

In contrast, the spectrum of nanorods was less clear even before the treatment with deoxyribonuclease. In this case, interpretation was more difficult due to the overlapping of carbonate bands at 1440 and 870 cm^{-1} that were a consequence of dissolved CO_2 from the atmosphere during the synthesis and a typical carbonate substitution of phosphate anions. Furthermore, it seems that the DNA incorporated inside nanorods could not be detected by FTIR due to presence of an opaque and thick HAp wall. Nevertheless, small signals around 1653 and 1220–1210 cm−1 could be envisaged and the phosphate band becomes broader with respect to that observed in the HAp spectrum.

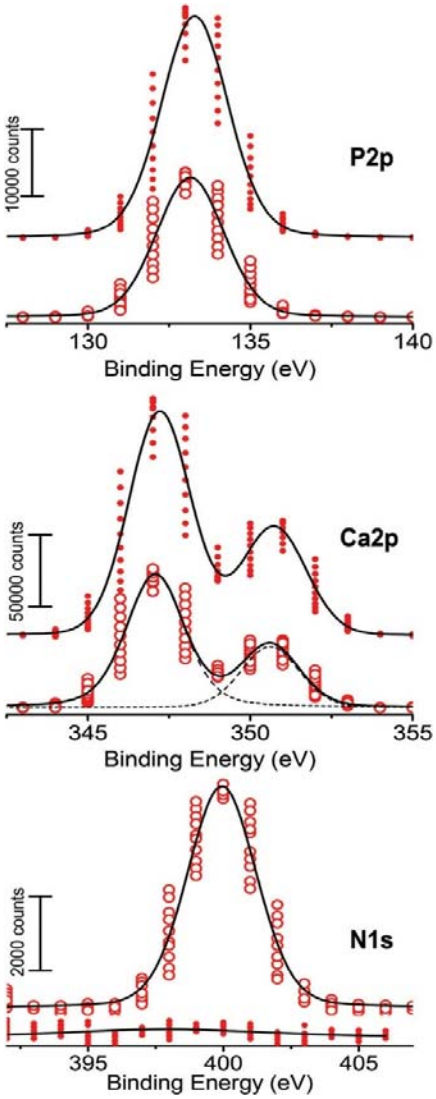

Figure Ann.II.10. High-resolution XPS spectra for HAp (solid circles) and HAp- DNA (open circles) nanocapsules: P2p, Ca2p and N1s regions. HAp-DNA samples were previously submitted to enzymatic digestion with deoxyribonuclease to eliminate the DNA adsorbed onto the surface.

Figure Ann.II.10. depicts the characteristic XPS spectra in the P 2p, Ca 2p and N 1s regions for HAp and HAp-DNA after the enzymatic digestion. The P 2p and Ca 2p peaks obtained before and after deconvolution, which are practically identical for the two systems, are in full agreement with those reported in the literature for natural HAp. The Ca 2p spectra present a doublet with Ca $2p_{3/2}$ and Ca $2p_{1/2}$, which is typically found for Ca^{2+} in inorganic calcium–oxygen compounds with binding energy at 347 eV and 351 eV, respectively.[33] Also, the single P 2p peak centered at 133 eV originates from the PO_4^{3-} anions of HAp nanocrystals.[33,34] As was expected, the N 1s signal is completely absent in HAp. In contrast, HAp-DNA samples digested with deoxyribonuclease to eliminate the DNA adsorbed onto the surface of the nanoparticles show a band centered at 400 eV, which has been attributed to the encapsulated biomolecule. UV-vis spectra, which are displayed in Figure Ann.II.11., clearly demonstrate the presence of DNA molecules in both nanocapsules and nanorod preparations since a characteristic absorption peak at 260 nm was detected in both cases. This absorbance increases after dissolution of the sample with the acid medium, as expected for DNA molecules encapsulated inside the HAp nanoparticles. It should be emphasized that such an increment is very remarkable in the nanorod preparation, corroborating the shielding effect hypothesis discussed above. Figure Ann.II.11. also shows the spectra of digested samples.

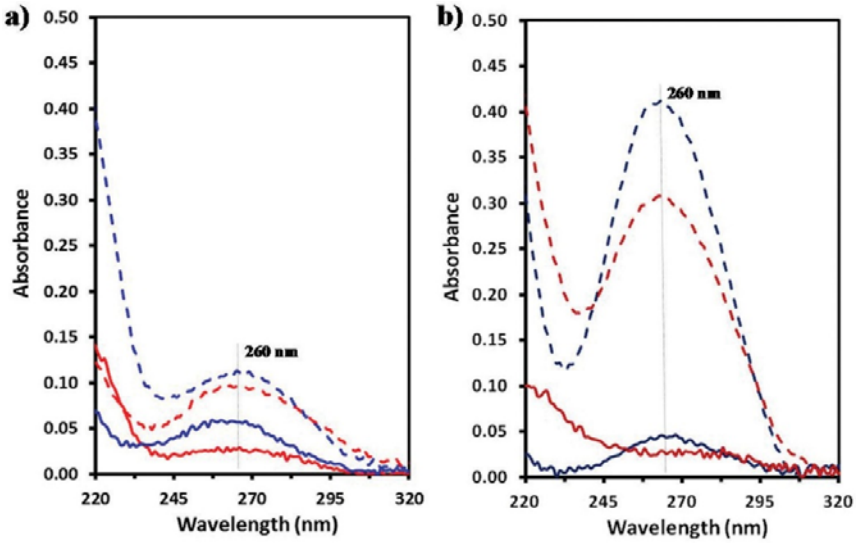

Figure Ann.II.11. UV-vis absorption spectra of the aqueous solution/dispersion of HAp-DNA nanocapsules (a) and nanocrystals (b) (with blue traces). Spectra from samples digested with deoxyribonuclease to eliminate adsorbed DNA are indicated with red traces, whereas those corresponding to samples dissolved with the acid medium are indicated with dashed traces.

As expected, the absorbance at 260 nm decreases considerably after enzymatic treatment, reaching a practically zero value for the nanorod sample. However, the significant absorbance detected after dissolution of the sample in acid medium unambiguously demonstrates the incorporation of DNA inside nanoparticles.

The quantification of DNA in nanoparticles was performed for the nanorod preparation due to a greater amount of sample being available. For this purpose, the absorbance measurement (A260) was multiplied by the well-known conversion factor of 50 $\mu g \cdot mL^{-1}$ for double-strand DNA) to get the total amount of DNA. Results indicate that approximately 11 µg and 33 µg of DNA are adsorbed on the surface or encapsulated inside the 1 mg of HAp nanorods, respectively. Accordingly, an encapsulating efficiency close to 25% is derived, considering that the DNA/HAp ratio from synthesis was 127 $\mu g \cdot mg^{-1}$.

Similar conclusions are derived from the electrophoretic pattern of HAp/DNA nanorods that is displayed in Fig. 12. Both the DNA superficially adsorbed and that incorporated inside the particles give rise to the high intense spot observed on lane 4.

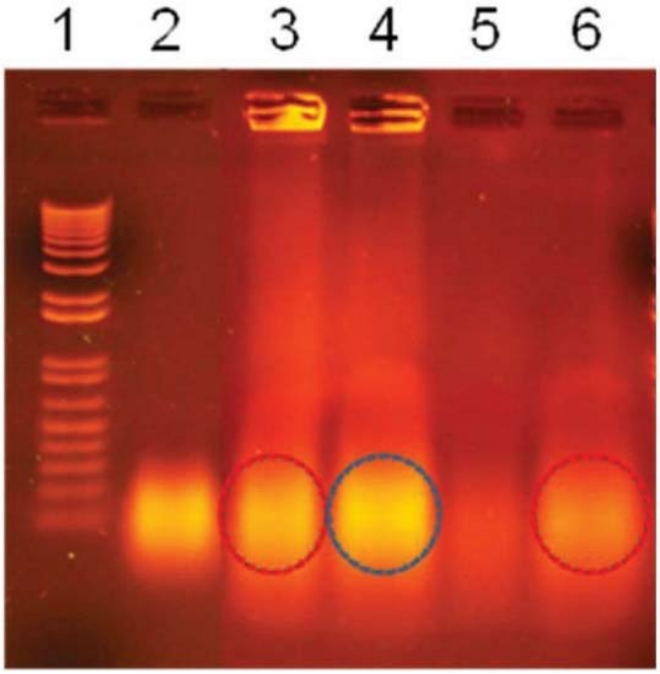

Figure Ann.II.12. Electrophoretic pattern of HAp-DNA nanocrystals. Lane 1: molecular weight marker. Lane 2: Fish sperm DNA. Lane 3: HAp-DNA nanocrystals. Lane 4: HAp-DNA nanocrystals dissolved with EDTA. Lane 5: HAp-DNA nanocrystals digested with deoxyribonuclease. Lane 6: HAp-DNA nanocrystals digested with deoxyribonuclease and then dis- solved with EDTA. Note that the intensity of the DNA signal in lane 4 (blue circle) is similar to the addition of the intensity of DNA signals in lanes 3 and 6 (red circles).

This corresponds to the particles digested with EDTA, which is capable of chelating calcium ions. The intensity of the latter spot is clearly higher than that observed for the spot of lane 3, which refers to the initially loaded particles (i.e. it is basically attributed to both DNA adsorbed on the surface and DNA internally loaded but able to migrate). The fluorescence observed in the wells of lanes 3 and 4, and even the continuous smear, reflect the restricted mobility of DNA in the gel, which is caused by a progressive release from the bigger particles. Lanes 5 and 6 correspond to particles in which the adsorbed DNA was previously digested with deoxyribonuclease to eliminate this superficial DNA. A high intense spot is observed after dissolution with EDTA (lane 6) while a low signal is detected before dissolution (lane 5), as expected for encapsulated DNA. Finally, Figure Ann.II.12. points out that the intensity of the DNA spot of lane 4 results from the addition of the signals of DNA adsorbed in the surface (lane 3) and DNA incorporated inside the particle (lane 6).

II.4. Conclusions

Classical MD simulations of inorganic Ca^{2+}, PO_4^{3-} and OH^- aqueous solutions in the presence and absence of DNA have shown that the biomolecule acts as a template for the nucleation and growth of HAp. This templating effect of DNA is accompanied by a change in the aggregation mechanism.

Thus, simulations show the formation of multiple calcium phosphate clusters in the absence of DNA, which incorporate OH^- anions after some ns transforming into nucleation centers for the formation of HAp. The simultaneous formation of multiple nucleation centers is fully consistent with the mechanism typically found for the crystallization of inorganic salts from their solutions. In contrast, simulations in the presence of the biomolecule reveal that calcium phosphate clusters are formed surrounding the DNA backbone. The phosphate groups of the biomolecule act as a very large nucleus for the growth of the HAp. As occurs in the absence of DNA, the formation of HAp around DNA is limited by the incorporation of OH^- anions to the cluster. In summary, MD simulations clearly indicate that DNA promotes the templated nucleation of HAp from a Ca^{2+}, PO_4^{3-} and OH^- containing inorganic solution. These conditions have been experimentally applied in the laboratory to create nanoparticles and nanocrystals with DNA inside. Nanoparticles show a spherical shape and a diameter of ~20 nm while nanocrystals are constituted of nanorods with a width of ~20 nm. After removal of all superficially adsorbed DNA by digestion with deoxyribonuclease, the presence of DNA inside nanospheres and nanocrystals has been unambiguously

determined by FTIR, XPS, UV-vis and gel electrophoresis. The biomineralization of DNA is particularly important for biomedical applications requiring the protection of the biomolecule from aggressive environmental conditions.

II.5. References

1. Narasaraju T.S.B., Phebe D.E., Some physico-chemical aspects of hydroxylapatite, *Journal of Material Sciences* (**1996**), *31*, 1–21.
   DOI: 10.1007/BF00355120

2. Weiner S., Wagner H.D., The material bone: structure-mechanical function relations, *Annual Reviews of Material Science* (**1998**), *28*, 271–298.
   DOI: 10.1146/annurev.matsci.28.1.271.

3. Fratzl P., Gupta H.S., Paschalis E.P., Roschger P., Structure and mechanical quality of the collagen–mineral nano-composite in bone, *Journal of Materials Chemistry* (**2004**), *14*, 2115–2123.
   DOI: 10.1039/B402005G

4. Tirrell M., Kokkoli E., Biesalski M., The role of surface science in bioengineered materials, *Surface Science* (**2002**), *500*, 61–83.
   DOI:10.1016/S0039-6028(01)01548-5.

5. George A., Veis A., Phosphorylated Proteins and Control over Apatite Nucleation, Crystal Growth, and Inhibition, *Chemical Reviews* (**2008**), *108*, 4670–4693.
   DOI: 10.1021/cr0782729.

6. Boskey A.L., Biomineralization: An Overview, *Connective Tissue Research* (**2003**), *44*, 5–9.
   DOI: 10.1080/03008200390152007.

7. Alford A.I., Hankenson K.D., Matricellular proteins: Extracellular modulators of bone development, remodeling, and regeneration, *Bone* (**2006**), *38*, 749–757.
   DOI: 10.1016/j.bone.2005.11.017.

8. Boskey A.L., *Bone mineralization, in Bone Mechanics Handbook*, ed. S. C. Cowin, CRC Press, Boca Raton, 2nd edn, pp. 5.1–5.31, (**2000**).

9. Baker R., Rogers K.D., Shepherd N., Stone N., New relationships between breast microcalcifications and cancer, *British Journal of Cancer* (**2010**), *103*, 1034–1039.
   DOI:10.1038/sj.bjc.6605873.

10. Zhu S.H., Huang B.Y., Zhou K.Z., Huang S.P., Liu F., Li Y.M., Xue Z.G..Long Z.G., Hydroxyapatite Nanoparticles as a Novel Gene Carrier, *Journal of Nanoparticle Research* (**2004**), *6*, 307–311.
    DOI:10.1023/B:NANO.0000034721.06473.23.

11. Kozlova D., Chernousova S., Knuschke T., Buer J., Westendorf A.M., Epple M., Cell targeting by antibody-functionalized calcium phosphate nanoparticles, *Journal of Materials Chemistry* (**2012**), *22*, 396–404.
    DOI: 10.1039/C1JM14683A.

12. Bisht S., Bhakta G., Mitra S., Maitra A., pDNA loaded calcium phosphate nanoparticles: highly efficient non-viral vector for gene delivery, *International Journal of Pharmaceutics* (**2005**), *288*, 157–168.
DOI:10.1016/j.ijpharm.2004.07.035.

13. Olton D., Li J., Wilson M.E., Rogers T., Close J., Huang L., Kumta P.N., Sfeir C., Nanostructured calcium phosphates (NanoCaPs) for non-viral gene delivery: Influence of the synthesis parameters on transfection efficiency. *Biomaterials* (**2007**), *28*, 1267–1279.
DOI: 10.1016/j.biomaterials.2006.10.026.

14. Brundin M., Figdor D., Sundqvist G., Sjögren U., DNA binding to hydroxyapatite: a potential mechanism for preservation of microbial DNA, *Journal of Endodontics* (**2013**), *39*, 211–216.
DOI:10.1016/j.joen.2012.09.013.

15. Jordan M., Schallhorn A., Wurm F.M., Transfecting mammalian cells: optimization of critical parameters affecting calcium-phosphate precipitate formation, *Nucleic Acids Research* (**1996**), *24*, 596–601.
DOI:10.1093/nar/24.4.596

16. Okazaki M., Yoshida Y., Yamaguchi S., Kaneno M., Elliot J.C., Affinity binding phenomena of DNA onto apatite crystals, *Biomaterials* (**2001**), *22*, 2459–2464.
DOI:10.1016/S0142-9612(00)00433-6.

17. Revilla-López, G., Casanovas J., Bertran O, Turon P.*, Puiggalí J.., Alemán C.,* Modeling biominerals formed by apatites and DNA, *Biointerphases* (**2013**), *8*, 10,1-15.
DOI:10.1186/1559-4106-8-10, Marked as “Highly accessed”

18. Grzeskowiak K., Goodsell D.S., Kaczor-Grzeskowiak M., Cascio D., Dickerson R.E., Crystallographic analysis of C-C-A-A-G-C-T-T-G-G and its implications for bending in B-DNA. *Biochemistry* (**1993**) *32*, 8923–8931.
DOI:10.1021/bi00085a025.

19. Phillips J.C., Braun R., Wang W., Gumbart J., Tajkhorshid E., Villa E., Chipot C., Skeel R.D., Kale L., Schulten K., Scalable molecular dynamics with NAMD. *Journal of Computational Chemistry* (**2005**), *26*, 1781–1802.
DOI: 10.1002/jcc.20289.

20. Cornell W.D,. Cieplak P., Bayly C.I., Gould I.R., Merz K.M., Ferguson D.M., Spellmeyer D.C., Fox T., Caldwell J.W., Kollman P.A., A second generation force field for the simulation of proteins, nucleic acids, and organic molecules. *Journal of American Chemical Society* (**1995**), *117*, 5179–5197.
DOI:10.1021/ja00124a002.

21. Duan Y., Chowdhury S., Lee M.C., Xiong G., Zhang W., Yang R., Cieplak P., Luo R., Lee T., Caldwell J., Wang J., Kollman P.A., A point-charge force field for molecular mechanics simulations of proteins based on condensed-phase quantum mechanical calculations. *Journal of Computational Chemistry* (**2003**), *24*, 1999–2012. DOI:10.1002/jcc.10349.

22. Hornak V., Abel R., Okur A., Strockbine B., Roitberg A., Simmerling C., Comparison of multiple Amber force fields and development of improved protein backbone parameters. *Proteins* (**2006**), *65*, 712–725. DOI:10.1002/prot.21123.

23. Bradbrook G.M., Gleichmann T., Harrop S.J., Habash J., Raftery J., Kalb J., Yariv J., Hillier I.H., Helliwell J.R., X-Ray and molecular dynamics studies of concanavalin-A glucoside and mannoside complexes Relating structure to thermodynamics of binding. *Journal of Chemical Society, Faraday Transactions* (**1998**), *94*, 1603–1611. DOI:10.1039/A800429C.

24. Jorgensen W.L., Chandrasekhar J., Madura J.D., Impey R.W., Klein M.L. Comparison of simple potential functions for simulating liquid water. *Journal of Chemical Phy*sics (**1983**), *79*, 926–935. DOI:10.1063/1.445869.

25. Darden T., York D., Pedersen L., Particle Mesh Ewald-an N.Log(N) method for Ewald sums in large systems. *Journal of Chemical Physics* (**1993**), *98*, 10089–10092. DOI:10.1063/1.464397.

26. Berendsen H.J.C., Postma J.P.M., van Gunsteren W.F., DiNola A., Haak J.R., Molecular dynamics with coupling to an external bath. *Journal of Chemical Physics* (**1984**), *81*, 3684–3690. DOI:10.1063/1.448118.

27. Ryckaert J.P., Ciccotti G., Berendsen H.J.C., Numerical integration of the Cartesian Equations of Motion of a System with Constraints: Molecular Dynamics of n-Alkanes. *Journal of Computational Physics* (**1977**), *23*, 327–341. DOI:10.1016/0021-9991(77)90098-5.

28. Harding, J.H., Duffy D.F., Sushko M.L., Rodger P.M., Quigley D., Elliot J.A., Computational techniques at the organic−inorganic interface in biomineralization, *Chemical Reviews* (**2008**), *108*, 4823–4854. DOI: 10.1021/cr078278y.

29. Hiughes J.M., Cameron M., Corwley K.D. Structural variations in natural F, OH, and Cl apatites. *American Mineralogist* (**1989**) *74*, 870–876.

30. Zhang Y., Lu J., A simple method to tailor spherical nanocrystal hydroxyapatite at low temperature, *Journal of Nanoparticle Research* (2007), *9*, 589–594. DOI: 10.1007/s11051-006-9177-3.

31. Wang P., Li C., Gong H., Jiang X., Wang H., Li K., Effects of synthesis conditions on the morphology of hydroxyapatite nanoparticles produced by wet chemical process, *Powder Technology* (**2010**), *203*, 315–321.
DOI:10.1016/j.powtec.2010.05.023.

32. Qi C., Zhu Y-J., Lu B-Q., Zhao X-Y., Zhao J., Chen F., Hydroxyapatite nanosheet-assembled porous hollow microspheres: DNA-templated hydrothermal synthesis, drug delivery and protein adsorption, *Journal of Materials Chemistry* (**2012**), *22*, 22642–22650.
DOI: 10.1039/C2JM35280J.

33. *Handbook of X-ray Photoelectron Spectroscopy*,ed. J. F. Moulder, J. Chastain, Physical Electronics Division, Perkin-Elmer Corporation, (**1995)**.

34 Chang M.C., Tanaka J., XPS study for the microstructure development of hydroxyapatite–collagen nanocomposites cross-linked using glutaraldehyde, Biomaterials (**2002**), *23*, 3879–3885.
DOI:10.1016/S0142-9612(02)00133-3.

Annex III

Restricted Puckering of Mineralized RNA-Like Riboses[4]

Abstract

The pseudorotational motions of highly hydroxylated pentafuranose sugars in the free state and tethered to hydroxyapatite have been compared. The conformation pentafuranose ring remains restricted at the North region of the pseudorotational wheel, which is the one typically observed for nucleosides and nucleotides in the double helix A-RNA, when the phosphate-bearing sugar is anchored to the mineral surface. Results indicate that the severe restrictions imposed by the mineral are responsible of the double helix preservation when DNA and RNA are encapsulated in crystalline nanorods.

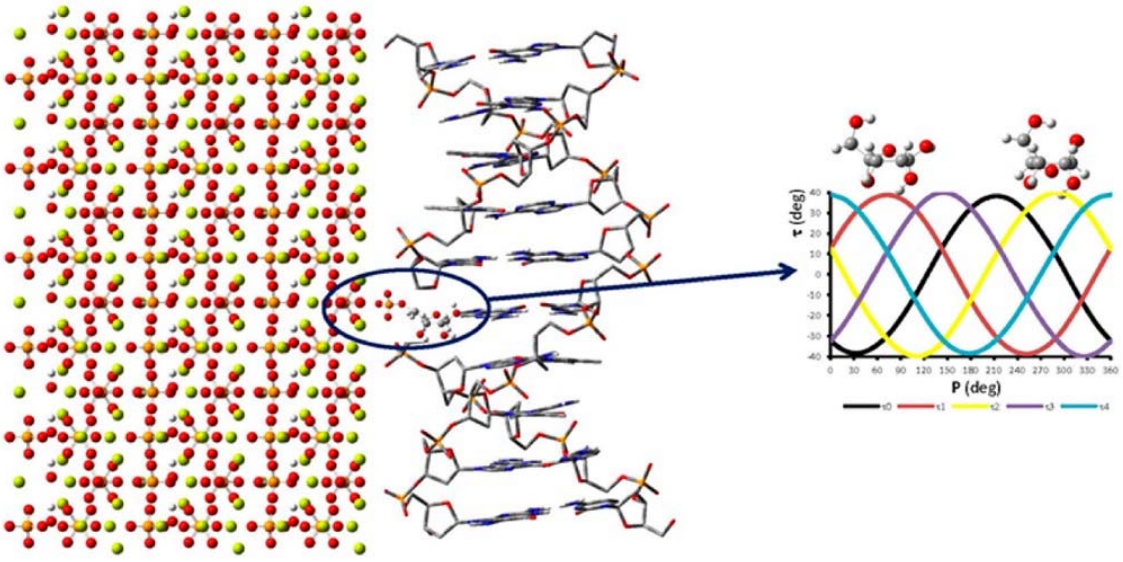

[4] Published in Casanovas J., Revilla-López G., Bertrán O., del Valle L.J., Turon P., Puiggalí J., Alemán C.. Restricted puckering of mineralized RNA-like riboses, *Journal of Physical Chemistry B*, (**2014**) *118*, 5075-5081. Reproduced with permission of American Chemical Society.

Annex III

Restricted Puckering of Mineralized RNA-Like Riboses

III.1 Introduction

Hydroxyapatite (HAp) has been a widespread building material in nature for millions of years.[1,2] Furthermore, since several decades ago, a number of biotechnological applications for nucleic acids (NA) separation and chemical protection have been reported. These are based in NA-HAp interactions at two complementary levels: HAp surface facets and NA-templated HAp nucleation. [1,2] The HAp-induced structural stabilization of the NAs has been suggested as a consequence of mineralization and the mechanism by which NAs are protected from chemical degradation. Only recently, the role of NA phosphate as a HAp crystallization promoter, an part of the mineral, has been revealed at atomic-level.[3,4] Further, NA flexibility is tightly bound to ribose and 2'-deoxyribose sugars conformational variability as reported for different chemical modifications[5,6] but little is known about its behavior when phosphate is embedded in the HAp crystal (i.e., the latter creates a rigid inflexible wall containing the phosphates of the biomolecules and the mineral). This rigidity can be transferred to the rest of the NAs through changes in the flexibility of their sugars, an aspect which is totally unknown.

Traditionally, the flexibility of pentofuranose sugars is described using the concept of pseudorotation (Figure Ann.III.1.), which allows unequivocal determination of the exact conformation of each five-membered ring in terms of two parameters, the phase of pseudorotation (P) and the puckering amplitude (τ_m).[7,8] Both P and τ_m are defined by endocyclic torsion angles (Figure Ann.III.2.). As canonical and non-canonical segments of functional NA and RNA duplexes are influenced by sugar pucker conformations,[9–11] work in this field has been essentially focused on the comparison of the pseudorotational equilibrium between abasic sugars and nucleosides.[7,8,12–21] In addition, sugars puckering is expected influence the hydrolysis of N-glycosidic bond.[22] In this work, we investigate the relationship between the sugar conformation and HAp. In particular, we are interested in highly hydroxylated pentafuranoses, which remain relatively unknown. As a first step, molecular modeling tools have been used as in our previous B-DNA study[3] to check that A-type RNA double helices can be encapsulated inside nanopores of crystalline HAp,

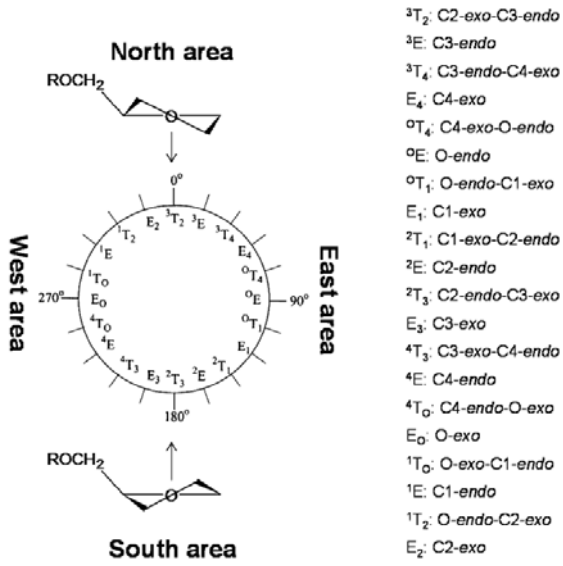

Figure Ann.III.1. Pseudorotational wheel of pentafuranose sugars (left). The North, East, South, and West regions are defined. Description of the conformations associated with the twist and envelope arrangements of the pentafuranose ring is also provided (right).

$Ca_{10}(PO_4)_6(OH)_2$ and hexagonal symmetry,[23] without undergoing significant alterations in the secondary structure. After this, the influence of the inorganic environment on the pseudorotational movement has been investigated. For this purpose, the pseudorotational spaces of β-D-ribofuranose (denoted **1** in Scheme III.1), a pentafuranose ring bearing four hydroxyl groups, β-D-ribofuranose 5-phosphate (denoted **2** in Scheme Ann.III.1), in which the hydroxyl group attached to the exocyclic methylene unit is replaced by a phosphate group, and 2 anchored to a HAp mineral wall have been determined using density functional theory (DFT) calculations.

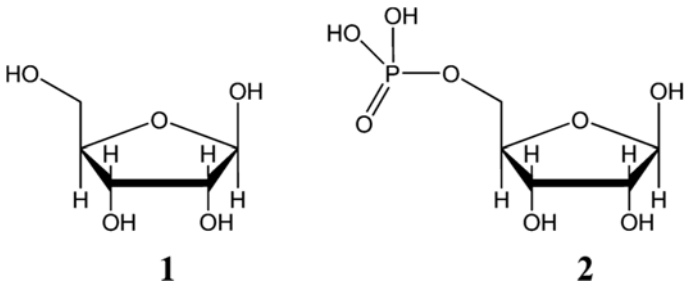

1 **2**

Scheme Ann.III.1

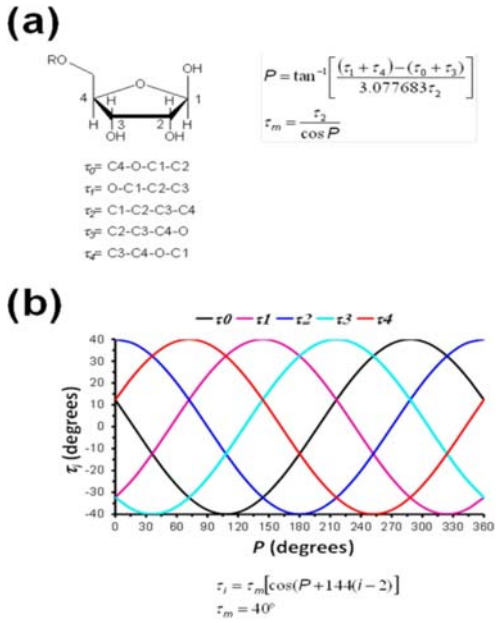

Figure Ann.III.2. (a) Endocyclic dihedral angles of pentafuranose sugars and expressions used to obtain the phase of pseudorotation (P) and the puckering amplitude (τ_m). (b) Variation of the endocyclic torsional angles with P (τ_m was set to 39°).

III.2. Methods

III.2.1. Force-Field Simulations

Both energy minimization and MD simulations were applied using the NAMD 2.6 program.[24] Models constructed to examine the stability of the A-RNA double helix embedded into HAp nanopores were minimized by applying 5×10^3 steps of steepest descent to relax the more important conformational and structural tensions. Then, a MD run of 3.0 ns in the NVT ensemble (constant number of particles, volume and temperature) at 298 K was carried out to equilibrate the systems and eliminate small structural tensions. After such thermal relaxation, the saved coordinates were submitted to a new energy minimization by applying 5×10^3 steps of steepest descent. In both energy minimizations and MD simulation, atoms contained in A-RNA were only allowed to move from their positions, the coordinates of the mineral being kept fixed at their crystallographic positions in all cases. It should be emphasized that all the systems were calculated in triplicate considering starting points that differ in the orientation of the A-RNA with respect to the apatite.

The potential energy was computed using the Amber forcefield.[25] All force-field parameters for DNA as well as the phosphate and hydroxyl groups were extracted from Amber ff03.[26] It should be noted that the ff03 parameters are identical to the ff99-SB27 ones for nucleic acids, phosphate and hydroxyl groups. Force-field parameters of Ca^{2+} were extracted from the work reported by Bradbrook et al.[28] The ability of this set of force-field parameters to reproduce the inorganic···organic interactions found in biominerals was recently proved.[3]

Puckering pseudorotation angles, P, and amplitudes, τ_m, were determined following Altona and Sundaralinga,[7,8] (Figure Ann.III.2a), using the same reference state for $P = 0.0°$. The pseudorotation space is divided into four equally sized quadrants, centered around $P = 0.0°$, $P = 90.0°$, $P = 180.0°$, and $P = 270.0°$, which are referred to as the North, East, South, and West quadrants (Figure Ann.III.1.), respectively. Structures to explore the pseudorotational properties were between $P = 0°$ and $P = 360°$ at 18° increments. Initially, dihedral angles internal to the ring were obtained using the formula displayed in Figure Ann.III.2b, τ_m being set to 39°. In addition to the pseudorotational angle P, model sugars 1 and 2 contain several torsion angles associated with exocyclic groups for which different conformations are possible. For each of the 20 ring dispositions generated to examine the pseudorotation movements, different structures were constructed by varying such dihedral angles associated with the exocyclic moieties to form stabilizing O–H···O hydrogen bonds. A total of 8, 14, and 6 structures were generated for each ring disposition of 1, 2, and 2 tethered to HAp, respectively. Accordingly, the number of starting structures for geometry optimization were 20 × 8 = 160, 20 × 14 = 280 and 20 × 6 = 120, respectively.

The endocyclic dihedrals τ_0 and τ_1 were constrained during geometry optimization to ensure the pentafuranose conformation, all other parameters being freely optimized. All quantum mechanical calculations were carried out with the Gaussian 09 program29 using the 6-311++G(d,p)[30,31] and 6-31G(d)[32] basis sets All pseudorotational energy surfaces were investigated at the DFT level of theory using a functional that combines the Becke's three-parameter hybrid functional (B3)33 with the Lee, Yang, and Parr (LYP)[34] expression for the nonlocal correlation (B3LYP).

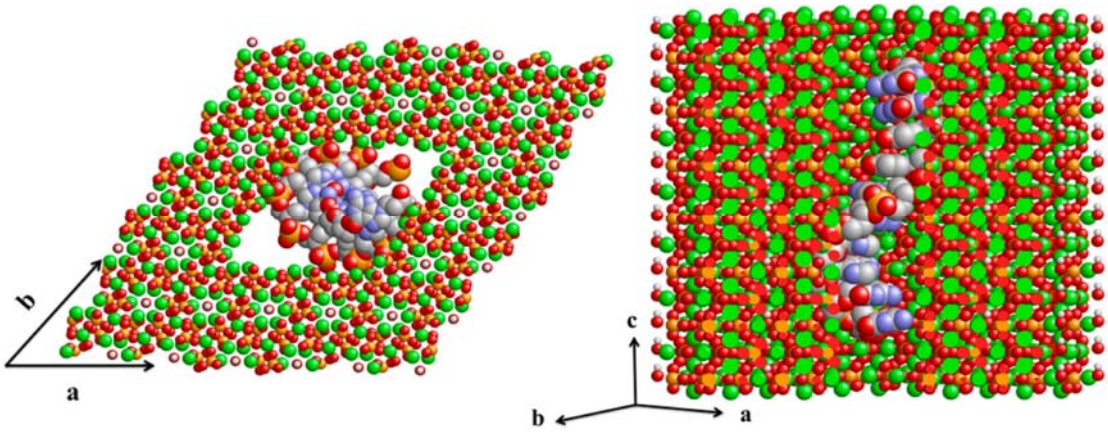

Figure Ann.III.3. Equatorial and axial projections of the biomineral obtained by embedding helical A-RNA into a HAp nanopore. Calcium is represented in green, phosphorus in orange, oxygen in red, nitrogen in blue, and hydrogen of HAp hydroxyl groups in white (hydrogen atoms belonging to the RNA have been omitted).

The influence of dispersion forces in the pseudorotational profile of 2 tethered to HAp was evaluated by including single point Grimme's empirical dispersion correction for dispersion[35–37] at the B3LYP/6-31G(d) optimized geometries. To avoid an overestimation of dispersion effects, the C6 coefficient for Ca^{2+} was set to zero.[38]

III.3. Results and discussion

Natural hydroxyapatite (HAp) has a hexagonal crystal structure with space group $P6_3/m$ and periods a = b = 9.42 Å, and c =6.87 Å.[23] The total number of atoms in the unit cell is 44, even though it only contains seven symmetrically independent atoms: two calcium ions, one forming single atomic columns parallel to the c axis and the other surrounding the hexagonal channel of hydroxyl in groups of the three calcium atoms at different heights; one phosphor and three oxygen atoms (forming PO_4^{3-} tetrahedral units; and the OH^- ions disordered along c about the mirror plane at z = 1/4. The occupancy of the OH^- sites was 50%, as necessary in a $P6_3/m$.

The chemical structure of the RNA dodecamer examined in this work is 5′-CGCGAAUUCGCG-3′, which corresponds to the Dickerson's dodecamer[39] used in our previous study[3] with DNA after replace thymine by uracile. This is a well-known sequence with three primary characteristic tracts: CG, AA and UU. The double helix was initially arranged in a typical A structure with pitch= 30 Å, 11 bases per turn, an axial rise of 2.79 Å

and a base-pair tilt of 16.7°. Giving the hexagonal symmetry of HAp and the molecular dimensions of the A-RNA dodecamer, HAp model (supercell) was constructed considering 6 × 6 × 7 unit cells. After this, a hole was generated in the center of the supercell, the dimensions of such hole being defined by the A-type double helix of RNA (i.e., steric conflicts between the apatite atoms and the A-RNA were not allowed). A hole of 2 × 2 × 7 units cells was the minimum required to accommodate the double helix without severe steric contacts. In order to completely avoid unfavorable steric interactions between the HAp and the biomolecule, some additional atoms and groups of atoms were translated at their border regions allowing us to maintain the electroneutrality of the supercells. The side length of this hole is 19 Å and its angle γ is 120°. The resulting model (i.e., supercell with a hole of appropriated dimensions at the center) consists of 9,856 atoms. In order to maintain the electrical neutrality of the system, Ca^{2+} ions were put at the minor groove of the RNA double helix. The positions of these ions were optimized by energy minimization while the coordinates of the rest of the atoms of the system were kept fixed.

Relaxation of the constructed models using MD simulations evidenced that encapsulation of the A-RNA double helix in constructed pores of HAp does not induce significant structural distortions in the secondary structure of the biomolecule (Figure Ann.III.3.).

The diameter of the minimum pore needed to encapsulate A-RNA, which is defined by the shortest internal diagonal, is 21 Å. Integration of A-form RNA into HAp crystals is favored because four phosphate groups at the double helix are located at distances (i.e., ∼7 and ∼13) very similar to those identified for a crystallographic plane of the HAp structure (i.e., 6.87 and 11.66 Å), which results in stabilizing interactions between the Ca^{2+} atoms of HAp and the phosphate groups of RNA backbone. This expected result is fully consistent with both MD predictions and experimental observations on DNA-HAp biominerals, especially those involving nanocrystals.[3,4] On the other hand, the ribose rings of encapsulated A-RNA remained between the typical C2-exo-C3-endo ($^3T_2$) and C3-endo (^3E) conformations (i.e., North region of the pseudorotational wheel).

Since RNA-HAp biominerals share the most relevant characteristics observed for DNA-HAp, the rest of the work has focused on evaluating the influence of the mineral on the potential energy for pseudorotation. For this purpose, in a first stage the pseudorotational space of **1** has been scanned by constructing 20 different twist and envelope conformations, which differ in the endocyclic torsional angles used to define *P* since τm was set to 39°

(Figure Ann.III.2.). For each of such 20 conformations, exocyclic hydroxyl groups were considered in 8 different dispositions, which result in structures that differ not only in the number of intramolecular hydrogen bonds but also in the their associated interaction pattern. All degrees of freedom other than the two endocyclic torsional angles used to preserve the *P* and τ_m values were optimized for the 20 × 8= 160 structures at both B3LYP/ 6-31G(d) and B3LYP/6-311+G(d,p) levels. Pseudorotational profiles for **1** were constructed considering the energy of the most stable structure for each value of *P* (Figure Ann.III.4.). Although the profiles obtained using the two basis sets are in excellent qualitative agreement, the flexibility of the furanose ring is considerably underestimated by the 6-31G(d) one. B3LYP/ 6-311+G(d,p) calculations corroborate the flexibility typically observed for all pentafuranose rings.[12–21] In spite of this common tendency, **1** presents features that are distinctive from less hydroxylated riboses and deoxyriboses. Three minima $^{3}T_{2}$ (*P* = 0.5°), $^{2}T_{1}$ (*P* = 144.7°) and ^{4}E (*P* = 235.4°) are clearly detected within a very narrow energy gap (<0.5 kcal/mol), the highest energy barrier (2.1 kcal/mol) corresponding to the ^{O}E (P = 93.4°). It should be noted that some X-ray and solution structures showing a ^{O}E sugar conformation were reported in early studies.[40,41] The positions of the three minima together with very low barriers found at the $^{2}T_{3}$ (P≈ 180°) and E_O (P ≈ 270°) regions indicate that of pseudorotational motion associated with the *North* ($^{3}T_{2}$) ↔ *South* ($^{2}T_{1}$) interconversion occurs through *West* (^{4}E) conformations (the different areas are defined in Figure Ann.III.1.). In contrast, for less hydroxylayed surgars the *North* ↔ *South* interconversion proceeds through the East area.[12–21]

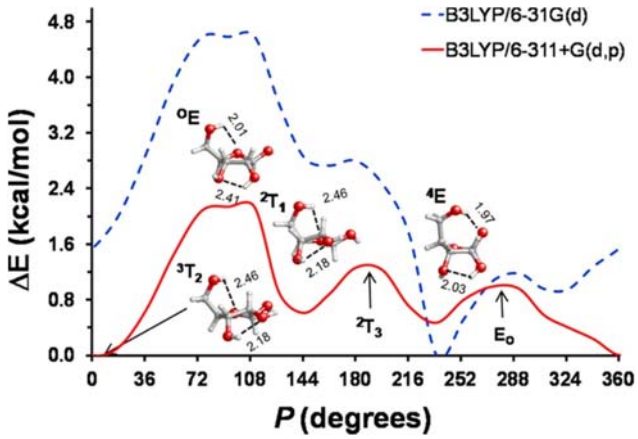

Figure Ann.III.4. Pseudorotational energy curves calculated for 1. Profiles were obtained through geometry optimization at the B3LYP/6-31G(d) and B3LYP/6-311+G(d,p) levels of 8 structures for each value of P, which ranged from 0° to 360° in steps of 18°. Energy profiles were constructed using the lowest energy structure for each value of P.

This important difference has been essentially attributed to the stabilizing effect of hydrogen bonds involving the hydroxyl groups attached to the C2 and C3 of **1** as well as to the extra gauche effect associated with higher number of OCCO dihedrals.[12–21]

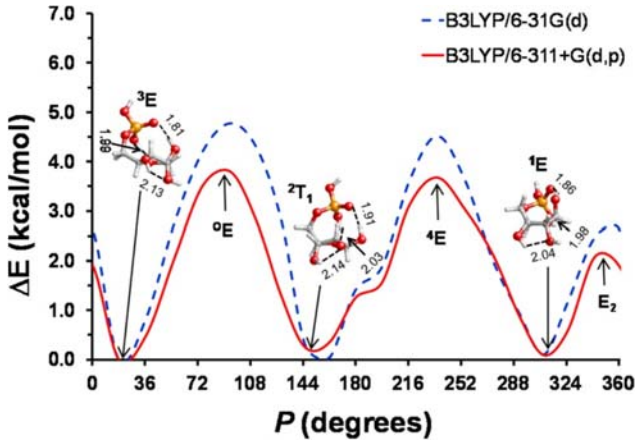

Figure Ann.III.5. Pseudorotational energy curves calculated for 2. Profiles obtained through geometry optimization at the B3LYP/6-31G(d) and B3LYP/6-311+G(d,p) levels of 14 structures for each value of P, which ranged from 0° to 360° in steps of 18°. These structures were constructed by varying the dihedral angles associated with the exocyclic moieties to form stabilizing O−H···O hydrogen bonds. Energy profiles were constructed using the lowest energy structure for each value of P.

The same methodology was applied to evaluate the pseudorotational energy profile of **2**, the substitution of the C4′-hydroxyl by phosphate increasing considerably the number of hydrogen bonding groups with respect to **1**. Accordingly, the number of initial structures constructed by varying the orientation of the exocyclic groups for each arrangement of the pentafuranose ring increased from 8 to 14. Results obtained after optimization of such 20 × 14 = 280 initial structures at the B3LYP/6-31G(d) and B3LYP/6-311+G(d,p) levels, which are displayed in Figure Ann.III.5., reveal significant changes with respect to **1**.

The $^{3}T_{2}$ and ^{4}E minima of **1** shift to ^{3}E (P = 18.1°) and ^{1}E (P = 308.7°), respectively, whereas the $^{2}T_{1}$ minimum remains (P = 145.1°). All these minima involve a hydrogen bonding network that is reinforced with respect to that found in **1** by strong phosphate···furarose interactions. Indeed each minimum presents two hydrogen bonds of such kind, the oxygen atoms of the phosphate moiety acting as donor in one and as acceptor in the other. Although the three minima are comprised within a relative energy gap of only 0.3 kcal/mol, they are separated by energy barriers of 3.8 (^{O}E, P = 94.5°), 3.7 (^{4}E, P = 235.7°) and 2.1 kcal/mol (E_2, P = 343.2°). These energy barriers are significantly higher than those

detected for the interconversion between the minima of **1**, which has been attributed to the repulsive steric interactions provoked by the phosphate at some pseudorotational regions (i.e., the phosphate moiety is bulkier than the hydroxyl group of **1**). On the other hand, it is worth to mention the excellent agreement between the pseudorotational profiles calculated with the two basis sets, which in this case is not only qualitative but also quantitative. This result has allowed us to examine, as a next step, the influence of the biomineralization in the pseudorotational flexibility of **2** using the smallest basis set only.

The influence of HAp mineral in the flexibility of the sugar was evaluated by considering a complex model constructed by combining the information derived from both experiments on crystalline nanorods of HAp containing DNA molecules inside and MD simulations devoted to examine the templating effect of the biomacromolecule on the nucleation and growth of crystalline HAp.[4,40,41] Accordingly, the phosphate moiety of compound **2** was tethered to a mineral wall. Thus, the whole system, which involves 62 atoms, consists on a single HAp unit cell with the phosphate moiety of **2** embedded in the $(10\bar{1}0)$ facet (Figure Ann.III.6a). This HAp wall restricts the number of initial structures with O−H···O hydrogen bonds that can be constructed for each arrangement of the pentafuranose ring, which decreases from 14 to 6, the resulting 6 × 20= 120 initial structures being optimized at the B3LYP/6-31G(d) level.

The pseudorotational profile displayed in Figure Ann.III.6b shows two minima, ${}^{3}T_{2}$ (P = 0.6°) and ${}^{2}T_{3}$ (P = 179.8°), which were identified in the curve calculated for **1** (Figure Ann.III.3.) as a minimum and a barrier, respectively. However, both steric and electrostatic interactions induced by the ions of the HAp wall increase the energy gap between these two conformations from 1.3 to 5.4 kcal/mol. Thus, although the *North* ↔ *South* equilibrium identified for the sugar moiety of ribufuranosyl-N-nucleosides was the ${}^{3}T_{2} \leftrightarrow {}^{2}T_{3}$,[7,8,12–21] the mineral practically vanishes the contribution of the ${}^{2}T_{3}$ conformation. Moreover, these two minima are separated by barriers at the *East* (${}^{O}E$, P = 94.9°) and *West* (${}^{4}T_{O}$, P = 255.0°) regions of 11.3 and 14.3 kcal/mol, respectively. It is worth noting that the ${}^{3}T_{2}$ minimum is fully consistent with the ribose conformations predicted by MD simulations for encapsulated A-RNA.

Dispersion forces may significant influence the pseudorotational profile of the calculated system. In order to evaluate this possibility, the previously discussed profile was refined by including single point Grimme's empirical correction for dispersion at the B3LYP/6-31G(d)

optimized geometries. The resulting profile, which is included in Figure Ann.III.6b, shows that dispersion forces do not affect the pseudorotational flexibility of the ring tethered to HAp. Accordingly, the overall results allow us to conclude that the pseudorotational flexibility of the sugar is practically inexistent when the double helix is embedded into the biomineral. Thus, the conformation pentafuranose ring remains restricted at the *North* region of the pseudorotational wheel, which is the one typically observed for nucleosides and nucleotides in the double helix A-RNA.

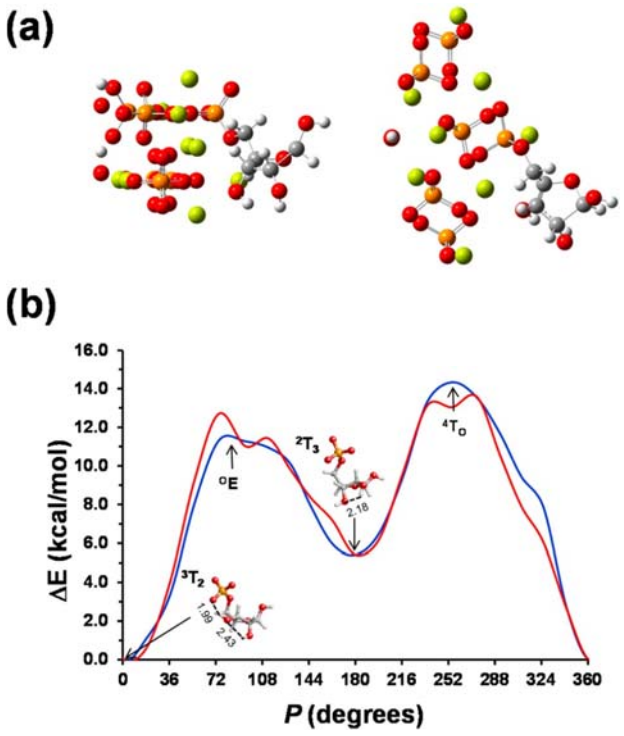

Figure Ann.III.6. (a) Side (left) and upper (right) views of the model complex used to represent the tethering of 2 to a HAp wall (top). (b) Pseudorotational energy curves calculated for 2 tethered to a HAp wall. Initially, the profile was obtained through geometry optimization at the B3LYP/6-31G(d) level of six structures for each value of P, which ranged from 0° to 360° in steps of 18°. These structures were constructed by varying the dihedral angles associated with the exocyclic moieties to form stabilizing intramolecular hydrogen bonds. The B3LYP/6-31G(d) energy profile (blue curve) was constructed using the lowest energy structure for each value of P. The energy profile including dispersion curves (red curve) was obtained by including Grimme's correction for dispersion at the B3LYP geometries.

Figure Ann.III.7a represents the variation of the exocyclic dihedral angle P−O−C−C4 with *P* obtained for **1**, **2** and **2** tethered to a HAp wall. Comparison of the profiles obtained for **2** in free-state and tethered to a HAp wall provides another prove of the drastic reduction provoked by biomineralization in the conformational flexibility of the sugar. Thus, the

exocyclic dihedral angle of **2** shows *gauche*+ → *gauche* - and *gauche* - → *gauche*+ conformational transitions at $P \approx 180°$ and $P \approx 325°$, respectively. In contrast, the HAp wall precludes such conformational transitions, the exocyclic dihedral angle keeping a gauche− conformation during the whole pseudorotational profile. It should be noted that small conformational movements, as the amplitude of the five membered ring, are not restricted by the HAp wall. This is evidenced in Figure Ann.III.7b, which represents the variation of τ_m against P for the three calculated systems.

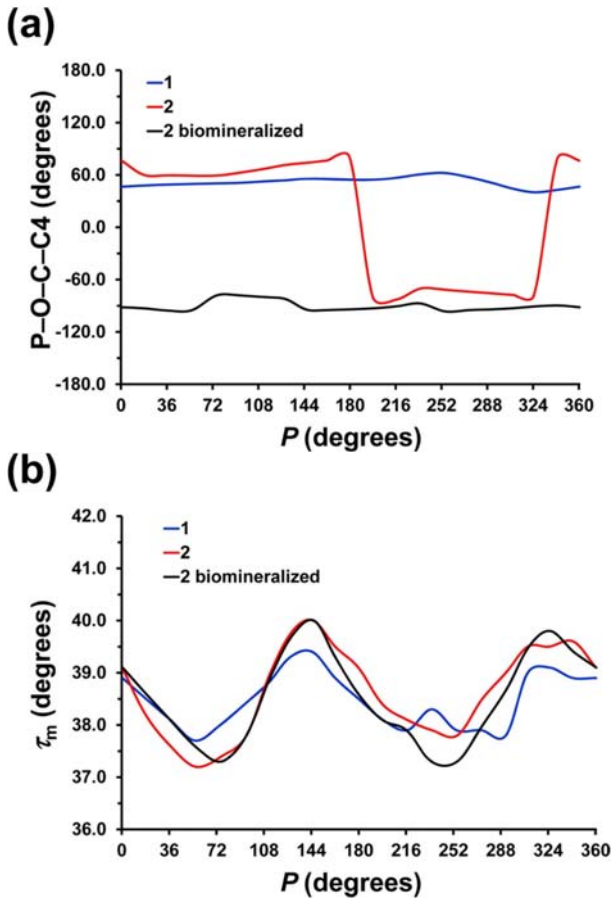

Figure Ann.III.7. Variation of the (a) exocyclic dihedral angle P−O−C−C4 and (b) τ_m with P for **1** (B3LYP/6-311+G(d,p) geometries), **2** (B3LYP/6-311+G(d,p) geometries) and **2** tethered to a HAp wall (B3LYP/6-31G(d) geometries). In all cases the profiles were derived from the geometries used to represent the pseudorotational energy displayed in Figures Ann.III.4., Ann.III.5. and Ann.III.6b.

III.4. Conclusions

The flexibility of sugar rings of RNA and DNA used as templates for HAp crystallization is completely eliminated by the mineral. This contributes to preserve the secondary structure of the biomolecule and of the associated functionality. Highly hydroxylated riboses are extra-stabilized by intramolecular hydrogen bonds, which is fully consistent with very recent experimental observations on RNA double helices modified by extra-hydroxylation.

III.5. References

1. Hench L.L., Wilson, J., Surface Active Materials. *Science* (**1984**), *226*, 630−636. DOI:10.1126/science.6093253.

2. Hartgerink, J. D.; Beniash, E.; Stupp, S. I. Self-Assembly and Mineralization of Peptide-Amphiphile Nanofibers. *Science* (**2001**), *294*, 1684−1688. DOI:10.1126/science.1063187.

3. Revilla-López G., Casanovas J., Bertran O., Turon P., Puiggalí J., Alemán C., Modeling biominerals formed by apatites and DNA, *Biointerphases* (**2013**), *8*, 10. DOI:10.1186/1559-4106-8-10.

4. Bertran, O., del Valle L.J., Revilla-López G., Chaves G., Cardús L., Casas M.T., Casanovas J., Turon P*, Puiggalí J.*, Alemán C*., Mineralization of DNA into nanoparticles of hydroxyapatite, *Dalton Transactions* (**2014**), *43*, 317-327. DOI:10.1039/c3dt52112e.

5. Martin-Pintado, N., Yahyaee-Anzahaee, M., Deleavey, G. F., Portella, G., Orozco, M., Damha, M. J., Gonzalez, C., Dramatic Effect of Furanose C2′-Substitution on Structure and Stability: Directing the Folding of the Human Telomeric Quadruplex with a Single Fluorine, Atom, *Journal of American Chemical Society* (**2013**), *135*, 5344−5347. DOI:10.1021/ja401954t.

6. Martin-Pintado, N., Deleavey, G. F., Portella, G., Campos-Olivas, R., Orozco, M., Damha, M. J., González, C., Backbone FC-H···O Hydrogen Bonds in 2′F-Substituted Nucleic Acids, *Angewandte Chemie, International Edition* (**2013**), *125*, 12065−12068. DOI:10.1002/anie.201305710.

7. Altona, C.; Sundaralingam, M. Conformational Analysis of the Sugar Ring in Nucleosides and Nucleotides. New Description Using the Concept of Pseudorotation. *Journal of American Chemical Society* (**1972**), *94*, 8205−8212. DOI:10.1021/ja00778a043.

8. Altona, C., Sundaralingam, M., Conformational Analysis of the Sugar Ring in Nucleosides and Nucleotides. Improved Method for the Interpretation of Proton Magnetic Resonance Coupling Constants, *Journal of American Chemical Society* (**1973**), *95*, 2333−2344. DOI:10.1021/ja00788a038.

9. Correll, C. C., Wool, I. G., Munishkin, A. The Two Faces of the Escherichia Coli 23SrRNA Sarcin/Ricin Domain: the Structure at 1.11 Å Resolution. *Journal of Molecular Biology* (**1999**), *292*, 275−287. DOI:10.1006/jmbi.1999.3072.

10. Ban, N., Nissen, P., Hansen, J., Moore, P. B., Steitz, T. A., The Complete Atomic Structure of the Large Ribosomal Subunit at 2.4 Å Resolution, *Science* (**2000**), *289*, 905−920. DOI:10.1126/science.289.5481.905.

11. Ng, H. L., Dickerson, R. E., Mediation of the A/B-DNA Helix Transition by G-Tracts in the Crystal Structure of Duplex CATGGGCCCATG., *Nucleic Acids Research* (**2002**), *30*, 4061−4067.
DOI:10.1093/nar/gkf515.

12. Plavec, J., Tong, W., J. Chattopadhyaya, J., How Do the Gauche and Anomeric Effects Drive the Pseudorotational Equilibrium of the Pentofuranose Moiety of Nucleosides? *Journal American Chemical Society* (**1993**), *115*, 9734−9746.
DOI:10.1021/ja00074a046.

13. Brameld, K. A., Goddard, W. A., III Ab Initio Quantum Mechanical Study of the Structures and Energies for the Pseudorotation of 5′-Dehydroxy Analogues of 2′-Deoxyribose and Ribose Sugars, *Journal of American Chemical Society* (**1999**), *121*, 985−993.
DOI:10.1021/ja982995f.

14. Pearlman, D. A., Kollman, P. A., Evaluating the Assumptions Underlying Force Field Development and Application, Using Free Energy Conformational Maps for Nucleosides, *Journal of American Chemical Society* (**1991**), *113*, 7167−7177.
DOI:10.1021/ja00019a012.

15. Barbe, S., Bre, M. L., Effect of a Water Molecule on the Sugar Puckering of Uridine, 2′-Deoxyuridine, and 2′-O-Methyl Uridine Inserted in Duplexes. *Journal of Computational Chemistry* (**2008**), *29*, 1353−1363.
DOI: 10.1021/jp075777u.

16. Rios-Font, R., Bertrán, J., Rodríguez-Santiago, L., Sodupe, M., Effects of Ionization, Metal Cationization and Protonation on 2′-Deoxyguanosine: Changes on Sugar Puckering and Stability of the Nglycosidic Bond, *Journal of Physical Chemistry B* (**2006**), *110*, 5767−5772.
DOI:10.1021/jp056089i.

17. Vokacova, Z., Matthias Bickelhaupt, F., Sponer, J., Sychrovsky, V., Structural Interpretation of J Coupling Constants in Guanosine and Deoxyguanosine: Modeling the Effects of Sugar Pucker, Backbone Conformation, and Base Pairing., *Journal of Physical Chemistry A* (**2009**), *113*, 8379−8386.
DOI:10.1021/jp902473v.

18. Boisbouvier, J., Bryce, D. L., O'Neil-Cabello, E., Nikonowicz, E. P., Bax, A. Resolution-Optimized NMR Measurement of 1DCH, 1DCC and 2DCH Residual Dipolar Couplings in Nucleic Acid Bases, *Journal of Biomolecular NMR* (**2004**), *30*, 287−301.
DOI: 10.1007/s10858-005-1846-5.

19. Marino, J. P., Landry, S. M., Varani, G., Tinoco, I., J-Coupling Restraints in RNA Structure Determination, *Accounts of Chemical Research* (**1999**), *32*, 614−623.
DOI:10.1021/ar9600392.

20. Munzarova, M. L., Sklenar, V., DFT Analysis of NMR Scalar Interactions Across the Glycosidic Bond in DNA, *Journal of American Chemical Society* (**2003**), *125*, 3649−3658.
DOI:10.1021/ja028931t.

21. Sychrovsky, V., Schneider, B., Hobza, P., Zidek, L., Sklenar, V., The Effect of Water on NMR Spin−Spin Couplings in DNA: Improvement of Calculated Values by Application of Two Solvent Models. *Physical Chemistry Chemical Physics* (**2003**), *5,* 734−739.
DOI:10.1039/B210553E.

22. Bianchet, M. A., Seiple, L. A., Jiang, Y. L., Ichikawa, Y., Amzel, L.M., Stivers, J. T., Electrostatic Guidance of Glycosyl Cation Migration Along the Reaction Coordinate of Uracil DNA Glycosylase. *Biochemistry* (**2003**), *42*, 12455−12460.
DOI:10.1021/bi035372+.

23. Hiughes J.M., Cameron M., Corwley K.D. Structural variations in natural F, OH, and Cl apatites. *American Mineralogist* (**1989**) *74*, 870–876.

24. Phillips, J. C., Braun, R., Wang, W., Gumbart, J., Tajkhorshid, E., Villa, E., Chipot, C., Skeel, R. D., Kale, L., Schulten, K., Scalable Molecular Dynamics with NAMD, *Journal of Computational Chemistry* (**2005**), *26*, 1781−1802.
DOI:10.1002/jcc.20289.

25. Cornell, W. D., Cieplak, P., Bayly, C. I., Gould, I. R., Merz, K. M., Ferguson, D. M., Spellmeyer, D. C., Fox, T., Caldwell, J. W., Kollman, P. A., A Second Generation Force Field for the Simulation of Proteins, Nucleic Acids, and Organic Molecules, *Journal of American Chemical Society* (**1995**), *117*, 5179−5197.
DOI:10.1021/ja00124a002.

26. Duan Y., Chowdhury S., Lee M.C., Xiong G., Zhang W., Yang R., Cieplak P., Luo R., Lee T., Caldwell J., Wang J., Kollman P.A., A point-charge force field for molecular mechanics simulations of proteins based on condensed-phase quantum mechanical calculations. *Journal of Computational Chemistry* (**2003**), *24*, 1999–2012.
DOI:10.1002/jcc.10349.

27. Hornak V., Abel R., Okur A., Strockbine B., Roitberg A., Simmerling C., Comparison of multiple Amber force fields and development of improved protein backbone parameters. *Proteins* (**2006**), *65*, 712–725.
DOI:10.1002/prot.21123.

28. Bradbrook G.M., Gleichmann T., Harrop S.J., Habash J., Raftery J., Kalb J., Yariv J., Hillier I.H., Helliwell J.R., X-Ray and molecular dynamics studies of concanavalin-A glucoside and mannoside complexes Relating structure to thermodynamics of binding. *Journal of Chemical Society, Faraday Transactions* (**1998**), *94*, 1603–1611.
DOI:10.1039/A800429C.

29. Frisch, M. J.; Trucks, G. W.; Schlegel, H. B.; Scuseria, G. E.; Robb, M. A.; Cheeseman, J. R.; Scalmani, G.; Barone, V.; Mennucci, B.; Petersson, G. A.; Nakatsuji, H.; Caricato, M.; Li, X.; Hratchian, H. P.; Izmaylov, A. F.; Bloino, J.; Zheng, G.; Sonnenberg, J. L.; Hada, M.; Ehara, M.; Toyota, K.; Fukuda, R.; Hasegawa, J.; Ishida, M.; Nakajima, T.; Honda, Y.; Kitao, O.; Nakai, H.; Vreven, T.; Montgomery, J. A.; Jr.; Peralta, J. E.; Ogliaro, F.; Bearpark, M.; Heyd, J. J.; Brothers, E.; Kudin, K. N.; Staroverov, V. N.; Kobayashi, R.; Normand, J.; Raghavachari, K.; Rendell, A.; Burant, J. C.; Iyengar, S. S.; Tomasi, J.; Cossi, M.; Rega, N.;Millam, J. M.; Klene, M.; Knox, J. E.; Cross, J. B.; Bakken, V.; Adamo, C.; Jaramillo, J.; Gomperts, R.; Stratmann, R. E.; Yazyev, O.; Austin, A. J.; Cammi, R.; Pomelli, C.; Ochterski, J. W.; Martin, R. L.; Morokuma, K.; Zakrzewski, V. G.; Voth, G. A.; Salvador, P.; Dannenberg, J. J.; Dapprich, S.; Daniels, A. D.; Farkas, Ö.; Foresman, J. B.; Ortiz, J. V.; Cioslowski, J.; Fox, D. J. Gaussian 09, Revision A.1; Gaussian, Inc.: Wallingford CT, (**2009)**.

30. Clark, T., Chandrasekhar, J., Spitznagel, G. W., von R. Schleyer, R., Efficient Diffuse Function-Augmented Basis Sets for Anion Calculations. III. The 3-21+G Basis Set for First-Row Elements, Li−F, *Journal of Computational Chemistry* (**1983**), *4*, 294−301. DOI:10.1002/jcc.540040303.

31. Frisch, M. J., Pople, J. A., Binkley, J. S., Self-consistent Molecular-Orbital Methods. 25. Supplementary Functions for Gaussian-Basis Sets. *Journal of Chemical Physics* (**1984**), *80*, 3265−3269. DOI:10.1063/1.447079.

32. Hariharan, P. C., Pople, J. A., Influence of Polarization Functions on MO Hydrogenation Energies. *Theoretica chimica acta* (**1973**), *28*, 213−222. DOI:10.1007/BF00533485.

33. Becke, A. D., A New Mixing of Hartree–Fock and Local Density-Functional Theories, *Journal of Chemical Physics* (**1993**), *98*, 1372−1377. DOI: 10.1063/1.464304.

34. Lee, C., Yang, W., Parr, R. G., Development of the Colle-Salvetti Correlation-Energy Formula into a Functional of the Electron Density, *Physical Reviews B* (**1988**), *37*, 785−789. DOI:10.1103/PhysRevB.37.785.

35. Grimme, S., Accurate Description of van der Waals Complexes by Density Functional Theory Including Empirical Corrections, *Journal of Computational Chemistry* (**2004**), *25*, 1463−1473. DOI:10.1002/jcc.20078.

36. Grimme, S., Semiempirical GGA-Type Density Functional Constructed with a Long-Range Dispersion Correction, *Journal of Computational Chemistry* (**2006**), *27,* 1787−1799. DOI:10.1002/jcc.20495.

37. Grimme, S., Antony, J., Ehrlich, S., Krieg, H., A Consistent and Accurate Ab Initio Parametrization of Density Functional Dispersion Correction (DFT-D) for the 94 Elements H-Pu, *Journal of Chemical Physics* (**2010**), *132*, 154104. DOI:10.1063/1.3382344.

38 Mignon, P., Ugliengo, P., Sodupe, M., Theoretical Study of the Adsorption of RNA/DNA Based on the External Surfaces of Na^+-Montmorillonite. *Journal of Physical Chemistry C* (**2009**), *113*, 13741−13749. DOI:10.1021/jp901699q.

39. Grzeskowiak, K., Goodsell, D. S., Kaczor-Grzeskowiak, M., Cascio, D., Dickerson, R. E. Crystallographic Analysis of C-C-A-A-G-CT-T-G-G and Its Implications for Bending in B-DNA, *Biochemistry* (**1993**), *32*, 8923−8931. DOI:10.1021/bi00085a025.

40. de Leeuw, H. P. M., Haasnot, C. A. G., Altona, C., Empirical Correlations between Conformational Parameters in β-D-Furanoside Fragments Derived from a Statistical Survey of Crystal Structures of Nucleic Acid Constituents Full Description of Nucleoside Molecular Geometries in terms of Four Parameters, *Israel Journal of Chemistry* (**1980**), *20*, 108−126. DOI:10.1002/ijch.198000059.

41. Hoffmann, R. A., van Wijk, J., Leeflang, B. R., Makerling, J. P., Altona, C., Vliegenthart, J. F. G., Conformational Analysis of the α-LArabinofuranosides Present in Wheat Arabinoxylans from Proton-Proton Coupling Constants, *Journal of American Chemical Society* (**1992**), *114*, 3710−3714. DOI:10.1021/ja00036a020.

Annex IV

Dissolving Hydroxyolite:

A DNA Molecule into Its Hydroxyapatite Mold[5]

Abstract

In spite of the clinical importance of hydroxyapatite (HAp), the mechanism that controls its dissolution in acidic environments remains unclear. Knowledge of such a process is highly desirable to provide better understanding of different pathologies, as for example osteoporosis, and of the HAp potential as vehicle for gene delivery to replace damaged DNA. In this work, the mechanism of dissolution in acid conditions of HAp nanoparticles encapsulating double-stranded DNA has been investigated at the atomistic level using computer simulations. For this purpose, four consecutive (multi-step) molecular dynamics simulations, involving different temperatures and proton transfer processes, have been carried out. Results are consistent with a polynuclear decalcification mechanism in which proton transfer processes, from the surface to the internal regions of the particle, play a crucial role. In addition, the DNA remains protected by the mineral mold and transferred proton from both temperature and chemicals. These results, which indicate that biomineralization imparts very effective protection to DNA, also have important implications in other biomedical fields, as for example in the design of artificial bones or in the fight against osteoporosis by promoting the fixation of Ca^{2+} ions.

---

[5] Published in Bertran O., Revilla-López G., Casanovas J., del Valle L.J., Turon P., Puiggalí J., Alemán C., Dissolving hydroxyolite: A DNA molecule into its hydroxyapatite mold, *Chemistry - A European Journal* (**2016**), *22*, 6631–6636. Reproduced with permission of John Wiley and Sons.

Annex IV

Dissolving Hydroxyolite:

A DNA Molecule into Its Hydroxyapatite Mold

IV.1. Introduction

Biomineralization involves the formation of inorganic materials in a biological environment. Certain biominerals composed of calcium phosphate (microcalcifications) are associated with pathogeneses of tissues such breast cancers, osteoarthritis, and vascular calcifications.[1-3] Currently, demineralization of double-stranded DNA (ds-DNA) with hydroxyapatite (HAp) is at the forefront of the emerging clinical and medical applications (gene therapy) because of its importance in the development of controlled vehicles for gene delivery to replace damaged DNA. In addition, clinical observations have evidenced that bone HAp dissolution in acid environments is directly related with the pathophysiology of cancer-associated bone pain and osteoporosis, even though their mechanisms remain poorly understood.[4,5] Bioactive particles made of DNA encapsulated and protected by HAp, recently named 'hydroxyolites' (HOli),[6] exhibit good cell absorption, significant transfection efficiency, and high biocompatibility. They are obtained by covering genetic material with HAp.[7-9] Dissolution of HOli is worthy of study because it is directly related to the transfection efficiency and, additionally, it can be connected with other biological processes because HOlis might release protected information encoded in DNA under certain conditions.[6] In recent years, the formation mechanism of HAp biominerals on ds-DNA soft templates has been investigated and characterized.[10-14] Nevertheless, the molecular mechanism that drives the particle dissolution and DNA demineralization remains widely unknown and controversial.[15-17] In this work we use a four-step approach based on atomistic molecular dynamics (MD) simulations to clarify the dissolution mechanism of HOli in acid environments, mimicking the physiological pH variations of the intracellular fluid encountered inside the cell cytosol and nucleus.

IV.2. Experimental Section

The potential energy was computed using the Amber force-field.[18] Force-field parameters for hydroxyl, Cl^- and PO_4^{3-} groups were extracted from Amber ff03.[19] Bonding parameters (i.e., stretching, bending, and torsion) for HPO_4^{2-} and $H_2PO_4^-$ were taken from Homeyer et al., [20]whereas van der Waals parameters were extracted from Amber ff03.[21]Atomic charges for the latter two anions were developed in-house using the methodology recommended in Amber ff03.[21]Force-field parameters of Ca^{2+}, Mg^{2+}, and H_3O^+ were extracted from the work reported by Bradbrook et al.,[21]Allner et al.,[22]and Baaden et al.,[23]respectively. All force-field parameters for DNA were extracted from Amber ff03.[21]It should be noted that the ff03 parameters are identical to the ff99-SB[24]ones for nucleic acids, phosphate and hydroxyl groups. The ability of this set of force-field parameters to reproduce the inorganic···organic interactions found in biominerals was recently proved.[8] The density of water in the simulation box was 1.00 $g \cdot cm^{-3}$ at a temperature of 298 K. The water molecules were represented using the TIP3P model.[25]All MD simulations were performed using the NAMD 2.6[26] code.

Once constructed, the initial model (i.e., HOli nanoparticle immersed into an acidic solution) as described in the Results and Discussion subsection, the initial simulation box (130 x 130 x 130 $Å^3$) was equilibrated using the following strategy. Before any of the multi-step MD trajectories, 5,000 steps of energy minimization were performed to relax conformational and structural tensions. Next, the system was heated and equilibrated by different consecutive MD runs. First, solvent, H_3O^+, and Cl^- ions were relaxed and homogeneously distributed in the box by 0.5 ns of NVT (constant volume and temperature) MD at 500 K, while keeping atoms belonging to HOLi (i.e., both HAp components and encapsulated ds-DNA) fixed. After this, thermal equilibration for 0.4 ns in the constant NVT ensemble at 298 K and a density relaxation for 0.4 ns in the constant NPT (constant pressure and temperature) ensemble at 298 K were performed. The last snapshot of the NPT MD was used as the starting point for the first production trajectory, MD1.

MD1 (298 K) is separated from the second production trajectory, MD2 (at 320 K), by a transition NPT trajectory in which the temperature was slowly increased (1 K per 50 ps). Similarly, MD2 is separated from the third production trajectory, MD3 (at 350 K) by a transition NPT trajectory in which the temperature was increased at a rate of 1 K per 50 ps. No transition was needed to evolve from MD3 to the fourth production trajectory, MD4.

MD1, MD2, MD3, and MD4 trajectories were 300, 200, 20, and 1750 ns long, respectively, and coordinates saved every 10 (MD1 and MD4), 5 (MD2), or 2 ps (MD3) were used for further analysis. It should be noted that transition trajectories were not considered for the analyses displayed in this work.

In order to ensure the reproducibility of the results, two different initial systems were considered. Accordingly, multistep MD1–MD4 trajectories were run in duplicate considering different initial positions not only for the atoms involved in the HOli nanoparticle but also for the H_2O, H_3O^+ , and Cl^- particles in the acidic solution. Results obtained for the two sets of multistep MD were very similar and, therefore, only the analyses for one of them are displayed in the figures. The production runs associated with this work involved a total of (300 + 200 + 20 + 1750) x2 ns = 4.54 ms. Atom pair distance cut-offs were applied at 16.0 Å to compute the van der Waals interactions. In order to avoid discontinuities in the Lennard–Jones potential, a switch function was applied to allow a continuous decay of the energy when the atom pair distances are larger than 14.0 Å. For electrostatic interactions, we computed the non-truncated electrostatic potential through Ewald summations.[27]The real space term was determined by the van der Waals cut-off (16 Å), while the reciprocal term was estimated by interpolation of the effective charge into a charge mesh with a grid thickness of 5 points per volume unit, that is, the particle-mesh Ewald PME) method.[28]

Both temperature and pressure were controlled by the weak coupling method, the Berendsen thermobarostat. The relaxation times used for the coupling were 1 and 10 ps for temperature and pressure, respectively. Bond lengths were constrained using the SHAKE algorithm[29]with a numerical integration step of 1 fs. Periodic boundary conditions were applied using the nearest image convention, and the nonbonded pair list was updated every 1000 steps (1 ps).

IV.3. Construction of the molecular Model

The model for the biomineral was constructed considering the following experimental observations: 1) carbonate and Mg^{2+} substitution in HAp, extensively observed in living organisms, may increase its solubility;[12-14] and 2) the solubility also increases with decreasing crystallinity.[30]Initially, a HAp nanoparticle of composition similar to that found

in previous experimental studies[12] was constructed using Ca^{2+}, Mg^{2+} , OH^- , PO_4^{3-}, and CO_3^{2-} ions. For this purpose, we used one of the small aggregates obtained in a previous work[12] as a starting point, which was spontaneously formed in neutral water from a bulk solution of the same ions. The rest of the ions were slowly added using the following strategy: i) a randomly chosen ion was placed at a position randomly chosen among all those that are within a distance d, with 5 Å < d < 10 Å, from any atom located at the surface of the nanoparticle; ii) the added ion was integrated with the nanoparticle through energy minimization. After this, the Dickerson's dodecamer (5'-CGCGAATTCGCG-3'), which is a well-known sequence that adopts a B-DNA double helix,[31] was placed in the center of such a nanoparticle, ions overlapping any atom of the ds-DNA being subsequently removed. In order to maintain the electrical neutrality of the system, Ca^{2+} ions were put at the minor groove of the double helix, as is frequently observed by X-ray diffraction.[32,33] The charge of the whole biomineral was neutralized by removing ions from the external surface (i.e. the final charge of the ds-DNA and the HAp nanocapsule was -20 and + 20, respectively). Next, the HOli nanoparticle was immersed in a water box of 130 x 130 x 130 $Å^3$ and the solvent molecules overlapping any atom of the mineral were removed. Finally, 1,000 water molecules were transformed into H_3O^+, which were neutralized with Cl^- ions put at relatively close sterically accessible positions, to mimic the acidic conditions. Obviously, the pH of the medium is very low with such a high number of H_3O^+ cations. However, it should be noted that approaches based on much higher concentrations in simulations, relative to the experiment, are frequently considered to allow events to occur on a shorter timescale. The resulting mineral mold, which contained 656 Ca^{2+}, 42 Mg^{2+}, 112 OH^-, 412 PO_4^{3-}, and 14 CO_3^{2-} ions, was surrounded by 50,552 water molecules, 1,000 H_3O^+, and 1,000 Cl^-. The total number of explicit atoms, including ds-DNA, was 160,328.

Two independent molecular models were constructed using this strategy because the study was performed using two sets of independent MD simulations. Although results discussed in this work correspond to one of such sets only, similar observation were obtained from the second set, giving consistency to their interpretation and discussion.

IV.4. Results and Discussion

Equilibration at 298 K and 1 bar (Figure Ann.IV.1a) was performed following the MD protocols described in the Methods section. The dissolution of the HOli was followed through changes in the Ca^{2+} distribution using two parameters: 1) the partial radial distribution function of Ca^{2+} ⋯Ca^{2+} pairs, g_{CaCa}, which is not expected to detect the first stages of dissolution process; and 2) a 1(L)–L profile, where 1(L) = 656/M(L), 656 is the total number of Ca^{2+} ions in the model, L is the edge of the identical cubes in which the simulation box was divided, and M(L) is the number of cubes of edge L containing at least one Ca^{2+}. Accordingly, 1(L) defines the average number of Ca^{2+} per occupied cube of edge L, the shape of the 1(L)–L profile being very sensitive to the migration of ions from the initial nanoparticle to the bulk solution. The distribution of the Ca^{2+} in equilibrated HOli is described in Figure Ann.IV.2.

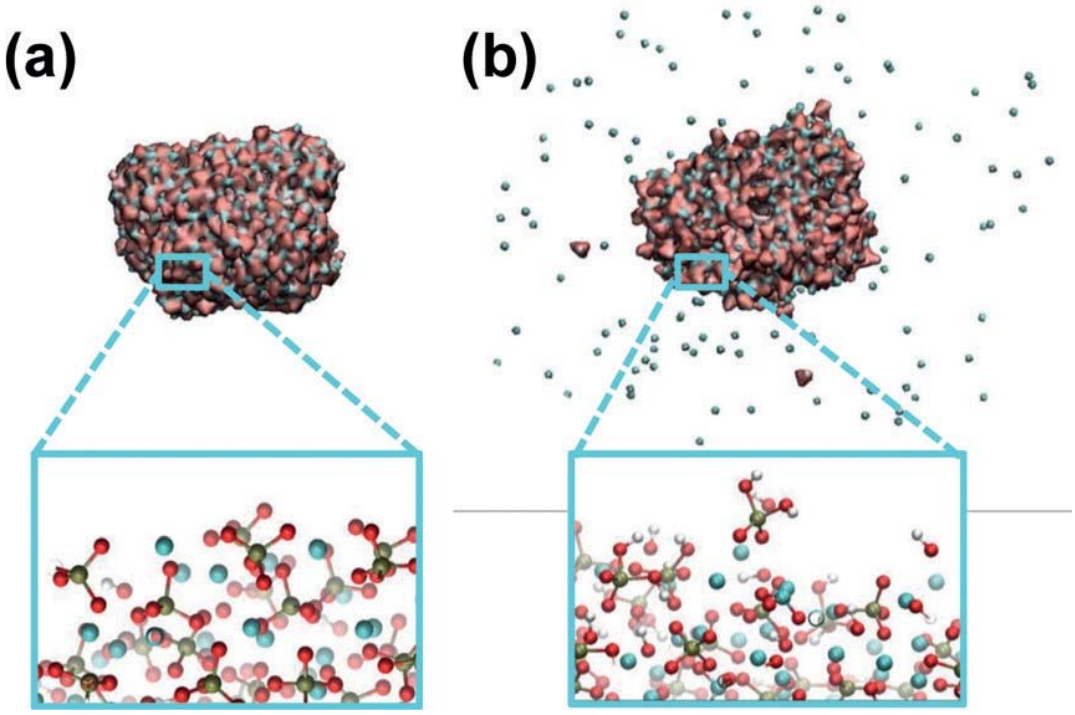

Figure Ann. IV.1. HOli nanoparticle: a) after equilibration; and b) after multi-step MD simulation (last snapshot). The distribution of the ions at the surface is illustrated in the magnifications. Brown, red, light grey, and blue balls represent P, O, H, and Ca, respectively.

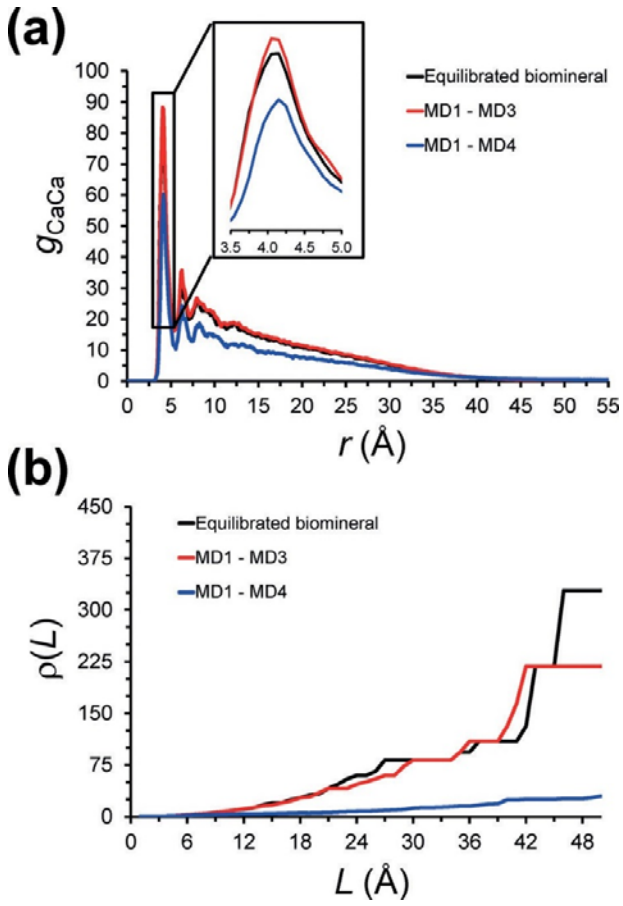

Figure IV.2. (a) Radial distribution functions of $Ca^{2+}\cdots Ca^{2+}$ pairs and (b) 1(L)–L curves calculated for HOli after equilibration, three consecutive runs at temperatures increasing from 298 to 350 K (MD1–MD3), and the latter trajectories plus a run of 1.75 ms at 350 K with proton transfer (MD1–MD4). The inset in (a) evidences the migration of the Ca^{2+} from the HOli surface to the solution during MD4.

The equilibrated HOli was the starting point of the first MD run (MD1), which corresponded to 300 ns of NPT MD at 298 K and 1 bar pressure. After this, both the g_{CaCa} and 1(L)–L profiles remained practically unchanged (Figure Ann.IV.S1.), evidencing that the dissolution process did not start yet. Then, the temperature was slowly increased to 320 K, a production run of 200 ns being subsequently conducted (MD2). The g_{CaCa} profile calculated for the last snapshot was again identical to that of the equilibrated HOli, whereas the 1(L)–L profile exhibited some differences (Figure Ann.IV.S2.). However, careful analysis of the results evidenced that such variations were not due to the migration of ions but to a change in the volume of the biomineral. Similar features were obtained when the temperature was slowly increased from 320 to 350 K and a production run of 20 ns (MD3)

was conducted (Figure Ann.IV.2.). Accordingly, the nanoparticle underwent small rearrangements produced by a thermal expansion, which resulted in a variation in the corresponding 1(L)–L curve. More specifically, the volume of the nanoparticle increased from 86,368 $Å^3$ at 298 K to 88,436 $Å^3$ (2.4 %) and 88,509 $Å^3$ (2.5 %) at 320 and 350 K, respectively.

The solubility of HAp in acid environments is known to increase with temperature.[34,35] However, simulations indicate that the description of the interactions at the nanoparticle/bulk interface is not enough to promote the HOli dissolution, independently of the temperature. The influence of the acidic conditions was introduced in the mechanism by considering reactions (1) [Eq. (1)] and (2) [Eq. (2)] in the next MD step:

$$PO_4^{3-} + H_3O^+ \rightarrow HPO_4^{2-} + H_2O \qquad (1)$$

$$HPO_4^{2-} + H_3O^+ \rightarrow H_2PO_4^- + H_2O \qquad (2)$$

These reactions were incorporated into the protocol considering variations in composition at time steps Δt. Specifically, the following changes were considered: a PO_4^{3-} (or HPO_4^{2-}) located at the HOli surface and a PO_4^{3-} from the solution separated by less than 3 Å were replaced by HPO_4^{2-} (or $H_2PO_4^-$) and H_2O, respectively. For each change, a new $H_3O^+ \cdot Cl^-$ pair was inserted at one of the boundaries of the simulation box to maintain the initial acidic conditions. After several trials, the time step Δt was fixed at 10 ns, this value providing a reasonable ratio between success and failures in the fulfilment of the above-mentioned distance requirement. To avoid the overconcentration of H_3O^+ and $H_2PO_4^-$ at the HOli surface, as well as to mimic the proton transfer process experimentally observed in HAp,[36,37] every five time steps, 5Δt = 50 ns, the conversion of an internal PO_4^{3-} (or $H_2PO_4^-$) into HPO_4^{2-} (or $H_2PO_4^-$) was considered. For this purpose, the internal PO_4^{3-} and HPO_4^{2-} ions were randomly chosen. This strategy was maintained for 1.75 ms at 350 K (MD4).

Changes in the g_{CaCa} and 1(L)–L profiles after 0.75 ms (Figure Ann.IV.S3.) evidenced that the nanoparticle was dissolving (i.e. , 25 Ca^{2+} migrated from the HOli surface to the solution). This dissolution process continued for the next 1 ms (Figure Ann.IV.2.). At the end of MD4, the intensity of the sharp peak at ≈ 4.1 Å in the g_{CaCa} profile decreased significantly (28 %) with respect to the equilibrated mineral, which was consistent with the drastic reduction of 1(L) at relatively small L values. The number of Ca^{2+} that migrated from

the nanoparticle to the solution accounted for 144 (i.e., 22 %) after 1.75 ms (Figure Ann.IV.1b). In addition, the proton transfer mechanism facilitated the dissolution of 7 Mg^{2+} (17 %), 4 OH^- (4 %), 63 PO_4^{3-} (16 %), 2 HPO_4^{2-}, and 1 CO_3^{2-} (7 %). This demineralization is dominated by the detachment of Ca^{2+} from the HOli nanoparticle (i.e., decalcification), the participation of Mg^{2+} ions in such process being very small at this stage.

Multi-step simulations suggest a decalcification for HOli dissolution, triggered by proton transfer and acid–base-based reactivity of the phosphate species. These results are in good agreement with experimental observations on the dissolution of HAp with different acids. [16,38]On the other hand, results reflect a polynuclear detachment of Ca^{2+} (Figure Ann.IV.3.).

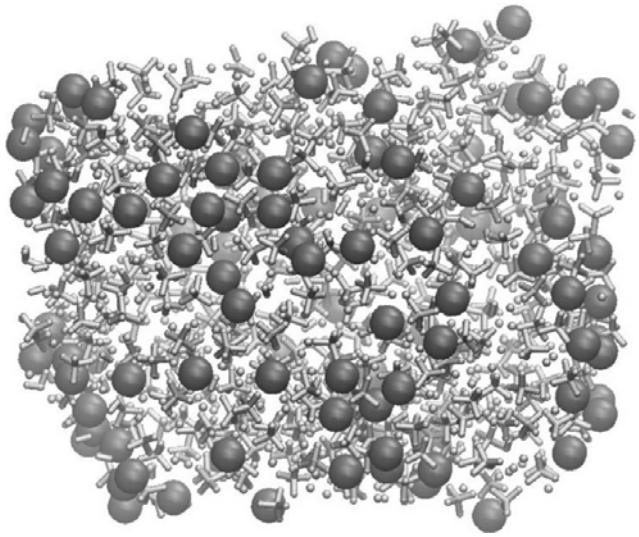

Figure Ann.IV.3. Dissolution of the HOli particle following a polynuclear mechanism. The initial nanoparticle (i.e., starting point for MD1) is displayed. All atoms are depicted with small light grey balls with the exception of Ca^{2+} detached from the surface along MD4 (i.e., the simulation considering proton transfer), which are represented by large dark grey balls. As it can be seen, Ca^{2+} ions detach from multiple centers widely distributed through the surface in the initial configuration. Accordingly, the decalcification process follows a poly-nuclear mechanism rather than a mononuclear one (i.e., detachment of Ca^{2+} ions from a few close centers).

Although some authors suggested that this mechanism is more probable for HAp dissolution in mild acid environments (pH within 5.0–7.2 and Ca/P molar ratios of 1.0–2.0), [39]other authors reported a mononuclear mechanism driven by the formation and growth of pits.[11]

Results obtained in this work provide direct evidence that Ca^{2+} is detached from multiple centers widely distributed on the surface. In addition, results show that Ca^{2+} mobility increases following the transformation of phosphates into $H_2PO_4^-$, thus reflecting changes in

the coordination caused by the steric and electrostatic components. The latter promotes dissolution of the biomineral (Figure Ann.IV.S4.). After detachment, Ca^{2+} preferentially coordinates with two Cl^- anions, but also with OH^- and Cl^- anions, in hydrated complexes (Figure Ann.IV.4a and b, respectively). These interaction patterns are supported by the partial radial distribution functions of $Ca^{2+}\cdots$Cl- (g_{CaCl}) pairs, which is displayed in Figure Ann.IV.4c. Thus, the g_{CaCl} profile shows broad and poorly defined peaks centered at ≈ 5.5 and ≈ 7.0 Å (marked with arrows) that corresponds to the above-mentioned complexes. Unfortunately, the partial radial distribution function of $Ca^{2+}\cdots OH^-$ (g_{CaOH}) pairs does not provide any additional information because the distance typically identified in complexes (2.6 Å in Figure Ann.IV.4b) is very close to the $Ca^{2+}\cdots OH^-$ in the HOli nanoparticle (Figure Ann.IV.S5a). Similarly, no relevant information has been extracted from the partial radial distribution function of $Ca^{2+}\cdots$H2O pairs (g_{CaWat}) because of the very large number of solvent molecules hydrating Ca^{2+} ions (Figure Ann.IV.S5b).

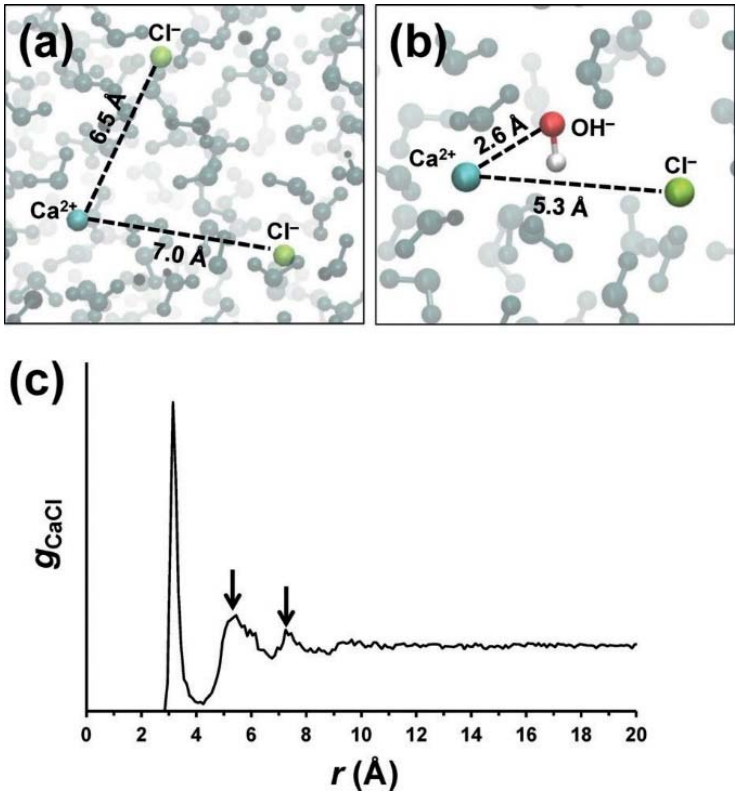

Figure Ann.IV.4. Representative complexes formed by detached Ca^{2+} ions: a) detached Ca^{2+} ions preferentially (≈ 75 % cases) form hydrated complexes with two Cl^- ions; b) hydrated complexes in which the detached Ca^{2+} coordinates one OH^- and one Cl^- are also relatively frequent (≈ 15 % cases). c) Radial distribution functions of $Ca^{2+}\cdots Cl^-$ pairs calculated for the last snap-shot of MD4. Arrows indicate the distances associated to complexes displayed in (a) and (b).

The structural stability of the ds-DNA can be assessed in Figure Ann.IV.5., which displays the temporal evolution of the root-mean-square deviation (RMSD) with respect to the ideal B-DNA double helix. The RMSD was calculated by considering all atoms different from hydrogen. The ds-DNA remains mostly unaltered through the whole range of examined temperatures. The average RMSD values calculated for MD1 (298 K), MD2 (320 K), and MD3 (350 K) are 0.42 ± 0.06, 1.02 ± 0.03, and 1.51 ± 0.01 Å, respectively. The RMSD increases slowly along MD4 as a consequence of the penetration of the protons. In spite of this, the average RMSD for the last 500 ns of MD4 (2.03 ± 0.04 Å) is still very low. This stability has been attributed to the reduction of the electrostatic strain at the biomolecule associated to the hydrogenated phosphates at the internal regions.

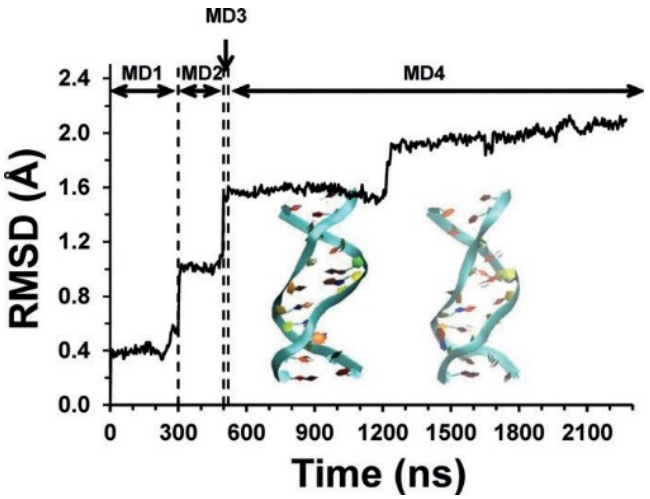

Figure Ann.IV.5. Evolution of the RMSD along the multi-step MD for the ds-DNA relative to the canonical B-DNA. The double helix is represented by using a ribbon model for the equilibrated system (starting point of MD1) and for the last snapshot of MD4.

HAp imparts protection against both temperature and chemicals to ds-DNA, which despite its fragility preserves the double helix. During its dissolution, HAp totally or partially protects DNA from physical and chemical stressing factors as well as from the aggression of biological factors, like enzymatic degradation. The HOli NP, which has to be understood as a DNA molecule in its HAp mold, has important implications in many fields. For example, these results are very useful for the development of novel strategies for gene therapy. Thus, biomineralization would facilitate DNA protection by the surrounding inorganic materials, while DNA transported at the surface of the mineral is attacked by endonucleases.[40]From the mass extinction events perspective (see Annex V), we discuss the formation and

resilience of HOli particles that may have made the difference for the survival of life.[6] Results from this work also suggests that HOli particles, when dissolving, can be also viewed as nanocontainers that store and preserve DNA or RNA from changing environmental conditions, which may have many applications in biomedicine and genetics biotechnology.

IV.5. Conclusions

This work sheds light on the atomic-level details of the acidic dissolution of HOli and HAp. This process happens following a decalcification mechanism where Ca^{2+} detachment is triggered by the initial hydration of phosphates, and it is enhanced by their further hydrogenation resulting from hydronium reactivity. The decalcification occurs through a polynuclear process: the escape of the calcium ions occurs through multiple independent centers widely distributed on the surface. Thus, the detachment of the calcium ions is caused by the important electrostatic alterations induced by the HPO_4^{2-} and $H_2PO_4^-$ species rather than by the detachment of neighboring calcium ions. This result has enormous implications for the development of therapies in which fixation of Ca^{2+} is crucial, as for example those related with the fight against osteoporosis. Also, results prove that HAp acts as a shield for ds-DNA molecules, protecting their functionality from temperature-stressing conditions and chemicals. Accordingly, HOli particles represent a very reliable alternative to conventional gene therapy strategies, in which genes are transported at the surface of the mineral and, therefore, undergo the attack of enzymes.

IV.6. References

1. Cox R.F., Hernandez-Santana A., Ramdass S., McMahon G., Harmey J.H., Morgan M.P., Microcalcifications in breast cancer: novel insights into the molecular mechanism and functional consequence of mammary mineralisation, *British Journal of Cancer* (**2012**), *106*, 525–537.
DOI:10.1038/bjc.2011.583.

2. Jin C., Frayssinet P., Pelker R., Cwirka D., Hu B., Vignery A., Eisenbarth S.C., Flavell R.A., NLRP3 inflammasome plays a critical role in the pathogenesis of hydroxyapatite-associated arthropathy, *Proceedings of National Academy of Sciences USA* (**2011**), *108*, 14867–14872.
DOI:10.1073/pnas.1111101108.

3. Sage A.P. , Tintut Y., Demer L.L., Regulatory mechanisms in vascular calcification, *Nature Reviews of Cardiology* (**2010**), *7*, 528 –536.
DOI:10.1038/nrcardio.2010.115.

.

4. Yoneda T., Hata K., Nakanishi M., Nagae M., Nagayama T., Wakabayashi H., Nishisho T., Sakurai T., Hiraga T., Involvement of acidic microenvironment in the pathophysiology of cancer-associated bone pain, *Bone* (**2011**), 48, 100–105.
DOI: 10.1016/j.bone.2010.07.009.

5. Dor Y., Cedar H., Principles of DNA methylation and their implications for biology and medicine, *Lancet* (**2018**), *392*, 777–786.
DOI: 10.1016/S0140-6736(18)31268-6.

6. Turon P., Puiggalí J., Bertrán O., Alemán C., Surviving Mass Extinctions through Biomineralized DNA, *Chemistry - A European Journal* (**2015**), *21*, 18892–18898, DOI:10.1002/chem.201503030.

7. Shen H., Tan J., Saltzman W.M., Surface-mediated gene transfer from nanocomposites of controlled texture, *Nature Materials* (**2004**), *3*, 569–574.
DOI:10.1038/nmat1179.

8. Sun B., Yi M., Yacoob C.C., Nguyen H.T., Shen H., Effect of surface chemistry on gene transfer efficiency mediated by surface-induced DNA-doped nanocomposites, *Acta Biomaterialia* (**2012**), *8*, 1109 – 1116.
DOI:10.1016/j.actbio.2011.12.005.

9. Sun B., Tran K.K., Shen H., Enabling customization of non-viral gene delivery systems for individual cell types by surface-induced mineralization, *Biomaterials* (**2009**), *30*, 6386–6393.
DOI:10.1016/j.biomaterials.2009.08.006.

10. Takeshita T., Matsuura Y., Arakawa S., Okamoto M., Biomineralization of hydroxyapatite on DNA molecules in SBF: morphological features and computer simulation, *Langmuir* (**2013**), *29*, 11975– 11981.
DOI:10.1021/la402589j.

11. Ngourn S.C., Butts H.A., Petty A.R., Anderson J.E., Gerdon A.E., Quartz crystal microbalance analysis of DNA-templated calcium phosphate mineralization. *Langmuir* (**2012**), *28*, 12151–12158.
DOI: 10.1021/la300949y.

12. Bertrán O., del Valle L.J., Revilla-López G., Rivas M., Chaves G., Casas M.T., Casanovas J., Turon P., Puiggalí J., Alemán C., Synergistic approach to elucidate the incorporation of magnesium ions into hydroxyapatite, *Chemistry- A European Journal* (**2015**), *21*, 2537–2546.
DOI:10.1002/chem.201405428.

13. Bertran O., del Valle L.J., Revilla-López G., Chaves G., Cardus L., Casas M.T., Casanovas J., Turon P., Puiggalí J., Alemán C., Mineralization of DNA into nanoparticles of hydroxyapatite, *Dalton Transactions* (**2014**), *43*, 317–327.
DOI: 10.1039/C3DT52112E.

14. Revilla-López G., Casanovas J., Bertran O., Turon P., Puiggalí J., Alemán C., Modeling biominerals formed by apatites and DNA, *Biointerphases* (**2013**), *8*, 10.
DOI:10.1186/1559-4106-8-10.

15. Wang L., Nancollas G.H., Calcium orthophosphates: crystallization and dissolution, *Chemical Reviews* (**2008**), *108*, 4628–4669.
DOI:10.1021/cr0782574.

16. Dorozhkin S.V., Dissolution mechanism of calcium apatites in acids: A review of literature, *World Journal of Methodology* (**2012**), *2*, 1–17.
DOI:10.5662/wjm.v2.i1.1.

17. Tang R.K., Orme C.A., Nancollas G.H., A new understanding of demineralization: The dynamics of brushite dissolution, *Journal of Physical Chemistry B* (**2003**), *107*, 10653–10657.
DOI:10.1021/jp0346312.

18. Cornell, W. D., Cieplak, P., Bayly, C. I., Gould, I. R., Merz, K. M., Ferguson, D. M., Spellmeyer, D. C., Fox, T., Caldwell, J. W., Kollman, P. A., A Second Generation Force Field for the Simulation of Proteins, Nucleic Acids, and Organic Molecules, *Journal of American Chemical Society* (**1995**), *117*,5179−5197.
DOI:10.1021/ja00124a002.

19. Duan Y., Chowdhury S., Lee M.C., Xiong G., Zhang W., Yang R., Cieplak P., Luo R., Lee T., Caldwell J., Wang J., Kollman P.A., A point-charge force field for molecular mechanics simulations of proteins based on condensed-phase quantum mechanical calculations. *Journal of Computational Chemistry* (**2003**), *24*, 1999–2012.
DOI:10.1002/jcc.10349.

20. Homeyer N., Horn A.H.C., Lanig H., Sticht H., AMBER force-field parameters for phosphorylated amino acids in different protonation states: phosphoserine, phosphothreonine, phosphotyrosine, and phosphohistidine, *Journal of Molecular Modelling,* (**2006**), *12*, 281–289.
DOI:10.1007/s00894-005-0028-4.

21. Bradbrook G.M., Gleichmann T., Harrop S.J., Habash J., Raftery J., Kalb J., Yariv J., Hillier I.H., Helliwell J.R., X-Ray and molecular dynamics studies of concanavalin-A glucoside and mannoside complexes Relating structure to thermodynamics of binding. *Journal of Chemical Society, Faraday Transactions* (**1998**), *94*, 1603–1611.
DOI:10.1039/A800429C.

22. Allnér O., Nilsson L., Villa A., Magnesium ion–water coordination and exchange in biomolecular simulations, *Journal of Chemical Theory and Computation* (**2012**), *8*, 1493–1502.
DOI: 10.1021/ct3000734.

23. Baaden M., Burgard M., Wipff G., TBP at the water− oil interface: the effect of TBP concentration and water acidity investigated by molecular dynamics simulations, *Journal of Physical Chemistry B* (**2001**), *105*, 11131–11141.
DOI: 10.1021/jp011890n.

24. Hornak V., Abel R., Okur A., Strockbine B., Roitberg A., Simmerling C., Comparison of multiple Amber force fields and development of improved protein backbone parameters. *Proteins* (**2006**), *65*, 712–725.
DOI:10.1002/prot.21123.

25. Jorgensen W.L., Chandrasekhar J., Madura J.D., Impey R.W., Klein M.L. Comparison of simple potential functions for simulating liquid water. *Journal of Chemical Phy*sics (**1983**), *79*, 926–935.
DOI:10.1063/1.445869.

26. Phillips, J. C., Braun, R., Wang, W., Gumbart, J., Tajkhorshid, E., Villa, E., Chipot, C., Skeel, R. D., Kale, L., Schulten, K., Scalable Molecular Dynamics with NAMD, *Journal of Computational Chemistry* (**2005**), *26*, 1781−1802.
DOI:10.1002/jcc.20289.

27. Darden T., York D., Pedersen L., Particle Mesh Ewald-an N.Log(N) method for Ewald sums in large systems. *Journal of Chemical Physics* (**1993**), *98*, 10089–10092.
DOI:10.1063/1.464397.

28. Berendsen H.J.C., Postma J.P.M., van Gunsteren W.F., DiNola A., Haak J.R., Molecular dynamics with coupling to an external bath. *Journal of Chemical Physics* (**1984**), *81*,3684–3690.
DOI:10.1063/1.448118.

29. Ryckaert J.P., Ciccotti G., Berendsen H.J.C., Numerical integration of the Cartesian Equations of Motion of a System with Constraints: Molecular Dynamics of n-Alkanes. *Journal of Computational Physics* (**1977**), *23*, 327–341. DOI:10.1016/0021-9991(77)90098-5.

.

30. Porter A.E., Patel N., Skepper J.N., Best S.M., Bonfield W, Comparison of in vivo dissolution processes in hydroxyapatite and silicon-substituted hydroxyapatite bioceramics, *Biomaterials* (**2003**), *24*, 4609–4620. DOI:10.1016/S0142-9612(03)00355-7.

31. Grzeskowiak, K., Goodsell, D. S., Kaczor-Grzeskowiak, M., Cascio, D., Dickerson, R. E. Crystallographic Analysis of C-C-A-A-G-CT-T-G-G and Its Implications for Bending in B-DNA, *Biochemistry* (**1993**), *32*, 8923−8931. DOI:10.1021/bi00085a025.

32. Sines C.C., McFail-Isom L., Howerton S.B., Van Derveer D., Williams L.D., Cations mediate B-DNA conformational heterogeneity. *Journal of American Chemical Society* (**2000**), *122*, 11048–11056. DOI:10.1021/ja002244p.

33. Hud N.V., Polak M., DNA-cation interactions: The major and minor grooves are flexible ionophores. *Current Opinion in Structural Biology* (**2001**) *11*, 293–301. DOI:10.1016/S0959-440X(00)00205-0.

34. Kumar R., Prakash K.H., Cheang P., Khor K.A., Involvement of acidic microenvironment in the pathophysiology of cancer-associated bone pain, *Langmuir* (**2004**), *20*, 5196–5200. DOI:10.1016/j.bone.2010.07.009.

35. Prakash K.H., Kumar R., Ooi C.P., Cheang P., Khor K.A. , Apparent solubility of hydroxyapatite in aqueous medium and its influence on the morphology of nanocrystallites with precipitation temperature, *Langmuir* (**2006**), *22*, 11002–11008. DOI:10.1021/la0621665.

36. Yashima M., Kubo N., Omoto K., Fujimori H., Fujii K., Ohoyama K., Diffusion path and conduction mechanism of protons in hydroxyapatite, *Journal of Physical Chemistry C* (**2014**), *118*, 5180. DOI:10.1021/jp412771f.

37. Misra D.N., Interaction of citric acid with hydroxyapatite: surface exchange of ions and precipitation of calcium citrate, *Journal of Dental Research* (**1996**), *75*, 1418–1425. DOI:10.1177/00220345960750061401.

38. Yoshioka M., Yoshida Y., Inoue S., Lambrechts P., Vanherle G., Nomura Y., Okazaki M., Shintani H., Van Meerbeek B., Adhesion/decalcification mechanisms of acid interactions with human hard tissues, *Journal of Biomedical Materials Research* (**2002**), *59*, 56– 62. DOI: 10.1002/jbm.1216.

39. Christoffersen M.R., Dohrup J., Christoffersen J., Kinetics of growth and dissolution of calcium hydroxyapatite in suspensions with variable calcium to phosphate ratio, *Journal of Crystal Growth* (**1998**), *186*, 283–290. DOI:10.1016/S0022-0248(97)00473-9.

40. Valle L.J., Bertran O., Chaves G, Revilla-López G., Rivas M., Teresa Casas M., Casanovas J., Turon P., Puiggalí J., Alemán C., DNA adsorbed on hydroxyapatite surfaces *Journal of Materials Chemistry B* (**2014**), *2*, 6953-6966. DOI: 10.1039/C4TB01184H.

IV. 7. Enclosure A. Additional information

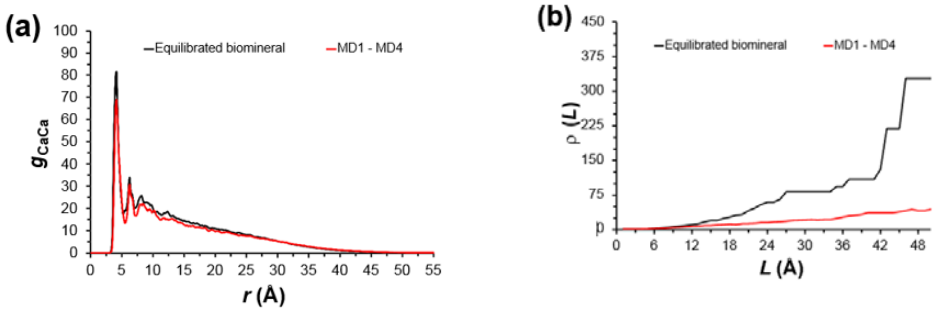

Figure Ann.IV.S1. (a) Radial distribution functions of $Ca^{2+}\cdots Ca^{2+}$ pairs and (b) ρ (L)-L curves calculated for the equilibrated hydroxyolyte and the biomineral after 300 ns at 298 K D1).

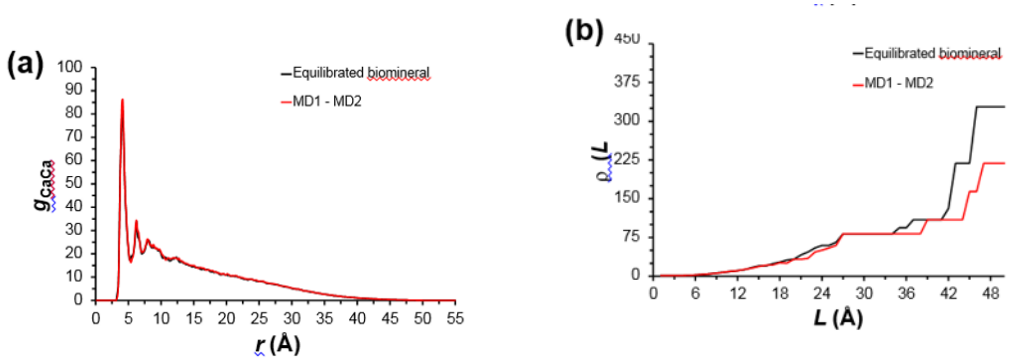

Figure Ann.IV. S2. (a) Radial distribution functions of $Ca^{2+}\cdots Ca^{2+}$ pairs and (b) ρ (L)-L curves calculated for the equilibrated hydroxyolyte and the biomineral after consecutive MD1 (300 ns at 298 K) and MD2 (200 ns at 320 K) trajectories.

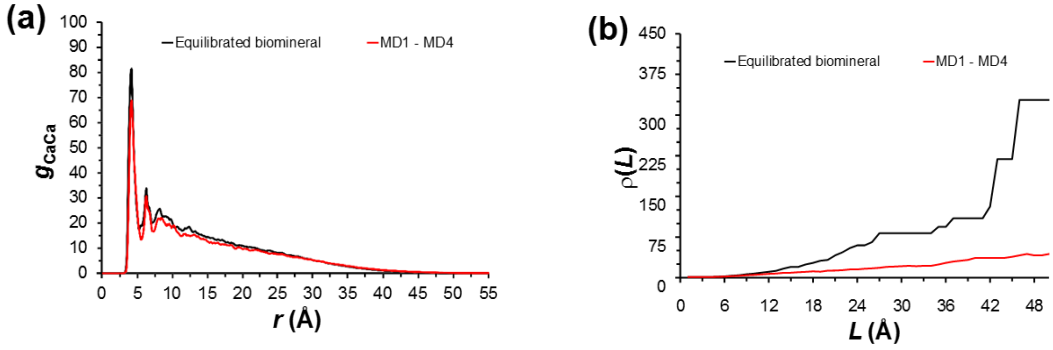

Figure Ann.IV.S3. (a) Radial distribution functions of $Ca^{2+}\cdots Ca^{2+}$ pairs and (b) ρ(L)-L curves calculated for the initial biomineral and the biomineral after consecutive MD1 (300 ns at 298 K), MD2 (200 ns at 320 K), MD3 (20 ns at 350 K) and 750 ns of MD4 (350 K with proton transfer) trajectories.

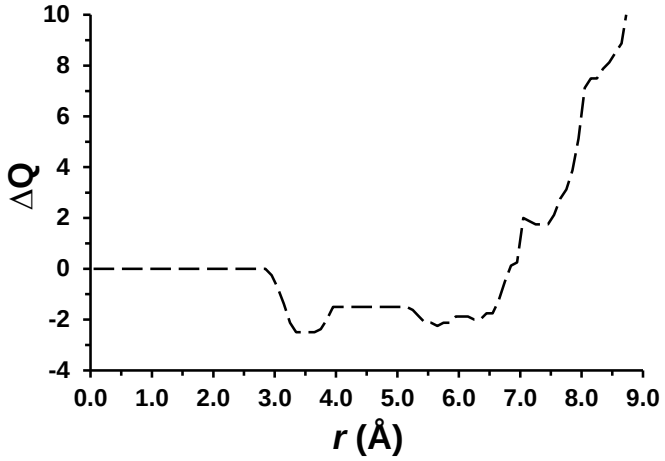

Figure Ann.IV.S4. For a Ca^{2+} (close to a HPO_4^{2-}) before the detachment from the hydroxyolite nanoparticle surface, representative profile displaying the difference (ΔQ) between the charge at the surface of the nanoparticle and the charge at the internal region (distance r from the Ca^{2+}). The negative ΔQ at low r values indicate that the Ca^{2+} is more attracted by the external side of the nanoparticle than by the internal one and, therefore, it tends to migrate. The electrostatic energy increment (calculated using a simple Coulombic approach) required by a Ca^{2+} ion surrounded by PO_4^{3-} to migrate from the surface nanoparticle to the bulk is +15.2 eV. According to this repulsive energy penalty, the Ca^{2+} ion remains at the surface. In contrast, the electrostatic energy required by a Ca^{2+} ion surrounded by HPO_4^{2-} to migrate from the surface nanoparticle to the bulk is -42.7 eV. Therefore, the gain of energy favors the spontaneous transfer of the Ca^{2+} ion from the surface of the nanoparticle to the bulk.

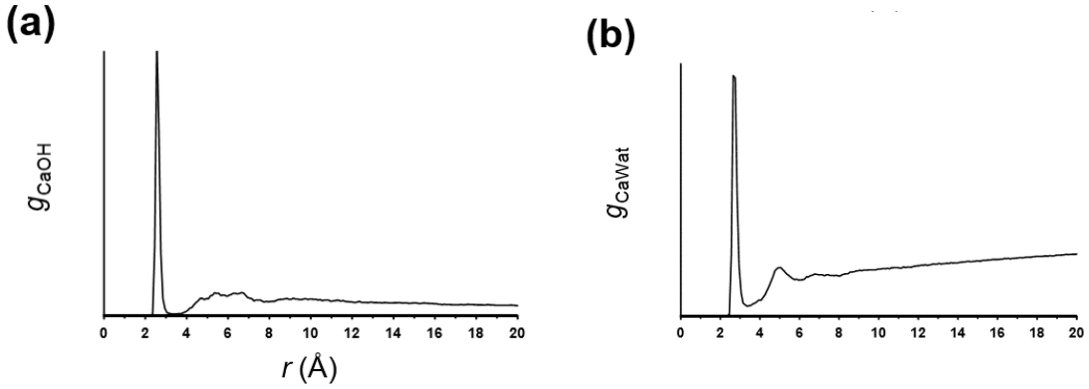

Figure Ann.IV.S5. Radial distribution functions of (a) $Ca^{2+}\cdots Cl^-$ and (b) $Ca^{2+}\cdots H_2O$ pairs at the end of MD4.

Annex V

Hydroxyapatite with Permanent Electrical Polarization: Preparation, Characterization, and Response against Inorganic Adsorbates[6]

Abstract

Permanently polarized hydroxyapatite (HAp) particles have been prepared by applying a constant DC of 500 V at 1000 ºC for 1 h to the sintered mineral. This process causes important chemical changes, as the formation of OH^- defects (vacancies), the disappearance of hydrogen phosphate ions at the mineral surface layer, and structural variations reflected by the increment of the crystallinity. As a consequence, the electrochemical properties and electrical conductivity of the polarized mineral increase noticeably compared with as-prepared and sintered samples. Moreover, these increments remain practically unaltered after several months. In addition, permanent polarization favors significantly the ability of HAp to adsorb inorganic bioadsorbates in comparison with as-prepared and sintered samples. The adsorbates cause a significant increment of the electrochemical stability and electrical conductivity with respect to bare polarized HAp, which may have many implications for biomedical applications of permanently polarized HAp.

---

[6] Published in Rivas M., del Valle L.J., Armelin E., Bertran O., Turon P., Puiggalí J., Alemán C., Hydroxyapatite with Permanent Electrical Polarization: Preparation, Characterization and Response Against Inorganic Adsorbates, *ChemPhysChem* (**2018**), *19*, 14, 1746-1755. Reproduced with permission of John Wiley and Sons.

Annex V

Hydroxyapatite with Permanent Electrical Polarization: Preparation, Characterization, and Response against Inorganic Adsorbates

V.1. Introduction

Hydroxyapatite (HAp), $Ca_{10}(PO_4)_6(OH)_2$, is the major inorganic component of biological hard tissues such as bone and tooth.[1,2] Synthetic HAp, which shows excellent ability to interact with living systems, has been investigated for biomedical applications, as for example drug and gene delivery, tissue engineering and bone repair.[3-7]

An important difference between amorphous calcium phosphate (ACP) and crystalline synthetic HAp (cHAp) is the alignment of the OH^- ions along the c-axis in the latter. The crystal structure of stoichiometric cHAp, which contains no OH^- defects, is monoclinic at room temperature.[8,9] However, the monoclinic cHAp changes to hexagonal phase at about 210 ºC, which means a change from an ordered to a disordered distribution of OH^- ions along the c-axis. The hexagonal phase becomes the most stable form of cHAp in the pH range of 4–12 because of the disorder caused by the presence of vacancies and presence of O_2^- ions in the columns of OH^- groups.[8,9] Although the properties of cHAp were altered by thermally induced changes in the positions of OH^- ions,[10-12] the observed effects were not stable at room temperature (i. e. the OH^- reorientation has a short relaxation time).

ACP and cHAp interact with different phosphates and a biophosphonate (BPs),[13] which is a very relevant topic in the field of biomaterials for biomedical applications. Thus, polyphosphate, which is an orthophosphate polymer found in mammalian organisms,[14] promotes mineralization and bone regeneration when adsorbed onto HAp by stabilizing basic cell growth and differentiation.[15-21] On the other hand, the oxygen atom that links the phosphate groups of pyrophosphates is replaced by a carbon atom in BPs, which results in the inhibition of both hydrolytic and enzymatic degradations.[22] The affinity of BPs towards HAp has been associated with the formation of strong interactions between the two species.[23,24] Indeed, BPs are primary agents in the current pharmacological arsenal against

different bone diseases (e. g. osteoporosis, Paget disease of bone and metastatic bone malignancies).[25]

In the last decades, Yamashita and co-workers[26-30] caused polarization effects in HAp samples by applying a constant DC electric field of 1.0–10.0 kV/cm at elevated temperature (300– 850 ºC) to samples previously sintered at 1250 ºC for 2 h. Results indicated that the polarization effects were consequence of the electrical dipoles associated with the formation of defects inside crystal grains and of the space charge polarization originated in the grain boundaries. The slow relaxation of such dipoles suggested that polarization was only partially maintained (semi-permanently), even though this effect was not quantified. In addition, the above mentioned thermally stimulated polarization process (TSP) was found to affect some surface properties as for example the wettability and adhesion of osteoblastic cells, which were higher onto semi-permanently polarized samples than onto non-polarized ones.[31,32]

In a very recent work, we used an alternative TSP strategy to prepare an electrophotocatalyst based on permanently polarized HAp particles.[33] More specifically, the new catalyst allows fixing nitrogen from N_2 and carbon from CO_2 and CH_4 to obtain both glycine and Alanine (D/L racemic mixture), the two simplest amino acids, using mild reaction conditions. In this work we disclose the enhanced electrochemical and electrical properties of permanently polarized cHAp comparing them with those of semi-permanently polarized samples, obtained using previously reported strategies.[26-30] Furthermore, the adsorption of phosphates and phosphonate onto permanently polarized cHAp samples has been examined. Results reflect the significant impact of the alternative conditions used for the TSP treatment on the adsorption process. Our findings indicate that the adhesion of inorganic phosphates and phosphonates can be tailored by controlling the conditions used for cHAp treatment, suggesting new applications for permanently polarized cHAp.

V.2. Methods

Materials. Ammonium phosphate dibasic [$(NH_4)_2HPO_4$; purity ≥ 99.0%], ammonium hydroxide solution 30% (NH_4OH; purity: 28-30%), tetrasodium pyrophosphate ($Na_4P_2O_7$), sodium triphosphate ($Na_5P_3O_{10}$) and aminotris(methylenephosphonic acid) (ATMP) were purchased from Sigma-Aldrich. Calcium nitrate [$Ca(NO_3)_2$; purity ≥ 99.0%] was purchased from Panreac (Barcelona, Spain). Ethanol (C_2H_5OH; purity ≥ 99.5%) was obtained from

Scharlab (Barcelona, Spain). Fetal bovine serum (FBS), for contact angle measurements, was purchased from Gibco.

Synthesis of cHAp. A simple procedure was used to prepare cHAp samples, the only difference being the thermal post-treatment applied to the reaction mixture.[34] Reagent conditions were adjusted to get a Ca/P ratio of 1.67: 15 mL of 0.5 M $(NH_4)_2HPO_4$ in deionized water (pH adjusted to 11 with an ammonia 30% w/w solution) were added dropwise (rate of 2 mL·min^{-1}) and under agitation (400 rpm) to 25 mL of 0.5 M $Ca(NO_3)_2$ in ethanol. After that, the reaction mixture was stirred 1 h by agitation (400 rpm) at room temperature. The resulting suspension was aged applying hydrothermal conditions (200 bar at 150 ºC for 24 h) during 24 h. The precipitate was separated by centrifugation and washed sequentially with deionized water and a 60/40 v/v mixture of ethanol-water (twice). A white powder was recovered after freeze-drying. cHAp obtained using this procedure have been denoted "as prepared" samples, hereafter abbreviated cHAp/p.

Sintering and thermally stimulated polarization process. Sintered cHAp samples, hereafter denoted cHAp/s, were prepared by heating the previously synthesized powders (i.e. cHAp/p) at 1000 ºC for 2 h in air. After this, powders were uniaxially pressed at 620 MPa for 10 min to obtain dense discs suitable for characterization. The dimensions of these specimens were 10 mm of diameter x 1.68 mm of thickness.

In order to get thermally stimulated polarized cHAp (cHAp/tsp), discs of sintered samples were sandwiched between stainless steel (AISI 304) plates, heated to 1000 ºC in air and, simultaneously, polarized for 1 h under application of a constant DC voltage (**V**). Subsequently, samples were cooled to room temperature, maintaining the DC voltage. Preliminary assays were performed using **V** values that ranged from 250 to 2000 V, the best results being obtained for 500 V. Accordingly, all experiments described in this work correspond to cHAP/tsp samples polarized using **V**= 500 V (DC field of 3 kV/cm).

X-Ray diffraction. The structure and crystallinity were studied by wide angle X-ray diffraction (WAXD). Patterns were acquired using a Bruker D8 Advance model with CuK_α radiation (λ = 0.1542 nm) and geometry of Bragg-Brentano, theta-2 theta. A one-dimensional Lynx Eye detector was employed. Samples were run at 40 kV and 40 mA, with a 2-theta range of 10-60, measurement steps of 0.02º, and time/step of 2-8 s. Diffraction profiles were processed using PeakFit v4 software (Jandel Scientific Software) and the

graphical representation performed with OriginPro v8 software (OriginLab Corporation, USA).

The crystallinity (χ_c) was obtained using the following expression:[35]

$$\chi_c = {V_{112/100}}/{I_{300}} \quad \text{(V.S2)}$$

where I_{300} is the intensity of the (300) reflection and $V_{112/300}$ is the intensity of the hollow between the (112) and (300) reflections, which disappears in non-crystalline samples.

X-ray photoelectron spectroscopy (XPS). XPS analyses were performed in a SPECS system equipped with a high-intensity twin-anode X-ray source XR50 of Mg/Al (1,253 eV/1487 eV) operating at 150 W, placed perpendicular to the analyzer axis, and using a Phoibos 150 MCD-9 XP detector. The X-ray spot size was 650 µm. The pass energy was set to 25 and 0.1 eV for the survey and the narrow scans, respectively. Charge compensation was achieved with a combination of electron and argon ion flood guns. The energy and emission current of the electrons were 4 eV and 0.35 mA, respectively. For the argon gun, the energy and the emission current were 0 eV and 0.1 mA, respectively. The spectra were recorded with pass energy of 25 eV in 0.1 eV steps at a pressure below 6×10^{-9} mbar. These standard conditions of charge compensation resulted in a negative but perfectly uniform static charge. The C 1s peak was used as an internal reference with a binding energy of 284.8 eV. High-resolution XPS spectra were acquired by Gaussian–Lorentzian curve fitting after s-shape background subtraction. The surface composition was determined using the manufacturer's sensitivity factors.

FTIR spectroscopy. Infrared absorption spectra were recorded with a Fourier Transform FTIR 4100 Jasco spectrometer in the 1800-700 cm-1 range. A Specac model MKII Golden Gate attenuated total reflection (ATR) equipment with a heating Diamond ATR Top-Plate was used.

Morphology. Scanning electron microscopy (SEM) studies were carried out using a Focused Ion Beam Zeiss Neon40 microscope operating at 5 kV, equipped with an energy dispersive X-ray (EDX) spectroscopy system. Samples were deposited on a silicon disc mounted with silver paint on pin stubs of aluminum, and sputter-coated with a thin layer of carbon to prevent sample charging problems.

Nuclear Magnetic Resonance (NMR). Solid state ^{31}P NMR spectra were acquired using a MHz WB Avance Bruker III-400 spectrometer, operating at a frequency of 400 MHz. Chemical shifts were calibrated using H_3PO_4 (85%) as internal standard. The sample spinning rate was 12 KHz.

Contact profilometry. The surface roughness (Rq) of the prepared HAp discs was determined using a stylus profilometer (Veeco, Plainview, NY, USA). Imaging of the samples was conducted using the following optimized settings: tip radius= 2.5 μm; stylus force= 1.5 mg; scan length= 1 μm; speed= 1.5 nm/s.

Contact angle. Measurements were carried out using the sessile drop method at room temperature on an OCA 15EC with SCA20 software (Data-Physics Instruments GmbH, Filderstadt, Germany). The solvents used for these experiments were deionized water and FBS. For contact angle (θ) measurements, the sessile drop was gently put on the surface of sample discs using a micrometric syringe with a proper metallic needle (Hamilton 500 μL). The ellipse method was used to fit a mathematical function to the measured drop contour. This procedure consists on approximate the drop contour to the line of an ellipse, deviations from the true drop shape being in the range of a few percent. The ellipse method provides accurate measure of the contact angle and holds the advantage that it is extremely fast. For each solvent, no less than ten drops were examined.

Cyclic voltammetry (CV). The electrochemical behavior was determined by CV using an Autolab PGSTAT302N equipped with the ECD module (Ecochimie, The Netherlands) with a three-electrode cell under a nitrogen atmosphere (99.995% in purity) at room temperature. A 0.1 M phosphate buffer saline solution (PBS; pH = 7.2 adjusted with NaOH) was used as the electrolyte in the three-electrode cell. The working compartment was filled with 30 mL of the electrolyte solution. Steel AISI 316 sheets of 1x1.5 cm^2 (thickness 0.1 cm) were used as both the working and the counter electrodes, and an Ag|AgCl electrode was used as the reference electrode which contained a KCl saturated aqueous solution (offset potential versus the standard hydrogen electrode, E^0 = 0.222 V at 25 °C). All potentials given in this work are referenced to this electrode. HAp discs prepared as described above were fixed on the working electrode using a two-side adhesive carbon layer. The initial and final potentials were -0.40 V, whereas a reversal potential of 0.80 V was considered. The scan rate was 50 mV/s.

The electroactivity, which indicates the ability to exchange charge reversibly, was evaluated by examining the similarity between the anodic and cathodic areas of the control voltammogram (i.e. the ratio between the reduction and oxidation charges). The electrochemical stability (i.e. loss of electroactivity, *LEA*), which decreases with the oxidation and reduction areas of consecutive control voltammograms, was determined using the following expression:

$$LEA = {}^{\Delta Q}/_{Q_{II}} \cdot 100 \quad \text{(V.S3)}$$

where ΔQ is the difference of voltammetric charge between the second cycle and the last cycle and QII is the voltammetric charge corresponding to the second cycle. In this work all values of LEA were referred to 1000 consecutive oxidation-reduction cycles.

The specific capacitance (SC; in F/g) of HAp in the electrode was calculated as:

$$SC = {}^{\Delta Q}/_{V_m} \quad \text{(V.S4)}$$

where Q is voltammetric charge, which is determined by integrating either the oxidative or the reductive parts of the cyclic voltammogram curve, Δ V is the potential window and m is the mass of polymer on the surface of the working electrode. The latter is derived from the productivity current and polymerization charge.[36]

Electrochemical Impedance Spectroscopy (EIS). EIS measurements were performed using an AUTOLAB PGSTAT302N in the 10 kHz to the 10 mHz frequency range and the amplitude of the sinusoidal voltage was 10 mV. All experiments were carried out at room temperature. Appropriated sized films were pressed in a disc format and were sandwiched between two stainless steel electrodes (diameter = 1.5 cm) assembled into an isolating resin holder.[37] The cell was tightened with screws to ensure constant pressure fastening. Films thickness was between 1.7 and 2.0 mm determined by a micrometer and the area was about 1.766 cm^2. Prior analyses, samples were previously dried by heating at 100 ºC in an oven overnight. After data collection, EIS results were then processed and fitted to an electrical equivalent circuit (EEC). All electrochemical assays (i.e. CV and EIS) were done in triplicate.

Adsorption onto treated cHAp. The concentration of the adsorbate in the working solutions was 100 mM for $P_2O_7^{4-}$ and 200 mM for both $P_3O_{10}^{5-}$ and ATMP, while the pH considered in this study was 7 in all cases. The concentration of $P_2O_7^{4-}$ was a half of that used for the other two adsorbates because of limitations in the solubility of the former specie. For the incubation, 500 µL of the working solution with the adsorbate were deposited onto 50 mg of cHAp. After overnight agitation at 25 ºC, adducts were separated by centrifugation at 6,500 rpm during 5 minutes at 4 ºC. Sediments were re-suspended in distilled water. After this process, which was repeated two times, the obtained pellets were frozen at -80 ºC for 3 h and, subsequently, the humidity was removed using a lyophilizer.

V.3. Results and Discussion

V.3.1. Preparation and Characterization

HAp was prepared by adding 0.5 M $(NH_4)_2HPO_4$ in de-ionized water to 0.5 M $Ca(NO_3)_2$ in ethanol, as it is detailed in Methods section.[38] The resulting suspension was aged applying hydrothermal conditions (16 bar at 150 ºC) during 24 h to produce cHAp. Samples obtained at this stage has been denoted "as prepared", hereafter abbreviated cHAp/p. Sintered cHAp samples, hereafter denoted cHAp/s, were prepared by heating previously synthesized cHAp/p at 1000 ºC for 2 h in air. Finally, thermally stimulated polarized cHAp (cHAp/tsp) was achieved using discs of sintered samples (10 mm of diameter x 1.68 mm of thickness), which were sandwiched between stainless steel (AISI 304) plates and polarized for 1 h under application of a constant DC voltage of 500 V (DC field of 3 kV/ cm) at 1000 ºC. After this, samples were allowed to cool to room temperature, maintaining the DC voltage.

The FTIR spectra of as prepared, sintered and permanently polarized cHAp are compared in Figure Ann.V.1a. The spectra, which show characteristic vibrational modes of PO_4^{3-} at υ_1 = 962 cm^{-1} and υ_3 = 1016, 1087 cm^{-1}, indicate that cHAp/tsp does not undergo major changes with respect to cHAp/p and cHAp/s. Analysis of WAXD measurements of as prepared and polarized samples were focused on peaks at 2θ = 32º–34º (Figure Ann.V.1b), which are characteristic of the (211), (112), and (300) cHAp reflections. The TSP process results in a very important increment of the crystallinity (i. e. from 0.43 ± 0.01 to 0.76 ± 0.02) which has been attributed to the formation of OH^- defects.

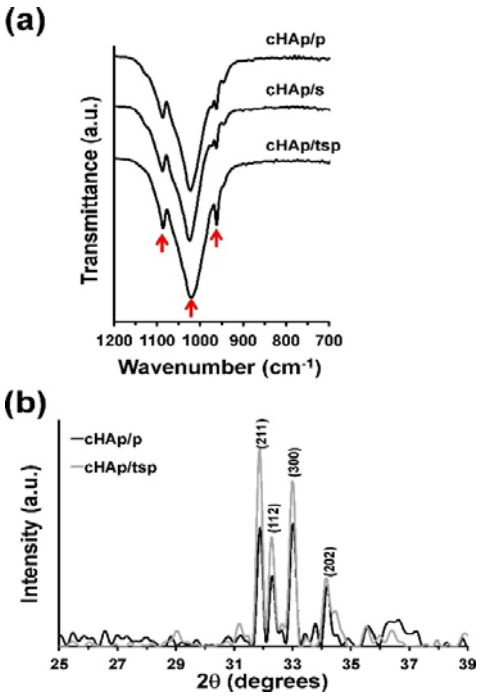

Figure Ann.V.1. (a) FTIR spectra of as-prepared, sintered, and polarized samples. (b) X-ray diffraction patterns of cHAp/p and cHAp/tsp. The samples were identified by the peaks at 2θ = 32º–34º.

Fujimori et al.[39] reported that OH^- ions scape from the HAp matrix above 800 ºC, such dehydration process resulting in the formation of vacancies and O_2^- ions. In addition to the formation of a small amount of OH^- defects, a monoclinic-to-hexagonal thermal phase transition occurs upon the application of such treatment to cHAp.[40] The hexagonal phase becomes the most stable at room temperature because of the order-disorder phase transition, which is accounted for by the change in the position of the OH^- ions.

The chemical composition, as determined by X-ray photoelectron spectroscopy (XPS), is consistent with the formation of thermally-induced OH^- vacancies (Table Ann.V.S1): the content of oxygen is around 2 wt.% lower for cHAp/s and cHAp/tsp than for cHAp/p. Although the Ca/P molar ratio of cHAp/p is very close to the stoichiometric value of 1.67, cHAp/s and cHAp/tsp exhibit a small reduction with respect to such ideal value (1.62 and 1.64, respectively), supporting the apparition of vacancies. Moreover, Figure Ann.V.2a compares the XPS spectra in the P 2p and Ca 2p regions for cHAp/p, cHAp/s and cHAp/tsp. The single P2p peak, which originates from PO_4^{3-} anions,[41,42] is centered at 132.2 eV for

cHAp/p, experiencing a slight shift towards higher and lower energies (ΔBE = + 0.4 and -1.0 eV) after sintering and TSP, respectively. The binding energies of the Ca 2p3/2 and Ca 2p1/2 peaks, which are detected at 346.1 and 349.6 eV, respectively, for cHAp/p,[41,42] shift to 346.5 and 350.0 eV for cHAp/s and to 345.1 and 348.6 eV for cHAp/tsp. These variations are consistent with structural changes associated to phase transitions.

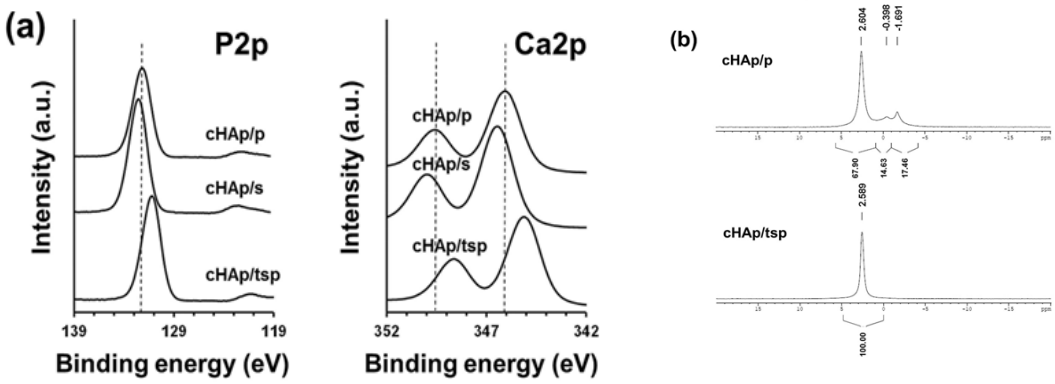

Figure Ann.V.2. (a) High-resolution XP spectra for cHAp samples: P 2p and Ca 2p regions. (b) Solid-state ^{31}P NMR spectra of cHAp/p and cHAp/tsp.

Figure Ann.V.2b compares the solid state ^{31}P NMR spectra of cHAp/p and cHAp/tsp, the spectrum of cHAp/s being displayed in Figure Ann.V.S1.. The main resonance peak in all samples (2.9 ppm) corresponds to bulk phosphate groups of HAp.[43] This peak is narrower for cHAp/s and HAp/tsp than for c/HAp/p, which is consistent with the increment of crystallinity mentioned above. The broad signals at approximately [-1,0] ppm and the shoulder at [0,1] ppm in both cHAp/p and cHAp/s are usually assigned to the lone protonated surfaces of phosphate groups arising from the disordered near surface layer.[44] Indeed, cHAp particles are frequently described as an ordered crystalline core surrounded by a disordered non-apatitic surface layer.[45] The shoulder at 4–6 ppm in cHAp/s (Figure Ann.V.S1.) has been attributed to the increment of HPO_4^{2-} ions at the disordered surface layer.[46,47] However, the most amazing result is the single peak observed in cHAp/tsp, which corresponds to phosphate groups. This evidences that the TSP exerts an important effect on the surface layer. Thus, the fingerprints of the surface OH^- ions leaving from the columns due to the TSP process are the disappearance of the surface HPO_4^{2-} ions and the formation of holes in the valence band to achieve the corresponding charge neutralization.

Figure Ann.V.3. compares the surface morphologies of cHAp/p, cHAp/s and cHAp/tsp. Although SEM micrographs of all samples are constituted by laminar crystals and fusiform rods, the amount of such elements increases upon the application of treatments, especially after TSP. Thus, crystals are bigger in cHAp/tsp than in cHAp/p and cHAp/s, which is consistent with the crystallinity changes discussed above. The surface roughness (Rq), as determined by contact profilometry, remained practically unaltered upon the application of thermal and TSP treatments (Table Ann.V.1).

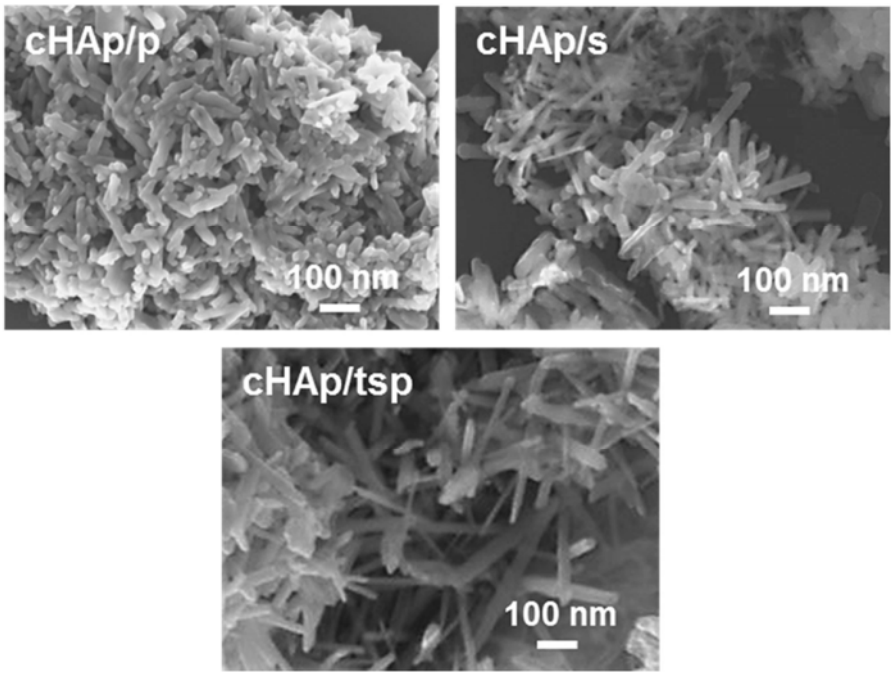

Figure Ann.V.3. SEM micrographs of cHAp/p, c/HAp/s, and cHAp/tsp particles.

The contact angle of water (θ_{water}) was ~ 4º for cHAp/p, cHAp/s and cHAp/tsp, indicating that the three are very hydrophilic materials, as it was expected because of their surface charge. In contrast, the contact angle of fetal bovine serum (θ_{FBS}) was significantly lower on cHAp/s and, especially, cHAp/tsp than on cHAp/p (Table Ann.V.1). This variation suggests that the reorganization of the ions induced by the thermal and TSP treatments increases the contribution of the polar component to the surface energy.

Table Ann.V.1. Roughness (R_q) and contact angle of water and fetal bobine serum drops (θ_{water} and θ_{FBS}) determined for cHAp/p, cHAp/s, and cHAp/tsp samples

Sample	R_q (nm)	θ_{water}	θ_{FSB}
cHAp/p	851± 194	3 ± 1	81 ± 2
cHAp/s	863 ± 158	4 ± 1	61 ± 2
cHAp/tsp	882 ± 92	4 ± 1	51 ± 2

V.3.2. Electrochemical Properties: Permanent versus Semi-permanent Polarization

Cyclic voltammograms recorded in phosphate buffer saline solution (PBS; pH 7.2) for cHAp/p, cHAp/s and cHAp/tsp fixed on steel are compared in Figure Ann.V.4a. Although cHAp/p exhibits higher electrochemical activity than bare steel (blank), the electroactivity increases considerably with thermal and TSP treatments (i. e. 46 % and 150 %, respectively). In the case of cHAp/tsp, such effect is accompanied of a significant enhancement of the anodic current intensity at the reversal potential. Thus, results evidence that the structural changes caused by the TSP treatment facilitate the diffusion of ions through the inorganic matrix and, therefore, the electrochemical response upon oxidation-reduction processes.

Treatments also affect the electrochemical stability, as is shown by the loss of electroactivity (*LEA*; Eqn V.S3) with the number of consecutive oxidation-reduction (redox) cycles (Figure Ann.V.4b). The electroactivity of all samples decreases rapidly during the first 100–150 redox cycles, experiencing a very slow reduction along the next cycles. After 1,000 cycles, the electroactivity decreased 72 %, 67 % and 60 % for cHAp/p, cHAp/s and cHAp/tsp, respectively, evidencing that structural changes caused by the TSP process enhances the stability of the electrochemical properties.

The behaviour followed by the specific capacitance (*SC*; Eqn V.S4) is fully consistent with that of the electroactivity. Although *SC* was small in all cases, the ability to store charge of cHAp/p (*SC* = 160 μF/g) resulted 71 % and 82 % smaller than those of cHAp/s and cHAp/tsp (*SC* = 560 and 890 μF/g, respectively). Also, the variation of the specific capacitance with the number of redox cycles (Figure Ann.V.4c) was similar to that described above for *LEA*.

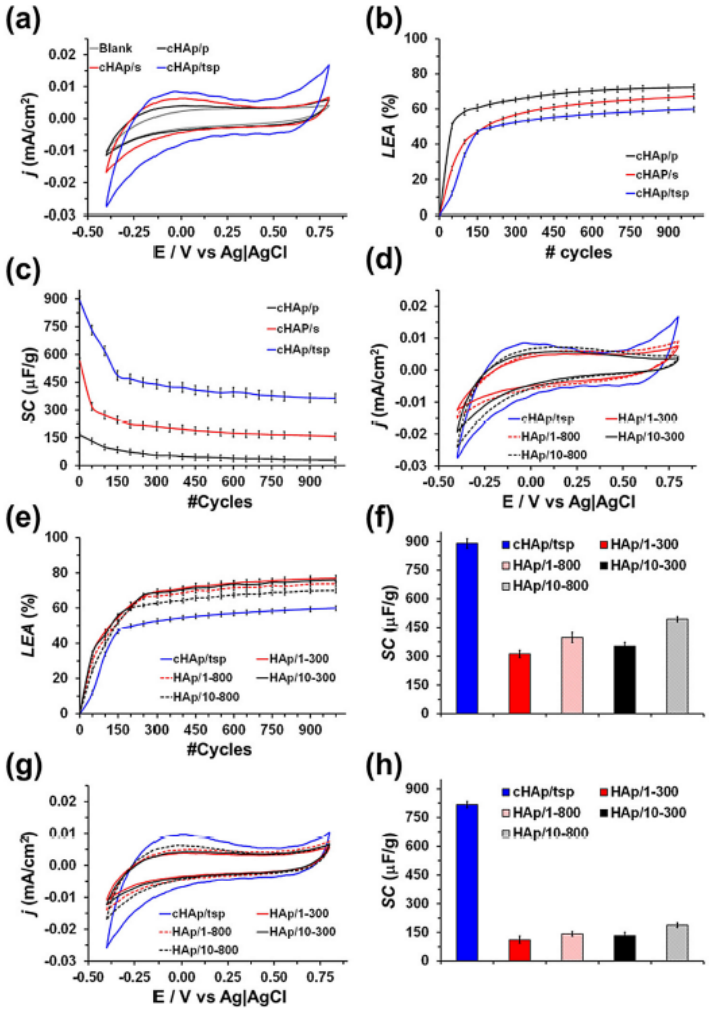

Figure Ann.V.4. (a) Control voltammograms and variation of both (b) the loss of electroactivity (LEA; Eqn S3) and (c) the specific capacitance (SC; Eqn S4) against the number of redox cycles in PBS (pH 7.2) for cHAp/p, c/HAp/s and cHAp/tsp. The voltammogram of bare steel (blank) is included in (a). (d–f) Comparison between the electrochemical properties of permanently polarized cHAp/tsp and different semi-permanently polarized HAp samples: (d) control voltammograms in PBS, (e) LEA against number of redox cycles, and (f) SC in PBS (pH 7.2). The labelling of the semi-permanently polarized HAp samples is described in the text. (g–h) Comparison between semi-permanently polarized and cHAp/tsp samples prepared three months before the measurements: (g) control voltammograms and (h) SC in PBS (pH 7.2). The scan rate was 50 mV/s in all cases.

To examine the influence of the preparation conditions in the electrochemical properties, semi-permanently polarized HAp samples were prepared following the procedure described by Yamashita and co-workers.[26-30] This can be summarized as follows: (i) HAp was synthesized by chemical precipitation; (ii) prepared HAp was dried at 850 ºC for 2 h; (iii)

dried HAp was sintered in saturated water vapor atmosphere at 1,250 ºC for 2 h; and (iv) sintered samples were electrically polarized in a DC field of 1 kV/cm at 300 ºC or 800 ºC for 1 h (hereafter HAp/1-300 or HAp/1-800, respectively) or a DC field of 10 kV/cm at 300 ºC or 850 ºC for 1 h (hereafter HAp/10-300 or HAp/10-850, respectively). It is worth noting that the DC field values (1 and 10 kV/cm) and the polarization temperatures (300 and 800 ºC) were selected to include the most diverse conditions employed for the preparation of semi-permanently polarized HAp. [26-30]

The voltammograms recorded for cHAp/tsp, HAp/1-300, HAp/1-800, HAp/10-300 and HAp/10-800 samples after 20 consecutive oxidation-reduction cycles are compared in Figure Ann.V.4d. The electrochemical activity of cHAp/tsp is at least 20% higher than that of the rest of the samples. Moreover, anodic and cathodic current densities at the final and reversal potentials, respectively, are significantly higher in absolute values for cHAp/tsp than for the other samples, reflecting a higher movement of charge during the oxidation and reduction processes. This feature is particularly noticeable for the anodic current density (i. e. 16.8 $\mu A/cm^2$ for cHAp/tsp while a value comprised between 4 and 9 $\mu A/cm^2$ for the other samples). Besides, the electrochemical stability and *SC* are considerably higher for cHAp/tsp than for semi-permanently polarized HAp samples (Figures Ann.V.4e and Ann.V.4f).

Results displayed in Figures Ann.V.4d–f are fully consistent with the highly crystalline organization and regular surface structure of cHAp/tsp. Indeed, the crystallinity of HAp/1-300, HAp/1-800, HAp/10-300 and HAp/10-800, as determined from the corresponding WAXD patterns, was lower than 0.63 ± 0.02, while cHAp/tsp exhibited a crystallinity of 0.76 ± 0.02. Moreover, the electrochemical behavior of semi-permanently polarized HAp samples is, independently of the polarization conditions (i. e. DC field and temperature), very similar to that displayed by cHAp/s (Figures Ann.V.4a–c), suggesting that application of a water vapor stream during the sintering process and/or the low temperature applied during the polarization process (≤ 800 ºC) do not inhibit the formation of disordered near surface layers with protonated phosphate groups. This lack of organization also affects the preservation of the electrochemical properties induced by the polarization process. This is reflected in Figures Ann.V.4g-h, which compare the voltammograms and *SC* of samples measured three months after being prepared and polarized. During such period, all samples were stored in the lab at room temperature under atmospheric conditions. As it can be seen, the electrochemical activity and *SC* of HAp/1-300, HAp/1-800, HAp/10-300 and HAp/10-

800 samples are very similar, suggesting that the distinctive properties induced by the magnitude of the DC field and the polarization temperature disappears after three months only. Indeed, the differences between such samples and cHAp/p (Figures Ann.V.4a and Ann.V.4c) are very small, which prove that the polarization effects induced by the conditions described by Yamashita and co-workers[26-30] are not enduring over time. In contrast, the properties of cHAp/tsp samples remain practically unchanged after three months (e. g. the *SC* decreased by 9 % only), demonstrating that temperatures higher than 800 ºC are crucial to achieve permanent polarization effects.

V.3.3. Electrical Properties: Permanent Versus Semi-Permanent Polarization

Electrochemical impedance spectroscopy (EIS) measurements were carried out to evaluate the ionic conductivity. This technique is expected to provide relevant information about the influence of the sintering and TSP processes in the resistivity of cHAp. Figure Ann.V.5a compares representative and reproducible Nyquist plots obtained for cHAp/p, cHAp/s and cHAp/tsp. In a Nyquist plot, the first semi-circular response corresponds to the electron transfer resistance at the higher frequency range, which controls the electron transfer kinetics of the redox probe on the electrode-solid disk interface. The diameter of the semi-circle defines the resistance of electron transfer, usually called bulk resistance (R_b). The Nyquist plot recorded for cHAp/p exhibits only one dielectric relaxation time (τ_1), which corresponds to a single charge transfer across the solid disk, showing that the material has a high bulk resistance (i. e. low ionic conductivity) in the dry state. Bode plots (Figure Ann.V.S2) show a phase angle close to 80º, which correspond to resistive materials in the dry state. The semi-circle diameter in Nyquist plots is much smaller for cHAp/s and, especially, for cHAp/tsp. Besides, a second time constant (τ_2) appears due to the significant structural modification occurred in cHAp, enabling fast charge transport across the disk. As discussed above, cHAp/s and cHAp/tsp present higher crystallinity and bigger crystals than cHAp/p. Therefore, the thermal treatment step promotes the growing of the crystals, while the TSP treatment is, apparently, responsible of the definition of good pathways for charge transportation.

The electrical equivalent circuit (EEC) used to fit the experimental data is shown in Figure Ann.V.5b. The EEC contains three important elements: R_b that represents the bulk resistance; and Q_b and Q_{dl} that describes the ideal capacitances from both the cHAp thick disk and the double layer between the metal-disk surfaces, respectively. R_S corresponds to the electrolyte resistance, even though it was considered ~ 0 $\Omega \cdot cm^2$ due to the absence of liquid electrolyte. The CPE_b is the real capacitance of the bulk disk, which accounts for the non- uniform diffusion among the films adhered to the electrode surface. On the other hand, CPE_{dl} is the real capacitance of the double-layer, which in turn is typically associated to the surface reactivity, surface heterogeneity and roughness (i. e. related to the electrode geometry and porosity). Also, the CPE impedance, which has been expressed as $Z_{CPE} = [Q \cdot (j\omega)^n]^{-1}$, represents an ideal capacitor and a pure resistor for n = 1 and n = 0, respectively, while it is associated with a diffusion process when n ~ 0.5.

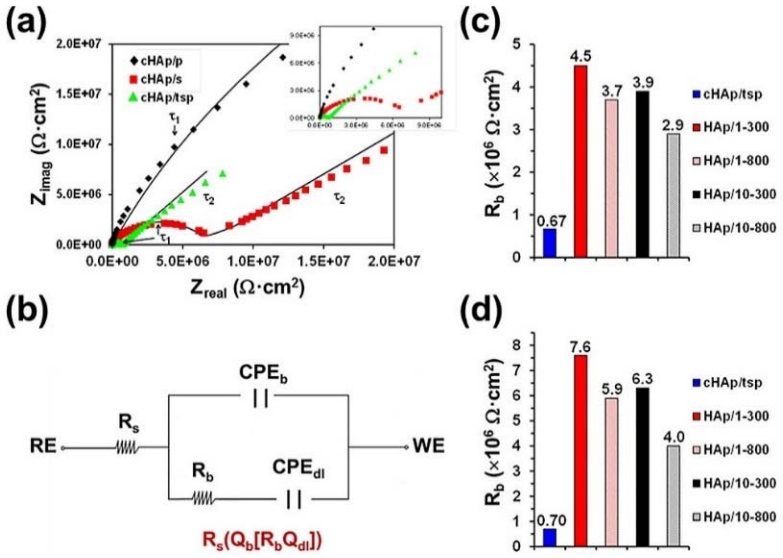

Figure Ann.V.5. (a) Nyquist plots for cHAp/p, cHAp/s, and cHAp/tsp. The inset represents the Nyquist behavior at high frequency. (b) Electrical equivalent circuit (EEC) used to fit the experimental data recorded for cHAp/s and cHAp/tsp: RS is the electrolyte resistance, CPE_b and R_b are the bulk constant phase element and resistance, respectively, CPEdl is the contribution of the double layer capacitance. (c,d) Comparison between the Rb values determined by EIS for permanently and semi-permanently polarized HAp samples: (c) fresh samples and (d) samples prepared using the same procedure that fresh samples and left in a dry environment for 3 months before the measurements.

All impedance data displayed in Figure Ann.V.5a were fitted with the EEC showed in the Figure Ann.V.5b, with exception of those obtained for cHAp/p. For EEC used the latter samples does not have the capacitance response from the double layer film and corresponds

to $R_s(R_bQ_b)$. The numerical evaluation of the EIS results is provided in Table Ann.V.2. The percentage error associated with each circuit element was lower than 5 % in all cases, reflecting the good quality of the experimental data fitting.

Table Ann.V.2. Data derived from the fitting of the experimental EIS results, recorded for cHAp/p, cHAp/s and cHAp/tsp dry discs, to the electrical equivalent circuits (EECs).

Sample	R_b (□ ·cm²)	Q_{dl} (F·cm⁻²·sⁿ⁻¹)	n	Q_b (F·cm⁻²·sⁿ⁻¹)	n
cHAp/p[a]	134.6 M	-	-	8.180×10^{-10}	0.76
cHAp/s[b]	6.43 M	1.248×10^{-8}	0.77	1.215×10^{-5}	0.44
cHAp/tsp[b]	0.67 M	4.558×10^{-7}	0.71	4.863×10^{-5}	0.55

[a] The EEC for cHAp/p is $R_s(R_bQ_b)$.
[b] The EEC for HAp/s and HAp/tso is displayed in Figure Ann.V.5b

The R_b obtained for cHAp/tsp is very low (6.7×10^5 Ω·cm²) with respect to cHAp/s (6.4 x 106 Ω·cm²), which indicates that the ionic conductivity increased by one order of magnitude when the TSP process is applied. Moreover, the R_b of cHAp/p (134.6 x 106 Ω·cm²) is two orders magnitude higher than that cHAp/s, evidencing that sintering also promotes charge transport. Another relevant change induced by the both the sintering and the TSP is the appearance of a second time constant (τ_2), indicating the creation of charge pathways inside the solid through the formation of larger crystals (Figure Ann.V.5a). This observation is in perfect agreement with SEM, NMR and cyclic voltammetry results discussed above. Overall, the conductive sites in cHAp/tsp seem to arise from the re-organization of the vacancies into channels, which are formed by the dehydroxylation of the crystals during the sintering. This re-structuration occurs during the TSP process and, as a result, ions are able to move along the crystals. This interpretation is in good agreement with results derived from other studies of HAp at high temperatures.[48,49] Figure Ann.V.5c compares the electrical resistivity, R_b, of cHAp/tsp with those of the samples prepared according to the protocol reported by Yamashita and co-workers[26-31] (i.e. HAp/1-300, HAp/1-800, HAp/10-300 and HAp/10-800). As it can be seen, the R_b of cHAp/tsp is the smallest, independently of the electric field and/or temperature used to prepare semi-permanently cHAp/tsp. Indeed, the R_b of samples prepared using the procedure described by Yamashita and co-workers[26-31] is similar to that of cHAp/s (6.4 x 106 Ω·cm²). Again, these results point out the importance of the high temperature (1,000 ºC) in the electrical

polarization step, which is necessary for the complete elimination of protons near surface layers and for the creation of both ordered structures and charge defects.

Inspection of samples three months after their preparation and polarization before the EIS measurements (Figure Ann.V.5d) reveals that R_b remains practically unchanged for cHAp/tsp (i.e. R_b increases 4 %), while the electrical resistivity of semi-permanently polarized samples experiences an increment that ranges from 38% (HAp/10-800) to 69% (HAp/1-300). Overall, observations reported in this and previous subsections confirm that cHAp/tsp shall be described as a permanently polarized cHAp.

V.3.4. Adsorption of Pyrophosphate, Triphosphate, and Trisphosphonate

In a recent study we examined the adsorption of sodium pyrophosphate ($P_2O_7^{4-}$), sodium triphosphate ($P_3O_{10}^{5-}$) and aminotris(methylenephosphonic acid) (ATMP), which is a phosphonic acid with chemical formula $N(CH_2PO_3H_2)_3$, onto cHAp/p.[13] In order to examine how both thermal and electric treatments have affected cHAp/s and cHAp/tsp substrates, a complete adsorption study have been conducted using the same inorganic adsorbates. The concentration of adsorbate in the incubation solutions was 100 mM for $P_2O_7^{4-}$ and 200 mM for both $P_3O_{10}^{5-}$ and ATMP, which provided clear adsorption signals for cHAp/p at pH 7.[13]

The contact angle of fetal bovine serum on bare cHAp/s and cHAp/tsp decreased after incubation, indicating that the hree inorganic adsorbates were successfully adsorbed (Figure Ann.V.S3.). The reduction of the contact angle with the adsorbate followed the same variation for the two cHAp substrates, $P_3O_{10}^{5-} < P_2O_7^{4-} \approx$ ATMP, suggesting that $P_3O_{10}^{5-}$ provides the higher surface energy. On the other, the XPS spectra in the Na 1s region reveals a peak centred at 1074.2 eV for cHAp/s and cHAp/tsp treated with $P_2O_7^{4-}$ and $P_3O_{10}^{5-}$ (Figures Ann.V.6a–b), corroborating the incorporation of these compounds. In contrast, the content of Na 1s in non-incubated samples and samples incubated in presence of ATMP is null (Figure Ann.V.6a). The ratios obtained using the Na 1s atomic percent compositions indicate that the adsorption of $P_2O_7^{4-}$ and $P_3O_{10}^{5-}$ is ~ 2 and ~ 1.5 times respectively, higher for cHAp/tsp than for cHAp/s (Table V.S1). A similar strategy was followed to characterize the adsorption of ATMP, which is clearly detected through the peaks at the N 1s region (Figure Ann.V.6c–d). The content of N 1s in non-incubated samples and samples incubated in presence of $P_2O_7^{4-}$ and $P_3O_{10}^{5-}$ is ≤ 0.40 wt.%, increasing to 3.18 and 4.08 wt.% for cHAp/s and cHAp/tsp samples with ATMP (Table V.S1), respectively. Assuming that the amount of

N_2 adsorbed from the atmosphere is the same for incubated and non-incubated samples, the adsorption of ATMP is ~ 1.4 times higher for cHAp/tsp than for cHAp/s. The two peaks detected at 404.3 and 402.5 eV for the latter samples have been attributed to nitrogen atoms of ATMP with different chemical environments (i.e. free and hydrogen bonded) Figure Ann.V.S4. compares the FTIR spectra of cHAp/p, cHAp/s and cHAp/tsp after incubation with $P_2O_7^{4-}$, $P_3O_{10}^{5-}$ and ATMP solutions at neutral pH. The P-O-P asymmetric stretching of $P_3O_{10}^{5-}$, which is a weak shoulder at around 890 cm^{-1} for cHAp/ p, transforms into a well-defined band for cHAp/s and, especially, cHAp/tsp (Figure Ann.V.S4a). This feature is fully consistent with XPS observations, corroborating that the sintering and TSP enhance significantly the ability of cHAp to adsorb $P_3O_{10}^{5-}$. Moreover, quantification through the ratio of integrated area of the peaks at 1016 cm^{-1} and 890 cm^{-1} indicated that the adsorption of $P_3O_{10}^{5-}$ onto cHAp/p is 2.0 and 2.6 times lower than onto cHAp/s and cHAp/tsp, respectively.

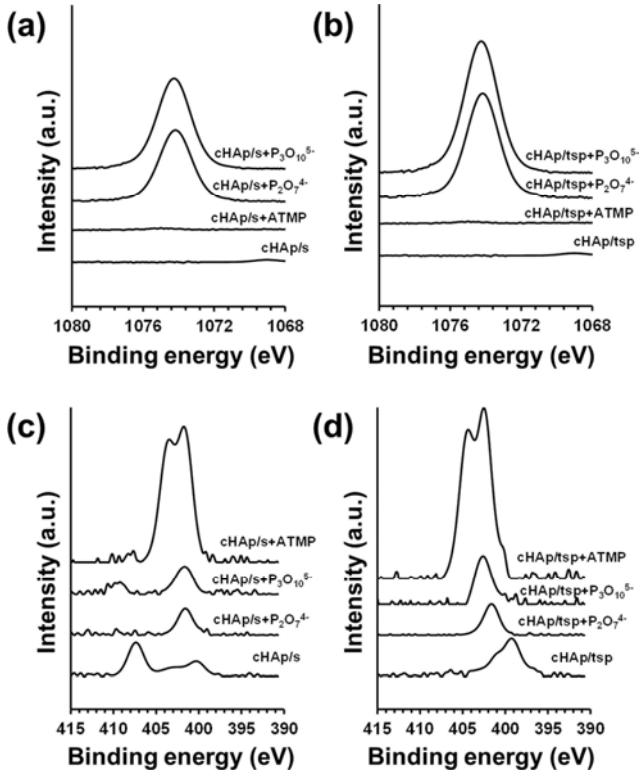

Figure Ann.V.6. High-resolution X-ray photoelectron spectra in the: (a,b) Na 1s and (c,d) N 1s regions for: a,c) cHAp/s and b,d) cHAp/tsp samples before and after incubation in $P_2O_7^{4-}$, $P_3O_{10}^{5-}$, and ATMP solutions at neutral pH.

This feature is much less clear for $P_2O_7^{4-}$ since the band at 890 cm^{-1} remains undetectable (Figure Ann.V.S4b). In this case, the only evidence of adsorption is the very weak shoulder at 740–750 cm^{-1} for cHAp/s and cHAp/tsp, which has been attributed to the P-O-P symmetric stretching. The atomic percent content of Na 1s detected by XPS in cHAp samples incubated with $P_3O_{10}^{5-}$ is considerably higher than in those incubated with $P_2O_7^{4-}$ (Table V.S1.), which is consistent with FTIR observations. This has been attributed to the fact that phosphate chains of increasing size adapt better their geometry to the crystallographic positions of the ions at the cHAp surfaces.

Finally, FTIR results for the different cHAp samples incubated with ATMP (Figure Ann.V.S4c) reveals trends similar to those observed for $P_3O_{10}^{5-}$. The band at 900 cm^{-1}, which corresponds to asymmetric vibrations of alkylphosphonic, is a shoulder for cHAp/p and a well-defined peak for cHAp/s and, especially cHAp/tsp. This variation, which is in agreement with XPS results, evidence that the ability to adsorb ATMP increases as follows: cHAp/p < cHAp/s < cHAp/tsp. The adsorption of ATMP onto of cHAp/s and cHAp/tsp was estimated to be, respectively, 2.2 and 3.0 times higher than onto cHAp/p.

V.3.5. Inorganic Adsorbates Affect the Electrochemical and Electrical Properties of the Materials

Cyclic voltammograms recorded for cHAp/p reflect that the electrochemical activity of untreated cHAp remain unaltered after the adsorption of $P_3O_{10}^{5-}$ a, $P_2O_7^{4-}$ or ATMP (Figure Ann.V.S5a). In contrast, electroactivity of incubated cHAp/s and cHAp/tsp samples is ~ 40 % and ~ 60 % higher than that of the non- incubated ones (Figures Ann.7a-b), suggesting that tested inorganic adsorbates facilitate the exchange of ions between the mineral matrix and the PBS electrolyte solution during the oxidation and reduction processes. However, the most striking feature refers to the variation of the electroactivity against the number of redox cycles. Thus, the loss of electroactivity of non- incubated cHAp/s and cHAp/tsp after 1000 redox cycles is ~ 72 % and ~ 60 %, respectively. The adsorption of $P_3O_{10}^{5-}$, $P_2O_7^{4-}$ or ATMP reduces these values drastically (Figures Ann.V.7c–d), demonstrating that that these species provide electrochemical protection to the mineral and improve the stability. For example, for cHAp/tsp the LEA after 1,000 cycles decreases from ~ 60 % to 21 %, 27 % or 29 % upon adsorption of $P_3O_{10}^{5-}$, $P_2O_7^{4-}$ or ATMP, respectively. This effect is practically inexistent for cHAp/p (Figure Ann.V.S5b), which has been

attributed to the fact that the amount of adsorbate onto the surface of untreated cHAp is smaller than onto cHAp/s and cHAp/tsp, as proved in the previous subsection.

Figures Ann.V.S6 and Ann.V.S7 display the EIS plots for cHAp/s and cHAp/tsp, respectively, after adsorption of $P_3O_{10}^{5-}$, $P_2O_7^{4-}$ or ATMP, while results derived from the fitting to the EEC displayed in Figure Ann.V.5b are listed in Table V.S2. The R_b determined for cHAp/s and cHAp/tsp samples without (bare) and with inorganic adsorbates are plotted in Figures Ann.V.7e and V.7f, respectively.

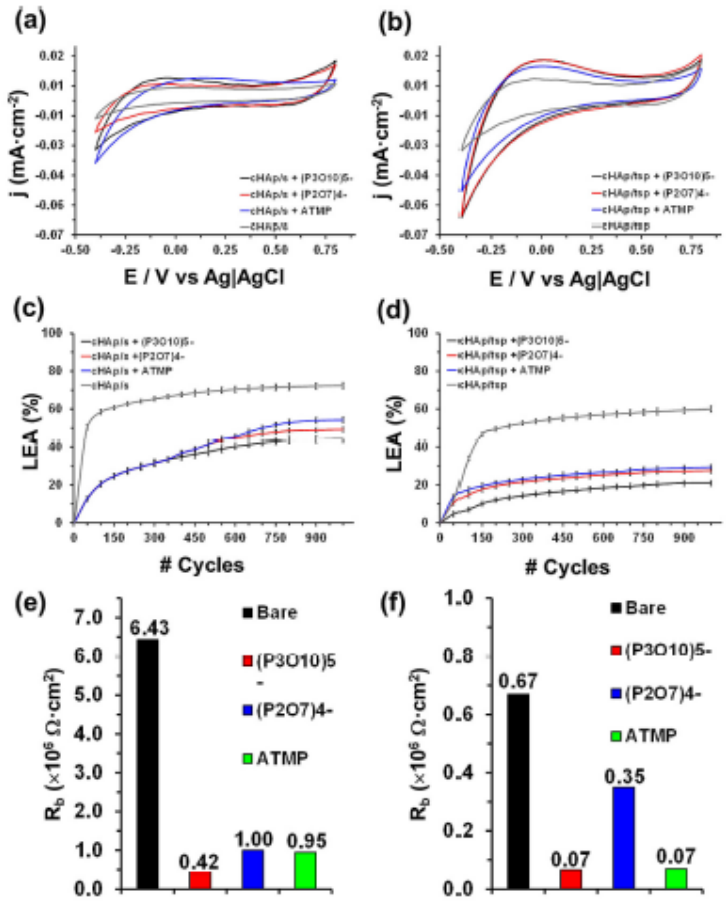

Figure Ann.V.7. (a,b) Control voltammograms and c,d) variation of the loss of electroactivity (LEA; Eqn S3) with the number of consecutive oxidation-reduction cycles in PBS for: (a,c) cHAp/s and (b,d) cHAp/tsp samples before and after incubation in $P_2O_7^{4-}$, $P_3O_{10}^{5-}$ and ATMP solutions at neutral pH. Comparison between the R_b values determined by EIS for: (e) cHAp/s and (f) cHAp/tsp before and after adsorption of $P_2O_7^{4-}$, $P_3O_{10}^{5-}$ and ATMP.

The adsorption of $P_3O_{10}^{5-}$ and ATMP exerts a remarkable influence in the electronic conductivity, this phenomenon being particularly remarkable for cHAp/tsp. Thus, the bulk

resistivity of cHAp/tsp with adsorbed $P_3O_{10}^{5-}$ and ATMP was 66.7 and 69.9 $k\Omega \cdot cm^2$, respectively, evidencing that such adsorbates promote the electron charge mobility inside the mineral. Structural changes obtained with the TSP treatment apparently favor the interaction with such adsorbates, forming better charge transfer channels.

V.4. Conclusions

cHAp/tsp has been prepared utilizing a TSP process according to which a constant DC voltage of 500 V (DC field of 300 $kV \cdot m^{-1}$) is applied at 1000 ºC for 1 h to cHAp/s. Analyses of the chemical and structural properties of the resulting cHAp/tsp have been evaluated using XPS, WAXD, solid state ^{31}P NMR and FTIR spectroscopy. Results evidence the disappearance of HPO_4^{2-} ions from the surface layer, which are typically identified in cHAp/p and, specially, cHAp/s, the apparition of OH^- vacancies and the enhancement of the crystallinity. However, the most distinctive characteristics of cHAp/tsp are the electrochemical properties (i. e. electrochemical activity and stability) and the electrical conductivity, which are considerably higher than those achieved by other authors[26-30] applying lower polarization temperatures to samples sintered in a saturated water vapor atmosphere. Moreover, re-evaluation of samples that were polarized three months before has shown that both the electrochemical and electrical properties of the cHAp/tsp remain practically unaltered, proving that the acquired polar- ization effects are permanent. This represents a very important advantage with respect to previously reported strategies since the properties of samples polarized at lower temperatures ($\leq$ 800 ºC) are very similar to those of cHAp/s after three months The ability to adsorb $P_3O_{10}^{5-}$, $P_2O_7^{4-}$ and ATMP is another remarkable characteristic of cHAp/tsp. XPS and FTIR results indicate that the adsorption of inorganic phosphates and phosphonates onto cHAp/tsp is around 1.5–2 times higher than onto cHAp/s, which in turn is about twice that of cHAp/p. These results are very important for biomedical applications, as for example the fabrication of HAp scaffolds with improved phosphate and phosphonate adsorption capacity for bone regeneration. In addition, the adsorption of inorganic phosphates and phosphonates imparts electrochemical stability and reduces the electrical resistance, opening new possibilities to the electrostimulation.

V.5. References

1. Dorozhkin, S.V., Epple, M. Biological and medical significance of calcium phosphates, *Angewandte Chemie International Edition* (**2002**), *41*, 3130–3146. DOI:10.1002/1521-3773(20020902)41:17<3130::AID-ANIE3130>3.0.CO;2-1.

2. Palmer L.C., Newcomb C.J., Kaltz S.R., Spoerke E.D., Stupp S.I., Biomimetic systems for hydroxyapatite mineralization inspired by bone and enamel, *Chemical Review*s (**2008**), *108*, 4754–4783. DOI:10.1021/cr8004422.

3. Ma M.Y., Zhu Y.J., Li L., Cao S.W., Nanostructured porous hollow ellipsoidal capsules of hydroxyapatite and calcium silicate: preparation and application in drug delivery, *Journal of Material Chemistry* (**2008**), *18*, 2722–2727. DOI:10.1039/B800389K.

4. K. W. Wang, L. Z. Zhou, Y. Sun, G. J. Wu, H. C. Gu, Y. R. Duan, F. Chen, Y. J. Zhu, Calcium phosphate/PLGA-mPEG hybrid porous nanospheres: A promising vector with ultrahigh gene loading and transfection efficiency, *Journal Materials Chemistry* (**2010**), *20*, 1161–1166. DOI: 10.1039/B917441A.

5. Tang Q.L., Zhu Y.J., Wu J., Chen F., Cao S.W., Calcium phosphate drug nanocarriers with ultrahigh and adjustable drug-loading capacity: One-step synthesis, in situ drug loading and prolonged drug release, *Nanomedicine: Nanotechnology, Biology and Medicine* (**2011**), *7*, 428–434. DOI: 10.1016/j.nano.2010.12.005.

6. Kim H-W., Knowles J.C., Kim H-E., Hydroxyapatite/poly (ε-caprolactone) composite coatings on hydroxyapatite porous bone scaffold for drug delivery, *Biomaterials* (**2004**), *25*, 1279–1287. DOI:10.1016/j.biomaterials.2003.07.003.

7. Suchanek W., Yoshimura M., Processing and properties of hydroxyapatite-based biomaterials for use as hard tissue replacement implants, *Journal Materials Research* (**1998**), *13*, 94–117. DOI: 10.1557/JMR.1998.0015.

8. Zhou H., Lee J., Nanoscale hydroxyapatite particles for bone tissue engineering, *Acta Biomaterialia* (**2011**), *7*, 2769–2781. DOI: 10.1016/j.actbio.2011.03.019.

9. Elliott J.C., Mackie P.E., Young R.A., Monoclinic hydroxyapatite, *Science* (**1973**), *180*, 1055–1057. DOI:10.1126/science.180.4090.1055.

10 Hitmi N., LaCabanne C., Young R.A., OH− reorientability in hydroxyapatites: effect of F^- and Cl^-, *Journal of Physics and Chemistry of Solids* (**1988**), *49*, 541–550. DOI:10.1016/0022-3697(88)90065-0.

11. Ikoma t., A. Yamazaki, S. Nakamura, M. Akao, Preparation and dielectric property of sintered monoclinic hydroxyapatite, *Journal of Materials Science Letters* (**1999**), *18*, 1225–1228.
DOI:10.1023/A:1006610521173.

12. Kalogeras I.M. , Vassilikou-Dova A., Katerinopoulou A., Axially dependent dielectric relaxation response of natural hydroxyapatite single crystals, *Journal of Applied Physics* (**2002**), *92*, 406.
DOI:10.1063/1.1481776.

13. Rivas M., Casanovas J., del Valle L.J., Bertran O., Revilla-López G., Turon P., Puiggalí J., Alemán C., An experimental-computer modeling study of inorganic phosphates surface adsorption on hydroxyapatite particles, *Dalton Transactions* (**2015**), *44*, 9980 – 9981.
DOI: 10.1039/C5DT00209E.

14. Kumble K.D., Kornberg A., Inorganic polyphosphate in mammalian cells and tissues, *Journal of Biological Chemistry* (**1996**), *270*, 5818–5822.
DOI:10.1074/jbc.270.11.5818.

15. Comeau P.A., Frei H., Yang C., Fernlund G., Rossi F.M., In vivo evaluation of calcium polyphosphate for bone regeneration, *Journal of Biomaterials Applications* (**2012**), *27*, 267–275.
DOI:10.1177/0885328211401933.

16. Siggers K., Frei H., Fernlund G., Rossi F.M., Effect of bone graft substitute on marrow stromal cell proliferation and differentiation, *Journal of Biomedical Materials Research Part A* (**2010**), *94*, 877–885.
DOI: 10.1002/jbm.a.32766.

17. Morita K., Doi K., Kubo T., Takeshita R., Kato S., Akagawa Y., Enhanced initial bone regeneration with inorganic polyphosphate-adsorbed hydroxyapatite, *Acta Biomaterialia* (**2010**), *6,* 2808–2815.
DOI:10.1016/j.actbio.2009.12.055.

18. Yuan Q., Kubo T., Doi K., Morita K., Takeshita R., Kato S., Shiba T., Akagawa Y., Effect of combined application of bFGF and inorganic polyphosphate on bioactivities of osteoblasts and initial bone regeneration, *Acta Biomaterialia* (**2009**), *5*, 1716–1724.
DOI:10.1016/j.actbio.2009.01.034.

19. Shiba T., Nishimura D., Kawazoe Y., Onodera Y., Tsutsumi K., Nakamura R., Ohshiro M., Modulation of mitogenic activity of fibroblast growth factors by inorganic polyphosphate, *Journal of Biologial Chemistry* (**2003**), *278*, 26788–26792.
DOI:10.1074/jbc.M303468200.

20. Hacchou Y., Uematsu T., Ueda O., Usui Y., Uematsu S., Takahashi M., Kawazoe Y., Shiba T., Kurihara S., Yamaoka M., Furusawa K., *Journal of Dental Research* (**2007**), *86*, 893– 897.
DOI:10.1177/154405910708600917.

21. Omelon S., Georgiou J., Henneman Z.J., Wise L.M., Sukhu B., Hunt T, Wynnyckyj, C., Holmyard D., Bielecki R., Grynpas R.D., Control of vertebrate skeletal mineralization by polyphosphates, *PLoS ONE* (**2009**), *4*, e5634.
DOI: 10.1371/journal.pone.0005634.

22. Kamat S.S., Raushel F.M., The enzymatic conversion of phosphonates to phosphate by bacteria, *Current Opinion of Chemical Biology* (**2013**), *17*, 589–596.
DOI:10.1016/j.cbpa.2013.06.006.

23. Nancollas G.H., Tang R., Phipps R.J., Henneman Z., Gulde S., Wu W., Mangood A., Russell R.G.G., Ebetino F.H., Novel insights into actions of bisphosphonates on bone: differences in interactions with hydroxyapatite, *Bone* (**2006**), *38*, 617–627.
DOI:10.1016/j.bone.2005.05.003.

24. Russell R.G.G., F. H. Ebetino, Mechanisms of action of bisphosphonates: similarities and differences and their potential influence on clinical efficacy, *Osteoporosis International.* (**2008**), *19*, 733–759.
DOI:10.1007/s00198-007-0540-8.

25. Gronich N., Rennet G., Nature Reviews. Beyond aspirin-cancer prevention with statins, metformin and bisphosphonates, *Nature Reviews Clinical Oncology* (**2013**), *10*, 625–642.
DOI: 10.1038/nrclinonc.2013.169.

26. Ueshima M., Nakamura S., Ohgaki M., Yamashita K., Electrovectorial effect of polarized hydroxyapatite on quasi-epitaxial growth at nano-interfaces, *Solid State Ionics* (**2002**), *151*, 29–34.
DOI:10.1016/S0167-2738(02)00600-8.

27. Ueshima M., Nakamura S., Yamashita K., Huge, millicoulomb charge storage in ceramic hydroxyapatite by bimodal electric polarization, *Advanced Materials* (**2002**), *14*, 591–595.
DOI:10.1002/1521-4095(20020418)14:8<591::AID-ADMA591>3.0.CO;2-7

28. Nakamura, M., Sekijima Y., Nakamura S., Kobayashi T., Niwa K., Yamashita K., Role of blood coagulation components as intermediators of high osteoconductivity of electrically polarized hydroxyapatite, *Journal Biomedical Materials Research* (**2006**), *79A*, 627– 634.
DOI:10.1002/jbm.a.30827.

29. Horiuchi N., Nakamura M., Nagai A., Katayama K., Yamashita K., Proton conduction related electrical dipole and space charge polarization in hydroxyapatite, *Journal of Applied Physics* (**2012**), *112*, 074901.
DOI: 10.1063/1.4754298.

30. Horiuchi N., Nakaguki S., Wada N., Nakamura M., Nagai A., Katayama K., Yamashita K., Polarization-induced surface charges in hydroxyapatite ceramics, *Journal of Applied Physics* (**2014**), *116*, 014902, 1-8.
DOI: 10.1063/1.4886235.

31. Nakamura M., Hori N., Namba S., Toyama T., Nishimiya N., Yamashita K., Wettability and surface free energy of polarised ceramic biomaterials, *Biomedical Material* (**2015**), *10*, 011001.
DOI:10.1088/1748-6041/10/1/011001.

32. Nakamura M., Nagai A., Hentunen T., Salonen J., Sekilima Y., Okura T., Hashimoto K., Toda Y., Monma H., Yamashita K., Surface Electric Fields Increase Osteoblast Adhesion through Improved Wettability on Hydroxyapatite Electret, *ACS Applied Materials and Interfaces* (**2009**), *1*, 2181–2189.
DOI:10.1021/am900341v.

.

33. Rivas M., del Valle L.J., Turon P., Alemán C., Puiggalí J., Sustainable synthesis of amino acids by catalytic fixation of molecular dinitrogen and carbon dioxide. *Green Chemistry* (**2018**), *20*, 685–693.
DOI: 10.1039/C7GC02911J.

34. Valle L.J., Bertrán O., Chaves G, Revilla-López G., Rivas M., Teresa Casas M., Casanovas J., Turon P., Puiggalí J., Alemán C., DNA adsorbed on hydroxyapatite surfaces *Journal of Materials Chemistry B* (**2014**), *2*, 6953-6966.
DOI: 10.1039/C4TB01184H.

35. Landi E., Tampieri A., Celotti G., Sprio S., Densification behaviour and mechanisms of synthetic hydroxyapatites, *Journal European Ceramics Society* (**2000**), *20*, 2377.
DOI: 10.1016/S0955-2219(00)00154-0.

36. Estrany F., Aradilla D., Oliver R., Alemán C., Densification behaviour and mechanisms of synthetic hydroxyapatites, *European Polymer Journal* (**2007**), *43*, 1876.
DOI:10.1016/S0955-2219(00)00154-0.

37. Müller F., Ferreira C.A., Azambuja D.S., Alemán C., Armelin E., Measuring the proton conductivity of ion-exchange membranes using electrochemical impedance spectroscopy and through-plane cell, *Journal Physical Chemistry B* (**2014**), *118*, 1102-1112.
DOI:10.1021/jp409675z.

38. Valle L.J., Bertran O., Chaves G, Revilla-López G., Rivas M., Teresa Casas M., Casanovas J., Turon P., Puiggalí J., Alemán C., DNA adsorbed on hydroxyapatite surfaces *Journal of Materials Chemistry B* (**2014**), *2*, 6953-6966.
DOI: 10.1039/C4TB01184H.

39. Fujimori H., Toya H., Ioku K., Goto S., Yoshimura M., In situ observation of defects in hydroxyapatite up to 1200° C by ultraviolet Raman spectroscopy, *Chemical Physics Letters* (**2000**), *325*, 383–388.
DOI:10.1016/S0009-2614(00)00695-3.

40. Ma G., Liu X.Y., Hydroxyapatite: hexagonal or monoclinic?, *Crystal Growth & Design* (**2009**), *9*, 2991–2994.
DOI:10.1021/cg900156w

41. *Handbook of X-ray Photoelectron Spectroscopy* (Eds.: J. F. Moulder, J. Chastain), Physical Electronics Division, PerkinElmer Corporation, (**1995**).

42. Chang M.C., Tanaka J., XPS study for the microstructure development of hydroxyapatite–collagen nanocomposites cross-linked using glutaraldehyde, *Biomaterials* (**2002**), *23*, 3879–3885.
DOI:10.1016/S0142-9612(02)00133-3.

43. Jarlbring M., Sandström D.E., Antzutkin O.N., Forsling W., Characterization of Active Phosphorus Surface Sites at Synthetic Carbonate-Free Fluorapatite Using Single-Pulse ^{1}H, ^{31}P, and ^{31}P CP MAS NMR, *Langmuir* (**2006**), *22*, 4787–4792.
DOI: 10.1021/la052837j.

44. Wang Y., Von Euw S., Fernandes F.M., Cassaignon S., Selmane M., Laurent G., Pehau-Arnaudet G., Coelho C., Bonhomme-Coury L., Giraud-Guillaume M-M., Babinneau F., Azars T., Nassif N., Water-mediated structuring of bone apatite, *Nature Material*s (**2013**), *12*, 1144–1153.
DOI: 10.1038/nmat3787.

45. Jager C., Welzel T., Meyer-Zaika W., Epple M.A., A solid‐state NMR investigation of the structure of nanocrystalline hydroxyapatite, *Magnetic Resonance in Chemistry* (**2006**), *44*, 573–580..
DOI: 10.1002/mrc.1774.

46. Osman M.B., Diallo-Garcia S., Herledan V., Brouri D., Toshioka T., Kubo J., Millot Y., Costentin G., Discrimination of surface and bulk structure of crystalline hydroxyapatite nanoparticles by NMR, *Journal of Physical Chemistry C* (**2015**), *119*, 23008–23020.
DOI:10.1021/acs.jpcc.5b08732.

47. Bertran O., Revilla-López G., Casanovas J., del Valle L.J., Turon P., Puiggalí J., Alemán C., Dissolving hydroxyolite: A DNA molecule into its hydroxyapatite mold, *Chemistry - A European Journal* (**2016**), *22*, 6631–6636.
DOI:10.1002/chem.201600703.

48. Gittings J.P., Bowen C.R., Dent A.C.E., Turner I.G., Baxter F.R., Chaudhuri J.B., Electrical characterization of hydroxyapatite-based bioceramics, *Acta Biomaterialia* (**2009**), *5*, 743–754.
DOI:10.1016/j.actbio.2008.08.012.

49. Lukic M.J., Jovalekic C., Markovic S., Uskolovic D., Enhanced high-temperature electrical response of hydroxyapatite upon grain size refinement, *Materials Research Bulletin*, (**2014**), *61*, 534–538.
DOI:10.1016/j.materresbull.2014.10.072

V.6. Enclosure B. Additional Information

Table Ann.V.S1. Ca, P, O, Na and N concentration (wt %) and Ca/P molar ratios determined by XPS of cHAP/p, cHAp/s and cHAp/tsp samples before and after incubation in presence of $P_2O_7^{4-}$, $P_3O_{10}^{5-}$ and ATMP.

	Ca (wt.%)	P (wt.%)	O (wt.%)	Na (wt.%)	N (wt.%)	Ca/P (molar)
cHAp/p	38.76	18.09	42.86	0.00	0.29 [a]	1.66
cHAp/s	39.76	19.01	40.95	0.00	0.28 [a]	1.62
cHAp/tsp	40.12	18.95	40.53	0.00	0.40 [a]	1.64
cHAp/s+ $P_2O_7^{4-}$	39.67	22.76	31.67	5.58	0.32	1.59
cHAp/s+ $P_3O_{10}^{5-}$	38.76	18.95	35.62	6.38	0.29	1.32
cHAp/s+ATMP	39.23	19.27	38.32	0.00	3.18 [b]	1.48
cHAp/tsp+ $P_2O_7^{4-}$	39.54	22.56	25.64	11.91	0.35	1.35
cHAp/tsp+ $P_3O_{10}^{5-}$	40.03	27.34	22.58	9.84	0.21	1.13
cHAp/tsp+ATMP	39.12	24.08	32.72	0.00	4.08 [b]	1.26

[a] The nitrogen found in cHAp/p, cHAp/s and cHAp/tsp is due to the adsorption of N_2 from the atmosphere. The nitrogen found in the cHAp/s+ATMP and cHAp/tsp+ATMP samples predominantly is due to the ATMP.

Table Ann.V.S2. Data of EIS results obtained from the electrical equivalent circuit (EEC) showed in the Figure Ann.V5b for cHAp/s and cHAp/tsp dry discs after adsorption of $P_2O_7^{4-}$, $P_3O_{10}^{5-}$ and ATMP.

Samples	R_b (Ω cm^2)	Q_{dl} (F cm^{-2} s^{n-1})	n	Q_b (F cm^{-2} s^{n-1})	n
cHAp/s + $P_3O_{10}^{5-}$	0.42 M	5.076×10^{-8}	0.81	1.573×10^{-5}	0.43
cHAp/s + $P_2O_7^{4-}$	1.00 M	3.647×10^{-8}	0.73	1.309×10^{-5}	0.50
cHAp/s + ATMP	0.95 M	2.159×10^{-8}	0.76	1.009×10^{-5}	0.42
cHAp/tsp + $P_3O_{10}^{5-}$	66.7 k	5.550×10^{-8}	0.81	7.792×10^{-4}	0.63
cHAp/tsp + $P_2O_7^{4-}$	0.35 M	1.373×10^{-8}	0.79	3.812×10^{-5}	0.49
cHAp/tsp + ATMP	69.9 k	5.699×10^{-8}	0.73	5.204×10^{-5}	0.48

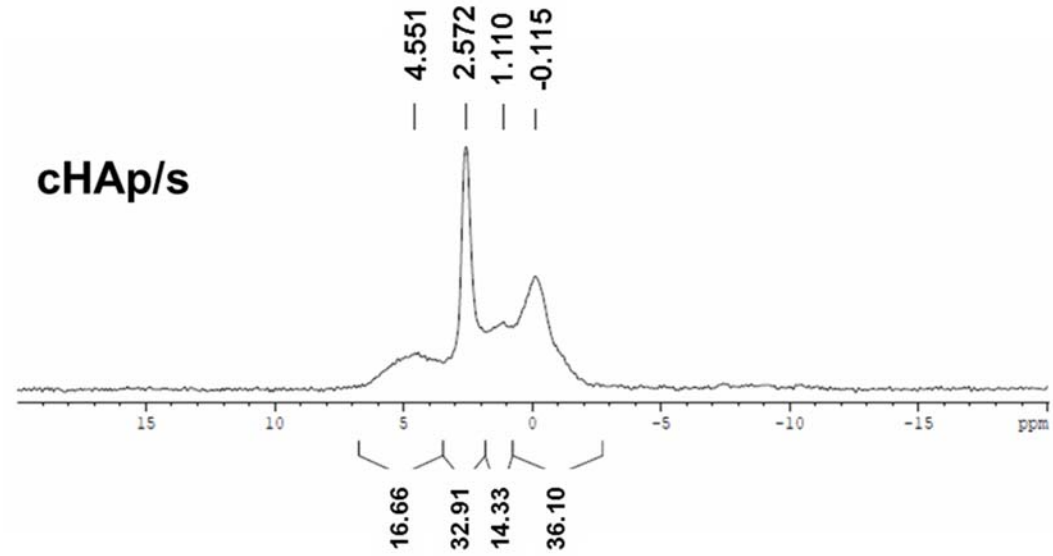

Figure Ann.V.S1. Solid state ^{31}P NMR spectrum of cHAp/s.

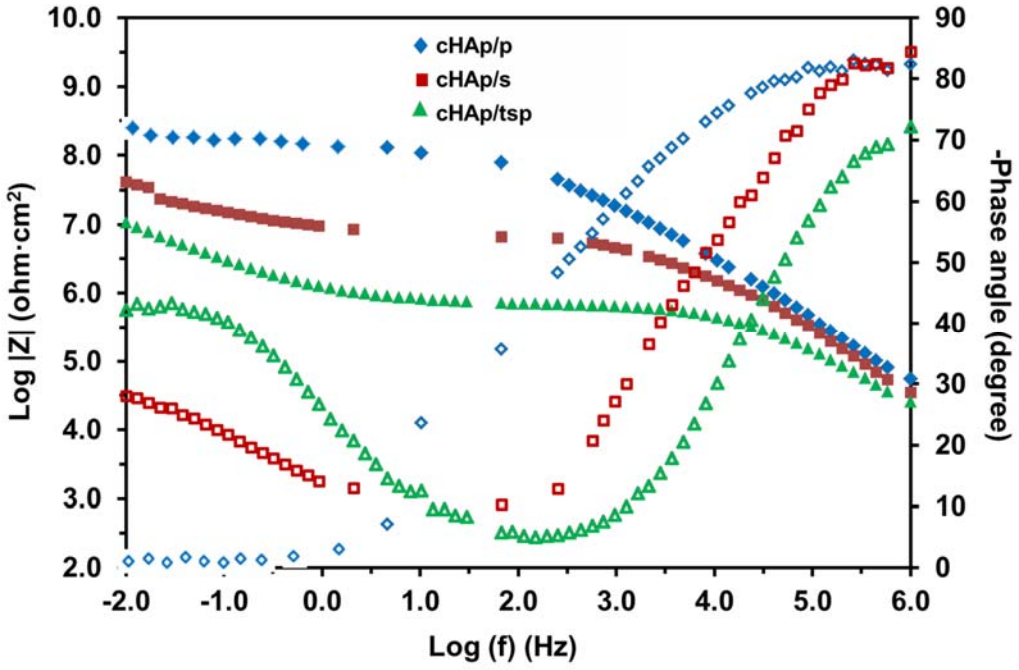

Figure Ann.V.S2. Bode plots for cHAp/p, cHAp/s and cHAp/tsp. Open symbols correspond to phase angle values whereas solid symbols correspond to Log|Z.

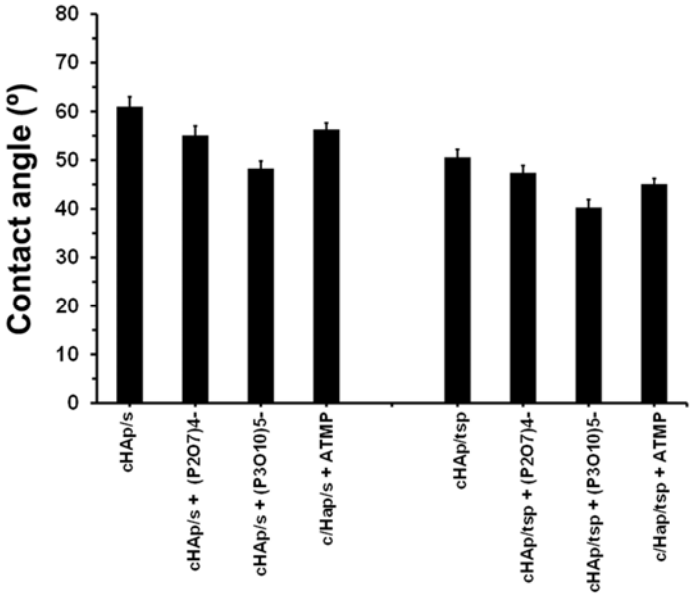

Figure Ann.V.S3. Contact angle of fetal bovine serum on cHAp/s and cHAp/tsp substrates before and after incubation with $P_2O_7^{4-}$, $P_3O_{10}^{5-}$ and ATMP solutions at neutral pH.

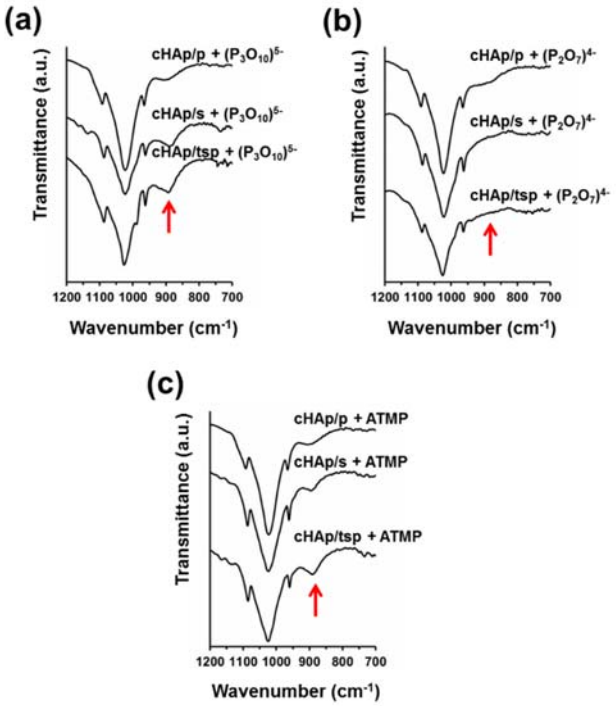

Figure Ann.V.S4. FTIR spectra of cHAp/p, cHAp/s and cHAp/tsp incubated in presence of (a) $P_3O_{10}^{5-}$ (200 mM), (b) $P_2O_7^{4-}$ (100 mM) and (c) ATMP (200 mM) at pH 7. Arrows indicate the position of the bands and shoulder used to identify the adsorption of the different adsorbates.

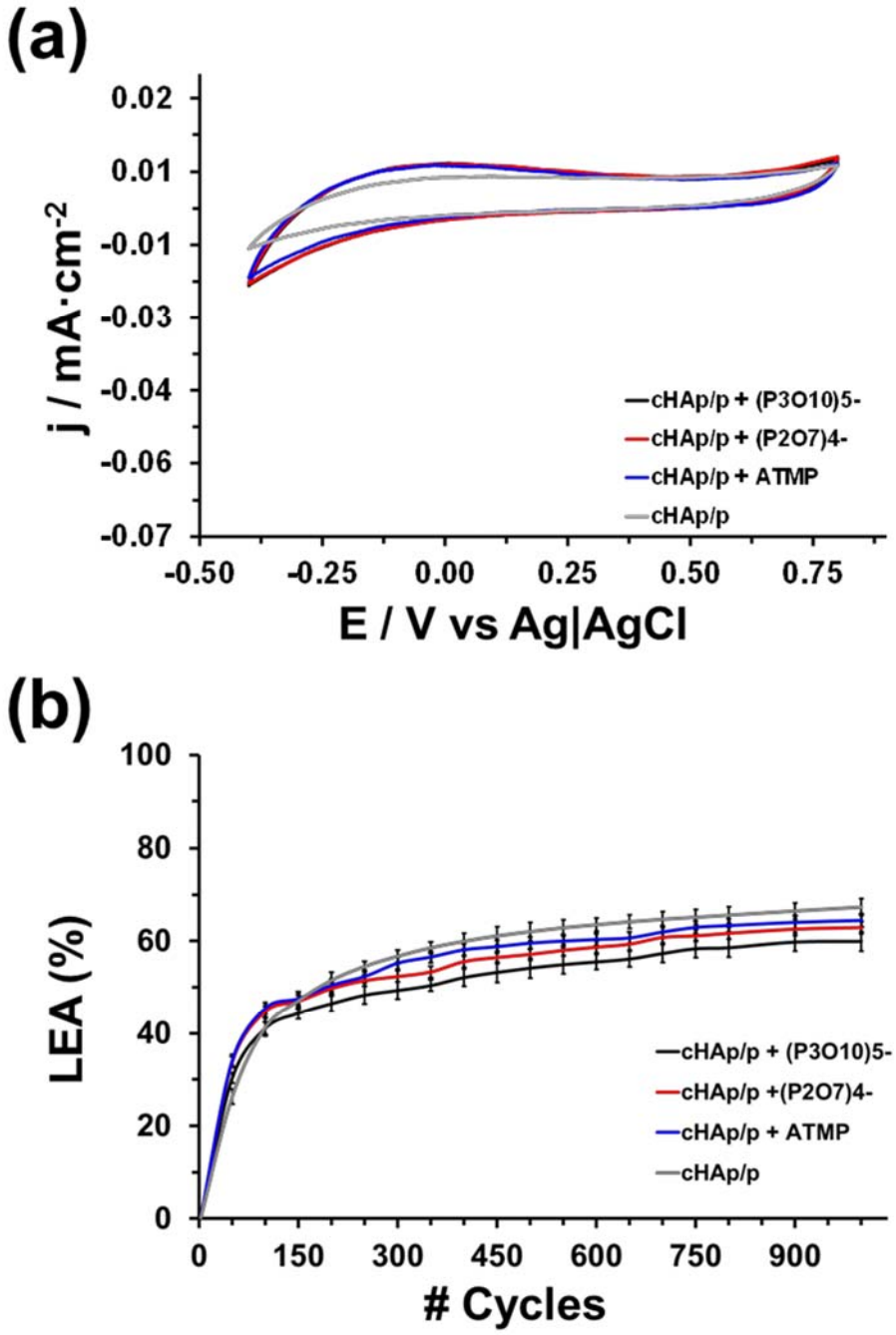

Figure Ann.V.S5. (a) Control voltammograms and (b) variation of the loss of electroactivity (LEA; Eqn S1) with the number of consecutive oxidation-reduction cycles in PBS for non-incubated and incubated cHAp/p samples.

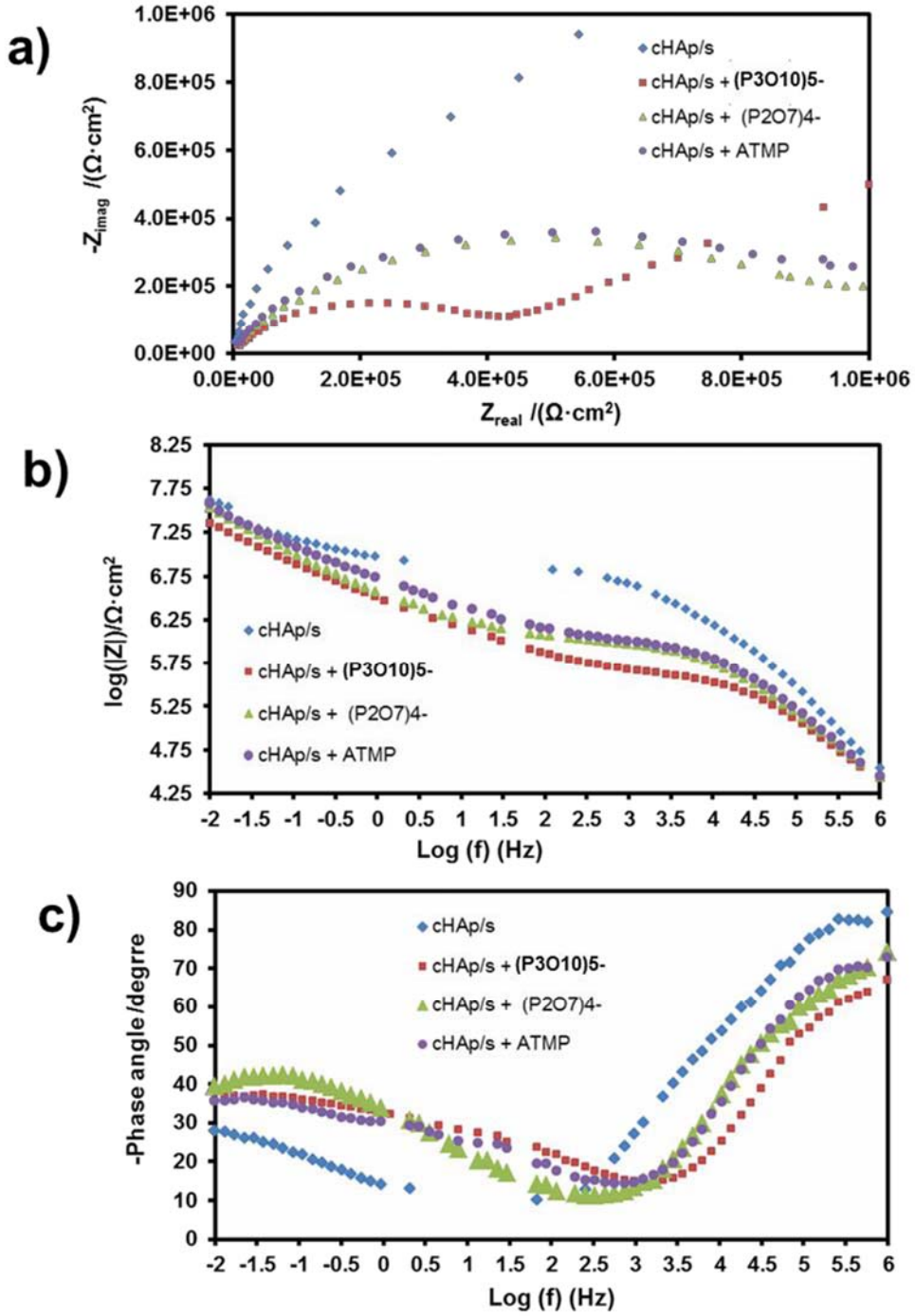

Figure Ann.V.S6. (a) Nyquist, (b) log |Z| and (c) phase angle plots for cHAp/s before and after incubation with $P_3O_{10}^{5-}$, $P_2O_7^{4-}$and ATMP.

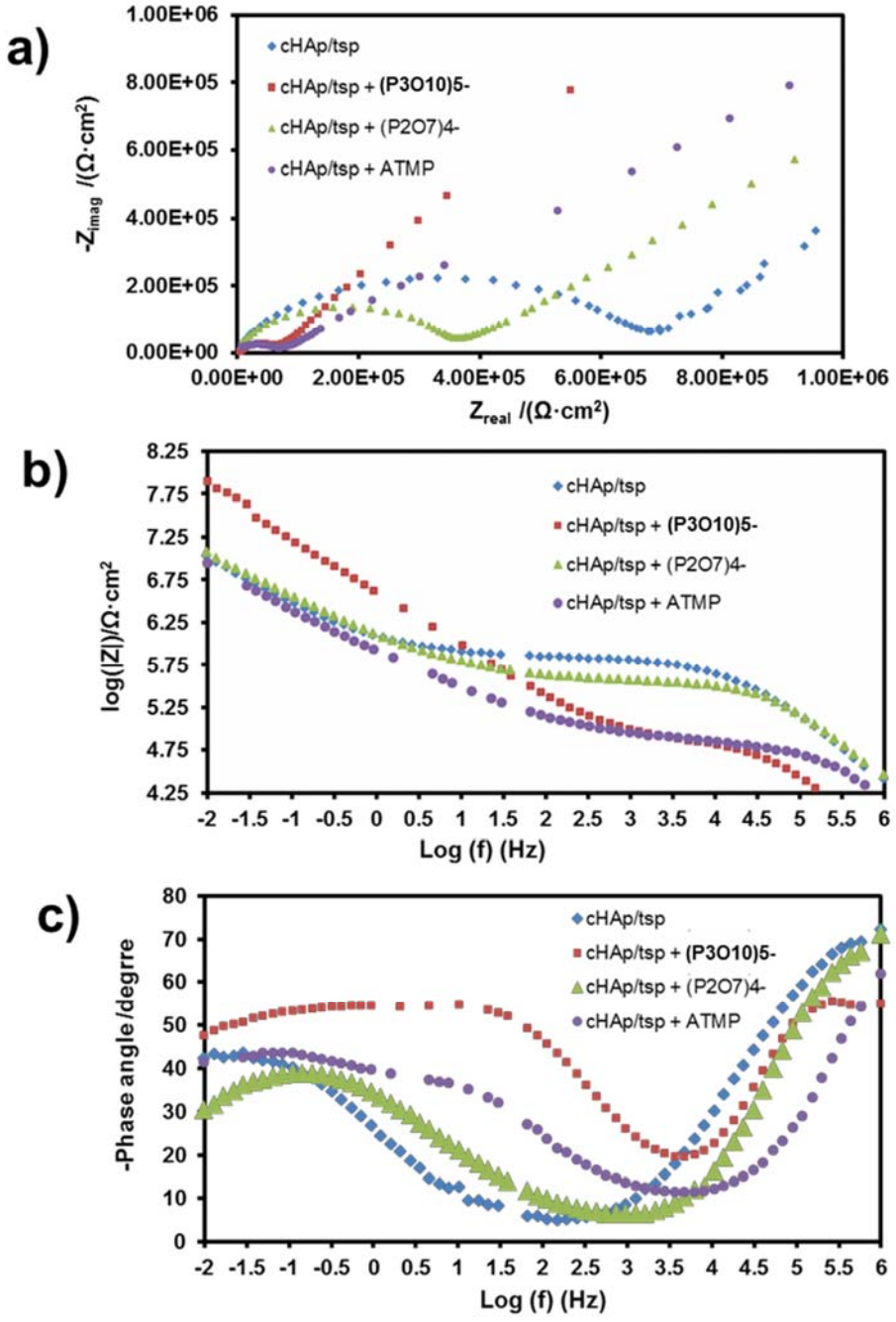

Figure Ann.V.S7. (a) Nyquist, (b) log |Z| and (c) phase angle plots for cHAp/tsp before and after incubation with $P_3O_{10}^{5-}$, $P_2O_7^{4-}$ and ATMP.

Annex VI

Sustainable synthesis of amino acids by catalytic fixation of molecular dinitrogen and carbon dioxide[7]

Abstract

The industrial process of nitrogen fixation is complex and results in a huge economic and environmental impact. It requires a catalyst and high temperature and pressure to induce the rupture of the strong N–N bond and subsequent hydrogenation. On the other hand, carbon dioxide removal from the atmosphere has become a priority objective due to the high amount of global carbon dioxide emissions (i.e. 36,200 million tons in 2015). In this work, we fix nitrogen from N_2 and carbon from CO_2 and CH_4 to obtain both glycine and alanine (D/L racemic mixture), the two simplest amino acids. The synthesis, catalyzed by polarized hydroxyapatite under UV light irradiation and conducted in an inert reaction chamber, starts from a simple gas mixture containing N_2, CO_2, CH_4 and H_2O and uses mild reaction conditions. At atmospheric pressure and 95 °C, the glycine and alanine molar yields with respect to CH_4 or CO_2 are about 1.9% and 1.6%, respectively, but they grow to 3.4% and 2.4%, when the pressure increases to 6 bar and the temperature is maintained at 95 °C. Besides, the minimum temperature required for the successful production of detectable amounts of amino acids is 75 °C. Accordingly, an artificial photosynthetic process has been developed by using an electrophotocatalyst based on hydroxyapatite thermally and electrically stimulated and coated with zirconyl chloride and a phosphonate. The synthesis of amino acids by direct fixation of nitrogen and carbon from gas mixtures opens new avenues regarding the nitrogen fixation for industrial purposes and the recycling of carbon dioxide.

---

[7] Published in Rivas M., del Valle L.J., Turon P., Alemán C., Puiggalí J., Sustainable synthesis of amino acids by catalytic fixation of molecular dinitrogen and carbon dioxide. *Green Chemistry* (**2018**), *20*, 685–693. Reproduced with permission of Royal Society of Chemistry.

Annex VI

Sustainable synthesis of amino acids by catalytic fixation of molecular dinitrogen and carbon dioxide

VI.1. Introduction

Nitrogen fixation is an extremely relevant process from an industrial perspective.[1] It is difficult to overestimate the impact of the Haber–Bosch process that yields ammonia and further results in more than 450 million tons of fertilizers per year, using more than 1% of the global energy supply.[2] Moreover, the synthesis of ammonia from nitrogen is constantly under research and only in the last decade new catalysts based on ruthenium and zirconium have been developed.[3] However, the environmental impact of the Haber– Bosch process is not negligible as natural gas or coal is used as an energy source (i.e. 1.87 tons of CO_2 are released per ton of ammonia produced and globally 245 million tons of CO_2 were released by the ammonia industry in 2010, equivalent to about 50% of the UK CO_2 emissions).[4] Thus, the outstanding benefits of nitrogen fixation are shadowed by their impact on environmental contamination. Furthermore, the catalytic reduction of dinitrogen under mild conditions has been achieved by using molybdenum catalysts. Shilov, in the 1980s, obtained a mixture of hydrazine and ammonia[5] and Schrock and co-workers[6,7] converted dinitrogen into ammonia with excellent yield using protons and electrons. Very recently, Kuriyama et al.[8] reported the catalytic reduction of molecular dinitrogen into ammonia and hydrazine by using iron complexes bearing an anionic ligand as catalysts under mild reaction conditions. However, to our knowledge, the nitrogen fixation into amino acids (AAs) using hydroxyapatite (HAp) has not been reported yet.

On the other hand, CO_2 recycling is an absolute necessity for our society knowing that its accumulation in the atmosphere is now approaching 1 Tera ton.[9] Significant steps have been taken towards the utilization of CO_2 in order to convert it into valuable chemicals (150 Mt urea, 100 Mt methanol, 70 Mt salicylic acid, 9.7 Mt formaldehyde and 0.7 Mt formic acid are the most produced).[10–12] In the last few years, catalytic reactions via carbon dioxide fixation have gained a prominent role as representative green processes with enhanced

sustainability.[13–16] However, by learning from nature, photosynthesis as performed by living organisms is the carbon fixation process par excellence. Efforts to mimic it synthetically have been elusive through time. The development of photosynthetic processes requires significant advances in new materials for light harvesting and the development of fast, stable, and efficient electrocatalysts.[17,18]

In this work, we introduce a new catalyst based on permanently polarized crystalline hydroxyapatite (p-cHAp) with enhanced electrical and photochemical properties that allows the coupling of nitrogen and carbon fixation processes. Such a catalyst family opens an interesting field of research where simple gas mixtures that usually do not react among themselves are combined to yield basic organic molecules, such as AAs, one of the main building blocks of life. More specifically, in this work we prove that glycine (Gly) and alanine (Ala) are produced at atmospheric pressure through an artificial photosynthetic nitrogen and carbon fixation reaction, starting from a weakly reducing atmosphere (N_2, H_2O, CO_2 and CH_4) and using UV radiation as a source of energy. This reaction represents a very simple alternative to the costly chemical and enzymatic processes used to produce commercially Gly and Ala.

VI.2. Experimental methods

VI.2.1. Preparation of polarized hydroxyapatite

The synthesis and characterization of aHAp and cHAp are described in detail in the Enclosure B. The sintering of aHAp, cHAp, montmorillonite and mica powders was carried out by heating them at 1000 °C for 2 h under air. After this, the samples were uniaxially pressed at 620 MPa for 10 min. Discs of 100 mm diameter, 1.7 mm thickness and sufficient mechanical consistence were finally obtained for all sintered materials (s-aHAp, s-cHAp, s-Nanofil 757 and s-LM).

In order to get thermally and electrically stimulated minerals, preliminary assays were performed with s-cHAp discs using DC voltages that ranged from 250 to 2000 V. For this purpose, s-cHAp discs were sandwiched between stainless steel (AISI 304) plates, heated in a furnace to 1000 °C in air and, simultaneously, polarized for 1 h under the application of a constant DC voltage of 500 V (3 kV cm^{-1}). Subsequently, the samples were cooled to room temperature, maintaining the DC voltage. The best results, in terms of both the mechanical

consistence and maximum adsorption capacity of phosphates and phosphonates, were obtained at 500 V. After this, the discs of s-cHAp, s-aHAp, s-Nanofil 757 or s-LM were polarized using the same procedure for 1 h under the application of a constant DC voltage of 500 V, and the resultant polarized systems are denoted as p-aHAp, p-cHAp, p-N757 and p-LM, respectively.

VI.2.2. Characterization of polarized hydroxyapatite

p-cHAp samples were characterized by cyclic voltammetry (CV), wide angle X-ray diffraction (WAXD) and FTIR spectroscopy as detailed and discussed in Enclosure B.

VI.2.3. Deposition of phosphonate and zirconyl chloride layers

3-Layered systems consisting of the successive deposition of ATMP, ZC and ATMP layers (Phos-ZC-Phos) onto a mineral substrate (i.e. s-cHAp, s-aHAp, s-Nanofil 757 or s-LM before and after being subjected to the thermally stimulated polarization process) were obtained by immersion in the corresponding aqueous solutions at room temperature for 5 h. The detailed experimental conditions are described in Enclosure B.

After different trials to evaluate the influence of the content of ZC (detailed in Enclosure B.) all the results displayed in this work, including the main text, correspond to the ZC layer de- posited from a 5 mM solution (unless another concentration is explicitly indicated).

VI.2.4. Synthesis of amino acids

A high pressure stainless steel reactor was designed ad hoc and employed to perform the synthesis of amino acids (AAs). The designed reactor, which is discussed in Enclosure B was equipped with three independent inlet valves for N_2, CH_4, and CO_2 and an outlet valve to recover the gaseous reaction products. A UV lamp (GPH265T5L/4, 253.7 nm) was also placed in the middle of the reactor to irradiate the catalyst directly, the lamp being protected by a UV transparent quartz tube. All surfaces were coated with a thin film of a perfluorinated polymer in order to avoid any contact between the reaction medium and the reactor surfaces, in this way discarding other catalytic effects.

Regarding the temperature range, the reactions were performed within 75–105 °C for reaction times between 2 and 96 h. The catalyst samples weighed approximately 150 mg and

0.5 mL of de-ionized liquid water were initially incorporated into the reaction chamber, except for assessing the water effect. The chamber was extensively purged with the first selected gas in order to eliminate the initial air content (i.e. N_2 or CO_2). After this, in order to reach the target pressure with the right mixture, each selected gas was introduced to increase the reaction chamber pressure (measured at room temperature) as described in Enclosure B. The yields of AAs were determined by using the areas of ^1H NMR signals corresponding to CH_2 (Gly) and CH_3 (Ala) protons, as is described in Enclosure B.

VI.2.5. Measurements

The synthesis of AAs was routinely verified by the ninhydrin (2,2-dihydroxyindane-1,3-dione) detection test for primary amines. On the other hand, quantitative analyses were performed by NMR spectroscopy and X-ray photoelectron spectroscopy (XPS). Morphological studies were performed by scanning electron microscopy (SEM). Analysis of volatile organic compounds has been carried out by gas chromatography. The details about the equipment and experimental conditions for such analyses are provided in the Enclosure B.

VI.3. Results and discussion

The catalyst design arises from the properties induced by the thermally stimulated polarization process to cHAp (discussed below). Specifically, p-cHAp exhibits electrical and electrochemical properties, both associated with charge transport phenomena, that remain practically unaltered with time (i.e. p-cHAp is a permanent polarization mineral). In order to take advantage of p-cHAp properties, other materials were necessary to complete the whole catalytic system. Thus, the requirements of the catalyst were, on one hand, a material able to transform an energy source, as for example UV radiation, into electron/hole pairs and, on the other hand, materials to bring in contact the gases used as reactants with the catalyst (i.e. adsorb the gases), which was essential to conduct the reactions. Obviously, the success of the catalyst was also based on the fact that it could avoid unfavourable synergies among the materials when they were combined. After evaluating different options, two materials, which correspond to those presented in this work, were selected: zirconia and a phosphonic acid with chelating properties. The details about the roles played by each component of the catalytic system are given throughout the whole work.

VI.3.1. Synthesis of amino acids at atmospheric pressure from an electrophotocatalyst based on polarized hydroxyapatite.

The new catalytic system, hereafter denoted as p-cHAp/Phos- ZC-Phos, is based on p-cHAp that is, subsequently, coated with 3 layers. One of them, the intermediate coating layer, is made of zirconyl chloride (ZC), which probably hydrolyzes into zirconia, and two of them are made of amino tris(methylene phosphonic acid) (Phos). p-cHAp is a mineral with electrical and electrochemical activity obtained by applying a thermally and electrically stimulated polarization process to crystalline hydroxyapatite (cHAp). More specifically, p-cHAp is prepared using a three-step process: (1) cHAp is obtained by adding $(NH_4)_2HPO_4$ in de-ionized water to $Ca(NO_3)_2$ in ethanol, and applying hydrothermal conditions to the resulting suspension for 24 h; (2) sintered cHAp is achieved by heating the cHAp synthesized in step 1 at 1,000 °C for 2 h in air; and (3) p-cHAp was produced by sandwiching discs of sintered cHAp (step 2) between stainless steel plates and polarizing for 1 h with a constant DC field of 3 kV cm−1 at 1000 °C. The bulk resistance of p-HAp (∼105 $\Omega \cdot cm^2$) is significantly lower than that of the as- prepared HAp (∼108 $\Omega \cdot cm^2$), indicating that the ionic conductivity increases by three orders of magnitude when the thermally stimulated polarization process is applied. Moreover, the ionic conductivity is preserved for a long time (i.e. the bulk resistance increases by only 4% after 3 months). Similarly, the electrochemical activity of p-HAp is ∼150% higher than that of the as-prepared HAp, which evidences that the polarization treatment facilitates the diffusion of ions through the mineral matrix. On the other hand, the adsorption capacity of phosphonates onto p-cHAp is around four times higher than that onto cHAp, ensuring an efficient contact between the p-cHAp and the Phos-ZC-Phos 3-layer (Figure Ann.VI.1a). Besides, ZC and Phos layers have been used to adsorb the gaseous reactants, essentially N_2 and CO_2, facilitating their reactivity. The details about the preparation of the catalyst and its components are provided in Enclosure B.

The synthesis of AAs was carried out in an inert reaction chamber under a weakly reducing atmosphere constituted of N_2 (0.33 bar), CO_2 (0.33 bar), CH_4 (0.33 bar) and liquid H_2O, using an UV lamp directly irradiating the catalyst and gas mixture (Figure Ann.VI.1b). The formation of primary amines adsorbed onto the solid substrate was shown by positive ninhydrin tests through the development of purple spots inside the catalyst recovered after the reaction (Figure Ann.VI.1c, left). Amine compounds were well dissolved in an acetone solution after vigorous stirring (Figure Ann.VI.1c, middle), contrasting with the uncolored

solid and solution (Figure Ann.VI.1c, right) observed under many other assayed reaction conditions and catalytic systems (see below).

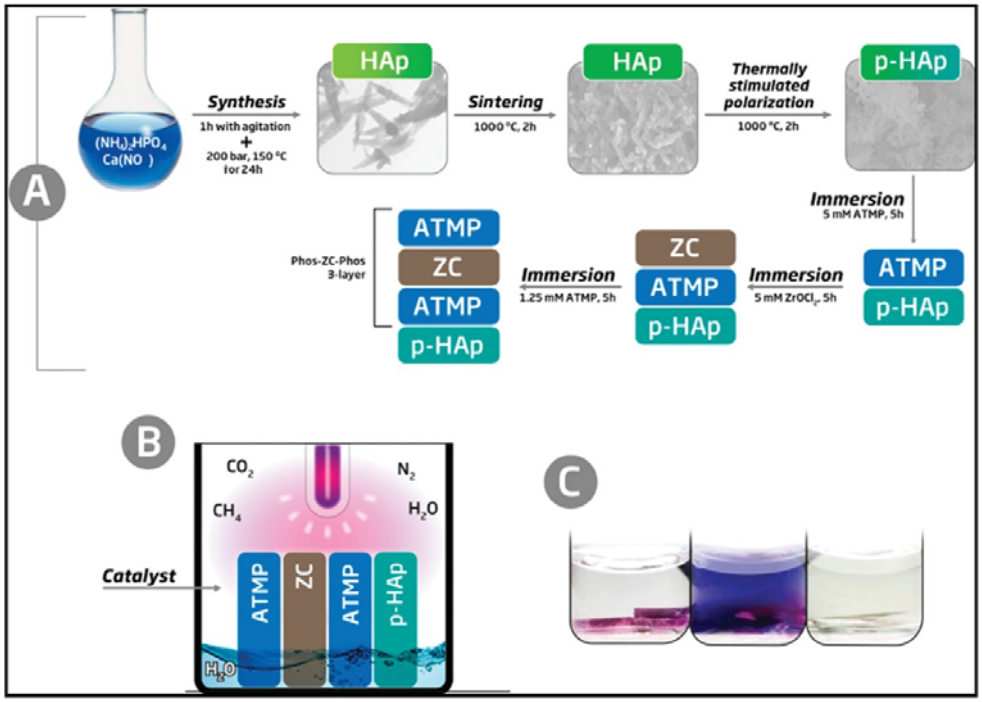

Figure Ann.VI.1. Schemes describing (a) the preparation of the p-cHAp/Phos-ZC-Phos catalytic system and (b) the reaction medium used to produce AAs. The details of the reactor are provided in Enclosure B. (c) Representative results of the ninhydrin test for a positive reaction before stirring (left) and after stirring (middle) and a negative reaction (right).

After 72 h at 95 °C, the clean synthesis of both Gly and Ala is demonstrated by the NMR spectra displayed in Figure Ann.VI.2. The ^{1}H NMR spectrum of the samples obtained by dissolving the catalyst and products of the reaction (Figure Ann.VI.2a) shows the presence of the catalyst signal corresponding to the Phos methylene group (doublet at 3.79–3.76 ppm) and the signals corresponding to the newly produced AAs such as methylene protons (singlet at 3.65 ppm) of Gly and both methine (quadruplet at 3.91–3.85 ppm) and methyl (doublet at 1.54–1.52 ppm) groups of Ala. The same compounds are also observed in the solid-state ^{13}C NMR spectrum (Figure Ann.VI.2b), where only peaks assigned to the Phos (54.34 and 53.00 ppm), Gly (171.95 and 41.26 ppm) and Ala (175.25, 50.25 and 16.01 ppm) units are detected. The ^{31}P NMR spectrum (Figure Ann.VI.2c) shows the presence of the p-HAp (7.21 ppm) and Phos (−0.03 ppm) peaks, but additional signals related to the products coming from the decomposition of the catalyst were not detected. With respect to CH_4 or

CO_2, the Gly and Ala molar yields at 95 °C after 72 h are 1.9% and 1.6%, respectively (Table Ann.VI.1). Instead, after 24 h at 95 °C no trace of Gly and Ala is detected by NMR. Furthermore, the formation of AAs is unsuccessful without the sustained exposure to the UV radiation, which appears to be a fundamental issue to generate radicals (e.g. •CH3 and •OH) needed for further reaction intermediates towards the final yielding of Ala and Gly. Photoemission spectroscopy (XPS) analyses show that the amines in AAs come from the molecular nitrogen and not from a hypothetical decomposition of the Phos. The N 1s spectra registered for different representative samples (Figure Ann.VI.3a) indicate that the peak at 399.5 eV, which is ascribed to the C–N of Phos, is observed with practically the same intensity when both negative and positive reactions (i.e. without and with sustained exposure to UV radiation) are monitored.

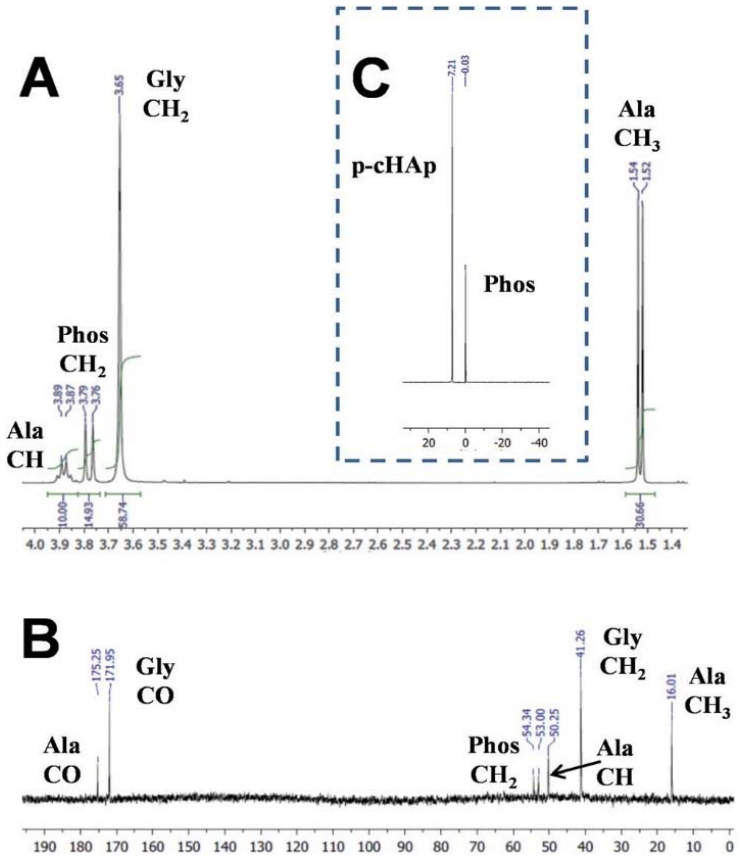

Figure Ann.VI.2. For samples obtained after the reaction (95 °C and 24 h) using a chamber pressure of 1 bar (i.e. 0.33 bar of each feeding reaction gas): (a) ^{1}H NMR spectrum of the solution obtained after the extraction of the AAs from the catalyst by dissolving the sample in deuterated water containing 100 mM of HCl and 50 mM of NaCl; and the solid state (b) ^{13}C - and (c) ^{31}P NMR spectra of the catalyst with the synthesized AAs.

However, only in the latter case bands at lower binding energies appear due to the formation of deprotonated and protonated amino groups (401.2 and 404.5 eV, respectively).[19] Furthermore, the amount of atomic nitrogen increased from 0% to 2.75–2.97% when the Phos-ZC-Phos 3-layer coating was added to the p-cHAp substrate. The nitrogen percentage, after the positive reaction, was increased up to 6.2%, which corroborates the fact that the formed AAs remain adsorbed into the catalysts.

The p-cHAp/Phos-ZC-Phos catalyst exhibits a rough and relatively irregular surface morphology (Figure Ann.VI.3b), which changed after the reaction due to the sporadic formation of micrometric prismatic crystals with the hexagonal basal plane parallel to the disk surface (Figure Ann.VI.3c). Although the ninhydrin test reflects the presence of AAs adsorbed inside the catalyst, micrographs also demonstrate the growth of AA crystals on the surface of the catalytic system. This behavior is consistent with the capacity of organophosphonate films for inducing the crystallization of oriented molecular sieves as proved by the growth of stable, vertically-oriented and one dimensional aluminum phosphate crystals.[20,21] On the other hand, the formation of AAs has also been proven by FTIR spectroscopy, which shows intense absorption bands in the amine region of the corresponding spectra, and characteristic X-ray diffraction patterns. Finally, chiral high-performance liquid chromatography (HPLC) analyses were carried out to quantify the ratio of D- and L-Ala adsorbed into the catalysts. As was expected, after dissolution of the catalysts after the reaction in a 0.1 M HCl solution with 50 mM NaCl, a racemic D-Ala : L-Ala mixture was determined.

VI.3.2. The effect of varying the pressure and the temperature

In order to increase the rate of the reaction, the chamber pressure was increased up to 6 bar by introducing 2 bar of each feeding reaction gas, while the temperature was kept fixed at 95 °C. After 24 h, the molar yields, expressed with respect to CH_4 or CO_2, are 1.9% and 1.3% for Gly and Ala, respectively (Table Ann.VI.1), which are pretty similar to those achieved at atmospheric pressure after 72 h. Moreover, at high pressure Gly and Ala molar yields increase to 3.4% and 2.4%, respectively, after 96 h. Amazingly, the reported molar yields of Gly and Ala, based on the same carbonaceous species, by the action of electric discharges on a mixture of CH_4, N_2, water and traces of ammonia were only 0.26% and

0.71%, respectively, increasing to 1.55% when the sum of the 10 produced AAs was considered.[22]

The effects of both the reaction time and the temperature in this catalytic process were studied considering a chamber pressure of 6 bar. The variation of the Gly/Phos and Ala/Phos ratios, which were determined from the areas of signals corresponding to CH_2 (Gly and Phos) and CH (Ala) protons in the ^1H NMR spectra, against the reaction time (from 2 to 96 h) reflects that Gly is produced first (Figure Ann.VI.3a), while Ala is subsequently derived from this simple AA. Thus, the Gly/Ala ratio decreases from 5.4 to 2.2, while a continuous increase of the Gly/Phos ratio with the reaction time is nevertheless observed (i.e. from 0.8 to 4.5). On the other hand, the minimum temperature required for the successful production of detectable amounts of Gly and Ala after 24 hours is 75 °C (Figure Ann.VI.3b). The Ala/Phos ratio increases progressively with the reaction temperature while the Gly/Phos ratio decreases at 105 °C due to the conversion of Gly into Ala, even though the (Gly + Ala)/Phos ratio still increases.

VI.3.3. Influence of changes in the catalytic system

Substitution of p-cHAp by p-aHAp, which is obtained by replacing cHAp by amorphous hydroxyapatite (aHAp) and by applying the same thermally and electrically stimulated polarization process, did not affect the production of AAs, even though the yield of Gly and Ala decreases to 0.92% and 0.65%, respectively (Table VI.1). The latter has been attributed to the partial thermal decomposition of aHAp during the sintering process, which gives rise to the formation of a β-tricalcium phosphate[23] causing a reduction of the electrochemical activity with respect to the samples obtained using cHAp. Conversely, negative results were obtained when p-cHAp was replaced by sintered s-cHAp (i.e. non-polarized), polarized silicates or aluminosilicates (mica), proving that the HAp and its electrochemical activity play an important role in the catalytic mechanism.

For the sake of completeness, the effectiveness of the substitution of the Phos-ZC-Phos 3-layer coating by two possible combinations of 2-layer coatings (Phos-ZC and ZC-Phos), by Phos monolayers or by a Phos/ZC mixture was also assayed. In all cases, negative results were obtained demonstrating the importance of the 3-layered architecture, and thus discarding a process based on the photodecomposition of Phos. In addition, both the capability of incorporating water molecules[24] and the effective role of metal/phosphonate

compounds as chelating ligands[25] are noteworthy due to the presence of free phosphonic acid groups. The results obtained after introducing the above-mentioned changes in the 3-layered p-HAp catalyst are summarized in Figure Ann.VI.4.

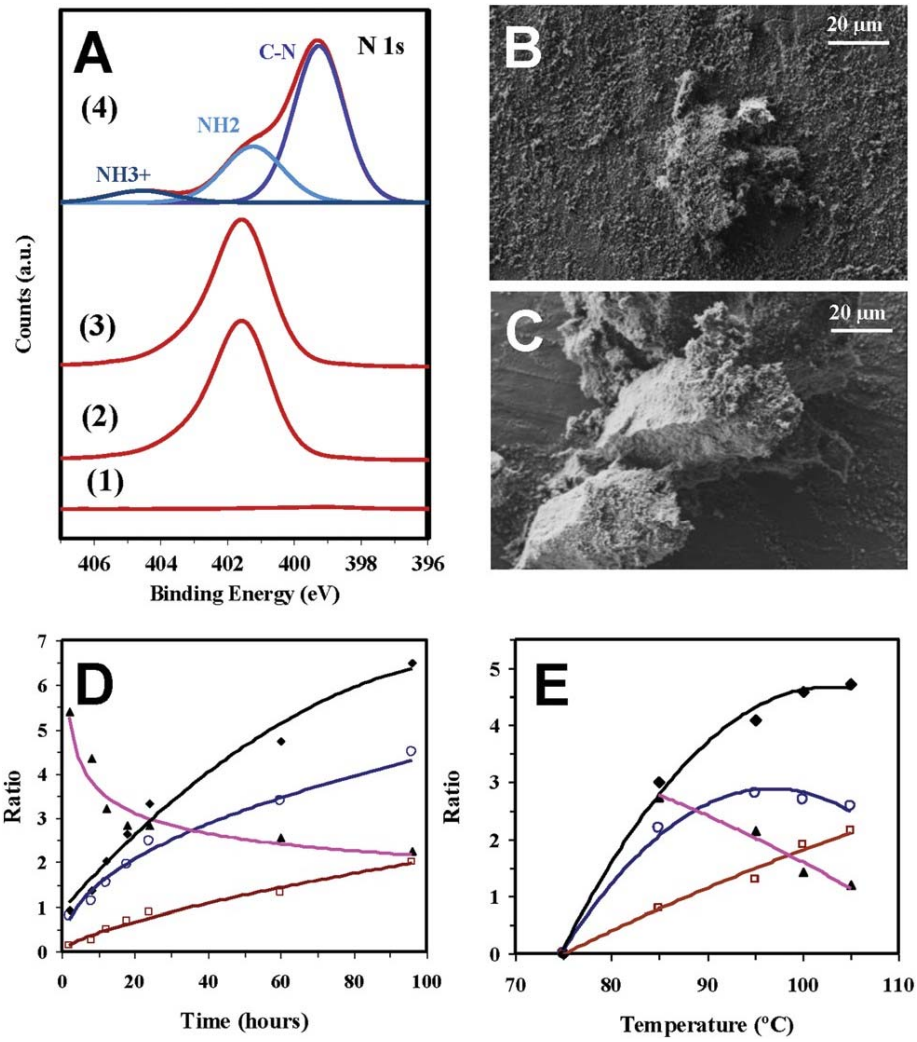

Figure Ann.VI.3. (A) N 1s high-resolution XPS spectra for (1) p-cHAp, (2) p-cHAp/Phos-ZC-Phos, and (3) p-cHAp/Phos-ZC-Phos after the negative reaction (i.e. without exposure to UV radiation) and (4) p-cHAp/Phos- ZC-Phos after the positive reaction (24 h at 95 °C). SEM micrographs before (B) and after (C) successful reaction using the p-HAp/Phos- ZC-Phos catalytic system (24 h at 95 °C). The reactions were performed at 1 bar. Variation of the Gly/Phos (○), Ala/Phos (□) (Gly + Ala)/Phos (◆) and Gly/Ala (▲) ratios versus (D) time for reactions performed at 95 °C and (E) temperature for reactions performed for 24 h using the p-cHAp/ Phos-ZC-Phos catalytic system prepared as displayed in Figure Ann.VI.1a. The reactions were performed at 6 bar.

VI.3.4. Molecular nitrogen and carbon dioxide fixation

Different experiments (Table Ann.VI.S5) have also been performed in order to determine the reactants that are essential to obtain AAs under the defined experimental conditions (UV radiation, 6 bar, 95 °C, and 24 h). The results indicate that N_2, CH_4, CO_2 and H_2O were all necessary, because the removal of any of them led to negative ninhydrin tests as well as an absence of the AA peaks in the corresponding NMR spectra (Figure Ann.VI.4.). As was expected, the yield of AAs systematically correlates with the pressure of N_2 in the reaction chamber (Table Ann.VI.1).

Table Ann.V.1. Influence of the experimental conditions (catalyst, pressure and time) in the molar yields of Gly and Ala expressed with respect to CH_4 or CO_2. The weight of AA per surface area of the catalyst is also displayed.

Experimental conditions			**Yield**	
Mineral	P (bar)	Time	Gly	Ala
p-cHAp	1[b]	24 h	-	-
p-cHAp	1[b]	72 h	1.9% (6.7 mg·cm^{-2})	1.6% (3.3 mg·cm^{-2})
p-cHAp	6[c]	24 h	1.9 % (6.6 mg·cm^{-2})	1.3% (2.7 mg·cm^{-2})
p-cHAp	6[c]	72 h	3.4 % (11.9 mg·cm^{-2})	2.4% (5.0 mg·cm^{-2})
p-aHAp	6[c]	72 h	0.9 % (3.2 mg·cm^{-2})	0.7% (1.3 mg·cm^{-2})
p-cHAp	5[d]	24 h	1.5 % (5.3 mg·cm^{-2})	0.9% (1.9 mg·cm^{-2})
p-cHAp	7[e]	24 h	2.4 % (8.3 mg·cm^{-2})	1.6% (3.3 mg·cm^{-2})

[a]Temperature was kept fixed at 95 ºC in all cases. [b]P_{N2} = 0.33 bar; P_{CH4} = 0.33 bar; P_{CO2} = 0.33 bar. [c]P_{N2} = 2 bar; P_{CH4} = 2 bar; P_{CO2} = 2 bar. [d]P_{N2} = 1 bar; P_{CH4} = 2 bar; P_{CO2} = 2 bar. [e]P_{N2} = 3 bar; P_{CH4} = 2 bar; P_{CO2} = 2 bar.

These observations support the idea that the nitrogen source for the AAs is N_2 and not Phos. Furthermore, the experiments performed without incorporating the coating to the catalyst failed to produce AAs (Table Ann.VI.S5), whilst XPS measurements evidenced that N_2 was adsorbed by the Phos layers of the coating (Table Ann.VI.S3). Altogether, these results support that the catalyst coating facilitates both the adsorption and further reactivity of N_2. This point is particularly relevant since most of the reported AA syntheses are based on ammoniacal solutions as the nitrogen source. It is well known that N_2 is fixed by means of some specific bacteria by the action of enzymes that have metal-sulfide active sites.[26] Numerous efforts have been made to develop metal-based catalysts to coordinate and activate N_2 through the formation of metal–dinitrogen complexes with limited success.[27] The

splitting of the N–N bond in bridging dinitrogen complexes was first achieved by Cummins, who showed how three-coordinate molybdenum amido-complexes react with dinitrogen at −35 °C to yield an unstable dinitrogen bridging complex that, subsequently, breaks down into two molecules of the nitride-complex.[28] Although some additional progress has been made in this area, the fixation of atmospheric N_2 remains a challenge because of the limited reactivity and the harsh conditions required to convert dinitrogen into useful nitrogen-containing organic compounds. The p-cHAp/Phos-ZC-Phos catalyst overcomes such drawbacks rendering nitrogen containing com- pounds under relatively mild reaction conditions.

Regarding carbon fixation, experiments performed without CH_4 in the initial mixture failed to produce AAs and, therefore, prove its role as a carbon source for the methyl group of Ala and for the methylene group of Gly (i.e. it again discards a synthetic route based on the decomposition of Phos). On the other hand, the carboxylic groups of the two AAs would appear to come from CO_2. The transformation of CO_2 into organic moieties under UV irradiation, mimicking photosynthesis, represents a very interesting approach for the minimization of CO_2 emissions and for developing sustainable industrial processes. Thus, the catalytic process reported in this work fulfils the very ambitious goals of artificial photosynthesis: to use earth-abundant and inexpensive materials converting them into highly appreciated organic compounds (i.e. AAs) of industrial and environmental significance. Although zirconium phosphonates are able to adsorb CO_2,[29] HAp has shown a noticeable capacity to incorporate carbonate and hydrogen carbonate from atmospheric CO_2 when dissolved in water[23,30] facilitating the formation of carboxylic groups. In this work, XPS experiments prove that both the p-cHAp substrate and the ZC layer are responsible for the CO_2 adsorption onto the catalyst, while Phos layers do not contribute.

Finally, water also displays a fundamental role in the synthesis of AAs (Figure Ann.VI.4.). In fact, water molecules do not appear as an element source of AAs, but they have a significant influence on the mechanism contributing to the formation of $^{\bullet}OH$ radicals and dissolving CO_2. Furthermore, hydration of Phos layers is also expected to play a major role in ionic mobility through such Phos layers.[31]

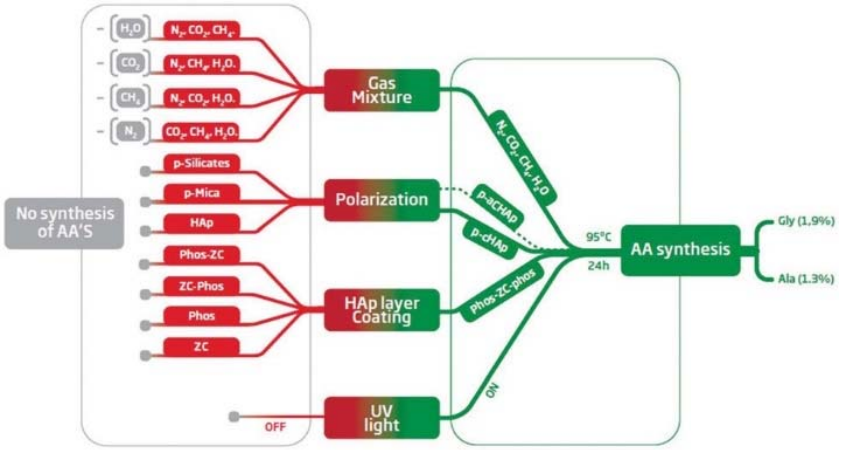

Figure Ann.VI.4. Summary of the results obtained using different experimental conditions: green and red boxes refer to the successful and unsuccessful production of AAs, respectively. The details about the 16 different experimental conditions are provided in the Enclosure B.

VI.2.5. Mechanism

Similar syntheses of AAs (mainly Gly and Ala) have been demonstrated when ammoniacal solutions saturated with methane were exposed to near-UV irradiation ($\lambda < 405$ nm) and even natural sunlight in the presence of the catalyst platinized TiO_2 powder.[32,33] The total yield of AAs after 72 h of irradiation with a xenon lamp was 472 nmol and after 312 h of exposure to sunlight was 2,140 nmol, which represented a very low conversion (molar yield: <0.01%).[32] The reaction mechanism proposed in this case was based on the electron/hole (e^-/h^+) pair produced when TiO_2 was irradiated with light having a higher energy of its band gap. However, the results were negative when CO_2 was employed as a carbon source instead of CH_4. The present work reveals an alternative way by obtaining organic nitrogen from molecular nitrogen instead of ammonia.

Our first hypothesis for the reaction mechanism of the processes presented in this work is the occurrence of water-splitting photocatalysis on the surface of p-cHAp, in a way that resembles the one on TiO_2 electrodes earlier reported by Fujishima and Honda.[34] Thus, the reaction is not successful without water, which is consistent with the fact that water plays an important role in the mechanism. The hydroxyl radical (•OH) photoproduction on those mineral surfaces is a well-known process that can be described as follows.[35] The photon energy is adsorbed and electrons are excited to the conduction band, leaving holes in the

valence band (h^+). These electron–hole pairs travel to the surface of the substrate to participate in water splitting. Thus, the transfer of electrons from water molecules to valence band holes forms $^{\bullet}OH$ (eqn (1)), whereas in the corresponding reductive reaction the transfer of electrons to O_2 molecules forms superoxide radical anions ($^{\bullet}O^{2-}$).

$$H_2O + h^+ \rightarrow {}^{\bullet}OH + H^+ \qquad \text{(VI.1)}$$

Because of the electrical properties of p-cHAp, we have hypothesized a similar process for the water photolysis on this mineral, regardless of the possible variations in the intermediate stages of the photooxidation and photoreduction reactions. It is worth noting that p-cHAp presents vacancies that originate from the transformation of hydrogen phosphate into phosphate during the thermally stimulated polarization process, as proved by NMR experiments. Therefore, its catalytic role should be comparable to that of activated TiO_2 surfaces.

Furthermore, Nishikawa[36] demonstrated that, after heat treatment, HAp becomes electroconductive by UV irradiation, leading to the formation of stable but very reactive $^{\bullet}O^{2-}$ by altering its own PO_4^{3-} groups. These features together with the electrochemical activity of p-cHAp, in combination with the Phos-ZC-Phos layers could produce an electrochemical capacitor,[37] explaining the electrophotocatalytic activation of the p-cHAp/Phos-ZC-Phos system. Accordingly, the mobility of $^{\bullet}O^{2-}$, which may produce $^{\bullet}OH$ in an aqueous environment, H^+ and vacancies could be the driving forces of this electrochemical mechanism. The high electrochemical activity of p-cHAp in comparison with the as-prepared and sintered cHAp is proved in Figure Ann.V.5., which presents the voltammetric charge per surface unit (Q) against the number of consecutive oxidation–reduction cycles. As can be seen, Q is significantly higher for p-HAp than for the two non-polarized samples, such a difference increasing with the number of redox processes.

As the hydroxyl radicals are very oxidative in nature, we suggest several possible reaction steps that could lead to the production of carbonaceous intermediates required for the production of Gly and Ala:

$$CH_4 + {}^{\bullet}OH \rightarrow {}^{\bullet}CH_3 + H_2O \qquad \text{(VI.2)}$$

$$^{\bullet}CH_3 + {}^{\bullet}OH \rightarrow :CH_2 + H_2O \qquad \text{(VI.3)}$$

On the other hand, the one electron reduction of CO_2 into its radical anion, $^{\bullet}CO_2^-$, is proposed as a net electron transfer process possible at the interface between p-cHAp and Phos-ZC-Phos:

$$CO_2 + e^- \rightarrow {}^{\bullet}CO_2^- \qquad \text{(VI.4)}$$

Although this process is expected to be disfavored, because of both the thermodynamic stability of CO_2 and the energy required for a stereochemical change in the geometry from a linear to a bent configuration, it has frequently been observed on HAp surfaces.[23,30] This step is consistent with the analysis of volatile compounds, which revealed the formation of small amounts of aldehydes. Thus, around 600 $\mu g \cdot m^{-3}$ of acetaldehyde and 90 $\mu g \cdot m^{-3}$ of formaldehyde were detected after 16 h of reaction at 95 °C.

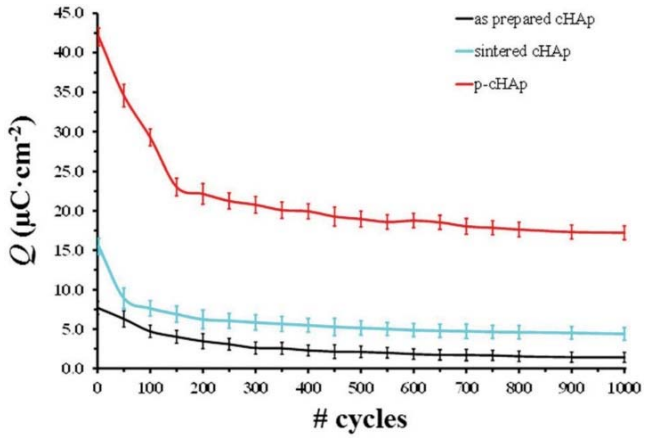

Figure Ann.VI.5. Variation of the electroactivity (voltammetric charge stored for reversible exchange in a redox cycle) of the as-prepared cHAp, sintered cHAp and p-HAp. In all cases, electroactivity measurements are expressed as voltammetric charge per surface unit (Q).

Besides, a number of mechanisms have been reported to explain the electrochemical transformation of N_2 into NH_3 through different steps that involve the N–N cleavage and the N protonation onto the catalyst surface.[38] Within this context, such a transformation could follow associative or dissociative mechanisms. In the associative mechanism, N_2 molecules adsorbed onto the catalysts are protonated sequentially without breaking the N–N bond until the first NH_3 molecule is produced, as occurs in the reaction of N_2-fixing by enzymes;[39]

while in the dissociative mechanism, the N_2 molecules dissociate immediately and nitrogen radicals are protonated as they are in the Haber–Bosch process.[40] After this the resulting NH_3 may be easily oxidized by $^{\bullet}OH$ to form $^{\bullet}NH_2$.[41] Then, Gly may be produced in the successive free-radical reactions involving $^{\bullet}NH_2$, $^{\bullet}CO_2^-$ and $^{\bullet}CH_3$ and the intermediate species. Finally, the transformation of Gly into Ala is possibly due to the -H-($C^{\alpha}H$) electrochemical removal and subsequent reaction with $^{\bullet}CH_3$.

VI.4. Conclusions

In summary, AAs are produced by using a new process based on electrophotosynthesis which uses a simple gas mixture. The process is able to fix nitrogen and carbon dioxide into organic species under mild reaction conditions, becoming an efficient and environmentally friendly synthesis. The newly developed electrophotocatalyst enhances the catalytic properties of cHAp to the extent that artificial photosynthesis is achieved, thus opening a new era in the treatment of contaminated atmospheres and nitrogen fixation research.

VI.5. References

1. Editorial comment, The Nitrogen Fix, *Nature* (**2013**), *501*, 6–6. DOI:10.1038/501006a.

2. Smith B.E., Nitrogenase reveals its inner secrets, *Science* (**2002**), *297*, 1654–1655. DOI:10.1126/science.1076659.

3. Macleod K.C., Holland P.L., Recent developments in the homogeneous reduction of dinitrogen by molybdenum and iron, *Nature Chemistry* (**2013**), *5*, 559–565. DOI:10.1038/nchem.1620.

4. Lan R., Irvine J.T.S., Tao S., Synthesis of ammonia directly from air and water at ambient temperature and pressure, *Scientific Reports* (**2013**), *3*, 1145. DOI:10.1038/srep01145.

5. Shilov A.E., Catalytic reduction of molecular nitrogen in solutions, *Russian Chemical Bulletin International Edition* (**2003**), *52*, 2555–2562. DOI: 10.1023/B:RUCB.0000019873.81002.60.

6. Yandulov D.V., Schrock R.R., Catalytic reduction of dinitrogen to ammonia at a single molybdenum center, *Science* (**2003**), *301*, 76–78. DOI:10.1126/science.1085326.

7. Schrock R.R., Reduction of dinitrogen, *Proceedings of National Academy of Sciencies. U. S. A.* (**2006**), *103*, 17087–17087. DOI:10.1073/pnas.0603633103.

8. Kuriyama S., Arashiba K., Nakajima K., Matsuo Y., Tanaka H., Ishii K.,Yoshizawa K., Catalytic transformation of dinitrogen into ammonia and hydrazine by iron-dinitrogen complexes bearing pincer ligand, *Nature Communications* (**2016**), *7*, 12181. DOI: 10.1038/ncomms12181.

9. Mikkelsen M., Jorgensen M., Krebs F.C., Synthesis and characterization of zwitterionic carbon dioxide fixing reagents, *International Journal of Greenhouse Gas Control* (**2010**), *4,* 452–458. DOI:10.1016/j.ijggc.2009.11.008.

10. Alper E., Orhan O.Y., CO_2 utilization: Developments in conversion processes, *Petroleum* (**2017**), *3*, 109–126. DOI:10.1016/j.petlm.2016.11.003.

11. Ola O., Maroto-Valer M.M., Mackintosh S., Turning CO_2 into valuable chemicals, *Energy Procedia* (**2013**), *37*, 6704–6709. DOI:10.1016/j.egypro.2013.06.603.

12. Aresta M., Dibenedetto A., Utilisation of CO_2 as a chemical feedstock opportunities and challenges, *Dalton Transactions* (**2007**), *28*, 2975–2992. DOI:10.1039/B700658F.

13. Song Q-W., Zhou Z-H., He L-N., Efficient, selective and sustainable catalysis of carbon dioxide, *Green Chemistry* (**2017**), *19*, 3707–3728.
DOI:10.1039/C7GC00199A.

14. Zhao B., Su Y., Process effect of microalgal-carbon dioxide fixation and biomass production: A review, *Renewable Sustainable Energy Reviews* (**2014**), *31*, 121–132.
DOI:10.1016/j.rser.2013.11.054.

15. Fleischer M., Blattmann H., Mülhaupt R., Glycerol-, pentaerythritol- and trimetylolpropane based polyurethanes and their cellulose carbonate composites prepared via the non-isocyanate route with catalytic carbon dioxide fixation, *Green Chemistry* (**2013**), *15*, 934–942.
DOI:10.1039/C3GC00078H.

16. Molla R.A., Iqubal Md. A., Ghosh K., Islam S.M., A route for direct transformation of aryl halides to benzyl alcohols via carbon dioxide fixation reaction catalyzed by a (Pd@N-GMC) palladium nanoparticle encapsulated nitrogen doped mesoporous carbon material, *Green Chemistry* (**2016**), *18*, 4649–4656.
DOI:10.1039/C6GC01038E.

17. Bar-Even A,, Noor E., Lewis N.E., Milo R., Design and analysis of synthetic carbon fixation pathways, *Proceedings of National Academy of Sciences. U. S. A*. (**2010**), *107*, 8889–8894.
DOI:10.1073/pnas.0907176107.

18. Dubois M.R., Dubois D.L., Development of molecular electrocatalysts for CO_2 reduction and H_2 production/oxidation, *Accounts of Chemical Research* (**2009**), *42*, 1974–1982.
DOI: 10.1021/ar900110c.

19. Tzvetkov G., Netzer F.P., Synchrotron X-ray photoemission study of soft X-ray processed ultrathin glycine- water ice films, *The Journal of Chemical Physics* (**2011**), *134*, 204704.
DOI:10.1063/1.3591337.

20. Feng S., Bein T., Growth of oriented molecular sieve crystals on organophosphonate films, *Nature* (**1994**), *368*, 834–836.
DOI:10.1038/368834a0.

21. Feng S., Bein T., Vertical aluminophosphate molecular sieve crystals grown at inorganic-organic interfaces, *Science* (**1994**), *265*, 1839–1841.
DOI: 10.1126/science.265.5180.1839.

22. Ring D., Wolman Y., Friedman N., Miller S.L., Prebiotic synthesis of hydrophobic and protein amino acids, *Proceedings of National Academy of Sciences U. S. A*. (**1972**), *69*, 765–768.
DOI:10.1073/pnas.69.3.765.

23. Bertran O., del Valle L.J., Revilla-López G., Rivas M., Chaves G., Casas M.T., Casanovas J., Turon P., Puiggalí J. Alemán C., Synergistic approach to elucidate the incorporation of magnesium ions into hydroxyapatite, *Chemistry – A European Journal* (**2015**), *21*, 2537–2546.
DOI:10.1002/chem.201405428.

24. Shah B., Chudasam U., Application of zirconium phosphonate - A novel hybrid material as an ion exchanger, *Desalinization and Water Treatment* (**2012**), *38*, 227–235.
DOI:10.1080/19443994.2012.664384.

25. Griffith C.S., De Los Reyes M., Scales N., Hanna J.V., Luca V., Hybrid inorganic-organic adsorbents. Part 1: Synthesis and characterization of mesoporous zirconium titanate frameworks containing coordinating organic functionalities, *ACS Applied Materials and Interfaces* (**2010**), *2*, 3436–3446.
DOI:10.1021/am100891u.

26. Thorneley R.N.F., New light on nitrogenase, *Nature* (**1992**), *360*, 553–560.
DOI:10.1038/360532a0.

27. Andino J.G., Mazumder S., Pal K., Caulton K.G., New approaches to functionalizing metal-coordinates N_2, *Angewandte Chemie, International Edition* (**2013**), *52*, 4726–4732.
DOI:10.1002/anie.201209168.

28. Laplaza C.E., Johnson M.J.A., Peters J.C., Odom A.L., Kim E., Cummins C.C., George G.N., Pickering I.J., Dinitrogen cleavage by three-coordinate molybdenum(III) complexes: Mechanistic and structural data, *Journal of American Chemical Society* (**1996**), *118*, 8623–8638.
DOI:

29. Lin X-Z., Yang Z-Z., He L-N, Yuan Z-Y., Mesoporous zirconium phosphonates as efficient catalysts for chemical CO_2 fixation, *Green Chemistry* (**2015**), *17*, 795–798.
DOI:10.1039/C4GC01709A.

30. Bertran O., del Valle L.J., Revilla-López G., Chaves G., Cardus L., Casas M.T., Casanovas J., Turon P., Puiggalí J., Alemán C., Mineralization of DNA into nanoparticles of hydroxyapatite, *Dalton Transactions* (**2014**), *43*, 317 –327.
DOI: 10.1039/C3DT52112E.

31. Katz H.E., Schilling M.L., Electrical properties of multilayers based on zirconium phosphate/phosphonate bonds, *Chemistry of Materials* (**1993**), 5, 1162–1166.
DOI: 10.1021/cm00032a021.

32. Reiche H., Bard A.J, Heterogeneous photosynthetic production of amino acids from methane-ammonia-water at platinum/titanium dioxide. Implications in chemical evolution*, Journal of American Chemical Society* (**1979**), *101*, 3127–3128.
DOI:10.1021/ja00505a054.

33. Dunn W.W., Aikawa Y., Bard A.J., Heterogeneous photosynthetic production of amino acids at Pt/TiO_2 suspensions by near ultraviolet light, *Journal of American Chemical Society* (**1981**), *103*, 6893–6897.
DOI: 10.1021/ja00413a020.

34. Fujishima A., Honda K., Electrochemical photolysis of water at a semiconductor electrode, *Nature* (**1972**), *238*, 37–38.
DOI:10.1038/238037a0.

35. Linsebigler A.L., Lu G., Yates Jr J.T., Photocatalysis on TiO_2 surfaces: Principles, mechanisms, and selected results, *Chemical Reviews* (**1995**), *95*, 735–758.
DOI:10.1021/cr00035a013.

36. Nishikawa H., Surface changes and radical formation on hydroxyapatite by UV irradiation for inducing photocatalytic activation, *Journal of Molecular Catalysis A: Chemistry* (**2003**), *206*, 331–338.
DOI:10.1016/S1381-1169(03)00414-X.

37. Aradilla D., Estrany F., Alemán C., Symmetric supercapacitors based on multilayers of conducting polymers, *Journal of Physical Chemistry C* (**2011**), *115*, 8430–8438.
DOI: 10.1021/jp201108c.

38. Back S., Jung Y., On the mechanism of electrochemical ammonia synthesis on the Ru catalyst, *Physical Chemistry Chemical Physics* (**2016**), *18*, 9161–9166.
DOI:10.1039/C5CP07363D.

39. Hoffman B.M., Dean D.R., Seefeldt L.C., Climbing nitrogenase: Toward a mechanism of enzymatic nitrogen fixation, *Accounts of Chemical Research* (**2009**), *42*, 609–619.
DOI:10.1021/ar8002128.

40. Rod T.H., Logadottir A. Nørskov J.K., Ammonia synthesis at low temperatures, *Journal of Chemical Physics* (**2000**), *112*, 5343–5347.
DOI:10.1063/1.481103.

41. Huang L., Li L., Dong W, Liu Y., Lou H., Removal of ammonia by OH radical in aqueous phase, *Environmental Science and Technology* (**2008**), *42*, 8070–8075.
DOI:10.1021/es8008216.

VI. Enclosure B

VI.C.1. Materials and Methods

VI.C.1.1. Materials

Diammonium hydrogen phosphate [$(NH_4)_2HPO_4$; purity ≥ 99.0%], ammonium hydroxide solution 30% (NH_4OH; purity: 28-30% w/w), calcium nitrate ($Ca(NO_3)_2$, zirconyl chloride (ZC: $ZrOCl_2 \cdot 8H_2O$), amino tris(methylene phosphonic acid (ATMP), 2,2-dihydroxyindane-1,3-dione (ninhydrin), Glycine (aminoacetic acid), L-Alanine ((S)-2-aminopropionic acid) and D-Alananine ((R)-2-aminopropionic acid) were purchased from Sigma-Aldrich. Pristine sodium montmorillonite (Nanofil 757, N757), denoted silicate in the main text, was purchased from Süd-Chemie (Germany) and layered mica (LM), denoted aluminosilicate, from Agar Scientific.

N_2, CH_4 and CO_2 gases with a purity of > 99.995% were purchased from Messer. Solvents (ethanol and acetone) were purchased from Scharlab. All experiments were performed with milli-Q water.

VI.C.1.2. Synthesis of amorphous (aHAp) and crystalline hydroxyapatite (cHAp)

15 mL of 0.5 M $(NH_4)_2HPO_4$ in de-ionized water (pH adjusted to 11 with an ammonium hydroxide 30 *w*/*w*-% solution) were added drop-wise (rate of 2 $mL \cdot min^{-1}$) and under agitation (400 rpm) to 25 mL of 0.5 M $Ca(NO_3)_2$ in ethanol. After that, the reaction mixture was stirred 1 h by agitation (400 rpm) at room temperature. The suspension was aged for 24 h at 37 ºC to achieve aHAP, whereas a hydrothermal treatment (200 bar at 150 ºC for 24 h) was subsequently applied to obtain cHAp. The precipitates were separated by centrifugation and washed sequentially with milli-Q water and a 60/40 *v*/*v* mixture of ethanol-water (twice). A white powder with the theoretical Ca/P ratio of 1.67 was recovered after freeze-drying.

VI.C.1.3. Sintering process

aHAp, cHAp, and montmorillonite and mica powders were sintered by firstly heating them in a laboratory furnace (Carbolite ELF11/6B/301) at 1000 ºC during 2 h at an air atmosphere and finally uniaxially pressed at 620 MPa for 10 min. Discs of 10 mm of diameter, 1.7 mm of thickness and sufficient mechanical consistence (s-aHAp, s-cHAp, s-Nanofil 757 and s-LM) were finally obtained.

VI.C.1.4. Thermally and electrically stimulated polarization process

In order to get thermally and electrically stimulated minerals, discs of s-cHAp, s-aHAp, s-Nanofil 757 or s-LM were sandwiched between stainless steel (AISI 304) plates, heated in the furnace to 1000 ºC in air and, simultaneously, polarized for 1 h under application of a constant DC voltage of 500 V. Subsequently, samples were cooled to room temperature, maintaining the DC voltage, the resultant polarized systems being denoted p-aHAp, p-cHAp, p-N757 and p-LM, respectively. These conditions were defined from preliminary assays with s-cHAp discs using DC voltages that ranged from 250 to 2000 V. The best results, in terms of both mechanical consistence and maximum adsorption capacity of phosphates and phosphonates (not shown), were obtained at 500 V.

VI.C.1.5. Characterization of polarized hydroxyapatite (p-cHAp)

The electrochemical behavior was determined by cyclic voltammetry (CV) using an Autolab PGSTAT302N equipped with the ECD module (Ecochimie, The Netherlands) with a three-electrode cell under a nitrogen atmosphere (99.995% in purity) at room temperature. A 0.1 M phosphate buffer saline solution (PBS; pH = 7.2 adjusted with NaOH) was used as the electrolyte in the three-electrode cell. The working compartment was filled with 30 mL of the electrolyte solution. Steel AISI 316 sheets of 1×1.5 cm^2 (thickness 0.1 cm) were used as both the working and the counter electrodes, and an Ag|AgCl electrode was used as the reference electrode which contained a KCl saturated aqueous solution (offset potential versus the standard hydrogen electrode, E^0 = 0.222 V at 25 °C). All potentials given in this report are referenced to this electrode. Polarized HAp (p-HAp) discs, prepared as described above, were fixed on the working electrode using a two-side adhesive carbon layer. The initial and final potentials were -0.40 V, whereas a reversal potential of 0.80 V was considered. The scan rate was 50 mV/s. The crystallinity and structure was studied by wide angle X-ray diffraction (WAXD). Patterns were acquired using a Bruker D8 Advance model with Cu K_α radiation (λ = 0.1542 nm) and geometry of Bragg-Brentano, theta-2 theta. A one-dimensional Lynx Eye detector was employed. Samples were run at 40 kV and 40 mA, with a 2-theta range of 10-60, measurement steps of 0.02º, and time/step of 2-8 s. Diffraction profiles were processed using PeakFit v4 software (Jandel Scientific Software) and the graphical representation performed with OriginPro v8 software (OriginLab Corporation, USA). The crystallite size (L), in the direction perpendicular to the (211) planes, was derived from X-ray diffraction profiles considering the (211) peak width and line broadening measurement using the Scherrer equation:[S1]

$$L = \frac{0.9\lambda}{\beta \cos \theta} \qquad \text{(VI.D.1)}$$

where λ is the wavelength (CuK_α), β is the full width at half maximum height of the (211) peak, θ is the diffraction angle and 0.9 is a shape factor.

The crystallinity (χ_c) was obtained using the following expression:[S2]

$$\chi_c = 1 - \frac{V_{112/300}}{I_{300}} \qquad \text{(VI.D.2)}$$

where I_{300} is the intensity of the (300) reflection and $V_{112/300}$ is the intensity of the hollow between the (112) and (300) reflections, which disappears in non-crystalline samples.

Cyclic voltammograms recorded in PBS for cHAp *as prepared*, *sintered* and *polarized* are compared in Figure Ann.VI.S1a. The electrochemical activity of *as prepared* cHAp is higher than that of steel AISI 316, which was used as a control. However, the electrochemical activity, which indicates the ability to exchange charge reversibly, increases considerably upon application of sintering and thermally and electrically stimulated polarization treatments (*i.e.* 41% and 159%, respectively). In the case of p-cHAp, such effect is accompanied by a significant enhancement of the anodic current intensity at the reversal potential. This behavior has been attributed to the structural changes caused by the thermally and electrically stimulated polarization treatment, which facilitates the diffusion of ions through the inorganic matrix and, therefore, the electrochemical response upon oxidation-reduction processes. These structural changes are reflected in Table Ann.VI.S1. The χ_c of p-cHAp and *as prepared* cHAp are 0.77±0.03 and 0.41±0.02, respectively, while the crystallite size of p-cHAp is around 40% larger than that of as prepared cHAp. The variation of χ_c and L has been related with the formation of OH^- defects.

On the other hand, cyclic voltammograms of polarized samples obtained using p-cHAp and p-aHAp are compared in Figure Ann.VI.S1b. As can be seen, the electrochemical activity of p-aHAp is very noteworthy, even though lower than that of p-cHAp. This reduction has been attributed to partial decomposition suffered by aHAp during the sintering process, which led to the formation of β-tricalcium phosphate (β-TCP: β-$Ca_3(PO_4)_2$). Thermal decomposition of aHAp at temperatures close to 1,000 ºC has also been reported by different authors.[S3,S4]

VI.C.1.6. Deposition of phosphonate and zirconyl chloride layers

A 3-layered system consisting in the successive deposition of ATMP, ZC and ATMP layers (Phos-ZC-Phos) onto a mineral substrate (*i.e.* s-cHAp, s-aHAp, s-Nanofil 757 or s-LM before and after being submitted to the thermally stimulated polarization process) was obtained by immersion in the corresponding aqueous solutions at room temperature for 5 h. Concentrations of ATMP solutions to obtain the first and third ATMP layers were 5 mM and 1.25 mM, respectively, whereas the concentration of ZC was varied from 1 mM to 10 mM. After each immersion the samples were dried at 37 ºC for 3 h. For the sake of completeness, 2-layered and 1-layered systems (*i.e.* Phos-ZC, ZC-Phos, Phos and ZC) were also considered.

VI.C.1.7. Synthesis of amino acids

A high pressure stainless steel reactor was designed *ad hoc* and employed to perform the synthesis of amino acids (AAs). The designed reactor, which is schematized in Figure Ann.VI.S1, was dotted with a manometer, an electric heater with a thermocouple and an external temperature controller. The reactor was also characterized by an inert reaction chamber coated with a perfluorinated polymer (120 mL) where both the catalyst and water were incorporated. The reactor was equipped with three independent inlet valves for N_2, CH_4, CO_2 and an outlet valve to recover the gaseous reaction products. A UV lamp (GPH265T5L/4, 253.7 nm) was also placed in the middle of the reactor to irradiate the catalyst directly, the lamp being protected by a UV transparent quartz tube. All surfaces were coated with a thin film of a perfluorinated polymer in order to avoid any contact between the reaction medium and the reactor surfaces, in this way discarding other catalyst effects.

Regarding temperature range, the reactions were performed within 75-105 ºC for reaction times ranging from 2 to 96 h. Catalyst samples weighed approximately 150 mg and 0.5 mL of de-ionized liquid water were initially incorporated into the reaction chamber, except for assessing the water effect. The chamber was extensively purged with the first selected gas in order to eliminate the initial air content. Each selected gas was introduced to increase the reaction chamber pressure (measured at room temperature) to the target pressure (*i.e.* 1 or 6 bar).

As mentioned in the previous sub-section, the concentration of ZC was varied from 1 mM to 10 mM for the preparation of Phos-ZC-Phos trilayer. However, the influence of the

content of ZC on the yield of Gly and Ala is very small. This is shown in Figure Ann.VI.S2, which displays the variation of the Gly/Phos and Ala/Phos ratios using p-cHAp/Phos-ZC-Phos catalytic systems in which the ZC layer was deposited from concentrations ranging from 1 to 10 mM. According to these results, all the results displayed in this work, including the main text, correspond to ZC layer deposited from a 5 mM solution (unless another concentration is explicitly indicated).

VI.C.2. Measurements

Synthesis of AAs was routinely verified by the ninhydrin (2,2-dihydroxyindane-1,3-dione) detection test for primary amines.[S5] To this end 0.5 mg of the solid recovered after reaction was immersed in a tube containing 0.2 *w*/*v*-% solution of ninhydrin in acetone and subsequently heated to 75 ºC in an oven. The development of purple coloured solutions indicated the formation of the 2-(1,3-dioxoindan-2-yl)iminoindane-1,3-dione chromophore. No yellow-orange coloured solutions were observed characteristic of the Schiff base generated by reaction with secondary amines.

^{1}H NMR spectra were acquired with a Bruker Avance III-400 spectrometer operating at frequencies of 400.1 MHz, 100.6, and 161.9 for ^{1}H, ^{13}C and ^{31}P, respectively. Chemical shifts were calibrated using tetramethylsilane as an internal standard. In order to remove the AAs from the catalyst, samples were dissolved in deuterated water containing 100 mM of HCl and 50 mM of NaCl.

^{1}H NMR spectra were analyzed for samples recovered after reaction times ranging from 2 to 96 h to detect the Gly/Phos and Ala/Phos ratios through the areas of signals corresponding to CH_2 protons at 3.65 ppm (Gly) and 3.79-3.76 ppm (Phos) and the CH_3 protons at 1.54-1.52 ppm (Ala).

$$\text{Gly/Phos} = (3 \times A_{3.65}) / A_{3.79\text{-}376} \quad \text{(VI.D.1)}$$

$$\text{Ala/Phos} = (2 \times A_{1.54\text{-}1.52}) / A_{3.79\text{-}376} \quad \text{(VI.D.2)}$$

$$\text{Gly/Ala} = (1.5 \times A_{3.65}) / A_{1.54\text{-}1.52} \quad \text{(VI.D.3)}$$

X-ray photoelectron spectroscopy (XPS) analyses were performed in a SPECS system equipped with a high-intensity twin-anode X-ray source XR50 of Mg/Al (1253 eV/1487 eV) operating at 150 W, placed perpendicular to the analyzer axis, and using a Phoibos 150 MCD-9 XP detector. The X-ray spot size was 650 μm. The pass energy was set to 25 and

0.1 eV for the survey and the narrow scans, respectively. Charge compensation was achieved with a combination of electron and argon ion flood guns. The energy and emission current of the electrons were 4 eV and 0.35 mA, respectively. For the argon gun, the energy and the emission current were 0 eV and 0.1 mA, respectively. The spectra were recorded at a pressure below 6×10^{-9} mbar. These standard conditions of charge compensation resulted in a negative but perfectly uniform static charge. The C1s peak was used as an internal reference with a binding energy of 284.8 eV. High-resolution XPS spectra were acquired by the Gaussian–Lorentzian curve fitting after s-shape background subtraction. The surface composition was determined using the manufacturer's sensitivity factors.

Scanning electron microscopy (SEM) studies were carried out using a Focused Ion Beam Zeiss Neon40 microscope operating at 5 kV, equipped with an energy dispersive X-ray (EDX) spectroscopy system. Samples were deposited on a silicon disc mounted with silver paint on pin stubs of aluminum, and sputter-coated with a thin layer of carbon to prevent sample charging problems.

Infrared absorption spectra were recorded with a Fourier Transform FTIR 4100 Jasco spectrometer in the 1800-700 cm^{-1} range. A Specac model MKII Golden Gate attenuated total reflection (ATR) equipment with a heating Diamond ATR Top-Plate was used.
X-ray powder diffraction patterns were recorded in the beamline BL11-NCD at ALBA synchrotron (Cerdanyola del Vallés, Barcelona, Spain) using a wavelength of 0.100 nm and an WAXS LX255-HS detector from Rayonix, which was calibrated with diffractions of standard of a Cr_2O_3 sample.

The separation of the synthesized AAs was performed by HPLC on a Agilent serie 1200 chromatograph using a Chirobiotic T (250 × 4.6 mm) column with a particle size of 5 μm. The mobile phase consisted of methanol:water (60:40 v/v) mixture. The flow rate was set at 1 mL/min and the volume of injected samples was 20 μL. The column temperature was maintained at 25ºC. Chromatograms were recorded at three wavelengths (205.4, 210.4 and 215.4 nm), but 210.4 nm was used for quantification purposes. Retention times of each AA were identified by comparing with the corresponding standard: 5.168 min (L-Ala), 5.781 min (Gly) and 7.463 min (D-Ala). Injected samples were obtained by extracting the AA from the catalyst after reaction (10 mg) using a mixture of 1 mL of methanol:water (60:40 v/v) by shaking during 5 min. After 30 min of sedimentation, the supernantant was filtered

using a PTFE 0.2 μm filter and finally, 20 μL of such a filtrate were injected into the HPLC equipment.

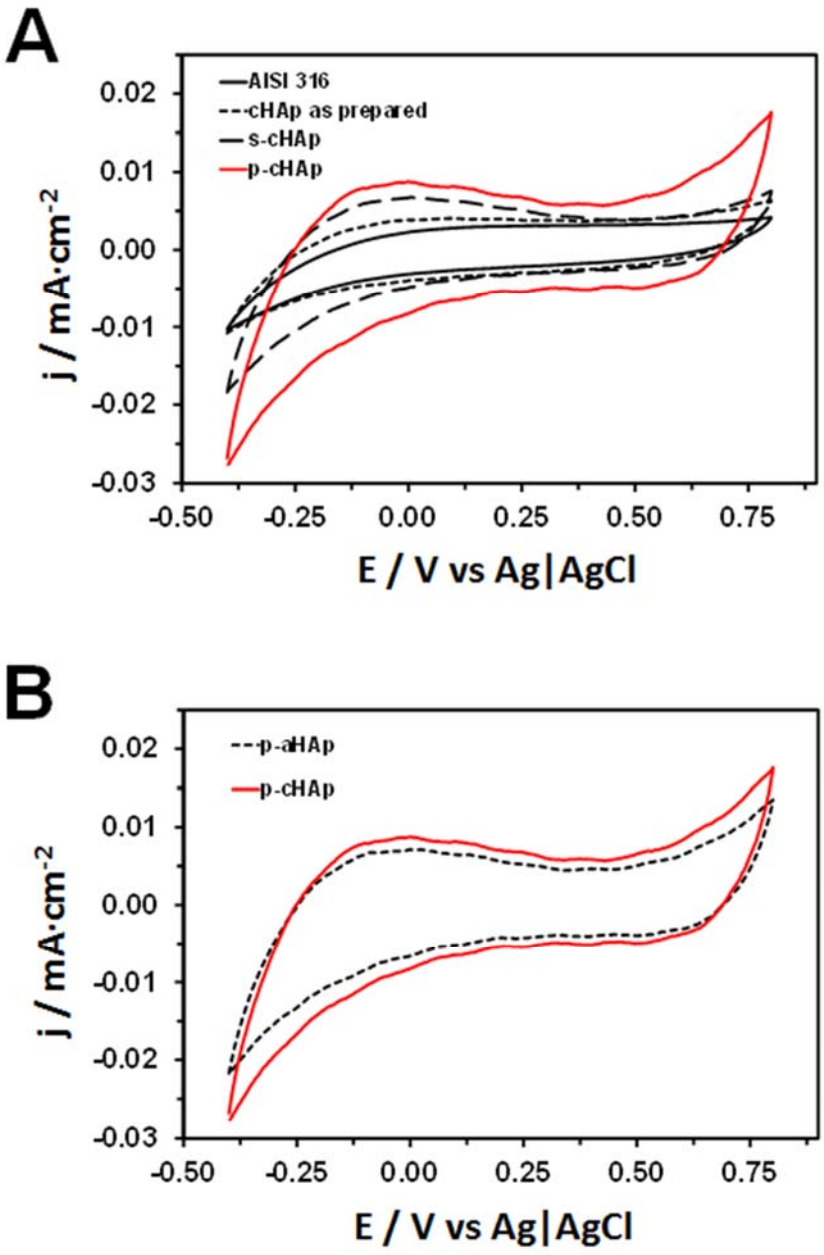

Figure Ann.VI.S1. Control cyclic voltammograms comparing the electrochemical activity of: (A) cHAp *as prepared*, *sintered* (s-cHAp) and *polarized* (p-cHAp); and (B) p-aHAp and p-cHAp.

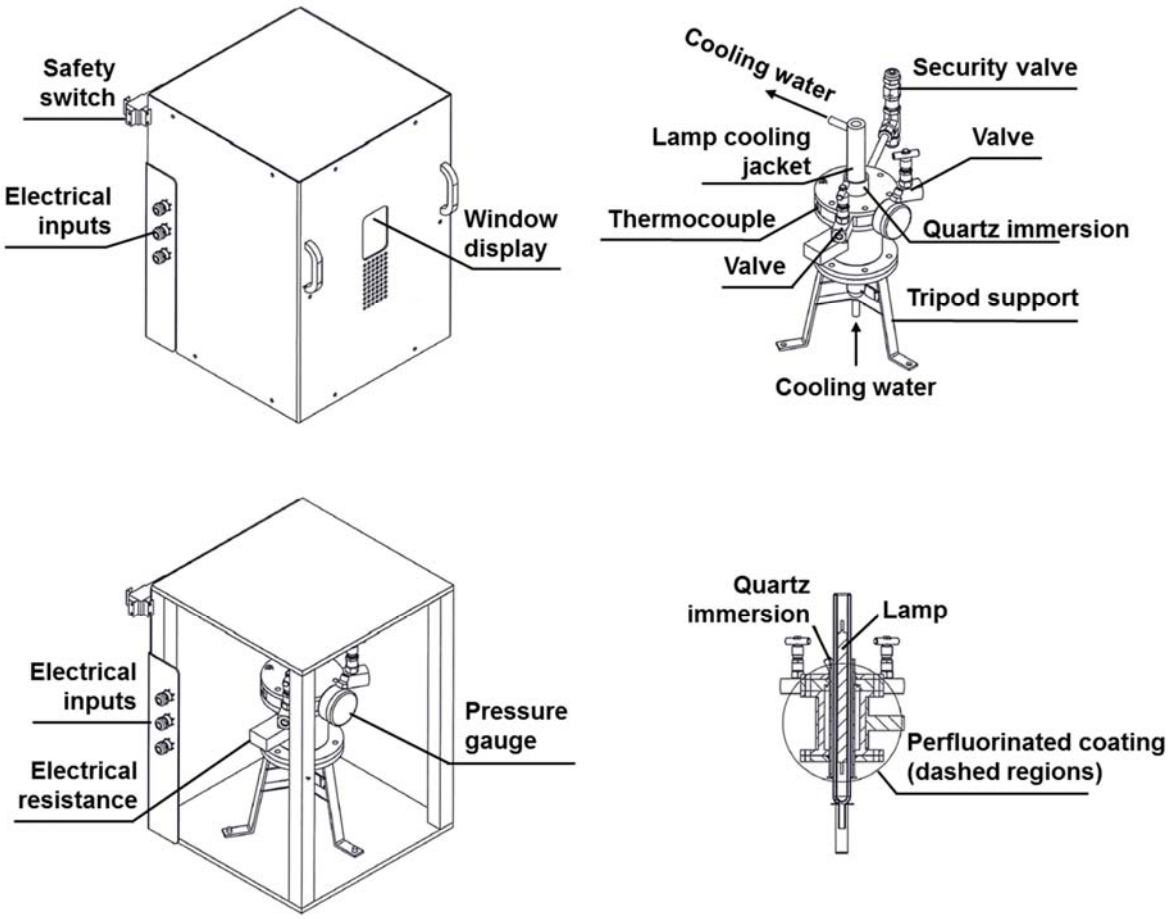

Figure Ann.VI.S2. Details of the reactor designed to synthesize AAs.

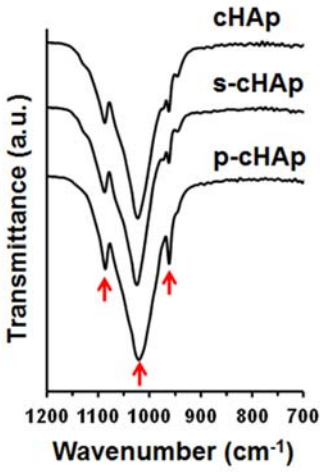

Figure Ann.VI.S3. FTIR spectra of cHAp *as prepared*, *sintered* (s-cHAp) and *polarized* (p-cHAp). The region comprised between 950 and 1200 cm^{-1} displays typical PO_4^{3-}bands. The spectra of cHAp, s-cHAp and p-cHAp show characteristic vibrational modes of PO_4^{3-} at ν_1= 962 cm^{-1} and ν_3= 1016, 1087 cm^{-1}.

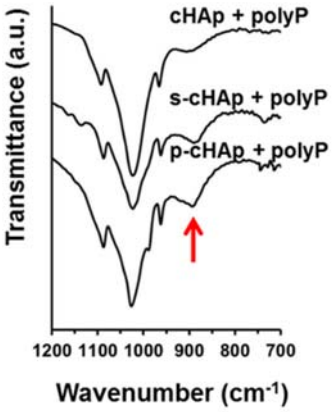

Figure Ann.VI.S4. FTIR spectra of cHAp as *prepared*, *sintered* (s-cHAp) and *polarized* (p-cHAp). incubated in presence of triphosphate (200 mM) at pH 7. The red arrow indicates the position of the band used to identify the adsorption of triphosphate (PolyP). The weak shoulder identified around 890 cm^{-1} for cHAp, which corresponds to the P–O–P asymmetric stretching, transforms into a well-defined adsorption band for s-cHAp and, especially, p-cHAp. This feature reflects that the application of thermal and thermally and electrically stimulated polarization processes enhance significantly the ability of cHAp to adsorb polyphosphates. Based on the FTIR spectra presented in Figures Ann.VI.S3. and Ann.VI.S4., the ability of cHAp samples to adsorb triphosphate was estimated using the ratio of integrated area of the peak at 1016 cm^{-1} (belonging to the mineral) and the integrated area of the peak at 890 cm^{-1} (belonging to polyP). Results indicated that the adsorption of polyP onto cHAp was 2.0 and 2.6 times lower than onto s-cHAp and p-cHAp, respectively. These results prove that properties of p-cHAp are clearly unique with respect to cHAp and s-cHAp.

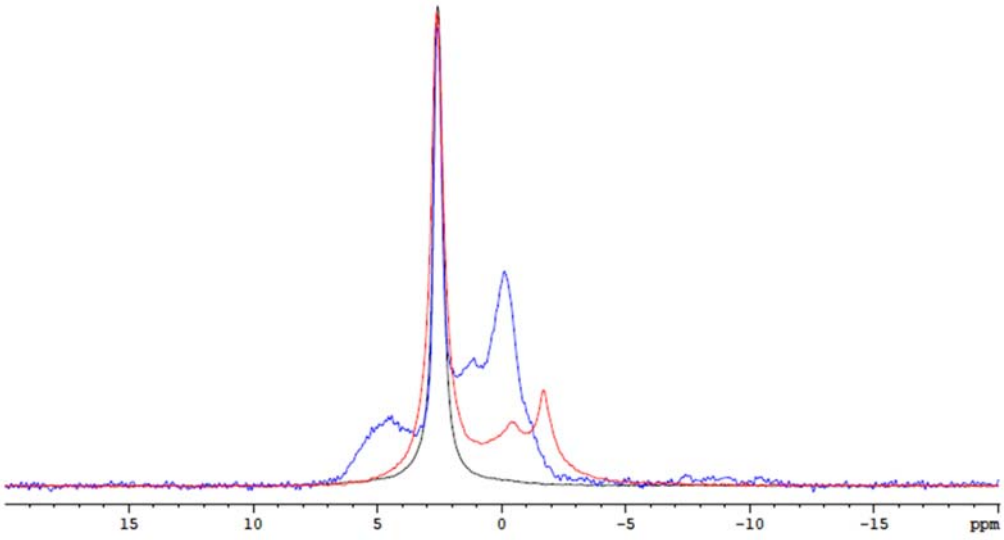

Figure Ann.VI.S5. Solid state ^{31}P NMR spectra of cHAp *as prepared* (in blue), *sintered* (s-cHAp; in red) and *polarized* (p-cHAp; in black). The main resonance peak, present in cHAp, s-cHAp and p-cHAp, at 2.9 ppm corresponds to bulk phosphate groups PO_4^{3-} of hydroxyapatites.[S7] Note that, compared to cHAp, the band width of s-cHAp and, particularly, p-cHAp samples are narrower, which is consistent with the higher crystallinity of the substrate (Crystallinity (%): cHAp= 42.67; s-cHAp=64.70; p-cHAp=75.50). The broad signals at approximately [-1, 0] ppm and a shoulder at [0,1] ppm, present in cHAp and s-cHAp, were usually assigned to the protonated surfaces phosphate groups arising from the disordered near surface layer.[S8] Indeed, hydroxyapatite particles are typically described as an ordered hydroxyapatite core surrounded by a disordered non-apatitic surface layer.[S9] The shoulder at 4-6 ppm, which is present in s-cHAp, is also due to the surface HPO_4^{2-} ions, when its amount in the surface layer is greater than a certain threshold.[S10] This increase in surface of HPO_4^{2-} ions in s-cHAp is caused by the more disordered surface layer due to the thermal process applied in s-cHAp particle treatment. The more unusual part is the only peak of typical bulk phosphate groups PO_4^{3-} of hydroxyapatites present in p-cHAp. *p*-cHAp particles treatment consists of applying a constant DC electric field of 500 V, heating simultaneously at 1000 ºC for 2 h. This thermally and electrically stimulated polarization process was found to exert different effects on the hydroxyapatite surface properties.[S11] The hydroxyapatite surface undergoes variations due to changes in the position of OH^- ions.[S12] Accordingly, the fingerprint of the surface OH^- ions leaving from the columns due to the thermally and electrically stimulated polarization process in p-cHAp is the disappearance of the surface HPO_4^{2-} ions and the formation of holes in the valence band (h^+) for charge neutralization.

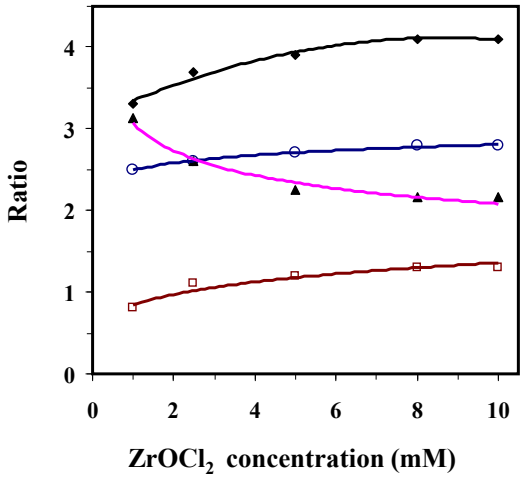

Figure Ann.VI.S6. Variation of Gly/Phos (○), Ala/Phos (□), (Gly+Ala)/Phos (♦) and Gly/Ala (▲) ratios for reactions performed at 95 ºC, 24 h and using the p-cHAp/Phos-ZC-Phos system versus the concentration of ZC solutions used to prepare the central ZC layer (see Figure Ann.VI.1a).

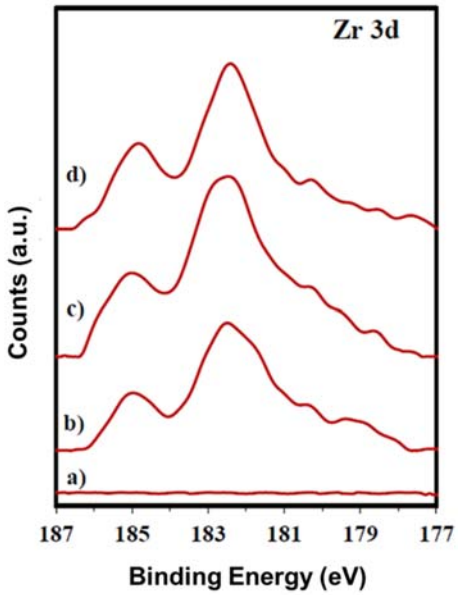

Figure Ann.VI.S7. Zr 3d high resolution XPS spectra for (a) p-cHAp, (b) p-cHAp/Phos-ZC-Phos, and (c) p-cHAp/Phos-ZC-Phos after negative reaction (*i.e.* without exposure to UV radiation) and (d) p-cHAp/Phos-ZC-Phos after positive reaction (24 h at 95 ºC). The Zr signals appeared as a resolved spin doublet at binding energies of 182.6 and 185.0 eV, which correspond to the 3d5/2 and 3d3/2, respectively.[S5] The measured Zr content was in the 1.26-1.29% interval for all samples having the Phos-ZC-Phos trilayer prepared using a 5 mM ZC solution, this percentage being independent of the progress of the reaction.

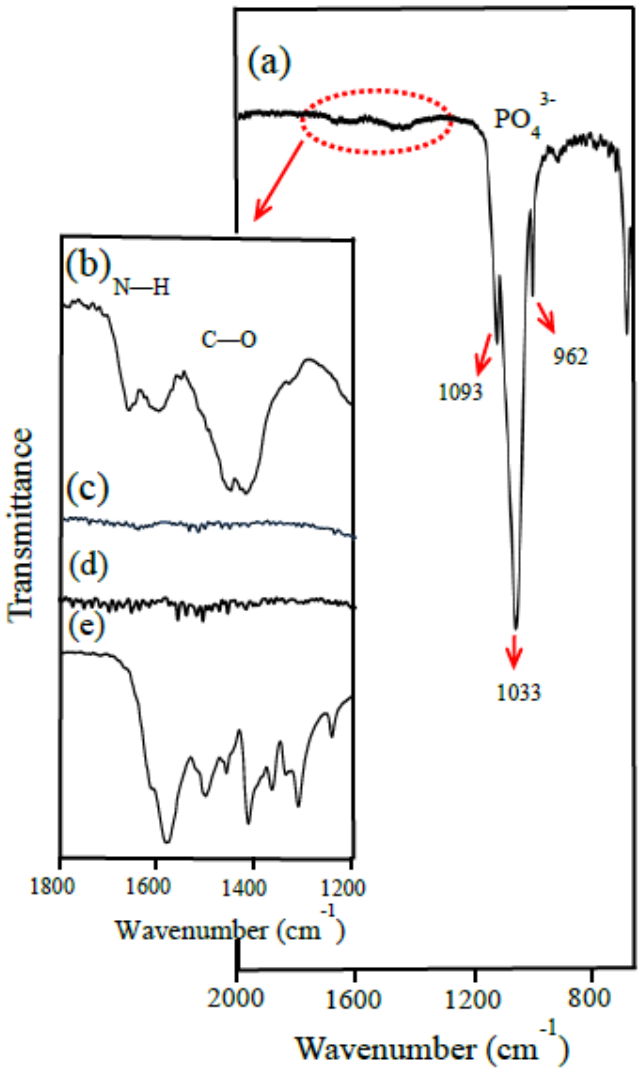

Figure Ann.VI.S8. (a) FTIR spectra of the sample after reaction for 24 h at 95 ºC. Insets compare the 1800-1200 cm^{-1} region for the above sample (b) after and (c) before reaction, (d) an unsuccessful reaction because of the lack of sustained exposure of the system to the UV radiation, and (e) a mixture of Gly and Ala (2:1 weight ratio). Despite the low sensitivity of the technique, the successfully formed AAs are identified by the broad and low-intensity bands at the 1600-1400 cm^{-1} region. It is worth noting that this region is completely flat in the spectra of samples before reaction and also for samples coming from a negative ninhydrin test (e.g. spectrum (c) for samples without UV radiation). On the contrary, AAs such as Gly and Ala have the most intense absorptions in this region (b). Obviously, FTIR spectra showed in all samples the characteristic peaks of HAp and specifically the three intense bands at 1093, 1033 and 962 cm^{-1} associated with the characteristic vibrational modes of PO_4^{3-} .

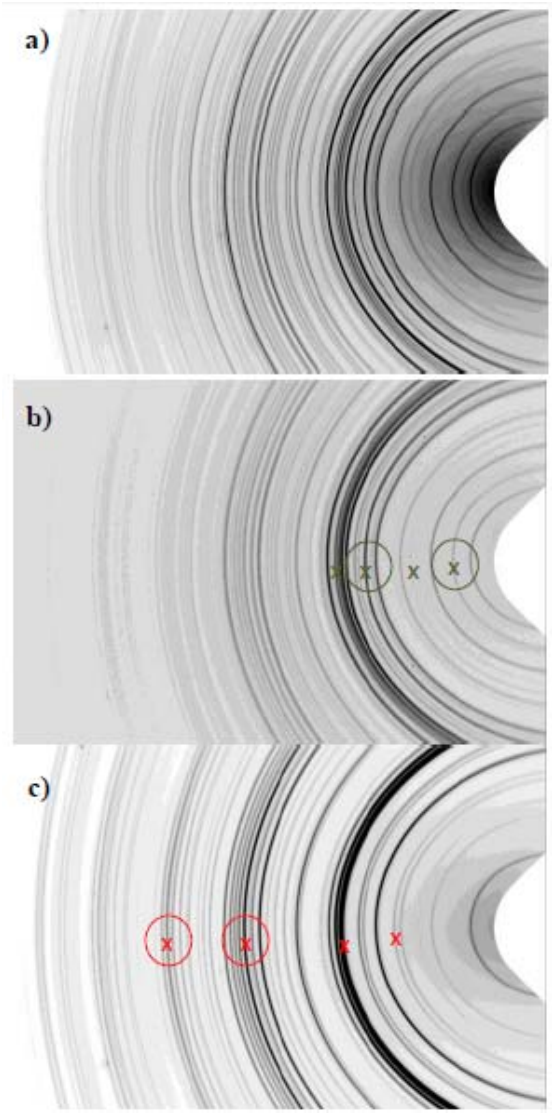

Figure Ann.VI.S9. X-ray diffraction patterns corresponding to (a) p-cHAp and the p-cHAp/Phos-ZC-Phos system (b) before and (c) after successful reaction for 24 h at 95 ºC. Gray crosses in **b)** point out the characteristic X-ray diffraction reflections of the catalytic system, which disappear after reaction, while red crosses in **c)** point out new reflections that can be observed after successful reaction. Circled symbols indicate the reflections that changed more drastically during reaction. Deposition of the 3-layer onto p-cHAp did not cause a significant changes in the X-ray diffraction pattern (a) and (b), whereas remarkable changes can be observed after chemical reaction (b) and (c). These correspond to the disappearance of some reflections (*i.e.* 0.648, 0.406, 0.321 and 0.282 nm) and the appearance /intensification of some reflections (*i.e.* 0.391, 0.282, 0.184 and 0.146 nm). It is clear that reaction gave rise to a slight transformation of the previous structure as reflected by the development of new crystals (Figure Ann.VI.3d). However, characteristic peaks of Ala and Gly were not clearly detected due to overlapping with reflections of catalysts, the development of different crystalline structures for the adsorbed AA, and the low amount of formed crystals.

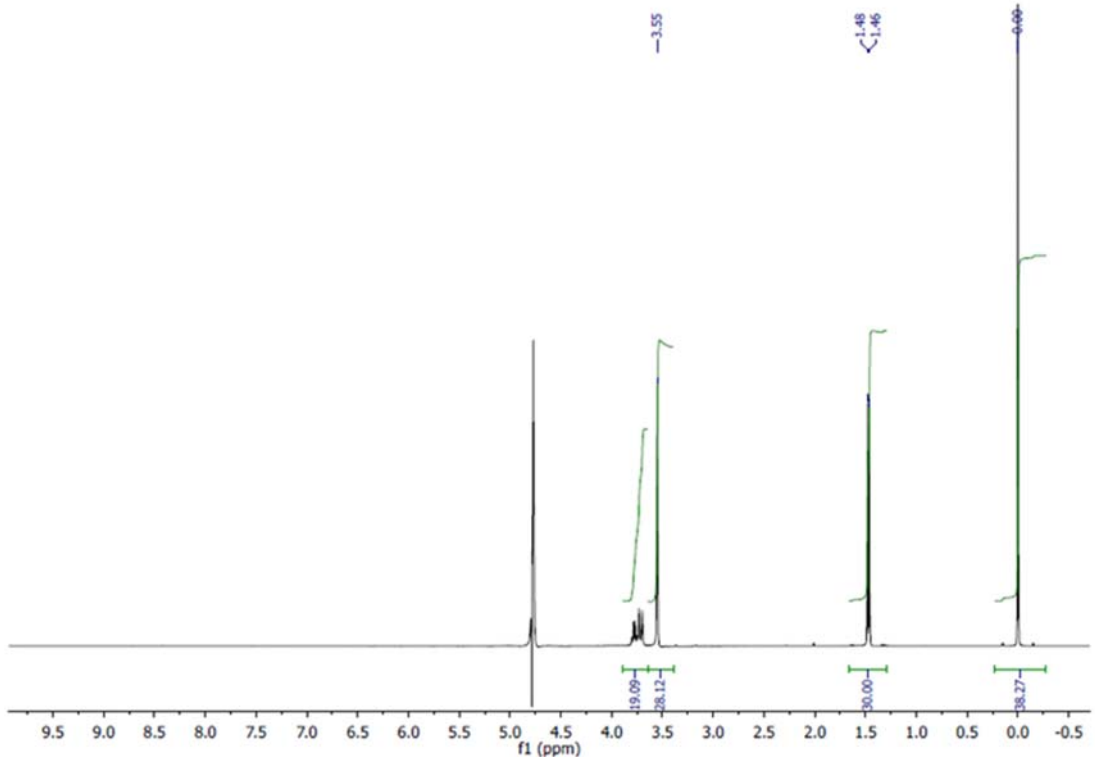

Figure Ann.VI.S10. ^{1}H-NMR spectra of samples obtained after reaction (95 ºC and 24 h) using a chamber pressure of 6 bar (*i.e.* 2 bar of each feeding reaction gas). The spectrum corresponds to the solution obtained after extract the AAs from the catalyst by dissolving the sample in deuterated water containing 100 mM of HCl and 50 mM of NaCl. Peaks for Gly and Ala are practically identical to those displayed in Figure Ann.VI.2 (*i.e*. using a chamber pressure of 1 bar – 0.33 bar of each feeding reaction gas).

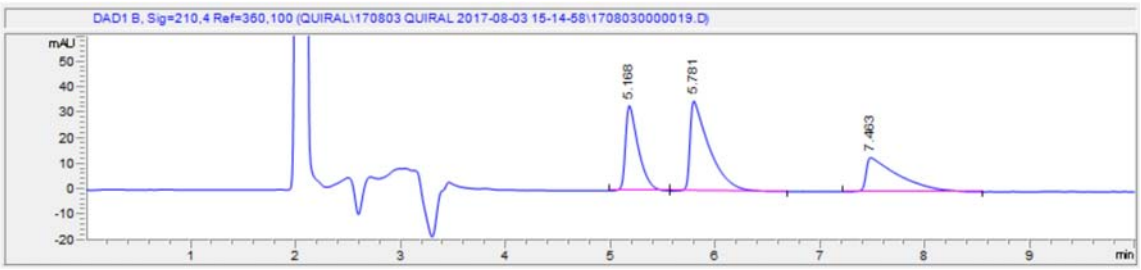

Figure Ann.VI.S11. Representative HPLC chromatogram (λ=210.4 nm) of a sample extracted from the catalyst after reaction shows the separation of Gly (5.781 min), L-Ala (5.168 min) and D-Ala (7.463 min). A racemic D-Ala:L-Ala mixture was obtained.

Table Ann.VI.S1. Structural parameters of cHAp, aHAp as prepared and after applying the thermally and electrically stimulated polarization treatment: crystallinity (χ_c) and length of the crystallites (L).

Sample	χ_c (%)	L (nm)
As prepared cHAp	0.41±0.02	61±2
p-cHAp	0.77±0.03	42±3
As prepared aHAp	0.09±0.01	10±1
p-aHAp	0.69±0.03	52±3

Table Ann.VI.S2. Atomic percent composition (Ca, P, O, C, N and Zr) of p-cHAP, p-cHAP/Phos-ZC-Phos, p-cHAP/Phos-ZC-Phos after negative reaction (*i.e.* without exposure to UV radiation), and p-cHAp/Phos-ZC-Phos after positive reaction (24 h at 95 ºC). Reactions were performed at 6 atm.

	Ca	P	O	C	N	Zr
p-cHAp	38.35	17.78	41.96	1.20	0.70	0.01
p-cHAp/Phos-ZC-Phos	34.79	16.21	42.46	1.73	3.12	1.69
p-cHAp/Phos-ZC-Phos (after negative reaction)[a]	25.43	11.86	44.78	5.45	10.72	1.76
p-cHAp/Phos-ZC-Phos (after positive reaction)[b]	22.87	10.46	44.69	7.87	12.43	1.68

[a] Without exposure to UV radiation. [b] 24 h at 95 ºC.

Table Ann.VI.S3. Atomic percent composition (Ca, P, O, C, N and Zr) of p-cHAp, p-cHAp/Phos and HAp/ZC before and after remain in a N_2 atmosphere. As it can be seen, the percentage of N increases considerably when N_2 is in contact with p-cHAp (71% of increment) and, especially, p-cHAp/Phos (261% of increment) indicating that the p-cHAp substrate and the ATMP layers are the catalyst components associated with the first step of the N_2 fixation (*i.e.* adsorption of the gas from the atmosphere). Besides, the increment of the percentage of N for p-cHAp/ZC (62%) is similar to that obtained for p-cHAp, indicating that the role of the ZC layer in the N_2 adsorption is null. Experiments were performed according to this protocol: i) heating of the sample until 400 ºC with an Ar flux during 30 min; ii) cooling down to 90 ºC; and ii) generation of a N_2 atmosphere applying a nitrogen flux of 5 mL/min diluted in an Ar flux of 45 mL/min during 30 min.

	Ca	**P**	**O**	**C**	**N**	**Zr**
p-cHAp	38.35	17.78	41.96	1.20	0.70	0.01
p-cHAp + N_2 atmosphere	38.70	17.81	41.05	1.22	1.20	0.02
p-cHAp/ZC	38.45	18.02	40.04	1.17	0.56	1.76
p-cHAp/ZC + N_2 atmosphere	37.15	17.07	41.8	1.25	0.91	1.82
p-cHAp/Phos	37.45	17.23	41.27	1.18	2.86	0.01
p-cHAp/Phos + N_2 atmosphere	35.90	16.46	36.04	1.24	10.35	0.01

Table VI.S4. Atomic percent composition (Ca, P, O, C, N and Zr) of p-cHAp, p-cHAp/Phos and HAp/ZC before and after remain in a CO_2 atmosphere. As it can be seen, the percentages of C and O increase considerably when CO_2 is in contact with p-cHAp (39% and 1.9% of increment, respectively) and, especially, p-cHAp/ZC (332% and 22% of increment, respectively) indicating that the p-cHAp substrate and the ZC layer are the catalyst components associated with the first step of the CO_2 fixation (*i.e.* adsorption of the gas from the atmosphere). Experiments were performed according to this protocol: i) heating of the sample until 400 ºC with an Ar flux during 30 min; ii) cooling down to 90 ºC; and ii) generation of a CO_2 atmosphere applying a nitrogen flux of 5 mL/min diluted in an Ar flux of 45 mL/min during 30 min.

	Ca	**P**	**O**	**C**	**N**	**Zr**
p-cHAp	38.35	17.78	41.96	1.20	0.70	0.01
p-cHAp + CO_2 atmosphere	37.45	17.45	42.77	1.67	0.65	0.01
p-cHAp/ZC	38.45	18.02	40.04	1.17	0.56	1.76
p-cHAp/ZC + CO_2 atmosphere	30.00	13.61	49.05	5.05	0.62	1.67
p-cHAp/Phos	37.45	17.23	41.27	1.18	2.86	0.01
p-cHAp/Phos + CO_2 atmosphere	37.35	17.40	40.56	1.69	2.98	0.02

Table Ann.VI.S5. Summary of experiments and results attained for the synthesis of AAs.[a]

Set	Conditions[a]	Ninhidrine test	Observations
1	p-cHAp/Phos-ZC-Phos N_2, CH_4, CO_2, H_2O / UV	+	Gly and Ala signals in NMR spectra. Increasing AAs/Phos ratio with reaction time. Increasing AAs/Phos ratio with reaction *T*. Increasing AA/Phos ratio with Zr content.
2	p-cHAp/Phos-ZC-Phos N_2, CH_4, CO_2, H_2O	-	UV radiation is fundamental.
3	cHAp/Phos-ZC-Phos N_2, CH_4, CO_2, H_2O / UV	-	Polarization of HAp is fundamental.
4	p-aHAp/Phos-ZC-Phos N_2, CH_4, CO_2, H_2O / UV	+	The crystalline structure of HAp is not fundamental for reaction.
5	p-N757/Phos-ZC-Phos N_2, CH_4, CO_2, H_2O / UV	-	The type of polarized support is important. Silicates do not work.
6	p-LM/Phos-ZC-Phos N_2, CH_4, CO_2, H_2O / UV	-	The type of polarized support is important. Mica does not work.
7	p-cHAp/Phos-ZC N_2, CH_4, CO_2, H_2O / UV	-	The trilayered system is fundamental. When missing one Phos layer does not work
8	p-cHAp/ZC-Phos N_2, CH_4, CO_2, H_2O / UV	-	The p-HAp/Phos interphase is fundamental.
9	p-cHAp/Phos N_2, CH_4, CO_2, H_2O / UV	-	The trilayered system is fundamental.
10	p-cHAp/ZC N_2, CH_4, CO_2, H_2O / UV	-	The trilayered system is fundamental.
11	Phos N_2, CH_4, CO_2, H_2O / UV	-	AAs cannot be derived from a simple decomposition of Phos.
12	Phos-Zr N_2, CH_4, CO_2, H_2O / UV	-	AAs cannot be derived from a simple decomposition of Phos using ZC as catalyst.
13	p-cHAp/Phos-ZC-Phos CH_4, CO_2, H_2O / UV	-	Substrate is able to fix molecular nitrogen. N_2 is essential as a nitrogen source.c
14	p-cHAp/Phos-ZC-Phos N_2, CO_2, H_2O / UV	-	CH_4 appears as the carbon source for CH_2 and CH_3 groups.
15	p-cHAp/Phos-ZC-Phos N_2, CH_4, H_2O / UV	-	CO_2 appears as the source of carbon (*i.e.* for carboxylic groups).
16	p-cHAp/Phos-ZC-Phos N_2, CH_4, CO_2 / UV	-	H_2O plays an important role in the … mechanism.

[a] Abbreviations denote the support (p-cHAp, p-aHAp, p-N757, p-LM) and the order of the different layers deposited onto its surface (Phos and ZC for phosphonate and zirconyl chloride, respectively). UV indicates that experiments were performed under UV radiation.

VI.C.3. References

S1. Klug H.P., Alexander L.E., *In X-Ray diffraction procedures: for polycrystalline and amorphous materials*. 2nd. Edition, John Wiley and Sons, New York, (**1974**).

S2. Landi E., Tampieri A., Celotti G., Sprio S., Densification behavior and mechanisms of synthetic hydroxyapatites, *Journal of the European Ceramics Society* (**2000**), *20*, 2377–2387.
DOI:10.1016/S0955-2219(00)00154-0.

S3. Ruhemann S., Triketohydrindene hydrate, *Journal of the Chemical Society, Transactions* (**1910**), *97*, 2025–2031.
DOI:10.1039/CT9109702025.

S4. Tang Q.L., Zhu Y.J., Wu J., Chen F., Cao S.W., Calcium phosphate drug nanocarriers with ultrahigh and adjustable drug-loading capacity: One-step synthesis, In Situ drug loading and prolonged drug release, *Nanomedicine: Nanotechnology, Biology and Medicine* (**2011**), *7*, 428–434
DOI:10.1016/j.nano.2010.12.005.

S5. Bertran O., del Valle L.J., Revilla-López G., Rivas M., Chaves G., Casas M.T., Casanovas J., Turon P., Puiggalí J. Alemán C., Synergistic approach to elucidate the incorporation of magnesium ions into hydroxyapatite, *Chemistry – A European Journal* (**2015**), *21*, 2537–2546.
DOI:10.1002/chem.201405428.

S6. Barr T.L., An ESCA study of the termination of the passivation of elemental metals, *Journal of Physical Chemistry* (**1978**), *82*, 1801–1810.
DOI:10.1021/j100505a006.

S7. Jarlbring M., Sandström D.E., Antzutkin O.N., Forsling W., Characterization of Active Phosphorus Surface Sites at Synthetic Carbonate-Free Fluorapatite Using Single-Pulse ^{1}H, ^{31}P, and ^{31}P CP MAS NMR, *Langmuir* (**2006**), *22*, 4787–4792.
DOI: 10.1021/la052837j.

S8. Wang Y., Von Euw S., Fernandes F.M., Cassaignon S., Selmane M., Laurent G., Pehau-Arnaudet G., Coelho C., Bonhomme-Coury L., Giraud-Guillaume M-M., Babinneau F., Azars T., Nassif N., Water-mediated structuring of bone apatite, *Nature Material*s (**2013**), *12*, 1144–1153.
DOI: 10.1038/nmat3787.

S9. Jager C., Welzel T., Meyer-Zaika W., Epple M.A., A solid‐state NMR investigation of the structure of nanocrystalline hydroxyapatite, *Magnetic Resonance in Chemistry* (**2006**), *44*, 573–580..
DOI: 10.1002/mrc.1774.

S10. Osman M.B., Diallo-Garcia S., Herledan V., Brouri D., Toshioka T., Kubo J., Millot Y., Costentin G., Discrimination of surface and bulk structure of crystalline hydroxyapatite nanoparticles by NMR, *Journal of Physical Chemistry C* (**2015**), *119*, 23008–23020.
DOI:10.1021/acs.jpcc.5b08732.

S11. Nakamura M., Hori N., Namba S., Toyama T., Nishimiya N., Yamashita K., Wettability and surface free energy of polarised ceramic biomaterials, *Biomedical Material* (**2015**), *10*, 011001.
DOI:10.1088/1748-6041/10/1/011001.

S12. Ikoma t., A. Yamazaki, S. Nakamura, M. Akao, Preparation and dielectric property of sintered monoclinic hydroxyapatite, *Journal of Materials Science Letters* (**1999**), *18*, 1225–1228.
DOI:10.1023/A:1006610521173.

Annex VII.

Permanently polarized hydroxyapatite, a process for its manufacture and uses thereof

(12) INTERNATIONAL APPLICATION PUBLISHED UNDER THE PATENT COOPERATION TREATY (PCT)

(19) World Intellectual Property Organization
International Bureau

(43) International Publication Date
08 February 2018 (08.02.2018)

WIPO | PCT

(10) International Publication Number
WO 2018/024727 A1

(51) International Patent Classification:
C01B 25/32 (2006.01) *A61L 27/12* (2006.01)

(21) International Application Number:
PCT/EP2017/069437

(22) International Filing Date:
01 August 2017 (01.08.2017)

(25) Filing Language: English

(26) Publication Language: English

(30) Priority Data:
16382381.8 02 August 2016 (02.08.2016) EP
16382524.3 11 November 2016 (11.11.2016) EP

(71) Applicants: **B. BRAUN SURGICAL, S. A.** [ES/ES]; Ctra. de Terrassa, 121, 08191 Rubi (ES). **UNIVERSITAT POLITÈCNICA DE CATALUNYA** [ES/ES]; Jordi Girona, 31, 08034 Barcelona (ES).

(72) Inventors: **TURON DOLS, Pau**; Carretera de Terrassa, 121, 08191 Rubi (ES). **DEL VALLE MENDOZA, Luis Javier**; Jordi Girona, 31, 08034 Barcelona (ES). **PUIGGALÍ BELLALTA, Jordi**; Jordi Girona, 31, 08034 Barcelona (ES). **ALEMÁN LLANSÓ, Carlos Enrique**; Jordi Girona, 31, 08034 Barcelona (ES).

(74) Agent: **OFICINA PONTI, S.L.P.**; C. Consell de Cent, 322, 08007 Barcelona (ES).

(81) Designated States *(unless otherwise indicated, for every kind of national protection available)*: AE, AG, AL, AM, AO, AT, AU, AZ, BA, BB, BG, BH, BN, BR, BW, BY, BZ, CA, CH, CL, CN, CO, CR, CU, CZ, DE, DJ, DK, DM, DO, DZ, EC, EE, EG, ES, FI, GB, GD, GE, GH, GM, GT, HN, HR, HU, ID, IL, IN, IR, IS, JO, JP, KE, KG, KH, KN, KP, KR, KW, KZ, LA, LC, LK, LR, LS, LU, LY, MA, MD, ME, MG, MK, MN, MW, MX, MY, MZ, NA, NG, NI, NO, NZ, OM, PA, PE, PG, PH, PL, PT, QA, RO, RS, RU, RW, SA, SC, SD, SE, SG, SK, SL, SM, ST, SV, SY, TH, TJ, TM, TN, TR, TT, TZ, UA, UG, US, UZ, VC, VN, ZA, ZM, ZW.

(84) Designated States *(unless otherwise indicated, for every kind of regional protection available)*: ARIPO (BW, GH, GM, KE, LR, LS, MW, MZ, NA, RW, SD, SL, ST, SZ, TZ, UG, ZM, ZW), Eurasian (AM, AZ, BY, KG, KZ, RU, TJ, TM), European (AL, AT, BE, BG, CH, CY, CZ, DE, DK, EE, ES, FI, FR, GB, GR, HR, HU, IE, IS, IT, LT, LU, LV, MC, MK, MT, NL, NO, PL, PT, RO, RS, SE, SI, SK, SM, TR), OAPI (BF, BJ, CF, CG, CI, CM, GA, GN, GQ, GW, KM, ML, MR, NE, SN, TD, TG).

Published:
— *with international search report (Art. 21(3))*

(54) Title: PERMANENTLY POLARIZED HYDROXYAPATITE, A PROCESS FOR ITS MANUFACTURE AND USES THEREOF

Figure 4

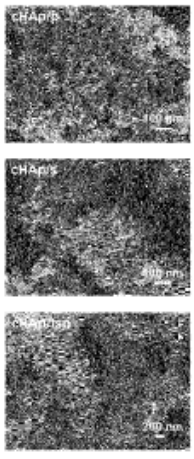

(57) Abstract: The present invention relates to a permanently polarized hydroxyapatite and a composition or material comprising thereof. The present invention further relates to a process for obtaining a permanently polarized hydroxyapatite and to different uses of the permanently polarized hydroxyapatite or the composition or material comprising thereof.

WO 2018/024727 A1

Annex VII.

Permanently polarized hydroxyapatite, a process for its manufacture and uses thereof

ABSTRACT

The present invention relates to a permanently polarized hydroxyapatite and a composition or material comprising thereof. The present invention further relates to a process for obtaining a permanently polarized hydroxyapatite and to different uses of the permanently polarized hydroxyapatite or the composition or material comprising thereof.

Annex VII.

Permanently polarized hydroxyapatite, a process for its manufacture and uses thereof

VII. 1. Field of the invention

The present invention relates to a permanently polarized hydroxyapatite, a process for manufacturing said permanently polarized hydroxyapatite and uses thereof.

VII.2 Background of the invention

Hydroxyapatite (HAp), $Ca_{10}(PO_4)_6(OH)_2$, is the major inorganic component of biological hard tissues such as bone and tooth.[1,2] Synthetic HAp, which shows excellent ability to interact with living systems, has been investigated for biomedical applications, as for example drug and gene delivery, tissue engineering and bone repair.[3-8]

An important difference between amorphous calcium phosphate (ACP) and crystalline synthetic HAp (cHAp) is the alignment of the OH^- ions along the *c*-axis in the latter. The crystal structure of stoichiometric cHAp, which contains no OH^- defects, is monoclinic at room temperature.[9,10] The monoclinic cHAp changes to hexagonal phase at about 210 ºC, which means a change from an ordered to a disordered distribution of OH^- ions along the *c*-axis. In addition to thermal phase transition, OH^- defects also cause a phase transition.[9,10] In this case, the hexagonal phase becomes the most stable form of cHAp in the pH range of 4-12 because of the disorder caused by the presence of vacancies and presence of oxygen radicals in the columns of OH^- groups. Although electrical and dielectric properties of cHAp were found to be altered by thermally-induced changes in the positions of OH^- ions,[11-13] the observed polarization effects were not stable at room temperature (*i.e.* the OH^- re-reorientation has a short relaxation time).

Yamashita and co-workers[14,15] provoked quasi-permanent polarization effects in the polycrystalline HAp samples by applying a constant DC electric field of 1.0-4.0 kV/cm to samples sintered previously at 1250 ºC for 2 h. This approach is based on a constant electric field at a temperature < 700 ºC. The maximum current density ($\sim 10^{-9}$ A/cm^2) determined by thermally stimulated depolarization current (TSDC) measurements was obtained when the

temperature in the polarization step was fixed at 400 ºC. Indeed, the current density was observed to decrease rapidly when the polarization temperature was higher than 450 ºC. Results indicated that the polarization was consequence of the electrical dipoles associated to the formation of defects inside crystal grains and of the space charge polarization originated in the grain boundaries. The thermally stimulated polarization process was found to exert different effects on the HAp surface properties.[16,17] Although the influence of polarization exhibited no effect on the surface roughness, crystallinity and constituent elements of cHAp, the wettability[16] and adhesion of osteoblastic cells is higher onto polarized samples than onto as prepared ones.[17] The latter phenomena were attributed to the increase in the surface free energies in comparison with non-polarized cHAp surfaces.

In this sense, document ES2323628 discloses that calcium hydroxyapatite in solid solution is obtained by sintering the prepared powder by a given method at 1200 ºC for 1-5 hours. The ceramic material can be polarized at a T higher than 1000 ºC or at a constant electric field higher than 100.000 V/cm. Nevertheless, the energy is not stored in such conditions and accordingly it is better to work under 1000 ºC or a voltage between 10 and 100.000 V/cm.

Fu, Cong et al. discloses in "Hydroxyapatite thin films with giant electrical polarization", Chemistry of Materials (2015) 27(4), 1164-1171, that carbonated hydroxyapatite formed on titanium and stainless steel electrodes and further hydrothermal crystallization at 200 ºC using a solution that contains 0.3 M of urea was found to display giant polarization with quasi-permanent stored charge in excess of 66.000 microcoulombs per square centimeter. In addition, this exjibited polarization on carbonated hydroxyapatite depends on the temperature and is not permanent. In contrast, the present invention does not disclose carbonated hydroxyapatite and the goal is to obtain a permanent polarization.

Recently, the present inventors examined the capacity of prepared ACP and cHAp to interact with different phosphates and a biophosphonate (BPs),[18] which is a very relevant topic in the field of biomaterials for biomedical applications. Thus, polyphosphate (polyP), which is an orthophosphate polymer found in mammalian organisms,[19] promotes bone regeneration when adsorbed onto HAp.[20-24] Specifically, polyP stabilizes basic cell growth and differentiation enhancing bone regeneration.[25-27] Further, other studies reported that polyP and pyrophosphate ($P_2O_7^{4-}$) inhibit HAp crystal growth.[28,29] More recently, Grynpas and coworkers[30] proposed that the production of polyP plays an important role in cartilage

mineralization and bone formation, which was attributed to the local accumulation of phosphate (PO_4^{3-}) and calcium (Ca^{2+}) through the formation of strong complexes. This hypothesis was supported by both the adsorption of polyP onto HAp and the correlation between the hydrolytic correlation of polyP in Ca^{2+}-polyP complexes and the increment of PO_4^{3-} and Ca^{2+} concentrations. On the other hand, in BPs the oxygen atom that links the phosphate groups of pyrophosphates is replaced by a carbon atom, which results in the inhibition of both hydrolytic and enzymatic degradations.[31] The affinity of BPs towards HAp increases by incorporating amino functionalities to the tertiary carbon atom, which has been associated to the formation of strong hydrogen bonds between the two species.[32,33] Furthermore, BPs are primary agents in the current pharmacological arsenal against different bone diseases (*e.g.* osteoporosis, Paget disease of bone and malignancies metastatic to bone).[34]

Recent observations evidenced that the adsorption of polyP and $P_2O_7^{4-}$ onto as prepared ACP and cHAp is favored at pH 7 with respect to basic pH 9, even though some limitations in the association processes were found when the results obtained using different adsorbate concentrations were compared.[18] Studies on the adsorption of amino-tris(methylenephosphonic acid), hereafter denoted ATMP, suggested that the affinity of ACP and cHAp towards this BP is lower than towards polyP and $P_2O_7^{4-}$.[18]

M. Ueshima, S. Nakamura, M. Oghaki, K. Yamashita, *Solid State Ionics* (***2002***), *151*, 29-34[63] disclose the polarization of bioactive (HAp) materials by preparing HAp powders via a precipitations reaction, then uniaxially pressing the powders into pellets and sintering those at 1250 ºC for 2 h under a water vapor stream. The obtained specimens are sandwiched between Pt electrodes, heated to room temperature, 300 ºC and 800 ºC in air, respectively, and then subjected to electrical polarization treatment in DC fields of 1 and 10 $kV \cdot cm^{-1}$ for 1 h and thereafter cooled to room temperature under polarization.

M. Nakamura, Y. Sekijima, S. Nakamura, T. Kobayashi, K. Niwa, K. Yamashita, *J. Biomed. Mater. Res*. (**2006**), *79A*, 627-634[62] disclose the preparation of polarized HAp samples as shown in the material and methods section wherein, in particular, the sinterization is carried out in saturated water vapor atmosphere at 1250 ºC for 2 hours and the samples are electrically polarized in a DC. field of 1.0 $kV\ cm^{-1}$ with a pair of platinum electrodes in air at 300 ºC for 1 h. Said polarized HAp are implanted into the tibia of rats in order to detect the interactions between the implanted HAp and blood coagulation components. The

mechanism of the enhanced osteoconductivity caused by electrical polarization is also discussed.

Accordingly, in view of above, the present inventors have surprisingly found that it is possible to obtain a permanently polarized hydroxyapatite with specific electrochemical and electrical properties associated with a huge range of possibilities of use as disclosed below.

VII. 3. Summary of the invention

A first aspect of the present invention relates to a permanently polarized hydroxyapatite and a composition or material comprising thereof.

A second aspect of the present invention relates to a process for obtaining a permanently polarized hydroxyapatite.

A third aspect of the present invention relates to another process for obtaining a permanently polarized hydroxyapatite.

A fourth aspect of the present invention relates to a permanently polarized hydroxyapatite obtained or obtainable by a process according to the second or third aspect of the present invention.

A fifth aspect of the present invention relates to different uses of the permanently polarized hydroxyapatite.

VII.4. Brief description of the drawings

Fig. Ann.VII.1. FTIR spectra of (a) cHAp and (b) ACP.

Fig. Ann.VII.2. X-ray diffraction patterns of the cHAp and ACP particles studied in this work: (a) cHAp/p and cHAp/tsp; and (b) ACP/p and ACP/tsp. cHAp and ACP samples were identified by the peaks at 2θ=32º–34º.

Fig. Ann.VII.3. High-resolution XPS spectra for (a) cHAp/p, (b) cHAp/s and (c) cHAp/tsp samples: P2p, Ca2p, and O1s regions.

Fig. Ann.VII.4. SEM micrographs of cHAp/p, c/HAp/s and cHAp/tsp particles.

Fig. Ann.VII.5. For cHAp/p, c/HAp/s and cHAp/tsp: (a) control voltammograms and variation of both (b) the loss of electroactivity (LEA in Eqn 2) and (c) the specific capacitance (C in Eqn 3) with the number of consecutive oxidation-reduction cycles in PBS.

Fig. Ann.VII. 6. (a) Nyquist and (b) Bode plots for cHAp/p, cHAp/s and cHAp/tsp. (c) Electrical equivalent circuit (EEC) used to fit the experimental data recorded for cHAp/s and cHAp/tsp: R_S is the electrolyte resistance, CPE_b and R_b are the bulk constant phase element and resistance, respectively, CPE_{dl} is the contribution of the double layer capacitance. Open symbols correspond to phase angle values whereas solid symbols correspond to Log|Z|, and black lines correspond to the fitted profile. Inset in figure (a) represents the Nyquist behavior at high frequency.

Fig. Ann.VII.7. Contact angle of the first and second FBS drops (θ_{FBS} and θ'_{FBS} in black and grey, respectively) for cHAp/s and cHAp/tsp samples before and after incubation in presence of $P_2O_7^{4-}$, polyP and ATMP.

Fig. Ann.VII.8. FTIR spectra of cHAp/p, cHAp/s and cHAp/tsp incubated in presence of (a) polyP (200 mM), (b) $P_2O_7^{4-}$ (100 mM) and (c) ATMP (200 mM) at pH 7. Arrows indicate the position of the bands and shoulder used to identify the adsorption of the different adsorbates.

Fig. Ann.VII.9. For (a and c) cHAp/s and (b and d) cHAp/tsp: (a and b) control voltammograms and (c and d) variation of the loss of electroactivity (LEA in Eqn 2) with the number of consecutive oxidation-reduction cycles in PBS for samples non-incubated and incubated in presence of $P_2O_7^{4-}$, polyP and ATMP.

Fig. Ann.VII.10. X-ray diffraction patterns of the cHAp/p and cHAp/s samples, which were identified by the peaks at 2θ=32º–34º.

Fig. Ann.VII.11. SEM micrographs of ACP/p, ACP/s and ACP/tsp particles. The nanospherical morphologies found in ACP/p transforms into fusiform nanorods in ACP/tsp, whereas the two morphologies seem to coexist in ACP/s.

Fig. Ann.VII.12. High-resolution XPS spectrum in the Na1s region for (a) cHAp/s and (b) cHAp/tsp samples before and after incubation in presence of ATMP, $P_2O_7^{4-}$ and polyP.

Fig. Ann.VII.13. High-resolution XPS spectrum in the N1s region for (a) cHAp/s and (b) cHAp/tsp samples before and after incubation in presence of ATMP.

Fig.Ann.VII.14. For cHAp/p: (a) control voltammogram and (b) variation of the loss of electroactivity (LEA in Eqn 2) with the number of consecutive oxidation-reduction cycles in PBS for samples non-incubated and incubated in presence of $P_2O_7^{4-}$, polyP and ATMP.

Fig.Ann.VII.15. a) Nyquist, (b) log |Z| and (c) phase angle plots for cHAp/s alone and incubated in presence of polyP (200 mM), $P_2O_7^{4-}$ (100 mM) and (c) ATMP (200 mM) at pH 7.

Fig.Ann.VII.16. a) Nyquist, (b) log |Z| and (c) phase angle plots for cHAp/tsp alone and incubated in presence of polyP (200 mM), $P_2O_7^{4-}$ (100 mM) and (c) ATMP (200 mM) at pH 7.

Fig.Ann.VII.17. Figure Ann.VII.17. shows the control voltammograms for cHAp/p, c/HAp/s and cHAp/tsp in PBS. The electrochemical activity, which is defined by the anodic and cathodic areas of the voltammogram, is noticeably higher for HAp/tsp than for HAp/s and HAp/p and the control (stainless steel, AISI 304, electrode).

Fig. Ann.VII. 18A-D. Figure Ann.VII.18A shows the ^{31}P spectrum of HAp sample as obtained by synthesis (cHAp/p) where the co-existence of crystalline and disordered phase(s) (amorphous calcium phosphate) is present. The crystallinity is 43%. Weak signals are probably due to hydrogenphosphate and dihydrogenphosphate. Figure Ann.VII.18B shows the ^{31}P spectrum of sintered HAp sample (cHAp/s) where a re-organization is observed. The co-existence of several crystalline and disordered phase(s) (amorphous calcium phosphate) is also present. The crystallinity is 65%. Weak signals are probably due to hydrogenphosphate and dihydrogenphosphate. Figure Ann.VII.18C shows the ^{31}P spectrum of HAp sample after permanent polarization according to the present invention (cHAp/tsp) where the crystallinity is 76%. Weak signals are no longer present. Figure Ann.VII.18D shows the overlapping of spectra from Figure Ann.VII.18A-C.

Fig.Ann.VII.19. ^{1}H (a), ^{13}C (b) and ^{31}P NMR (c) spectra of a set 1 sample (Table Ann.VII.4) obtained after reaction for 24 h at 95 ºC and using a 5 mM $ZrOCl_2$ solution for preparing the layered system.

Fig.Ann.VII.20. Variation of Gly/Phos (○), Ala/Phos (□) (Gly+Ala)/Phos (♦) and Gly/Ala (▲) ratios versus time for reactions performed at 95 ºC using set1 samples (Table 4) prepared from a 5 mM $ZrOCl_2$ solution (a), versus temperature for reactions performed during 24 h using the same sample (b) and versus concentration of zirconium oxychloride solutions (c) for reactions performed at 95 ºC, 24 h and using set 1 samples.

Fig.Ann.VII.21. High resolution XPS spectra for (a) p-cHAP, (b) p-cHAP + Phos-Zr-Phos, c) p-cHAP + Phos-Zr-Phos after negative reaction (e.g. without exposure to UV radiation) and d) p-CHAP + Phos-Zr-Phos after positive reaction (24 h at 95 ºC): N1s, and Zr3d regions.

Fig.Ann.VII.22. SEM micrograps of a set 1 sample before (a) and after (b) reaction for 24 h at 95 ºC and using a 5 mM $ZrOCl_2$ solution for preparing the layered system.

Fig.Ann.VII.23. a) FTIR spectra of a set 1 sample after reaction for 24 h at 95 ºC and using a 5 mM $ZrOCl_2$ solution for preparing the layered system. Insets compare the 1700-1500 cm^{-1} region for the above sample after (b) and before reaction (d), a set 2 sample after reaction (c) and a mixture of glycine and alanine (2:1 weight ratio) (e).

Fig.Ann.VII.24. X-ray diffraction patterns corresponding to polarized c-HAp (a) and the set 1 sample before (b) and after (c) reaction for 24 h at 95 ºC and using a 5 mM $ZrOCl_2$ solution for preparing the layered system. Gray crosses point out characteristic X-ray diffraction reflections of the catalyst that disappear after reaction whereas red crosses point out new reflections that can be observed after reaction. Circled symbols indicate the reflections that changed more drastically during reaction.

Fig.Ann.VII.25. Voltammogram after 20 consecutive oxidation and reduction cycles For cHAp/tsp (prepared according to our conditions) and the polarized mineral prepared according to the conditions of Nakamura et al. and Ueshima et al. with samples as prepared.

Conditions of Nakamura et al. (*J. Biomed. Mater. Res*. (**2006)**, *79A*, 627-634):

i) Synthesis by precipitation at room temperature;

ii) Drying at 850 ºC for 2 h.

iii) Calcination at 1250 ºC in saturated water atmosphere for 2h

iv) Polarization at 1 kV/cm for 1h at 300 or 800 ºC

Conditions of Ueshima et al. (Solid State Ionics 2002, 151, 29-34):

i) Synthesis by precipitation at room temperature;

ii) Drying at 850 ºC for 2 h

iii) Calcination at 1250 ºC in saturated water atmosphere for 2 h

iv) Polarization at 10 kV/cm for 1h at 300 or 850 ºC

Fig.Ann.VII.26. Loss of electrochemical activity against the number of oxidation-reduction cycles for cHAp/tsp (prepared according our conditions) and the polarized mineral prepared according to the conditions of Nakamura et al. and Ueshima et al. with samples as prepared.

Conditions of Nakamura et al. (*J. Biomed. Mater. Res*. (**2006)**, *79A*, 627-634):

i) Synthesis by precipitation at room temperature;

ii) Drying at 850 ºC for 2 h

iii) Calcination at 1250 ºC in saturated water atmosphere for 2 h

iv) Polarization at 1 kV/cm for 1h at 300 or 800 ºC

Conditions of Ueshima et al. (Solid State Ionics 2002, 151, 29-34):

i) Synthesis by precipitation at room temperature;

ii) Drying at 850 ºC for 2 h

iii) Calcination at 1250 ºC in saturated water atmosphere for 2 h

iv) Polarization at 10 kV/cm for 1h at 300 or 850 ºC.

Fig.Ann.VII.27. Comparative table between the system of the present invention and those of state of the art with respect to the electrical resistance and surface capacitance with the following conditions with samples as prepared:

Conditions of Nakamura et al. (*J. Biomed. Mater. Res*. (**2006)**, *79A*, 627-634):

i) Synthesis by precipitation at room temperature;

ii) Drying at 850 ºC for 2h

iii) Calcination at 1250 ºC in saturated water atmosphere for 2 h

iv) Polarization at 1 kV/cm for 1h at 300 or 800 ºC

Conditions of Ueshima et al. (Solid State Ionics 2002, 151, 29-34):

i) Synthesis by precipitation at room temperature;

ii) Drying at 850 ºC for 2h

iii) Calcination at 1250 ºC in saturated water atmosphere for 2 h

iv) Polarization at 10 kV/cm for 1h at 300 or 850 ºC.

Fig.Ann.VII.28. Re-evaluation of the samples as in Figure Ann.VII.25 after 3 months.

Fig.Ann.VII.29. Re-evaluation of the samples as in Figure Ann.VII.27 after 3 months.

VII. 5. Detailed description of the invention

In a first aspect, the present invention relates to permanently polarized hydroxyapatite characterized in that its crystallinity is over 65%, preferably, over 70%, more preferably, over 75%, and its corresponding ^{31}P NMR spectrum is as shown on Figure Ann.VII.18C.

In the present invention, the term "permanently polarized" means that the hydroxyapatite has undergone a complete structural redistribution, almost perfect, with a high crystallinity degree, i.e. particularly with a low amount of amorphous calcium phosphate and the presence of vacancies detected by increased electrochemical activity and the accumulation of charge per unit mass and surface. It has an electrochemical activity and ionic mobility which do not disappear over. The chemical differences between the permanently polarized hydroxyapatite and the corresponding synthesized and sintered hydroxyapatite are shown on RMN ^{31}P spectra according to Figure Ann.VII.18A-C.

Figure Ann.VII.s Ann.VII.18A-C display the solid state ^{31}P NMR spectra of cHAp/p, cHAp/s and cHAp/tsp samples (according to the present invention). The main resonance peak, present in cHAp/p, cHAp/s and cHAp/tsp at 2.9 ppm corresponds to bulk phosphate groups PO_4^{3-} of hydroxyapatites.[56] Compared to cHAp/p, the line width of both cHAp/s and HAp/tsp samples are narrower, which is consistent with the increment of χ_c mentioned above. The broad signals at approximately [-1,0] ppm and a shoulder at [0,1] ppm, present in cHAp/p and cHAp/s, were usually assigned to the lone protonated surfaces phosphate groups arising from the disordered near surface layer.[57] Indeed, hydroxyapatite particles are typically described as an ordered hydroxyapatite core surrounded by a disordered non-apatitic surface layer.[58] The shoulder at 4-6 ppm, which is present in cHAp/s, is also due to the surface HPO_4^{2-} ions, when its amount in the surface layer is greater that a certain threshold.[59] This increase in surface HPO_4^{2-} ions in cHAp/s is caused by the more disordered surface layer due to the thermal process applied in cHAp/s particle treatment. The more unusual part is the only peak of typical bulk phosphate groups PO_4^{3-} of hydroxyapatites present in cHAp/tsp. Thus, such particles undergo a treatment consisting in a constant DC electric field of 500 V, heating simultaneously at 1000 ºC for 2 h. This thermal and electrical stimulation process (TSP) process was found to exert different effects on the hydroxyapatite surface properties.[60] Like the hydroxyapatite surface undergoes variations due to changes in the position of OH^- ions.[61] Accordingly, the fingerprint of the surface OH^- ions leaving from the columns due to the thermally and electrical stimulated polarization process in p-cHAp is

the disappearance of the surface HPO_4^{2-} ions and formation of holes in the valence band for the corresponding charge neutralization.

The present invention further relates to a composition or material comprising the permanently polarized hydroxyapatite as defined herein.

In a further embodiment, said composition or material is a medical, in particular pharmaceutical, composition or material.

In another further embodiment, said composition or material further comprises at least one of the followings: silicates; biocompatible polymers, including but not limited thereto, polylactic acid (PLA), poly lactic-co-glycolic acid (PGLA), polyglycolide (PGA), polydioxanone (PDO), polyhydroxybutyrate (PHB), polysaccharides and proteins such as collagen; organometallic compounds and metal ions, preferably selected from Mg, Sr, Fe, Mn, Zr, Au, and Ti, more preferably Zr.

In a second aspect, the present invention relates to a process for obtaining a permanently polarized hydroxyapatite, preferably as defined in any of the embodiments of the first aspect, comprising the steps of:

(a) obtaining sintered samples of hydroxyapatite and/or amorphous calcium phosphate at a temperature between 700 ºC and 1200 ºC;

(b) applying a constant or variable DC voltage between 250 V and 2500 V for at least 1 minute at a temperature between 900 °C and 1200 °C or
applying an equivalent electric field between 1.49 kV/cm and 15 kV/cm for at least 1 minute at a temperature between 900 °C and 1200 °C or
applying an electrostatic discharge between 2500 V and 1500000 V for less than 10 minutes at a temperature between 900 ºC and 1200 ºC or
applying an equivalent electric field between 148.9 kV/cm and 8928 kV/cm for less than 10 minutes at a temperature between 900 ºC and 1200 ºC;

(c) cooling the samples while applying the constant or variable DC voltage or the equivalent electric field, preferably to room temperature or
cooling the samples while applying the electrostatic discharge or the equivalent electric field, preferably to room temperature.

The process and the permanently polarized hydroxyapatite obtained or obtainable by that process has in particular the following advantages:

The sintering temperature as defined in step (a) is lower than that of Yamashita and co-workers[14] and advantageously avoids some undesirable phase transitions.

The current density of the obtained permanently polarized hydroxyapatite using a temperature as defined in step (b), which is the so-called polarization temperature, is several orders of magnitude higher than that achieved by Yamashita and co-workers[14] using a polarization temperature of 350 °C to 400 ºC (~10^{-5} A/cm^2 and ~10^{-9} A/cm^2, respectively), proving the success of the inventors' treatment. It is worth noting that this was an unexpected result since Yamashita and coworkers[14] found that the current density decreases in the interval between 450 and 700 ºC. The success of the inventors' treatment has been attributed to the combination of the sintering temperature and a very high polarization temperature (between 900 ºC and 1200 °C).

In a preferred embodiment, the sintered samples of hydroxyapatite obtained in step a) are selected from the group consisting of sintered samples of crystalline hydroxyapatite, sintered samples of amorphous hydroxyapatite and a mixture of said sintered samples. More preferably, the sintered samples of hydroxyapatite obtained in step a) are sintered samples of crystalline hydroxyapatite.

In a further embodiment, the sintered samples obtained in step a) are sintered samples of hydroxyapatite. The sintered samples of hydroxyapatite are preferably selected from the group consisting of sintered samples of crystalline hydroxyapatite, sintered samples of amorphous hydroxyapatite and a mixture of said sintered samples. More preferably, the sintered samples obtained in step a) are sintered samples of crystalline hydroxyapatite.

In another further embodiment, the sintered samples obtained in step a) are sintered samples of hydroxyapatite and amorphous calcium phosphate. The sintered samples of hydroxyapatite are preferably selected from the group consisting of sintered samples of crystalline hydroxyapatite, sintered samples of amorphous hydroxyapatite and a mixture of said sintered samples. More preferably, the sintered samples obtained in step a) are sintered samples of crystalline hydroxyapatite and amorphous calcium phosphate.

In a yet another embodiment, the sintered samples obtained in step a) are sintered samples of amorphous calcium phosphate.

The sintering step (a) is a thermal treatment of a ceramic at a temperature lower than its melting point. In the instant case, the sintering step is carried out at a temperature between

700 °C and 1200 ºC, preferably between 700 °C and 1150 ºC, more preferably between 800 °C and 1100 ºC, and most preferably about 1000 ºC.

Also, importantly, the process according to the second aspect of the present invention applies a constant DC voltage (see step (b)) and / or constant electric field as disclosed in the state of the art. When a constant DC voltage is applied the corresponding electric field is zero.

In a further embodiment, the constant or variable DC voltage or the equivalent electric field is applied in step (b) for 0.5 hours to 1.5 hours. In another embodiment, the constant or variable DC voltage or the equivalent electric field is applied in step (b) for about 1 hour.

In another further embodiment, the DC voltage applied in step (b) is about 500 V. Such a DC voltage would be equivalent to a constant electric field of 3.0 $kV \cdot cm^{-1}$.

In a yet another embodiment, the temperature in step (b) is at least 1000 ºC.

In a third aspect, the present invention relates to a process for obtaining a permanently polarized hydroxyapatite, preferably as defined in any of the embodiments of the first aspect, comprising the steps of:

(a) obtaining sintered samples of hydroxyapatite and/or amorphous calcium phosphate;

(b) heating the samples obtained in (a) at between 900 ºC and 1200 ºC;

(c) applying a constant or variable DC voltage between 250 V and 2500 V for at least 1 minute or, applying an equivalent electric field between 1.49 kV/cm and 15 kV/cm for at least 1 minute or, applying an electrostatic discharge between 2,500 V and 1,500,000 V for less than 10 minutes or, applying an equivalent electric field between 148.9 $kV \cdot cm^{-1}$ and 8928 $kV \cdot cm^{-1}$ for less than 10 minutes;

(d) cooling the samples maintaining the DC voltage or the equivalent electric field, preferably to room temperature, or cooling the samples maintaining the electrostatic discharge or the equivalent electric field, preferably to room temperature

In a preferred embodiment, the sintered samples of hydroxyapatite obtained in step a) are selected from the group consisting of sintered samples of crystalline hydroxyapatite, sintered samples of amorphous hydroxyapatite and a mixture of said sintered samples. More preferably, the sintered samples of hydroxyapatite obtained in step a) are sintered samples of crystalline hydroxyapatite.

In a further embodiment, the sintered samples obtained in step a) are sintered samples of hydroxyapatite. The sintered samples of hydroxyapatite are preferably selected from the group consisting of sintered samples of crystalline hydroxyapatite, sintered samples of amorphous hydroxyapatite and a mixture of said sintered samples. More preferably, the sintered samples obtained in step a) are sintered samples of crystalline hydroxyapatite.

In another further embodiment, the sintered samples obtained in step a) are sintered samples of hydroxyapatite and amorphous calcium phosphate. The sintered samples of hydroxyapatite are preferably selected from the group consisting of sintered samples of crystalline hydroxyapatite, sintered samples of amorphous hydroxyapatite and a mixture of said sintered samples. More preferably, the sintered samples obtained in step a) are sintered samples of crystalline hydroxyapatite and amorphous calcium phosphate.

In a yet another embodiment, the sintered samples obtained in step a) are sintered samples of amorphous calcium phosphate.

The sintering step (a) is a thermal treatment of a ceramic at a temperature lower than its melting point. In the instant case, the sintering step is preferably carried out at a temperature between 700 °C and 1200 °C, more preferably 700 °C and 1150 ºC, even more preferably 800 °C and 1100 °C, and most preferably about 1000 ºC.

Also, importantly, the process according to the third aspect of the present invention applies a constant DC voltage (see step (c)) and/or a constant electric field as disclosed in the state of the art. When a constant DC voltage is applied the corresponding electric field is zero.

In a further embodiment, the constant or variable DC voltage or the equivalent electric field is applied in step (c) for 0.5 hours to 1.5 hours. In another embodiment, the constant or variable DC voltage or the equivalent electric field is applied in step (c) for about 1 hour.

In another further embodiment, the DC voltage applied in step (c) is about 500 V.

In a yet another embodiment, the temperature in step (b) is at least 1000 ºC.

The advantages mentioned in the context of the process according to the second aspect of the present invention do analogously apply with respect to the process according to the third aspect of the present invention.

In a fourth aspect, the present invention relates to a permanently polarized hydroxyapatite obtained or obtainable by a process according to the second aspect or third aspect of the

present invention. With regard to further features and advantages of the permanent polarized hydroxyapatite and process, reference is made to the embodiments described in the first and second aspect of the present invention.

In a fifth aspect, the present invention relates to the following uses of the permanently polarized hydroxyapatite.

The present invention further relates to the use of the permanently polarized hydroxyapatite as defined herein or the composition or material comprising said permanently polarized hydroxyapatite as defined herein in biomedical applications. Preferably, said biomedical application is selected from cementum for teeth, bone, prosthesis, medical devices, drug-delivery,gene therapy and tissue regeneration.

The present invention further relates to the use of the permanently polarized hydroxyapatite as defined herein or the composition or material comprising said permanently polarized hydroxyapatite as defined herein as electrodes.

The present invention further relates to the use of the permanently polarized hydroxyapatite as defined herein or the composition or material comprising said permanently polarized hydroxyapatite as defined herein for doping polymers.

The present invention further relates to the use of the permanently polarized hydroxyapatite as defined herein or the composition or material comprising said permanently polarized hydroxyapatite as defined herein as a catalyst, preferably as a photoelectrocatalyst or an electrocatalyst. Preferably, the use as a catalyst is in a reaction for the synthesis of organic molecules, in particular amino acids, preferably natural amino acids. Advantageously, the permanently polarized hydroxyapatite may exhibit superior catalytic performance and high adsorption capacity as further illustrated in the following.

The present inventors have found that the permanently polarized hydroxyapatite as defined herein or the composition or material comprising said permanently polarized hydroxyapatite as defined herein, can be used as a component in a layered, in particular trilayered, catalyst system based on (zirconium) amino tris(methylene phosphonic acid) which allows to catalyze the synthesis of natural amino acids, such as glycine and alanine. This synthesis takes place in the solid state with a significant yield and without rendering noticeable by-products as demonstrated by NMR spectroscopy. The reaction can be performed at a relatively low temperature (75-105 ºC), short time (e.g. less than 24 h) and

low pressure (e.g. less than 50 bar) but exposition to UV radiation is indispensable. The catalyst is able to fix molecular nitrogen which acts as the nitrogen source and adsorb CO_2. Carbon dioxide and methane are involved in the production of carboxylic groups and both methylene and methyl groups, respectively. Water also affects the catalyst modifying its dielectric behavior and contributing to ionic mobility. These results are very interesting since it is provided a new and clean synthesis process of organic molecules, such as amino acids that could proceed in the solid state, avoiding the dissolution of reactants in great water volumes as proposed in former prebiotic synthesis. The capacity of fixing molecular nitrogen and using a mildly reducing atmosphere (N_2, CO_2, H_2O and CH_4) are also noticeable points of the new catalyst system. This surprising use opens the possibility of employing this catalyst family to get amino acids from a mildly reducing atmosphere (i.e. containing H_2O, CH_4, N_2 and CO_2,) instead of the less probable reducing atmosphere (H_2O, CH_4, NH_3 and H_2). Furthermore, the use of this catalyst by adsorbing CO_2 allows to obtain organic compounds (such as the production of amino acids as shown in the example section), while reducing the amount of CO_2 in the atmosphere which represents a clear contribution to the existing environmental problems due to high CO_2 volume concentrations in the atmosphere (green house effect).

This catalyst is based on the efficient zirconium oxychloride and amino tris(methylene phosphonic acid) trilayered system, abbreviated hereinafter as Phos-Zr-Phos. Nevertheless, the compound supporting the trilayered system should play a determinant rule to anchor properly the first phosphonate layer. This feature will be also evaluated comparing the results from a layered silicate (e.g. sodium montmorillonite), a layered aluminosilicate (e.g. mica) and a calcium phosphate compound (HAp, ($Ca_{10}(PO_4)_6(OH)_2$)) able to establish strong ionic interactions between its calcium ions and the deposited phosphonate layer. The application of a thermally stimulated polarization to HAp enhanced the electrochemical activity and stability and the electrical conductivity, while increased significantly the adsorption of phosphates and phosphonates (particularly the amino tris(methylene phosphonic acid, ATMP) with respect to non-treated (as synthesized) HAp particles. (See example section for further details about this process).

The present invention further relates to the use of the permanently polarized hydroxyapatite as defined herein or the composition or material comprising said permanently polarized hydroxyapatite as defined herein for supporting, preferably adsorbing, organic

molecules. Preferably, said molecules are selected from carbohydrates, amino acids, lipids, DNA, RNA, biopolymers and ATP. More preferably, said biopolymers are selected from polylactic acid (PLA), poly lactic-co-glycolic acid (PGLA), polyhydroxybutyrate (PHB), polydioxanone (PDO), polysaccharides and proteins and organo-metallic compounds.

The present invention further relates to the use of the permanently polarized hydroxyapatite as defined herein or the composition or material comprising said permanently polarized hydroxyapatite as defined herein for supporting, preferably adsorbing, phosphorous containing compounds such as pyrophosphate, triphosphate, triphosphonate and/or polyphosphates. The polyphosphates are preferably selected from any of the polyphosphates having from 1 to 50,000 monomer units or any combination thereof.

The present invention further relates to the use of the permanently polarized hydroxyapatite as defined herein or the composition or material comprising said permanently polarized hydroxyapatite as defined herein for supporting, preferably adsorbing, organometallic compounds, preferably metal phosphonates. The organo-metallic compounds are preferably compounds containing metal ions wherein the metal ions are selected from the group consisting of transition metals, lanthanides and combinations thereof. More preferably, the organometallic compounds are compounds containing metal ions wherein the metal ions are selected from the group consisting of Sr, Mg, Fe, Mn, Zr, Au, Ti and mixtures of at least two of said compounds.

The present invention further relates to the use of the permanently polarized hydroxyapatite as defined herein or the composition or material comprising said permanently polarized hydroxyapatite as defined herein for molecular recognition, preferably racemic resolution.

The present invention further relates to the permanently polarized hydroxyapatite as defined herein or the composition or material comprising said permanently polarized hydroxyapatite as defined herein for use in the treatment of bone degradation and/or bone malignancies, such as osteoporosis.

The present invention further relates to DNA/RNA for use in the treatment of diseases, wherein the DNA/RNA is administered by means of the permanently polarized hydroxyapatite as defined herein or the composition or material comprising said permanently polarized hydroxyapatite as defined herein. The DNA/RNA is preferably selected from the group consisting of double-stranded or single-stranded DNA or RNA cointaining sequences

related to diseases (i.e. cancer, neuronal diseases or diseases related to tissue calcifications) and mixtures of at least two of said DNA/RNA. The diseases are preferably selected from the group consisting of genetic disorders including, but not limited thereto, Achondroplasia, Alpha-1 Antitrypsin Deficiency, Antiphospholipid Syndrome, Autism, Autosomal Dominant Polycystic Kidney Disease, Breast cancer, Charcot-Marie-Tooth, Colon cancer, Cri du chat, Crohn's Disease, Cystic fibrosis, Dercum Disease, Down Syndrome, Duane Syndrome, Duchenne Muscular Dystrophy, Factor V Leiden Thrombophilia, Familial Hypercholesterolemia, Familial Mediterranean Fever, Fragile X Syndrome, Gaucher Disease, Hemochromatosis, Hemophilia, Holoprosencephaly, Huntington's disease, Klinefelter syndrome, Marfan syndrome, Myotonic Dystrophy, Neurofibromatosis, Noonan Syndrome, Osteogenesis Imperfecta, Parkinson's disease, Phenylketonuria, Poland Anomaly, Porphyria, Progeria, Prostate Cancer, Retinitis Pigmentosa, Severe Combined Immunodeficiency (SCID), Sickle cell disease, Skin Cancer, Spinal Muscular Atrophy, Tay-Sachs, Thalassemia, Trimethylaminuria, Turner Syndrome, Velocardiofacial Syndrome, WAGR Syndrome, Wilson Disease) and diseases related to tissue calcifications including, but not limited thereto, diseases related to small and large arteries, heart valves, brain (where it is known as cranial calcification), joints and tendons, such as knee joints and rotator cuff tendons, soft tissues like breasts, muscles, and fat, kidney, bladder, and gallbladder.

The present invention further relates to the use of the permanently polarized hydroxyapatite as defined herein or the composition or material comprising said permanently polarized hydroxyapatite as defined herein as a component in a solid-state battery. As used herein, a solid-state battery is a battery that has both solid electrodes and solid electrolytes. As a group, these materials are very good conductors of ions, which is necessary for good electrolyte and electrode performance, and are essentially insulating toward electrons, which is desirable in electrolytes but undesirable in electrodes. The high ionic conductivity minimizes the internal resistance of the battery, thus permitting high power densities, while the high electronic resistance minimizes its self-discharge rate, thus enhancing its charge retention.

The present invention further relates to the use of the permanently polarized hydroxyapatite as defined herein or the composition or material comprising said permanently polarized hydroxyapatite as defined herein as a component in an energy harvesting chip which is a chip that can generate their own energy. Energy harvesting is defined as the

conversion of ambient energy into usable electrical energy. When compared with the energy stored in common storage elements, like batteries and the like, the environment represents a relatively inexhaustible source of energy. Consequently, energy harvesting (i.e. scavenging) methods must be characterized by their power density, rather than energy density.

The present invention is now further illustrated by reference to the following examples which do not intend to limit the scope of the invention.

VII.6 Examples

VII.6.1. Process for obtaining permanently polarized HAp and ACP

Materials. Ammonium phosphate dibasic [$(NH_4)_2HPO_4$; purity ≥ 99.0%], ammonium hydroxide solution 30% (NH_4OH; purity: 28-30%), tetrasodium pyrophosphate ($Na_4P_2O_7$)), sodium triphosphate (polyP) and ATMP were purchased from Sigma-Aldrich. Calcium nitrate [$Ca(NO_3)_2$; purity ≥ 99.0%] was purchased from Panreac (Barcelona, Spain). Ethanol (C_2H_5OH; purity ≥ 99.5%) was obtained from Scharlab (Barcelona, Spain). Fetal bovine serum (FBS), for contact angle measurements, was purchased from Gibco.

Synthesis of HAp and ACP. A simple procedure was used to prepare ACP and cHAp samples, the only difference being the thermal post-treatment applied to the reaction mixture.[35] Reagent conditions were adjusted to get a Ca/P ratio of 1.67. For both ACP and cHAp, 15 mL of 0.5 M $(NH_4)_2HPO_4$ in de-ionized water (pH adjusted to 11 with an ammonia 30% w/w solution) were added drop-wise (rate of 2 $mL \cdot min^{-1}$) and under agitation (400 rpm) to 25 mL of 0.5 M $Ca(NO_3)_2$ in ethanol. After that, the reaction mixture was stirred 1 h by agitation (400 rpm) at room temperature. In the case of ACP the resulting suspension was aged for 24 h at 37 ºC, whereas hydrothermal conditions were applied during 24 h for cHAp. In the hydrothermal synthesis the crystal growth is performed in an apparatus consisting of a steel pressure vessel called an "autoclave", in which a nutrient is supplied along with water. In the instant case, the temperature was 150 ºC and the pressure was 200 bar.

In both cases, the precipitate was separated by centrifugation and washed sequentially with de-ionized water and a 60/40 v/v mixture of ethanol-water (twice). A white powder was recovered after freeze-drying. ACP and cHAp obtained using this procedure have been denoted "*as prepared*" samples, hereafter abbreviated ACP/p and cHAp/p, respectively.

Sintering and thermally stimulated polarization process. Sintered cHAp and ACP samples, hereafter denoted cHAp/s and ACP/s, respectively, were prepared by heating the previously synthesized powders at 1000 ºC for 2 h in air. This temperature is lower than that used by Yamashita and co-workers.[14,15] After this, powders were uniaxially pressed at 620 MPa for 10 min to obtain dense discs suitable for characterization. The dimensions of these specimens were 10 mm of diameter × 1.68 mm of thickness.

In order to get thermally stimulated polarized ACP and cHAp (ACP/tsp and cHAp/tsp, respectively), discs of sintered samples were sandwiched between stainless steel (AISI 304) plates, heated to 1000 ºC in air and, simultaneously, polarized for 1 h under application of a constant DC voltage (**V**). This polarization temperature as disclosed herein is out of the temperature values (i.e. < 700 ºC) employed by Yamashita and co-workers,[14,15] who indicated that temperatures higher 450 ºC have a negative impact in the polarization process, leading to a reduction in the current intensity of the polarized samples. Subsequently, samples were cooled to room temperature, maintaining the DC voltage. Preliminary assays were performed using **V** values that ranged from 250 to 2000 V (i.e. a constant electric field from 1.49 to 11.9 kV/cm), the best results being obtained for 500 V (i.e. 2.98 kV/cm). Accordingly, all experiments described in this work correspond to ACP/tsp and cHAP/tsp samples polarized using **V**= 500 V.

VII.6.2. Characterization of the permanently polarized HAp and ACP

X-Ray diffraction. The crystallinity and structure was studied by wide angle X-ray diffraction (WAXD). Patterns were acquired using a Bruker D8 Advance model with Cu K_α radiation (λ= 0.1542 nm) and geometry of Bragg-Brentano, theta-2 theta. A one-dimensional Lynx Eye detector was employed. Samples were run at 40 kV and 40 mA, with a 2-theta range of 10-60, measurement steps of 0.02º, and time/step of 2-8 s. Diffraction profiles were processed using PeakFit v4 software (Jandel Scientific Software) and the graphical representation performed with OriginPro v8 software (OriginLab Corporation, USA).

The crystallite size (L) in the direction perpendicular to the (211) planes was derived from X-ray diffraction profiles considering the (211) peak width and line broadening measurement using the Scherrer equation:[36]

$$L = \frac{0.9\lambda}{\beta \cos \theta} \quad (1)$$

where λ is the wavelength (CuK_α), β is the full width at half maximum height of the (211) peak, θ is the diffraction angle and 0.9 is a shape factor.

The crystallinity (χ_c) was obtained using the following expression:[37]

$$\chi_c = 1 - \frac{V_{112/300}}{I_{300}} \quad (2)$$

where I_{300} is the intensity of the (300) reflection and $V_{112/300}$ is the intensity of the hollow between the (112) and (300) reflections, which disappears in non-crystalline samples.

X-ray photoelectron spectroscopy (XPS). XPS analyses were performed in a SPECS system equipped with a high-intensity twin-anode X-ray source XR50 of Mg/Al (1253 eV/1487 eV) operating at 150 W, placed perpendicular to the analyzer axis, and using a Phoibos 150 MCD-9 XP detector. The X-ray spot size was 650 μm. The pass energy was set to 25 and 0.1 eV for the survey and the narrow scans, respectively. Charge compensation was achieved with a combination of electron and argon ion flood guns. The energy and emission current of the electrons were 4 eV and 0.35 mA, respectively. For the argon gun, the energy and the emission current were 0 eV and 0.1 mA, respectively. The spectra were recorded with pass energy of 25 eV in 0.1 eV steps at a pressure below 6×10^{-9} mbar. These standard conditions of charge compensation resulted in a negative but perfectly uniform static charge. The C1s peak was used as an internal reference with a binding energy of 284.8 eV. High-resolution XPS spectra were acquired by Gaussian–Lorentzian curve fitting after s-shape background subtraction. The surface composition was determined using the manufacturer's sensitivity factors.

FTIR spectroscopy. Infrared absorption spectra were recorded with a Fourier Transform FTIR 4100 Jasco spectrometer in the 1800-700 cm^{-1} range. A Specac model MKII Golden Gate attenuated total reflection (ATR) equipment with a heating Diamond ATR Top-Plate was used.

Morphology. Scanning electron microscopy (SEM) studies were carried out using a Focused Ion Beam Zeiss Neon40 microscope operating at 5 kV, equipped with an energy dispersive X-ray (EDX) spectroscopy system. Samples were deposited on a silicon disc

mounted with silver paint on pin stubs of aluminum, and sputter-coated with a thin layer of carbon to prevent sample charging problems.

Contact profilometry. The surface roughness (Rq) of the prepared HAp discs was determined using a stylus profilometer (Veeco, Plainview, NY, USA).

Contact angle. Measurements were carried out using the sessile drop method at room temperature on an OCA 15EC with SCA20 software (Data-Physics Instruments GmbH, Filderstadt, Germany). The solvents used for these experiments were deionized water and FBS, contact angles being determined for both the first and second drop (θ and θ', respectively). For θ measurements, the sessile drop was gently put on the surface of sample discs using a micrometric syringe with a proper metallic needle (Hamilton 500 μL). The ellipse method was used to fit a mathematical function to the measured drop contour. This procedure consists on approximate the drop contour to the line of an ellipse, deviations from the true drop shape being in the range of a few percent. The ellipse method provides accurate measure of the contact angle and holds the advantage that it is extremely fast. For each solvent, no less than ten drops were examined. Measures of θ' were performed using the same procedure, even though an equilibration time of 1 min. was applied after depositing the second drop onto the first one.

Determination of water content. HAp discs were dried in an oven (100 ºC) for 15 h. After this, samples reached the room temperature in a desiccator, being immediately weighted. Next, samples were immersed in deionized water for 1 hour. Samples were removed, patted dry with a lint free cloth, and weighted. The water content, expressed as increment in weight percent, was calculated as follows:

$$M_W(\%) = \frac{(W_W - W_D)}{W_D} \times 100 \qquad (1)$$

where M_W is the water content of the sample, W_W is the weight of the wet sample, and W_D the weight of the dried sample. W_W and W_D were determined using a Sartorius CPA26P analytical micro-balance.

Cyclic voltammetry (CV). The electrochemical behavior was determined by CV using an Autolab PGSTAT302N equipped with the ECD module (Ecochimie, The Netherlands) with a three-electrode cell under a nitrogen atmosphere (99.995% in purity) at room temperature. A 0.1 M phosphate buffer saline solution (PBS; pH = 7.2 adjusted with NaOH) was used as

the electrolyte in the three-electrode cell. The working compartment was filled with 30 mL of the electrolyte solution. Steel AISI 316 sheets of 1×1.5 cm^2 (thickness 0.1 cm) were used as both the working and the counter electrodes, and an Ag|AgCl electrode was used as the reference electrode which contained a KCl saturated aqueous solution (offset potential versus the standard hydrogen electrode, E^0 = 0.222 V at 25 °C). All potentials given in this report are referenced to this electrode. HAp discs prepared as described above were fixed on the working electrode using a two-side adhesive carbon layer. The initial and final potentials were -0.40 V, whereas a reversal potential of 0.80 V was considered. The scan rate was 50 mV/s.

The electroactivity, which indicates the ability to exchange charge reversibly, was evaluated by examining the similarity between the anodic and cathodic areas of the control voltammogram. The electrochemical stability (*i.e.* loss of electroactivity, LEA), which decreases with the oxidation and reduction areas of consecutive control voltammograms, was determined using the following expression:

$$LEA = \frac{\Delta Q}{Q_{II}} 100 \qquad (2)$$

where ΔQ is the difference of voltammetric charge between the second cycle and the last cycle and Q_{II} is the voltammetric charge corresponding to the second cycle. In this work all values of *LEA* were referred to 1000 consecutive oxidation-reduction cycles.

The specific capacitance (*SC*; in F/g) of HAp in the electrode was calculated as:

$$SC = \frac{Q}{\Delta V m} \qquad (3)$$

where Q is voltammetric charge, which is determined by integrating either the oxidative or the reductive parts of the cyclic voltammogram curve, ΔV is the potential window and m is the mass of polymer on the surface of the working electrode. The latter is derived from the productivity current and polymerization charge.[38]

Electrochemical Impedance Spectroscopy (EIS). EIS measurements were performed using an AUTOLAB PGSTAT302N in the 10 kHz to the 10 mHz frequency range and the amplitude of the sinusoidal voltage was 10 mV. All experiments were carried at room temperature. Appropriated sized films were pressed in a disc format and were sandwiched between two stainless steel electrodes (diameter = 1.5 cm) assembled into an isolating resin

holder.[39] The cell was tightened with screws to ensure constant pressure fastening. Films thickness was between 1.68 and 2.00 mm determined by a micrometer and the area was about 1.766 cm^2. Prior analyses, samples were previously dried by heating at 100 ºC in an oven overnight. After data collection, EIS results were then processed and fitted to an electrical equivalent circuit (EEC).

Adsorption onto treated cHAP. The concentration of the adsorbate in the working solutions was 100 mM for $P_2O_7^{4-}$ and 200 mM for both polyP and ATMP, while the pH considered in this study was 7 in all cases. The concentration of $P_2O_7^{4-}$ was a half of that used for the other two adsorbates because of limitations in the solubility of the former specie. For the incubation, 500 μL of the working solution with the adsorbate were deposited onto 50 mg of cHAp. After overnight agitation at 25 ºC, adducts were separated by centrifugation at 6500 rpm during 5 minutes at 4 ºC. Sediments were re-suspended in distilled water. After this process, which was repeated two times, the obtained pellets were frozen at -80 ºC for 3 h and, subsequently, the humidity was removed using a lyophilizer.

VII.6.3. Chemical characterization and choice of samples for electrochemical and adsorption assays

The FTIR spectra of the studied cHAp and ACP samples, which show typical PO_4^{3-} bands at the region comprised between 950 and 1200 cm^{-1}, are compared in Figure Ann.VII. 1.. The spectra of cHAp/p, cHAp/s and cHAp/tsp show characteristic vibrational modes of PO_4^{3-} at ν_1= 962 cm^{-1} and ν_3= 1016, 1087 cm^{-1}, the resemblance between the three spectra indicating that cHAp/p does not undergo significant structural changes when sintered and polarized. In contrast, the apparition of new bands and shoulders (*i.e.* at 970 and 1037 cm^{-1}), as well as the shifts in the existing bands (*i.e.* from 963 and 1090 cm^{-1} to 947 and 1098 cm^{-1}, respectively), in the spectra of ACP/s and ACP/tsp evidence important structural re-organizations in ACP/p after thermal and polarization treatment. Powder ACP samples heated at temperatures ranging between 600 and 1000º C were characterized by Raynaud *et al.*.[40] The apparition of new FTIR bands were attributed to the formation of a structure formed by cHAp and tricalcium phosphate (TCP) phases.

Structural analyses of cHAp and ACP particles by WAXD were focused on peaks at 2θ=32º–34º, which are characteristic of the (211), (112), and (300) HAp reflections.

Although the comparison between the diffraction patterns recorded for cHAp/p and cHAp/tsp reveal small structural changes (Figure Ann.VII.2a), the thermally stimulated polarization process provokes important increments in both the crystallinity (χ_c) and the crystallite size (L). Thus, the χ_c of cHAp/p and cHAp/tsp samples was 0.42±0.01 and 0.75±0.02, respectively, while the crystallite size of cHAp/tsp, L= 86±2 nm, was around 40% larger than that of cHAp/p (L= 61±2 nm). The variation of χ_c and L has been attributed to the formation of OH^- defects. Fujimori *et al.*[41] reported that OH^- ions scape from the HAp matrix above 800 ºC, this dehydration process giving place to the formation of vacancies and O^{2-} ions. In addition to the induction of a small amount of OH^- defects, a monoclinic-to-hexagonal thermal phase transition occurs upon the application of such treatment.[42-44] The hexagonal phase becomes most stable at room temperature because of the order-disorder phase transition, which is accounted for by the change in the position of the OH^- ions.[42-44] Although the structural differences between monoclinic and hexagonal HAP are small (Figure Ann.VII.2a) they are sufficient to exert a strong impact on some of its properties (see next subsections). The diffraction pattern recorded in this work for cHAp/s (χ_c= 0.65±0.02 and L= 86±3 nm) is compared in Figure Ann.VII.10 with that of cHAp/p.

Figure Ann.VII.3. compares the characteristic XPS spectra in the P 2p, Ca 2p and O 1s regions for cHAp/p, cHAp/s and cHAp/tsp. For cHAp/p the single P2p peak centered at 132.2 eV, which originates from the PO_4^{3-} anions,[45,46] undergoes a slight shift towards higher and lower energies (Δ_{BE}= +0.4 and -1.0 eV) upon the application of sintering and thermally stimulated polarization treatment, respectively. The binding energies of the Ca $2p_{3/2}$ and Ca $2p_{1/2}$ peaks, which are detected at 346.1 and 349.6 eV, respectively, for cHAp/p,[45,47] experience shifts to 346.5 and 350.0 eV for cHAp/s and to 345.1 and 348.6 eV for cHAp/tsp. These variations are fully consistent with the existence of structural changes associated to phase transitions. Moreover, inspection of the chemical composition as determined by XPS, which is displayed in Ann.VII.Table 1, is consistent with the formation of thermally-induced OH^- vacancies. Thus, the content of oxygen is around 2 wt.% lower for cHAp/s and cHAp/tsp than for cHAp/p. Interestingly, the Ca/P molar ratio of the cHAp/p samples is very close to the stoichiometric value of 1.67. However, cHAp/s and cHAp/tsp experience a small reduction with respect to such ideal value, supporting the apparition of vacancies. On the other hand, the nitrogen found in cHAp/p, cHAp/s and cHAp/tsp, which

ranges from 0.28 to 0.40 wt.%, has been attributed to the adsorption of N_2 from the atmosphere.

Table Ann.VII.1. Ca, P, O, Na and N concentrations (wt %) and Ca/P molar ratios determined by XPS of cHAp/p, cHAp, cHAp/s, cHAp/tsp samples before and after incubation in presence of $P_2O_7^{4-}$, PolyP and ATMP.

	Ca	P	O	Na	N	Ca/P
cHAp/p	38.76	18.09	42.86	0.00	0.29	1.66
cHAp/s	39.76	10.01	40.95	0.00	0.28	1.62
cHAp/tsp	40.12	18.95	40.53	0.00	0.40	1.64
cHAp/s + $P_2O_7^{4-}$	39.67	22.76	31.67	5.58	0.32	1.59
cHAp/s + PolyP	38.76	18.95	35.62	6.38	0.29	1.32
cHAp/s + ATMP	39.23	19.27	38.32	0.00	3.18	1.48
cHAp/tsp + $P_2O_7^{4-}$	39.54	22.56	25.64	11.91	0.35	1.35
cHAp/tsp + PolyP	40.03	27.34	22.58	9.84	0.21	1.13
cHAp/tsp + ATMP	39.12	24.08	32.72	0.00	4.08	1.26

Comparison of the diffraction patterns recorded for ACP samples as prepared and after conducting the thermally stimulated polarization process (ACP/p and ACP/tsp, respectively) is provided in Figure Ann.VII.2b. In this case, changes are very drastic, as is also reflected by the growth of χ_c and L from 0.05±0.02 and 5±1 nm for ACP/p to 0.74±0.03 and 52±3 nm for ACP/tsp. The structure exhibited by the crystalline fraction of ACP/p is identical to that observed for cHAp/p. However, the sintering process provokes the apparition of β-tricalcium phosphate (β-TCP: β-$Ca_3(PO_4)_2$) as the predominant phase. Although the high peaks at 2θ = 31.3º and 34.6º match well with those of the β-TCP card (#09-0169) in the Joint Committee on Powder Diffraction Standards (*JCPDS)*, the coexistence cHAp as a minor phase of ACP/tsp is probed by the persistent peak positions at 2θ= 31.9º, 32.3º, 33.0º and 34.3º. These results suggest that the thermally stimulated polarization process induces partial decomposition of ACP/p, leading to the formation of β-TCP. A similar behavior was reported by different authors for sintered ACP (ACP/s) at 1100 ºC (*i.e.* without applying any electric field),[5,47,48] and corroborated by our observation in the diffraction obtained for the samples prepared in this work by heating ACP/p to 1000 ºC for 2 h in air (not shown). SEM

micrographs displayed in Figure Ann.VII.10 reflect the drastic structural changes undergone by ACP/p samples when treated thermally and electrically.

Because of the predominance of the β-TCP phase in ACP/tsp transition, the rest of the present work (*i.e.* surface and electrochemical properties, as well as adsorption ability) has been focused on the comparison between cHAp/p and cHAp/tsp. For the sake of completeness, such comparison has been extended to sintered cHAp samples (named cHAp/s).

VII.6.4. Surface characterization

The surface morphologies of cHAp/p, cHAp/s and cHAp/tsp samples are compared in Figure Ann.VII.4. As it can be seen, SEM micrographs corroborate previously discussed WAXD results. cHAp/p samples are constituted by laminar crystals and fusiform rods, the same elements being also identified in cHAp/s and cHAp/tsp. However, the amount of such elements increases upon the application of external treatments, especially the thermal stimulation polarization. Thus, crystals are bigger in HAp/tsp than in cHAp/p and c/HAp/s, which is consistent with the χ_c variation discussed above. On the other hand, micrographs clearly reflect that the crystallite size increases with the increasing amount of crystals (*i.e.* WAXD results showed that L varies as follow: cHAp/tsp > cHAp/s > cHAp/p).

Table Ann.VII.2 indicates that, although the surface roughness (Rq) of cHAp/p samples remained practically unaltered upon the application of the polarization and/or thermal treatments, the surface energy changed considerably. The contact angle of water (θ_{water}) was ~4º for cHAp/p, cHAp/s and cHAp/tsp, indicating that the three are very hydrophilic materials, as it was expected because of their surface charge. In contrast, the contact angle in FBS (θ_{FBS}) was significantly lower for cHAp/s and cHAp/tsp than for cHAp/p (Table Ann.VII.2). This variation in the wetting suggests that the re-organization of the ions induced by the thermal and, especially, the polarization treatments increases the contribution of the polar component to the surface energy. In order to support the relative increase of the dispersive contribution with respect to the polar one, the contact angle of the second water and FBS drops (θ'_{water} and θ'_{FBS}, respectively) were determined for the three surfaces (see Methods section). Although the surfaces were less wetted than with the first drop, the behavior was practically identical to that described above (Table 2). Thus, the three

hydrophilic materials led to very similar θ'_{water} values while the differences among θ'_{FBS} values were similar to those obtained for θ_{FBS}.

Table Ann.VII.2. Roughness (Rq), contact angle of the first and second water drops (θ_{water} and θ'_{water}), contact angle of the first and second FBS drops (θ_{FBS} and θ'_{FBS}), and water content after immersion in deionized water (Mw) determined for cHAP/p, cHAp/s and cHAp/tsp samples.

Sample	Rq (nm)	θ_{water} (º) / θ'_{water} (º)	θ_{FBS} (º) / θ'_{FBS} (º)	Mw (%)
cHAp/p	851±194	3±1 / 6±1	81±2 / 96±2	-
cHAp/s	863±158	4±1 / 4±1	61±2 / 71±2	7±1
cHAp/tsp	882±92	4±1 / 4±1	51±2 / 62±2	13±1

In order to complement this information, water absorption assays were performed using the procedure described in the Methods section (Eqn VII.1). Unfortunately, cHAp/p discs broke immediately after water immersion, no measurement being possible in that case. However, the water content determined for cHAp/s and cHAp/tsp samples after immersion in deionized water, which is displayed in Table Ann.VII.2, were fully consistent with the θ_{FBS} and θ'_{FBS} values. Accordingly, water adsorption was 5% higher for HAp/tsp than for HAp/s.

VII.6.5. Electrochemical and electrical properties

Cyclic voltammograms recorded in PBS for cHAp/p, cHAp/s and cHAp/tsp fixed on steel are compared in Figure Ann.VII.5a. As it can be seen, the electrochemical activity of cHAp/p is higher than that of steel, which was used as a control. However, the electroactivity increases considerably with thermal and electrical treatments (*i.e.* 46% and 150%, respectively). In the case of cHAp/tsp, such evident effect is accompanied of a significant enhancement of the anodic current intensity at the reversal potential. This behavior suggests that the structural changes provoked by the thermally stimulated polarization treatment facilitate the diffusion of ions through the inorganic matrix and, therefore, the electrochemical response upon oxidation-reduction processes. On the other hand, the current density cHAp/tsp obtained using a polarization temperature range as disclosed herein is several orders of magnitude higher than that achieved by Yamashita and co-workers[14] using

a polarization temperature of 350-400 ºC (~10^{-5} A/cm^2 and ~10^{-9} A/cm^2, respectively), proving the success of our treatment. It is worth noting that this was an unexpected result since Yamashita and coworkers[14] found that the current density decreases in the interval between 450 and 700 ºC. The success of the inventors' treatment has been attributed to the combination of the sintering temperature, which is lower than that of Yamashita and co-workers[14] and avoids some undesirable phase transitions, and a very high polarization temperature (between 700 ºC and 1200 °C).

Treatments also affect the electrostability, as is reflected by the variation of the LEA (Eqn VII.2) with the number of consecutive oxidation-reduction cycles (Figure Ann.VII.5b). As it can be seen, in all cases the electrochemical stability decreases rapidly during the first 100-150 redox cycles, the reduction of the LEA being considerably slower along the next cycles. After 1000 cycles, the electroactivity decreased 72%, 67% and 60% for cHAp/p, cHAp/s and cHAp/tsp, respectively, evidencing that structural changes caused by thermally stimulated polarization process also enhances the stability of the electrochemical properties. The behavior followed by the specific capacitance (C in Eqn VII.3) is fully consistent with that of the electroactivity. Thus, although C is very small in all cases, the ability to store charge of cHAp/p (C= $16 \cdot 10^{-5}$ F/g·cm^2) is 71% and 82% smaller than those of cHAp/s and cHAp/tsp (C= $56 \cdot 10^{-5}$ and $89 \cdot 10^{-5}$ F/g·cm^2, respectively). The variation of the specific capacitance with the number of redox cycles (Figure Ann.VII.5c) was similar to that described above for LEA.

EIS measurements were carried out to evaluate the ionic conductivity inside the prepared HAp samples. Thus, this technique will provide information about the influence in the electrical properties of the inner interfaces created inside the material by the thermally stimulated polarization process. Figure Ann.VII.6. compares representative Nyquist plots obtained for cHAp/p, cHAp/s and cHAp/tsp. In a Nyquist plot, the first semi-circular response corresponds to the electron transfer resistance at the higher frequency range, which controls the electron transfer kinetics of the redox probe on the electrode-solid disk interface. The diameter of the semi-circle defines the resistance of electron transfer, usually called bulk resistance (R_b). The Nyquist plot recorded for cHAp/p (Figure Ann.VII.6a) exhibits only one dielectric relaxation time (τ), which corresponds to a single charge transfer across the solid disk, indicating that the material has a high bulk resistance (*i.e.* low ionic conductivity) in the dry state. Bode plots (Figure Ann.VII.6b) show phase angles close to 80º, which

correspond to resistive materials in the dry state. The semi-circle diameter in Nyquist plots (Figure Ann.VII.6a) is considerably smaller for cHAp/s and, especially, for cHAp/tsp, even though a second time constant appears. This feature has been attributed to a significant structural modification inside the HAp crystals that allows fast transport of charge across the disk. According to WAXD and SEM observations, cHAp/s and cHAp/tsp samples present higher more concentration of crystals as well as bigger crystals than cHAp/p. Therefore, the thermal treatment step promotes the growing of the crystal, while the thermally stimulated polarization treatment is that responsible is responsible of the definition of good pathways for charge transportation. This is reflected in the numerical evaluation of the EIS results (Table Ann.VII.3.).

The electrical equivalent circuit (EEC) used to fit the experimental data is shown in Figure Ann.VII.6c. The EEC contains three important elements: R_b that represents the bulk resistance; and Q_b and Q_{dl} that describes the ideal capacitances from both the cHAp thick film and double layer between the metal-disk surfaces, respectively. R_S corresponds to the electrolyte solution resistance, even though it was considered ~0 $\Omega \cdot cm^2$ due to the absence of liquid electrolyte. The CPE_b real capacitance accounts for the non-uniform diffusion among the films adhered to the electrode surface. The CPE_{dl} real capacitance is typically associated to the surface reactivity, surface heterogeneity and roughness, which in turn are related to the electrode geometry and porosity. Also, the CPE impedance, which has been expressed as $Z_{CPE} = [Q\ (j\omega)^n]^{-1}$, represents an ideal capacitor and a pure resistor for n= 1 and n= 0, respectively, while it is associated with a diffusion process when n~ 0.5. All impedance data displayed in Figure Ann.VII.6a were fitted with the EEC showed in the Figure Ann.VII.6c, with exception of those obtained for cHAp/p. For EEC used the latter samples does not have the capacitance response from the double layer film and corresponds to $[R_s(R_bQ_b)]$.

According to Table Ann.VII.3, the R_b is very low (6.7×10^5 $\Omega \cdot cm^2$) for the cHAp/tsp sample compared to the cHAp/s one (6.4×10^6 $\Omega \cdot cm^2$), which indicates that the ionic conductivity increased by one order of magnitude when the thermal treatment is combined with the polarization one. Another relevant change is the appearance of a second time constant (τ) when larger crystals were obtained and these crystals were polarized at 500 V (Figure Ann.VII.6a). This feature indicates the creation of charge pathways inside the solid, which is reflected by the CPE_b.

Table Ann.VII.3. Data of EIS results obtained from the electrical equivalent circuit (EEC) showed in the Figure Ann.VII.6c for cHAp/s and cHAp/tsp dry discs[a] after exposure to several treatment processes and after the phosphates inorganic molecules adsorption.

Samples	R_b (Ω cm^2)	Q_{dl} (F cm^{-2} s^{n-1})	n	Q_b (F cm^{-2} s^{n-1})	n
cHAp/p [a]	134.6×10^{-6}	-	-	8.180×10^{-10}	0.76
cHAp/s	6.43×10^{-6}	1.248×10^{-8}	0.77	1.215×10^{-5}	0.44
cHAp/tsp	0.67×10^{-6}	4.558×10^{-7}	0.71	4.863×10^{-5}	0.55
cHAp/s + polyp	0.42×10^{-6}	5.076×10^{-8}	0.81	1.573×10^{-5}	0.43
cHAp/s + $P_2O_7^{4-}$	1.00×10^{-6}	3.647×10^{-8}	0.73	1.309×10^{-5}	0.50
cHAp/s + ATMP	0.95×10^{-6}	2.159×10^{-8}	0.76	1.009×10^{-5}	0.42
cHAp/tsp + polyp	66.7×10^{-3}	5.550×10^{-8}	0.81	7.792×10^{-4}	0.63
cHAp/tsp + $P_2O_7^{4-}$	0.35×10^{-6}	1.373×10^{-8}	0.79	3.812×10^{-5}	0.49
cHAp/tsp + ATMP	69.9×10^{-3}	5.699×10^{-8}	0.73	5.204×10^{-5}	0.48

[a] The EEC for cHAp/p is $R_s(R_bQ_b)$.

The last observation is in perfect agreement with both SEM micrographs and the electrochemical response determined by CV. According to Chaudhuri and co-workers,[49] the conductive sites in dry HAp should be considered as the channels along which ions are able to move by thermally activated hopping (such as the columnar OH^- ions or protons) while the capacitive sites are immobile ions. In contrast, Lukic *et al*.,[50] who found that the conductivity of HAp increases with temperature, attributed this behavior to geometric factors as growing of grain size. Liu and Shen[51] showed extensive dehydroxylation during the sintering of cHAp above 900 ºC, OH^- ions being responsible of the conductivity at high temperatures (*i.e.* in the range of 700-1000 ºC).

VII.6.6. Adsorption of pyrophosphate, triphosphate and trisphosphonate

In a very recent study we examined the adsorption of $P_2O_7^{4-}$, polyP and amino-ATMP onto cHAp/p.[12] In order to examine how both thermal and electric treatments affect the adsorption of the same inorganic compounds, a complete study has been carried using cHAp/s and cHAp/tsp samples as substrates. According to our previous work, the

concentration of adsorbate in the working solutions was 100 mM for $P_2O_7^{4-}$ and 200 mM for both polyP and ATMP, which provided clear adsorption signals for cHAp/p at pH 7.

Figure Ann.VII.7a compares the contact angles for both the first and second FBS drop (θ_{FBS} and θ'_{FBS}, respectively) determined for cHAp/s and cHAp/tsp before and after incubation in presence of the inorganic adsorbates. As it can be seen, the FBS-wettability of the two substrates increased upon incubation, suggesting that the three inorganic adsorbates were successfully adsorbed. Moreover, the reduction of the contact angle with the adsorbate followed the same variation for the two cHAp substrates: polyP < $P_2O_7^{4-}$ ≈ ATMP. Accordingly, the surface energy becomes higher upon the adsorption of polyP than upon the adsorption of $P_2O_7^{4-}$ and ATMP, independently of the treatment applied to the cHAp particles.

Adsorption of $P_2O_7^{4-}$, polyP and ATMP was also examined by using XPS. Comparison of the characteristic XPS spectrum in the Na1s region for cHAp/s and cHAp/tsp before and after incubation in presence of inorganic adsorbates reveals a peak centered at 1074.2 eV for samples treated with $P_2O_7^{4-}$ and polyP (Figure Ann.VII.12.). This signal, which is identical to those reported by Gaskell *et al.*[52,53] for $Na_4P_2O_7 \cdot 10H_2O$ and $Na_5P_3O_{10}$, corroborates the incorporation of these compounds onto the surface of the two treated cHAp. In contrast the content of Na in non-incubated samples and samples incubated in presence of ATMP is null (Table 1). The ratios obtained using the Na1s atomic percent compositions indicate that the adsorption of $P_2O_7^{4-}$ and polyP is, respectively, ~2 and ~1.5 times higher for cHAp/tsp than for cHAp/s. A similar strategy was followed to identify the adsorption of ATMP, which is clearly detected through the peaks at the N1s region (Figure Ann.VII.S4.). Thus, the content of N in non-incubated samples and samples incubated in presence of $P_2O_7^{4-}$ and polyP is ≤ 0.40 wt.%, increasing to 3.18 and 4.08 wt.% for cHAp/s and cHAp/tsp samples incubated in presence of ATMP (Table Ann.VII.1). Assuming that the amount of N_2 adsorbed from the atmosphere is the same for incubated and non-incubated samples, the adsorption of ATMP is ~1.4 times higher for cHAp/tsp than for cHAp/s. The two peaks detected at 404.3 and 402.5 eV (Figure Ann.VII.13.) for the latter samples have been attributed to nitrogen atoms of ATMP with different chemical environments (*i.e.* free and hydrogen bonded).[54]

Figure Ann.VII.8. compares the FTIR spectra of cHAp/p, cHAp/s and cHAp/tsp after incubation in solution with $P_2O_7^{4-}$, polyP and ATMP at neutral pH. FTIR spectra of $P_2O_7^{4-}$, polyP and ATMP were reported in our previous work.[12] For polyP, the weak shoulder

identified at around 890 cm^{-1} for cHAp/p (Figure Ann.VII.8a), which corresponds to the P–O–P asymmetric stretching, transforms into a well-defined adsorptions band for cHAp/s and, especially, cHAp/tsp. This feature is fully consistent with XPS observation, corroborating that the application of thermal and thermally stimulated polarization processes enhance significantly the ability of cHAp to adsorb polyP. Based on the FTIR spectra presented in Figure Ann.VII.1 and 8, the ability of cHAp samples to adsorb polyP was estimated using the ratio of integrated area of the peak at 1016 cm^{-1} (belonging to the mineral) and the integrated area of the peak at 890 cm^{-1} (belonging to polyP). Results indicated that the adsorption of polyP onto cHAp/p was 2.0 and 2.6 times lower than onto cHAp/s and cHAp/tsp, respectively, which is in good agreement with XPS results.

Unfortunately, this feature was much less clear for $P_2O_7^{4-}$. Thus, the band at 890 cm^{-1} remained undetectable in the spectra displayed in Figure Ann.VII.8b, where the only evidence of adsorption is the very weak shoulder at 740-750 cm^{-1} for cHAp/s and cHAp/tsp that has been attributed to the P–O–P symmetric stretching. It should be noted that the atomic percent content of Na1s detected by XPS in cHAp samples incubated with polyP is considerably higher than in those incubated with $P_2O_7^{4-}$ (Table 1), which is consistent with FTIR observations. Also, previous quantum mechanical calculations considering the (100) and (001) surfaces of cHAp evidenced that the adsorption of polyP is favored with respect to that of $P_2O_7^{4-}$.[18] Thus, the ability of the adsorbate to adapt its geometry to the crystallographic positions of the ions at the cHAp surfaces increases with the size of phosphate chain. Therefore, adsorbed $P_2O_7^{4-}$ was found to be significantly strained in comparison to adsorbed polyP.

FTIR results for the different cHAp samples incubated with ATMP (Figure Ann.VII.8c) reveals similar trends to those observed for polyP. Thus, the shoulder identified for cHAp/p at 900 cm^{-1}, which corresponds to asymmetric vibrations of alkylphosphonic,[55] transforms into a relatively intense and well defined peak for cHAp/s and, especially, cHAp/tsp. This variation is in agreement with XPS results, indicating that the ability of the different cHAp samples to adsorb ATMP increase in the following way: cHAp/p < cHAp/s < cHAp/tsp. The adsorption of ATMP onto of cHAp/s and cHAp/tsp was estimated to be, respectively, 2.2 and 3.0 times higher than onto cHAp/p, supporting XPS data.

VII.6.7. Adsorption-induced electrochemical protection and enhanced electrical conductivity

Cyclic voltammograms recorded for cHAp/p incubated in presence of polyP, $P_2O_7^{4-}$ and ATMP (Figure Ann.VII.14a) are very similar to those displayed in Figure Ann.VII.5a, suggesting that the amount of adsorbate at the mineral surface is not enough to alter the redox behavior. In contrast, cyclic voltammograms of incubated cHAp/s and, especially, cHAp/tsp are considerably different from those of non-incubated samples. This is clearly reflected in Figure Ann.VII.9a and 9b, which compares the voltammograms recorded for incubated and non-incubated samples. Thus, the electroactivity of incubated cHAp/s and cHAp/tsp samples is higher than that of non-incubated samples by ~60% and ~40%, respectively, suggesting that adsorbed molecules facilitates the exchange of ions between the mineral matrix and the PBS electrolyte solution during the oxidation and reduction processes.

However, the most striking feature refers to the variation of the electroactivity against the number of redox cycles. Thus, comparison of the LEA (Eqn VII.2) measured for incubated and non-incubated cHAp/p (Figure Ann.VII.14b) indicates that the electrochemical stability of the latter is lower (~10%) than that of samples with adsorbed polyP, $P_2O_7^{4-}$ or ATMP. This feature, which suggests that adsorbate molecules provide electrochemical protection to the mineral, is significantly enhanced for cHAp/s and cHAp/tsp, as is evidenced in Figure Ann.VII.9c and 9d, respectively. Thus, after 1000 redox cycles the loss of electroactivity of non-incubated cHAp/s and cHAp/tsp is higher than those of incubated samples by ~20% and ~25%, respectively. The LEA values of incubated cHAp/tsp are particularly striking (*i.e.* 21%, 27% and 29% for polyP, $P_2O_7^{4-}$ and ATMP, respectively). These low values evidence that the application of the thermally stimulated polarization treatment enhances not only the adsorption capacity but also improves the electrochemical activity and stability.

EIS results (Table Ann VII.3.) reflect the positive effects of adsorbed PolyP and ATMP in the ionic conductivity of treated cHAp samples in comparison to adsorbed $P_2O_7^{4-}$. This phenomenon is particularly remarkable for cHAp/tsp, which display the lowest bulk resistance (66.7 and 69.9 $k\Omega \cdot cm^2$ for samples with adsorbed PolyP and ATMP, respectively), evidencing that PolyP and ATMP promote the electron charge mobility inside the dry film. Thus, structural changes produced by the thermally stimulated polarization treatment favors the interaction of the mineral with both PolyP and ATMP, forming better charge transfer

channels. The alignment of the OH^- ions along the *c*-axis in cHAp/tsp samples seems to play a crucial role in the formation of such interaction. Figure Ann.VII.15. and Figure Ann.VII.16. compare the Nyquist and Bode plots recorded for cHAp/s and cHAp/tsp, respectively, with the three examined adsorbates.

VII.6.8. Particular use of permanently polarized hydroxyapatite as a catalyst component in the synthesis of amino acids

VII.6.8.1. Synthesis of amorphous (aHAp) and crystalline hydroxyapatite (cHAp)

15 mL of 0.5 M $(NH_4)_2HPO_4$ in de-ionized water (pH adjusted to 11 with an ammonia 30 *w*/*w*-% solution) were added drop-wise (rate of 2 $mL \cdot min^{-1}$) and under agitation (400 rpm) to 25 mL of 0.5 M $Ca(NO_3)_2$ in ethanol. After that, the reaction mixture was stirred 1 h by agitation (400 rpm) at room temperature. The suspension was aged for 24 h at 37 ºC to get aHAP, whereas a hydrothermal treatment (200 bar at 150 º C for 24 h) was subsequently applied to get cHAp. The precipitate was separated by centrifugation and washed sequentially with de-ionized water and a 60/40 *v*/*v* mixture of ethanol-water (twice). A white powder with the theoretical Ca/P ratio of 1.67 was recovered after freeze-drying.

VII.6.8.2. Sintering process

aHAp, cHPAp and montmorillonite powders were subsequently sintered by firstly heating them in a laboratory furnace (Carbolite ELF11/6B/301) at 1000 ºC during 2 h at an air atmosphere and finally uniaxially pressed at 620 MPa for 10 min. Discs of 100 mm of diameter and 1.7 mm of thickness were finally obtained.

VII.6.8.3. Thermally stimulated polarization process

In order to get thermally stimulated polarized HAp, Nanofil 757 and LM systems, the corresponding discs samples were sandwiched between stainless steel (AISI 304) plates, heated in the furnace to 1000 ºC in air and, simultaneously, polarized for 1 h under application of a constant DC voltage of 500 V, which was previously reported as the optimal one for adsorption assays performed with polarized HAp.[2] Polarized samples will be named as p-cHAp, p-aHAp, p-N757 and p-LM. It should be pointed out that HAp could not be

polarized if the sample was not previously sintered since the disk had not the sufficiently consistence and broke during the polarization process.

VII.6.8.4. Deposition of phosphonate and Zirconium oxychloride ($ZrOCl_2$) layers

A trilayered system consisting in the successive deposition of ATMP, *Zirconium oxychloride* and ATMP layers onto the appropriate substrate (i.e. mica, sintered aHAp and cHAp or silicate before and after being submitted to the polarization process) was obtained by immersion in the corresponding aqueous solutions at room temperature for 5 h. Concentrations of ATMP solutions to get the first and second AMTP layers were 5 mM and 1.25 mM, respectively, whereas the concentration of *Zirconium oxychloride* was varied in the different experiments (i.e. from 1 mM to 10 mM, respectively). After each immersion the samples were dried at 37 ºC for 3 h. Fort the sake of completeness bilayered and monolayered systems (i.e. Pho-Z, Pho, Z) were also considered.

VII.6.8.5. Synthesis of amino acids

A high pressure stainless steel reactor was employed to perform the synthesis of amino acids (AAs). The designed reactor was dotted with a manometer, an electric heater with a thermocouple and an external temperature controller. The reactor was also characterized by an inert reaction chamber of teflon (120 mL) where catalyst and water were incorporated, three independent inlet valves for N_2, CH_4, CO_2 and an outlet valve to recover the gaseous reaction products. An UV lamp (GPH265T5L/4, 253.7 nm) was also placed in the middle of the reactor to irradiate directly the solid sample, being the lamp protected by a UV transparent quartz tube. This was coated with a thin film of teflon in order to avoid any contact between the reaction medium and the silicate and therefore to discard other catalyst effects.

Reactions were performed in the 75-105 ºC temperature range for reaction times between 2 and 96 h. Solid samples weighted approximately 150 mg and 0.5 mL of de-ionized liquid water were initially incorporated in the reaction chamber if it was considered necessary. The chamber was extensively purged with the first selected gas in order to eliminate the initial air content (i.e. N_2 or CO_2). Each selected gas was introduced to increase the reaction chamber pressure (measured at room temperature) in two or three atmospheres (i.e. the final pressure at room temperature was always 6 bar).

VII.6.8.6. Measurements

Synthesis of amino acids was routinely verified by the ninhydrin (2,2-dihydroxyindane-1,3-dione) detection test for primary amines. To this end 0.5 mg of the solid recovered after reaction was immersed in a tube containing 0.2 *w*/*v*-% solution of ninhydrin in acetone and subsequently heated to 75 ºC in an oven. The development of purple coloured solutions indicated the formation of the 2-(1,3-dioxoindan-2-yl)iminoindane-1,3-dione chromophore. Yellow-orange coloured solutions were on the contrary characteristic of the Schiff base generated by reaction with secondary amines, while uncoloured solutions derived from tertiary amines such as ATMP.

NMR spectra were acquired with a Bruker Avance III-400 spectrometer operating at frequencies of 400.1 MHz, 100.6, and 161.9 for ^{1}H, ^{13}C and ^{31}P, respectively. Chemical shifts for ^{1}H and ^{13}C were calibrated using tetramethylsilane as an internal standard. Samples were dissolved in deuterated water containing 100 mM of HCl and 50 mM of NaCl.

X-ray photoelectron spectroscopy (XPS) analyses were performed in a SPECS system equipped with a high-intensity twin-anode X-ray source XR50 of Mg/Al (1253 eV/1487 eV) operating at 150 W, placed perpendicular to the analyzer axis, and using a Phoibos 150 MCD-9 XP detector. The X-ray spot size was 650 μm. The pass energy was set to 25 and 0.1 eV for the survey and the narrow scans, respectively. Charge compensation was achieved with a combination of electron and argon ion flood guns. The energy and emission current of the electrons were 4 eV and 0.35 mA, respectively. For the argon gun, the energy and the emission current were 0 eV and 0.1 mA, respectively. The spectra were recorded with pass energy of 25 eV in 0.1 eV steps at a pressure below 6×10^{-9} mbar. These standard conditions of charge compensation resulted in a negative but perfectly uniform static charge. The C1s peak was used as an internal reference with a binding energy of 284.8 eV. High-resolution XPS spectra were acquired by Gaussian–Lorentzian curve fitting after s-shape background subtraction. The surface composition was determined using the manufacturer's sensitivity factors.

Scanning electron microscopy (SEM) studies were carried out using a Focused Ion Beam Zeiss Neon40 microscope operating at 5 kV, equipped with an energy dispersive X-ray (EDX) spectroscopy system. Samples were deposited on a silicon disc mounted with silver

paint on pin stubs of aluminum, and sputter-coated with a thin layer of carbon to prevent sample charging problems.

Infrared absorption spectra were recorded with a Fourier Transform FTIR 4100 Jasco spectrometer in the 1800-700 cm^{-1} range. A Specac model MKII Golden Gate attenuated total reflection (ATR) equipment with a heating Diamond ATR Top-Plate was used.

X-ray powder diffraction patterns were obtained in the beamline BL11-NCD at ALBA synchrotron (Cerdanyola del Vallés, Barcelona, Spain), by using a wavelength of 0.100 nm and an WAXS LX255-HS detector from Rayonix which was calibrated with diffractions of standard of a Cr_2O_3 sample.

VII.6.8.7. Results

Samples coming from reactions using the Pho-Zr-Pho trilayered catalyst supported onto polarized cHAp and an reducing atmosphere constituted by N_2, CO_2, CH_4 and H_2O (set 1 in Table 4) gave rise to positive ninhydrin tests, suggesting therefore the formation of primary amines. In fact, purple spots were developed inside the recovered solids after reaction, indicating that amine compounds were mainly absorbed into the solid substrate. These compounds were well dissolved in the acetone solution after vigorous stirring, contrasting with the uncolored solid/solutions observed for other assayed reaction conditions (e.g. set 2 and sets 4 to 13 in Table Ann.VII.4).

^{1}H NMR spectra (Figure Ann.VII.19a) showed only the presence after reaction of the phosphonate methylene group (i.e. doublet at 3.79-3.76 ppm) and signals corresponding to methylene protons of glycine (singlet at 3.65 ppm) and both methine (quadruplet at 3.91-3.85 ppm) and methane (doublet at 1.54-1.52 ppm) groups of alanine. The same compounds were also evidenced in the ^{13}C NMR spectrum (Figure Ann.VII.19b) where only peaks assigned to the phosphonate (54.34 and 53.00 ppm), glycine (171.95 and 41.26 ppm) and alanine (175.25, 50.25 and 16.01 ppm) units could be detected. It is noteworthy that no by-products were observed and consequently a very clean process for production of glycine and alanine was developed.

Set	Conditions[a]	Ninhidrine test	Observations
1	p-cHAp/Phos-ZC-Phos N_2, CH_4, CO_2, H_2O / UV	+	Gly and Ala signals in NMR spectra. Increasing AAs/Phos ratio with reaction time. Increasing AAs/Phos ratio with reaction *T*. Increasing AA/Phos ratio with Zr content.
2	p-cHAp/Phos-ZC-Phos N_2, CH_4, CO_2, H_2O	-	UV radiation is fundamental.
3	p-aHAp/Phos-ZC-Phos N_2, CH_4, CO_2, H_2O / UV	+	The crystalline structure of HAp is not fundamental for reaction.
4	cHAp/Phos-ZC-Phos N_2, CH_4, CO_2, H_2O / UV	-	Polarization of HAp is fundamental.
5	p-N757/Phos-ZC-Phos N_2, CH_4, CO_2, H_2O / UV	-	The type of polarized support is important.
6	p-LM/Phos-ZC-Phos N_2, CH_4, CO_2, H_2O / UV	-	The type of polarized support is important.
7	p-cHAp/Phos-ZC N_2, CH_4, CO_2, H_2O / UV	-	The trilayered system is fundamental.
8	p-cHAp/ZC-Phos N_2, CH_4, CO_2, H_2O / UV	-	The trilayered system is fundamental.
9	p-cHAp/Phos N_2, CH_4, CO_2, H_2O / UV	-	The trilayered system is fundamental.
10	p-cHAp/ZC N_2, CH_4, CO_2, H_2O / UV	-	The trilayered system is fundamental.
11	Phos	-	AAs cannot be derived from a simple decomposition of Phos using ZC as catalyst.
12	Phos-Zr N_2, CH_4, CO_2, H_2O / UV	-	AAs cannot be derived from a simple decomposition of Phos.
13	p-cHAp/Phos-ZC-Phos CH_4, CO_2, H_2O / UV	-	Substrate is able to fix molecular nitrogen. Molecular nitrogen is essential.
14	p-aHAp/Phos-ZC-Phos N_2, CO_2, H_2O / UV	-	CH_4 appears as the carbon source for CH_2 and CH_3 groups.
15	p-cHAp/Phos-ZC-Phos N_2, CH_4, H_2O / UV	-	CO_2 appears as the source for carboxylic groups.
16	p-cHAp/Phos-ZC-Phos N_2, CH_4, CO_2 / UV	-	H_2O plays an important role in the … mechanism.

Table Ann.VII.4. Summary of experiments and results attained for the synthesis of amino acids (AAs).[a]

[a] Abbreviations denote the support (p-aHAp, aHAp, p-N757, p-LM) and the order of the different layers deposited onto its surface (Phos and ZC for phosphonate and Z*irconium oxychloride*, respectively). UV indicates that experiments were performed under UV radiation.

^{1}H NMR spectra were analyzed for samples recovered after different reaction times (i.e. from 2 to 96 h), being possible to detect the ratios between glycine and phosphonate units (Gly/Phos), alanine and phosphonate units (Ala/Phos) and obviously between glycine and alanine unis (Gly/Ala). Specifically, the areas of signals corresponding to CH_2 protons at 3.65 and 3.79-3.76 ppm and the CH_3 protons at 1.54-1.52 ppm were considered:

$$\text{Gly/Phos} = (3 \times A_{3.65}) / A_{3.79\text{-}376} \quad \text{(VII.1)}$$

$$\text{Ala/Phos} = (2 \times A_{1.54\text{-}1.52}) / A_{3.79\text{-}376} \quad \text{(VII.2)}$$

$$\text{Gly/Ala} = (1.5 \times A_{3.65}) / A_{1.54\text{-}1.52} \quad \text{(VII.3)}$$

Results plotted in Figure Ann.VII.20a allow deducing that glycine is firstly produced and alanine is subsequently derived from this simple amino acid. Thus, the Gly/Ala ratio decreases from 5.4 to 2.2, being nevertheless observed a continuous increase of the Gly/Phos ratio with the reaction time (i.e. from 0.8 to 4.5).

Figure Ann.VII.20b allows estimating the effect of reaction temperature and specifically that a minimum value (i.e. 75 ºC) is required to get a detectable amount of amino acids after 24 h of reaction. The Ala/Phos ratio continuously increased with reaction temperature while the Gly/Phos ratio started to decrease at the maximum assayed temperature (105 ºC) as a result of conversion of glycine into alanine. Nevertheless, the ratio between the total amino acid content and the phosphonate content still increased at this temperature.

Figure Ann.VII.20c shows as the content of the Zirconium oxychloride has a practically negligible influence on the Gly/Phos and Ala/Phos ratios, as presumable for a catalyst. Nevertheless, samples prepared from solutions with a very low concentration of $ZrOCl_2$ (1 mM) led to significantly lower ratios as a consequence of the defective trilayered system. Logically, alanine was in this case the amino acid more disfavoured (i.e. the Gly/Ala ratio was maximum).

Experiments have also been assayed without exposure to the UV radiation (set 2), being in this case unsuccessful the formation of amino acids. Thus, the sustained exposure to UV logically appears as a fundamental issue to get radicals (e.g. $^{\cdot}CH_3$) for further reaction towards formation of alanine and even glycine.

XPS analysis was fundamental to corroborate that amino acids were derived from the molecular nitrogen and not from a hypothetical decomposition of the phosphonate compound. Note that this point cannot be inferred from the NMR spectra since the increase of Gly/Phos could also be related to a decomposition process. Figure Ann.VII.21a shows the XPS spectra in the N1s region for different representative samples and specifically as a peak around 399 eV appears when phosphonate is incorporated onto the surface of p-cHAp. This peak is associated to the nitrogen in the C-N bond and is observed with practically the same intensity when both negative and positive reactions took place. Only in the last case additional peaks corresponding to the deprotonated (NH_2) and protonated (NH_3^+) amino groups were observed at 400.3 eV and 403.8.4 eV, respectively.[32] The amount of nitrogen increased from 0% to 2.75-2.97% when the Phos-Zr-Phos trilayer was deposited onto the p-cHAP substrate and to 6.2% after positive reaction (i.e. set 1 for 24 h at 95 ºC). XPS spectra allowed determining the decrease of Ca/P ratio from a typical value of 1.64 for HAp to 1.26-1.29 when the trilayer was deposited onto the HAp surface. XPS spectra showed also Zr signals (Figure Ann.VII.21b) which appeared as a resolved spin doublet at binding energies of 182.6 (3d5/2) and 185 eV (3d3/2). The measured Zr content was in the 1.26-1.29% range for all samples having the Phos-Zr-Phos trilayer prepared from a 5 mM *Zirconium oxychloride* solution, being this percentage independently of the progress of the reaction.

Deposition of the trilayered system on HAp gave rise to a rough and relative irregular disk surface as shown in the SEM micrograph corresponding to a polarized sample (Figure Ann.VII.22a). This surface slightly changed after reaction since a sporadic formation of regular crystals was detected. Figure Ann.VII.22b shows the growth of micrometric prismatic structures where the hexagonal basal plane tended to be parallel to the disk surface. In fact, it has been reported the capacity of organophosphonate films for inducing crystallization and grown of oriented molecular sieves. In this way, stable, vertically oriented and one dimensional aluminium phosphate crystals were able to grow over the hybrid layers. Cannel systems that could be applied as new catalytic membranes with true molecular selectivity and even for controlling the access of determined size to a sensor surface were formed. In any case, the present results demonstrate that amino acid crystals can also grow onto the surface of the trilayered catalyst but it should also be taken into account that the nynhydrin test revealed the presence of absorbed amino acids inside the disk sample.

Significant differences between set 1 samples before and after reaction can be observed in the FTIR spectra despite the low sensitivity of the technique. Thus, broad and low-intensity bands in the 1600-1400 cm^{-1} region could only be observed in the second case (Figure Ann.VII.23.). It is worth noting that this region is completely flat in the spectra of samples before reaction and also for samples coming from a negative ninhydrin test (e.g. set 2 samples). On the contrary, amino acids such as glycine and alanine have the most intense absorptions in this region (see inset of Figure Ann.VII.23.). Logically, FTIR spectra showed the characteristic peaks of HAp and specifically the three intense bands at 1093, 1033 and 962 cm^{-1} associated to the characteristic vibrational modes of PO_4^{3-} were always observed.

Deposition of the trilayered systems over the polarized c-HAp did not cause a significant change on the X-ray diffraction pattern (Figure Ann.VII.24a and 24b) whereas remarkable changes can be observed after chemical reaction (Figure Ann.VII.24b and 24c).

VII.6.9. Influence of changes on the catalyst system and the polarized support on the synthesis of amino acids

Amino acids were also detected when p-aHAp was employed instead of p-cHAp and the experimental conditions of set 1 were maintained. Nevertheless, we preferred to insist on p-cHAp since the amorphous sample suffered a partial decomposition during the sintering process, which led to the formation of β-tricalcium phosphate (β-TCP: β-$Ca_3(PO_4)_2$) as the predominant phase.

Different assays have been performed in order to evaluate the importance of the type of substrate of the catalytic system. Amino acids were only detected when polarized HAp was employed (e.g. sets 1 and 3 in Table Ann.VII.4), being highly significant the negative results obtained when sintered HAp (set 4) was used as a substrate and also when other systems such as silicates (e.g. Nanofil 757, set 5) and aluminosilicates (e.g. layered mica, set 5) were tested even after being polarized under similar conditions to those applied for p-cHAp.

The suitability of the HAp contribution is interesting since it plays a fundamental role in living systems and specifically constitutes their most abundant inorganic component. The relationship between HAp and biological molecules (e.g. proteins like collagen and even DNA constituted by a phosphate skeleton) has nowadays enhanced an intensive research on

its use for different biomedical applications (e.g. drug and gene delivery, bone repair and tissue engineering among others).

In this sense, it is also remarkable that the metal/phosphonate layered system is also able to molecular recognition and consequently a selective binding of an enantiomeric compound from a racemic solution can be achieved. Furthermore, the high insolubility and stability towards thermal treatments and chemical reactants of zirconium phosphonates have opened other potential applications such as viral vectors in gene delivery. The positive charge of amino-functionalized phosphonates (e. g. the aminoethoxy derivative) allows the direct intercalation of negatively charged DNA molecules. Moreover, binding is pH sensitive being found that the conformation of DNA could be almost retained during intercalation and release processes.

For the sake of completeness we have also assayed the effectiveness of the two possible bilayered (deposition of a first layer of Phos or Zr and subsequent deposition of the second complementary layer, sets 7 and 8, respectively) and monolayer (sets 9 and 10) systems. In all cases, negative results were attained demonstrating that a stable Phos-Zr complex with a nucleation activity was only attained using the trilayered architecture. Probably dissolution of components in the water reaction medium should also be taken into account when bilayered and monolayer arrangements are considered.

Table Ann.VII.4 reports also the results attained when only phosphonate (set 11) and even a mixture of phosphonate and *Zirconium oxychloride* (set 12) were introduced into the reactor instead of the coated polarized support. These assays are also relevant since help discarding a process based on the decomposition of AMTP. Note that in this case the amount of AMTP submitted to UV irradiation and able to react with the selected reducing atmosphere was much higher than required in the trilayered system.

VII.7. Comparative Figures Ann.VII. with respect of prior art

The voltammograms recorded after 20 consecutive oxidation-reduction cycles are displayed in Figure Ann.VII.25.. The similarity between the areas of the anodic and cathodic scans, which correspond to the associated to the oxidation and reduction processes, respectively, have been used to determine the electrochemical activity. As it can be seen, the area of the cHAp/tsp voltammogram is at least 20% higher than the areas of those recorded for the different ACP/polarized samples, indicating that the former material presents higher

ability to store charge reversibly than the latter samples. Moreover, a significant difference is also detected in the anodic and cathodic current densities at the final and reversal potentials, respectively. The current densities are significantly higher, in absolute values, for cHAp/tsp than for the other samples, reflecting a higher movement of charge during the oxidation and reduction processes. This feature is particularly noticeable for the anodic current density. Thus, anodic current density determined for cHAp/tsp is 16.8 $\mu A/cm^2$ while that of the other samples ranges between 4 and 9 $\mu A/cm^2$.

Figure Ann.VII.26. displays the variation of electrochemical activity with the number of redox cycles (electrostability) with respect to the first cycle. Results prove that the excellent results of cHAp/tsp in comparison with all the ACP/polarized samples. After 1000 consecutive oxidation-reduction cycles, the loss of electrochemical activity (LEA) is at least 10% lower for cHAp/tsp than for the other samples. Moreover, the cHAp/tsp preserves the highest electrostability in all cases, independently of the number of cycles, evidencing that this property is inherent to its structure.

Results represented in Figures Ann.VII.25. and 26 are fully consistent with a highly organized and regular structure of cHAp/tsp, which is in agreement with RMN observations. Thus, the latter technique allowed us not only to identify the highly crystalline organization of cHAp/tsp but also to evidence the lack of protonated surfaces phosphate groups arising from the disordered near surface layer, as is typically observed in the rest of samples, as for example prepared and sintered HAp).

Finally, the comparative table of Figure Ann.VII.27. shows that the electrical resistivity of cHAp/tsp is one order of magnitude smaller than those of ACP/polarized samples, which in turn are practically identical to that of cHAp/s ($0.67 \times 10^7\ \Omega \cdot cm^2$, as mentioned above). This feature points out the importance of the temperature in the electrical polarization step. Accordingly, temperatures higher than 900 ºC are necessary to eliminate completely the protons near surface layers, facilitating the creation of both an ordered organization and charge defects able to move with the electric field. In contrast, the similarity between cHAp/s and ACP/polarized in terms of electrical resistivity reflects that these feature are not achieved when polarization is carried out at temperatures lower than 900ºC.

The samples tested in Figures Ann.VII.25. and Ann.VII.27. were re-evaluated after three months as shown in Figures Ann.VII.28. and 29., respectively.

In particular, the electrochemical behavior of all samples was re-evaluated (storage was done at ambient conditions, without any special care) by cyclic voltammetry (see Figure Ann.VII.28.). Results indicate that cHAp/tsp (according to the present invention) remains practically unaltered, as is evidenced by comparison with the voltammogram displayed in Figure Ann.VII.25.. In contrast, all other ACP/polarized samples (according to Nakamura et al. and Ueshima et al.) converge to the same behavior, which is similar to that displayed by cHAp/s. Thus, the electroactivity of cHAp/tsp is significantly higher than that of ACP/polarized samples. This feature supports the importance of the polarization temperature as well as the permanent polarized character of cHAp/tsp. In opposition, the changes observed in ACP/polarized samples after three months indicate that the polarization imparted at temperatures < 850 ºC is not permanent but only temporal.

As shown in Figure Ann.VII.29., the specific capacitance (capacitance per unit of mass, abbreviated SC) of cHAp/tsp decreases 8% after three months (storage was done at ambient conditions, without any special care). In contrast ACP/polarized samples prepared according to Yamashita and co-workers (Nakamura et al. and Ueshima et al.) present a drastic reduction of the SC, which ranges from 50% to 64%. As it can be seen in the previous Table (Figure Ann.VII.27.), the SC of cHAp/tsp is higher than those of ACP/polarized by one order of magnitude. A similar effect is observed in the electrical resistance. The value of cHAp/tsp increases 9% after 3 months, while the resistances of ACP/polarized prepared using the procedures of Yamashita and co-workers increase around 60-70%.

In view of the above results, it is concluded that the hydroxyapatite, as obtained by the present invention, is different from those disclosed in the prior art. It is apparent from the experimental data that the hydroxyapatite of the present invention shows a significant different behavior and it is effectively a permanently polarized hydroxyapatite, whereas those disclosed in the prior art are only temporal polarized hydroxyapatites.

VII. 8. Claims

1. Permanently polarized hydroxyapatite, characterized in that its crystallinity is over 65% and its corresponding RMN ^{31}P spectrum is as shown on Figure Ann.VII.18C.

2. Process for obtaining a permanently polarized hydroxyapatite, preferably a permanently polarized hydroxyapatite according to claim 1, comprising the steps of:

(a) obtaining sintered samples of hydroxyapatite and/or amorphous calcium phosphate at a temperature between 700 ºC and 1200 ºC;

(b) applying a constant or variable DC voltage between 250 V and 2500 V or an equivalent electric field between 1.49 kV/cm and 15 kV/cm for at least 1 minute at a temperature between 900 ºC and 1200 ºC or

applying an electrostatic discharge between 2500 V and 1500000 V or an equivalent electric field between 148.9 kV/cm and 8928 kV/cm for less than 10 minutes at a temperature between 900 ºC and 1200 ºC;

(d) cooling the samples while applying the constant or variable DC voltage or the equivalent electric field or

cooling the samples while applying the electrostatic discharge or the equivalent electric field.

3. Process according to claim 2, wherein the sintered samples of hydroxyapatite obtained in step a) are selected from the group consisting of sintered samples of crystalline hydroxyapatite, sintered samples of amorphous hydroxyapatite and a mixture of said sintered samples.

4. Process according to claim 2 or 3, wherein the sintered samples obtained in step a) are sintered samples of crystalline hydroxyapatite and amorphous calcium phosphate.

5. Composition or material comprising the permanently polarized hydroxyapatite according to claim 1.

6. Composition or material according to claim 5, further comprising at least one of the followings: silicates; biocompatible polymers selected from polylactic acid (PLA), poly

lactic-co-glycolic acid (PGLA), polyglycolide (PGA), polydioxanone (PDO), polyhydroxybutyrate (PHB), polysaccharides and proteins such as collagen; and metal ions.

7. Use of the composition or material according to any of claims 5 or 6 or the polarized hydroxyapatite according to claim 1 in biomedical applications, wherein said biomedical application is preferably selected from cementum for teeth, bone, prosthesis, medical devices, drug-delivery, gene therapy and tissue regeneration.

8. Use of the composition or material according to any of claims 5 or 6 or the polarized hydroxyapatite according to claim 1 as electrodes.

9. Use of the composition or material according to any of claims 5 or 6 or the polarized hydroxyapatite according to claim 1 for doping polymers.

10. Use of the composition or material according to any of claims 5 or 6 or the polarized hydroxyapatite according to claim 1 as a catalyst.

11. Use according to claim 10, wherein said catalyst is a photoelectrocatalyst or an electrocatalyst.

12. Use according to claim 10 or 11, wherein said use as a catalyst is in a reaction for the synthesis of organic molecules, in particular natural amino acids.

13. Use of the composition or material according to any of claims 5 or 6 or the polarized hydroxyapatite according to claim 1 for adsorbing organic molecules, wherein said organic molecules are preferably selected from carbohydrates, amino acids, lipids, DNA, RNA, biopolymers selected from polylactic acid (PLA), poly lactic-co-glycolic acid (PGLA), polyhydroxybutyrate (PHB), polydioxanone (PDO), polysaccharides and proteins, and ATP.

14. Use of the composition or material according to any of claims 5 or 6 or the polarized hydroxyapatite according to claim 1 as a component in a solid state battery.

15. Use of the composition or material according to any of claims 5 or 6 or the polarized hydroxyapatite according to claim 1 as a component in an energy harvesting chip.

VII.9. Figures

Figure Ann.VII.1.

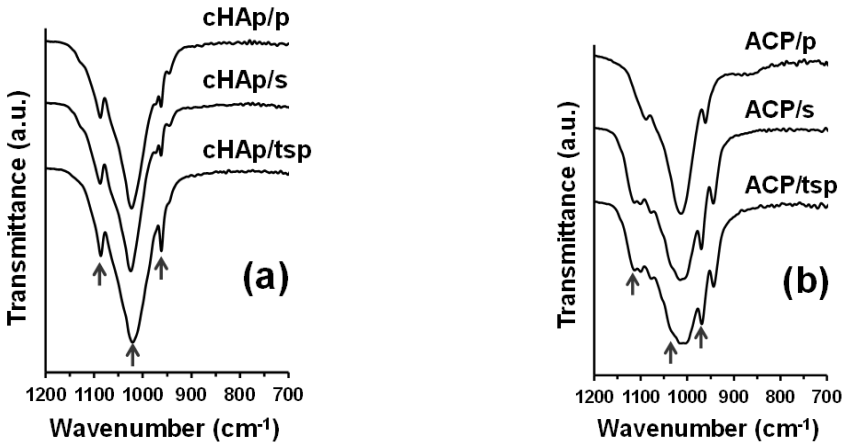

Figure Ann.VII.2.

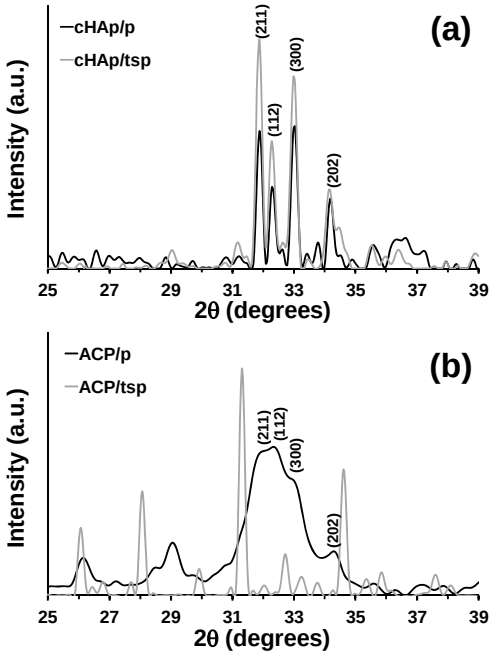

Figure Ann.VII.3.

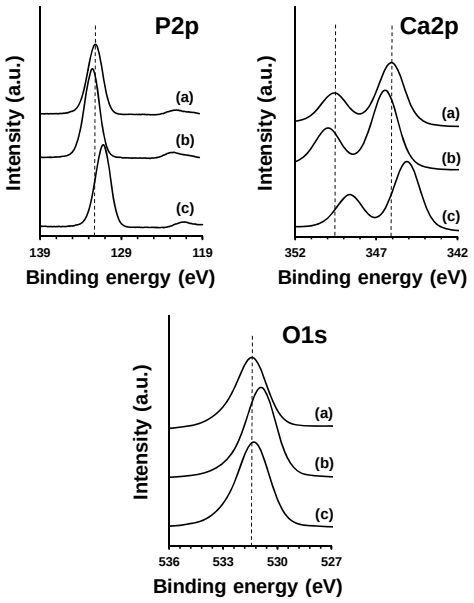

Figure Ann.VII.4.

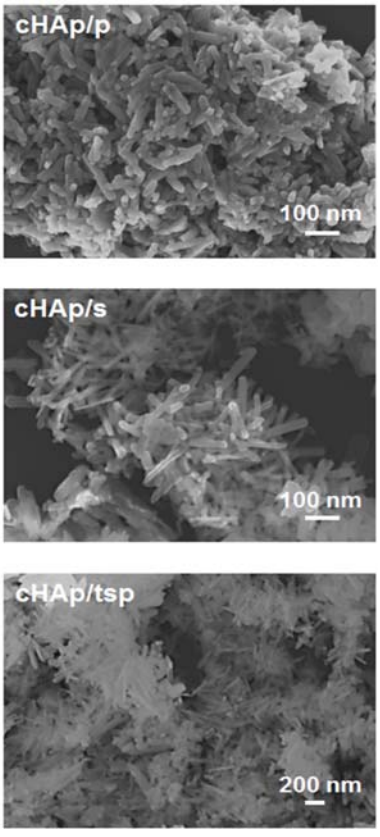

Figure Ann.VII.5.

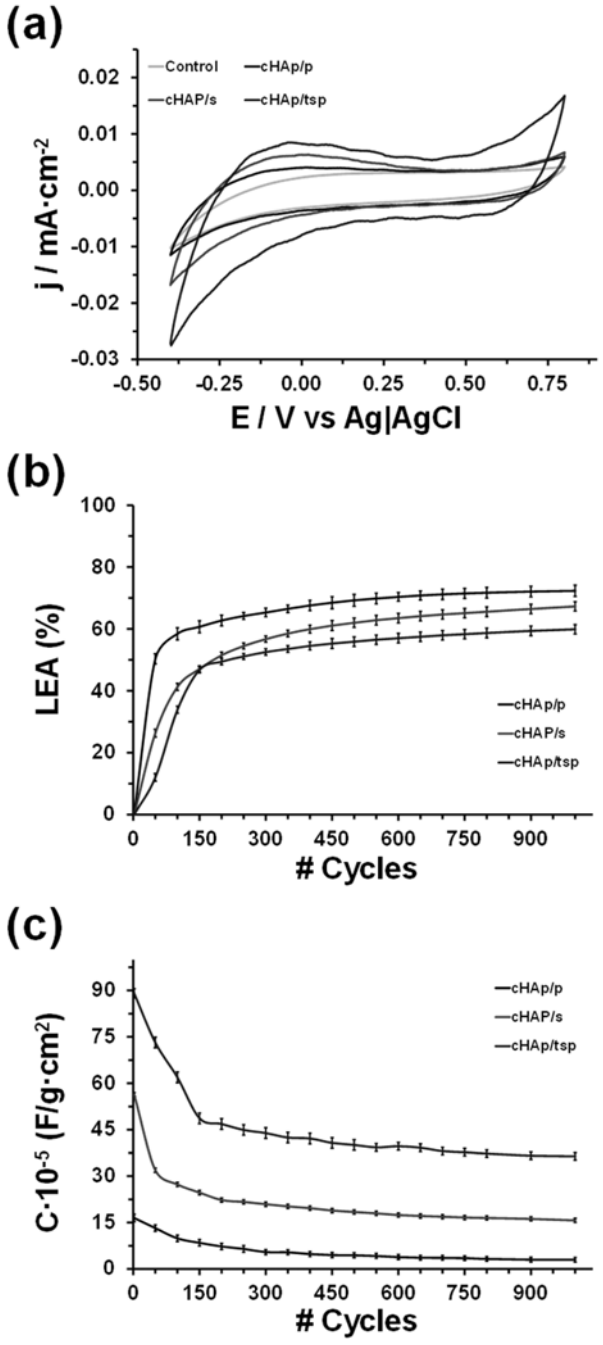

Figure Ann.VII.6.

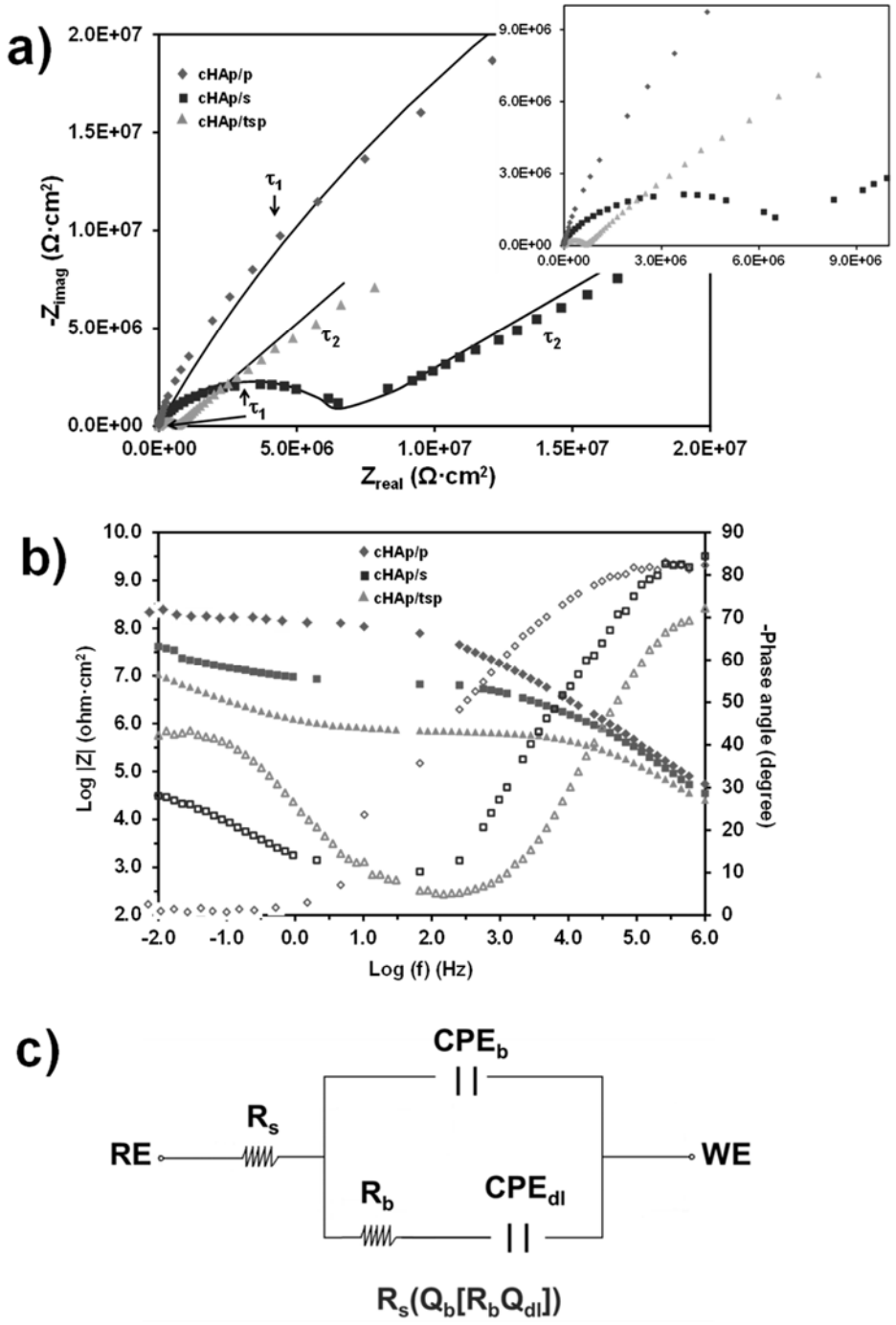

Figure Ann.VII.7.

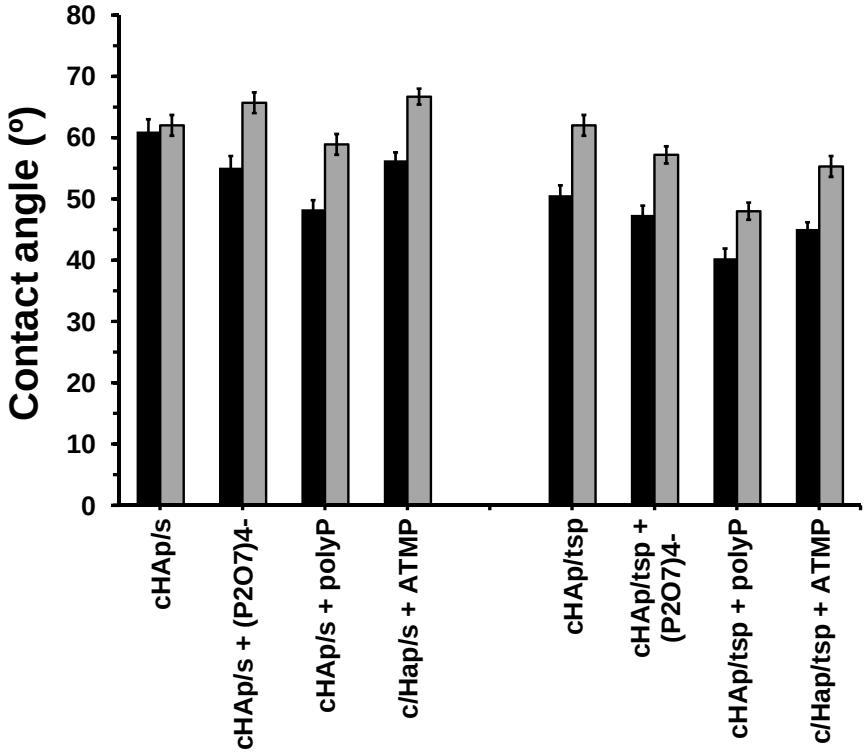

Figure Ann.VII.8.

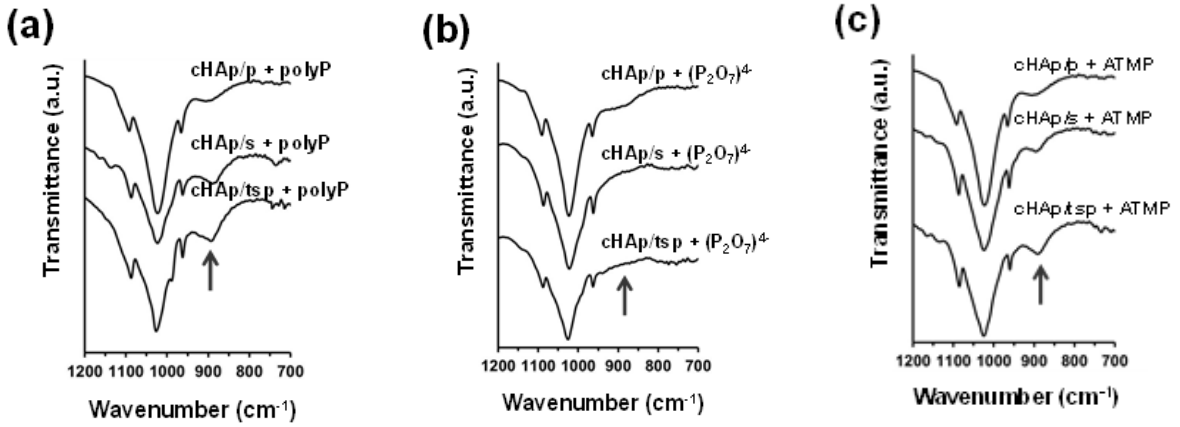

Figure Ann.VII.9.

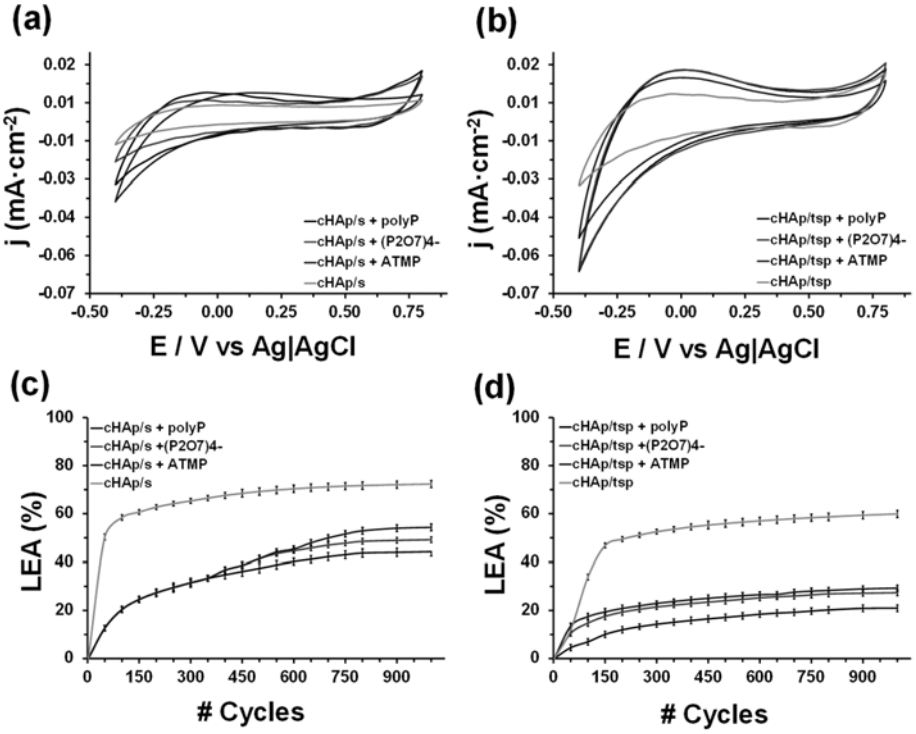

Figure Ann.VII.10.

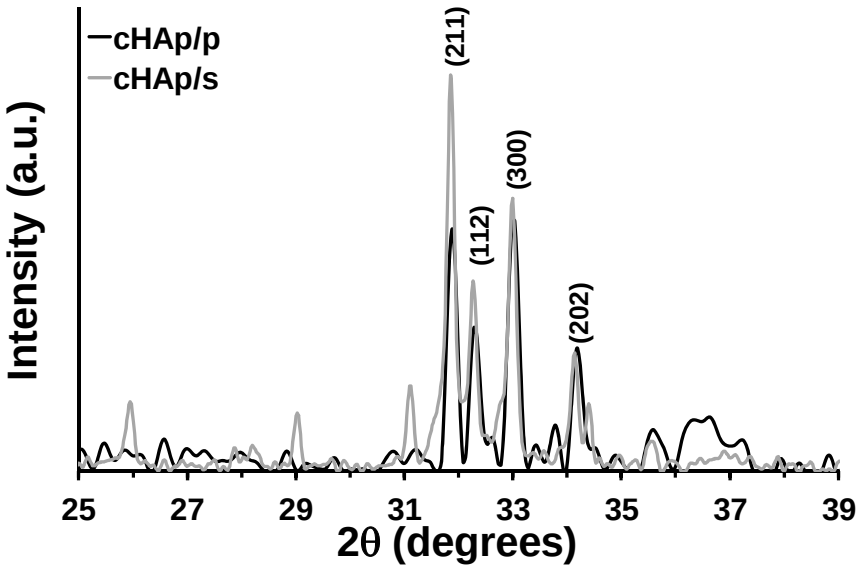

Figure Ann.VI.11.

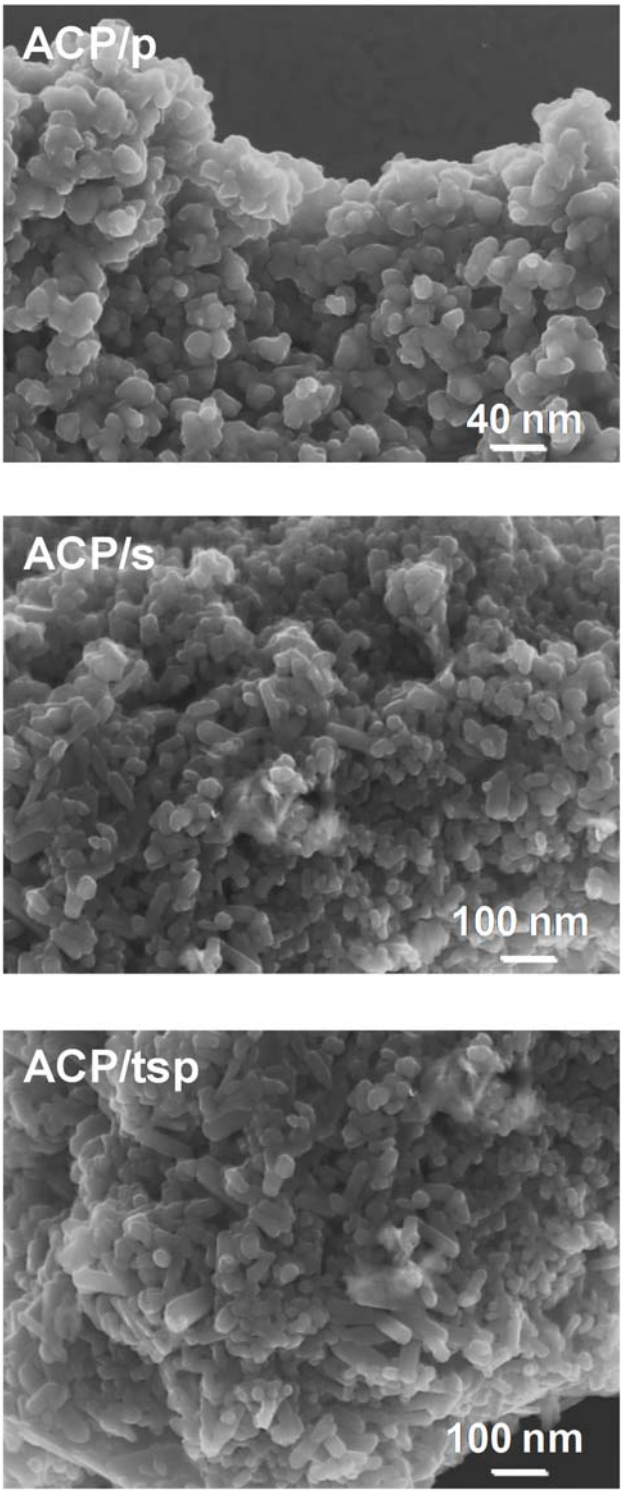

12/27

Figure Ann.VII.12.

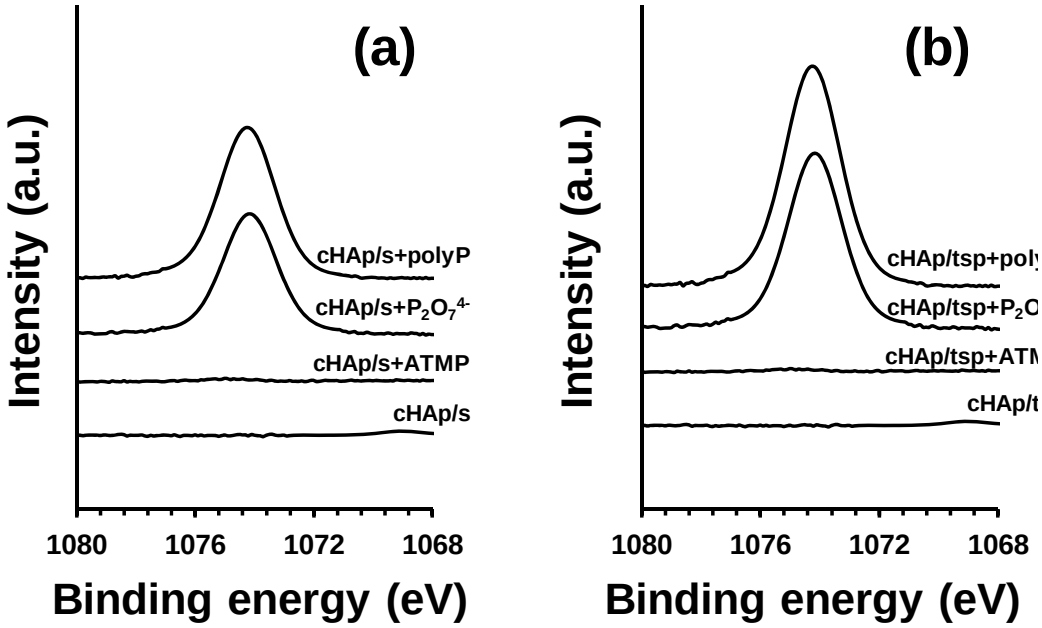

13/27

Figure Ann.VII.13.

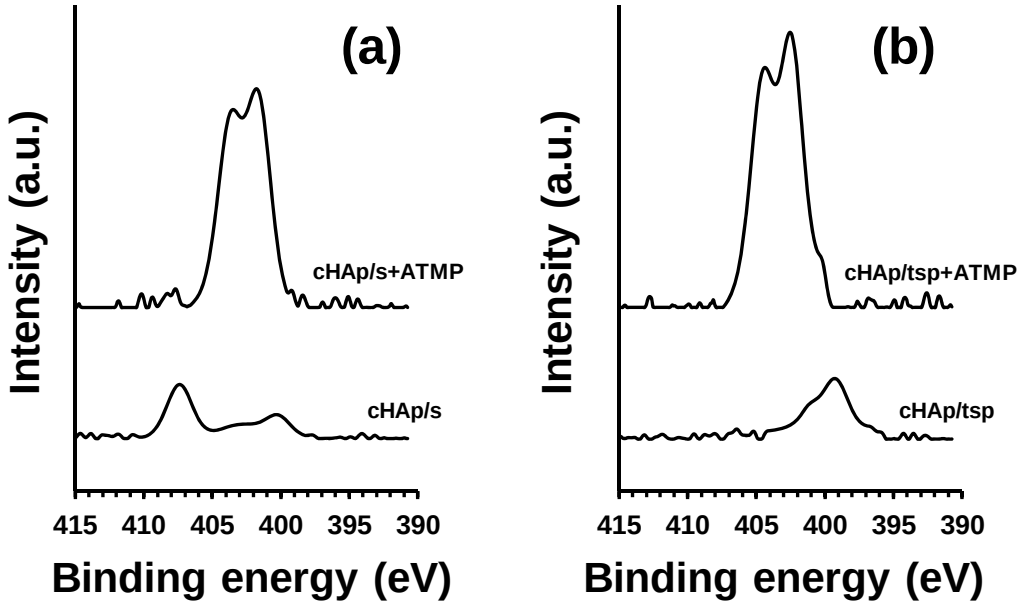

Figure Ann.VII.14.

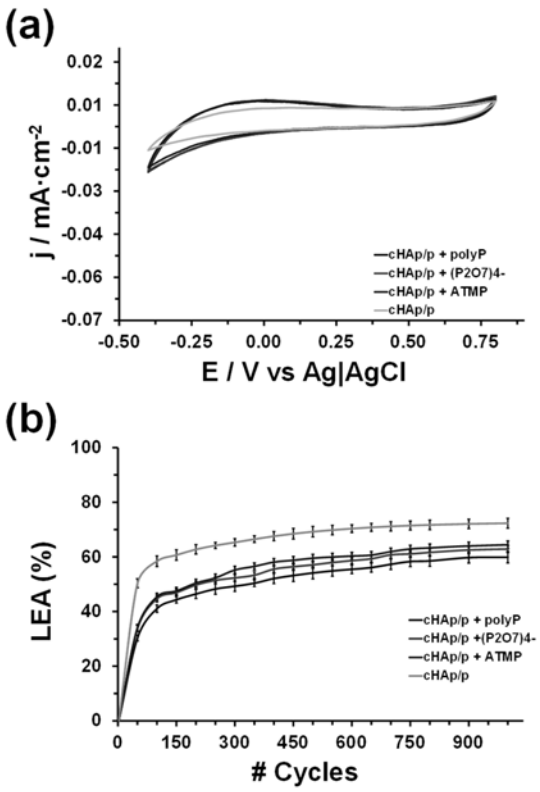

Figure Ann.VII.15.

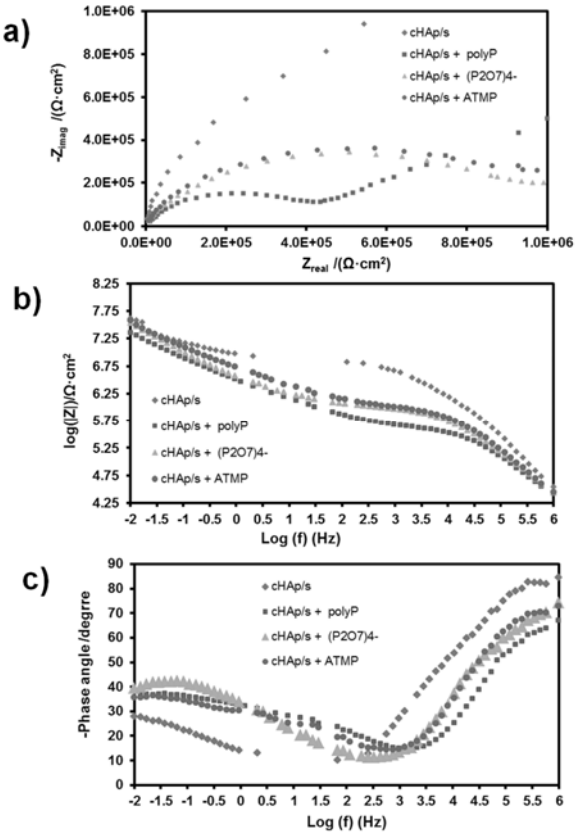

Figure Ann.VII.16.

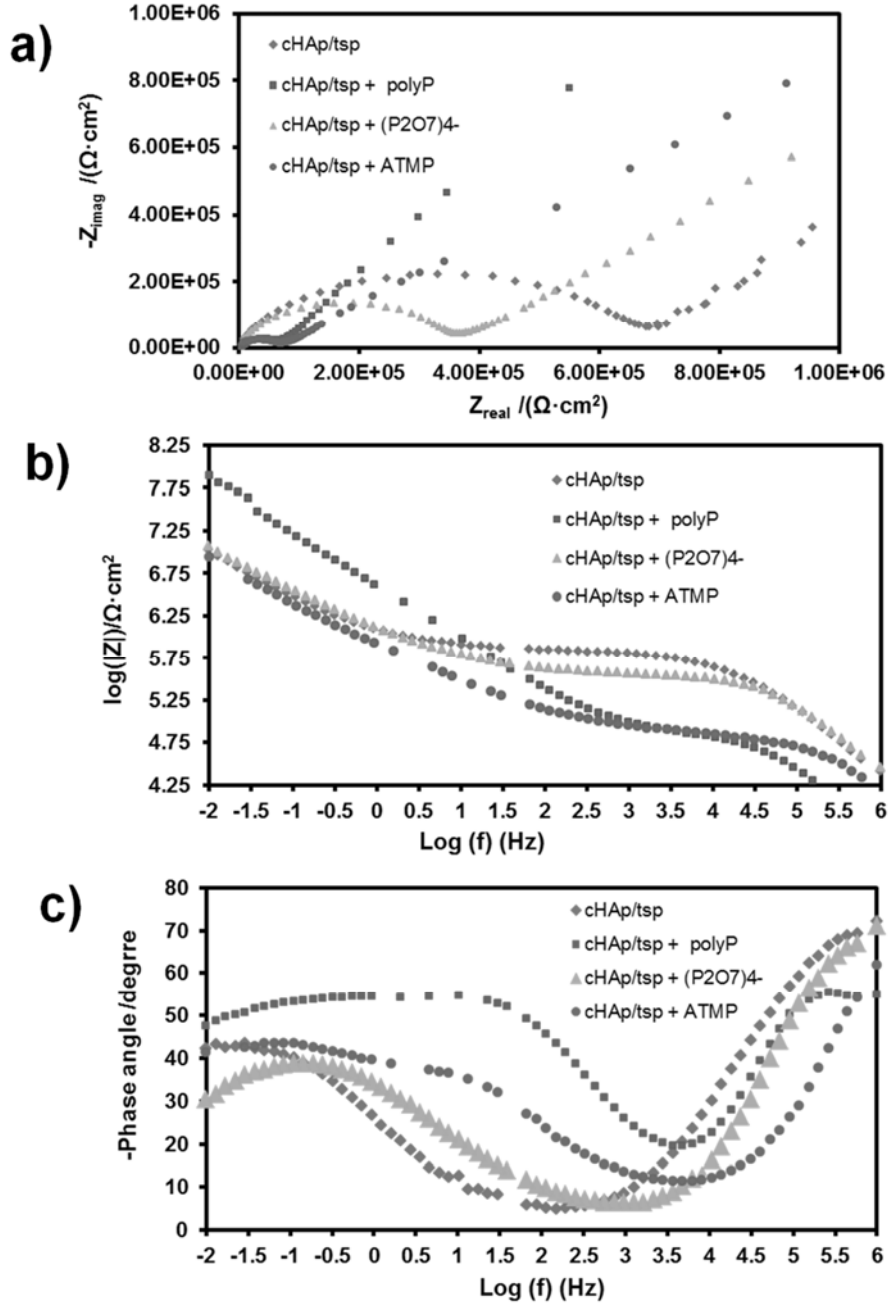

Figure Ann.VII.17.

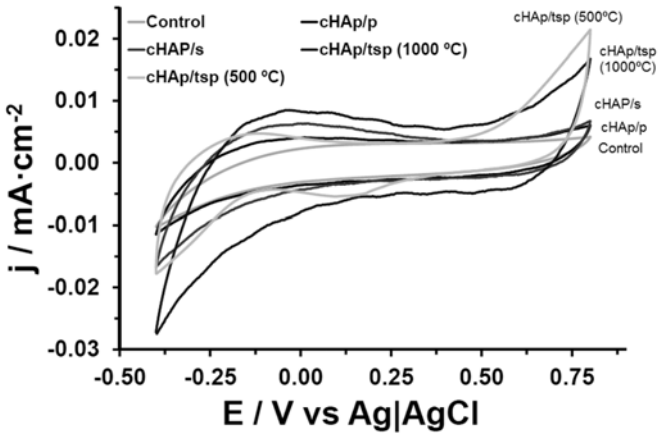

Figure Ann.VII.18.

A) B)

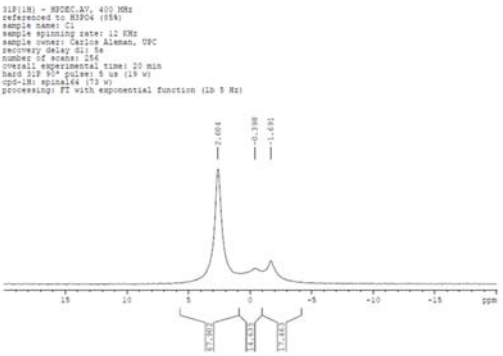

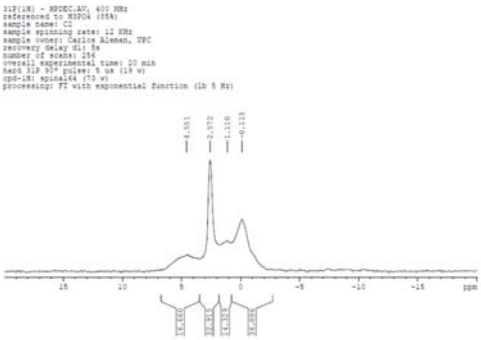

C) D)

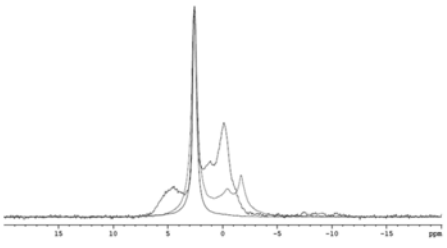

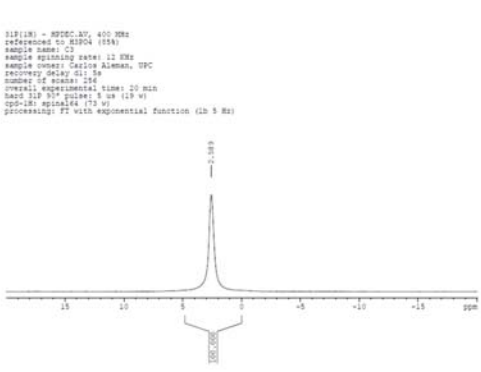

Figure Ann.VII.19.

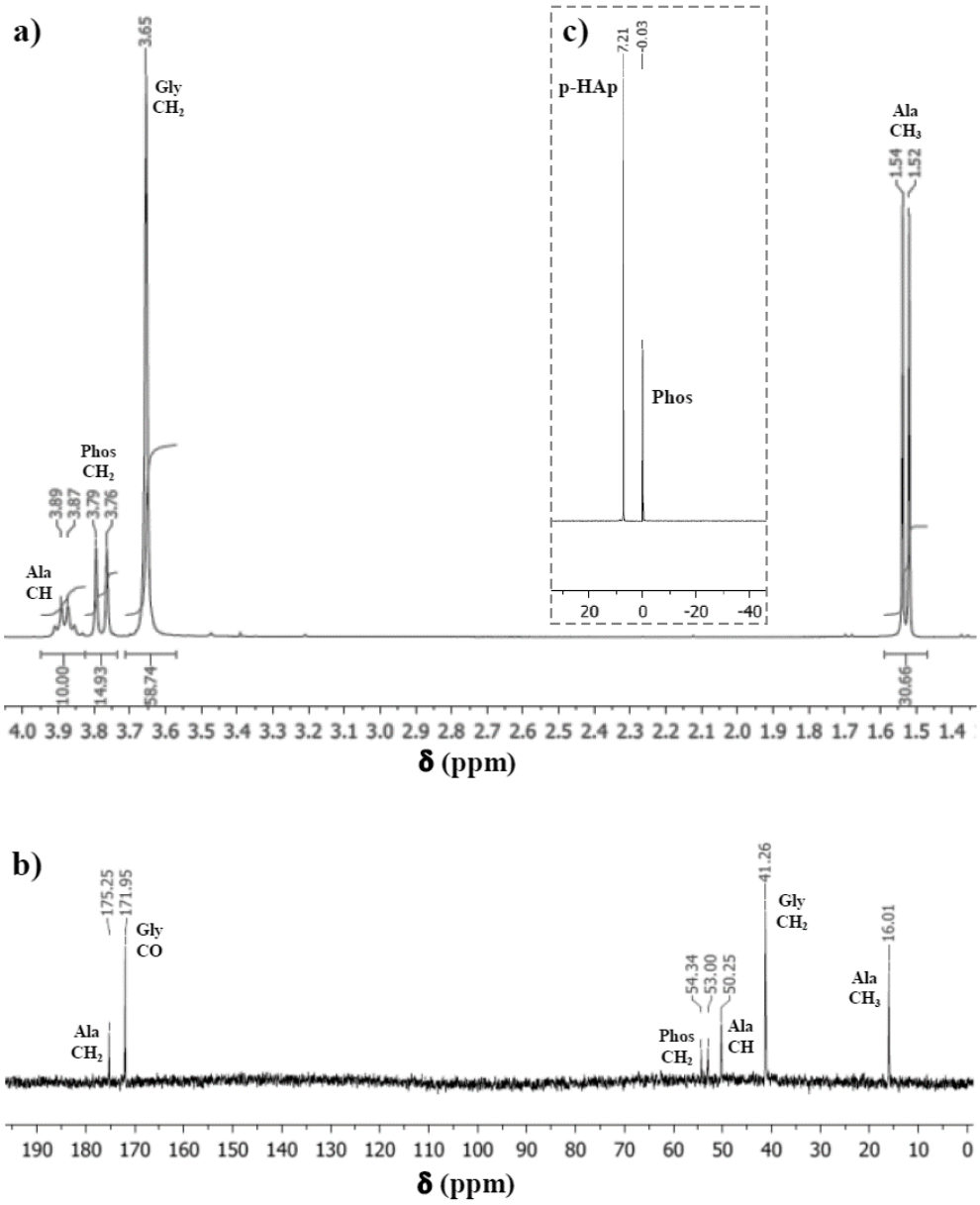

Figure Ann.VII.20.

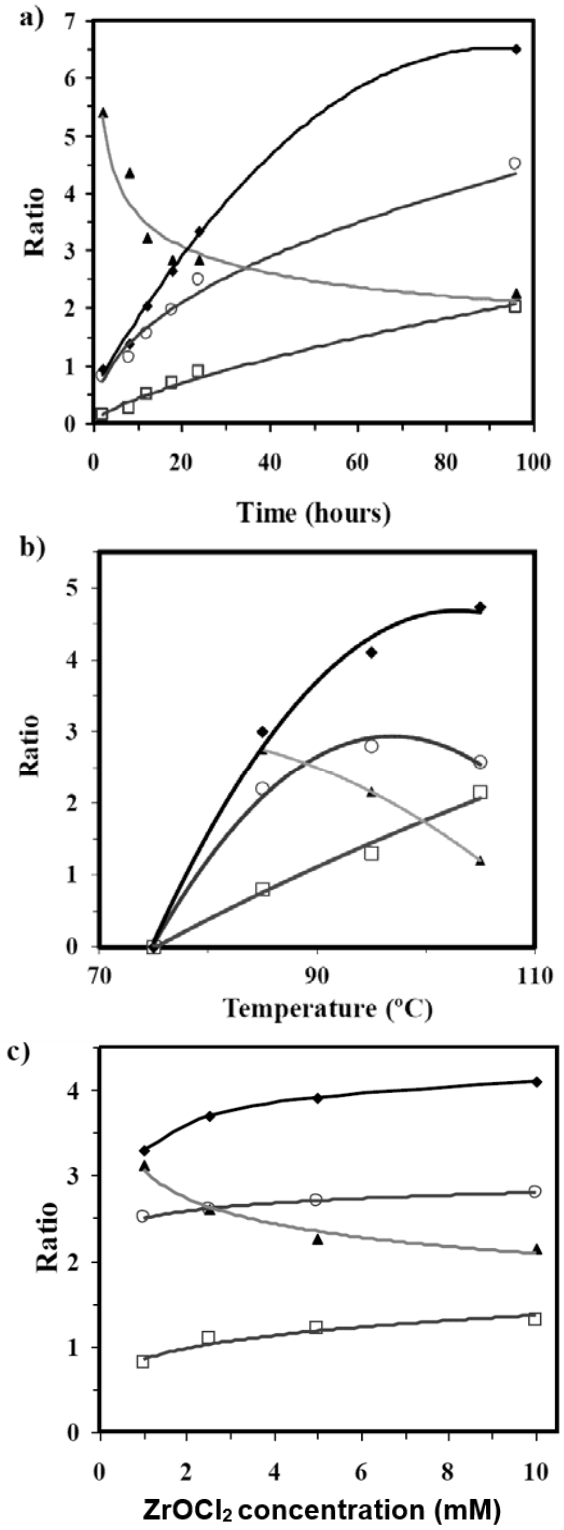

Figure Ann.VII.21.

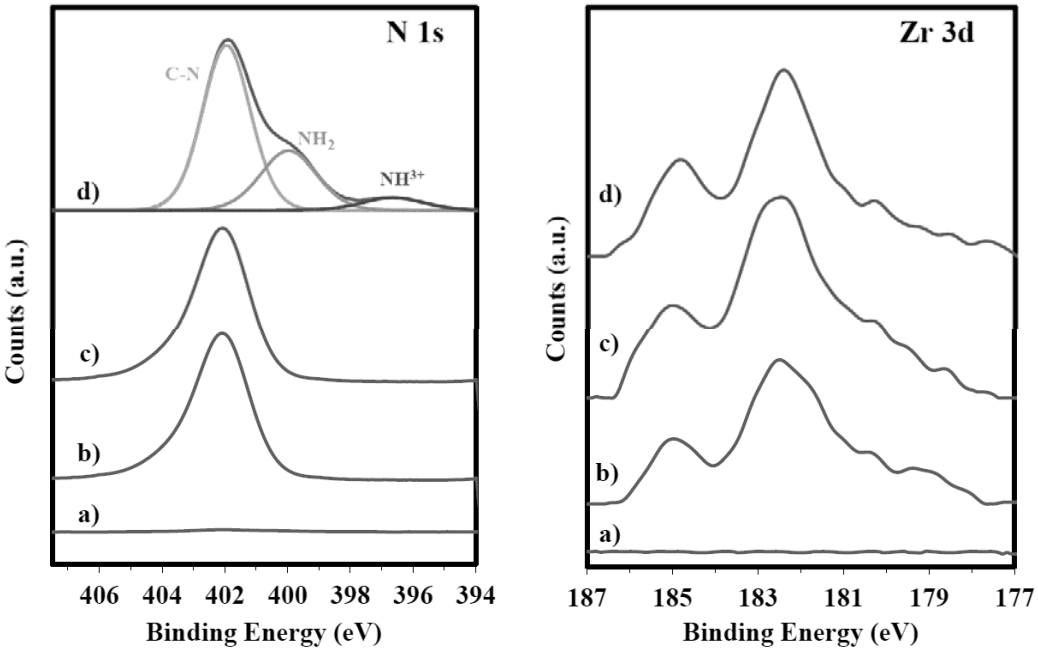

Figure Ann.VII.22.

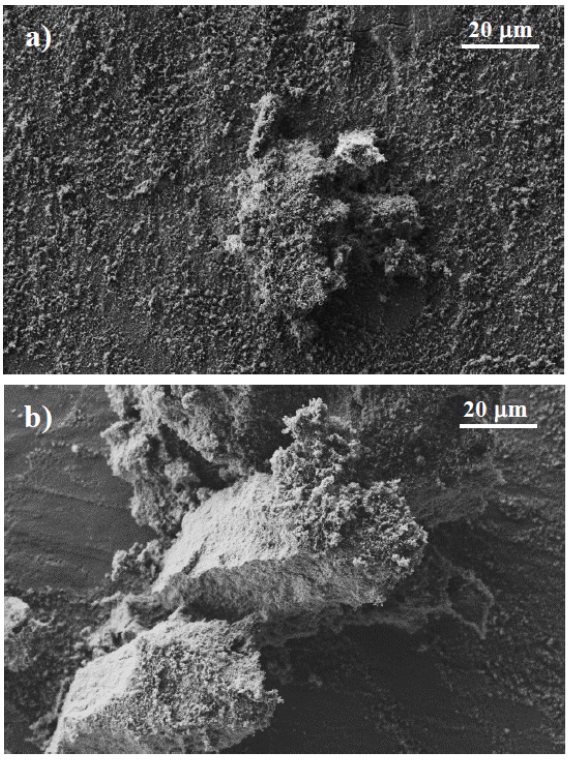

Figure Ann.VII.23.

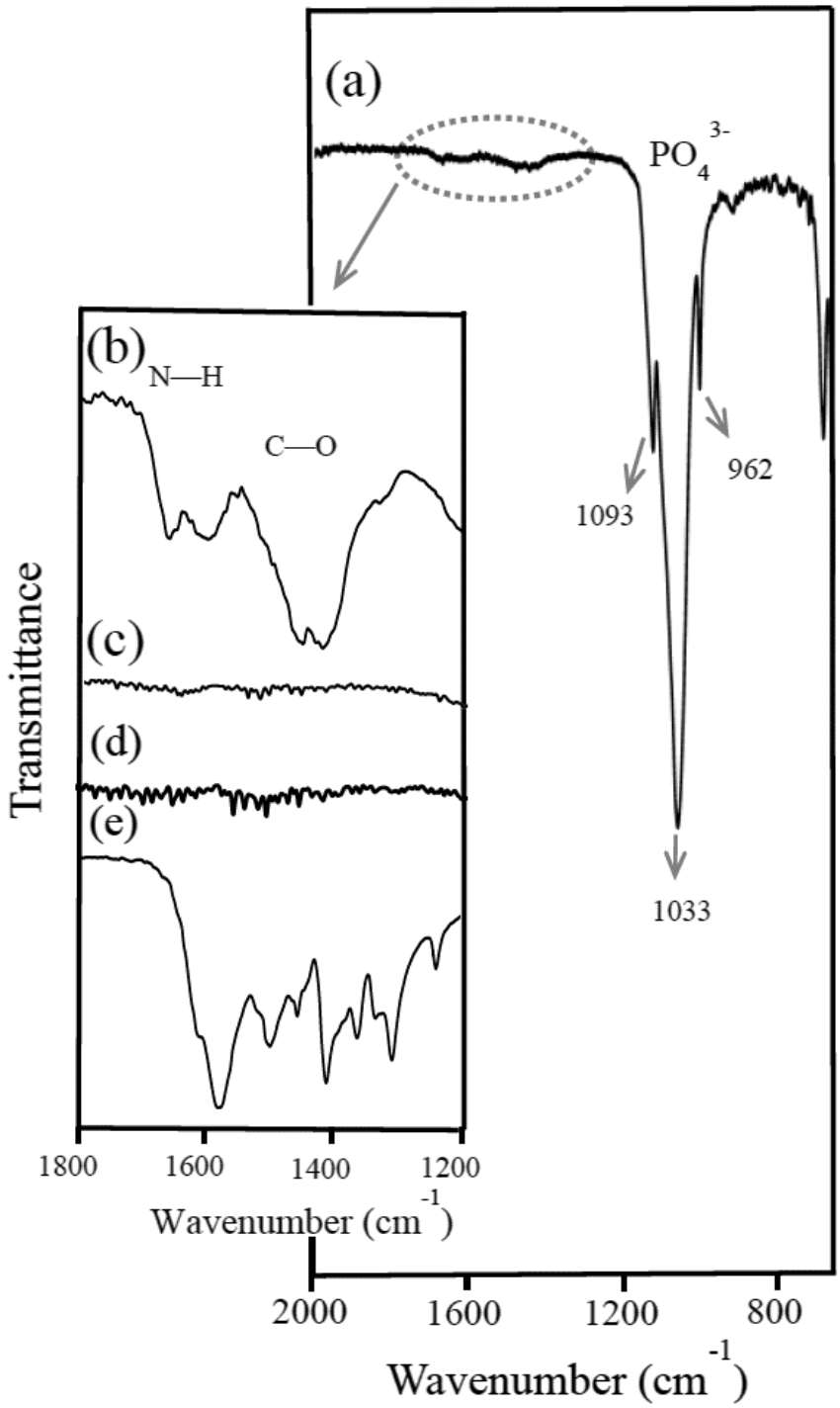

Figure Ann.VII.24.

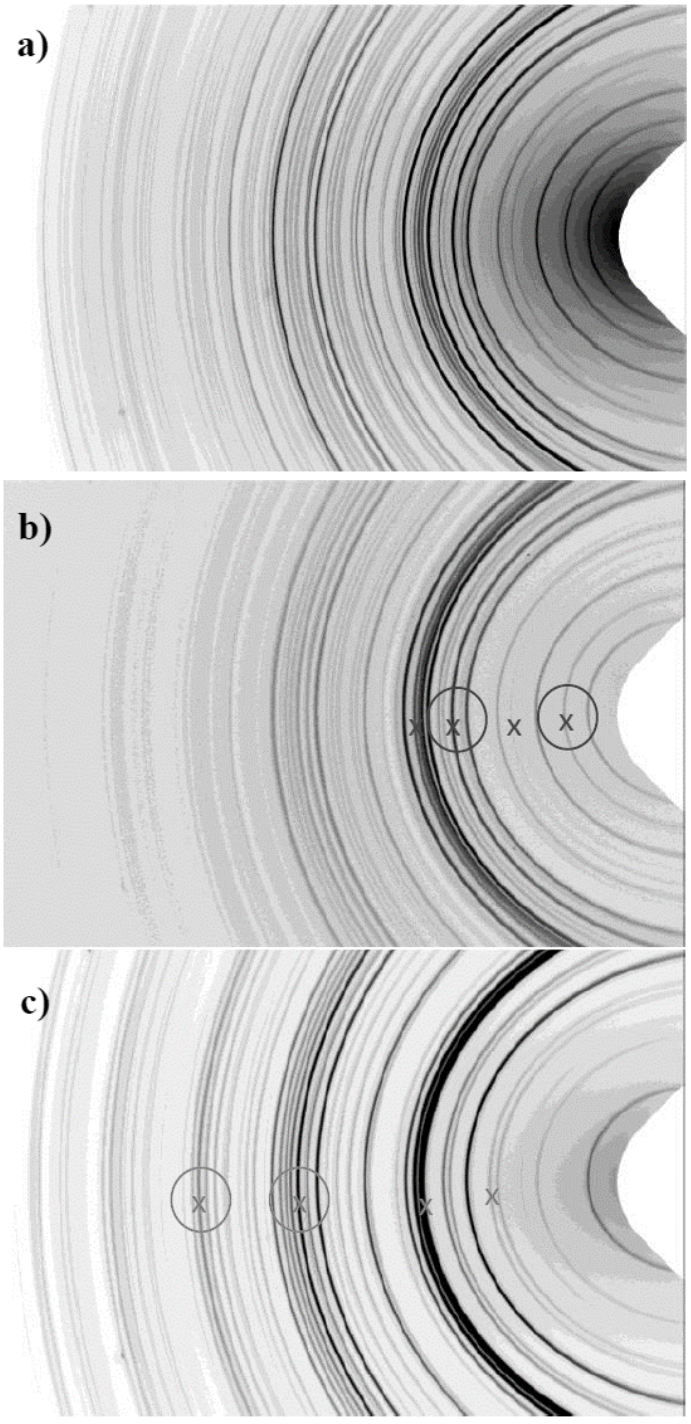

Figure Ann.VII.25.

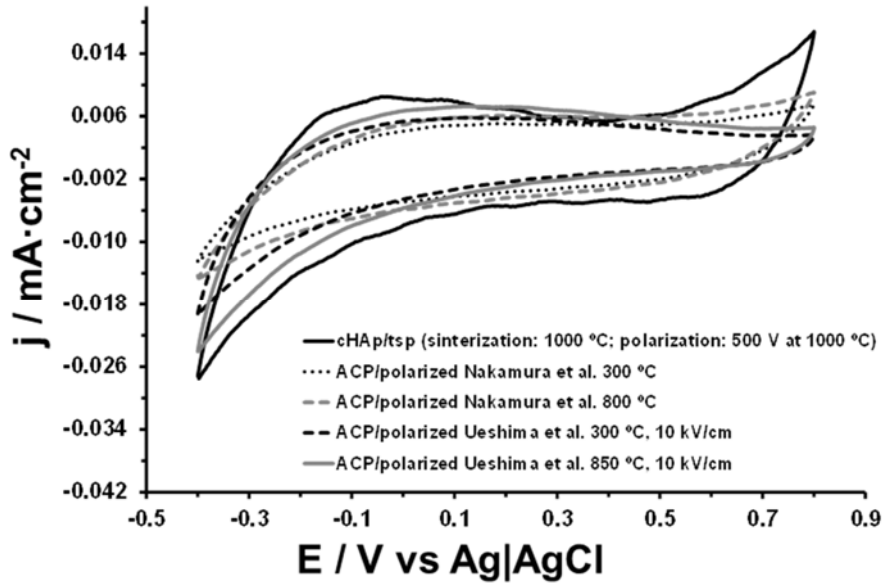

Figure Ann.VII.26.

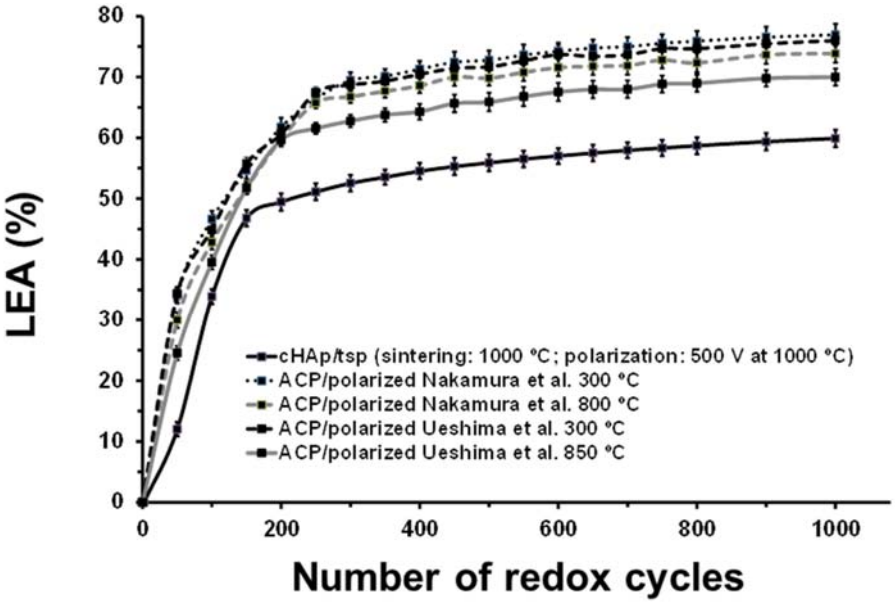

Figure Ann.VII.27.

SAMPLES AS PREPARED

System	Electrical resistance ($\Omega \cdot cm^2$)	Surface capacitance ($\mu F/g$)
cHAp/tsp	$0.67 \cdot 10^6$	386±16
Nakamura et al. 300 ºC	$0.45 \cdot 10^7$	136±14
Nakamura et al. 800 ºC	$0.37 \cdot 10^7$	173±27
Ueshima et al. (300 ºC)	$0.39 \cdot 10^7$	153±15
Ueshima et al. (850ºC)	$0.29 \cdot 10^7$	249±9

Figure Ann.VII.28.

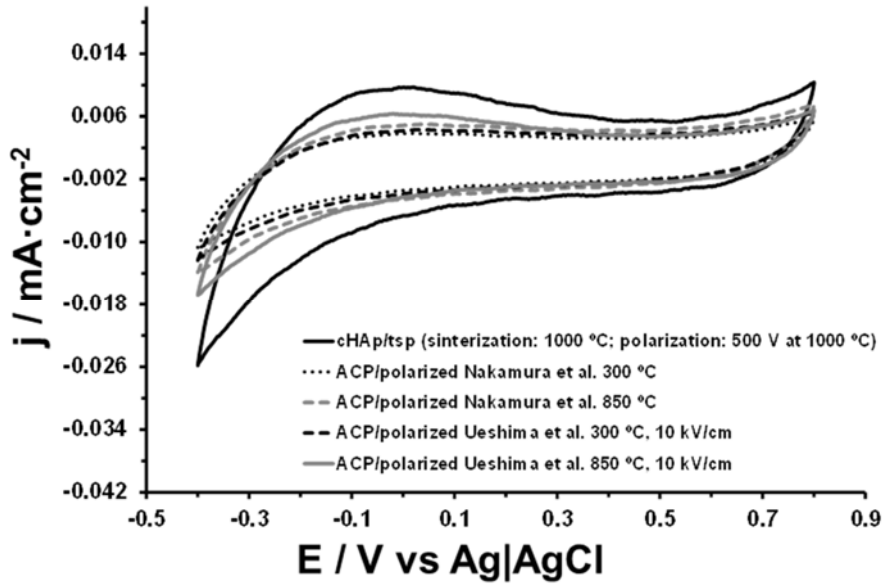

Figure Ann.VII.29.

RE-EVALUATION OF THE SAME SAMPLES AFTER 3 MONTHS

System	Electrical resistance ($\Omega \cdot cm^2$)	Surface capacitance ($\mu F/g$)
cHAp/tsp	$0.73 \cdot 10^6$	356±7
Nakamura et al. 300 °C	$0.76 \cdot 10^7$	49±9
Nakamura et al. 800 °C	$0.59 \cdot 10^7$	71±12
Ueshima et al. (300 °C)	$0.63 \cdot 10^7$	58±9
Ueshima et al. (850°C)	$0.47 \cdot 10^7$	94±12

VII. 10. References

1. Dorozhkin, S.V., Epple, M. Biological and medical significance of calcium phosphates, *Angewandte Chemie International Edition* (**2002**), *41*, 3130–3146. DOI:10.1002/1521-3773(20020902)41:17<3130::AID-ANIE3130>3.0.CO;2-1.

2. Palmer L.C., Newcomb C.J., Kaltz S.R., Spoerke E.D., Stupp S.I., Biomimetic systems for hydroxyapatite mineralization inspired by bone and enamel, *Chemical Review*s (**2008**), *108*, 4754–4783. DOI:10.1021/cr8004422.

3. Ma M.Y., Zhu Y.J., Li L., Cao S.W., Nanostructured porous hollow ellipsoidal capsules of hydroxyapatite and calcium silicate: preparation and application in drug delivery, *Journal of Material Chemistry* (**2008**), *18*, 2722–2727. DOI:10.1039/B800389K.

4. K. W. Wang, L. Z. Zhou, Y. Sun, G. J. Wu, H. C. Gu, Y. R. Duan, F. Chen, Y. J. Zhu, Calcium phosphate/PLGA-mPEG hybrid porous nanospheres: A promising vector with ultrahigh gene loading and transfection efficiency, *Journal Materials Chemistry* (**2010**), *20*, 1161–1166. DOI: 10.1039/B917441A.

5. Tang Q.L., Zhu Y.J., Wu J., Chen F., Cao S.W., Calcium phosphate drug nanocarriers with ultrahigh and adjustable drug-loading capacity: One-step synthesis, In Situ drug loading and prolonged drug release, *Nanomedicine: Nanotechnology, Biology and Medicine* (**2011**), *7*, 428–434 DOI:10.1016/j.nano.2010.12.005.

6. Kim H-W., Knowles J.C., Kim H-E., Hydroxyapatite/poly (ε-caprolactone) composite coatings on hydroxyapatite porous bone scaffold for drug delivery, *Biomaterials* (**2004**), *25*, 1279–1287. DOI:10.1016/j.biomaterials.2003.07.003.

7. Suchanek W., Yoshimura M., Processing and properties of hydroxyapatite-based biomaterials for use as hard tissue replacement implants, *Journal Materials Research* (**1998**), *13*, 94–117. DOI: 10.1557/JMR.1998.0015.

8. Zhou H., Lee J., Nanoscale hydroxyapatite particles for bone tissue engineering, *Acta Biomaterialia* (**2011**), *7*, 2769–2781. DOI: 10.1016/j.actbio.2011.03.019.

9. Elliott J.C., Mackie P.E., Young R.A., Monoclinic hydroxyapatite, *Science* (**1973**), *180*, 1055–1057. DOI:10.1126/science.180.4090.1055.

10. Ma G., Liu X.Y., Hydroxyapatite: hexagonal or monoclinic?, *Crystal Growth & Design* (**2009**), *9*, 2991–2994. DOI:10.1021/cg900156w

11. Hitmi N., LaCabanne C., Young R.A., OH− reorientability in hydroxyapatites: effect of F^- and Cl^-, *Journal of Physics and Chemistry of Solids* (**1988**), *49*, 541–550. DOI:10.1016/0022-3697(88)90065-0.

12. Ikoma t., A. Yamazaki, S. Nakamura, M. Akao, Preparation and dielectric property of sintered monoclinic hydroxyapatite, *Journal of Materials Science Letters* (**1999**), *18*, 1225–1228. DOI:10.1023/A:1006610521173.

13. Kalogeras I.M. , Vassilikou-Dova A., Katerinopoulou A., Axially dependent dielectric relaxation response of natural hydroxyapatite single crystals, *Journal of Applied Physics* (**2002**), *92*, 406. DOI:10.1063/1.1481776.

14. Horiuchi N., Nakamura M., Nagai A., Katayama K., Yamashita K., Proton conduction related electrical dipole and space charge polarization in hydroxyapatite, *Journal of Applied Physics* (**2012**), *112*, 074901. DOI:10.1063/1.4754298.

15. Horiuchi N., Nakaguki S., Wada N., Nakamura M., Nagai A., Katayama K., Yamashita K., Polarization-induced surface charges in hydroxyapatite ceramics, *Journal of Applied Physics* (**2014**), *116*, 014902, 1-8. DOI:10.1063/1.4886235.

16. Nakamura M., Hori N., Namba S., Toyama T., Nishimiya N., Yamashita K., Wettability and surface free energy of polarised ceramic biomaterials, *Biomedical Material* (**2015**), *10*, 011001. DOI:10.1088/1748-6041/10/1/011001.

17. Nakamura M., Nagai A., Hentunen T., Salonen J., Sekilima Y., Okura T., Hashimoto K., Toda Y., Monma H., Yamashita K., Surface Electric Fields Increase Osteoblast Adhesion through Improved Wettability on Hydroxyapatite Electret, *ACS Applied Materials and Interfaces* (**2009**), *1*, 2181–2189. DOI:10.1021/am900341v.

18. Rivas M., Casanovas J., del Valle L.J., Bertran O., Revilla-López G., Turon P., Puiggalí J., Alemán C., An experimental-computer modeling study of inorganic phosphates surface adsorption on hydroxyapatite particles, *Dalton Transactions* (**2015**), *44*, 9980 – 9981. DOI:10.1039/C5DT00209E.

19. Kumble K.D., Kornberg A., Inorganic polyphosphate in mammalian cells and tissues, *Journal of Biological Chemistry* (**1996**), *270*, 5818–5822. DOI:10.1074/jbc.270.11.5818.

20. Doi K., Kubi T., Takeshita R., Kajihara S., Kato S., Kawazoe Y., Shiba T., Akagawa Y., Inorganic polyphosphate adsorbed onto hydroxyapatite for guided bone regeneration: an animal study, *Dental Materials Journal* (2014), **33**, 179–186. DOI: 10.4012/dmj.2013-275.

21. Comeau P.A., Frei H., Yang C., Fernlund G., Rossi F.M., In vivo evaluation of calcium polyphosphate for bone regeneration, *Journal of Biomaterials Applications* (**2012**), *27*, 267–275.
DOI:10.1177/0885328211401933.

22. Siggers K., Frei H., Fernlund G., Rossi F.M., Effect of bone graft substitute on marrow stromal cell proliferation and differentiation, *Journal of Biomedical Materials Research Part A* (**2010**), *94*, 877–885.
DOI: 10.1002/jbm.a.32766.

23. Morita K., Doi K., Kubo T., Takeshita R., Kato S., Akagawa Y., Enhanced initial bone regeneration with inorganic polyphosphate-adsorbed hydroxyapatite, *Acta Biomaterialia* (**2010**), *6,* 2808–2815.
DOI:10.1016/j.actbio.2009.12.055.

24. Yuan Q., Kubo T., Doi K., Morita K., Takeshita R., Kato S., Shiba T., Akagawa Y., Effect of combined application of bFGF and inorganic polyphosphate on bioactivities of osteoblasts and initial bone regeneration, *Acta Biomaterialia* (**2009**), *5*, 1716–1724.
DOI:10.1016/j.actbio.2009.01.034.

25. Shiba T., Nishimura D., Kawazoe Y., Onodera Y., Tsutsumi K., Nakamura R., Ohshiro M., Modulation of mitogenic activity of fibroblast growth factors by inorganic polyphosphate, *Journal of Biologial Chemistry* (**2003**), *278*, 26788–26792.
DOI:10.1074/jbc.M303468200.

26. Kawazoe Y., Shiba T., Nakamura R., Mizuno A., Tsutsumi K., Uematsu T., Yamaoka M., Shindoh M. Kohgo T., Induction of calcification in MC3T3-E1 cells by inorganic polyphosphate*Journal of Dental Research* (**2004**), ***83***, 613–618.
DOI: 10.1177/154405910408300806.

27. Hacchou Y., Uematsu T., Ueda O., Usui Y., Uematsu S., Takahashi M., Kawazoe Y., Shiba T., Kurihara S., Yamaoka M., Furusawa K., *Journal of Dental Research* (**2007**), *86*, 893–897.
DOI:10.1177/154405910708600917.

28. Fleisch H., Bisaz S., Mechanism of calcification: inhibitory role of pyrophosphatem Nature (**1962**), *195*, 911–911.
DOI: 10.1038/195911a0.

29. Fleish H., Russel R., Straumann F, Effect of pyrophosphate on hydroxyapatite and its implications in calcium homeostasis, Nature (**1966**), *212*, 901–903.
DOI: 10.1038/212901a0.

30. Omelon S., Georgiou J., Henneman Z.J., Wise L.M., Sukhu B., Hunt T, Wynnyckyj, C., Holmyard D., Bielecki R., Grynpas R.D., Control of vertebrate skeletal mineralization by polyphosphates, *PLoS ONE* (**2009**), *4*, e5634.
DOI: 10.1371/journal.pone.0005634.

31. Kamat S.S., Raushel F.M., The enzymatic conversion of phosphonates to phosphate by bacteria, *Current Opinion of Chemical Biology* (**2013**), *17*, 589–596. DOI:10.1016/j.cbpa.2013.06.006.

32. Ebetino F.H.,Russell R.G.G., *Journal of Bone Mineralization Research* (2005), **20**, 259.

33. Russell R.G.G., Ebetino F.H., Mechanisms of action of bisphosphonates: similarities and differences and their potential influence on clinical efficacy, *Osteoporosis International.* (**2008**), *19*, 733–759. DOI:10.1007/s00198-007-0540-8.

34. Gronich N., Rennet G., Nature Reviews. Beyond aspirin-cancer prevention with statins, metformin and bisphosphonates, *Nature Reviews Clinical Oncology* (**2013**), *10*, 625–642. DOI: 10.1038/nrclinonc.2013.169.

35. Valle L.J., Bertrán O., Chaves G, Revilla-López G., Rivas M., Teresa Casas M., Casanovas J., Turon P., Puiggalí J., Alemán C., DNA adsorbed on hydroxyapatite surfaces *Journal of Materials Chemistry B* (**2014**), *2*, 6953-6966. DOI: 10.1039/C4TB01184H.

36. Klug H.P., Alexander L.E., In X-Ray diffraction procedures: for polycrystalline and amorphous materials. 2nd. Edition, John Wiley and Sons, New York, (**1974**).

37. Landi E., Tampieri A., Celotti G., Sprio S., Densification behavior and mechanisms of synthetic hydroxyapatites, *Journal of the European Ceramics Society* (**2000**), *20*, 2377–2387. DOI:10.1016/S0955-2219(00)00154-0.

38. Estrany F., Aradilla D., Oliver R., Alemán C., Densification behaviour and mechanisms of synthetic hydroxyapatites, *European Polymer Journal* (**2007**), *43*, 1876. DOI:10.1016/S0955-2219(00)00154-0.

39. Müller F., Ferreira C.A., Azambuja D.S., Alemán C., Armelin E., Measuring the proton conductivity of ion-exchange membranes using electrochemical impedance spectroscopy and through-plane cell, *Journal Physical Chemistry B* (**2014**), *118*, 1102-1112. DOI:10.1021/jp409675z.

40. Raynaud S., Champion E., Bernache-Assollant, Thomas P., Calcium phosphate apatites with variable Ca/P atomic ratio I: synthesis, characterization and thermal stability of powders. *Biomaterials* (**2002**), *23*, 1065-1072. DOI:10.1016/S0142-9612(01)00218-6.

41. Fujimori H., Toya H., Ioku K., Goto S., Yoshimura M., In situ observation of defects in hydroxyapatite up to 1200° C by ultraviolet Raman spectroscopy, *Chemical Physics Letters* (**2000**), *325*, 383–388. DOI:10.1016/S0009-2614(00)00695-3.

42. Elliott J.C., Mackie P.E., Young R.A., Monoclinic hydroxyapatite, *Science* (**1973**), *180*, 1055–1057.
DOI:10.1126/science.180.4090.1055.

43. Hitmi N., LaCabanne C., Young R.A., OH− reorientability in hydroxyapatites: effect of F^- and Cl^-, *Journal of Physics and Chemistry of Solids* (**1988**), *49*, 541–550.
DOI:10.1016/0022-3697(88)90065-0.

44. Ma G., Liu X.Y., Hydroxyapatite: hexagonal or monoclinic?, *Crystal Growth & Design* (**2009**), *9*, 2991–2994.
DOI:10.1021/cg900156w.

45. *Handbook of X-ray Photoelectron Spectroscopy* (Eds.: J. F. Moulder, J. Chastain), Physical Electronics Division, PerkinElmer Corporation, (**1995**).

46. Chang M.C., Tanaka J., XPS study for the microstructure development of hydroxyapatite–collagen nanocomposites cross-linked using glutaraldehyde, *Biomaterials* (**2002**), *23*, 3879–3885.
DOI:10.1016/S0142-9612(02)00133-3.

47 Bertran O., del Valle L.J., Revilla-López G., Rivas M., Chaves G., Casas M.T., Casanovas J., Turon P., Puiggalí J. Alemán C., Synergistic approach to elucidate the incorporation of magnesium ions into hydroxyapatite*, Chemistry – A European Journal* (**2015**), *21*, 2537–2546.
DOI:10.1002/chem.201405428.

48. Ming-Hung I., Shih W-J., Hon M-H., Wang M-C., Ming-Hung I., Shih W-J., Hon M-H., Wang M-C., The Properties of Sintered Calcium Phosphate with [Ca]/[P] = 1.50 *International Journal of Molecular Science* (**2012)**, *13*, 13569-13586.
DOI:10.3390/ijms131013569.

49. Gittings J.P., Bowen C.R., Dent A.C.E., Turner I.G., Baxter F.R., Chaudhuri J.B., Electrical characterization of hydroxyapatite-based bioceramics, *Acta Biomaterialia* (**2009**), *5*, 743–754.
DOI:10.1016/j.actbio.2008.08.012.

50. Lukic M.J., Jovalekic C., Markovic S., Uskolovic D., Enhanced high-temperature electrical response of hydroxyapatite upon grain size refinement, *Materials Research Bulletin*, (**2014**), *61*, 534–538.
DOI:10.1016/j.materresbull.2014.10.072.

51. Liu Y., Shen Z., Dehydroxylation of hydroxyapatite in dense bulk ceramics sintered by spark plasma sintering, Journal of the European Ceramic Society (**2012**), *32*, 11, 2691-2696.
DOI: 10.1016/j.jeurceramsoc.2012.02.025.

52. Tarafder S., Banerjee S., Bandyopadhyay A., Bose S., Electrically polarized biphasic calcium phosphates: adsorption and release of bovine serum albumin, Langmuir (**2010**), *26*, 16625–16629.
DOI: 10.1021/la101851f.

53. Gaskell K.J., Asunkis A.L., Sherwood P.M.A.. Sodium Pyrophosphate Decahydrate ($Na_4P_2O_7 \cdot 10H_2O$) by XPS. *Surface Science Spectra* (**2004**), *9*, 135-142.
DOI: 10.1116/11.20030111.

54. Gaskell K.J., Asunkis A.L., Sherwood P.M.A., *Sodium Tripolyphosphate ($Na_5P_3O_{10}$) by XPS*. Surface Science Spectra (2004), 9, 166-173.
DOI: 10.1116/11.20030113.

55. Dalmoro V., dos Santos J.H.Z., Armelin E., Alemán C., Azambuja D., A synergistic combination of tetraethylorthosilicate and multiphosphonic acid offers excellent corrosion protection to AA1100 aluminum alloy, Applied Surface Science (**2013**), *273*, 758–768.
DOI: 10.1016/j.apsusc.2013.02.131.

56. Jarlbring M., Sandström D.E., Antzutkin O.N., Forsling W., Characterization of Active Phosphorus Surface Sites at Synthetic Carbonate-Free Fluorapatite Using Single-Pulse ^{1}H, ^{31}P, and ^{31}P CP MAS NMR, *Langmuir* (**2006**), *22*, 4787–4792.
DOI: 10.1021/la052837j.

57. Wang Y., Von Euw S., Fernandes F.M., Cassaignon S., Selmane M., Laurent G., Pehau-Arnaudet G., Coelho C., Bonhomme-Coury L., Giraud-Guillaume M-M., Babinneau F., Azars T., Nassif N., Water-mediated structuring of bone apatite, *Nature Material*s (**2013**), *12*, 1144–1153.
DOI: 10.1038/nmat3787.

58. Jager C., Welzel T., Meyer-Zaika W., Epple M.A., A solid‐state NMR investigation of the structure of nanocrystalline hydroxyapatite, *Magnetic Resonance in Chemistry* (**2006**), *44*, 573–580.
DOI: 10.1002/mrc.1774.

59. Osman M.B., Diallo-Garcia S., Herledan V., Brouri D., Toshioka T., Kubo J., Millot Y., Costentin G., Discrimination of surface and bulk structure of crystalline hydroxyapatite nanoparticles by NMR, *Journal of Physical Chemistry C* (**2015**), *119*, 23008–23020.
DOI:10.1021/acs.jpcc.5b08732.

60. Nakamura M., Hori N., Namba S., Toyama T., Nishimiya N., Yamashita K., Wettability and surface free energy of polarised ceramic biomaterials, *Biomedical Material* (**2015**), *10*, 011001.
DOI:10.1088/1748-6041/10/1/011001.

61. Ikoma t., A. Yamazaki, S. Nakamura, M. Akao, Preparation and dielectric property of sintered monoclinic hydroxyapatite, *Journal of Materials Science Letters* (**1999**), *18*, 1225–1228.
DOI:10.1023/A:1006610521173.

62. Nakamura, M., Sekijima Y., Nakamura S., Kobayashi T., Niwa K., Yamashita K., Role of blood coagulation components as intermediators of high osteoconductivity of electrically polarized hydroxyapatite, *Journal Biomedical Materials Research* (**2006**), *79A*, 627– 634.
DOI:10.1002/jbm.a.30827.

63. Ueshima M., Nakamura S., Ohgaki M., Yamashita K., Electrovectorial effect of polarized hydroxyapatite on quasi-epitaxial growth at nano-interfaces, *Solid State Ionics* (**2002**), *151*, 29–34.
DOI:10.1016/S0167-2738(02)00600-8.